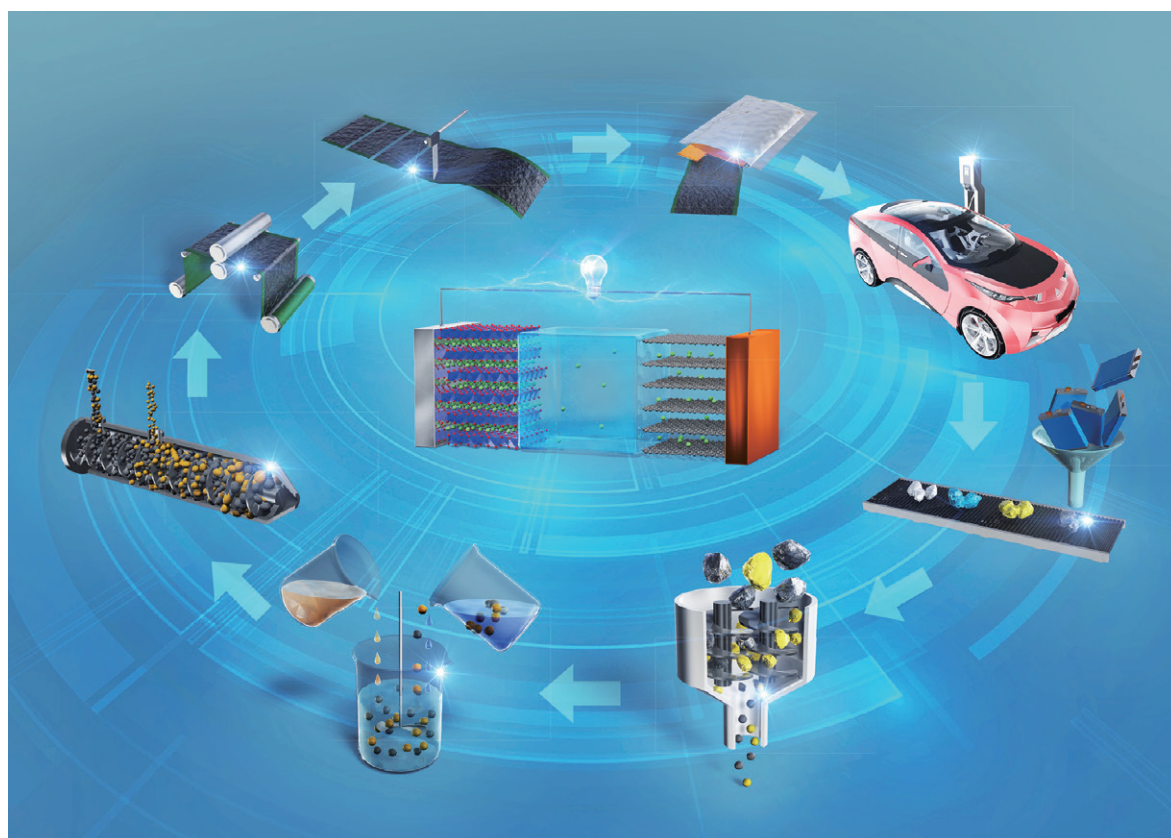


# KONA Powder and Particle Journal

No.40 (2023)



Hosokawa Powder Technology Foundation

available online-[www.kona.or.jp](http://www.kona.or.jp)

## About this Journal

KONA Powder and Particle Journal is a refereed scientific journal that publishes articles in the field of powder and particle science and technology annually since 1983. This journal is distributed free of charge to the members of scientific communities and universities and research libraries throughout the world by the Hosokawa Powder Technology Foundation ([www.kona.or.jp](http://www.kona.or.jp)) established by Mr. Masuo Hosokawa in 1991.

The Chinese character “粉” in the cover is pronounced as “KONA” in Japanese, and means "Powder", which was hand-written by Mr. Eiichi Hosokawa, the founder of the Hosokawa Micron Corporation ([www.hosokawamicon.co.jp/en/global.html](http://www.hosokawamicon.co.jp/en/global.html)).

### About the Cover

The fast increasing demand for lithium-ion and future types of lithium batteries requires the further development of an economically and, at the same time, ecologically sustainable supply and production circle. Starting with the processing of the primary raw materials and especially secondary, recycled materials, over the extraction of the valuable materials, their refinement to battery grade intermediates, the (re)synthesis of active and passive materials to the production of the cell components like electrodes and finally the battery cells and systems. Sustainability can only be achieved if the end-of-life battery systems are used as secondary material source for the production of new battery cells, through which the recycling of the materials and the re-synthesis or re-conditioning of the active materials becomes mandatory. By this milling, dispersing, classification and sorting processes get a central role within the circular processing of lithium-ion batteries and next battery generations. Review on this topic is discussed on pp. 50–73.



Headquarters of Hosokawa Micron Corporation

## Editorial Board

### Editor-in-Chief

M. Naito (Osaka Univ., *Japan*)

### Asian / Oceanian Editorial Board

X.S. Cai (Univ. of Shanghai for Sci. & Tech., *China*)  
 T. Charinpanitkul (Chulalongkorn Univ., *Thailand*)  
 Y.F. Chen (Chinese Academy of Sciences, *China*)  
 H. Choi (Changwon National Univ., *Korea*)  
 S. Das (Indian Institute of Technology, *India*)  
 M. Fuji (Nagoya Institute of Technology, *Japan*)  
 E. Iritani (Nagoya Univ., *Japan*)  
 H. Kage (Kyushu Institute of Technology, *Japan*)  
 A. Kawasaki (Tohoku Univ., *Japan*)  
 D.J. Lee (National Taiwan Univ., *Taiwan*)  
 J.H. Li (Chinese Academy of Sciences, *China*)  
 H. Makino (CRIEPI, *Japan*)  
 S. Matsusaka (Kyoto Univ., *Japan*)  
 K. Okuyama (Hiroshima Univ., *Japan*)  
 Y. Otani (Kanazawa Univ., *Japan*)  
 Y. Sakka (NIMS, *Japan*)  
 Y.-S. Shen (Univ. of New South Wales, *Australia*)  
 Y. Shirakawa (Doshisha Univ., *Japan*)  
 H. Takeuchi (Gifu Pharmaceutical Univ., *Japan*)  
 W. Tanthapanichakoon (The Royal Society of Thailand, *Thailand*)  
 C.H. Wang (National Univ. of Singapore, *Singapore*)  
 S. Watano (Osaka Metropolitan Univ., *Japan*)

### Secretariat

T. Yokoyama (Hosokawa Powder Tech. Foundation, *Japan*)  
 L. Cui (Hosokawa Micron Corp., *Japan*)

### European / African Editorial Board

#### Chairman

G.M.H. Meesters (Delft Univ. of Technology, *Netherlands*)  
 G. Biskos (The Cyprus Institute, *Cyprus*)  
 F. Bourgeois (Univ. of Toulouse, *France*)  
 M.-O. Coppens (Univ. College London, *UK*)  
 A. Kwade (TU Braunschweig, *Germany*)  
 A. Mainza (Univ. of Cape Town, *South Africa*)  
 M.G. Rasteiro (Univ. of Coimbra, *Portugal*)  
 J.M. Valverde (Univ. of Seville, *Spain*)

#### Secretariat

S. Sander (KONA Europe e.V., *Germany*)  
 S. Wilk (KONA Europe e.V., *Germany*)

### American Editorial Board

#### Chairman

B.M. Moudgil (Univ. of Florida., *USA*)  
 A.J. Hickey (Univ. of North Carolina, *USA*)  
 A. Misra (Univ. of Kansas, *USA*)  
 A.D. Rosato (New Jersey Institute of Technology, *USA*)  
 L.M. Tavares (UFRJ, *Brazil*)  
 W.-N. Wang (Virginia Commonwealth Univ., *USA*)  
 Q. Zhang (Univ. of Manitoba, *Canada*)

#### Secretariat

C.C. Huang (Hosokawa Micron Intl. Inc., *USA*)

### Publication Office

Hosokawa Powder Technology Foundation ([www.kona.or.jp](http://www.kona.or.jp))  
 (in the headquarters building of Hosokawa Micron Corporation)  
 1-9, Shodaitajika, Hirakata-shi, Osaka 573-1132, Japan  
 E-mail: [contact\\_zainq@hmc.hosokawa.com](mailto:contact_zainq@hmc.hosokawa.com)

Printing Office: Nakanishi Printing Co., Ltd., Japan

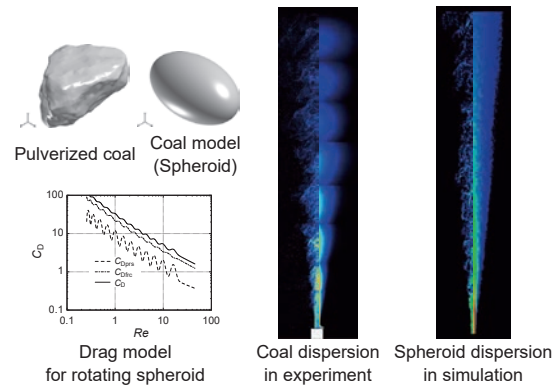
Publication Date: 10 January 2023

<Editorial>

1 Editor's Preface

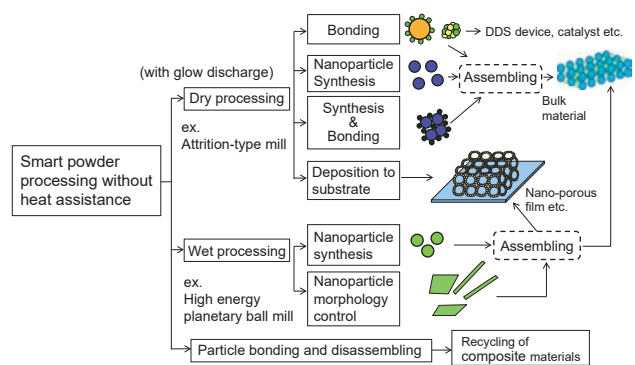
<Review Papers>

3 Analysis and Modeling of Non-Spherical Particle Motion in a Gas Flow



Hiroaki Watanabe and Wei Zhang

14 Smart Powder Processing for Excellent Advanced Materials and Its Applications



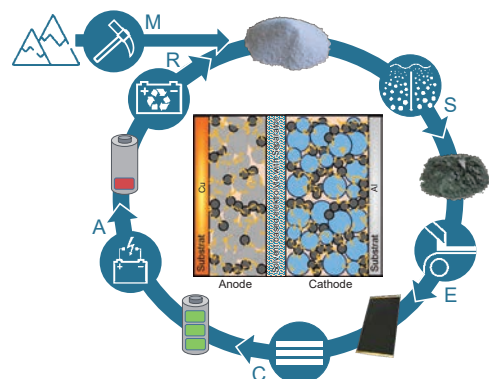
Makio Naito, Takahiro Kozawa, Akira Kondo and C.C. Huang

29 Interfacial Engineering of Particulate & Surfactant Systems for Enhanced Performance in Industrial Applications



Jiaqi Dong and Brij M. Moudgil

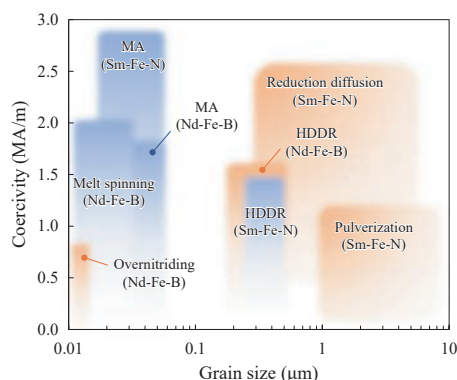
50 Comminution and Classification as Important Process Steps for the Circular Production of Lithium Batteries



Arno Kwade, Marcel Möller, Jannes Müller, Jutta Hesselbach, Sabrina Zellmer, Stefan Doose, Julian Mayer, Peter Michalowski, Malcolm Powell and Sandra Breitung-Faes

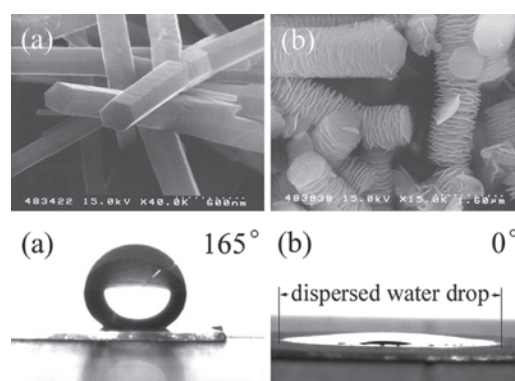
**74 Recent Research Trend in Powder Process Technology for High-Performance Rare-Earth Permanent Magnets**

Kenta Takagi, Yusuke Hirayama, Shusuke Okada, Akihide Hosokawa and Wataru Yamaguchi



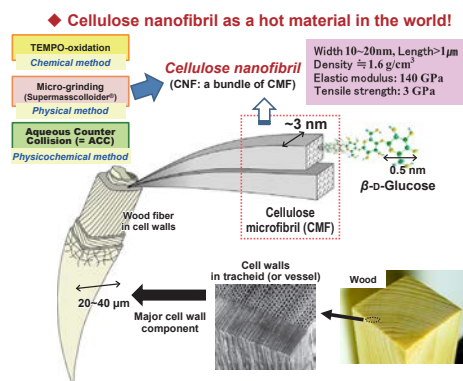
**94 Morphology Control of Transition Metal Oxides by Liquid-Phase Process and Their Material Development**

Shu Yin and Takuya Hasegawa



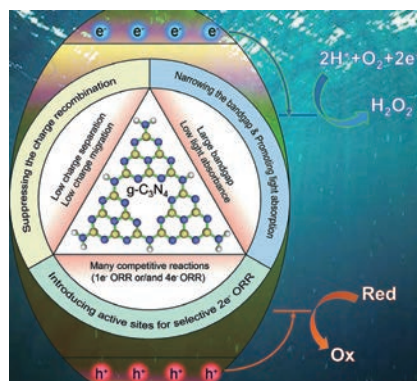
**109 Cellulose Nanofibrils Pulverized from Biomass Resources: Past, Present, and Future Perspectives**

Tetsuo Kondo



**124 Functionalized Graphitic Carbon Nitrides for Photocatalytic H<sub>2</sub>O<sub>2</sub> Production: Desired Properties Leading to Rational Catalyst Design**

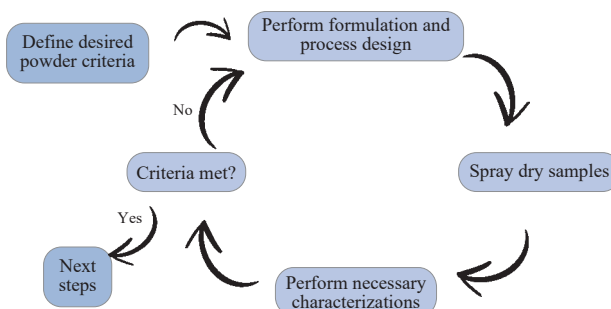
Zhengyuan Teng, Wenan Cai and Teruhisa Ohno



**149 Mechanistic Formulation Design of Spray-Dried Powders**

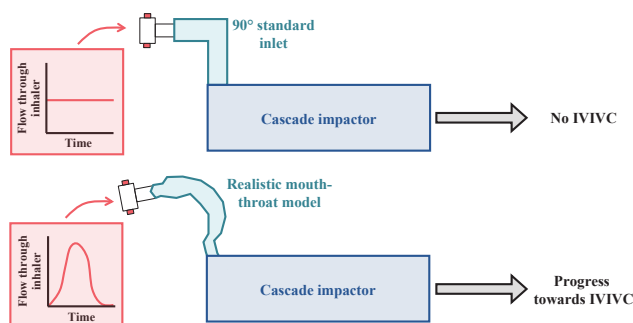
Mani Ordoubadi, Hui Wang and Reinhard Vehring

Mechanistic Design of Spray-Dried Powders



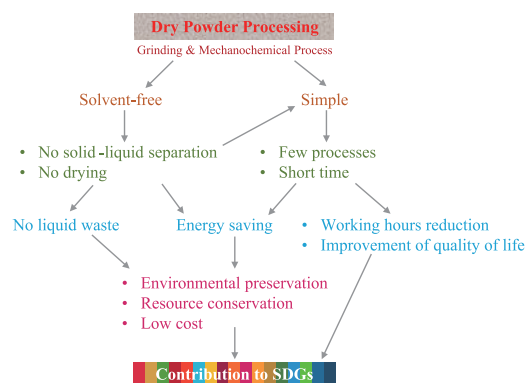
**172 Performance Testing for Dry Powder Inhaler Products: Towards Clinical Relevance**

Sara E. Maloney, Jeffrey B. Mecham and Anthony J. Hickey



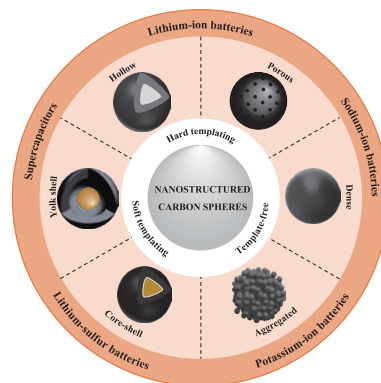
**186 Environmentally Friendly Green Synthesis of Fine Particles by Dry Mechanical Processes Toward SDGs: A Review**

Tomohiro Iwasaki



**197 Recent Advances in the Fabrication and Functionalization of Nanostructured Carbon Spheres for Energy Storage Applications**

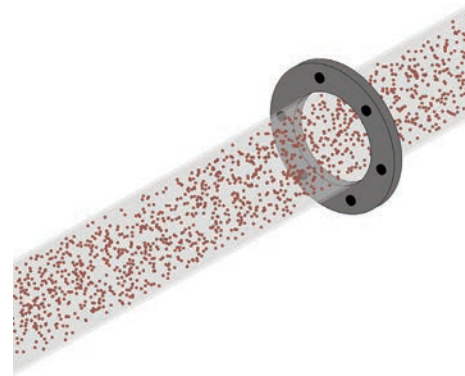
Kiet Le Anh Cao, Ferry Iskandar, Eishi Tanabe and Takashi Ogi



<Original Research Papers>

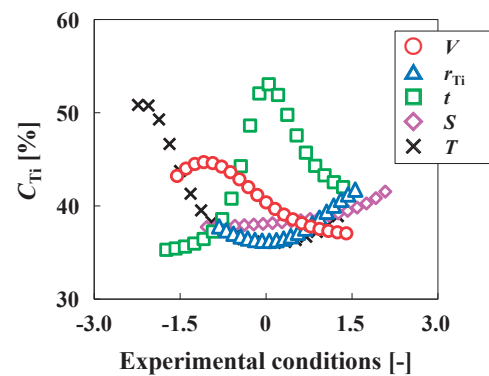
**219 Computational Fluid Dynamic Modelling of Fully-Suspended Slurry Flows in Horizontal Pipes with Different Solids Concentrations**

Gianandrea Vittorio Messa, Qi Yang, Maria Graça Rasteiro, Pedro Faia, Vaclav Matoušek, Rui C. Silva and Fernando Garcia



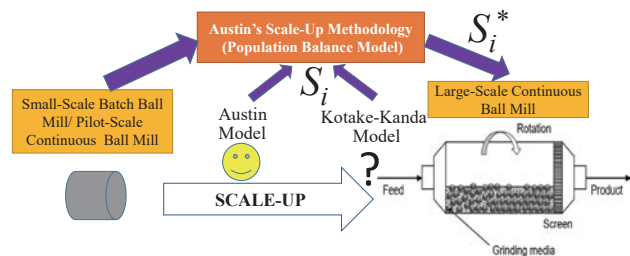
**236 Evaluation of a Coating Process for SiO<sub>2</sub>/TiO<sub>2</sub> Composite Particles by Machine Learning Techniques**

Taichi Kimura, Riko Iwamoto, Mikio Yoshida, Tatsuya Takahashi, Shuji Sasabe and Yoshiyuki Shirakawa



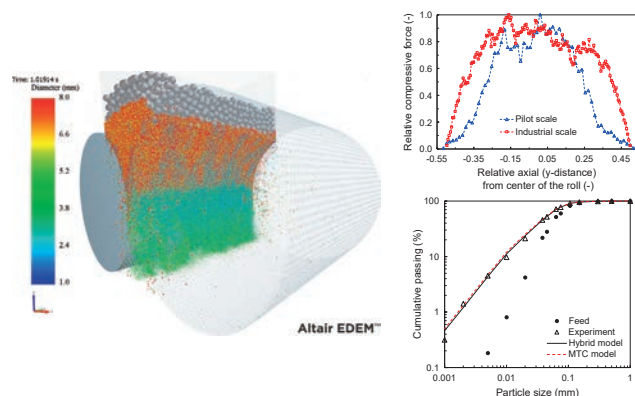
**250 On the Similarity of Austin Model and Kotake–Kanda Model and Implications for Tumbling Ball Mill Scale-Up**

Ecevit Bilgili



**262 A Hybrid PBM-DEM Model of High-Pressure Grinding Rolls Applied to Iron Ore Pellet Feed Pressing**

Victor A. Rodriguez, Túlio M. Campos, Gabriel K.P. Barrios, Gilvandro Bueno and Luís Marcelo Tavares

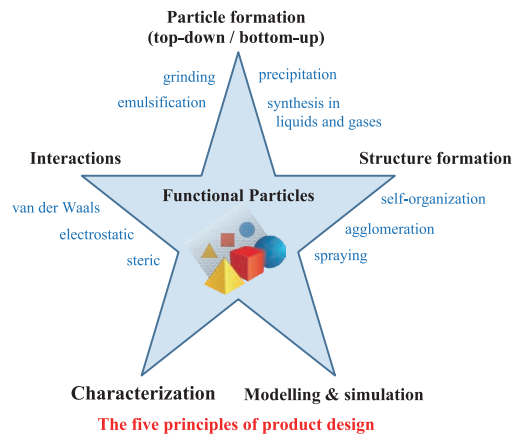


<Information Articles>

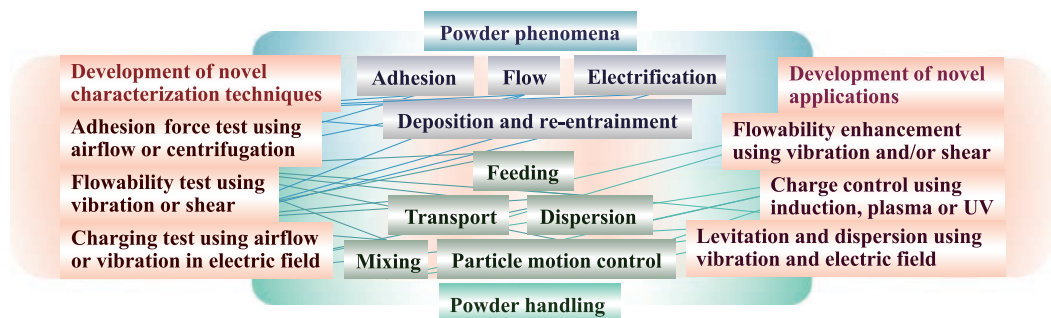
277 The 54th Symposium on Powder Technology and Special Lecture for the 30th Anniversary of the Establishment of HPTF



279 The KONA Award 2021



Selected research achievements for the KONA Award 2021 (Awardee: Prof. Dr. Wolfgang Peukert): Particle based product innovations by understanding and controlling particle interactions.



Selected research achievements for the KONA Award 2021 (Awardee: Prof. Dr. Shuji Matsusaka): Advanced characterization of fine particles and the development of novel powder handling systems.

281 General Information

粉

KONA

Powder and Particle Journal

Impact factor: 3.919 CiteScore: 5.7 Indexed in Scopus, Web of Science and DOAJ

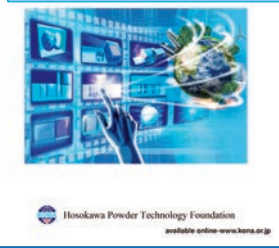
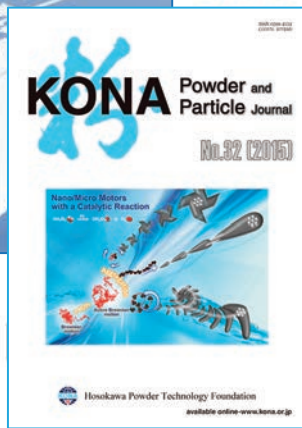
<Diamond Open Access> FREE for Reading & Publication

- 1983 First publication
- 1990 3 editorial blocks worldwide
- 2009 Registered in Web of Science
- 2013 Registered-published on J-STAGE
- 2014 Started Advance Publication
- 2016 Introduced CC-BY license
- 2017 Adopted Editorial Manager®
- 2019 Registered in DOAJ
- 2021 Registered on J-STAGE Data

About the journal

KONA Journal is a peer-reviewed, international, interdisciplinary and *Diamond OA* journal that publishes articles on powder and particle science and technology.

This journal has been published annually since 1983 and is distributed free of charge to researchers, members of the scientific communities, universities and research libraries throughout the world, by Hosokawa Powder Technology Foundation established by Mr. Masuo Hosokawa in 1991.



- Characterization
- Computer simulation
- Nanotechnology
- Material science
- Powder process
- Particle formation
- Dry powders & granules
- Aerosols & Colloids & Slurry
- Metals & Ceramics & Minerals
- Organic-inorganic composites
- Biomaterials & Pharmaceuticals
- Secondary battery, Fuel cell
- Electronic materials
- 3D printer
- Recycling
- etc.



URL: <http://www.kona.or.jp/>



HOSOKAWA Powder Technology Foundation (HPTF)



## Editor's Preface

### Makio Naito, Editor-in-Chief

*Professor, Osaka University, Japan*



I am very honored to be the Editor-in-Chief of “KONA Powder and Particle Journal” starting June 2022 as the successor of Emeritus Professor, Kikuo Okuyama. It is my great pleasure to publish the latest issue of the Journal No. 40 (2023). I have been working on the research and development of powder characterization, powder processing, and their applications for advanced materials for over 40 years, because powder technology is very attractive field for my research works. As you know, “powder”, an assemblage of small solid particles, exhibits very unique behavior. For example, depending on the circumstances, a powder can behave like a gas, a liquid, or a solid. Also, because of its larger specific surface area and smaller volume relative to a bulk material, powder can have very unique properties. This is especially true for “nanoparticles”, which offer a wide range of industrial applications ubiquitous in our daily life and create promising materials for scientific and technical innovations in the future. Furthermore, the 2030 Agenda for Sustainable Development (the 2030 Agenda) is a set of international development goals from 2016 to 2030, which was adopted by the United Nations Sustainable Development Summit held in September 2015 building on the success of Millennium Goals (MDGs). The 2030 Agenda listed “Sustainable Development Goals (SDGs)” consisting of 17 goals and 169 targets in order to eradicate poverty and realize a sustainable world. Powder technology is the key to achieve these goals for a sustainable society worldwide.

To contribute to the advancement of powder technology on a global scale, Mr. Masuo Hosokawa, the second President of Hosokawa Micron Corporation published the first issue of “KONA Powder and Particle Journal” in 1983. Then, he founded Hosokawa Powder Technology Foundation in 1991, and shifted the management issues of the KONA Journal to it. Besides, Mr. M. Hosokawa proposed the concept of “nanoparticle technology” long before the United State President Bill Clinton’s National Nanotechnology Initiative in 2000. As a chief editor, Mr. M. Hosokawa decided to inaugurate the Nanoparticle Technology Handbook to advance the development of powder technology. Subsequently, the Foundation published the Nanoparticle Technology Handbook in Japanese in 2006, which was translated into English and published as the first edition of the Nanoparticle Technology Handbook in 2007 by Elsevier. Since then, nanoparticle technology has rapidly advanced, and been applied broadly and in many new applications. Therefore, the Handbook was updated twice in 2012 and 2018, respectively, after Mr. M. Hosokawa passed away in 2010. Then, the third edition was organized by four editors, including myself (The chief editor), and Dr. Kohei Hosokawa (the President of Hosokawa Micron Corporation), contributing to the success of the publication.

The KONA Journal has evolved for over 40 years. In 1990, three Editorial Boards (Asian/Oceania, Europe/Africa and America) were established to manage the Journal worldwide. After the involvement of the Foundation management, the KONA Journal was registered in Web of Science in 2009. Furthermore, it was registered and published on J-STAGE in 2013. Besides, Advanced Publication started in 2014. DOAJ was registered in 2019. J-STAGE Data was registered in 2021. Today, “KONA Powder and Particle Journal” is a peer-reviewed, international open access journal. It is published on-line annually on the homepage of Hosokawa Powder Technology Foundation.

With the great effort of all Editorial Board Members, the impact factor of the Journal in 2021 has reached 3.919 showing the KONA Journal is highly evaluated as an international, academic journal. I would like to express my sincere appreciation to all Board Members for their contributions to the success of the KONA Journal publication. Aiming at higher quality journal in the future, I would like to emphasize the following issues for the Journal:

Firstly, the KONA Journal should keep aiming to publish mainly review articles on powder science and technology. As former Editor-in-Chief, Prof. Kikuo Okuyama mentioned at the preface of No. 37 (2020), review articles are especially important to fulfill demands from researchers and engineers who are looking for reliable sources which summarize all the rapidly advancing research to understand the recent research trends, latest information, and future tasks in the special subjects. Recent technology has rapidly advanced in the diverse areas including information technology and materials informatics. Powder technology is also rapidly developing by interacting with the new technologies. Such cutting-edge review articles will give readers the newest information through the KONA Journal.

Secondly, the KONA Journal should continue fostering development of powder science and technology and promoting the synergetic interactions with diverse science and technology communities. Research related to powder and particles has widely spread from advanced materials including ceramics, polymers, metals and composites, medical devices and pharmaceuticals to information technology. Research area for sustainable society is also very important. The KONA Journal should bridge the gaps between powder technology and diverse technology communities, to become more attractive journal for readers from various disciplines.

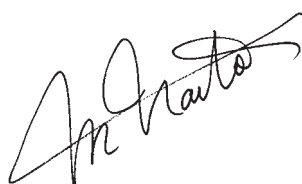
Thirdly, the continuous financial and human support from Hosokawa Powder Technology Foundation is critical to achieve higher quality of the KONA Journal. The 54<sup>th</sup> Symposium on Powder Technology was held on September 5, 2022 at the Imperial Hotel Osaka, in conjunction with the 30<sup>th</sup> Anniversary event of the Foundation. At the opening address, Mr. Yoshio Hosokawa, the President of the Foundation and the Chairman of Hosokawa Micron Corporation, introduced the history of the Foundation, and emphasized that the KONA Journal is now a highly evaluated academic international journal, contributing to the development of powder science and technology in the world. As the new Editor-in-Chief, I would like to express my sincere appreciation to the great support of the Foundation.

At last but not the least, taking use of this opportunity, I would like to express my gratitude to all paper reviewers shown here for the successful publication of the “KONA Powder and Particle Journal” (No. 40), and my sincere thanks to all those who have contributed to the publication of the journal.

FUJI, Masayoshi  
HICKEY, Anthony  
KAGE, Hiroyuki  
KANO, Junya  
KAWASAKI, Akira

KWADE, Arno  
MAKINO, Hisao  
MAZZINGHY, Douglas Batista  
MUTTIL, Pavan  
SAKAI, Mikio

SAKKA, Yoshio  
SANDER, Steffen  
SHIRAKAWA, Yoshiyuki  
TAKEDA, Shin-ichi  
TAVARES, Luis Marcelo



Makio Naito  
Editor-in-Chief  
Professor, Osaka University  
October, 2022



# Analysis and Modeling of Non-Spherical Particle Motion in a Gas Flow<sup>†</sup>

Hiroaki Watanabe<sup>1\*</sup> and Wei Zhang<sup>2</sup>

<sup>1</sup> Department of Advanced Environmental Science and Engineering, Kyushu University, Japan

<sup>2</sup> China College of Mechanical and Transportation Engineering, China University of Petroleum-Beijing, China

## Abstract

This paper describes the reviews of the recent works in analysis, modeling, and simulation of the motion of a non-spherical particle. The motion of the non-spherical particles was analyzed in detail by means of a fully resolved direct numerical simulation (DNS). From the DNS data, the PDF-based drag coefficient model was proposed and applied to the particle dispersion simulation in an isotropic turbulent flow to assess the effect of the particle shape by comparing it with the motion of a spherical particle. Moreover, the model was applied to a large-eddy simulation (LES) of particle dispersion in an axial jet flow and validated by comparing it with the experimental data. Results showed that the effect of the particle shape was clearly observed in the characteristics of the particle dispersion in the isotropic turbulent flow by evaluating the deviation from the Poisson distribution ( $D$  number) and the radial distribution function (RDF). It was found that the non-spherical particle's representative Stokes number becomes larger as the sphericity increases. Furthermore, it was also revealed that the effects of the particle size distribution and the shape observed in the experiment was precisely captured by the LES that coincided with the trend found in the isotropic turbulent flow.

**Keywords:** non-spherical particle, modeling, numerical simulation, experiment, DNS, LES

## 1. Introduction

A dispersed gas-particle two-phase flow is frequently utilized in many industrial applications, such as conveyance and energy conversion systems of solid materials. It is an urgent issue to reduce the environmental impact of these facilities for a low-carbon society. To design such highly efficient devices, it is essential to deeply understand the behavior of particles in a fluid flow.

A non-spherical particle is frequently seen in the industry as a pulverized solid particle such as coal which may behave in a different motion from a spherical particle. A great many efforts have been conventionally made to investigate the motion of the non-spherical particle. The majority of the works were dedicated to a spheroidal particle. Feng J. et al. (1995) performed a three-dimensional computation of the force and torque acting on an ellipsoid settling slowly in a viscoelastic fluid. They found that the signs of the perturbation pressure and velocity around the particle for inertia were reversed by viscoelasticity and the torques were also opposite signs. It was also found that the equilibrium tilt angle was a function of the elasticity num-

ber which was the ratio of the Weissenberg number and the Reynolds number. Broday D. et al. (1998) investigated the motion of non-neutrally buoyant prolate spheroidal particles freely rotating or fixed with orientations in vertical shear flows. They revealed that the spheroids freely moving translated along periodic trajectories with no net lateral drift, whereas the particles with fixed orientations were unstable with the drift velocity growing exponentially with time. The conditions for the unstable motion were also discussed as a function of the particle shape, via its aspect ratio and its inertia. Mortensen P.H. et al. (2008) performed a direct numerical simulation (DNS) of prolate ellipsoidal particles suspended in a turbulent channel flow. It was found that the ellipsoidal particles tend to align with the mean flow direction in the near-wall region, while the orientation became isotropic in the core region. In addition, when the particle inertia increases, the particles were less oriented in the spanwise direction and more oriented in the wall-normal direction.

Mathematical modeling of the complex motion of the non-spherical particle has been also examined in many works. Haider A. and Levenspiel O. (1989) proposed the explicit equations for the drag coefficient of falling non-spherical particles by fitting the experimental data of isometric and disk type solids with classification in terms of the sphericity. In this work, the drag coefficient is a function of the sphericity and Reynolds number, and the

<sup>†</sup> Received 1 March 2022; Accepted 15 April 2022  
J-STAGE Advance published online 18 June 2022

\* Corresponding author: Hiroaki Watanabe;  
Add: 6-1 Kasuga-koen, Kasuga, Fukuoka 816-8580, Japan  
E-mail: [whiroaki@tse.kyushu-u.ac.jp](mailto:whiroaki@tse.kyushu-u.ac.jp)  
TEL: +81-92-583-7674 FAX: +81-92-592-8447



orientation is not considered. Holzer A. and Sommerfeld M. (2008) also proposed a simple correlation formula for the drag coefficient of arbitrarily shaped particles by introducing the crosswise and lengthwise sphericities in addition to the normal sphericity into the drag coefficient equation based on a number of the experimental and numerical studies. Rosendahl L. (2000) developed the particle shape description based on the minor axis, the aspect ratio, and the superelliptic exponent to account for the shape effect of ellipsoids and cylinders and Zastawny M. et al. (2012) extended the model to account for the drag force, the lift force, the pitching torque, and the torque caused by the rotation of the particles based on the fully resolved DNS. They should be in useful forms when the orientation of the particle is considered in a Lagrangian particle tracking simulation.

In the modeling of the motion of the non-spherical particle in the earlier stage, the sphericity is simply used to consider the effect of the non-sphericity on the drag coefficient and the other related parameters to characterize the particle motion, while it cannot consider the effect of oscillation and rotating in a fluid flow. In the later stage, the effect of rotation is considered by introducing the orientation such as the crosswise and lengthwise sphericities. In the CFD framework, conventionally the Reynolds-averaged Navier-Stokes (RANS) simulation in which the entire scale of the turbulent eddy is modeled and the time-averaged quantities are evaluated is mainly used as a standard tool to predict the particle behavior in the industry due to its lower computational cost in spite of its lower accuracy for a long time (e.g. Watanabe H. and Otaka M. (2006), Watanabe H. et al. (2015), Hashimoto N. and Watanabe H. (2016)). However, with the great advance in computer performance, massively parallel large-scale computing by means of a large-eddy simulation (LES) in which the eddies in the subgrid-scale are only modeled and the fully unsteady phenomena can be considered is expected to be a new standard tool (e.g. Kurose R. et al. (2009), Muto M. et al. (2019), Ahn S. et al. (2019), Watanabe H. and Kurose R. (2020)). In such a highly fidelity unsteady simulation framework, the motion models which can consider the oscillation and rotation of the particle would be essential.

While the models taking the orientation of the particles into account have been proposed in some existing works, as mentioned earlier, another modeling strategy will be reported hereafter in this paper. In typical industrial applications, a tremendous number of particles exist in a fluid flow such as a pulverized coal combustion boiler. Here we introduce a concept of probability density function (PDF) to model the motion of non-spherical particles. In **Section 2**, the motion model of the non-spherical particle is developed by a fully resolved DNS. In **Section 3**, the model proposed here is assessed in an isotropic turbulent flow by means of a DNS with the point mass approximation. In **Section 4**, the

model is applied to an LES of a turbulent axial jet flow and validated with the experiment.

## 2. Modeling of non-spherical particle motion

In this section, the motion of a single non-spherical particle is numerically investigated by means of a fully resolved gas-particle two-phase flow DNS. The DNS data is analyzed to formulate the effects of the non-sphericity in the motion equation. The Basset-Boussinesq-Oseen (B.B.O.) equation is expressed as,

$$\rho_p V_p \frac{d\mathbf{v}}{dt} = \mathbf{F}_D + \mathbf{F}_L + \mathbf{F}_B + \mathbf{F}_{\text{prs}} + \mathbf{F}_{\text{mass}} + \mathbf{F}_{\text{Basset}}, \quad (1)$$

where  $\rho_p$ ,  $V_p$ , and  $\mathbf{v}$  are the density, volume, and velocity of the particle, respectively.  $\mathbf{F}_D$ ,  $\mathbf{F}_L$ ,  $\mathbf{F}_B$ ,  $\mathbf{F}_{\text{prs}}$ ,  $\mathbf{F}_{\text{mass}}$ , and  $\mathbf{F}_{\text{Basset}}$  are the drag force, lift force, buoyancy, pressure gradient, virtual mass, and Basset history term, respectively. In this study, because the drag force mainly contributes to the motion of the particle in the pulverized coal combustion field, we pay special attention to  $\mathbf{F}_D$  via modeling of the drag coefficient  $C_D$ .

The drag force is regarded as the summation of the contributions of the pressure and frictions as,

$$\mathbf{F}_D = \mathbf{F}_{D\text{prs}} + \mathbf{F}_{D\text{fric}}. \quad (2)$$

And the drag coefficient can be also expressed as,

$$C_D = \frac{\mathbf{F}_D}{\frac{1}{2} \rho_f |\mathbf{u} - \mathbf{v}|^2 A} = C_{D\text{prs}} + C_{D\text{fric}}, \quad (3)$$

where  $A$  is the projection area of the particle to the flow direction. As shown in Eqn. (3),  $C_D$  is also considered as a sum of  $C_{D\text{prs}}$  and  $C_{D\text{fric}}$  which are influenced by the pressure and the friction, respectively.  $C_D$  for a spherical particle can be regarded as a simple function of the Reynolds number  $Re$  and as mentioned earlier, many works propose the drag curve equations. Clift R. et al. (1978) summarized some of the most popular expressions, and provided the following recommendation as,

$$C_D = 3/16 + 24/Re \quad \text{for } Re < 0.01, \quad (4)$$

$$C_D = \frac{24}{Re} (1 + 0.1315 Re^{0.82 - 0.05 \log Re}) \quad \text{for } 0.01 < Re \leq 20, \quad (5)$$

$$C_D = \frac{24}{Re} (1 + 0.1935 Re^{0.6305}) \quad \text{for } 20 < Re \leq 260, \quad (6)$$

where  $Re$  is based on the slip velocity and particle size as,

$$Re = \frac{\rho_f |\mathbf{u} - \mathbf{v}| d}{\mu}, \quad (7)$$

where  $d$  is the diameter of the particle and  $\mu$  is the viscosity of the fluid, respectively.

Eqns (1) to (6) are only suitable for a spherical particle. A non-spherical particle is typically assessed by the

sphericity which is defined as the ratio of the surface area of a sphere to that of a given particle where the sphere and the given particle have the same volume as,

$$\phi = \frac{S_{\text{sphere}}}{S_{\text{particle}}} = \frac{\pi^{1/3} (6V_{\text{particle}})^{2/3}}{S_{\text{particle}}}. \quad (8)$$

According to the examination by Haider A. and Levenspiel O. (1989),  $C_D$  becomes larger as  $\phi$  decreases.

## 2.1 The arbitrary Lagrangian-Eulerian (ALE) method

To deeply understand the six-degree of freedom for a particle motion, the arbitrary Lagrangian-Eulerian (ALE) method is employed (Hirt C.W. et al. (1974)). The governing equations of the ALE method are expressed as,

$$\frac{\partial \rho_f}{\partial t} + ((\mathbf{u} - \mathbf{u}') \cdot \nabla) \rho_f = -\rho_f \nabla \cdot \mathbf{u}, \quad (9)$$

$$\frac{\partial \mathbf{u}}{\partial t} + ((\mathbf{u} - \mathbf{u}') \cdot \nabla) \mathbf{u} = -\frac{1}{\rho_f} \nabla p + \frac{1}{\rho_f} \nabla p \cdot \boldsymbol{\sigma} + \mathbf{g}, \quad (10)$$

where  $\rho_f$  and  $\mathbf{u}$  are the fluid density and velocity, respectively,  $\mathbf{u}'$  the mesh velocity,  $p$  the pressure,  $\boldsymbol{\sigma}$  the surface stress tensor. The ALE method is equivalent to the Eulerian method when  $\mathbf{u}' = 0$  and is equivalent to the Lagrangian method when  $\mathbf{u}' = \mathbf{u}$ . Here, the particle velocity  $\mathbf{v}$  is employed as  $\mathbf{u}'$  to consider the Lagrangian particle motion. The slip velocity  $\mathbf{u} - \mathbf{v}$  appears when the particle translates, rotates and oscillates. This means that the entire computational grid around the particle moves in the ALE method.

The motion of the single particle is calculated by the governing equations of a rigid body as,

$$m \frac{d^2 \mathbf{z}}{dt^2} = \mathbf{F}, \quad (11)$$

$$\mathbf{I} \frac{d^2 \boldsymbol{\alpha}}{dt^2} + \frac{d\boldsymbol{\alpha}}{dt} \times \left( \mathbf{I} \frac{d\boldsymbol{\alpha}}{dt} \right) = \mathbf{M}, \quad (12)$$

where  $m$  is the particle mass,  $\mathbf{I}$  the moment of inertia of particle,  $\mathbf{z}$  the displacement angle,  $\boldsymbol{\alpha}$  the rotation angle,  $\mathbf{F}$  the force on the particle,  $\mathbf{M}$  the torque on the particle, which are obtained by considering the integration of the fluid force over the surface and the gravity. Subsequently, we can calculate the moving and angular velocities of the particle. The presented numerical procedure was implemented into the unstructured FVM parallel computing solver FFR-Comb (NuFD/FrontFlowRed extended by Kyushu Univ., Kyoto Univ., CRIEPI, and NuFD) (Zhang W. et al., 2018a; 2018b). The presented ALE method has been properly validated by comparing with the correlation expression of the drag coefficient curve by Cliff R. et al. (1978) and with the experiment of the falling particles in water by Mordant N. et al. (2000). See more details of this DNS in Zhang W. et al. (2018b).

## 2.2 Computational details

To observe the motion characteristics of various particle shapes, pulverized coal and spheroidal particles are examined. Fig. 1 shows the shapes of the particles. The 3D data of the coal particle was obtained by the X-ray CT scanner. The shape of the spheroidal particle was determined by the equivalent volume. In our preliminary examination, the spheroid with the equivalent volume shows the closest behavior of the coal particle rather than the spheroids with the equivalent surface area and sphericity. Fig. 2 shows the computational grid for the coal particle. The computational domain is discretized with about 12 million cells and is divided into 1,024 regions for the MPI parallel computing. It takes approximately 15,000 node-hour for one case. The grid resolution around the particle is confirmed to be enough to resolve the boundary layer thickness formed on the surface within the range of the particle Reynolds number  $Re$  in this study following the theorem by Schlichting et al. (1955) and the examination by Muto et al. (2012).

The flow velocity was set to 15 m/s, and the particle was placed in the upward flow at the beginning of the computation. The particle was released at  $t = 0$  without the initial velocity. The major axis of each particle was set in the vertical direction. The initial  $Re$  was estimated as 45.

## 2.3 Results and discussion

Fig. 3 shows the drag curves for (a) coal particle and (b) spheroid with the equivalent volume. In Fig. 3,  $C_{D_{\text{Dprs}}}$  and  $C_{D_{\text{Dfric}}}$  are also displayed as well as  $C_D$ . It is found that the  $C_D$  curve oscillates for the both particles. Because the major axis is set in the vertical direction, the initial projection area in the fluid direction is small and it is located in unstable equilibrium. With the small disturbance of the pressure or friction variation on the surface, the particle starts oscillating and rotating. It is found that the contribution of  $C_{D_{\text{Dfric}}}$  is dominant, while the large oscillation is observed for  $C_{D_{\text{Dprs}}}$ . It is also understood that the trend for the spheroid shows a good agreement with that for the coal particle.

Fig. 4 shows the drag curves with the various initial angles of the major axis of the spheroid. Here, the two-digit number after “EV” (equivalent to the volume) in the figure displays the initial angle from the horizontal axis. In spite

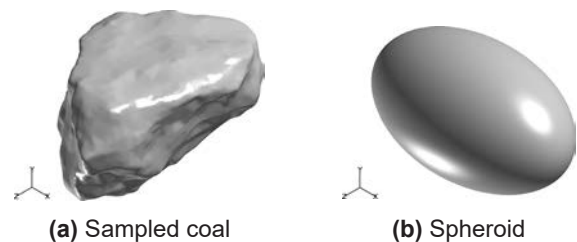
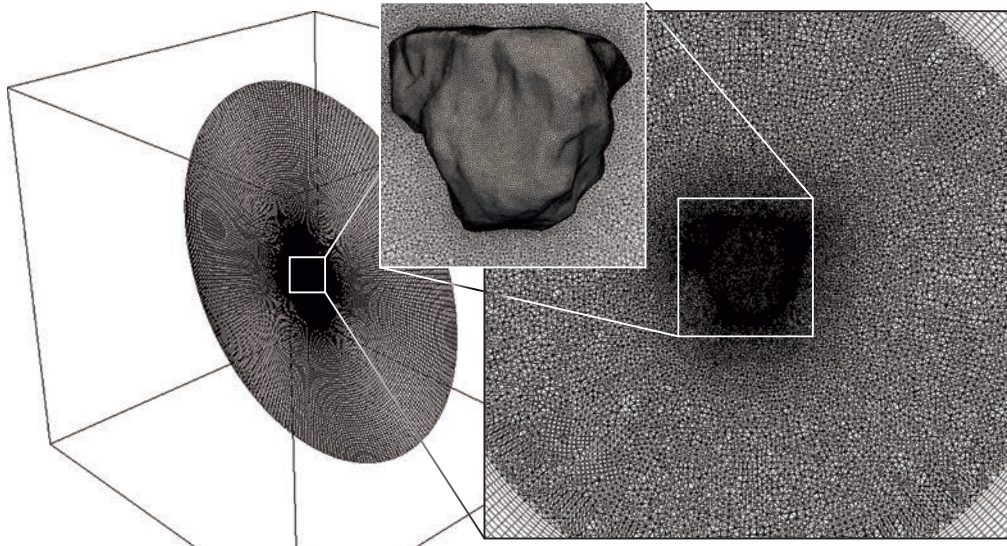
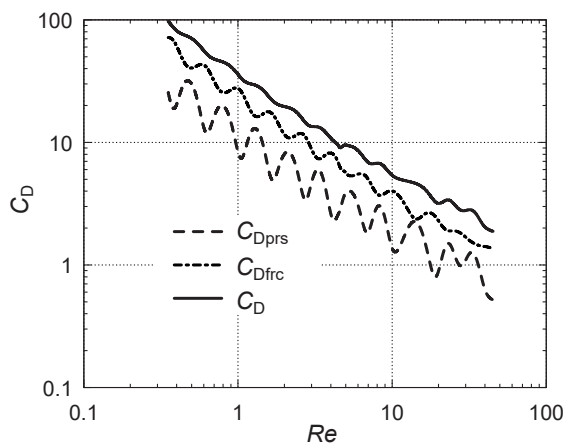


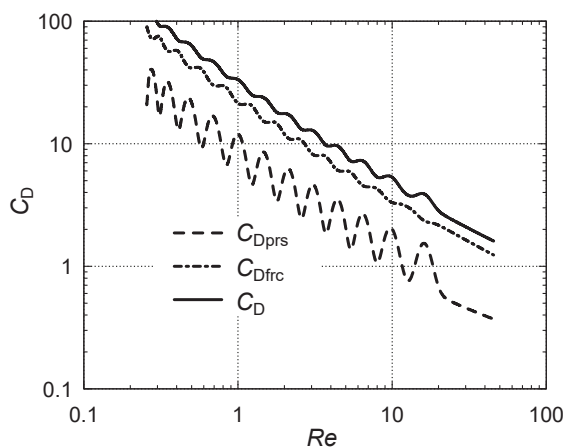
Fig. 1 Shapes of (a) sampled pulverized coal particle, and (b) spheroid with equivalent volume. Reprinted with permission from Ref. (Zhang et al., 2018a). Copyright: (2018) Elsevier B.V.



**Fig. 2** Computational grid for sampled coal particle. Reprinted with permission from Ref. (Zhang et al., 2018a). Copyright: (2018) Elsevier B.V.



**(a)** Sampled coal



**(b)** Spheroid

**Fig. 3** Drag curves for **(a)** sampled pulverized coal particle, and **(b)** spheroid with equivalent volume. Reprinted with permission from Ref. (Zhang et al., 2018a). Copyright: (2018) Elsevier B.V.

of the difference in the timing to start the oscillation among the cases, all the oscillating curves are located within a certain range of the maximum and minimum smooth

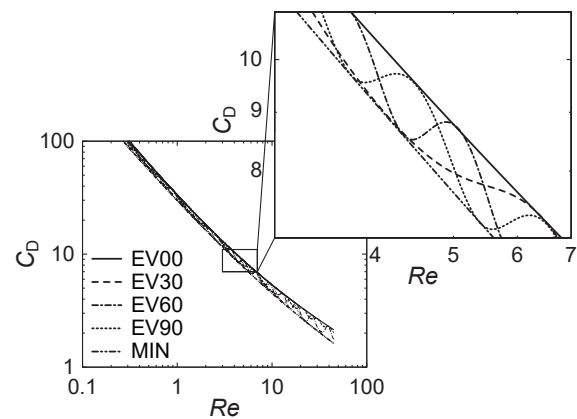


**Fig. 4** Drag curves for spheroid with equivalent volume with various initial angles. Reprinted with permission from Ref. (Zhang et al., 2018a). Copyright: (2018) Elsevier B.V.

curves. The trend of the oscillation is analyzed in terms of the probability density in **Fig. 5**. Here, the probability density function (PDF) of the sine curve is displayed as well in **Fig. 5**. It is revealed that the PDF of the sine curve can precisely reproduce that of the spheroid particle. From this consideration, the characteristics of the oscillating  $C_D$  can be formulated by the following simple expression as,

$$\log C_D = \log C_{D_{\min}} + (\log C_{D_{\max}} - \log C_{D_{\min}}) \cdot \frac{\sin(2\pi\theta + 1)}{2}, \quad (13)$$

where  $\theta$  is the random number from 0 to 1, and  $C_{D_{\max}}$  and  $C_{D_{\min}}$  are determined by the computation of the six-degree of freedom motion of the target particle and those can be approximated by the expressions by Haider A. and Haider A. and Levenspiel O. (1989) and Clift R. et al. (1978) as,

$$C_D = \frac{24}{Re} (1 + A Re^{B-C \cdot \log Re}) \quad \text{for } 0.01 < Re \leq 10, \quad (14)$$

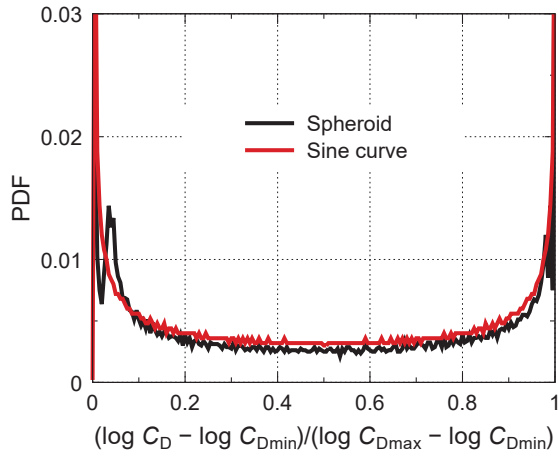


**Fig. 5** PDFs of drag coefficient for spheroid and sine curve. Reprinted with permission from Ref. (Zhang et al., 2018a). Copyright: (2018) Elsevier B.V.

$$C_D = \frac{24}{Re}(1 + X Re^Y) \quad \text{for } 10 < Re \leq 100. \quad (15)$$

Here, the model parameters,  $A$ ,  $B$ ,  $C$ ,  $X$ , and  $Y$  are determined by the computation as mentioned earlier.

### 3. Dispersion of non-spherical particles in an isotropic turbulent flow

In this section, the non-spherical particle motion model developed in the previous section is applied to the Eulerian-Lagrangian two-way coupling DNS with employing the particle-source-in cell (PSI-CELL) model (Crowe C.T. et al. (1977)) to observe the effects of non-sphericity.

#### 3.1 Governing equations

The governing equations for the fluid flow consist of the mass and momentum conservations as,

$$\frac{\partial \rho_f}{\partial t} + \frac{\partial \rho_f u_j}{\partial x_j} = 0, \quad (16)$$

$$\frac{\partial \rho_f u_i}{\partial t} + \frac{\partial \rho_f u_j u_i}{\partial x_j} = -\frac{\partial p}{\partial x_i} + \frac{\partial \sigma_{ij}}{\partial x_j} + S_{u_i}, \quad (17)$$

where  $u_i$  and  $\sigma_{ij}$  are the fluid velocity and stress tensor, respectively.  $S_{u_i}$  is the source term of the interphase momentum transfer and evaluated by,

$$S_{u_i} = -\frac{1}{\Delta V} \sum^N \frac{m}{\tau_p} \frac{Re}{24} C_D (u_i - u_p), \quad (18)$$

where  $u_p$  is the particle velocity and  $\Delta V$  the control volume.  $\tau_p$  is the particle response time. The Stokes number  $St$  characterizing the behavior of particles in a fluid flow is defined with the Kolmogorov time scale  $\tau_k$  as,

$$St = \frac{\tau_p}{\tau_k}. \quad (19)$$

The particles are treated as mass points and tracked by the Lagrangian manner. The gravity and lift forces are

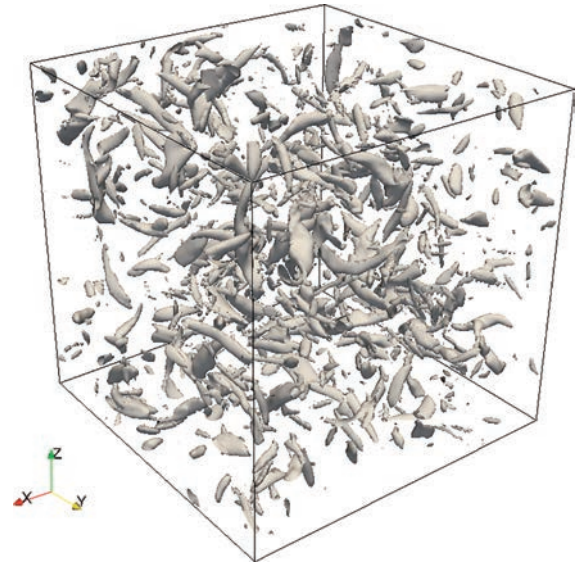


**Fig. 6** Computational domain and vortex visualization of isotropic turbulent flow. Reprinted with permission from Ref. (Zhang et al., 2018a). Copyright: (2018) Elsevier B.V.

ignored. The effects of the pressure gradient, virtual mass, and Basset history term are neglected. The motion equations for the particles are expressed as,

$$\frac{dx_p}{dt} = u_p, \quad (20)$$

$$\frac{du_p}{dt} = \frac{1}{\tau_p} \frac{Re}{24} C_D (u_i - u_p), \quad (21)$$

where  $x_p$  is the particle position.

#### 3.2 Computational details

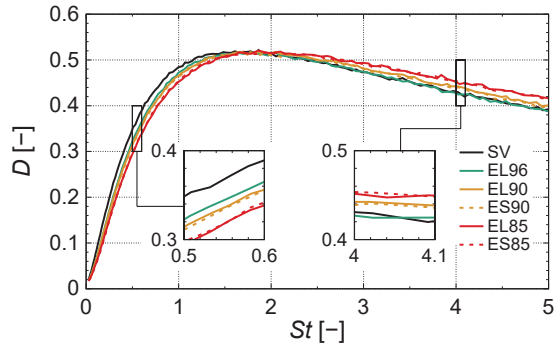
**Fig. 6** shows the computational domain displaying the distribution of the vortices distinguished by the second invariant of the velocity gradient tensor,  $Q = 10,000$ . The domain is a  $(2\pi)^3 \text{ cm}^3$  cube divided by  $128^3$  grids. All boundaries are set as periodic boundaries. The isotropic turbulent field generated in this study has the RMS (root mean square) of the velocity of 2.7 m/s and the Taylor's microscale-based Reynolds number of 60 which is closed to the condition by Ooi A. et al., (1999). The isotropic turbulent flow is evaluated by the energy spectrum field and  $St$  is controlled by varying the particle size. The one spherical and five different sphericity spheroidal particles are examined. **Table 1** shows the particle properties. All the model parameters for each particle shape are obtained by the computation of the six-degree of freedom motion of the target particle as described in **Section 2**. See more details of this DNS in Zhang W. et al. (2018b).

#### 3.3 Results and discussion

The characteristics of the particle dispersion is evaluated by the  $D$  number (Fessler J.R. et al. (1994)) which shows the deviation between the target particles dispersion and

**Table 1** Cases performed in isotropic turbulent flow.

Cases	Sphericity [-]	Diameter of equivalent volume sphere [m]
SV	1.00	$4.23 \times 10^{-5}$
EL96	0.96	$4.23 \times 10^{-5}$
EL90	0.90	$4.23 \times 10^{-5}$
ES90	0.90	$3.43 \times 10^{-5}$
EL85	0.85	$4.23 \times 10^{-5}$
ES85	0.85	$2.91 \times 10^{-5}$


**Fig. 7** Computational domain and vortex visualization of isotropic turbulent flow. Reprinted with permission from Ref. (Zhang et al., 2018a). Copyright: (2018) Elsevier B.V.

the Poisson distribution defined as,

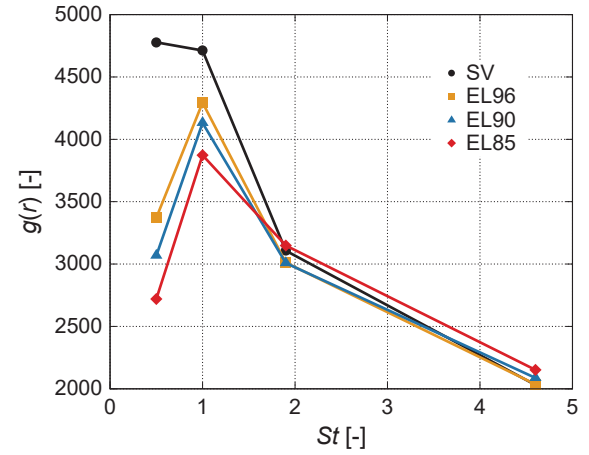
$$D = \frac{\sigma - \sigma_{\text{Poi}}}{\lambda}, \quad (22)$$

where  $\sigma$  and  $\sigma_{\text{Poi}}$  are the standard deviations, and  $\lambda$  is the mean number of particles in each small box which is set to analyze  $D$ . In this study,  $24^3$  boxes are applied to the whole domain. **Fig. 7** shows the variation of  $D$  with the various  $St$  for the six cases. It is found that the effect of the sphericity changes at the point where the peak value of  $D$  appears. In the region of the smaller  $St$  from the point of the peak,  $D$  becomes larger with increasing the sphericity. On the other hand, in the larger  $St$  region, the trend is opposite. In other words, as the sphericity increases, the  $D$  curve shifts toward the larger  $St$  direction. This means that the spheroid's apparent (representative) Stokes number  $St^*$ , which represents the dispersion behavior becomes larger.

The characteristics of the particle dispersion is also analyzed by the radial distribution function (RDF) which describes the characteristics of particle clustering in terms of its length scale. RDF is defined as,

$$g(r_i) = \frac{N_p(i) / \Delta V_i}{N_p / V}, \quad (23)$$

where  $N_p = N(N-1)/2$  is the total number of particle pairs and  $V$  is the volume of the whole domain.  $N_p(i)$  is the total number of particle pairs with a distance between  $r_i + \Delta r/2$


**Fig. 8** Sum of  $g(r)$  values conditioned by  $r/\eta < 12$  for each case. Reprinted with permission from Ref. (Zhang et al., 2018a). Copyright: (2018) Elsevier B.V.

and  $r_i - \Delta r/2$ .  $\Delta V_i$  is the volume of the shell located at a distance  $r_i$  with the thickness  $\Delta r$ . **Fig. 8** shows the RDF variation with varying  $St$  for the representative four cases. In **Fig. 8**, RDF is evaluated as the sum of  $g(r)$  conditioned by  $r/\eta < 12$ , where  $\eta$  is the Kolmogorov length scale. In the condition to analyze  $D$ ,  $r/\eta$  can be approximately estimated as around 12. It is found in **Fig. 8** that as  $St$  increases,  $g(r)$  initially increases and then decreases after appearing the peak value at  $St = 1.0$  except SV. These trends agree with the result observed in **Fig. 7**.

#### 4. Dispersion of non-spherical particles in a turbulent jet flow

In this section, the non-spherical particle motion model developed in **Section 2** is applied to the Eulerian-Lagrangian two-way coupling LES to investigate the particle dispersion behavior in a more practical condition. The model results are compared with the experimental results.

##### 4.1 Governing equations

The governing equations of the fluid and particle motions are almost the same as described in **Section 3**, while the variables are evaluated with the spatial and Favre filtering in the coarser grid. The subgrid-scale (SGS) terms are considered by the dynamic Smagorinsky model proposed by Moin P. et al. (1991). The interphase momentum transfer is evaluated by the PSI-CELL method.

##### 4.2 Experimental and computational details

**Fig. 9** shows the schematic diagram of the targeted cold flow experiment. The particles are transported by the airflow and injected vertically by the coaxial jet burner. The particle image velocimetry (PIV) method is used to measure particle motion. The laser sheet is applied at different heights of 0, 20, 30, 60, 90, 120, 150, 180, and 210 mm from the burner exit. At each height, 1,000 graphics are taken and processed to obtain the time-averaged profiles.



In the experiment, the two cases, pulverized coal, and spherical polymer particles are used to observe the effect of the particle's shape. The densities of coal and polymer are almost the same about  $1,200 \text{ kg/m}^3$ . The averaged flow velocity is set to  $7.59 \text{ m/s}$  and the particle mass flux is set to  $1.29 \times 10^{-4} \text{ kg/s}$ . **Fig. 10** shows the particle mass flux of the different diameters.

The computational domain is a  $360 \text{ mm}$  height cylinder with a diameter of  $100 \text{ mm}$ . The axial jet burner is located at the center of the bottom which has a  $6 \text{ mm}$  diameter and  $60 \text{ mm}$  height. The number of cells is  $11.5$  million. **Table 2** shows the four cases performed in this study. As shown in **Fig. 10**, the particle size distribution is expressed by the representative six diameters in the simulation. The model

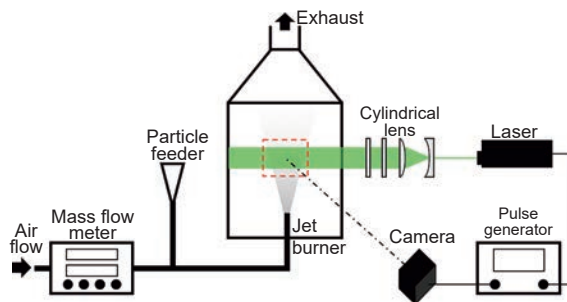


**Fig. 9** Schematics of experimental configuration. Reprinted with permission from Ref. (Zhang et al., 2018b). Copyright: (2018) Elsevier B.V.

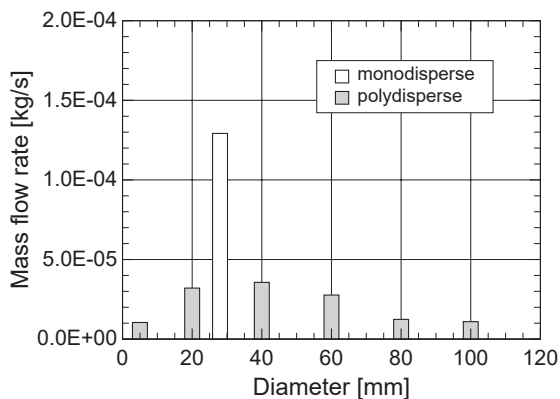


**Fig. 10** Particle mass fluxes of different diameters for monodispersed and polydispersed cases.

**Table 2** Cases performed in turbulent axial jet flow.

Cases	Particle shape (model)	Diameter [m]	Note
COAL	Non-spherical	Polydispersed	Exp
POLYMER	Spherical	$2.8 \times 10^{-5}$	Exp
SPE_S	Spherical	$2.8 \times 10^{-5}$	CFD
SPE_R	Spherical	Polydispersed	CFD
SPO_S	Spheroid	$2.8 \times 10^{-5}$	CFD
SPO_R	Spheroid	Polydispersed	CFD

parameters in Eqns. (14) and (15) for the spheroidal particle with the sphericity of  $0.85$  are employed to approximate the non-spherical coal particle behavior.

### 4.3 Results and discussion

**Fig. 11** shows the instantaneous and the time-averaged distributions of the Mie scattering intensity obtained by the experiment for (a) pulverized coal COAL and (b) monodispersed polymer POLYMER, and the distributions of the particle number density by the simulation for (c) monodispersed sphere SPE\_S, (d) polydispersed sphere SPE\_R, (e) monodispersed spheroid SPO\_S, and (f) polydispersed spheroid SPO\_R, respectively. Here, the left-hand side of each figure displays the instantaneous distribution, and the right-hand side displays the time-averaged distribution. With focusing on the experimental result, the region that shows the high intensity of Mie scattering for COAL appears near the burner nozzle exit, while that for POLYMER appears at the downstream region from the nozzle exit. For POLYMER the number density of the particles increases once due to the interaction between the turbulent eddies and the particles, while the particles for COAL simply disperse the downstream. In the higher region, the difference turns clearer. POLYMER clusters strongly from the middle to the higher region. In the simulation result, the same concentration downstream from the nozzle exit can be found for the monodispersed cases, SPE\_S and SPO\_S, while the simple dispersion is observed for the polydispersed cases, SPE\_R and SPO\_R. The trend obtained by the simulation agrees with that observed in the experiment. It can be considered that the difference in the region where the peak value of the Mie scattering intensity appears between the two cases in the experiment is mainly attributed to the particle size distribution. It is also found that the higher number density region appears downstream for the spheroid cases rather than that for the sphere cases. This is affected by the difference in the particle shape. In the higher region, while the polydispersed cases tend to randomly disperse in space, the monodispersed cases cluster and form the branch-shaped structure.

**Fig. 12** shows the instantaneous distribution of the particles near the burner nozzle exit for the sphere cases, (a) SPE\_S and (b) SPE\_R. For SPE\_R, the number of the smaller particles which have a short response time is large. They are entrained well by the vortices and the ring-like structure is formed at the nozzle exit. For SPE\_S, since the particles are larger enough to be less likely to trace the vortices due to the longer response time than those observed in SPE\_R, the ring-like structure does not appear.

**Fig. 13** shows the time-averaged width of the region where the traveling particles exist (the dispersion width) in the axial direction. The particle dispersion width monotonously increases in the axial direction for all cases. Between the sphere cases, since the dispersion width for

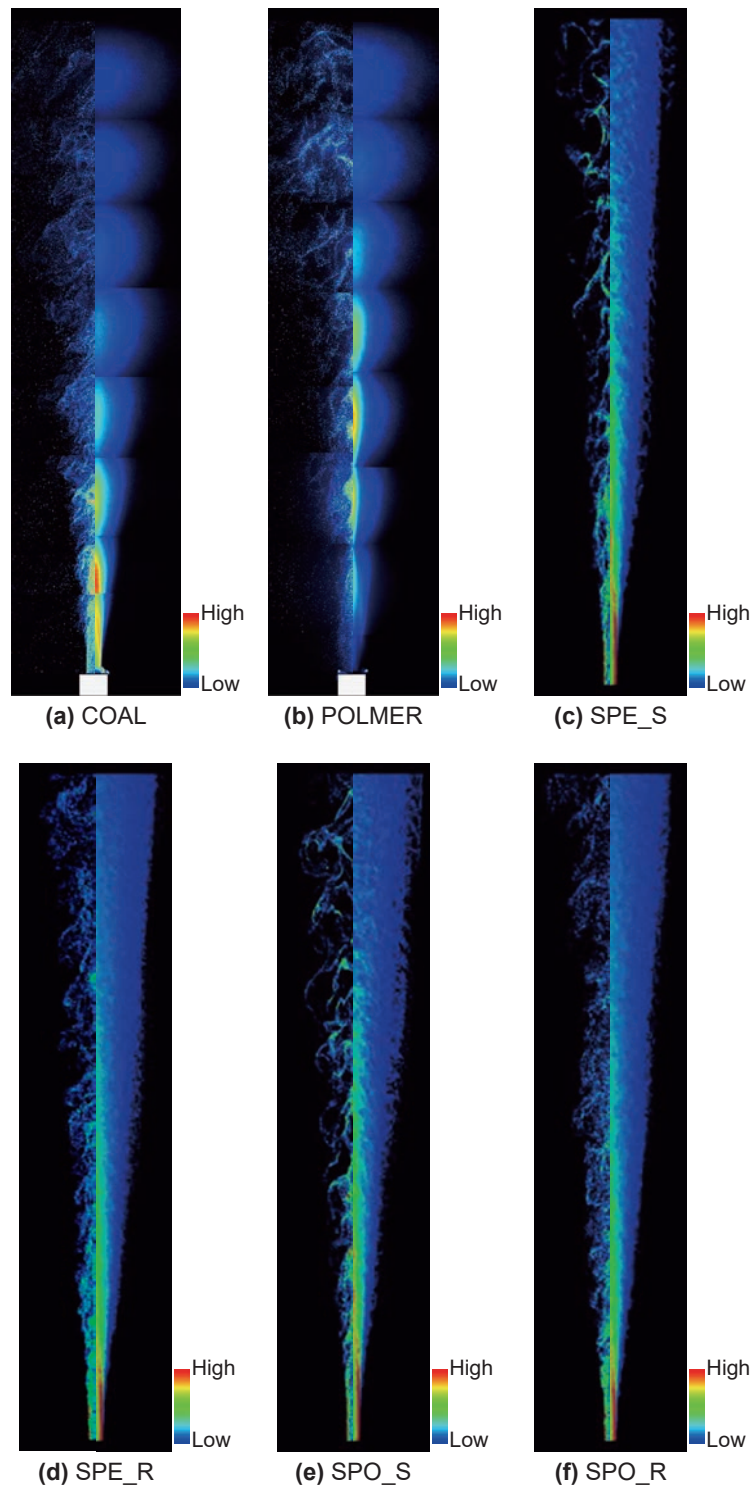


**Fig. 11** Mie scattering intensity in experiments (a) COAL and (b) POLYMER, and number density in CFD (c) SPE\_S, (d) SPE\_R, (e) SPO\_S, and (f) SPO\_R. Reprinted with permission from Ref. (Zhang et al., 2018b). Copyright: (2018) Elsevier B.V.

SPE\_R is larger than that for SPE\_S in the entire region, the particle size distribution significantly affects the dispersion width. On the other hand, between the spheroid cases, the difference in the dispersion width is not observed. It is considered that the particle shape affects the dispersion width.

The characteristic length of the particle clustering is analyzed by RDF as described in the previous section.

**Fig. 14** shows the variation of RDF in the characteristic length scale. It is found that RDF is significantly affected by the particle size distribution, since the monodispersed cases and the polydispersed cases respectively show the individual trend. While RDFs for SPE\_S and SPO\_S are almost the same in the upstream region at  $z = 30$  mm, SPE\_R shows a higher value than SPO\_R in the shorter length scale region. In the middle stream at  $z = 90$  mm, the

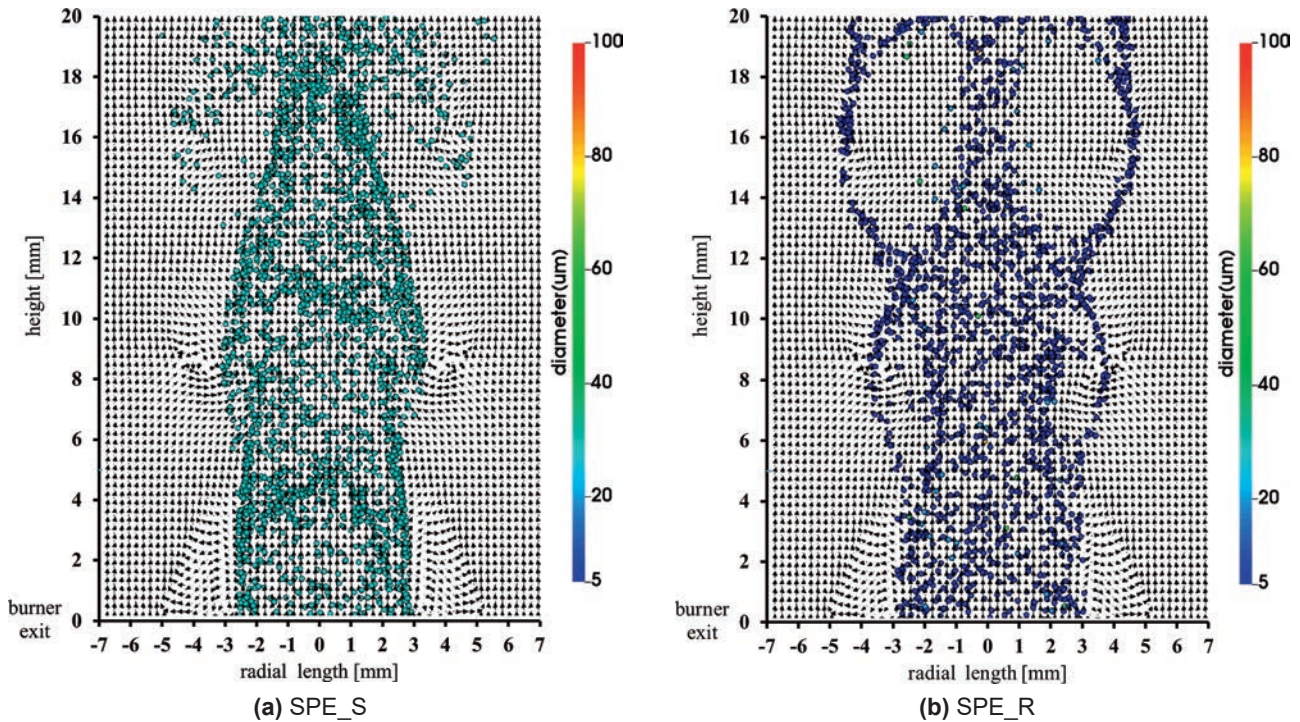


**Fig. 12** Instantaneous particle distribution near burner nozzle exit for (a) SPE\_S and (b) SPE\_R. Reprinted with permission from Ref. (Zhang et al., 2018b). Copyright: (2018) Elsevier B.V.

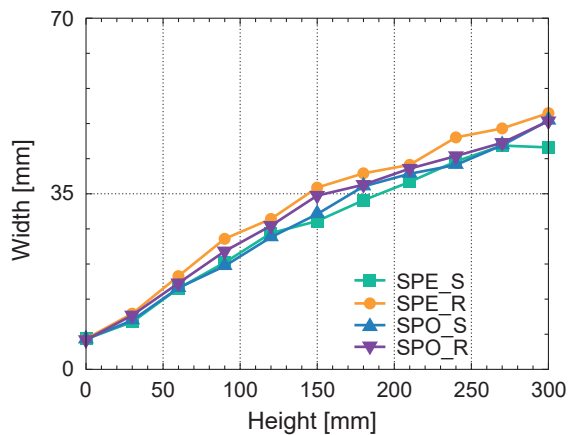


**Fig. 13** Variation of particle dispersion width in axial direction.

difference between SPE\_R and SPO\_R becomes smaller, whereas the value for SPO\_S becomes slightly higher than that for SPE\_S. And then, in the downstream region at  $z = 180$  mm, RDF for SPE\_R almost agrees with that for SPO\_R, while the difference between SPE\_S and SPO\_S becomes marked. From this observation, it is revealed that the effect of the particle shape on their dispersion becomes marked toward the downstream, although the particle size distribution tends to suppress this trend. This behavior should be characterized by the Stokes number. The non-sphericity of the particle changes its apparent Stokes number. In the region where the apparent Stokes number is smaller than the order of unity, the particle dispersion is suppressed, and in contrast, the particle dispersion is enhanced by the larger apparent Stokes number, as dis-

cussed in the previous section. It is considered that the trend observed in the turbulent axial jet in this section also follows this fact.

## 5. Conclusions

This paper describes the reviews of the recent works in the analysis, modeling, and simulation of the motion of a non-spherical particle. The motions of the non-spherical pulverized coal, sphere, and spheroidal particles were analyzed in detail by means of the fully resolved DNS of the six-degree of freedom particle motion by employing the ALE method. It was found that the motion of pulverized coal particle can be reproduced by the spheroidal particle with the equivalent volume. From the detailed analysis of the motion of the spheroidal particle, it was revealed that the PDF of the sine curve can capture the variation of the drag coefficient due to the particle oscillation and rotation.

The motion model based on the six-degree of freedom motion DNS was applied to the particle dispersion simulation in an isotropic turbulent flow by mean of the point mass approximation DNS. The results showed that the effect of the particle shape was clearly observed in the characteristics of the particle dispersion by evaluating the  $D$  number and RDF. It was found that the non-spherical particle's representative Stokes number becomes larger as the sphericity increases.

Furthermore, the proposed motion model was applied to the LES of particle dispersion in an axial jet flow and validated by comparing it with the experimental data. It was revealed that the effects of the particle size distribution

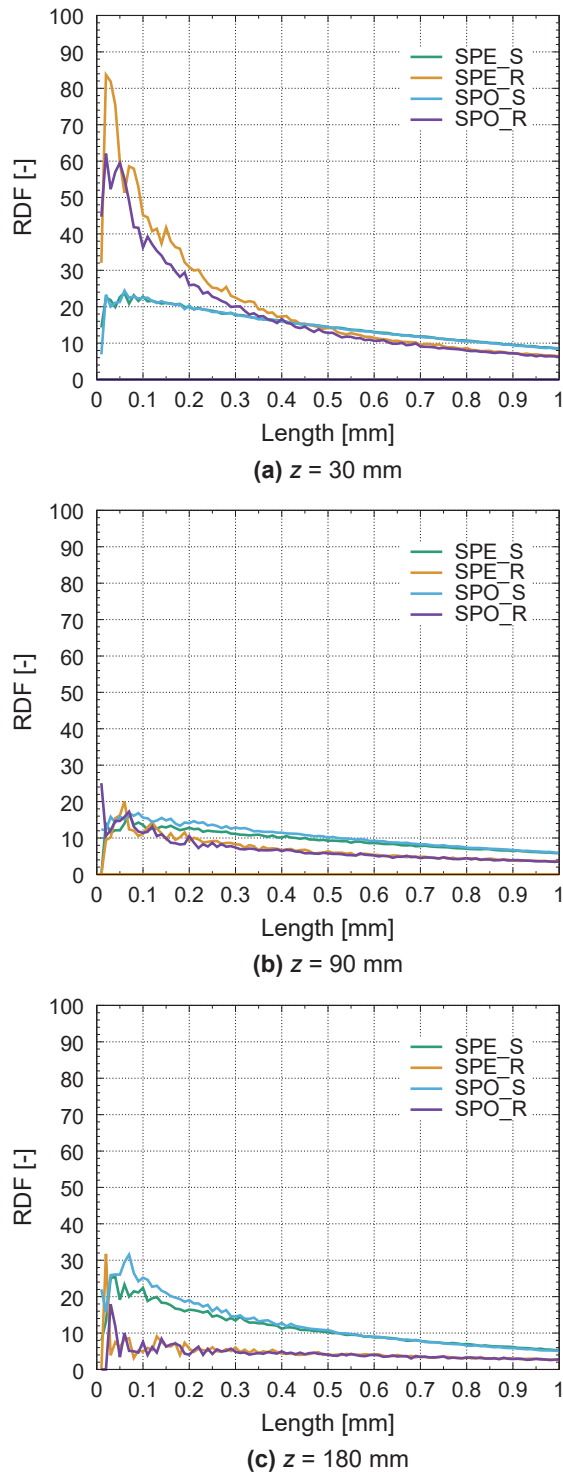


**Fig. 14** Variation of RDF in characteristic length scale for (a)  $z = 30$  mm, (b)  $z = 90$  mm (c)  $z = 180$  mm. Reprinted with permission from Ref. (Zhang et al., 2018b). Copyright: (2018) Elsevier B.V.

and the shape observed in the experiment were precisely captured by the LES that coincided with the trend found in the isotropic turbulent flow.

### Acknowledgements

This study was partly supported by JSPS KAKENHI Grant No. 25420173 and 16K06125, and a grant from the

Information Center of Particle Technology, Japan. HW is grateful to Dr. Kazuki Tainaka of CRIEPI for his great support to conduct the PIV measurement in the experiment.

### Nomenclature

DNS	Direct numerical simulation
LES	Large-eddy simulation
PIV	Particle image velocimetry
RANS	Reynolds-averaged Navier-Stokes simulation
SGS	Subgrid scale
$A$	projection area of particle ( $\text{m}^2$ )
$C_D$	drag coefficient
$d$	particle size (m)
$D$	$D$ number (-)
$F$	force acting on particle ( $\text{kg m s}^{-2}$ )
$g$	gravity ( $\text{m s}^{-2}$ ), radial distribution function
$l$	length (m)
$m$	particle mass (kg)
$N_p$	total number of particle pairs (-)
$p$	pressure (Pa)
$r$	distance of particle pairs (m)
$Re$	Reynolds number (-)
$St$	Stokes number (-)
$t$	time (s)
$\mathbf{u}$	fluid velocity ( $\text{m s}^{-1}$ )
$\mathbf{u}'$	mesh velocity ( $\text{m s}^{-1}$ )
$V$	volume of domain ( $\text{m}^3$ )
$V_p$	particle volume ( $\text{m}^3$ )
$\mathbf{v}$	particle velocity ( $\text{m s}^{-1}$ )
$\phi$	sphericity (-)
$\eta$	Kolmogorov length scale (m)
$\lambda$	mean number of particles (-)
$\mu$	gas viscosity (Pa s)
$\rho_f$	gas density ( $\text{kg m}^{-3}$ )
$\rho_p$	particle density ( $\text{kg m}^{-3}$ )
$\sigma$	stress tensor, standard deviation
$\sigma_{\text{Poi}}$	standard deviation of Poisson distribution
$\tau_p$	particle response time (s)

### References

- Ahn S., Watanabe H., Kitagawa T., Numerical investigation on the detailed structure of a coaxial coal jet flame using large-eddy simulation with elementary reactions, *Energy and Fuels*, 33 (2019) 4621–4631. DOI: 10.1021/acs.energyfuels.9b00734
- Brodady D., Fichman M., Shapiro M., Gutfinger C., Motion of spheroidal particles in vertical shear flows, *Physics of fluids*, 10 (1998) 86–100. DOI: 10.1063/1.869552
- Clift R., Grace J.R., Weber M.E., *Bubbles, Drops, and Particles*, Academic Press, 1978, ISBN: 9780121769505.
- Crowe C.T., Sharma M.P., Stock D.E., The particle-source-in cell (PSI-CELL) model for gas-droplet flows, *Journal of Fluids Engineering*, 99 (1977) 325–332. DOI: 10.1115/1.3448756
- Feng J., Joseph D.D., Glowinski R., Pan T.W., A three-dimensional computation of the force and torque on an ellipsoid settling

- slowly through a viscoelastic fluid, *Journal of Fluid Mechanics*, 25 (1995) 1–16. DOI: 10.1017/S0022112095002217
- Fessler J.R., Kulick J.D., Eaton J.K., Preferential concentration of heavy particles in a turbulent channel flow, *Physics of Fluids*, 6 (1994) 3742–3749. DOI: 10.1063/1.868445
- Haider A., Levenspiel O., Drag coefficient and terminal velocity of spherical and nonspherical particles, *Powder Technology*, 58 (1989) 63–70. DOI: 10.1016/0032-5910(89)80008-7
- Hashimoto N., Watanabe H., Numerical analysis on effect of furnace scale on heat transfer mechanism of coal particles in pulverized coal combustion field, *Fuel Processing Technology*, 145 (2016) 20–30. DOI: 10.1016/j.fuproc.2016.01.024
- Hirt C.W., Amsden A.A., Cook J.L., An arbitrary Lagrangian-Eulerian computing method for all flow speeds, *Journal of Computational Physics*, 14 (1974) 227–253. DOI: 10.1016/0021-9991(74)90051-5
- Holzer A., Sommerfeld M., New simple correlation formula for the drag coefficient of non-spherical particles, *Powder Technology*, 184 (2008) 361–365. DOI: 10.1016/j.powtec.2007.08.021
- Kurose R., Watanabe H., Makino, H., Numerical simulation of pulverized coal combustion, *KONA Powder and Particle Journal*, 27 (2009) 144–156. DOI: 10.14356/kona.2009014
- Moin P., Squires K., Cabot W., Lee S., A dynamic subgrid-scale model for compressible turbulence and scalar transport, *Physics of Fluids A: Fluid Dynamics*, 3 (1991) 2746–2757. DOI: 10.1063/1.858164
- Mordant R., Pinton, J.-F., Velocity measurement of a settling sphere, *European Physical Journal B*, 18 (2000) 343–352. DOI: 10.1007/PL00011074
- Mortensen P.H., Andersson H.I., Gillissen J.J.J., Boersma B.J., On the orientation of ellipsoidal particles in a turbulent shear flow, *International Journal of Multiphase Flow*, 34 (2008) 678–683. DOI: 10.1016/j.ijmultiphaseflow.2007.12.007
- Muto M., Tsubokura M., Oshima N., Negative magnus lift on a rotating sphere at around the critical Reynolds number, *Physics of Fluids*, 24 (2012), 014102. DOI: 10.1063/1.3673571
- Muto M., Watanabe H., Kurose R., Large eddy simulation of pulverized coal combustion in multi-burner system—effect of in-furnace blending method on NO emission—, *Advanced Powder Technology*, 30 (2019) 3153–3162. DOI: 10.1016/j.appt.2019.09.024
- Ooi A., Martin J., Soria J., Chong M.S., A study of the evolution and characteristics of the invariants of the velocity-gradient tensor in isotropic turbulence, *Journal of Fluid Mechanics*, 381 (1999) 141–174. DOI: 10.1017/S0022112098003681
- Rosendahl L., Using a multi-parameter particle shape description to predict the motion of non-spherical particle shapes in swirling flow, *Applied Mathematical Modelling*, 24 (2000) 11–25. DOI: 10.1016/S0307-904X(99)00023-2
- Schlichting H., Gersten K., Krause E., Oertel H., *Boundary-layer Theory*, Vol. 7, Springer (1955), ISBN 0-07-055334-3.
- Watanabe H., Otaka M., Numerical simulation of coal gasification in entrained flow coal gasifier, *Fuel*, 85 (2006) 1935–1943. DOI: 10.1016/j.fuel.2006.02.002
- Watanabe H., Kurose R., Modeling and simulation of coal gasification on an entrained flow coal gasifier, *Advanced Powder Technology*, 31 (2020) 2733–2741. DOI: 10.1016/j.appt.2020.05.002
- Watanabe H., Tanno K., Umetsu H., Umemoto S., Modeling and simulation of coal gasification on an entrained flow coal gasifier with a recycled CO<sub>2</sub> injection, *Fuel*, 142 (2015) 250–259. DOI: 10.1016/j.fuel.2014.11.012
- Zastawny M., Mallouppas G., Zhao F., van Wachem B., Derivation of drag and lift force and torque coefficients for non-spherical particles in flows, *International Journal of Multiphase Flow*, 39 (2012) 227–239. DOI: 10.1016/j.ijmultiphaseflow.2011.09.004
- Zhang W., Tainaka K., Ahn S., Watanabe H., Kitagawa T., Experimental and numerical investigation of effect of particle shape and size distribution on particles' dispersion in a coaxial jet flow, *Advanced Powder Technology*, 29 (2018a) 2322–2330. DOI: 10.1016/j.appt.2018.06.008
- Zhang W., Watanabe H., Kitagawa T., Numerical investigation of effects of particle shape on dispersion in an isotropic turbulent flow, *Advanced Powder Technology*, 29 (2018b) 2048–2060. DOI: 10.1016/j.appt.2018.05.011

## Authors' Short Biographies



### Hiroaki Watanabe

Prof. Hiroaki Watanabe received his Ph.D. from Kyoto University in 2008. He worked as a researcher at Central Research Institute of Electric Power Industry from 1998 to 2014. He joined Department of Mechanical Engineering at Kyushu University as an Associate Professor in 2014 and became a Full Professor of Department of Advanced Environmental Science and Engineering in 2020. His research interest is mathematical modeling and simulation of multiphase turbulent reacting flows. Modeling of co-combustion of solid carbon fuels with carbon-free gaseous fuels is currently being examined.



### Wei Zhang

Dr. Zhang Wei received his Ph.D. from Kyushu University in 2017 and then worked as a doctoral researcher at Kyushu University for half a year. He moved to Nagoya University and worked as a designated Assistant Professor from 2018 to 2020. Now he is a Lecturer working in the College of Mechanical and Transportation Engineering, China University of Petroleum-Beijing. He mainly works on the numerical simulation of gas-solid multiphase reacting flows for carbon conversion, such as the CO<sub>2</sub> methanation, and the gasification of carbon fuels including coal, biomass, and petroleum coke.



# Smart Powder Processing for Excellent Advanced Materials and Its Applications<sup>†</sup>

Makio Naito<sup>1\*</sup>, Takahiro Kozawa<sup>1</sup>, Akira Kondo<sup>1</sup> and C.C. Huang<sup>2</sup>

<sup>1</sup> Joining and Welding Research Institute, Osaka University, Japan

<sup>2</sup> Hosokawa Micron Powder Systems, USA

## Abstract

To create advanced materials with minimal energy consumption and environmental impacts, a green and sustainable powder processing technology is essential. The authors have developed this technique based on powder grinding technology. In this paper, the authors will explain the recent progress of the smart powder processing, and its applications. Firstly, particle bonding process, and novel one-pot processing methods to synthesize nanoparticles, to create nanostructured composite granules and to form nano-porous films on substrates in dry phase will be discussed. Their applications on the advanced material fabrications contributing to the sustainable economy will also be explained. Then, the use of grinding technology in wet processing to synthesize nanoparticles and control their morphology will be explained. Smart powder processing can be a foundation to move forward material development technologies and create many more high-quality advanced materials in the future.

**Keywords:** smart powder processing, particle bonding, lithium-ion battery, fuel cell, thermal insulation material

## 1. Introduction

The 2030 Agenda for Sustainable Development (the 2030 Agenda) is a set of international development goals from 2016 to 2030, which was adopted by the United Nations Sustainable Development Summit held in September 2015 building on the success of Millennium Development Goals (MDGs). The 2030 Agenda listed “Sustainable Development Goals (SDGs)” consisting of 17 goals and 169 targets in order to eradicate poverty and realize a sustainable world. The SDGs are universal goals applicable, not only to developing countries but also developed countries.

Powder technology directly contributes to achieve these goals with a wide range of powder processing technology, and the development of advanced materials is one of the key issues to promote the achievements of these goals (Hosokawa et al., 2007; Naito et al., 2010; 2018). Recently, some novel powder processing techniques have been developed to fabricate the advanced materials. Smart powder processing is a green and sustainable powder processing technology, because it creates advanced materials without consuming a large amount of energy.

In this paper, the authors introduce a smart powder processing developed based on powder grinding technology. Grinding process produces fine particles by giving feed materials the mechanical forces strong enough to break them. From a different viewpoint, the process is thought to be a useful method to act an effective force onto the surface of fine particles for their bonding. This function can be applied for many kinds of particle design and structural control without any heat treatment. **Fig. 1** shows the smart powder processing so far developed by the authors, which was developed based on the concept of the particle bonding process to make advanced composites (Koishi, 1987; Yokoyama et al., 1987; Naito et al., 1993; 2009; Naito and Abe, 2006; Naito and Kondo, 2016). The particle bonding process developed by the authors has many unique features. For examples, it establishes direct bonding between particles without any heat treatment or binders of any kind in the dry phase through the enhanced particle surface activation induced by mechanical energy and the high intrinsic surface reactivity of nanoparticles to fabricate desired composite particles.

As a result, a new one-pot processing method to synthesize nanoparticles without applying extra heat was achieved using particle bonding technique. Furthermore, both the synthesis of nanoparticles and their bonding with other kind of particles to make nanocomposite granules could be completed at the same time, which leading to the possibility of controlling the nano/microstructure of the composite particles/granules and resulting in customized

<sup>†</sup> Received 28 July 2021; Accepted 22 September 2021  
J-STAGE Advance published online 13 November 2021

\* Corresponding author: Makio Naito;  
Add: 11-1, Mihogaoka, Ibaraki, Osaka 567-0047, Japan  
E-mail: m-naito@jwri.osaka-u.ac.jp  
TEL: +81-6-6879-8660 FAX: +81-6-6879-8680



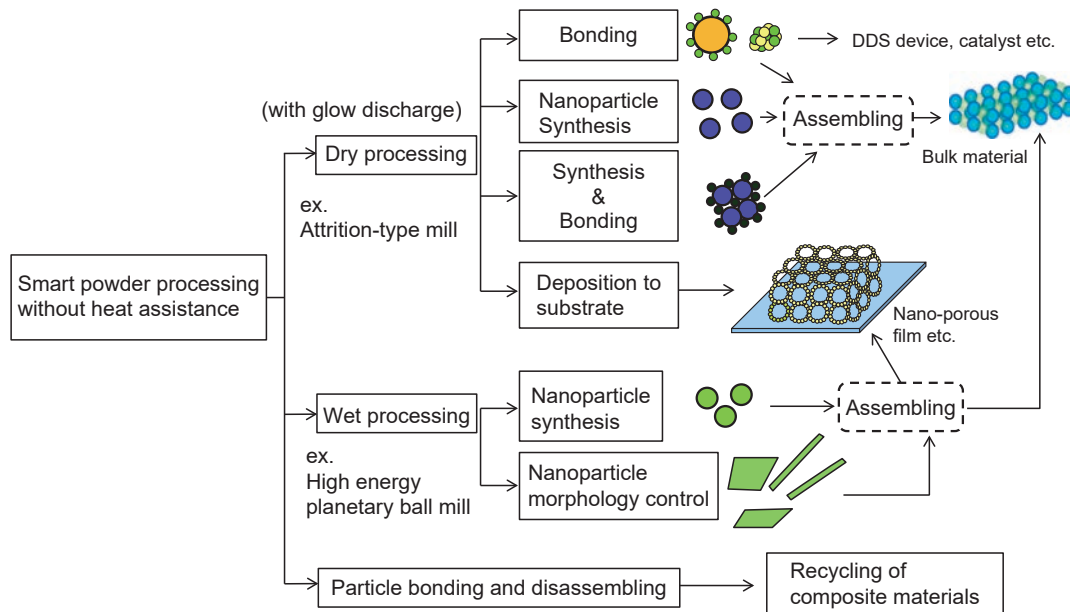


Fig. 1 Smart powder processing developed based on powder grinding technology.

nano/micro structural new materials by a simple manufacturing process. Besides, as shown in Fig. 1, coating nanoparticles on the substrate to form mechanically deposited nano-porous film was also demonstrated. At the first part of this paper, the dry process of the smart powder processing and its applications for developing advanced materials which contribute to saving energy and providing clean energy are explained (Naito and Kondo, 2016; Naito et al., 2009).

Based on the powder grinding technology, the authors recently developed wet mechanical processing method to synthesize nanoparticles and control their morphology from raw materials in liquid without any heat assistance as shown in Fig. 1. At the second part of this paper, the wet process of the smart powder processing will be explained.

In addition, controlling the bonding between different kinds of materials could also make it possible to disassemble them for the purpose of recycling their elemental components. It led to the development of novel technology for recycling composite materials as demonstrated in the literatures (Naito et al., 2009; 2011; Kondo et al., 2010; 2012).

## 2. Particle bonding process

Grinding process is to use mechanical forces from the grinding machines to fracture materials into small pieces. From a different viewpoint, the mechanical forces can also be applied on the surface of particles to create inter-particle bonding effects. Table 1 shows the equipment having been applied for making composite particles (Naito et al., 1993). As seen in the Group I, most kinds of fine grinding

Table 1 Main machines used for particle bonding.

Type/machines		
I	Impaction-type pin mill, disc mill	
	Centrifugal classifying type	
	Attrition-type mill	
	Ball mill tumbling vibration planetary centrifugal fluidizing	
	Agitated ball mill mixing vessel type	
	Jet mill	
	Mortar	
	II	Cylindrical vessel type with rotating disc
		Elliptical vessel type with high-speed elliptical rotor

machines can be used in the particle bonding process. Group II shows the intensive mixing apparatus used for particle bonding applications. Several commercial particle bonding machines have been developed based on their mechanical principles. For example, the MECHANO FUSION® System has a rotating chamber and a fixed arm head with a certain gap against the inside wall of the chamber (Yokoyama et al., 1987; Naito et al., 1993). During its processing, the powder material is pushed next to the inside wall of the rotating chamber by the centrifugal force and is compressed through the gap against the fixed arm head, wherein receiving various kinds of forces, such

as compression, shear, attrition, impact and rolling forces. The processed powder is then dispersed by a scraper in the chamber. Particle bonding effect is created as the above actions repetitively applied to the powder material during the chamber rotation. In addition, an electric discharge option is available to generate glow discharge in vacuum between the fixed arm head and the rotating chamber during the operation to activate nanoparticles (Naito and Abe, 2006).

Prevailing parameters affecting the particle bonding process are summarized in the Fig. 2 (Naito and Kondo, 2016), including the properties of powder materials and the processing conditions.

The properties of powder materials affect the structure and bonding mechanism of composite particles. For making core/shell type composite particles, the particle size ratio between core particles and shell particles should be properly selected. The mixing ratio is also an important factor to form composite particles with a desired structure. For example, the weight fraction of fine particles  $n$  is calculated by the following equation (Naito et al., 1993) assuming the fine particles are closely allocated onto the surface of core particle, and  $d_p \gg d_a$ .

$$n = \left( 1 + \frac{\sqrt{3}}{2\pi} \times \frac{\rho_p}{\rho_a} \times \frac{d_p}{d_a} \right)^{-1} \quad (1)$$

where  $d_p$  : core particle diameter  
 $d_a$  : fine particle diameter  
 $\rho_p$  : true density of core particles  
 $\rho_a$  : true density of fine particles

Eq. (1) is a starting guideline to determine the fine particle fraction. In practice, the fine particle fraction can be selected in a wide range.

As to the bonding mechanism, it depends on the combinations of powder materials and processing conditions. At the contact surfaces between particles, extremely high local temperature and strong mechanical stress were observed

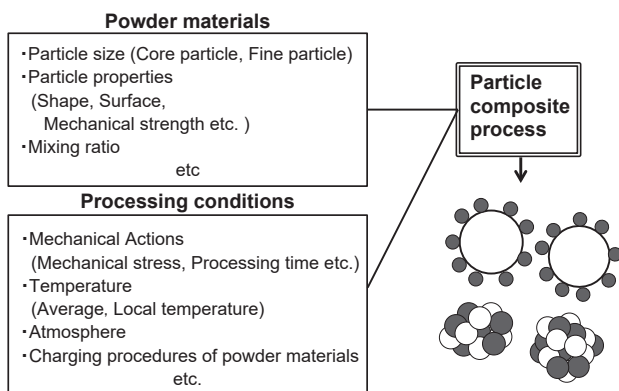


Fig. 2 Factors controlling particle bonding process. Reproduced with permission from Ref. (Naito and Kondo, 2016). Copyright 2016, Elsevier.

(Dachille and Roy, 1960). The local temperature between particles could be ten times higher than the apparent temperature of processing chamber (Nogi et al., 1996). Such a high local temperature could create unique phenomena such as micro-welding or chemical interaction between fine particles and core particles, or among fine particles (Lian et al., 2015).

Apparently, processing conditions such as mechanical actions from the machine rotation can directly affect the performance of particle bonding process. For coating a core particle with fine guest particles, the particle bonding process is proposed as shown in Fig. 3 (Naito et al., 1993). The rotation speed of rotor or chamber and the processing time determine the mechanical actions and its repeated number for processing the powder mixture. This includes two steps: First, the surfaces of fine particles and core particles are mechanically activated, as a result, fine particles adhere onto the surfaces of core particles as the solid line in shown Fig. 3. At this step (Region I in Fig. 3), the BET specific surface area of the composites gradually decreases with processing time. However, at the second step (Region II in Fig. 3), as fine particles deposited on the surfaces of core particles are gradually compacted, BET specific surface area starts leveling off with the processing time, which resulting in lower porosity, smaller pore size, higher mechanical strength of surface layers and stronger bonding between surface layers and core particle. Therefore, the apparent density (porosity and pore size) and strength of surface layers can be controlled by adjusting the rotation speed and its processing time. However, the surface layer formed on the core particle can be fractured

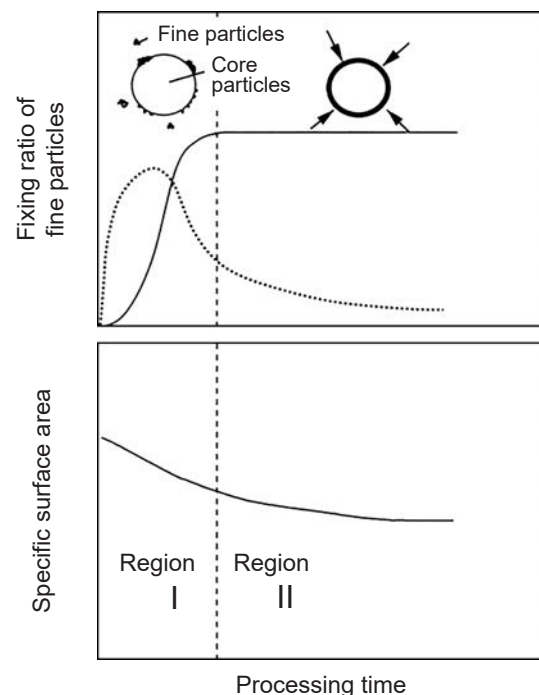


Fig. 3 Particle bonding process for core/fine particles.



after certain processing time if the rotation speed is too high as the dotted line shown in Fig. 3, due to the effect of surface grinding on composite particles (Naito et al., 1993). Besides, Distinct Element Method (DEM) simulation was also applied to a high-speed mixer (Endoh et al., 2004), and to an attrition-type mill (Soda et al., 2012) respectively to elucidate the particle bonding process. Both papers concluded that the motion of core particles, their contact forces and frequencies are important factors to control the particle bonding process.

Temperature and atmosphere during the mechanical processing also affect the performance of particle bonding process. Like the powder grinding operation, particle bonding process generates a large amount of heat. Temperature control is essential when processing heat-sensitive materials. Besides, the processing atmosphere is also important to process powder materials in the dry phase for better products.

To custom the structure of composite particles, the charging procedures of powder materials are critical. Fabricating composite particles with a uniform surface layer of fine particles can be achieved by adding a small amount of fine particles repeatedly into the processed powder at certain time intervals (Naito et al., 1998). As to the multi-layered composite particle, it can be created by adding different kinds of fine powders at certain time intervals. These techniques have been used for many industries including the applications for drug delivery systems (Fukumori et al., 2005).

### 3. Application of particle bonding process for advanced materials

Particle Bonding Process has a lot of potential to develop various kinds of advanced materials. In this section, the authors introduce the following four kinds of advanced materials which are applied for the purpose of energy saving and clean energy related issues.

#### 3.1 Development of high performance thermal insulation materials

The fabrication of highly performance thermal insulation materials by particle bonding process was reported earlier (Abe et al., 2005; Abe et al., 2008). Interest in thermal insulation materials has been intensified globally, because energy saving issues signified the importance of efficient thermal insulation. In this study, nanoparticle bonding process was used to make composite fibers coated with porous fumed silica layer in the dry phase. Fig. 4 shows the proposed dry processing method to fabricate fumed silica compact by using composite fibers (Abe et al., 2005). Fumed silica / fiber composites porously coated with silica nanoparticles were fabricated at the first stage and then compacted into a board by dry pressing. The composites were produced by a particle bonding process without collapsing the fiber glass and with nano-scale pores made by the fumed silica. The proposed method had the advantage of preventing contacts between fibers in the compacts due to the existence of coating layer.

Table 2 shows the composition of the thermal insulation

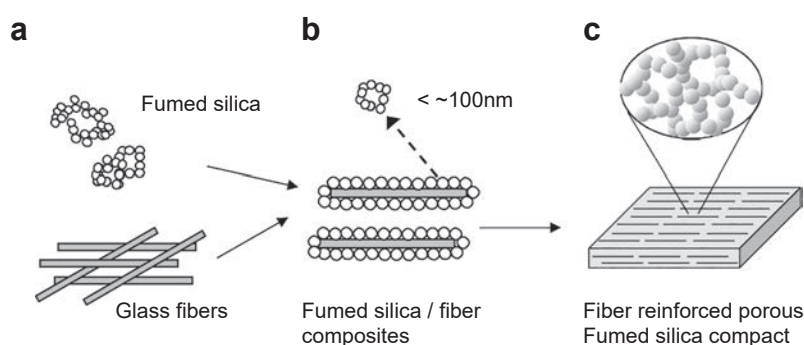


**Fig. 4** Fabrication method of fibrous fumed silica compacts: (a) mixing of raw materials, (b) particle bonding to coat glass fiber with fumed silica, (c) dry pressing of the composites from (b) to produce bulk body. Reproduced with permission from Ref. (Abe et al., 2005). Copyright 2005, John Wiley and Sons.

**Table 2** Composition of the thermal insulation board.

Material	Compounding ratio (mass%)	Average diameter
Fumed silica nano particle (Hydrophilic or hydrophobic)	60	10 nm (Hydrophilic) 12 nm (Hydrophobic)
SiC particle	20	3.3 $\mu\text{m}$
Glass fiber	20	10 $\mu\text{m}$

board (Lian et al., 2015). When the hydrophilic fumed silica nanoparticle is used as starting material, the bonding between hydrophilic glass fiber and nanoparticles in addition to the bonding between nanoparticles is well formed due to the dehydration reaction between OH group on the particle surface. **Fig. 5** shows the thermal conductivity of the hydrophilic fumed silica compact specimens (Lian et al., 2015). The light weight board with 86 % porosity (apparent bulk density: 405 kg/m<sup>3</sup>) was obtained, and its thermal conductivity was 0.031 W/mK at 600 °C. They were lower than molecular conductivity of still air (0.05 W/mK at 400 °C) and at the same level as those obtained from silica aerogel (Kwon et al., 2000) and fumed silica compacts (Smith and Hust, 1989). These results indicated that the obtained compacts had the nano-scale porous structure. The mechanical strength of the compacts depends on their apparent density and the amount of glass fibers as determined by the bending strength. In this case, three-point bending strength was 0.3 MPa. This made it possible to machine the compacts for various applications.

On the other hand, the surface chemical structure of the fumed silica also affects the bonding mechanism between nanoparticles and that between nanoparticles and glass fiber (Lian et al., 2015; 2017). When the hydrophobic fumed silica was used as starting material as shown in **Table 2**, the thermal conductivity of the obtained specimen showed lower value than that made by hydrophilic fumed silica as shown in **Fig. 5**. Since the hydrophobic methyl group decomposed around 400 °C, the thermal conductivity of the compact after 400 °C heat treatment was also measured, and found it was increased by the heat treatment, but still lower than that of the compact with hydrophilic fumed silica. Microscopic observation results made clear that the surface layer thickness of hydrophobic fumed silica on the surface of glass fiber was thinner than that of hydrophilic fumed silica due to weaker bond between particles. Therefore, the hydrophobic fumed silica contributed to lower thermal conductivity of the compact. It means that the raw powder properties are also critical to achieve higher perfor-

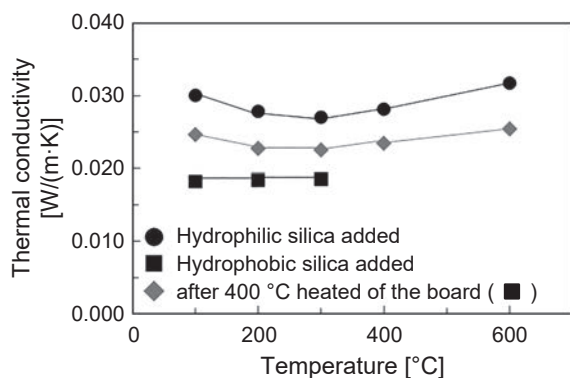


**Fig. 5** Thermal conductivity of thermal insulation boards for temperature. Reproduced with permission from Ref. (Lian et al., 2015). Copyright 2015, Elsevier.

mance for the thermal insulation materials. For example, when fumed alumina nanoparticle and ceramic fiber were selected as the starting powder materials, the thermal conductivity of the obtained bulk compact could achieve lower value than 0.065 W/mK at 1,000 °C. It is a very promising result for thermal insulation materials at very high temperature applications (Tasaka et al., 2020).

### 3.2 Development of fuel cell electrodes

Fuel cell is touted to be the power generation of 21st century because of their high energy efficiency and clean exhaust. The application of particle bonding process for the fuel cell development has been focusing on making composite particles to reduce its production costs and increase the long-term stability of cells and stacks by lowering its operation temperature without losing power density. For controlling the microstructure of composite electrodes, various kinds of composite particles such as large core-particles coated with nanoparticles (Fukui et al., 2004; Hagiwara et al., 2006; Misono et al., 2006) and inter-dispersed composite mixture consisting of several kinds of nanoparticles (Sato et al., 2009) have been successfully fabricated using the particle bonding process.

For the solid oxide fuel cell (SOFC), nickel-yttria stabilized zirconia (Ni-YSZ) was widely used SOFC anode material due to its excellent electrochemical properties at high temperatures. **Fig. 6** shows NiO-YSZ inter-dispersed composite particles consisting of NiO and YSZ nanoparticles processed by particle bonding process (Sato et al., 2009). **Fig. 6(a)** is the SEM micrograph of the composite particles. **Fig. 6(b)** is the detailed structure of a composite particle observed by TEM. NiO and YSZ phases in the composite particle were identified by EDX analysis in the micrograph. The micrograph indicates successful fabrication of the composite particles. NiO and YSZ nanoparticles were well dispersed and their sizes were in good agreement with those estimated from the specific surface area of starting particles (NiO: 160 nm and YSZ: 75 nm).

**Fig. 7** shows SEM micrographs of the anode made of composite particles before the reduction operation, just

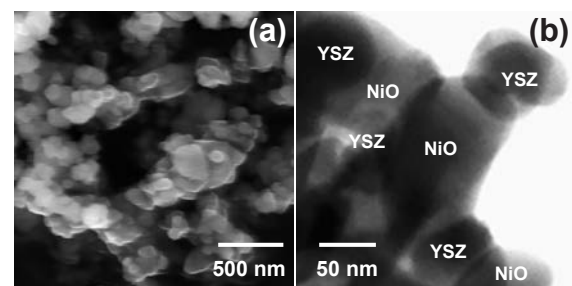


**Fig. 6** NiO-YSZ inter-dispersed composite particles: (a) SEM image, (b) TEM image. Reproduced with permission from Ref. (Sato et al., 2009). Copyright 2009, Elsevier.

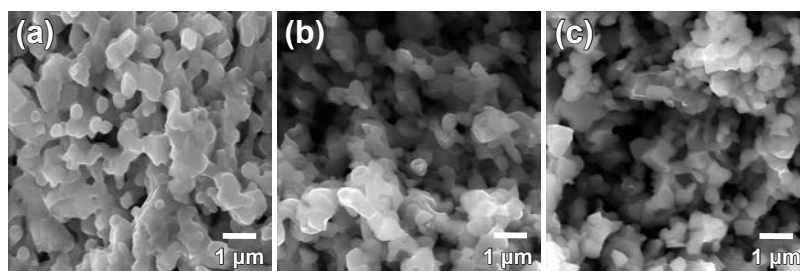


**Fig. 7** Cross-sectional SEM images of the anode: (a) before reduction (b) after reduction (c) after long-term stability test at 700 °C for 920 h. Reproduced with permission from Ref. (Sato et al., 2009). Copyright 2009, Elsevier.

after the reduction operation, and after the long-term stability test at 700 °C for 920 h (Sato et al., 2009). Before the reduction operation, the grain size of the anode was smaller than 1 μm without unusually large ones. The NiO shrunk when it was reduced to Ni and producing porous structure in the anode. Thus, the uniform porous structure after reduction as seen in the **Fig. 7(b)** suggests that Ni was uniformly distributed around the three-dimensional YSZ framework in the entire anode. In addition, there was no significant structural change even after the long-term stability test. The grain size was kept at about 0.5 μm without large grains, which indicating the insignificant grain growth of Ni in the anode made of inter-dispersed composite particles under the testing conditions and exhibiting lower polarization than the anode made of coated composite particles prepared by the authors (Fukui et al., 2004). Controlling the microstructure of composite particles as the starting materials for SOFC anode fabrication is the key to improve its performance.

Particle bonding process is also effective to develop superior electrode of molten carbide fuel cell (MCFC). For example, Ni particles uniformly coated with fine CoO particles were prepared by particle bonding process (Fukui et al., 2000; 2001). A new cathode structure, where the NiO core coated with an outer layer of lithiated cobalt and nickel solid-solution oxide (Li(Co,Ni) oxide), was formed by oxidation and lithiation using the CoO/Ni composite particles. As a result, the solubility of nickel in this Li(Co,Ni) oxide layer into carbonate melt decreased to two-thirds of that of NiO when used as a cathode for MCFCs. Other examples made by the particle bonding process were filament shaped Ni particle uniformly coated by CoO fine particles, and that by MgFe<sub>2</sub>O<sub>4</sub> fine particles as starting material, respectively. The cathode made by the starting composite particles showed lower solubility of nickel into carbonate melt (Fukui et al., 2003).

Furthermore, particle bonding process was applied to develop low-platinum catalyst for polymer electrolyte fuel cell (PEFC) (Munakata et al., 2011). Composite catalyst consisting of tungsten carbide (WC) and platinum/carbon (Pt/C) was fabricated by bonding them together in the dry phase. Small Pt particles with thin carbon layer was

observed on the surface of WC particles in the composite catalyst by TEM analysis. The composite catalyst showed a similar catalytic reactivity to that from pristine Pt/C catalyst for hydrogen oxidation with about 25 % of Pt loading (Munakata et al., 2011). It suggests that the particle bonding process is a promising way to develop low cost catalysts for PEFC.

### 3.3 Development of CNT/Al composites

The advanced carbon nanomaterials with extraordinary mechanical and physical properties, represented by carbon nanotubes (CNTs) and graphene nanosheets, are regarded as ideal reinforcements for developing high performance structural composites. Recently, great efforts have been done to develop carbon nanotubes reinforced aluminum matrix composites, due to the urgent need in many areas such as transportation for advanced light weight structural materials with good stiffness and ductility. For this purpose, a new powder metallurgy route via combination of particle bonding process and shift-speed ball milling process was developed (Chen et al., 2018; 2019). At first, CNTs were well dispersed and uniformly coated on the surface of 6061 Al particles by particle bonding process. Then, the composite particles were processed by a planetary ball mill at low rotation speed for 6 h to make CNT/6061Al flake particles, and processed at high rotation speed for 1 h to make cold welded CNT/6061 Al particles. The obtained composite particles were cold pressed, consolidated by sintering, and hot extruded into rod samples. As a result, the extruded 1.5 mass% CNT/6061Al composites exhibited simultaneous enhancement in Young's modulus, tensile strength and ductility, compared to the counterpart without particle bonding process at the first step (Chen et al., 2018).

### 3.4 Development of all-solid-state Li-ion batteries and traditional Li-ion batteries

All-solid-state Li batteries (ASS-LIBs) are suitable applications of 5 V-class cathode materials with high energy densities. However, it was hard to fabricate bulk-type batteries composed of a mixture of active materials and

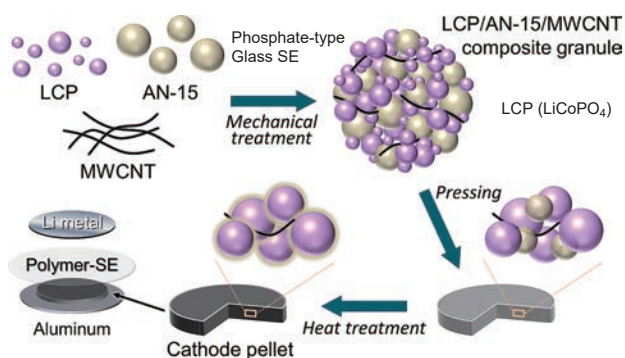


**Fig. 8** The assembling process of bulk-type all-solid-state Li-ion batteries. Reproduced with permission from Ref. (Kozawa et al., 2019b). Copyright 2019, Springer Nature.

solid electrolytes because of the difficulty of ensuring a conductive path and suppressing the formation of reactive layers at the interface. To solve this problem, the authors proposed the assembling procedures of the composite cathode and the ASS-LIBs as shown in Fig. 8 (Kozawa et al., 2019b). The first step was the mechanical treatment of the composite  $\text{LiCoPO}_4$  (LCP) granules by particle bonding process. The granule was inter-dispersed composite particle containing the LCP, phosphate-type glass solid electrolyte (AN-15), and multi-walled carbon nanotubes (MWCNT) as the conductive material. They were homogeneously dispersed and organized a network structure as shown in Fig. 8. Then, the produced composite granules were shaped into pellets by pressing. The heat treatment at low temperature brought the AN-15 in close contact with the LCP through softening. The ASS-LIB were assembled by using a Li metal anode and a polymer-solid electrolyte (polymer-SE) film, so that the properties of composite LCP cathodes could be evaluated.

Fig. 9 shows STEM-EELS measurements performed at the interface between LCP and AN-15 solid electrolyte of the cathode pellet. The spectra were collected with a step size of 2 nm. The interface between LCP bulk and SE bulk (AN-15) did not reveal any gaps. The EELS data for the Co-M edge at  $\sim 780$  eV was collected in the direction from SE bulk to LCP bulk. It revealed no band of the Co-M edge was detected in the region of existence of AN-15. It was concluded that the mechanical and subsequent heat treatment resulted in a good interface between LCP and the AN-15 particles without any Co diffusion. As a result, the first discharge capacity was a bit lower than that of traditional LCP/Li battery using organic liquid electrolytes, but the discharge capacities kept higher value up to 20 cycles. In another case, the inter-dispersed composite granule of  $\text{LiCoO}_2/\text{Li}_{1.3}\text{Al}_{0.3}\text{Ti}_{1.7}(\text{PO}_4)_3$  was fabricated by the particle bonding process to make the cathode for ASS-LIBs with good results (Nakamura et al., 2016).

Furthermore, the particle bonding process was also applied to improve the anode performance of traditional

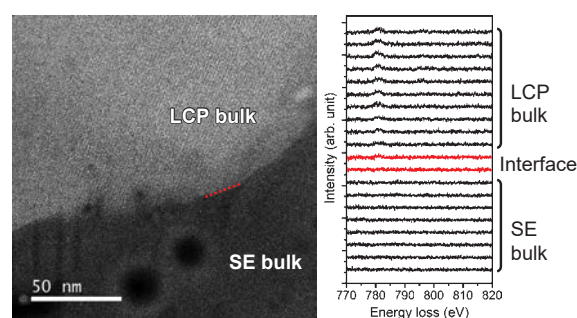


**Fig. 9** STEM-EELS measurements performed at the interface between LCP and AN-15 solid electrolyte (SE) of the cathode pellet. Reproduced with permission from Ref. (Kozawa et al., 2019b). Copyright 2019, Springer Nature.

Li-ion batteries. For example, silicon can be used as anode material due to its high theoretical specific capacity and a relatively low working voltage. However, silicon experiences the large volume changes up to 300 % associated with lithium ion, which leads to poor electrochemical properties caused by loss of the electrical contact between active materials and other effects. To overcome this problem, a new structure of the anode was proposed (Lee et al., 2020). It is the silicon/graphite granular composite with uniform amorphous carbon coating layer. Besides, the granule has uniform inner free space to buffer the volume change of silicon. Actually, the granule was prepared by spray-drying process, and its outer layer was coated with pitch by particle bonding process. Then, the composite granule was heated at  $800^\circ\text{C}$  to form the amorphous carbon coating layer. The pouch cell made by using the composite granule showed good long-term cycle properties with the capacity retention 71 % over 500 cycles at 1 C rate.

#### 4. One-pot mechanical synthesis of nanoparticles without heat assistance

Material synthesis at low temperature using particle bonding process began with the attempt to create  $\text{MgB}_2$  from raw powders (Abe et al., 2003; 2006). Mechanically processed large magnesium particles and submicron amorphous boron particles could embed boron particles into the surface of magnesium particle. Also,  $\text{MgB}_2$  was found at this embedded region after being annealed at a low temperature under argon atmospheric pressure.

Particle bonding process with low temperature plasma discharge was also applied to dope  $\text{TiO}_2$  nanoparticles with nitrogen without providing any heat (Abe et al., 2006), which usually accomplished (Asahi et al., 2001) at  $500\sim 600^\circ\text{C}$  under  $\text{NH}_3$  flow. Since high temperature could cause undesirable grain-size growth of  $\text{TiO}_2$  nanoparticles, particle bonding process with low temperature plasma discharge was preferable for this application (Naito and Abe, 2006).  $\text{NH}_3$  (10 %)/Ar plasma was generated at different

gas pressures in a particle bonding processing chamber, where an anatase  $\text{TiO}_2$  powder with a BET specific surface area of  $300 \text{ m}^2/\text{g}$  was processed and uniformly irradiated. As generated plasma irradiation at 300 Pa, the  $\text{TiO}_2$  powder had a specific surface area of  $283 \text{ m}^2/\text{g}$ , and, noticeable absorption in visible light range was observed. In addition, the powder showed an improvement of the photo-catalytic oxidation activity of  $\text{CH}_3\text{CHO}$  under visible light. These results indicate that the presented plasma-enhanced particle bonding processing is capable of modifying  $\text{TiO}_2$  nano-powder to improve its photo-reactivity without much reduction in specific surface area.

Using the features of particle bonding process, new one-pot processing to synthesize nanoparticles without any heat support was developed. First, a rapid synthesis of perovskite type lanthanum manganite starting with a mixture of industrial grade powders was demonstrated (Sato et al., 2006; Ohara et al., 2008a). Traditionally,  $\text{LaMnO}_{3+\delta}$  was synthesized through the solid-state reaction of component oxide powders such as  $\text{La}_2\text{O}_3$  and  $\text{Mn}_3\text{O}_4$  at  $1300 \text{ }^\circ\text{C}$ , which required many manufacturing steps. Particle size enlargement during the thermal reaction and limited degree of chemical homogeneity with some impurities during the powder processing have been an issue for its producers. However, with the rapid mechano-chemical synthesis, one-pot synthesis of  $\text{LaMnO}_{3+\delta}$  from a mixture of industrial grade  $\text{La}_2\text{O}_3$  and  $\text{Mn}_3\text{O}_4$  could be accomplished without using any heat. The one-pot processing was applied mechanical forces from the particle bonding process to achieve the solid state reaction on the powder mixture without using ball media.

Adding to the synthesis of  $\text{LaMnO}_{3+\delta}$ , **Table 3** summarizes the examples of nanoparticles synthesized by the one-pot mechanical method. It shows various kinds of composite oxides have been synthesized by the one-pot processing. For example, YAG: $\text{Ce}^{3+}$  phosphor is used for white light emitting diodes (LEDs) of next generation lighting. LED is a highly energy-efficient lighting technology, and has the potential to fundamentally change the future of lighting. Widespread use of LED lighting can have

greatest impact on energy savings worldwide. However, YAG: $\text{Ce}^{3+}$  phosphor has been manufactured by solid-state reaction at over  $1600 \text{ }^\circ\text{C}$ . To achieve low cost manufacturing of the phosphor with more energy saving process, drastic decrease of the calcination temperature is essential.

To decrease the synthetic temperature of solid-state reaction, the addition of  $\text{BaF}_2$  and  $\text{YF}_3$  was usually used as fluxes. Therefore, the authors achieved the YAG: $\text{Ce}^{3+}$  nanoparticle synthesis by applying the one-pot mechanical synthesis from  $\text{Y}_2\text{O}_3$ ,  $\text{Al}_2\text{O}_3$  and  $\text{CeO}_2$  with  $\text{BaF}_2$  (Kanai et al., 2017) and those with  $\text{YF}_3$  (Kanai et al., 2018). This synthesis route is very promising as a novel energy saving process. The only concern was the flux must be removed from the product after the synthesis. Now, further research work to develop one-pot synthesis of YAG: $\text{Ce}^{3+}$  without any flux materials is on-going.

## 5. One-pot mechanical process to synthesize nanoparticles and their bonding to make nanocomposite granules

The motivation to make nanocomposite granules was raised by the development of the cathode of lithium-ion batteries (LIBs). For example, lithium-ion phosphate ( $\text{LiFePO}_4$ ) is one of the key cathode materials for use in large-format LIBs, due to its intrinsic structural and chemical stability that leads to the safety and long cycle life of the batteries. Nevertheless, it has two main obstacles inherent to the practical applications i.e. slow kinetics of lithium-ion diffusion coefficient and poor electronic conductivity. To improve these undesirable properties, the particle size reduction to nano-scale dimensions and the conductive coating on their surfaces become necessary. However, these two approaches lead to another problem i.e. decreasing packing density of electrode, which causes an issue on the energy density of LIBs. One of the breakthrough for this unfavorable problem is to prepare granule particle which has the internal pores to encourage the penetration of electrolyte. As a result, the ideal structure of the

**Table 3** Examples of synthesized nanoparticles and its applications by the one-pot mechanical method.

Synthesized nanoparticles	Applications
$\text{BaTiO}_3$ (Kondo et al., 2006; Ohara et al., 2008b)	Dielectric material
$\text{LiCoO}_2$ (Kondo et al., 2014)	Li-ion battery
$\text{LiMnPO}_4$ (Yoshida et al., 2013)	
$\text{LiFePO}_4$ (Kozawa et al., 2014a; 2015)	
$\text{LiCoPO}_4$ (Matsuoka et al., 2017)	
$\text{LiNi}_{0.5}\text{Mn}_{1.5}\text{O}_4$ (Kozawa et al., 2014b; Kozawa and Naito, 2015)	
$\text{La}_{0.8}\text{Sr}_{0.2}\text{MnO}_3$ (LSM) (Chaichanawong et al., 2006)	Fuel cell (SOFC)
$\text{La}_{0.6}\text{Sr}_{0.4}\text{Co}_{0.2}\text{Fe}_{0.8}\text{O}_3$ (Xi et al., 2015)	
$\text{Y}_{2.97}\text{Al}_3\text{O}_{12}:\text{Ce}^{3+}_{0.03}$ (Kanai et al., 2017; 2018)	Phosphor for LED

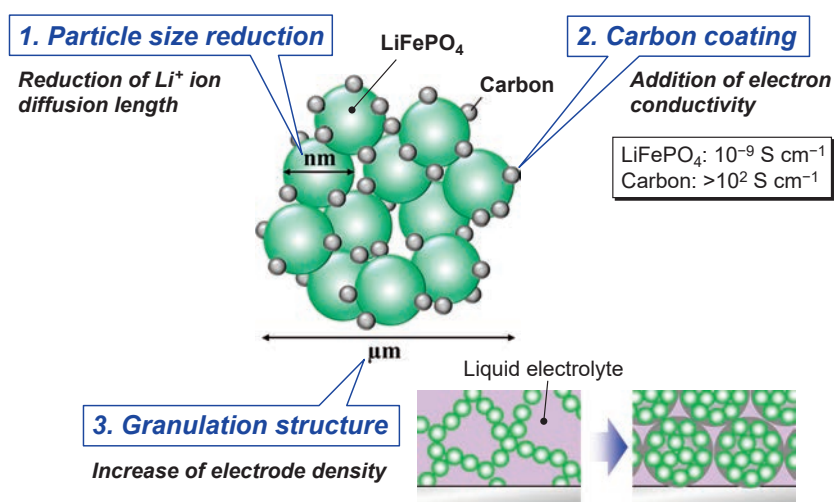


**Fig. 10** LiFePO<sub>4</sub>/C composite granule consisting of nano-sized LiFePO<sub>4</sub> and carbon.

starting material of LiFePO<sub>4</sub> cathode is designed as shown in **Fig. 10** (Kozawa et al., 2014a).

To make the structure, conventional process begins with the synthesis of LiFePO<sub>4</sub> by solid-state reaction which needs calcination step controlling the atmosphere by flowing inert or slightly reductive gases to prevent the oxidation from Fe(II) to Fe(III). Then, the surface coating on the synthesized LiFePO<sub>4</sub> with a carbon, and the subsequent granulation process is required to prepare the aimed LiFePO<sub>4</sub>/C composite granule as shown in **Fig. 10**. However, an ultimate synthesis method for the structure is a direct formation from raw materials under ambient atmosphere.

To achieve this purpose, one-pot mechanical process was applied. Starting materials, Li<sub>2</sub>CO<sub>3</sub>, FeC<sub>2</sub>O<sub>4</sub>·2H<sub>2</sub>O and NH<sub>4</sub>H<sub>2</sub>PO<sub>4</sub> were selected, and ketjen black was used as conductive carbon. The additive of carbon was also helpful to improve the flow abilities of raw powders. The powders were put into the chamber of attrition-type mill and the mechanical synthesis was carried out below 4,500 rpm for 20 min. The processing of attrition-type mill was done under ambient atmosphere.

**Fig. 11** shows the XRD patterns of the products (Kozawa et al., 2014a). In spite of the presence or absence of carbon, LiFePO<sub>4</sub> was formed by the mechanical treatment under ambient atmosphere. Synthesis of LiFePO<sub>4</sub> usually requires inert or reductive gases to prevent the iron oxidation. Therefore, this process has a great advantage over the conventional LiFePO<sub>4</sub> synthesis. The effect of carbon addition appeared in the formation of by-product phase. In the case of the mechanical treatment without carbon, impurities were detected as by-products. The oxidation state of iron in Li<sub>3</sub>Fe<sub>2</sub>(PO<sub>4</sub>)<sub>3</sub> is trivalent, so that iron oxidation takes place during the mechanical treatment without carbon. On the other hand, by adding the carbon, the formation of trivalent iron compound was suppressed, though trace

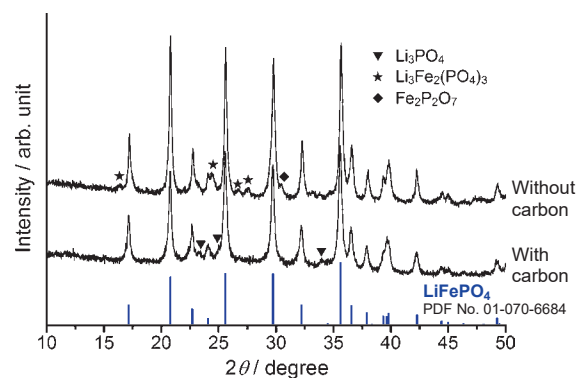


**Fig. 11** XRD patterns of LiFePO<sub>4</sub> synthesized by one-pot mechanical process. Reproduced with permission from Ref. (Kozawa et al., 2014a). Copyright 2014, Elsevier.

amount of Li<sub>3</sub>PO<sub>4</sub> was detected. The carbon addition on the mechanical treatment exerted an important role in the prevention of iron oxidation as well as the improvement of conductivity and powder flow ability. Besides, applying higher electric power in the mechanical synthesis, a single phase of LiFePO<sub>4</sub> could be obtained in a shorter time.

**Fig. 12** shows the microstructure of nanoporous LiFePO<sub>4</sub>/C composite granules prepared by the one-pot mechanical process (Kozawa et al., 2015). As expected from **Fig. 10**, the granule was composed of synthesized LiFePO<sub>4</sub> nanoparticles, and its inside had nanoporous structure as shown on the fracture surface in **Fig. 12**, **Fig. 13** shows the discharge capacity and coulombic efficiency against the cycle number at 0.1 C rate (Kozawa et al., 2015). The discharge capacity gradually increased and reached to 130 mAh/g after 15 cycles. This might be due to the slow penetration of electrolyte into the granules while the coulombic efficiency kept constant at 94–96 % during the cycles. Further design improvement of the granule including the pore structure should be done to advance the performance of the cathode.

The one-pot mechanical process was also applied to prepare nanocomposite granules as the starting materials for the cathode of SOFC (Hosokawa et al., 2014; Xi et al., 2016). In this case, the one-pot mechanical process achieved not only electrocatalyst nanoparticles synthesis from the raw powder materials but also their bonding with solid electrolyte nanoparticles to form inter-dispersed composite granules. The purpose of the composite granule was to create the triple phase boundary (TPB) region as broad as possible while maintaining sufficient porous channels for gas diffusion in the resultant cathode. Actually, the authors prepared the following two kinds of composite granules for this purpose. The first one was the combination of strontium doped lanthanum manganite (LSM) as electrocatalyst and scandium stabilized zirconia (ScSZ) as solid electrolyte (Hosokawa et al., 2014). The second one was the combination of  $\text{La}_{0.6}\text{Sr}_{0.4}\text{Co}_{0.2}\text{Fe}_{0.8}\text{O}_3$  (LSCF) as electrocatalyst and  $\text{Ce}_{0.9}\text{Gd}_{0.1}\text{O}_{1.95}$  (GDC) as solid electrolyte (Xi et al., 2016).

In the latter case, commercially available  $\text{La}_2\text{O}_3$ ,  $\text{Sr}(\text{OH})_2$ ,  $\text{Co}_3\text{O}_4$  and  $\text{Fe}_2\text{O}_3$  with stoichiometric quantities were put into the chamber with one-fifth of the total amount of GDC nanoparticles, and then, the powders were mechanically treated under ambient atmosphere without external heating. During the mechanical processing, one-

fifth of the total amount of GDC powder was added every 4 min. The total processing time was 20 min. The XRD pattern of the composite particles after 20 min. processing exhibited mainly LSCF and GDC phase, and they formed inter-dispersed nanocomposite granules wherein both elements were uniformly dispersed. The obtained cathode after sintering exhibited a finely composed porous structure consisting of fine grains ranging from nano to submicron sizes. It indicated that quite low polarization resistance in the intermediate temperature range. The obtained results suggest that the one-pot mechanical process is a very promising, simple, and energy-saving approach for producing high-quality LSCF-GDC composite powders.

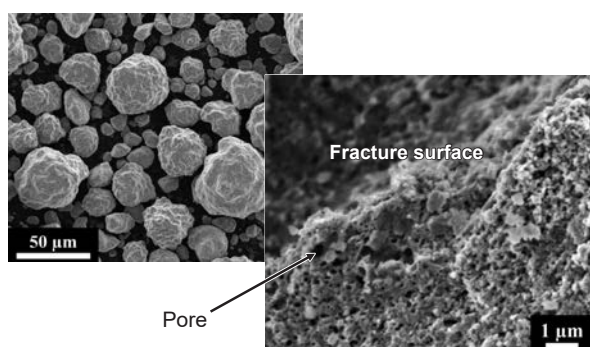
## 6. Mechanically assisted deposition of nanocomposite film by one-pot processing

To make porous composite films with a large surface area for chemical sensing and energy storage/conversion, direct deposition of mechanically activated nanocomposite particles on the substrates in the dry phase is desirable.

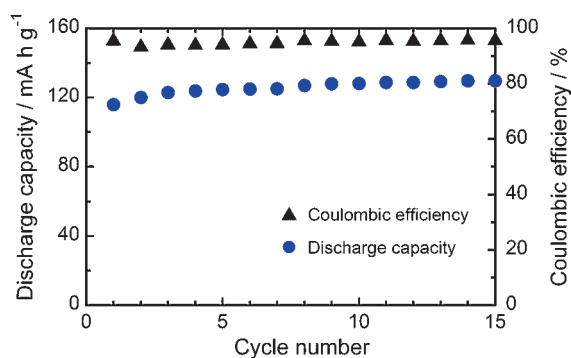
Primarily, the apparatus used in this study (Abe et al., 2012) consisted of a closed vessel and a feather-type rotor. As an example, the anode of Nickel-yttria stabilized zirconia (Ni-YSZ) cermet was fabricated on YSZ substrate by this apparatus. NiO/YSZ composite particles were first put into the chamber and dispersed by the rotor. The dispersed and mechanically activated particles were then transported to the substrate and deposited on it. As reported by Akedo (Akedo, 2006), dense ceramic layer consisting of fractured particles or deformed particles could be successfully formed on the substrate when the ceramic particles speeded up to 100–500 m/s. On the contrary, it was demonstrated that the fine aggregates or clusters could be bonded together at a much lower impact speed of about 30 m/s for making the porous films. Besides, the rapid film formation was found with the nanoparticles due to their high specific surface area.

Fig. 14 shows the effect of the processing time on the thickness of the deposited film with the NiO-YSZ nanoparticles ( $120 \text{ m}^2/\text{g}$ ) (Abe et al., 2012). Noticeable film formation was found at  $\sim 10$  min after starting the process, which indicating that the fine aggregates of the nanocomposite particles were formed and activated in the early stage of the processing and started to deposit on the substrate at an impact speed of about 30 m/s. No unusually large grain was found on the porous film after the heat treatment at  $1200^\circ\text{C}$ . The fine composite microstructure was a result of the homogeneously distributed NiO and YSZ nanograins in the deposited film. The polarization of the porous film as the anode of SOFC showed good performance as reported by Abe etc. (Abe et al., 2012).

The deposition process can be also applied to suppress



**Fig. 12** Microstructure of nanoporous  $\text{LiFePO}_4/\text{C}$  composite granules. Reproduced with permission from Ref. (Kozawa et al., 2015). Copyright 2015, Elsevier.



**Fig. 13** Cycle performance of the synthesized  $\text{LiFePO}_4/\text{C}$  composite granules at 0.1 C rate. Reproduced with permission from Ref. (Kozawa et al., 2015). Copyright 2015, Elsevier.

the mold growth on the surface of materials (Nomura et al., 2018). Mold growth can trigger a variety of serious human health problem such as allergies and asthma. Designing surface unfavorable for the adhesion of fungal spores was considered an effective method to prevent fungal growth. In this study, the effect of hydrophilic surface treatment on the adhesion of fungal spores onto substrates was investigated using *Aspergillus oryzae* as a model fungus. The glass substrate coated with hydrophilic fumed silica (BET equivalent diameter: 7 nm) was prepared using this method. As a result, the fungal spores that strongly adhered on the coated glass substrate under atmosphere conditions were easily removed by lightly hand-washing in water. In addition, the removal ratio of the fungal spores on the coated glass was higher than that on plasma-treated glass. Atomic force microscopy revealed that there was almost no adhesive force between the spores and the glass substrate coated with fumed silica.

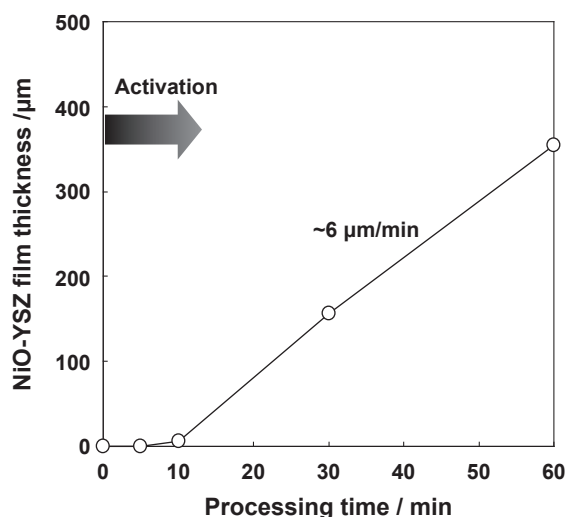


**Fig. 14** Relationship between film thickness and processing time. Reproduced with permission from Ref. (Abe et al., 2012). Copyright 2012, John Wiley and Sons.

## 7. Wet mechanical processing to synthesis nanoparticles and their morphology control

Wet mechanical processing has been used to synthesize particles for years. For example, particle synthesis via solid-solution reaction incorporating mechanical actions by using a multi-ring media mill was pioneered by Riman's group (Shuk et al., 2001; Suchanek et al., 2002). However, variations of particle synthesized by conventional wet mechanical approach are still limited, and the particle preparation with specific morphologies has not been accomplished yet.

The authors applied grinding apparatus used for the particle bonding to synthesize nanoparticles with a unique structure in the wet phase. At first, the synthesis of unique morphology of lithium titanate hydrate,  $\text{Li}_{1.8}\text{H}_{0.19}\text{Ti}_2\text{O}_5 \cdot x\text{H}_2\text{O}$  (LHTO) was done by applying a high energy planetary ball mill (Suzuki et al., 2017). This material is used as a precursor of  $\text{Li}_4\text{Ti}_5\text{O}_{12}$  (LTO), a typical LIB anode material. The traditional hydrothermal methods to synthesize LHTO were constrained by the restrictive preparation requirements, such as handling moisture-sensitive titanium precursors and high concentration NaOH solutions. In contrast, the high energy planetary ball mill enabled us to achieve the synthesis and morphology control of LHTO only by using low-cost materials (LiOH and  $\text{TiO}_2$ ) at room temperature.

**Fig. 15** shows the TEM images of the raw  $\text{TiO}_2$  powder and the products after planetary ball milling at 150 G up to 10 h (Suzuki et al., 2017). The  $\text{TiO}_2$  powder used consisted of ultrafine nanoparticles of approximately 5 nm in diameter. After the planetary ball milling, thin sheets of LHTO were formed, and the widespread LHTO sheets were formed after 3 h as shown in the figure. Then, the LHTO sheet was transformed into the nanotube morphology by curling after 5 and 10 h. Direct formation of LHTO

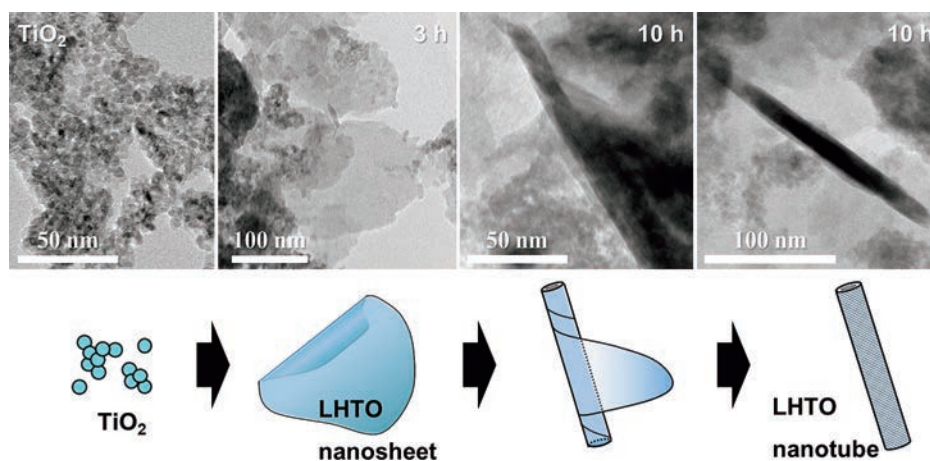


**Fig. 15** TEM images of the raw  $\text{TiO}_2$  particles and the products after milling at 150 G for 3 h and 10 h. Reproduced with permission from Ref. (Suzuki et al., 2017). Copyright 2017, Elsevier.



nanotubes was successfully achieved by the wet mechanical method. Then, thermal treatment of the LHTO nanotubes was conducted at 500 °C. As a result, an LTO phase with a spinel structure was obtained, and the nanotube morphology of LHTO was retained in the LTO product. The anode properties of the prepared LTO nanotubes exhibited a first discharge capacity of 160 mAh/g at 0.1 C rate.

To clarify whether the normal or tangential component of collisions makes a larger contribution on the synthesis of LHTO, the effect of collision direction on a reaction rate of LHTO was studied through the combined analysis of the experimental results and the simulated ball motion by Distinct Element Method (DEM) (Kozawa et al., 2021b). As a result, collisions of balls in the normal direction were found to contribute strongly to the wet mechanochemical reaction.

The wet mechanical processing was also applied for the morphology-controlled  $\text{NH}_4\text{MnPO}_4 \cdot \text{H}_2\text{O}$  (Kozawa et al., 2019a) and  $\text{NH}_4\text{CoPO}_4 \cdot \text{H}_2\text{O}$  (ACP) (Kozawa et al., 2021a), respectively. For the latter case, ACP platelets were synthesized via the wet mechanical processing of  $\text{NH}_4\text{H}_2\text{PO}_4$  and  $\text{Co}(\text{OH})_2$  in water using a planetary ball mill. The formation of ACP was achieved by the dissolution-precipitation reaction, involving the gradual dissolution of water-insoluble  $\text{Co}(\text{OH})_2$  into the  $\text{NH}_4\text{H}_2\text{PO}_4$ -dissolved acidic solution. The use of  $\text{Co}(\text{OH})_2$  with a brucite-type structure allowed the ready formation of the layered ACP phase. Despite the ball milling treatment, ACP particles with platelet morphologies were produced, and their sizes and shapes were varied, depending on the milling conditions. The formed ACP platelets were subjected to grinding, consequently affording a decrease in size and subsequent dissolution. However, an increase in supersaturation led to the recrystallization and crystal growth of the ACP platelets. This dissolution-recrystallization cycle during milling allows the repeated growth of the ACP platelets. The ACP powder was converted into  $\text{LiCoPO}_4$ , while maintaining the shape and size, by a simple solid-state reaction with  $\text{Li}_2\text{CO}_3$ . The flake-like LCP cathode exhibited a charge/discharge plateau at ~4.8 V and a better discharge capacity of 109 mAh/g because of the high specific surface area and small platelet thickness (Kozawa et al., 2021a). Other applications of the wet mechanical processing including the synthesis of  $\text{Sr}_3\text{Al}_2(\text{OH})_{12}$  hydrogarnet (Kozawa et al., 2018), and the fabrication of composite cathode of  $\text{LiMn}_2\text{O}_4$  coated by  $\text{LiMnPO}_4$  (Kozawa et al., 2020) have been investigated.

## 8. Conclusions

Smart powder processing was developed based on powder grinding technology. It is a very promising technique for achieving green and sustainable manufacturing,

as well as developing advanced materials contributing to establishing sustainable economy. In this paper, the authors explained the recent progress of the smart powder processing, and its applications. At first, the authors introduced particle bonding process, novel one-pot process to synthesize nanoparticles, process to create nanostructured composite granules, and process to form nano-porous films on substrates in the dry phase. Then, the authors discussed the wet smart processing with grinding technology. Smart powder processing can be a foundation to move forward material development technologies and create many more high-quality advanced materials in the future.

## References

- Abe I., Sato K., Abe H., Naito, M., Formation of porous fumed silica coating on the surface of glass fibers by a dry mechanical processing technique, *Advanced Powder Technology*, 19 (2008) 311–320. DOI: 10.1163/156855208X314976
- Abe H., Abe I., Sato K., Naito M., Dry powder processing of fibrous fumed silica compacts for thermal insulation, *Journal of the American Ceramic Society*, 88 (2005) 1359–1361. DOI: 10.1111/j.1551-2916.2005.00317.x
- Abe H., Kimitani T., Naito, M., Influence of  $\text{NH}_3/\text{Ar}$  plasma irradiation on physical and photocatalytic properties of  $\text{TiO}_2$  nanopowder, *Journal of Photochemistry and Photobiology A: Chemistry*, 183 (2006) 171–175. DOI: 10.1016/j.jphotochem.2006.03.013
- Abe H., Naito M., Nogi K., Kondo A., Fukui T., Ohara S., Matsuda M., Miyake M., Formation of  $\text{MgB}_2$  superconducting phase from Mg and B composite particles produced by mechanical mixing, in: *Characterization & Control of Interfaces for High Quality Advanced Materials: Ceramic Transactions* (eds K. Ewsuk, K. Nogi, M. Reiterer, A. Tomsia, S.J. Glass, R. Waesche, K. Uematsu and M. Naito), 146 (2006) 277–282. DOI: 10.1002/9781118406038.ch34
- Abe H., Naito M., Nogi K., Matsuda M., Miyake M., Ohara S., Kondo A., Fukui T., Low temperature formation of superconducting  $\text{MgB}_2$  phase from elements by mechanical milling, *Physica C*, 391 (2003) 211–216. DOI: 10.1016/S0921-4534(03)00932-8
- Abe H., Naito M., Sato K., Mechanically assisted deposition of nickel oxide–yttria stabilized zirconia nanocomposite film and its microstructural evolution for solid oxide fuel cells anode application, *International Journal of Applied Ceramic Technology*, 9 (2012) 928–935. DOI: 10.1111/j.1744-7402.2012.02780.x
- Asahi R., Morikawa T., Ohwaki T., Aoki K., Taga, Y., Visible-light photocatalysis in nitrogen-doped titanium oxides, *Science*, 293 (2001) 269–271. DOI: 10.1126/science.1061051
- Akedo J., Aerosol deposition of ceramic thick film at room temperature densification mechanism of ceramic layers, *Journal of the American Ceramic Society*, 89 (2006) 1834–1839. DOI: 10.1111/j.1551-2916.2006.01030.x
- Chaichanawong J., Sato K., Abe H., Murata K., Fukui T., Charinpanitkul T., Tanthapanichakoon W., Naito M., Formation of strontium-doped lanthanum manganite ( $\text{La}_{0.8}\text{Sr}_{0.2}\text{MnO}_3$ ) by mechanical milling without media balls, *Advanced Powder Technology*, 17 (2006) 613–622. DOI: 10.1163/156855206778917751
- Chen M., Fan G., Tan Z., Xiong D., Guo Q., Su Y., Zhang J.,

- Li Z., Naito M., Di Z., Design of an efficient flake powder metallurgy route to fabricate CNT/6061Al composites, *Materials and Design*, 142 (2018) 288–296. DOI: 10.1016/j.matdes.2018.01.044
- Chen M., Fan G., Tan Z., Yuan C., Xiong D., Guo Q., Su Y., Naito M., Li Z., Tailoring and characterization of carbon nanotube dispersity in CNT/6061Al composites, *Materials Science & Engineering. A*, 757 (2019) 172–181. DOI: 10.1016/j.msea.2019.04.093
- Dachille F., Roy R., High-pressure phase transformations in laboratory mechanical mixers and mortars, *Nature*, 186 (1960) 34. DOI: 10.1038/186034a0
- Endoh S., Szepvolgyi J., Hotta T., Naito M., Izumi K., Experimental and theoretical analysis of mechanical coating process of particles with the theta composer, *Chemical Engineering Communications*, 191 (2004) 1259–1270. DOI: 10.1080/00986440490464174
- Fukui T., Murata K., Ohara S., Abe H., Naito M., Nogi K., Morphology control of Ni-YSZ cermet anode for lower temperature operation of SOFC, *Journal of Power Sources*, 125 (2004) 17–21. DOI: 10.1016/S0378-7753(03)00817-6
- Fukui T., Ohara S., Okawa H., Hotta T., Naito M. Properties of NiO cathode coated with lithiated Co and Ni solid solution oxide for MCFCs, *Journal of Power Sources*, 86 (2000) 340–346. DOI: 10.1016/S0378-7753(99)00416-4
- Fukui T., Ohara S., Okawa H., Naito M., Nogi K., Synthesis of metal and ceramic composite particles for fuel cell electrodes, *Journal of the European Ceramic Society*, 23 (2003) 2835–2840. DOI: 10.1016/S0955-2219(03)00296-6
- Fukui T., Okawa H., Hotta T., Naito M., Yokoyama T., Synthesis of CoO/Ni composite powders for molten carbonate fuel cells, *Journal of the American Ceramic Society*, 84 (2001) 233–235. DOI: 10.1111/j.1151-2916.2001.tb00639.x
- Fukumori Y., Ichikawa H., Uemura T., Sato K., Abe H. Naito, M., Process performance of dry powder coating for preparing controlled release microcapsules by a high speed mixer, *Proceedings of 8th International Symposium on Agglomeration*, Bangkok, Thailand, March 16–18 (2005) 31–38.
- Hagiwara A., Hobara N., Takizawa K., Sato K., Abe H., Naito M., Preparation and evaluation of mechanochemically fabricated LSM/ScSZ composite materials for SOFC cathodes, *Solid State Ionics*, 177 (2006) 2967–2977. DOI: 10.1016/j.ssi.2006.08.021
- Hosokawa K., Kondo A., Okumiya M., Abe H., Naito M., One-step mechanical processing to prepare LSM/ScSZ composite particles for SOFC cathode, *Advanced Powder Technology*, 25 (2014) 1430–1434. DOI: 10.1016/j.apt.2013.12.006
- Hosokawa M., Nogi K., Naito M., Yokoyama T., *Nanoparticle Technology Handbook*, 1st Ed., Elsevier, 2007, ISBN: 9780080558028.
- Kanai K., Fukui Y., Kozawa T., Kondo A., Naito M., Effect of BaF<sub>2</sub> powder addition on the synthesis of YAG phosphor by mechanical method, *Advanced Powder Technology*, 28 (2017) 50–54. DOI: 10.1016/j.apt.2016.07.017
- Kanai K., Fukui Y., Kozawa T., Kondo A., Naito M., Effect of flux powder addition on the synthesis of YAG phosphor by mechanical method, *Advanced Powder Technology*, 29 (2018) 457–461. DOI: 10.1016/j.apt.2017.11.002
- Koishi M., Biryushi Sekkei, *Kogyo Chousakai*, 1987, ISBN:978-4769340508
- Kondo A., Abe H., Isu N., Miura M., Mori A., Ohmura T., Naito M., Development of light weight materials with low thermal conductivity by making use of waste FRP, *Journal of the Society of Powder Technology, Japan*, 47 (2010) 768–772. DOI: 10.4164/sptj.47.768
- Kondo A., Nakamura E., Kozawa T., Abe H., Naito M., Yoshida J., Nakanishi S., Iba H., One-pot mechanical synthesis of the nanocomposite granule of LiCoO<sub>2</sub> nanoparticles, *Advanced Powder Technology*, 25 (2014) 1280–1284. DOI: 10.1016/j.apt.2014.03.005
- Kondo A., Ohmura T., Abe H., Kano J., Naito M., Development of recycling process for waste FRP mortar pipe, *Journal of the Society of Powder Technology, Japan*, 49 (2012) 827–831. DOI: 10.4164/sptj.49.827
- Kondo A., Sato K., Abe H., Naito M., Shimoda H., Mechanochemical synthesis of barium titanate from nanocrystalline BaCO<sub>3</sub> and TiO<sub>2</sub>, in: *Characterization and Control of Interfaces for High Quality Advanced Materials II: Ceramic Transactions* (eds K. Ewsuk, K. Nogi, R. Waesche, Y. Umakoshi, T. Hinklin, K. Uematsu, T. Tomsia, H. Abe, H. Kamiya and M. Naito), 198 (2006) 375–380. DOI: 10.1002/9781118144145.ch57
- Kozawa T., Fukuyama K., Kondo A., Naito M., Wet mechanical route to synthesize morphology-controlled NH<sub>4</sub>MnPO<sub>4</sub>·H<sub>2</sub>O and its conversion reaction into LiMnPO<sub>4</sub>, *ACS Omega*, 4 (2019a) 5690–5695. DOI: 10.1021/acsomega.9b00026
- Kozawa T., Fukuyama K., Kondo A., Naito M., Wet milling synthesis of NH<sub>4</sub>CoPO<sub>4</sub>·H<sub>2</sub>O platelets: formation reaction, growth mechanism, and conversion into high-voltage LiCoPO<sub>4</sub> cathode for Li-ion batteries, *Materials Research Bulletin*, 135 (2021a) 111149. DOI: 10.1016/j.materresbull.2020.111149
- Kozawa T., Fukuyama K., Kushimoto K., Ishihara S., Kano J., Kondo A., Naito M., Effect of ball collision direction on a wet mechanochemical reaction, *Scientific Reports*, 11 (2021b) 210. DOI: 10.1038/s41598-020-80342-w
- Kozawa T., Harata T., Naito M., Fabrication of an LiMn<sub>2</sub>O<sub>4</sub>@LiMnPO<sub>4</sub> cathode for improved cycling performance at high temperatures, *Journal of Asian Ceramic Societies*, 8 (2020) 309–317. DOI: 10.1080/21870764.2020.1743413
- Kozawa T., Kataoka N., Kondo A., Nakamura E., Abe H., Naito M., One-step mechanical synthesis of LiFePO<sub>4</sub>/C composite granule under ambient atmosphere, *Ceramics International*, 40 (2014a) 16127–16131. DOI: 10.1016/j.ceramint.2014.07.043
- Kozawa T., Kataoka N., Kondo A., Nakamura E., Abe H., Naito M., Facile preparation of porous LiFePO<sub>4</sub>/C composite granules by mechanical process, *Materials Chemistry and Physics*, 155 (2015) 246–251. DOI: 10.1016/j.matchemphys.2015.02.038
- Kozawa T., Kondo A., Fukuyama K., Naito M., Koga H., Shimo Y., Saito T., Iba H., Inda Y., Oono T., Katoh T., Nakajima K., Bulk-type all-solid-state batteries with mechanically prepared LiCoPO<sub>4</sub> composite cathodes, *Journal of Solid State Electrochemistry*, 23 (2019b) 1297–1302. DOI: 10.1007/s10008-019-04218-4
- Kozawa T., Kondo A., Nakamura E., Abe H., Naito M., Koga H., Nakanishi S., Iba H., Rapid synthesis of LiNi<sub>0.5</sub>Mn<sub>1.5</sub>O<sub>4</sub> by mechanical process and post-annealing, *Materials Letters*, 132 (2014b) 218–220. DOI: 10.1016/j.matlet.2014.06.097
- Kozawa T., Naito M., Facile preparation of core@shell and concentration-gradient spinel particles for Li-ion battery cathode materials, *Science and Technology of Advanced Materials*, 16 (2015) 015006. DOI: 10.1088/1468-6996/16/1/015006
- Kozawa T., Suzuki Y., Naito M., Scalable synthesis of Sr<sub>3</sub>Al<sub>2</sub>(OH)<sub>12</sub> hydrogarnet by wet milling and its thermal decomposition behavior, *Materials Chemistry and Physics*, 212 (2018) 245–251. DOI: 10.1016/j.matchemphys.2018.03.060
- Kwon Y.G., Choi S.Y., Kang E.S., Baek, S.S., Ambient-dried

- silica aerogel doped with  $\text{TiO}_2$  powder for thermal insulation, *Journal of Materials Science*, 35 (2000) 6075–6079. DOI: 10.1023/A:1026775632209
- Lee D., Kondo A., Lee S., Myeong S., Sun S., Hwang I., Song T., Naito M., Paik U., Controlled swelling behavior and stable cycling of silicon/graphite granular composite for high energy density in lithium ion batteries, *Journal of Power Sources*, 457 (2020) 228021. DOI: 10.1016/j.jpowsour.2020.228021
- Lian T.W., Kondo A., Kozawa T., Akoshima M., Abe H., Ohmura T., Tuan W.H., Naito M., Effect of hydrophobic nano-silica on the thermal insulation of fibrous silica compacts, *Journal of Asian Ceramic Societies*, 5 (2017) 118–122. DOI: 10.1016/j.jascer.2017.03.003
- Lian T.W., Kondo A., Kozawa T., Ohmura T., Tuan W.H., Naito M., Effect of fumed silica properties on the thermal insulation performance of fibrous compact, *Ceramics International*, 41 (2015) 9966–9971. DOI: 10.1016/j.ceramint.2015.04.076
- Matsuoka M., Kondo A., Kozawa T., Naito M., Koga H., Saito T., Iba H., Effect of carbon addition on one-step mechanical synthesis of  $\text{LiCoPO}_4/\text{C}$  composite granules and their powder characteristics, *Ceramics International*, 43 (2017) 938–943. DOI: 10.1016/j.ceramint.2016.10.022
- Misono T., Murata K., Fukui T., Chaichanawong J., Sato K., Abe H., Naito M., Ni-SDC cermet anode fabricated from NiO-SDC composite powder for intermediate temperature SOFC, *Journal of Power Sources*, 157 (2006) 754–757. DOI: 10.1016/j.jpowsour.2006.01.074
- Munakata H., Tashita T., Kanamura K., Kondo A., Naito M., Development of low-platinum catalyst for fuel cells by mechano-chemical method, *Journal of the Society of Powder Technology, Japan*, 48 (2011) 364–369. DOI: 10.4164/sptj.48.364
- Naito M., Abe H., Particle bonding technology for composite materials -microstructure control and its characterization, in: *Characterization and Modeling to Control Sintered Ceramic Microstructures and Properties: Ceramic Transactions, C. DiAntonio (Ed.)*, 157 (2006) 69–76. DOI: 10.1002/9781118407080.ch8
- Naito M., Abe H., Kondo A., Smart powder processing for energy and environment, *WIT Transactions on Ecology and the Environment*, 154 (2011) 51–59. DOI: 10.2495/CHEM110061
- Naito M., Abe H., Kondo A., Yokoyama T., Huang C.C., Smart powder processing for advanced materials, *KONA Powder and Particle Journal*, 27 (2009) 130–141. DOI: 10.14356/kona.2009013
- Naito M., Hotta T., Asahi S., Tanimoto T., Endoh S., Effect of processing conditions on particle composite process by a high-speed elliptical-rotor-type mixer, *Kagaku Kogaku Ronbunshu*, 24 (1998) 99–103. DOI: 10.1252/kakoronbunshu.24.99
- Naito M., Kondo A., Chapter 8 - Smart Powder Processing for Green Technologies, in: *Singh M., Ohji T., Asthana R. (Eds.), Green and Sustainable Manufacturing of Advanced Material*, Elsevier, Oxford, 2016, pp.197-221, ISBN: 978-0-12-411497-5. DOI: 10.1016/B978-0-12-411497-5.00008-4
- Naito M., Kondo A., Yokoyama T., Applications of comminution techniques for the surface modification of powder materials, *ISIJ International*, 33 (1993) 915–924. DOI: 10.2355/isijinternational.33.915
- Naito M., Okumiya M., Abe H., Kondo A., Huang C.C., Powder processing issues for high quality advanced ceramics, *KONA Powder and Particle Journal*, 28 (2010) 143–152. DOI: 10.14356/kona.2010013
- Naito M., Yokoyama T., Hosokawa K., Nogi K., Nanoparticle Technology Handbook, Third Edition, Elsevier, 2018, ISBN: 978-0-444-64110-6. DOI: 10.1016/C2017-0-01011-X
- Nakamura E., Kondo A., Matsuoka M., Kozawa T., Naito M., Koga H., Iba H., Preparation of  $\text{LiCoO}_2/\text{Li}_{1.3}\text{Al}_{0.3}\text{Ti}_{1.7}(\text{PO}_4)_3$  composite cathode granule for all-solid-state lithium-ion batteries by simple mechanical method, *Advanced Powder Technology*, 27 (2016) 825–829. DOI: 10.1016/j.apt.2015.10.013
- Nogi K., Naito M., Kondo A., Nakahira A., Niihara K., Yokoyama T., New method for elucidation of temperature at the interface between particles under mechanical stirring, *Journal of the Japan Society of Powder and Powder Metallurgy*, 43 (1996) 396–401. DOI: 10.2497/jjspm.43.396
- Nomura T., Minamiura M., Fukamachi K., Yumiyama S., Kondo A., Naito M., Adhesion control of fungal spores on solid surfaces using hydrophilic nanoparticles, *Advanced Powder Technology*, 29 (2018) 909–914. DOI: 10.1016/j.apt.2018.01.007
- Ohara S., Abe H., Sato K., Kondo A., Naito M., Effect of water content in powder mixture on mechanochemical reaction of  $\text{LaMnO}_3$  fine powder, *Journal of the European Ceramic Society*, 28 (2008a) 1815–1819. DOI: 10.1016/j.jeurceramsoc.2007.11.014
- Ohara S., Kondo A., Shimoda H., Sato K., Abe H., Naito M., Rapid mechanochemical synthesis of fine barium titanate nanoparticles, *Materials Letters*, 62 (2008b) 2957–2959. DOI: 10.1016/j.matlet.2008.01.083
- Sato K., Abe H., Misono T., Murata K., Fukui T., Naito M., Enhanced electrochemical activity and long-term stability of Ni-YSZ anode derived from NiO-YSZ interdispersed composite particles, *Journal of the European Ceramic Society*, 29 (2009) 1119–1124. DOI: 10.1016/j.jeurceramsoc.2008.07.050
- Sato K., Chaichanawong J., Abe H., Naito M., Mechanochemical synthesis of  $\text{LaMnO}_3$  fine powder assisted with water vapor, *Materials Letters*, 60 (2006) 1399–1402. DOI: 10.1016/j.matlet.2005.11.038
- Smith D.R., Hust J.G., Microporous fumed-silica insulation board as a candidate standard reference material of thermal resistance, U.S., National Institute of Standards and Technology, NISTIR 89-3901, 1989.
- Soda R., Yagi K., Kano J., Saito F., Naito M., DEM simulation of the powder composite process by a mechanical method, *Journal of Smart Processing*, 1 (2012) 218–223. DOI: 10.7791/jspmee.1.218
- Shuk P., Suchanek W.L., Hao T., Guliver F., Riman R.E., Senna M., TenHuisen K.S., Janas V.F., Mechanochemical-hydrothermal preparation of crystalline hydroxyapatite powders at room temperature, *Journal of Materials Research*, 16 (2001) 1231–1234. DOI: 10.1557/JMR.2001.0170
- Suchanek W.L., Shuk P., Byrappa K., Riman R.E., TenHuisen K.S., Janas V.F., Mechanochemical-hydrothermal synthesis of carbonated apatite powders at room temperature, *Biomaterials*, 23 (2002) 699–710. DOI: 10.1016/S0142-9612(01)00158-2
- Suzuki S., Kozawa T., Murakami T., Naito M., Mechanochemical-hydrothermal synthesis of layered lithium titanate hydrate nanotubes at room temperature and their conversion to  $\text{Li}_4\text{Ti}_5\text{O}_{12}$ , *Materials Research Bulletin*, 90 (2017) 218–223. DOI: 10.1016/j.materresbull.2017.02.011
- Tasaka T., Ohmura T., Hagihara S., Kondo A., Naito M., Effect of temperature history on the thermal and mechanical properties of fibrous fumed alumina compacts, *Journal of the Society of Powder Technology, Japan*, 57 (2020) 612–618. DOI:

10.4164/sptj.57.612

Yokoyama T., Urayama K., Naito M., Kato M., Yokoyama T., The Angmill mechanofusion system and its applications, *KONA Powder and Particle Journal*, 5 (1987) 59–68. DOI: 10.14356/kona.1987011

Yoshida J., Nakanishi S., Iba H., Kondo A., Abe H., Naito M., One-step mechanical synthesis of the nanocomposite granule of  $\text{LiMnPO}_4$  nanoparticles and carbon, *Advanced Powder Technology*, 24 (2013) 829–832. DOI: 10.1016/j.

apt.2013.01.010

Xi X., Kondo A., Kozawa T., Naito M., LSCF-GDC composite particles for solid oxide fuel cells cathodes prepared by facile mechanical method, *Advanced Powder Technology*, 27 (2016) 646–651. DOI: 10.1016/j.ap.2016.02.022

Xi X., Kondo A., Naito M., Simple mechanical process to synthesize  $\text{La}_{0.6}\text{Sr}_{0.4}\text{Co}_{0.2}\text{Fe}_{0.8}\text{O}_3$  perovskite for solid oxide fuel cells cathode, *Materials Letters*, 145 (2015) 212–215. DOI: 10.1016/j.matlet.2015.01.116

## Authors' Short Biographies



### Makio Naito

Makio Naito is a Professor at the Joining and Welding Research Institute (JWRI), Osaka University in Japan. He served as the President of The Society of Powder Technology, Japan from 2015 to 2019. His publications cover a wide range of studies in the fields of advanced materials and novel powder processing and characterization. He has received several prestigious awards including the Richard M. Fulrath Award from the American Ceramic Society (ACerS) in 2002 and the KONA Award in 2019. He has been a Fellow of the ACerS since 2010, and serves on the ACerS Board of Directors from 2020.



### Takahiro Kozawa

Takahiro Kozawa is an Assistant Professor at the Joining and Welding Research Institute (JWRI), Osaka University in Japan. He received his Ph.D. in science from Kochi University in 2012. He was fellowships (DC1, PD) from the Japan Society for Promotion of Science from 2011 to 2012. He became a specially designated researcher at JWRI in 2012 and has been in his current position since 2014. His research interests include the R&D on environment-friendly powder synthesis methods and particle design of energy materials such as lithium-ion and solid-state batteries.



### Akira Kondo

Akira Kondo received B.S. and M.S. degrees in chemical engineering from Nagoya University, Japan in 1989 and 1991, respectively. He received Ph.D. degree in material science from Osaka University in 1999. He was with Hosokawa Micron Corp. from 1991 to 2005, where he engaged in the R&D of powder processing technology. He became a specially designated researcher at the Joining and Welding Research Institute (JWRI), Osaka University in 2005, and is engaged in the R&D of powder processing for advanced materials.



### C.C. Huang

C. C. Huang is the Director of Technology at Hosokawa Micron Powder Systems, an operating unit of Hosokawa Micron International Inc., a global supplier of systems and equipment related to material sciences and engineering. He holds an M.S. degree in engineering from Illinois Institute of Technology and a Ph.D. degree in chemical engineering from West Virginia University. He specializes in powder and nanoparticle processing, powder characterization, powder granulation, and fluidization. He has published over 30 articles and 8 patents, chaired several meetings, and is an active member in a number of scientific and engineering societies.

# Interfacial Engineering of Particulate & Surfactant Systems for Enhanced Performance in Industrial Applications<sup>†</sup>

Jiaqi Dong and Brij M. Moudgil\*

Center for Particulate and Surfactant Systems (CPaSS), Department of Materials Science and Engineering, University of Florida, USA

## Abstract

Particulate and surfactant systems are an integral part either in processing or product lines in essentially every major industry, including Energy and Minerals, Pharmaceutical, Agriculture & Food, Microelectronics, Healthcare, Cosmetics, Consumer Products, and Analytical Instrumentation & Services. In most applications, product and process specifications depend on the synergistic or competitive interactions between the particles and reagent schemes. The primary goal of our research efforts has been to generate the structure-property-performance correlations-based knowledge and technology platforms for industry to develop more sustainable products and processes. Engineering the physicochemical/mechanical properties of surfaces, particles, and self-assembling surfactant systems enables their enhanced performance in industrial applications. Specifically, understanding and control of the nano and atomic-scale forces between particles and synthesis of functionalized particles form the foundation for targeted contributions in biomedical, advanced materials and minerals, sensor, and coating technologies. A synoptic overview of selected projects is presented in this review. Additional details can be found in the topic-specific references listed at the end of this manuscript.

**Keywords:** interfacial engineering, functionalized particles, antibacterial coatings, antiscalant additives, corrosion inhibitors, precision particles

## 1. Introduction

Over the last few decades, the theme of research at the Particle Engineering Research Center (PERC) and subsequently at the Center for Particulate and Surfactant Systems (CPaSS—NSF Industry/University Cooperative Research Center) has been focused on developing the structure-property-performance correlations in the particle and surfactant systems. In most projects, control of forces between particles in suspensions and functionalization of particles form the foundation of targeted advances in separations, dispersion & flocculation, and coating technologies.

## 2. Synopsis of selected research topics

### 2.1 Competitive adsorption

Controlled adsorption of molecules on selected particles or moieties is necessary for achieving the desired separation of minerals, and also for the release of active ingredients in drug formulations. Center researchers have devoted considerable efforts to understand the selectivity principles and develop guidelines for achieving selective

coatings of surfactant/polymers on targeted surfaces. For example, Engelhard Corporation has commercialized the “site blocking agent” concept developed in our research (Behl et al., 1993; 1996). Researchers in the pharmaceutical industry and microelectronic manufacturing, especially chemical mechanical polishing (CMP) slurry developers have also recognized the relevance and significance of our work on competitive (selective) adsorption of polymer and surfactant molecules.

The synthesis of functional particles has been a major focus of the Center research endeavors. An inorganic crystalline Cryptomelane type hydrous manganese dioxide was synthesized and successfully evaluated in ion exchange columns for selective removal of potassium ions from sodium ions. The synthesis protocol of this material was designed based on the “ion memory effect” displayed by specific minerals. Selective uptake by such functional materials is achieved by controlling the spatial arrangement of the structural ions. The objective of this work was to design an environmentally-benign water recycling technique in paper manufacturing (Prakash and Moudgil, 1995).

A novel flotation process based on in-situ generation of gas bubbles on the ink particles as they detach from the fibers was developed to deink wastepaper by PERC researchers (El-Shall et al., 2005).

<sup>†</sup> Received 3 August 2021; Accepted 24 November 2021  
J-STAGE Advance published online 29 January 2022

\* Corresponding author: Brij M. Moudgil;  
Add: 1180 Center Drive, Gainesville, FL 32603, USA  
E-mail: [bmoudgil@perc.ufl.edu](mailto:bmoudgil@perc.ufl.edu)  
TEL: +1-352-846-1194 FAX: +1-352-846-1196

## 2.2 Dispersion and flocculation—science and technology

Efforts to optimize CMP slurries revealed, to our knowledge, for the first time that shear and normal forces between particles and surfaces must be controlled independently of each other to achieve maximum removal rate with minimal defects (Basim et al., 2003). Additionally, selective adsorption of surfactants on various wafer components formed the basis of next-generation selective polishing slurries later commercialized by a university spin-off company. These findings also led to the development of reagent schemes for controlling the structure of particulate agglomerates (flocs) for the dewatering of suspensions. Additionally, the development of the theoretical basis and experimental measurements of mechanical properties of self-assembled surfactant structures, such as micelles at interfaces, revealed that specific materials could catalyze the structure formation process on surfaces at a lower concentration than in the bulk (Rabinovich et al., 2005 and Singh et al., 2001). Based on this work, new reagent schemes were proposed for wafer polishing slurries and for crystal habit modification additives.

The synthesis of nanoscale rough surfaces coupled with modeling the effect of nanoscale roughness and humidity on interparticle forces have provided new insights into aggregation and dry dispersion phenomena important to devising the dedusting schemes (Rabinovich et al., 2002).

## 2.3 Cross-contamination in powder mixtures

Changes in the particulate behavior in a mixture under storage and handling have been an enigma to scientists in the past. It has been well known that particulate systems can exhibit different bulk behavior even when the physical and surface chemical properties such as shape and size, size distribution, zeta potential, and viscosity of the systems are similar. In this regard, research on cross-contamination of powders has shown that even slight contact between two solid surfaces may be sufficient for atomic/nanoscale material transfer from one surface to the other, thereby reducing the selectivity of reagent coatings on the two surfaces. When apatite and dolomite particles were gently mixed, the transfer of material was too small to be detected by conventional surface analytical tools such as EDA, ESCA, SEM, TEM, but was sufficient to result in measurable changes in their zeta potential. It was further determined that the cross-contamination in particulate mixtures could be controlled with chemical additives (Mehta N, 1993).

## 2.4 Polyhydroxy fullerenes (PHF)—their novel properties and applications

A new phenomenon, namely the optical ignition of poly hydroxyl fullerenes (PHF), was discovered in our laboratory (Krishna et al., 2010; 2016a). This discovery led to the synthesis of carbon nanostructures without the use of any

metal catalysts (Krishna et al., 2010). It resulted in practical uses of PHF in designing new antimicrobial coatings, selective ablation of cancerous cells, new herbicides, and plant growth promoters. (Gao et al., 2011; 2016; Krishna et al., 2015; 2016b; Sharma et al., 2013a).

## 2.5 Effect of kaolin clays on casting rate

In a recently completed project on the engineering of clays, the characterization of clay samples from different locations revealed that morphology, crystallinity, and shape of the clay particles play a major role in the dewatering behavior and casting rate of ceramic products. (Badr et al., 2021).

## 2.6 Science and technology of odor control

In an odor control study, porous silica particles impregnated with nano copper deposits were reported to be much more efficient odor control materials. However, challenges were encountered by an industry partner when attempts were made to scale up the process. A systematic characterization of the product formulation steps revealed that not only the chemical composition of the copper catalyst but also the morphology of the nano deposits in the pores played a critical role in achieving the optimal product performance (Singh et al., 2010).

## 3. Review highlights of selected research themes

### 3.1 Particle assisted removal of microbes from surfaces

In general, antibiotic-based strategies have limited efficacy owing to bacterial persistence and resistance to antibiotics. As a result, there has been an alarming growth of multi-drug-resistant pathogens. It is well known that non-alcohol-based cleansing formulations although may reduce 99.9%+ bacteria and yet leave enough bacteria to cause infection. The need for alternative approaches has never been greater. The current project aimed at the removal of microbes rather than killing them.

Proper handwashing using soap, as per CDC guidelines, is quite effective. Soap molecules can outright kill the microbes or decrease the force of adhesion between the microbe and the skin. However, quite often in practice, due to lack of time, water or soap, improper handwashing can leave enough microbes on the skin to cause infections. Choices of more effective antimicrobial soaps are restricted due to health and safety regulations. Alcohol-based sanitizers are known to kill all microbes, but their repeated use without the application of skin emollients can lead to an increased risk of infection due to skin damage. For these reasons, engineered particles were developed to achieve higher efficacy of soap-based handwashing practices.

Considering that the microbes are negatively charged, the proposed hypothesis was investigated using positively

charged (cationic) silica particles. Silica particles (isoelectric point around pH of 2.8) are negatively charged under natural pH conditions (about pH 5.6) and can exhibit a positive charge when coated with polyethyleneimine (PEI). *E. coli* and VITRO-SKIN<sup>®</sup> served as the bacteria and skin surface, respectively. A brief description of the experimental procedures is given below. Additional details are provided in Nandakumar (2018).

Materials and reagents employed in this study and their respective sources (in parenthesis) are as follows: Silica of different particle sizes and Polyethyleneimine—M<sub>n</sub>10,000 (Sigma-Aldrich, USA); Ampicillin sodium salt and Neutralizer D/E broth (Thermo Fisher Scientific); Artificial skin substrate -VITRO-SKIN<sup>®</sup> (IMS Inc. USA); *Escherichia coli*—ATCC 25922GFP (ATCC).

In order to remove any organic contaminants from the obtained silica surface, 1 g of the particles were treated with 1 M HCl for 60 min and thoroughly washed before conditioning with 40 mL of 2 wt % polyethylene imine—PEI, at pH 10.5 for 17 hours in a rotisserie. After recovering the PEI coated silica particles via centrifugation and washing them to remove excess PEI, they were lyophilized using a LABCONCO<sup>®</sup> freeze drier for storage purposes. Modified or unmodified silica particle suspensions were prepared in 0.5 % Tween 80 solution unless otherwise noted.

Brookhaven ZetaPlus<sup>®</sup>, and Coulter<sup>®</sup> LS13320 were employed for zeta potential and particle size measurements, respectively. For determining the amount of polymer coating, elemental analysis on a Carlo Erba NA1500 CNHS elemental analyzer was employed.

As per manufacturers protocol, 1.5 cm × 1.5 cm patch of VITRO-SKIN<sup>®</sup> was hydrated overnight using glycerol: water (15:85) binary mixture in a humidity chamber. Anton Paar<sup>®</sup> Physica Electro Kinetic Analyzer was used to measure the zeta potential. Surface energy was determined via contact angle measurements with water, glycerol, ethylene glycol, and diiodomethane, using the Owens-Wendt model (Owens and Wendt, 1969).

The surface energy of the *E. coli* strain (ATCC 25922GFP) was determined using a light scattering technique described elsewhere (Zhang X. et al., 2015). MATS (Microbial Adhesion to Solvents) assays were used to study the bacterial cell surface properties, including hydrophobic components and electron donor groups according to the protocol established (Bellon-Fontaine et al., 1996; Hamadi and Latrache, 2008). Bacterial adhesion to solvent was estimated by Eq. (1) (Bellon-Fontaine et al., 1996), where  $A_0$  is the optical density at 600 nm of the aqueous suspension before mixing,  $A$  is the optical density of the aqueous suspension after mixing with the solvent pair.

$$\% \text{ adherence} = \left(1 - \frac{A}{A_0}\right) * 100 \quad (1)$$

Interactions of modified and unmodified silica particles

with bacteria were assessed by enumerating remnant bacterial population on the substrate following treatment with particles. Removal efficacy was calculated using Eq. (2).

$$\begin{aligned} \log_{10} \text{ bacterial removal} \\ = \log_{10} \text{ Inoculum on skin} \\ - \log_{10} \text{ bacteria remaining on skin} \end{aligned} \quad (2)$$

The plate count method was used to estimate the cell density in the suspension, and the results were reported in terms of the total number of bacteria recovered as CFU. A wide-field fluorescence microscope (Cytation 5) was employed to assess cell membrane damage and cell viability.

In order to determine the extent of bacterial killing by the particles, tests were conducted by contacting the modified silica particles with *E. coli*. The cell viability illustrated in Fig. 1 established that the modified particles by themselves do not kill the bacteria and hence would be suitable for removal studies.

Test results plotted in Fig. 2 demonstrated that modified silica particles interact strongly with *E. coli* cells and can reduce bacterial concentrations by four log orders in 30 seconds in contrast to a maximum of 1.5 log reduction with unmodified control particles.

### 3.2 Particle design parameters for the removal of *E. coli* from artificial skin

A major hypothesis of this study was that microbial removal is possible only if the particle-bacterial interactions are strong enough to overcome the bacterial–substrate adhesion forces. Furthermore, particle size and density should be such that they impart enough shear force to remove the microbe-particle construct from the skin under handwashing conditions (e.g., fluid velocity, the volume of water, or time—20 seconds). Additionally, there need to be enough particles (particle loading, wt %) in the

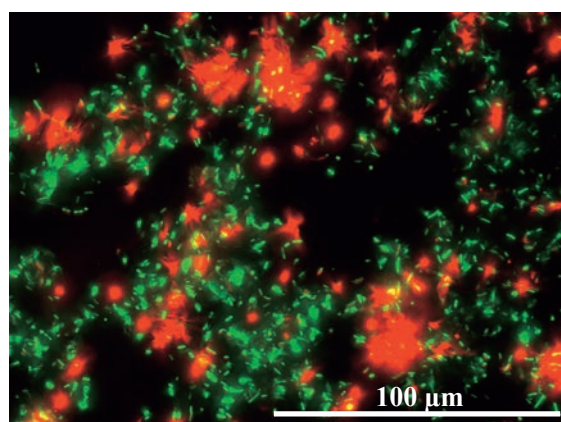


**Fig. 1** Viability of microbes when attached to modified particles using fluorescence microscopy. Green—viable microbes attached to particles. Red—inactive microbes (Red intensity enhanced). Reprinted with permission from Ref. (Nandakumar et al., 2019). Copyright: (2019) Elsevier.

system to efficiently cleanse the skin. Accordingly, the role of adhesion forces (zeta potential), particle size, fluid velocity, and particle loading were systematically evaluated (Nandakumar et al., 2019).

It is observed from Fig. 2 that an additional 2.5 log bacterial reduction on the skin surface is possible with the modified particles. It was further determined that the removal of bacteria dispersed on the skin (e.g., *E. coli*) was easier than the aggregated ones, e.g., *S. aureus*, see Fig. 3 (Nandakumar, 2018).

Overall, this approach exhibited the potential of using modified particles to remove bacteria from surfaces as an alternative to kill-based methodologies.

### 3.3 Microbial disease control in the citrus plants: controlled release of insect repellants

In the past, engineered particle coatings have been successfully employed to control plant diseases in pear, apple, and cotton plants. Particle coatings of foliage primarily compromise the ability of insects to visualize, settle, feed, move and oviposit. They can also mask the color of the leaves and stems, making it difficult for insects to recognize them from a distance (Grafton-Cardwell et al., 2013; Glenn, 2012; Puterka et al., 2005; Wenninger et al., 2009). Sometimes the films themselves can be toxic to insects.

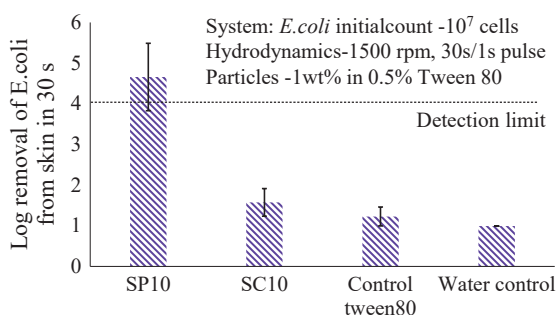


**Fig. 2** Removal of *E. coli* using modified and unmodified silica particles. Reprinted with permission from Ref. (Nandakumar et al., 2019). Copyright: (2019) Elsevier.

Center researchers were approached to study the potential of particle coatings for managing the “Citrus Greening” diseases, which was detected by the Florida citrus growers back in 2005. “Citrus greening” (also known as the Huanglongbing or HLB) is a bacterial disease transmitted by an insect, the Asian citrus Psyllid (ACP). ACP attacks the younger flush making them more prone to infection, thus increasing the vulnerability of citrus trees during flush. The disease reduces the quality and quantity of the fruit yield, thereby threatening the economic viability of the Florida citrus industry. Some of the methods used and/or suggested to control citrus greening are as follows:

- Spraying of insecticides to control the insect attack. However, repetitive applications are required.
- Quarantine of infected trees, although it controls the spreading of the disease, the cost is a major drawback.
- Applying particulate (kaolin clay) coatings is effective in suppressing the disease, but rain fastness and exposure due to leaf growth remain major challenges.

Kaolin-based coatings have been reported to control the spread of the disease to varying degrees of success. However, the development of gaps upon the growth of leaves and washing off the coatings due to rains reduce their effectiveness for protection from the insects. Interestingly, contrary to conventional thinking, particle coatings are not only non-phytotoxic, but they improve water use efficiency. Hydrophobized Kaolin films have been shown to reduce heat stress by reflecting sunlight from the white film surface, and the porous nature of the films allows efficient gaseous exchange, thereby maintaining healthy photosynthesis in the plants (Glenn and Puterka, 2004; Puterka et al., 2005).

A systematic study was conducted to overcome a major limitation of the emerging gaps in the coatings due to leaf growth. Two approaches were proposed to overcome this challenge (i) developing a coating that slowly released an insect repellent such as garlic oil and (ii) coating the foliage with colored clays that masked the olfactory cues,

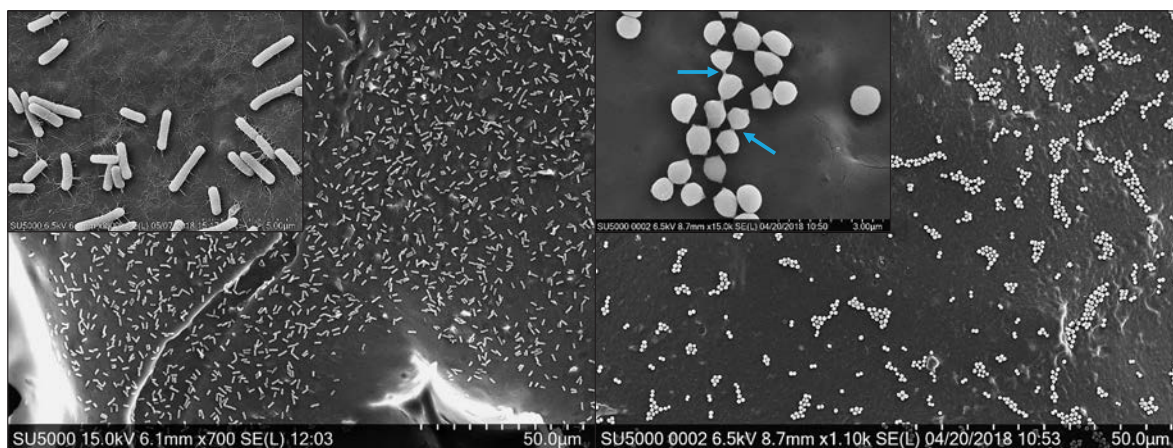


**Fig. 3** *E. coli*—dispersed on skin (left); *S. aureus*—agglomerated on skin (right).



thus keeping the insects away from the citrus trees. These coatings were to also incorporate additives that enhance the rain fastness of the particles to the leaves.

### 3.4 Encapsulation of garlic oil (insect repellent) in unmodified and modified clays

The uptake of garlic oil (GO) was investigated using modified montmorillonite (MMT), surfactant treated montmorillonite (NMMT), and Claytone® 40 (hydrophobized montmorillonite). Pristine kaolin clays were employed as the negative control.

**Fig. 4** shows that the highest uptake of GO was achieved in modified MMT clays such as Claytone 40 and NMMT (0.4 g GO/g clay), followed by unmodified MMT (0.2 g GO/g clay). The uptake of GO in pristine kaolin clays is almost negligible (0.04 g GO/g clay), possibly due to the lack of intergallery spacing and the hydrophilic nature of the kaolin clays (Narayanan et al., 2012; Sharma et al., 2013b).

Among the montmorillonite clays, the trend is consistent with the intergallery spacings ( $d_{001}$ ) measured with the help of an X-ray diffractometer—Claytone 40 > NMMT > MMT. The increase in the intergallery spacing of Claytone 40 (29 Å) in the presence of GO (34 Å) suggests possible encapsulation of GO in between the layers. Similar results have also been reported in the literature for the sorption of aromatic compounds in Claytone 40. These set of experiments reinforced our hypothesis that the intergallery spacings and the hydrophobic nature of the clays are important for the integration of GO to the clays.

### 3.5 Release profile of encapsulated garlic oil

Preliminary data of release profile of GO from the clays is plotted in **Fig. 5**. The cumulative release of GO after four days from Claytone 40 is 13 % of the total encapsulated garlic oil (0.4 g/g of clay) as compared to 34 % of 0.2 g of GO uptaken in 1 g of unmodified MMT, and 84 % GO alone. It is hypothesized that uptake of GO in the clays is primarily due to electrostatic attraction between the modified clays and the garlic oil, along with uptake of GO within

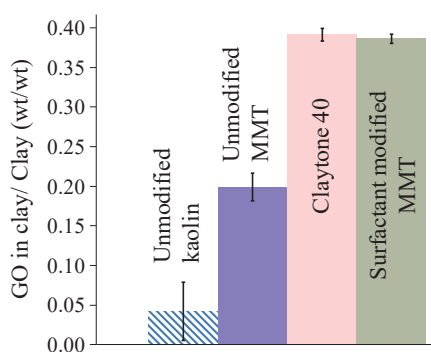


**Fig. 4** Uptake of GO in unmodified MMT, modified MMT, and unmodified kaolin clays (clay = 1 g; the initial amount of GO = 0.4 g) (error bars with one std dev). Reprinted with permission from Ref. (Sharma et al., 2013b). Copyright: (2013) The Authors, patented in U.S.

the hydrophobic pores. This study indicated the potential of controlled release of insect repellants as a methodology for crop protection purposes (Sharma et al., 2013b).

### 3.6 Colored clays as an optical and physical deterrent for insect attack of citrus plants

This project aimed to investigate if colored clays with reflectance in the visible range can prevent feeding on the citrus leaves by the Asian Citrus Psyllid (ACP), especially feeding on the fresh flush (fresh leaves). Colored kaolin clays were formulated using select dyes, including FDA-certified colorants, and approved for agricultural use by the EPA (list §180.920).

Basic dyes were used to prepare the colored kaolin clays (Moudgil et al., 2017; Sharma et al., 2015). Several clays from different suppliers were evaluated, and only a white clay sample was selected for further processing. Clay particles surfaces were modified using cationic surfactants and/or polymers, followed by mixing them with the dyes. This step was essential to prevent the leaching of the dyes from the clay particle suspensions. Zeta potential of the unmodified clays was determined to be about -31 mV and changed to +5 mV to +22 mV when treated with the acidic dyes, and -13 mV to -23 mV upon treatment with the basic dyes. Zeta potential was measured using a Zeta Plus Analyzer from Brookhaven instruments.

Ten different colored clays were developed using dyes—FD&C Blue 1, FD&C Red 40, Basic Blue 54, Crystal Violet, and FD&C Yellow 6, D&C Violet 2, as shown in **Fig. 6**. The optical properties of the colored clays were characterized using an integrating sphere (Lambda 800 UV-vis Spectrometer) for total reflectance measurements. These measurements were carried out by depositing a clay film on a glass slide.

It was determined that the majority of the colored clay coatings increased the reflectance in the 400–500 nm range relative to the uncoated leaves. The colorant strength of the

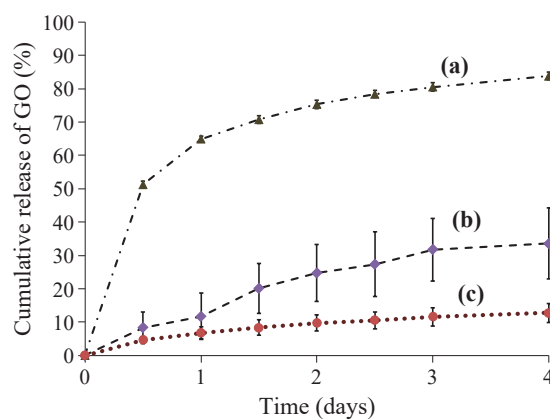


**Fig. 5** The release profile of (a) GO alone, (b) GO from unmodified MMT, and (c) GO from Claytone 40. (Temp 22 °C; error bars with one std. deviation). Reprinted with permission from Ref. (Sharma et al., 2013b). Copyright: (2013) The Authors, patented in U.S.

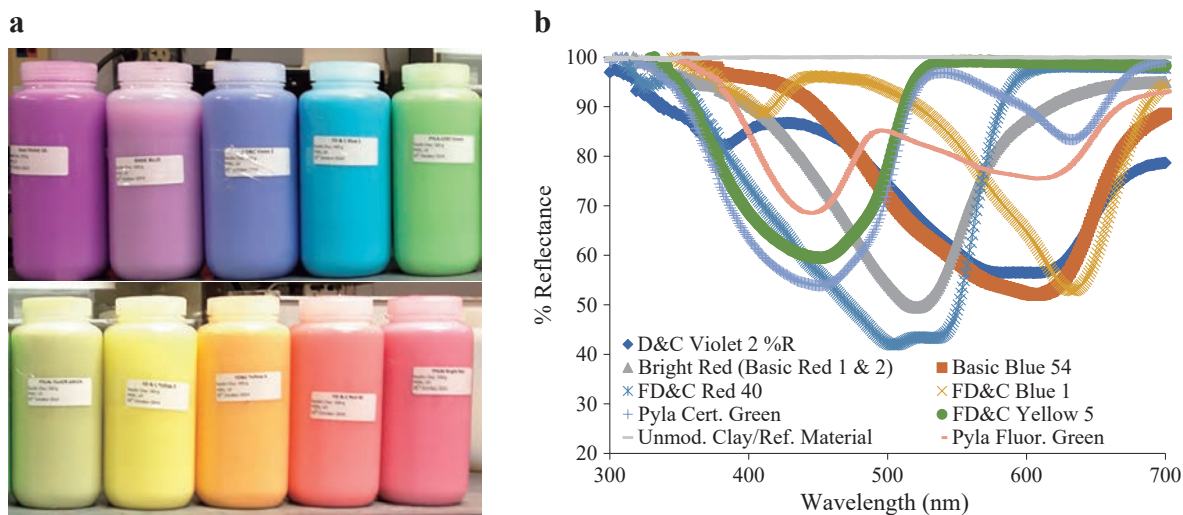


**Fig. 6 (a)** Colored Kaolin clays developed with surfactants and dyes. **(b)** The reflectance spectrum of the colored clays. Reprinted with permission from Ref. (Moudgil et al., 2017). Copyright: (2017) The Authors, patented in U.S.

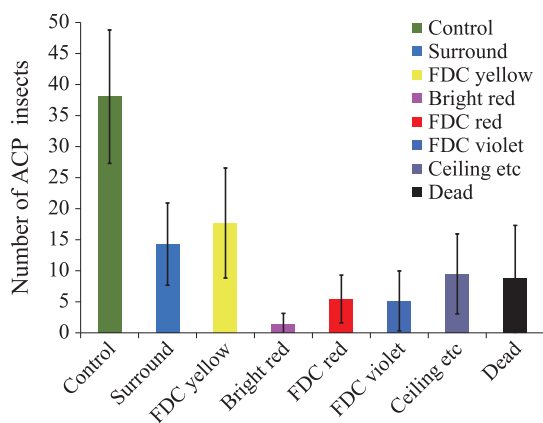


**Fig. 7** The choice of ACP to go to the tree coated with different colored clays as compared to Surround® and uncoated leaves. Reprinted with permission from Ref. (Moudgil et al., 2017). Copyright: (2017) The Authors, patented in U.S.

coated leaves was found to depend on the thickness of the coating.

### 3.7 Effect of the colored coatings on inhibition of Asian Citrus Psyllid (ACP) insect

The selected colored clay formulations were applied to the leaves of citrus plants to deter the Asian Citrus Psyllid *Diaphorina citri*. One hundred psyllids were released in the cage, and they had 24 hours to choose a location before counts were made. Fig. 7 shows the results from the treatment, and the values are the numbers of psyllids on each tree.

It is observed from Fig. 7 that ACP has a very low preference for Bright red, followed by FDC red- and violet-colored trees. FDC Yellow clays seem to attract more insects than Surround® coated (white) trees (control). These measurements indicated the potential of colored clay coatings in managing the ACP attack of the fresh flush.

### 3.8 Rain fastness enhancement

Several formulations were prepared with different adjuvants to determine how well the clay particles adhere to the citrus foliage. Adjuvants were selected based on their ability to act as stickers, binders, or viscosity modifiers. Some of the adjuvants tested resulted in the desorption of the dye from the clays. The colored clay formulations containing Kollicoat, i.e., a pharmaceutical excipient—polyvinyl acetate dispersed in water and stabilized with povidone and sodium dodecyl sulfate, Polymer adjuvant, i.e., sodium polyacrylate, and Xanthan gum yielded coatings with enhanced rain fastness properties.

Several colored clay formulations containing different concentrations of the three adjuvants were sprayed onto the citrus plants, along with white only and colored clays only (no adjuvants) as controls. The coatings were evaluated for color intensity after 1–2, 4–5, and 7 cm of rainfall (see Fig. 8). Kollicot and polymer additives were determined to be the best adjuvants for improving both spreading and rain fastness of the colored kaolin clays, withstanding up to 7 cm rain (Moudgil et al., 2017).

### 3.9 Multimodal contrast agents for cancer detection and treatment

Methods for early detection of cancer using low-cost means remain a critical need. This requires tools that can yield high resolution and sensitivity without compromising the safety of patients. Data from complementary imaging modalities are often evaluated to enable early and accurate detection. Currently employed techniques such as Computed Tomography (CT), Positron Emission Tomography (PET), Magnetic Resonance Imaging (MRI), and Ultrasound possess different detection limits, spatial-temporal resolution, accuracy, and long-term safety upon multiple exposures. However, none of these methods, when

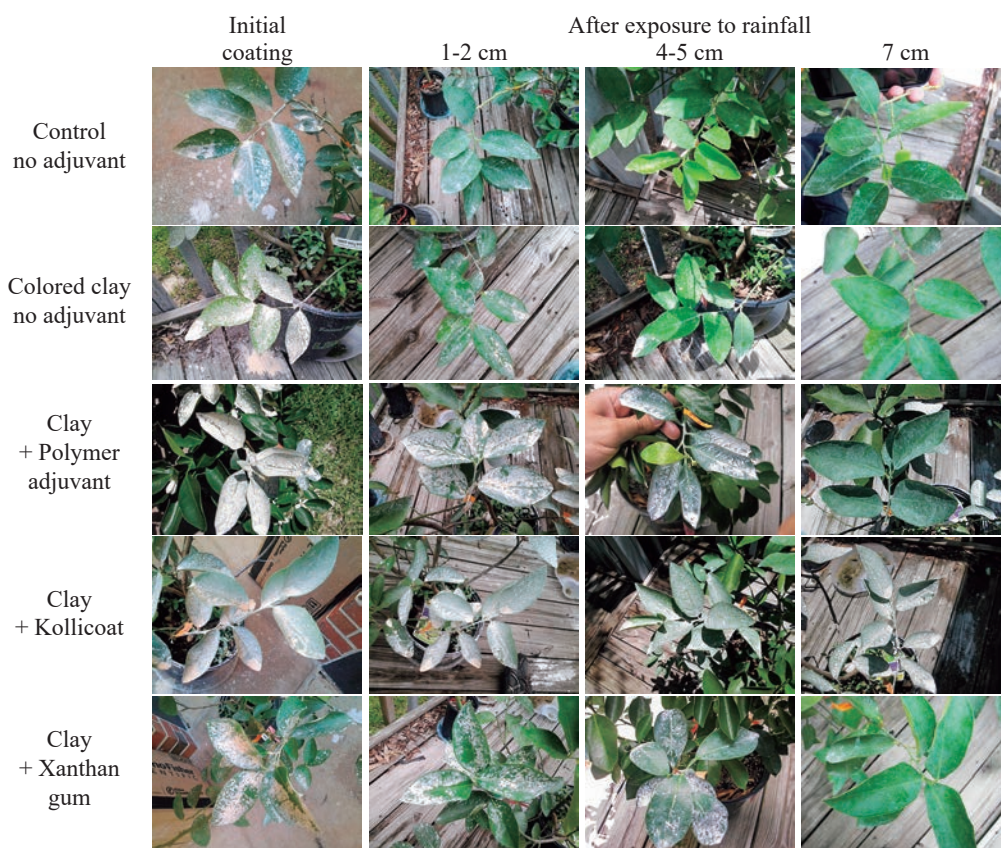


**Fig. 8** Images of citrus plants coated with clay, dyed-clay, dyed clay + polymer adjuvant, dyed clay + Kollicoat and dyed clay + Xanthan gum before and after exposure to 1–2 cm, 4–5 cm and 7 cm rainfall. Reprinted with permission from Ref. (Moudgil et al., 2017). Copyright: (2017) The Authors, patented in U.S.

used by themselves (alone), yield the required structural and functional information at affordable costs. Availability of safe multimodal—multifunctional contrast agents can promote early detection and treatments. Also, they can enable deep tissue imaging capabilities with some of the currently employed detection tools.

Photo Acoustic tomography (PAT) is a noninvasive imaging technique that employs nonionizing radiation (visible to near-infrared region) to contrast biological tissue and cells. Absorption of “pulsed” incident light by the biological tissue generates an acoustic signal (ultrasound) which is processed to obtain an image of the object. Furthermore, it is possible to image deep tissue because of the lower scattering of the ultrasound waves. However, enhancements in detection are needed for better resolution of the healthy and diseased tissue and cells. Multimodal contrast agents can enhance low-cost imaging using the capabilities of PAT. This may allow high-resolution *in vivo* imaging of patients with metallic implants who are, otherwise, unable to undergo MRI imaging.

Previously reported attempts to develop contrast agents, although successful but were of limited applicability because of their relatively larger size (120–150 nm). Gold-silica hybrid material termed gold speckled silica (GSS) nanoparticles were synthesized using nonionic water-in-oil

(W/O) emulsion technique. An outline of the synthesis protocol is presented below; additional details can be found in the related publications (Hahn et al., 2011; Sharma et al., 2010).

### 3.10 Synthesis and evaluation of Gd doped GSS nanoparticles as Multimodal contrast agents

The synthesis of the multimodal nanoparticles involved the following steps, (i) preparing the W/O microemulsion by mixing Tx-100 (nonionic surfactant), cyclohexane, and n-hexanol as co-surfactant with the appropriate amount of water. Adding the predetermined amount of TEOS (tetraethyl orthosilicate) in the beginning to the microemulsion and equilibrating the mixture for 30 minutes, (ii) initiating the hydrolysis and polymerization of TEOS by adding  $\text{NH}_4\text{OH}$ . Equilibrating the mixture for 24 hours and adding TSPETE (N-trimethoxysilyl propyl ethylenediamine triacetic acid trisodium salt) and TEOS for modifying the silica nanoparticles, followed by stirring overnight, (iii) adding Gd (III) acetate solution and stirring for another four hours, (iv) adding  $\text{HAuCl}_4$ , and 1.1 M solution of reducing agent (hydrazine hydrate) and stirring for ~12 hours, (v) separating the Gd doped GSS nanoparticles from the micro-emulsion by adding ethanol. Centrifuging the solution to recover nanoparticles of gold, (vi) washing the particles

thoroughly with ethanol and with water to remove surfactant molecules completely. (vii) redispersing the particles in nano-pure water for further characterization. As shown in Fig. 9, the gold speckled silica particles (GSS) were 25–60 nm in size, were fluorescent, and exhibited visible NIR absorbance (Sharma et al., 2010). Gd doped GSS particles exhibited unique photothermal properties, which are suitable for PAT imaging and possessing high relaxivity for MRI purposes (Sharma et al., 2012).

Fig. 10 illustrates the following: a) membrane labeled with Alexa Fluor<sup>®</sup> 488 WGA dye; b) nucleus stained with TO-PRO-3 stain; c) NIR Fluorescence from ICG–SiO<sub>2</sub> nanoparticles; d) an overlay of Fluorescence from the ICG–SiO<sub>2</sub> (pseudo-colored–red) showing the labeling and internalization of the breast cancer cells with the dye-doped nanoparticles. e) Pre-injection epifluorescence image (IVIS, Caliper) of the mouse with 745 nm excitation and 840 nm emission showing minimum background tissue fluorescence; f) NIR fluorescence signal from immediately after the first injection of Gd-doped ICG–SiO<sub>2</sub> nanoparticles showing the increase in signal with minimal interference from the background fluorescence; g) NIR fluorescence immediately following the second injection of Gd-doped ICG nanoparticles. The ROI quantification shows an increase in signal pre- and post-injections.

Gaps in the gold speckled silica surface permit water exchange between the Gd in the silica core and the bulk water, necessary for obtaining an efficient MR contrast. Simultaneously, the metal-dielectric interface generates an efficient PAT contrast enabling the applicability of these particles for diagnostic as well as therapeutic purposes.

Imaging and photothermal ability of the fluorescently doped GSS nanoparticles were evaluated in vitro by injecting GSS nanoparticles intratumorally into nu/nu mice bearing human breast cancers. The tumor region was irradiated with a NIR laser (output 500 mW) for 10 minutes. More than 60 % GSS loaded cells underwent necrotic death as compared to 30 % in control experiments (Sharma et al., 2010). These experiments indicated the suitability of using sub 50 nm NIR absorbing and luminescent GSS nanoparticles for imaging as well as their in-vitro and in-vivo photothermal ablation properties. Further studies were suggested to establish the viability of the GSS type nanoparticles applications for detecting and treating cancerous tissues in practical biological settings.

### 3.11 Self-stimulating photocatalytic antimicrobial coatings

Contact or touch-based infections are more common than generally recognized. Any contact with common

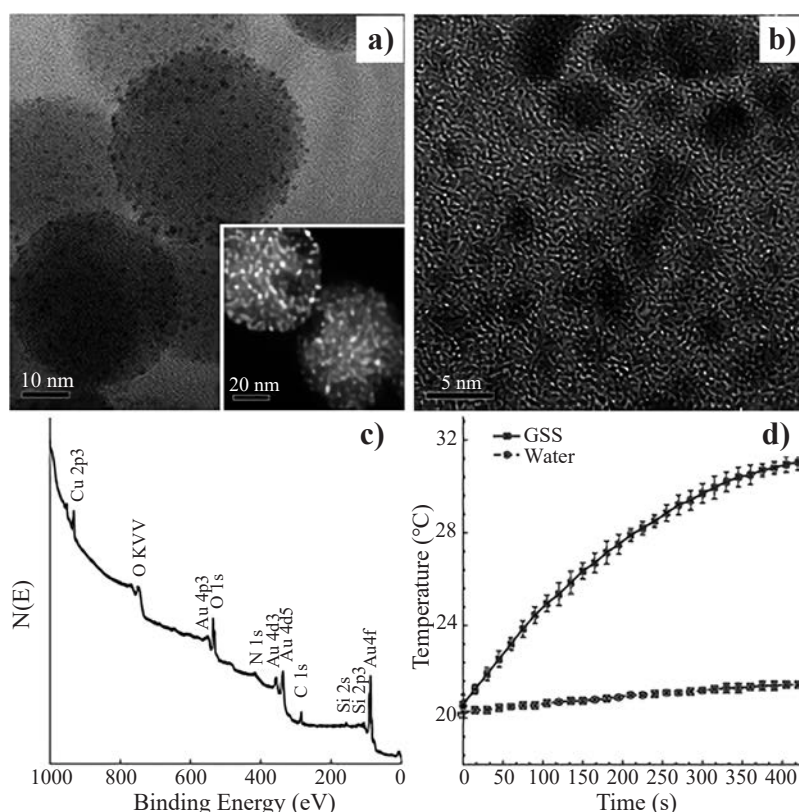


**Fig. 9** Characterization of rhodamine doped gold speckled silica (GSS) nanoparticles (a) representative TEM image of ca. 40 nm rhodamine doped GSS nanoparticles GSS showing the speckled silica surface; inset Z-contrast digital TEM; (b) higher magnification showing irregular shaped, discontinuously placed, 1–5 nm crystalline nano-gold deposits on silica; (c) representative XPS spectra; (d) ca. 11 °C increase in temperature of pegylated GSS nanoparticles in water suspension. Reprinted with permission from Ref. (Sharma et al., 2010). Copyright: (2010) Royal Society of Chemistry.

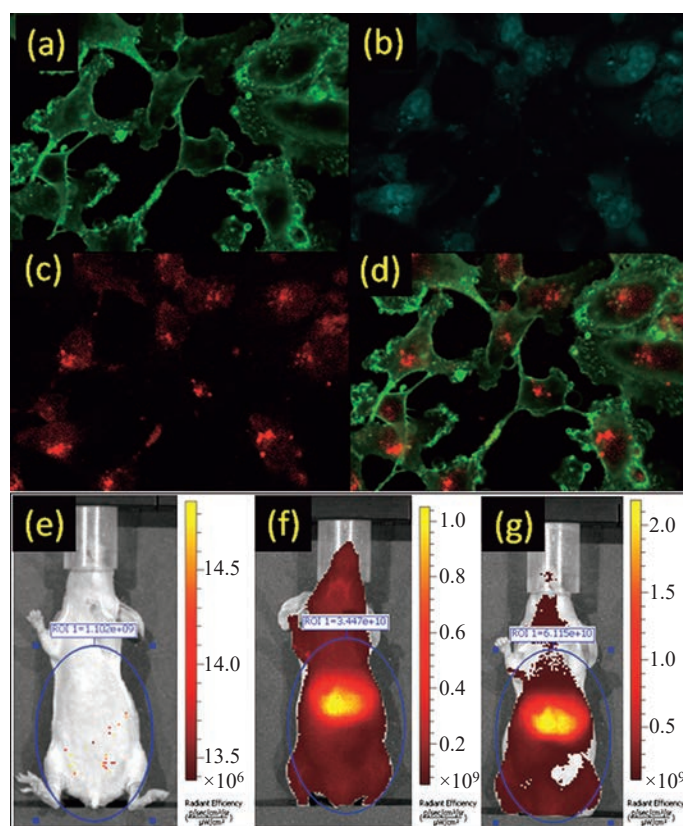


**Fig. 10** In vitro and in vivo functional evaluation of ICG–SiO<sub>2</sub> and Gd-doped ICG–SiO<sub>2</sub> nanoparticles. NIR fluorescent image of breast cancer MDA-MB-231 cells. Reprinted with permission from Ref. (Sharma et al., 2012). Copyright: (2012) John Wiley & Sons.

surfaces, including cell phones, keyboards, door handles, clothes, taps, and mops, can transmit infectious microbes. Currently available antimicrobial coatings that slowly release silver or copper ions have a limited lifetime, difficult to employ, and are relatively costly. In contrast, TiO<sub>2</sub> coatings that photo-catalytically mineralize organic contaminants are self-cleaning and produce no toxic by-products, and are relatively inexpensive. However, a major limitation of the TiO<sub>2</sub> by itself has been the need for UV light since, by itself, it exhibits poor photocatalytic properties in visible light.

Among the various techniques investigated for enhancing the photocatalytic property of TiO<sub>2</sub> in visible light include mixing TiO<sub>2</sub> with organic dyes—by far the least complicated method. However, degradation of the dye itself poses a major limitation of this approach. This is attributed to the generation of the reactive oxygen species (ROS) because of the transfer of light-initiated carriers to the TiO<sub>2</sub> surface and their reaction with the surrounding water/oxygen molecules. Interestingly, polyhydroxy fullerenes (PHF) behave the same way as organic dyes and are comparatively more efficient in scavenging electrons. Degradation of the PHF molecules can be tailored by synthesizing the number and placement of hydroxyl groups on the core fullerene structure.

Basic concept: The observation with the dye-sensitized

solar cells became the basis of the contaminant-activated photocatalysis concept. It was hypothesized that a dye such as Mordant Orange or Procion Red, when coated on pristine TiO<sub>2</sub>, can enhance photocatalysis by absorbing visible light and transferring the generated electrons to the TiO<sub>2</sub> surface. Similarly, when a bacterium such as *Staphylococcus aureus* comes in contact with the TiO<sub>2</sub>—dye construct, it should get mineralized. In another scenario, if the bacterium (or any other organic entity) is capable of absorbing the visible light, it should lead to its own degradation (“self-stimulating photocatalytic degradation”) by the generated ROS species (Krishna et al., 2018). The organic “contaminant” activated photocatalytic concept, along with measured visible light spectra of various surfaces, with and without different coatings, is presented in Fig. 11. Methods, protocols, and tools employed in this research are briefly described below. Additional details are provided by Krishna et al.

### 3.12 Coating formulations and testing protocols

The preparation of photocatalytic coating formulations involved sonicating 10 mg of anatase in 20 mL water at pH 9.5 for 30 minutes. Rutile and silica coatings, with and without PHF, were prepared in the same fashion. Coating formulations were used for further testing within an hour of their preparation.

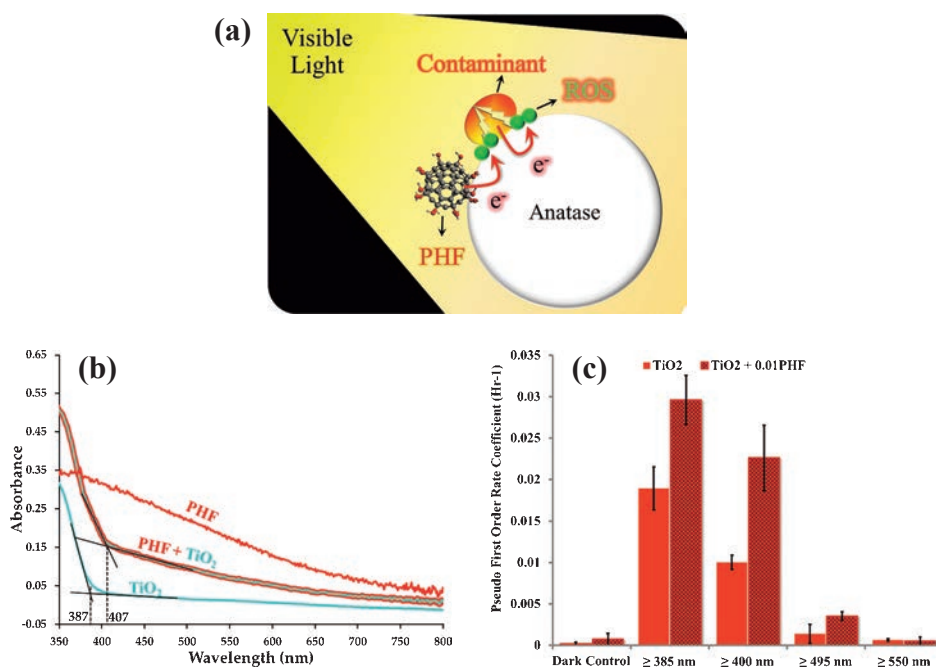


**Fig. 11** Contaminant-activated photocatalysis. (a) schematic of microbial mineralization with PHF as an auxiliary light harvester. (b) Ground-state absorption spectra for anatase (TiO<sub>2</sub>), polyhydroxy fullerenes (PHF), and PHF+ TiO<sub>2</sub>. (c) Pseudo first-order rate coefficients for degradation of Mordant Orange dye on anatase (TiO<sub>2</sub>) and anatase + 0.01 (w/w) PHF (TiO<sub>2</sub> + 0.01PHF) coatings. Dark control measures the ability of the photocatalytic coatings to degrade dye in the dark.  $N = 10$ . Reprinted with permission from Ref. (Krishna et al., 2018). Copyright: (2018) the authors, published by nature, Scientific Reports.

The efficacy of the photocatalytic coatings was tested using ceramic tiles. 0.4 mL of coating formulation was applied to the tile surface and dried for one hour at 40 °C in the dark. Subsequently, the second coat of the same or different coating material was applied. Organic dye or *S. aureus* suspension was applied to the dried surfaces. In *S. aureus*, a suspension ( $2\text{--}3 \times 10$  CFU/mL) was spread onto each coated tile surface, yielding a surface loading of 6400–9600 CFU/cm. *S. aureus*-coated tiles were dried in the dark in a biosafety cabinet for 3 hours.

### 3.13 Two-layer coating strategy

First, applying a layer of rutile (or silica) on the surface to be treated, followed by a thin coating of anatase, was devised to protect the base surface from any damage caused by the reactive oxygen species formed due to photocatalysis. Preliminary experiments employing an MRSA surrogate (ATCC 25923) showed promising results.

### 3.14 Testing in a beta facility

Commercial equipment was employed to apply the coatings, with a commercial primer (BioShield NuTiO) used as the binder between the two coatings. Coated surfaces were tested for antimicrobial efficacy using the bacterial count technique (Krishna et al., 2018). The efficacy of the coatings on various surfaces is illustrated by the results plotted in Fig. 12.

It was anticipated that visible light-absorbing organic

contaminants, including bacteria and viruses, when in contact with pristine TiO<sub>2</sub> (anatase), can further accelerate the contaminant degradation rate. Considering the wide-ranging applications of TiO<sub>2</sub> in paints, food products, pharmaceuticals, and polymer composites, possible photocatalytic activity aspects should be considered when designing such products (Georgieva et al., 2013; Krishna et al., 2006; Nandakumar et al., 2017; Zhao et al., 2009).

### 3.15 Inhibition of scale formation by surfactant and polymeric additives

Several industrial processes are adversely impacted by the crystallization of minerals or the formation of “scale” on the surface of the processing equipment. Examples include phosphoric acid manufacturing for fertilizer production, desalination plants, boilers for steam production, and water treatment facilities. Scale deposition severely reduces the process efficiency and requires frequent cleanings that cost money. In phosphoric acid manufacturing, multistage evaporators are frequently used to obtain 52–55 wt % P<sub>2</sub>O<sub>5</sub> phosphoric acid. The concentrated phosphoric acid gets supersaturated with respect to calcium sulfate and other scale-forming constituents, which subsequently accumulate on the pipe walls. These deposits reduce the output of the system and require frequent removal to maintain efficiency (Carr et al., 2014). Even a thin layer of deposits can create significant resistance to heat transfer.

Over the last several decades, research attempts have

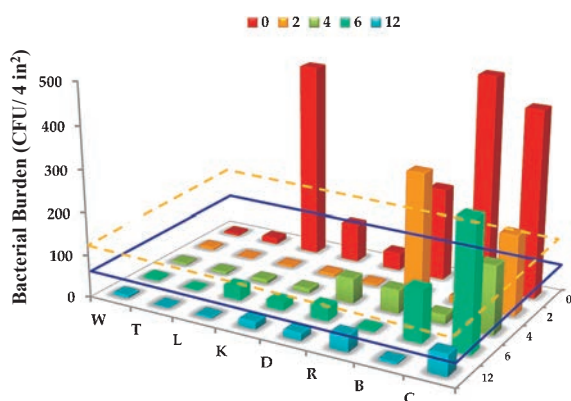


**Fig. 12** Beta facility testing. For a given surface, the bars represent counts ( $n = 3$ ) as a function of time from 0 to 12 months. W = Wall; T = Thermostat; L = Locker; K = Knob; D = Soap Dispenser; R = Bathroom Rail; B = Bed Rail; C = Counter. Blue dashed line --the threshold of microbial counts for benign surfaces, and the yellow dashed line - - the average microbial counts on copper surfaces in a clinical trial. Reprinted with permission from Ref. (Krishna et al., 2018). Copyright: (2018) the authors, published by nature, Scientific Reports.

continued to identify the additives that at least might delay the scale formation if not eliminate it outright. In the phosphoric acid production plants, research approaches have focused on the use of water-soluble inhibitors that may block the development of the supercritical nuclei or retard the growth of the calcium sulfate crystals. Several theories have been proposed for antiscaling properties of different additives, but the inhibitors that can perform at a plant scale on a consistent basis have been lacking. Over the last decade, Solvay researchers have developed and demonstrated an antiscalant technology using Phosflow<sup>®</sup> that substantially reduces the fouling issue in the wet-process phosphoric acid production plants (Carr et al., 2014).

Phosphoric acid is produced by reacting phosphate rock (tricalcium phosphate) with sulfuric acid at high temperatures. This reaction generates calcium sulfate as the byproduct, some of which can deposit on heat exchanger walls when the phosphoric acid is concentrated. Calcium sulfate exists in three forms: calcium sulfate dihydrate,  $\text{CaSO}_4 \cdot 2\text{H}_2\text{O}$  (Di-hydrate or DH); calcium sulfate hemihydrate,  $\text{CaSO}_4 \cdot 0.5\text{H}_2\text{O}$  (also known as bassanite); and calcium sulfate anhydrous,  $\text{CaSO}_4$  (anhydrite). Plants generally produce gypsum (calcium sulfate dihydrate) initially, which over time can be baked into anhydrite ( $\text{CaSO}_4$ )—which is dense and difficult to remove (Carr et al., 2014). It has been proposed that in a system supersaturated with DH, first crystals of hemihydrate ( $\text{CaSO}_4 \cdot 0.5\text{H}_2\text{O}$  (HH)) precipitate out, which subsequently hydrate into DH. Once the HH crystals are formed, they start to grow into nanorods. At low to medium supersaturation ratios, both bassanite and gypsum crystals seem to form. At high supersaturation ratios, only gypsum precipitates have been observed (no Bassanite). It was further reported that the existence of the

precursor phase (bassanite) could be increased by adding carboxylic acid (Polat and Sayan, 2017). Changes in crystal morphology were also observed. Inhibition of scale through the complexation and adsorption of an additive is not unique to  $\text{CaSO}_4$ . A comprehensive review of calcium sulfate precipitation is presented in Driessche et al. (2017).

In order to understand the underlying mechanisms of the Phosflow<sup>®</sup> (PF) technology, a systematic study was conducted. Turbidity and induction time measurements were used to calculate the inhibition efficiency ( $E$ ), the surface energy ( $\gamma$ ), the nucleation rate ( $J_s$ ), the free energy ( $\Delta G_{cr}$ ), and the critical nucleus size ( $r$ ). Solubility changes, SEM, FTIR, and XRD, were employed as investigative tools in the in-situ study of how additives affect mineral crystallization on surfaces. It was anticipated that a basic understanding of the scale formation process would allow the development of commercially viable other (greener) additives not only for phosphoric acid plants but also for other systems (Tanquero et al., 2021).

Experimental protocols employed are briefly described below. Reagent grade chemicals, including phosphoric and sulfuric acids, and calcium hydrogen phosphate monobasic  $\text{CaH}_4(\text{PO}_4)_2 \cdot 2\text{H}_2\text{O}$  were purchased from the Fisher Scientific Company and were used as received. Polyethyleneimine of different molecular weights (Mn 0.6 k, 1.8 k, 10 k, and 60 k) was obtained from Sigma Aldrich and Acros Organics Co.

Predetermined volume and ratio of phosphoric and sulphuric acid solutions were added to a 500-mL beaker and heated to 88 °C. The desired amount of calcium phosphate monobasic monohydrate, a specific volume of deionized water or water containing a polymeric additive, along with a corresponding amount of 32.5 g/g (mass%) sulphuric acid was added to the beaker. The reaction temperature was kept constant at 88 °C. The turbidity of the resulting reaction product was measured at different times throughout the reaction using a HACH 2100AN Turbidimeter. Particle Size measurements were conducted using the Accusizer 780 AD. Recovered solids were imaged using an Olympus Optical Microscope.

The effect of PhosFlow (PF) addition is illustrated by Fig. 13 and data given in Tables 1 and 2. PF addition increased the induction time, reduced the surface free energy for nucleation, and delayed the growth of the gypsum (Carr et al., 2014; Tanquero et al., 2021; Zhang L. et al., 2015).

Effects of polymeric additives: Different pathways by which polymeric scale inhibitors can affect nucleation and growth processes include: (a) chelating the active ions in the nucleating solutions (Jamialahmadi and Müller-Steinhagen, 2007); (b) adsorption onto nuclei interfering in nucleation and/or crystal growth (He et al., 1994); (c) dispersion of the scale-forming species (Amjad, 1988); and (d) increasing the local viscosity of the medium thereby affecting the kinetics of the nucleation and growth processes

(Driessche et al., 2017).

Chemical structure, molecular weight, and dosage of additives all are known to govern the efficacy of polymeric type inhibitors (Abdel-Aal et al., 2015; Jain et al., 2019; Akyol et al., 2006). Based on the literature review, three polymeric additives—Poly(acrylic acid) (PAA), Poly(diallyldimethylammonium chloride) (PDADMAC), and Polyethyleneimine (PEI) were selected for the present study. Screening tests revealed that only PEI has the potential of affecting the scale formation in the phosphoric acid system. As shown in Fig. 14, PEI effectiveness increased with an increase in polymer molecular weight, and the optimal concentration was determined to be around 40 ppm.

Higher interfacial energies upon PEI addition and morphological changes suggested a plausible mechanism

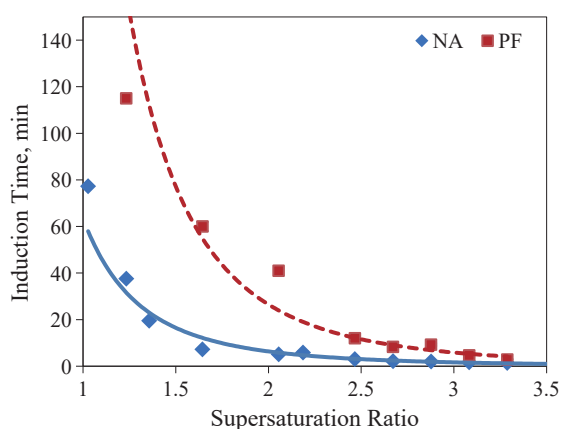


**Fig. 13** Effect of PhosFlow (PF) on the induction time as a function of supersaturation ratio. Note: the legend NA and PF represent without additive and with additive PhosFlow, respectively. Reprinted with permission from Ref. (Tanquero et al., 2021). Copyright: (2021) Canadian Journal of Chemical Engineering.

involving adsorption of the polymer molecules on specific crystal faces resulting in inhibition of nuclei growth. Another possibility was stated to be the polymer changing the stability of the precursor molecules, thus prolonging their induction period. The exact role of PEI as a scale inhibitor requires further studies, including monitoring of the structural and morphological changes of the crystals formed, especially during phase changes. In this regard, techniques such as cryo-TEM or small-angle X-ray scattering have been successfully employed to probe molecular-scale mechanisms (Sleutel et al., 2014).

### 3.16 Surfactant coatings for corrosion inhibition

Corrosion of metal structures, pipelines, boilers, and other industrial equipment is a major challenge in the manufacturing sector. It is estimated by NACE International and other sources that the industrial impact of corrosion

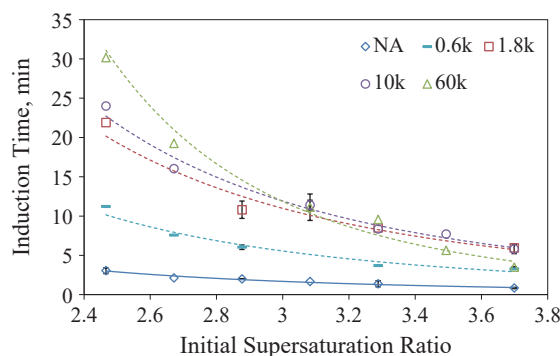


**Fig. 14** Effect of PEI molecular weight on the induction time as a function of supersaturation ratio. Reprinted with permission from Ref. (Tanquero et al., 2021). Copyright: (2021) Canadian Journal of Chemical Engineering.

**Table 1** Effect of different supersaturation ratio of calcium sulfate on nucleation rate and free energy change for formation of critical nucleus size.

Supersaturation ratio	Nucleation rate $J_s$ $10^{28}$ nuclei/cm <sup>3</sup> ·s		Gibbs free energy $\Delta G$ $10^{-20}$ kJ/mol	
	Without PF	With PF	Without PF	With PF 75 ppm
2.466	9.19	22.43	1.19	0.75
2.672	13.35	28.33	1.00	0.63
2.877	17.53	33.60	0.87	0.54
3.083	21.56	38.25	0.76	0.48

**Table 2** Effect of different supersaturation ratio of calcium sulfate on critical nucleus size and the number of molecules per a nucleus with and without PF.

Supersaturation ratio	Critical nucleus radius $10^{-8}$ cm		Number of molecules per a nucleus	
	Without PF	With PF	Without PF	With PF (75 ppm)
2.466	4.68	4.01	5	3
2.672	4.30	3.68	4	3
2.877	4.00	3.42	3	2
3.083	3.76	3.21	3	2



in the US alone is in excess of \$500B per year. Corrosion inhibition strategies include designing new materials for corrosion resistance, minimizing contact with corrosive elements, and/or applying protective coatings. The application of organic corrosion inhibitors is quite common in oil and water transport pipelines. Surfactant blends constitute most of the corrosion inhibitors.

Most of the effective inhibitors comprise heteroatoms such as O, N, S, and  $\pi$  bonds, which enable them to attach to the metal surface (Bockris et al., 2000). The specific chemical nature of a given corrosion inhibitor (CI) depends on the environment (nature of ions, pH, temperature, etc.). Organic corrosion inhibitors, especially surface-active agents (surfactants), have been reported to be some of the most effective inhibitors due to their ability to form self-assembled films at interfaces, as shown in Fig. 15 (Fuchs-Godec, 2009; Zhu et al., 2016; 2017). These barrier layers inhibit the transport of corrosion, causing ionic species to and from the surface.

Despite their advantages and wide usage, the scientific understanding of corrosion inhibition using surfactants at the molecular level is not comprehensive. One of the major aims of the current research was to characterize the surfactant films formed on the steel surface to gain a better understanding of the corrosion inhibition mechanism. A brief description of the materials, methods and experimental protocols is outlined below. Additional details can be found elsewhere (Rajopadhye, 2018).

The standard practice for laboratory immersion corrosion testing of metals (ASTM G31) was followed to prepare the test samples. AISI1010 carbon steel rod (Obtained from McMaster-Carr, composition: C 0.13 %, Mn 0.4 %, P 0.04 %, S 0.05 % and balance Fe) was used to fabricate the working electrode. A circular rod of the cross-section area of 0.08 cm<sup>2</sup> (accurate within  $\pm 1$  %) was coated in epoxy resin such that only the circular cross-section of the rod at the end was exposed to the electrolyte while immersed in the test solution. The exposed end of the steel rod was polished using 600, 800, 1000, and 1200 grit silicon carbide abrasive pads to remove the surface oxide layer,

followed by fine polishing using 1  $\mu$  colloidal silica slurry and diamond paste. The RMS surface roughness of the polished specimen was determined to be  $\sim 25$  nm using AFM surface topography. The steel specimen thus prepared was degreased by sonicating in ethanol followed by thorough rinsing using DI water and dried by the jet of nitrogen gas. The steel surface thus prepared was exposed to the test solution no later than 30 minutes after the polishing was done in order to keep surface oxidation to a minimum level.

The surfactants investigated in this study were purchased from Sigma-Aldrich (research-grade) and were used as received. All the surfactant solutions were prepared by adding the calculated amounts of surfactants to triple distilled DI water (Resistivity of 18.1 M $\Omega$ .cm) to prepare the stock solutions. These stock solutions were used to prepare the desired concentration by successive dilutions.

All the electrochemical investigations were performed in a standard 3-electrode electrochemical cell, Multiport<sup>TM</sup> (supplied by Gamry Instruments Inc.), connected to the Reference3000<sup>TM</sup> potentiostat (Model number 20215, supplied by Gamry Instruments Inc.) equipped with an inbuilt lock-in amplifier. The saturated calomel electrode (SCE) housed inside the Luggin capillary was used as a reference electrode, whereas a high-density graphite rod was used as an auxiliary electrode. 800 mL of test solution was transferred to the Gamry Multiport<sup>TM</sup> electrochemical cell after the solution pH was adjusted. The cell was closed by placing the glass lid with a Viton O-ring to seal the vessel. All the tests were performed at  $25 \pm 1$  °C. The temperature of the test solutions was maintained by circulating water through the jacket around the electrochemical cell. All experiments were repeated multiple times to ensure the reproducibility of the data.

### 3.17 Effect of nature of the surfactant head group on corrosion inhibition

In an attempt to isolate the effect of the head group chemical nature, octadecyl trimethyl ammonium bromide (OTAB) was selected as a counterpart to oleic imidazoline (OI), an active ingredient in commercial corrosion inhibitor

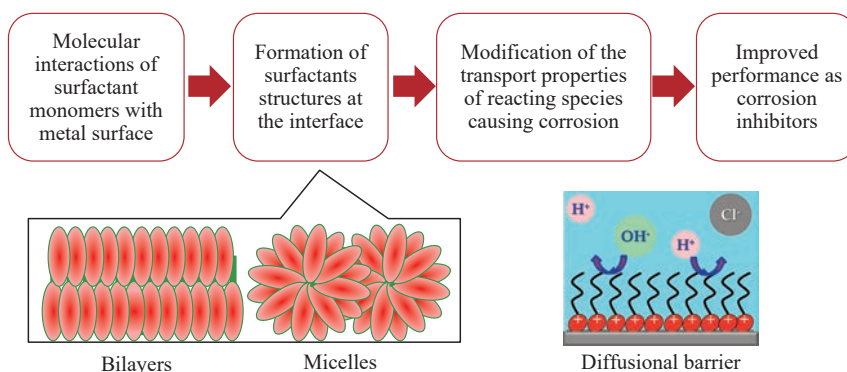


**Fig. 15** Self-assembled surfactant structure as a diffusional barrier to the transport of corrosion causing species. Reprinted with permission from Ref. (Rajopadhye, 2018). Copyright: (2018) University of Florida.

blends. They both have 18 carbon atoms in their hydrocarbon chain, albeit different chain structures—OTAB straight chain; OI with a double bond in the hydrocarbon chain. The inhibition efficiency of the two surfactants was determined to be 78 % vs. 83 % for OI and OTAB, respectively, indicating that the contributions from the two polar head groups are relatively well matched.

### 3.18 Effect of hydrophobic interactions on corrosion inhibition

The corrosion inhibition contribution of the hydrophobic effects due to the chain-chain interactions was investigated by comparing the inhibition performances of different inhibitors with the same head group chemistry but varying chain lengths. Several homologous members (from 10 to 18 CH<sub>2</sub> groups) of quaternary ammonium bromide (TAB) were tested at the same bulk concentration for their corrosion inhibition efficiency. It was determined that the corrosion rate decreased with an increase in the hydrocarbon chain length. Both corrosion rate and the polarization resistance are plotted as a function of hydrocarbon chain length in Fig. 16.

The observed results can be explained based on the degree of surface activity of the surfactant molecules. Higher surface activity due to higher chain length results in higher and probably denser surface coverage, thereby providing more corrosion protection. Therefore, in spite of the same number of molecules being present in the bulk solution for each surfactant, better corrosion protection was provided by OTAB as compared to DTAB since a higher number of OTAB molecules are expected to be adsorbed at the interface due to their higher surface activity, thereby blocking a greater number of active sites for corrosion.

### 3.19 Effect of surfactant concentration

Comparison of the corrosion inhibition efficiency as a function of DTAB and OI concentration in Fig. 17 revealed that optimal corrosion inhibition occurs at a lower concen-

tration than their respective critical micelle concentration (CMC) values. OI was determined to be more effective than DTAB, possibly due to the stronger electrochemical interaction of the imidazoline ring with the steel surface resulting in more effective corrosion protection.

The initial part with the higher slope in both the plots represents the region where the corrosion rate is increasingly reduced as more and more active sites are blocked by the adsorbed inhibitor molecules. This region is fairly straight-lined, indicating that the corrosion inhibition is directly proportional to the surface coverage by the surfactant molecules. The second part, also almost straight-lined, albeit with a relatively lower slope, indicates almost complete coverage of the surface with monolayer and/or surfactant aggregate structures. The corrosion protection in this region was attributed to the blocking of the active corrosion sites as well as the resistance to the transport of corrosive species through the surfactant aggregates.

The inflection point in each plot represents a structural change in the adsorbed layer from monolayer to multilayer (bilayers or micelles!). Concentration at the inflection

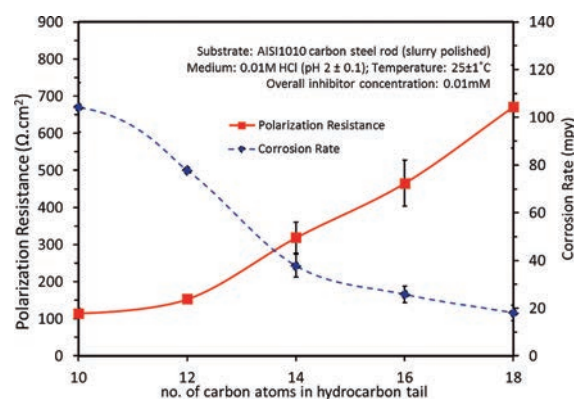


Fig. 16 Corrosion rate (CR) and the polarization resistance (Rp) for AISI1010 carbon steel exposed to 0.01 M HCl solution in the presence of the homologous series of TAB inhibitors at 0.01 mM concentration at 298 K. Reprinted with permission from Ref. (Rajopadhye, 2018). Copyright: (2018) University of Florida.

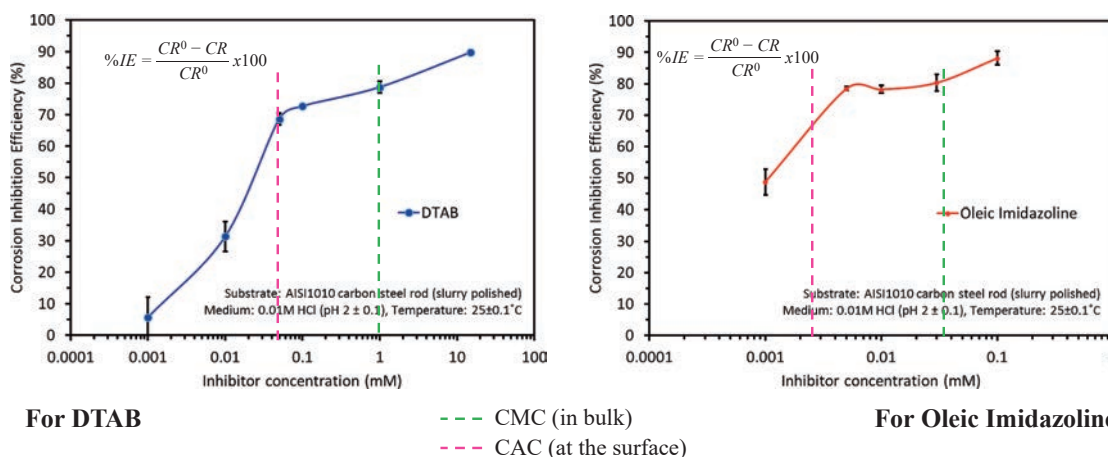


Fig. 17 Comparison of corrosion inhibition efficiency of DTAB and OI as a function of concentration. Reprinted with permission from Ref. (Rajopadhye, 2018). Copyright: (2018) University of Florida.

point is termed as the critical aggregate concentration (CAC), the concentration at which the aggregate structures start forming at the interface. The CAC value for DTAB (0.05 mM) is about an order of magnitude higher than for OI (CAC = 0.005 mM). This could be due to the higher surface activity of OI molecules as compared to DTAB as a result of differences in their hydrocarbon chain lengths. Interestingly, the CAC values ( $CAC_{DTAB} = 0.07$  mM and  $CAC_{OI} = 0.008$  mM) are lower than the bulk CMCs of the two surfactants ( $CMC_{DTAB} = 15$  mM and  $CMC_{OI} = 0.03$  mM), indicating the possibility of the metal surface catalyzing the self-structuring process resulting in the aggregation taking place on the surface (CAC) at a lower concentration than in bulk (CMC) (Singh et al., 2001).

### 3.20 Surfactant adsorption mechanism

The mode of adsorption for the OI-type additives has been reported to be chemical in nature. In the present study, adsorption of DTAB and OI was determined to obey the Langmuir adsorption isotherm. The free energy calculations of 9.3 kJ/mol for DTAB and 9.4 kJ/mol for OI are more indicative of the physical adsorption mechanism. The literature reports are inconclusive in this regard (Keera et al., 2012; Zhu et al., 2015; 2017). Further investigations are required to reach a conclusive determination about the adsorption mechanism of the most effective corrosion inhibitors.

Overall, the two key contributions to corrosion inhibition – physical (the hydrophobic interactions between the chains) and electrochemical (the head group interactions with the surface) were isolated in this study by varying one component while keeping the other constant. It was demonstrated that the physical contributions play an equally important role in determining the corrosion inhibition properties of the surfactant-based inhibitors. The chain-chain interactions of surfactant molecules that drive them to the interface determine the number of surfactant molecules available for adsorption and thus dictate the overall surface coverage and the corrosion inhibition efficiency.

### 3.21 Precision gold nanoparticles synthesis

Precision particles of very narrow size distribution, especially metal (e.g., gold) nanoparticles, are needed for advanced sensor applications and as reference materials for toxicology assessments. Additional commercial applications of such particles are limited due to their high cost. Narrowly sized gold nanoparticles (AuNPs) can cost up to \$10,000 per gram AuNPs. One of the major reasons for their high cost is their labor-intensive batch production which is susceptible to batch-to-batch variation. The aim of this project was to develop a continuous production technique that is scalable for cost-effectively and high-throughput production of precise metal nanoparticles. AuNPs can

be synthesized using the Turkevich method. The average particle size, size distribution, and morphology were characterized by UV-visible spectroscopy, Dynamic Light Scattering (DLS), and Transmission Electron Microscopy (TEM). Chemical composition was analyzed with XPS, FT-IR, and ICP-MS Spectrometry. The precision of nanoparticles, i.e., size distribution, was quantified using the polydispersity index, PDI (ISO13321, 1996).

Over the last decades, nanoparticle synthesis using flow chemistry has attracted more attention because of its automation capability and potential for low-cost production of high-precision nanomaterials (Nightingale et al., 2014; Stitt, 2002). Typical flow chemistry involves the mixing of reactants in a chip-based microfluidic cell under specific conditions (Wagner et al., 2008). However, relatively low throughput and reactor fouling are some of the major limitations of microfluidic reactors for nanoparticle synthesis. Moreover, attempts to scale up such reactors often lead to the loss of precision control of the particle properties such as the size and size distribution.

In this study, initial efforts to produce narrowly sized gold nanoparticles using a single-phase flow reactor were unsuccessful primarily due to reactor fouling. The attempts to overcome reactor fouling by changing the reactor material, flow rate, and particle synthesis chemistry were not successful. However, these attempts revealed that most likely fouling was caused by heterogeneous nucleation and the growth of gold on the reactor surface. Fouling in continuous nanoparticle synthesis can be overcome in carefully designed two-phase or biphasic flow systems that comprise two immiscible fluids. In the biphasic reactor, the continuous phase is selected such that it preferentially wets the reactor surface, and the dispersed phase consists of reactant solution. In the present study, silicone oil was selected as the continuous phase since it was expected to wet the reactor surface, Perfluoro alkoxy, or PFA tubing. Gold chloride ( $HAuCl_4$ ) and trisodium citrate ( $Na_3C_6H_5O_7$ ) constituted the two aqueous phase reactants. A schematic of the flow reactor is illustrated in Fig. 18.

As shown in Fig. 19, silicone oil was introduced from both sides of the cross-junction (IDEX, ETFE P-723) as the continuous phase and droplets of aqueous reactants were generated when the already mixed solution of the two reactants was merged into the silicone oil. Each aqueous droplet dispersed in the silicone oil acted as an individual mini reactor. Additional experimental details can be found in the publication (Dong et al., 2022). It is important that the system conditions of concentrations, flow rate, and temperature, and pressure are controlled such that the aqueous reagents are completely mixed during their flow in the channel before the mixed reactants are discharged/dispersed into the non-aqueous phase. It should be noted that to avoid nucleation before complete mixing of the reactants, the channel temperature is maintained at room

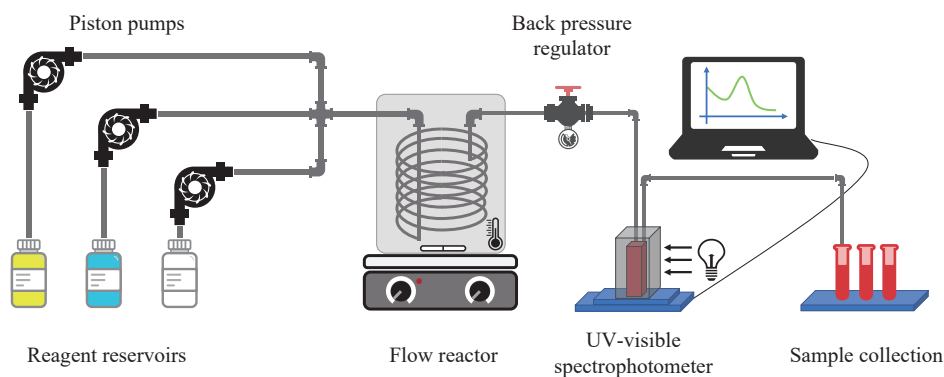


**Fig. 18** The layout of the flow reactor system used for gold nanoparticle synthesis. Reprinted with permission from Ref. (Dong et al., 2022). Copyright: (2022) The Authors, published by KONA Powder and Particle Journal.

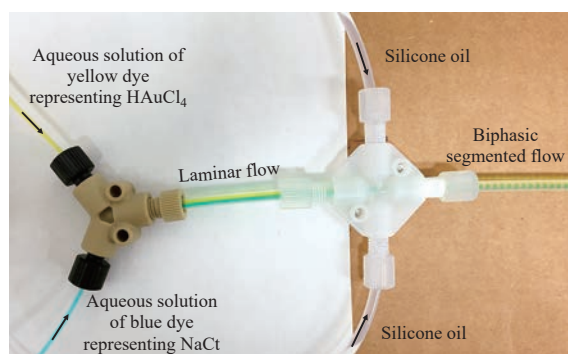


**Fig. 19** Experimental setup showing the generation of liquid-liquid biphasic segmented flow. The yellow and blue dye represent  $\text{HAuCl}_4$  and  $\text{NaCl}$  solutions, respectively. Reprinted with permission from Ref. (Dong et al., 2022). Copyright: (2022) The Authors, published by KONA Powder and Particle Journal.

temperature to slow the precipitation reaction kinetics; and to accelerate the kinetic process, the droplets of the mixed reactants are heated to  $100\text{ }^\circ\text{C}$  as soon as they are dispersed in the non-aqueous phase.

No fouling was observed in the biphasic flow reactor. Moreover, as indicated in **Figs. 20** & **21**, the gold nanoparticles produced were consistent over several hours of biphasic reactor operation. This was attributed to the elimination of fouling and the much more efficient mixing of the reactants due to the recirculating flow fields encountered inside of each aqueous segment/droplet dispersed in the continuous fluid. The precision of the nanoparticles produced was determined by calculating the polydispersity index (PDI) values. Polydispersity index values of the gold nanoparticles ( $\text{PDI} = 0.068$ ) were determined to be very close to the PDI of the reference material generated in batch synthesis ( $\text{PDI} = 0.065$ ). Overall, it was determined that fouling in the continuous flow reactors can be overcome by avoiding the nucleation reaction in the vicinity of the reactor surface; otherwise, it could impact the particle properties and the reaction yield.

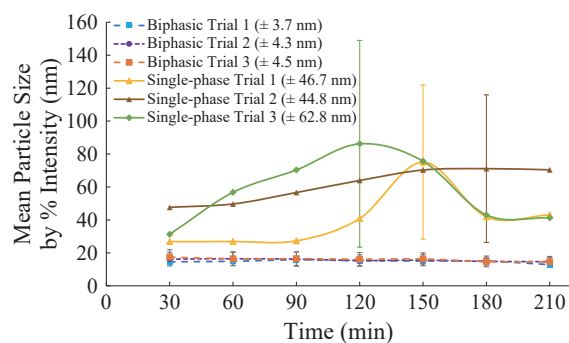


**Fig. 20** DLS measurement of the mean particle size of the AuNPs synthesized in biphasic flow reactor. Reprinted with permission from Ref. (Dong et al., 2022). Copyright: (2022) The Authors, published by KONA Powder and Particle Journal.

#### 4. Concluding remarks

Although there have been considerable advances in particle synthesis, functionalization, characterization, and performance assessment methodologies, a number of challenges remain that need to be overcome before large-scale applications of engineered particulate systems become a reality. Some of the challenges and opportunities, especially related to the fields of research discussed in this paper, are outlined below.

In the area of particle assisted microbe adhesion and removal from household surfaces, skin, bio-implants, hospital and general use fabrics, etc. in the form of sprays & coatings, controlled release devices, and wipes, there is a critical need for a better understanding of the mechanisms of bacterial interactions with different types of surfaces and engineered particulates including polymers, inorganic, metal, skin, etc. (D'Accolti et al., 2018; Varshney et al., 2021). Qualitative or semi-quantitative information about the mode of microbial adhesion exists, but there is a lack of quantitative data on the various forces involved in microbial adhesion and removal. Reliable data is needed to develop robust modeling and simulation schemes. Specifically, in the handwashing applications field, reducing the time it takes to wash off the microbial contaminants below

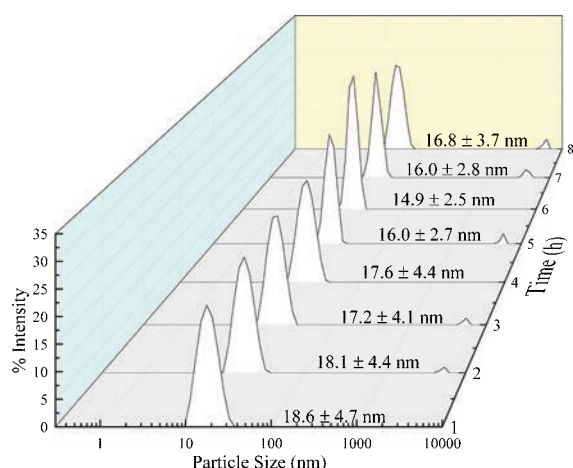


**Fig. 21** DLS measurements of particle size and size distribution of gold nanoparticle samples synthesized using liquid-liquid biphasic flow reactor. The particle size and size distribution remained constant in the 8-hours uninterrupted experiment. Reprinted with permission from Ref. (Dong et al., 2022). Copyright: (2022) The Authors, published by KONA Powder and Particle Journal.

a safe threshold is an important goal. Furthermore, developing suitable hand hygiene, body cleansing formulations, and detergency for water-stressed regions of the world is fast becoming an acute necessity.

Large-scale applications of particulate coatings for crop protection require low-cost functionalized materials such as clays for foliar applications not only for protection from insects but also for on-demand delivery of actives and micronutrients to the plants. Moreover, functionalized particles must not cause any harmful effects to crop quality and yield. Multifunctional particle formulations and smart aggregates for on-demand delivery purposes can help reduce the dependence on chemicals that might otherwise result in the generation of antibiotic-resistant microbes. Selective killing of only harmful insects and bacteria, leaving the healthy microbes and insects intact, remains a prized long-term goal.

On the particulate systems mediated disinfectant front using photocatalytic coatings, considerable progress has been made in identifying suitable doping additives to enhance photocatalysis under visible light. However, the low rate of disinfection requiring relatively longer disinfection times remains a major competitive disadvantage for large-scale applications. Additionally, nanotoxicity continues to be a challenge for titania-based disinfection coatings (Jafari et al., 2020; Liao et al., 2020; Rtimi et al., 2019). Bismuth oxide coatings have been reported to outperform other photocatalytic materials, including titania. However, long exposure times are required for microbial inactivation (Ratova et al., 2018). For the disinfection of surfaces, increasing the efficacy of applied coatings to reduce the frequency of disinfectant applications is a critical need.

Practical application of surfactants for corrosion in-

hibition has been a theme of several studies not only to enhance the effectiveness of current formulations but also to develop greener surfactant coatings (Sliem et al., 2019; Zhuang et al., 2021). Facilities for testing the efficacy of formulations under field conditions of high temperature, pressure, salinity, pH, flow conditions and particulate contamination, etc., are scarce. Suggestions for setting up a flow loop incorporating above mentioned parameters should yield the data needed for developing robust predictive models (Zhu et al., 2017).

Biomedical applications of nanoparticles continue to be a strong driver for advanced applications of engineered particulate systems for the detection and treatment of cancer. Several comprehensive review articles have summarized the latest developments in this regard. Despite the positive outlook, major challenges need to be overcome before large-scale clinical implementation of such materials becomes a reality. These include toxicity, long term biodistribution, biodegradability, in addition to protocols for large scale production of multimodal particles at low cost (Aghebati-Maleki et al., 2020; Gallo et al., 2013; Han et al., 2019; Hsu et al., 2020; Luo et al., 2021; Silva et al., 2019; Thanapandiyaraj et al., 2018).

Despite several studies across the globe, the toxicity of nanoparticles continues to be a major obstacle for their large-scale usage in biomedical, consumer goods, healthcare, and pharmaceutical products. Lack of availability of well-characterized reference materials for conducting comprehensive toxicological assessments has been a problem for industrial and academic researchers alike. In the USA, the National Institute of Environmental Health Sciences (NIEHS) has funded several groups to generate the required data. Most recently, NIEHS funded a consortium led by the Center for Nanotechnology and Nanotoxicology, T.H. Chan School of Public Health, Harvard University in collaboration with MIT, University of Maine, and the University of Florida to create a repository of well-characterized engineered nanomaterials for toxicological studies. Availability of precise nanoparticles (narrowly sized and/or with specifically designed functionalities) at low cost, however, remains a barrier because of batch production of such particles that invariably involves numerous iterations to generate modest quantities of narrowly sized nanoparticles thereby driving up their prices. In this regard, biphasic continuous flow reactors have shown promise pending their successful scale up for larger-scale production (Dong et al., 2022).

In recent years, AI has become a popular tool for complex materials and systems design, simulation, and optimization. For example, Shams et al. employed AI methods to estimate and optimize the silver nanoparticle concentration on the treated silk fabrics for antimicrobial properties (Shams Nateri et al., 2019). Vinoth and Datta used the artificial neural network and genetic algorithm to

design a novel nanoparticle reinforced polymer composite for replacements in hip joints (Vinoth and Datta, 2020). Mahmoud et al. implemented the artificial neural network to simulate and predict the removal efficiency of several organic contaminants from aqueous systems using iron nanoparticle sorbents (Mahmoud et al., 2018).

AI techniques have also been utilized in various biomedical applications, including image inspection via machine learning, histopathology examination, making unbiased medical decisions, molecular and medicine performance modeling (Chaddad et al., 2021; Jin et al., 2020). AI has the ability to precisely detect nanoparticle biomarkers or contrast agents in biological systems from medical imaging modalities (Zhang et al., 2021). It also has the potential to predict and model the property and response of a hypothetical contrast agent in specific systems. The main limitation of AI applications remains the lack of professional data curation and quality assurance (Bi et al., 2019). Other challenges include validating the predictive AI models, understanding the fundamental mechanisms of the AI models, and reaching a consensus in the research community about the AI outcomes (Bi et al., 2019).

Greater interactions among the industry and academic researchers not only would advance the field of particle and powder technology-mediated processes and products but also help create a well-trained cadre of sorely needed young researchers and practitioners in the field. Additionally, meaningful collaborations among physical scientists and engineers, life scientists, and clinicians are necessary to develop nanoparticle-based sensors, multimodal contrast agents, and other health monitoring and treatment devices. Overall, in the last few decades, there have been tremendous advances in the field, and more exciting new discoveries are expected in the coming years, especially with the advent of AI-mediated particulate systems-related innovations.

## Acknowledgments

The authors convey special thanks to Dr. P. Sharma, Dr. V. Krishna, Dr. V. Nandakumar, and Dr. J. Tanquero for their valuable assistance with some of the figures incorporated in this paper. The authors acknowledge the financial support of the National Science Foundation Center for Particulate and Surfactant Systems (CPaSS) and the industry members (NSF Award #1362060, NSF Award #1602032). Any opinions, findings, and conclusions or recommendations expressed in this material are those of the authors and do not necessarily reflect the views of the National Science Foundation or the CPaSS industry members.

## References

Abdel-Aal E.A., Abdel-Ghaffar H.M., El Anadouli B.E., New findings about nucleation and crystal growth of reverse osmosis desalination scales with and without inhibitor, *Crys-*

- tal Growth and Design*, 15 (2015) 5133–5137. DOI: 10.1021/acs.cgd.5b01091
- Aghebati-Maleki A., Dolati S., Ahmadi M., Baghbanzadeh A., Asadi M., Fotouhi A., Yousefi M., Aghebati-Maleki L., Nanoparticles and cancer therapy: perspectives for application of nanoparticles in the treatment of cancers, *Journal of Cellular Physiology*, 235 (2020) 1962–1972. DOI: 10.1002/jcp.29126
- Akyol E., Bozkurt A., Öner M., The effects of polyelectrolytes on the inhibition and aggregation of calcium oxalate crystallization, *Polymers for Advanced Technologies*, 17 (2006) 58–65. DOI: 10.1002/pat.693
- Amjad Z., Calcium sulfate dihydrate (gypsum) scale formation on heat exchanger surfaces: the influence of scale inhibitors, *Journal of Colloid and Interface Science*, 123 (1988) 523–536. DOI: 10.1016/0021-9797(88)90274-3
- Badr M.S.H., Yuan S., Dong J., El-Shall H., Bermudez Y.A., Ortega D.C., Lopez-Rendon J.E., Moudgil B.M., The properties of Kaolin from different locations and their impact on casting rate, *KONA Powder and Particle Journal*, 38 (2021) 251–259. DOI: 10.14356/kona.2021002
- Basim G.B., Vakarelski I.U., Moudgil B.M., Role of interaction forces in controlling the stability and polishing performance of CMP slurries, *Journal of Colloid and Interface Science*, 263 (2003) 506–515. DOI: 10.1016/S0021-9797(03)00201-7
- Behl S., Moudgil B.M., Prakash T.S., Control of active sites in selective flocculation. I. Mathematical model, *Journal of Colloid and Interface Science*, 161 (1993) 414–421. DOI: 10.1006/jcis.1993.1483
- Behl S., Willis M.J., Young R.H., Colored titaniferous coating pigment obtained as a flocculated by-product in a kaolin purification process, United States Patent, (1996) US5584394A.
- Bellon-Fontaine M.N., Rault J., van Oss C.J., Microbial adhesion to solvents: a novel method to determine the electron-donor/electron-acceptor or Lewis acid-base properties of microbial cells, *Colloids and Surfaces B: Biointerfaces*, 7 (1996) 47–53. DOI: 10.1016/0927-7765(96)01272-6
- Bi W.L., Hosny A., Schabath M.B., Giger M.L., Birkbak N.J., Mehrtash A., Allison T., Arnaout O., Abbosh C., Dunn I.F., Mak R.H., Tamimi R.M., Tempany C.M., Swanton C., Hoffmann U., et al., Artificial intelligence in cancer imaging: clinical challenges and applications, *CA: A Cancer Journal for Clinicians*, 69 (2019) 127–157. DOI: 10.3322/caac.21552
- Bockris J.O'M., Reddy A.K.N., Gamboa-Aldeco M.E., *Modern Electrochemistry 2A-Fundamentals of Electrode Processes*, Springer New York LLC, 2000, ISBN: 9780306461675. DOI: 10.1007/b113922
- Carr J., Zhang L., Davis M., Ravishankar S.A., Flieg G., Scale controlling chemical additives for phosphoric acid production plants, *Procedia Engineering*, 83 (2014) 233–242. DOI: 10.1016/j.proeng.2014.09.043
- Chaddad A., Katib Y., Hassan L., Future artificial intelligence tools and perspectives in medicine, *Current Opinion in Urology*, 31 (2021) 371–377. DOI: 10.1097/MOU.0000000000000884
- D'Accolti M., Soffritti I., Piffanelli M., Bisi M., Mazzacane S., Caselli E., Efficient removal of hospital pathogens from hard surfaces by a combined use of bacteriophages and probiotics: potential as sanitizing agents, *Infection and Drug Resistance*, 11 (2018) 1015–1026. DOI: 10.2147/IDR.S170071
- Dong J., Lau J., Svoronos S.A., Moudgil B.M., Continuous synthesis of precision gold nanoparticles using a flow reactor, *KONA Powder and Particle Journal*, 39 (2022) 2022011. DOI: 10.14356/kona.2022011
- Driessche A.E.S., Stawski T.M., Benning L.G., Kellermeier M., Calcium sulfate precipitation throughout its phase

- diagram, In: Van Driessche A., Kellermeier M., Benning L., Gebauer D. (eds), *New Perspectives on Mineral Nucleation and Growth*. Springer, Cham., 2017, pp. 227–256. DOI: 10.1007/978-3-319-45669-0\_12
- El-Shall H., Moudgil B.M., El-Midany A., Separation of ink particles from waste paper by fine-bubbles, *KONA Powder and Particle Journal*, 23 (2005) 122–128. DOI: 10.14356/kona.2005015
- Fuchs-Godec R., Effects of surfactants and their mixtures on inhibition of the corrosion process of ferritic stainless steel, *Electrochimica Acta*, 54 (2009) 2171–2179. DOI: 10.1016/j.electacta.2008.10.014
- Gallo J., Long N.J., Aboagye E.O., Magnetic nanoparticles as contrast agents in the diagnosis and treatment of cancer, *Chemical Society Reviews*, 42 (2013) 7816–7833. DOI: 10.1039/c3cs60149h
- Gao J., Krishna V., Bai W., Koopman B.L., Moudgil B.M., Indeglia P.A., Folta K.M., Georgieva A.T., Functionalized fullerenes as a biomass stimulant and a life extension agent, United States Patent, (2016) US9399756B2.
- Gao J., Wang Y., Folta K.M., Krishna V., Bai W., Indeglia P., Georgieva A., Nakamura H., Koopman B., Moudgil B., Polyhydroxy fullerenes (fullerols or fullerlenols): beneficial effects on growth and lifespan in diverse biological models, *PLoS ONE*, 6 (2011) 19976–19985. DOI: 10.1371/journal.pone.0019976
- Georgieva A.T., Pappu V., Krishna V., Georgiev P.G., Ghiviriga I., Indeglia P., Xu X., Fan Z.H., Koopman B., Pardalos P.M., Moudgil B., Polyhydroxy fullerenes, *Journal of Nanoparticle Research*, 15 (2013) 1690. DOI: 10.1007/s11051-013-1690-6
- Glenn D.M., Puterka G.J., Chapter 1- Particle films: a new technology for agriculture, in: Janick J. (Ed.), *Horticultural Reviews*, 2004, pp. 1–44. DOI: 10.1002/9780470650882.ch1
- Glenn D.M., The mechanisms of plant stress mitigation by kaolin-based particle films and applications in horticultural and agricultural crops, *HortScience Horts*, 47 (2012) 710–711. DOI: 10.21273/hortsci.47.6.710
- Grafton-Cardwell E.E., Stelinski L.L., Stansly P.A., Biology and management of Asian citrus psyllid, vector of the Huanglongbing pathogens, *Annual Review of Entomology*, 58 (2013) 413–432. DOI: 10.1146/annurev-ento-120811-153542
- Hahn M.A., Singh A.K., Sharma P., Brown S.C., Moudgil B.M., Nanoparticles as contrast agents for in-vivo bioimaging: current status and future perspectives, *Analytical and Bioanalytical Chemistry*, 399 (2011) 3–27. DOI: 10.1007/s00216-010-4207-5
- Hamadi F., Latrache H., Comparison of contact angle measurement and microbial adhesion to solvents for assaying electron donor–electron acceptor (acid–base) properties of bacterial surface, *Colloids and Surfaces B: Biointerfaces*, 65 (2008) 134–139. DOI: 10.1016/j.colsurfb.2008.03.010
- Han X., Xu K., Taratula O., Farsad K., Applications of nanoparticles in biomedical imaging, *Nanoscale*, 11 (2019) 799–819. DOI: 10.1039/c8nr07769j
- He S., Oddo J.E., Tomson M.B., The inhibition of gypsum and barite nucleation in NaCl brines at temperatures from 25 to 90 °C, *Applied Geochemistry*, 9 (1994) 561–567. DOI: 10.1016/0883-2927(94)90018-3
- Hsu J.C., Nieves L.M., Betzer O., Sadan T., Noël P.B., Popovtzer R., Cormode D.P., Nanoparticle contrast agents for X-ray imaging applications, *Wiley Interdisciplinary Reviews: Nanomedicine and Nanobiotechnology*, 12 (2020) e1642. DOI: 10.1002/WNAN.1642
- ISO13321, Methods for determination of particle size distribution part 8: photon correlation spectroscopy, International Organization for Standardisation (ISO), (1996).
- Jafari S., Mahyad B., Hashemzadeh H., Janfaza S., Gholikhani T., Tayebi L., Biomedical applications of TiO<sub>2</sub> nanostructures: recent advances, *International Journal of Nanomedicine*, 15 (2020) 3447–3470. DOI: 10.2147/IJN.S249441
- Jain T., Sanchez E., Owens-Bennett E., Trussell R., Walker S., Liu H., Impacts of antiscalants on the formation of calcium solids: implication on scaling potential of desalination concentrate, *Environmental Science: Water Research & Technology*, 5 (2019) 1285–1294. DOI: 10.1039/C9EW00351G
- Jamialahmadi M., Müller-Steinhagen H., Heat exchanger fouling and cleaning in the dihydrate process for the production of phosphoric acid, *Chemical Engineering Research and Design*, 85 (2007) 245–255. DOI: 10.1205/cherd06050
- Jin P., Ji X., Kang W., Li Y., Liu H., Ma F., Ma S., Hu H., Li W., Tian Y., Artificial intelligence in gastric cancer: a systematic review, *Journal of Cancer Research and Clinical Oncology*, 146 (2020) 2339–2350. DOI: 10.1007/s00432-020-03304-9
- Keera S.T., Farid N.A., Mohamed K.Z., Imidazoline derivatives as corrosion inhibitors of carbon steel in crude oils and associated water, *Energy Sources, Part A: Recovery, Utilization and Environmental Effects*, 34 (2012) 1371–1383. DOI: 10.1080/15567036.2010.481657
- Krishna V., Bai W., Han Z., Yano A., Thakur A., Georgieva A., Tolley K., Navarro J., Koopman B., Moudgil B., Contaminant-activated visible light photocatalysis, *Scientific Reports*, 8 (2018) 1894. DOI: 10.1038/s41598-018-19972-0
- Krishna V., Moudgil B., Koopman B., Systems and methods based on radiation induced heating or ignition of functionalized fullerenes, United States Patent, (2016a) US9475028B2.
- Krishna V., Moudgil B., Koopman B., Functionalized fullerenes as antifungal agents, United States Patent, (2016b) US9314027B2.
- Krishna V., Noguchi N., Koopman B., Moudgil B., Enhancement of titanium dioxide photocatalysis by water-soluble fullerenes, *Journal of Colloid and Interface Science*, 304 (2006) 166–171. DOI: 10.1016/j.jcis.2006.08.041
- Krishna V., Stevens N., Koopman B., Moudgil B., Optical heating and rapid transformation of functionalized fullerenes, *Nature Nanotechnology*, 5 (2010) 330–334. DOI: 10.1038/nnano.2010.35
- Krishna V., Zawoy K., Moudgil B.M., Koopman B.L., Stevens N.I., Powers K.W., Devices for thermally induced transformations controlled by irradiation of functionalized fullerenes, United States Patent, (2015) US9011309B2.
- Liao C., Li Y., Tjong S.C., Visible-light active titanium dioxide nanomaterials with bactericidal properties, *Nanomaterials*, 10 (2020) 124 (56pp). DOI: 10.3390/nano10010124
- Luo D., Wang X., Burda C., Basilion J.P., Recent development of gold nanoparticles as contrast agents for cancer diagnosis, *Cancers*, 13 (2021) 1825 (16pp). DOI: 10.3390/cancers13081825
- Mahmoud A.S., Mostafa M.K., Abdel-Gawad S.A., Artificial intelligence for the removal of benzene, toluene, ethyl benzene and xylene (BTEX) from aqueous solutions using iron nanoparticles, *Water Science and Technology: Water Supply*, 18 (2018) 1650–1663. DOI: 10.2166/ws.2017.225
- Mehta N, Flocculation Behavior of Apatite with Polyacrylic Acid, MS Thesis, University of Florida, Gainesville, FL, 1993.
- Moudgil B.M., Musella S.C., Etxeberria E., Rogers M.E., Brodersen C.R., Sharma P., Colored clays for agricultural and other industrial applications, United States Patent, (2017) US9763440B2.
- Nandakumar V., Physicochemical Aspects of Bacterial Adhesion on Surfaces and Strategies to Remove Adhered

- Bacteria from Surfaces, Doctoral Dissertation, University of Florida, Gainesville, FL, 2018. <https://ufdc.ufl.edu/UFE0052040/00001>
- Nandakumar V., Han Z., Fritz Z., Krishna V., Koopman B., Moudgil B., Visible light photocatalytic bacterial inactivation on titanium dioxide coatings, *KONA Powder and Particle Journal*, 34 (2017) 234–240. DOI: 10.14356/kona.2017011
- Nandakumar V., Huang C., Pulgar A., Balasubramanian V., Wu G., Chandar P., Moudgil B.M., Particle assisted removal of microbes from surfaces, *Journal of Colloid and Interface Science*, 533 (2019) 190–197. DOI: 10.1016/j.jcis.2018.08.043
- Narayanan A., Sharma P., Moudgil B.M., Applications of engineered particulate systems in agriculture and food industry, *KONA Powder and Particle Journal*, 30 (2012) 221–235. DOI: 10.14356/kona.2013021
- Nightingale A.M., Phillips T.W., Bannock J.H., De Mello J.C., Controlled multistep synthesis in a three-phase droplet reactor, *Nature Communications*, 5 (2014) 3777. DOI: 10.1038/ncomms4777
- Owens D.K., Wendt R.C., Estimation of the surface free energy of polymers, *Journal of Applied Polymer Science*, 13 (1969) 1741–1747. DOI: 10.1002/app.1969.070130815
- Polat S., Sayan P., Determination of the effects of carboxylic acids on calcium sulfate dihydrate crystallization, *Chemical Engineering and Technology*, 40 (2017) 1354–1361. DOI: 10.1002/ceat.201600525
- Prakash T.S., Moudgil B.M., Removal of chloride and potassium ions from the recovery boiler salt cake, in: *TAPPI Proceedings—International Environmental Conference*, 1995, pp. 161–174, ISBN:0898529360.
- Puterka G.J., Glenn D.M., Pluta R.C., Action of particle films on the biology and behavior of pear psylla (Homoptera: Psyllidae), *Journal of Economic Entomology*, 98 (2005) 2079–2088. DOI: 10.1093/jee/98.6.2079
- Rabinovich Y.I., Adler J.J., Esayanur M.S., Ata A., Singh R.K., Moudgil B.M., Capillary forces between surfaces with nanoscale roughness, *Advances in Colloid and Interface Science*, 96 (2002) 213–230. DOI: 10.1016/S0001-8686(01)00082-3
- Rabinovich Y.I., Vakarelski I.U., Brown S.C., Singh P.K., Moudgil B.M., Mechanical and thermodynamic properties of surfactant aggregates at the solid-liquid interface, *Journal of Colloid and Interface Science*, 270 (2004) 29–36. DOI: 10.1016/j.jcis.2003.09.005
- Rajopadhye A., Understanding the Fundamental Role of Surfactant Structures in the Inhibition of Carbon Steel Corrosion in Acidic Medium, Doctoral Dissertation, University of Florida, Gainesville, FL, 2018. [https://ufl-flvc.primo.exlibrisgroup.com/permalink/01FALSC\\_UFL/175ga98/alma990366927060306597](https://ufl-flvc.primo.exlibrisgroup.com/permalink/01FALSC_UFL/175ga98/alma990366927060306597)
- Ratova M., Redfern J., Verran J., Kelly P.J., Highly efficient photocatalytic bismuth oxide coatings and their antimicrobial properties under visible light irradiation, *Applied Catalysis B: Environmental*, 239 (2018) 223–232. DOI: 10.1016/j.apcatb.2018.08.020
- Rtimi S., Dionysiou D.D., Pillai S.C., Kiwi J., Advances in catalytic/photocatalytic bacterial inactivation by nano Ag and Cu coated surfaces and medical devices, *Applied Catalysis B: Environmental*, 240 (2019) 291–318. DOI: 10.1016/j.apcatb.2018.07.025
- Shams Nateri A., Hasanlou E., Hajipour A., Using adaptive neuro-fuzzy and genetic algorithm for simultaneously estimating the dye and AgNP concentrations of treated silk fabrics with nanosilver, *Pigment and Resin Technology*, 48 (2019) 20–28. DOI: 10.1108/PRT-11-2017-0096
- Sharma P., Bengtsson N.E., Walter G.A., Sohn H.B., Zhou G., Iwakuma N., Zeng H., Grobmyer S.R., Scott E.W., Moudgil B.M., Gadolinium-doped silica nanoparticles encapsulating indocyanine green for near infrared and magnetic resonance imaging, *Small*, 8 (2012) 2856–2868. DOI: 10.1002/sml.201200258
- Sharma P., Brown S.C., Singh A., Iwakuma N., Pyrgiotakis G., Krishna V., Knapik J.A., Barr K., Moudgil B.M., Grobmyer S.R., Near-infrared absorbing and luminescent gold speckled silica nanoparticles for photothermal therapy, *Journal of Materials Chemistry*, 20 (2010) 5182–5185. DOI: 10.1039/c0jm00354a
- Sharma P., Moudgil B.M., Walter G.A., Grobmyer S.R., Santra S., Jiang H., Brown S.C., Scott E.W., Zhang Q., Bengtsson N., Multimodal nanoparticles for non-invasive bio-imaging, United States Patent, (2013a) US8361437B2.
- Sharma P., Narayanan A., El-Shall H.E., Moudgil B.M., Engineered particulate systems for controlled release of pesticides and repellants, WIPO (PCT), (2013b) WO2013123176A1.
- Sharma P., Brodersen C., Rogers M., Etxeberria E., Optical and physical deterrent for preventing ACP vector attack on citrus, Citrus Research and Development Foundation (CRDF), CATP13 Proposal #860, Gainesville, United States, 2015.
- Silva C.O., Pinho J.O., Lopes J.M., Almeida A.J., Gaspar M.M., Reis C., Current trends in cancer nanotheranostics: metallic, polymeric, and lipid-based systems, *Pharmaceutics*, 11 (2019) 22 (40pp). DOI: 10.3390/pharmaceutics11010022
- Singh A., Krishna V., Angerhofer A., Do B., MacDonald G., Moudgil B., Copper coated silica nanoparticles for odor removal, *Langmuir*, 26 (2010) 15837–15844. DOI: 10.1021/la100793u
- Singh P.K., Adler J.J., Rabinovich Y.I., Moudgil B.M., Investigation of self-assembled surfactant structures at the solid-liquid interface using FT-IR/ATR, *Langmuir*, 17 (2001) 468–473. DOI: 10.1021/la000981t
- Sleutel M., Lutsko J., Van Driessche A.E.S., Durán-Olivencia M.A., Maes D., Observing classical nucleation theory at work by monitoring phase transitions with molecular precision, *Nature Communications*, 5 (2014) 5598. DOI: 10.1038/ncomms6598
- Sliem M.H., Afifi M., Bahgat Radwan A., Fayyad E.M., Shibl M.F., Heikal F.E.-T., Abdullah A.M., AEO7 surfactant as an eco-friendly corrosion inhibitor for carbon steel in HCl solution, *Scientific Reports*, 9 (2019) 2319 (16pp). DOI: 10.1038/s41598-018-37254-7
- Stitt E.H., Alternative multiphase reactors for fine chemicals: a world beyond stirred tanks?, *Chemical Engineering Journal*, 90 (2002) 47–60. DOI: 10.1016/S1385-8947(02)00067-0
- Tanquero J.G., Abdel-Aal E.-S.A., Farinato R.S., El-Shall H., Moudgil B.M., Inhibition of calcium sulphate hemihydrate crystallization under simulated conditions of phosphoric acid evaporation, *The Canadian Journal of Chemical Engineering*, (2021). DOI: 10.1002/cjce.24210
- Thanapandiyaraj R., Rajendran T., Mohammedgani P.B., Performance analysis of various nanocontrast agents and CAD systems for cancer diagnosis, *Current Medical Imaging Formerly Current Medical Imaging Reviews*, 15 (2018) 831–852. DOI: 10.2174/1573405614666180924124736
- Varshney S., Sain A., Gupta D., Sharma S., Factors affecting bacterial adhesion on selected textile fibres, *Indian Journal of Microbiology*, 61 (2021) 31–37. DOI: 10.1007/s12088-020-00903-5
- Vinoth A., Datta S., Design of the ultrahigh molecular weight polyethylene composites with multiple nanoparticles: an artificial intelligence approach, *Journal of Composite Materials*,



- 54 (2020) 179–192. DOI: 10.1177/0021998319859924
- Wagner J., Tshikhudo T.R., Köhler J.M., Microfluidic generation of metal nanoparticles by borohydride reduction, *Chemical Engineering Journal*, 135 (2008) S104–S109. DOI: 10.1016/j.cej.2007.07.046
- Weninger E.J., Stelinski L.L., Hall D.G., Roles of olfactory cues, visual cues, and mating status in orientation of *Diaphorina citri* Kuwayama (Hemiptera: Psyllidae) to four different host plants, *Environmental Entomology*, 38 (2009) 225–234. DOI: 10.1603/022.038.0128
- Zhang H., Meng D., Cai S., Guo H., Chen P., Zheng Z., Zhu J., Zhao W., Wang H., Zhao S., Yu J., He Y., The application of artificial intelligence in lung cancer: a narrative review, *Translational Cancer Research*, 10 (2021) 2478–2487. DOI: 10.21037/tcr-20-3398
- Zhang L., Carr J., Chen T.H.-L., Primary amine-containing polymers useful as scale inhibitors, WIPO (PCT), (2015) WO2015123294A1.
- Zhang X., Zhang Q., Yan T., Jiang Z., Zhang Xinxin, Zuo Y.Y., Quantitatively predicting bacterial adhesion using surface free energy determined with a spectrophotometric method, *Environmental Science and Technology*, 49 (2015) 6164–6171. DOI: 10.1021/es5050425
- Zhao J., Krishna V., Hua B., Moudgil B., Koopman B., Effect of UVA irradiance on photocatalytic and UVA inactivation of *Bacillus cereus* spores, *Journal of Photochemistry and Photobiology B: Biology*, 94 (2009) 96–100. DOI: 10.1016/j.jphotobiol.2008.10.006
- Zhu Y., Free M.L., Woollam R., Durnie W., A review of surfactants as corrosion inhibitors and associated modeling, *Progress in Materials Science*, 90 (2017) 159–223. DOI: 10.1016/j.pmatsci.2017.07.006
- Zhu Y., Free M.L., Yi G., Experimental investigation and modeling of the performance of pure and mixed surfactant inhibitors: aggregation, adsorption, and corrosion inhibition on steel pipe in aqueous phase, *Journal of The Electrochemical Society*, 162 (2015) C582–C591. DOI: 10.1149/2.09415010jes
- Zhu Y., Free M.L., Yi G., The effects of surfactant concentration, adsorption, aggregation, and solution conditions on steel corrosion inhibition and associated modeling in aqueous media, *Corrosion Science*, 102 (2016) 233–250. DOI: 10.1016/j.corsci.2015.10.012
- Zhuang W., Wang X., Zhu W., Zhang Y., Sun D., Zhang R., Wu C., Imidazoline Gemini surfactants as corrosion inhibitors for carbon steel X70 in NaCl solution, *ACS Omega*, 6 (2021) 5653–5660. DOI: 10.1021/acsomega.0c06103

## Authors' Short Biographies



### Jiaqi Dong

Jiaqi Dong received his B.S. in Materials Science and Engineering from the Illinois Institute of Technology in 2013. He then attended the University of Florida as a graduate student and received his M.S. in Materials Science and Engineering in 2016. Currently, he is a Ph.D. candidate under the supervision of Dr. Brij Moudgil and Dr. Bahar Basim at the Center for Particulate and Surfactant Systems (CPaSS). His current research focus is metallic nanoparticle synthesis and functionalization using flow chemistry.



### Brij M. Moudgil

Dr. Brij M. Moudgil is a Distinguished Professor of Materials Science and Engineering at the University of Florida. He received his B.E from the Indian Institute of Science, Bangalore, India, and his M.S. and Eng.Sc.D degrees from Columbia University, New York. His current research interests are in surfactant and polymer adsorption, dispersion and aggregation of fine particles, adhesion, and removal of microbes from surfaces, synthesis of functionalized nanoparticles, anti-scaling and surfactant mediated corrosion inhibitors, photocatalytic degradation of hazardous microbes, and nanotoxicity. He has published more than 400 technical papers and has been awarded over 25 patents. He is a member of the U.S National Academy of Engineering.



# Comminution and Classification as Important Process Steps for the Circular Production of Lithium Batteries<sup>†</sup>

Arno Kwade<sup>1,2\*</sup>, Marcel Möller<sup>1</sup>, Jannes Müller<sup>1</sup>, Jutta Hesselbach<sup>2</sup>, Sabrina Zellmer<sup>2</sup>, Stefan Doose<sup>1</sup>, Julian Mayer<sup>1</sup>, Peter Michalowski<sup>1</sup>, Malcolm Powell<sup>3</sup> and Sandra Breitung-Faes<sup>1</sup>

<sup>1</sup> Institute for Particle Technology, Technical University of Braunschweig, Germany

<sup>2</sup> Fraunhofer Institute for Surface Engineering and Thin Films IST, Germany

<sup>3</sup> University of Queensland, Australia

## Abstract

Lithium-ion batteries (LIBs) provide the largest source of electrical energy storage today. This paper covers the use of comminution processes and, thus, crushers and mills for particle breakage and dispersing, as well as classifiers for particle separation within the process chain, from the raw material to the final lithium battery cell and its recycling at end of life. First of all, the raw materials for the active material production have to be produced either by processing primary raw materials, or by recycling the spent lithium batteries. The end-of-life battery cells have to be shredded, the materials separated and then milled in order to achieve the so-called black mass, which provides a secondary material source with very valuable components. Using these materials for the synthesis of the cathode active materials, milling has to be applied in different stages. The natural graphite, increasingly used as anode material, has to be designed in mills and classifiers for achieving targeted properties. Nanosized silicon is produced by nanomilling using stirred media mills as a primary option. Conductive additives for LIBs, like carbon black, have to be dispersed in a solvent with machines like planetary mixers, extruders or stirred media mills. In the future, mechanochemical synthesis of solid electrolytes will especially require additional application of comminution processes.

**Keywords:** graphite, silicon, battery recycling, active material synthesis, solid state batteries, electrode production

## 1. Introduction

The most popular energy storage system today is the lithium-ion battery (LIB). LIBs offer superior performance in terms of energy density (Wh/L) and specific energy (Wh/kg), as well as lifetime and cycling stability. Moreover, due to their mass production, their costs decrease continuously and, due to increasing application knowledge, the safety is steadily improving. Regarding LIB cell costs, about 75 % is attributed to the materials used for the cell production (Kwade et al., 2018). A schematic presentation of an electrochemical basic unit consisting of cathode, separator and anode, as well as electrolyte, is shown in **Fig. 1 left**. Both electrodes consist of particles which are bound to each other and to a current collector by a binder. As active material on the cathode side, particles consisting of lithium transition metal oxides (e.g. NMC, NCA, LMNO) or a lithium metal phosphate (e.g. LFP) are used together with carbon

based conductive additives like carbon black, carbon nano tubes (CNT) and/or fine graphite particles. On the anode side, as a rule, natural or synthetic graphite particles with tailored surface functionalizations are employed together with small amounts of carbon-based conductive additives. Recently, the specific capacity of the anodes has been increased by adding smaller amounts of silicon, which has about a 10 times higher specific capacity than graphite, despite possessing severe cycling stability challenges due to extreme volume changes during cycling.

In addition to the development of improved active materials, comprehensive research is being conducted on the development of solid electrolytes for the so-called All-Solid-State Batteries (ASSB) as next generation lithium battery technology (Janek and Zeier, 2016). As depicted in **Fig. 1 right**, such ASSB cells have a solid electrolyte acting as ionic conductor within the cathode, as well as a separator layer between anode and cathode. Solid electrolytes can be sulfide, polymer and/or oxide based, among others, and are produced by mechanochemical processes. Lithium based anodes can be employed in an ASSB, avoiding, or at least strongly minimizing, lithium dendrite growth, as well as significantly increasing the energy density.

Another promising lithium battery cell type is the

<sup>†</sup> Received 12 June 2021; Accepted 29 September 2021  
J-STAGE Advance published online 23 April 2022

\* Corresponding author: Arno Kwade;

<sup>1</sup> Add: Volkmaroder Str. 5, 38104 Braunschweig, Germany

<sup>2</sup> Add: Bienroder Weg 54 e, 38108 Braunschweig, Germany

E-mail: a.kwade@tu-braunschweig.de

TEL: +49-531-391-9603 FAX: +49-531-9633



Lithium-Sulfur-Battery (LiS), which has the potential to achieve very high specific capacities, which is especially important for aerospace applications or application within trucks (Zhao et al., 2020). Similar to ASSB, these cells have a lithium-based anode and a cathode based on a sulfur-carbon composite material. Both liquid electrolyte and solid electrolytes can be employed.

Today the different materials have to be produced from primary resources mainly by mining and subsequent mineral processing. For the metals lithium, nickel, cobalt, manganese, aluminum and copper, as well as for graphite, almost 3 million tons in 2025 (with approx. 0.5 million tons of nickel and graphite) and about 7 million tons will be required in 2030 (with approx. 1 million tons of nickel and graphite) overall according to the Electric Vehicle Outlook 2018 of Bloomberg New Energy Finance (Bloomberg NEF, 2018). Therefore, the conservation of primary material resources, and interdependence on individual primary resources and raw material producers, is an important task for the coming years. Moreover, the actual development challenges are the improvement of the fast-charging behavior and the CO<sub>2</sub>-footprint of the LIB. In order to reduce the

CO<sub>2</sub>-footprint and to become independent of the primary raw material resources, the buildup and establishment of a circular economy, especially circular production of LIB, is a major task for the near future. Within the circular production, the End-of-Life (EoL) battery systems have to be dismantled and the components have to be fed to a recycling process, resulting in secondary raw materials that are used to produce new battery active materials, especially cathode active materials. The overall recycling process can consist of mechanical (especially shredding, milling), classification and sorting, thermal, hydrometallurgical and/or pyrometallurgical process steps (Doose et al., 2021b). According to existing or proposed regulations in the different regions of the world (e.g. newly proposed EU directive), batteries must be recycled at high recycling rates, especially for reuse of the transition metals as Ni, Co and Cu, with up to 95 % recovery, as well as for Li and the overall battery system with at least 70 % recovery. A schematic outline of the circular production of lithium batteries, especially lithium-ion batteries, is shown in Fig. 2.

The primary, and increasingly the secondary, raw materials are used as the basis for the production/synthesis of the cathode and anode active materials. Within the production of these particulate active materials, milling and classification processes play a major role for tailoring the particle size distributions and particle shapes, as well as dispersing calcinated materials. The particle size distributions and particle shapes are important for the subsequent electrochemical performance and cycling stability of the LIB cells.

For the production of the anodes and cathodes, the different components (as shown in Fig. 1) have to be well dispersed in a solvent by using mixing and milling devices. The resulting microstructure of the carbon-based conductive additives is decisive for the future cell performance.

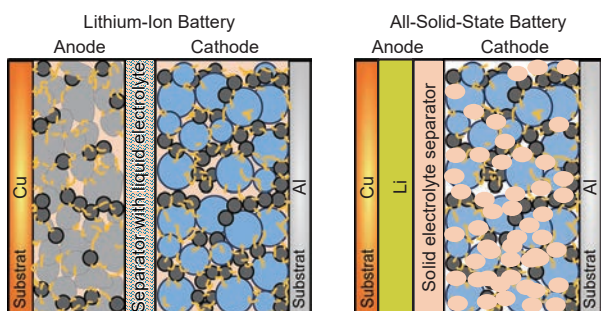


Fig. 1 Compartment of Lithium-Ion Battery (LIB) (left) and all-solid-state battery (ASSB) (right).

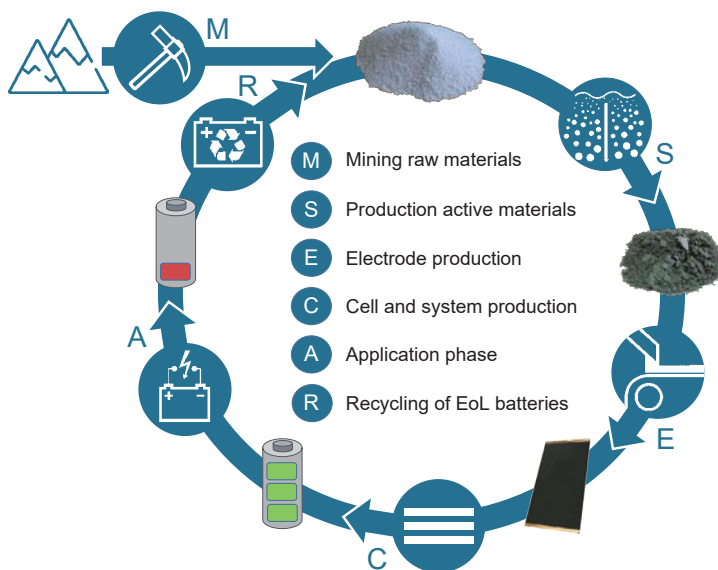


Fig. 2 Circular production of LIB.

After production, the electrodes are assembled together with the separator to form the battery cell, as described in detail for example in the literature (Kwade et al., 2018). The cells can be cylindrical, prismatic or pouch types, and are lastly filled with electrolyte, formatted, aged and closed to be shipped for integration into a battery system for application in electromobility, stationary storage or power tools. After the application phase, usually lasting more than ten years, the lithium-ion batteries reach their end of life and have to be shipped to a dismantling and recycling facility.

Finally, besides the critical discussion and further presentation of the perspective of milling, dispersing and classification processes for today's LIB based on liquid electrolytes, an outlook of milling and classification processes for the production of ASSB will be given. The synthesis of solid electrolytes is often achieved through mechanochemical synthesis within planetary, vibration or agitated ball mills. Moreover, mills are often employed for the preparation of the composite materials for the cathode. Another possible application is the production of composite materials for LiS battery cells, which have high potential for usage in aviation, due to their low weight in relation to their storage capacity.

## 2. Raw material supply

Today, the raw materials for the cathode active material production, mainly ores with transition metals, and for the anode active material production, i.e. natural graphite and synthetic graphite, as well as silicon, are extracted from primary natural resources. However, the electromobility and energy turnaround can only be successful if the materials used for the production of the energy storage devices underly a circular economy: i.e. closed material cycles. Therefore, besides primary resources, the use of EoL batteries as secondary material source is growing in importance. Within the processing of both primary and secondary raw materials, comminution, classification and sorting processes play a major role.

### 2.1 Processing of primary raw materials

Mineral processing is the link between mining and chemical beneficiation of valuable elements, like lithium, for battery applications. The valuable minerals upon which our industrialized society depends have been formed and or laid down in host rock, from which they need to be extracted. The minerals are embedded and dispersed in many forms and structures, presenting a wide range of requirements for their recovery from different ore bodies. Most valuable metals occur naturally in the form of their oxides, sulfides, silicates, carbonates or similar. Extractive processing usually involves the conversion of the mineral into the valuable metal, or for lithium to a soluble component like  $\text{LiCO}_3$  (Amarante et al., 1999; Talens Peiró et al., 2013; Lee, 2015). Mineral processing is responsible

for concentrating the raw mined rock, which generally contains the valuable minerals in concentrations from a few percent down to parts per million, to a concentrate stream with 10 % to 40 % valuables that is sent for refining to the end metal product. In order to concentrate the minerals, they have to be mechanically separated from the host rock to be exposed to a recovery process. The exposure should be sufficient to differentiate particles that contain the valuable minerals from those that are barren, or have an extremely low grade of valuables. The recovery process can be physical (density, magnetic susceptibility), based on surface chemistry (flotation), or exposure to a lixiviant used to dissolve the minerals (leaching), each requiring a different degree of mineral exposure. The size to which the rock needs to be reduced depends upon the mineral association and recovery process. The process of rock breakage for liberation of the minerals is known as comminution.

Predictions that mineral processing would become less important in favor of hydro- and pyrometallurgy are only true for a few special cases (Moskvitch, 2014). For most ores, including lithium containing pegmatites, mechanical breakage and concentration creates reactive surfaces suited to hydrometallurgical recovery of the valuable components (Baláz, 2003). For lithium ores, concentration is followed by either calcination or roasting, and then a leaching step. Both are often followed by a carbonate precipitation (Barbosa et al., 2014; Amer, 2008; Sitando and Crouse, 2012; Yan et al., 2012).

In order to reduce the particle size by about a thousand-fold, a number of progressive breakage stages are required. Blasting of in-situ rock, followed by primary crushing, provides a minus 200 mm feed of rock. This can be stage-crushed to minus 12 mm for grinding in tumbling ball mills that use steel grinding media, and produce products in the range of 80 % passing (P80) 60  $\mu\text{m}$  up to 80 % passing 1 mm. Large semi-autogenous grinding (SAG) mills that contain a mixture of rock and steel balls as grinding media are common for large ore bodies of low grade. SAG mills are fed direct from the primary crusher, have up to 24 MW power draw, and process 1500 to 3500 tons per hour (tph) of ore. They are generally followed by one to three ball mills. For a required grind size finer than 60  $\mu\text{m}$ , stirred mills are generally used as the final grinding stage. These provide a lower energy use for fine grinding, and the higher energy density reduces the footprint of the equipment (Palaniandy et al., 2015; Taylor et al., 2020).

Most commonly, hydrocyclones are used to classify the product by size prior to the recovery process. However, these are intrinsically inefficient and allow coarse oversize to be passed on, and fine final product to return to the mill and be over-ground. Additionally, the milling process is non-selective, resulting in overgrinding of material as is passing along a mill. More extensive descriptions of the comminution process can be found in works such as

those of Wills' Mineral Processing Technology (Wills and Napier-Munn, 2006).

Comminution is exceedingly energy-intensive, using 2–3 % of the electrical energy consumed worldwide energy and around 40 % of energy in mining (Ballantyne and Powell, 2014). The energy requirement rises almost exponentially with finer grinding, but linearly with the production of fine product (Ballantyne et al., 2015), emphasizing the need to improve processing at the fine end (minus 500  $\mu\text{m}$ ), or reduce the need to produce material below this size. Due to this energy intensity, the need to drive down the energy cost is a significant factor in reducing the environmental cost of producing metals. This has led to many ongoing process improvements designed to reduce energy consumption.

Alternate circuits that include high pressure grinding rolls (HPGR) (Schönert, 1988) are becoming more common for hard-rock applications, as they offer a reduction in energy use, but they still need to be fed by conventional crushers and require ball mills to produce the final grind size, compromising the overall energy savings. Selective breakage of minerals along the grain boundaries has long been a pathway pursued to reduce energy and improve recoveries. It has been met with limited success thus far, such as in the application of microwave pretreatment (Kingman, 2006), or electrical fragmentation (Parker et al., 2015), but remains an important area of research.

In light of the high energy use and low efficiency of breakage and selection of minerals, a major research thrust is captured in the work of Powell (2019): “The objective of industrial comminution processes is to conduct the minimum degree of breakage required to permit recovery of the valuable minerals or satisfy product quality needs.”

There is a compromise between energy use and adequate liberation of the minerals to enable their recovery. Too little breakage results in minerals remaining trapped (unliberated) and not recovered or too coarse for the recovery process to select. Too much breakage results in loss through fines (slimes) that cannot be selected. The objective of breaking the rock into a narrow size range, well suited to recovery, is severely compromised by the relatively crude nature of the crushing, milling and classification equipment used for bulk processing of ores. Fine screens are providing greatly improved classification compared to hydro cyclones, but are currently only suited to lower throughput operations (less than 500 tph). However, they show greater promise in light of finding that the change in classification can improve the liberation characteristics of the ore, increasing recoveries while reducing energy needs (Frausto et al., 2021).

Powell has proposed flexible circuit design to improve the balance of energy applied to the rock, and enable early selection and progressive rejection of waste material. Considerable research and process development is being

applied to coarser recovery processes, such as coarse flotation, that allow coarser product sizes to be recovered. Another approach to improving recoveries is by increasing the surface reactivity through mechanochemical treatment—the addition of chemical reagents combined with mechanical grinding (Dessemond et al., 2019).

Overall, the extraction of raw materials will remain essential to the production of batteries for many decades to come, as demand far outstrips available resource in the circular economy. Due to the high energy and environmental footprint of current production processes, improving the efficiency of this production is an important aspect of sustainable energy production.

## 2.2 Secondary raw materials from recycling

In order to achieve an economically and ecologically sustainable battery production, the recycling of the circulated lithium-ion batteries is of tremendous importance (Peters et al., 2017; Kwade and Diekmann, 2018; Zhao et al., 2020). According to Xu et al. (2020), the circulating batteries in consumer products, EV application and other use cases will increase many times by 2030. To cover the raw material demand in the targeted sustainable production of LIB, recycling represents a central and elementary bridge between LIB at end-of-life or production scrap, and the production of new cells (Habib et al., 2020).

### 2.2.1 Recycling impact on battery value chain

The key element to reduce the carbon footprint, minimize raw material dependencies and increase sustainability of batteries, is the recycling of the recyclables within the battery to reuse them in a new production cycle (Velázquez-Martínez et al., 2019).

Approaches to achieve this goal are described in the literature in wide variety, and are already successfully implemented at the research and, in some cases, the industrial level (Brückner et al., 2020; Velázquez-Martínez et al., 2019; Zeng et al., 2014; Arshad et al., 2020; Kwade and Diekmann, 2018). However, the ambitious targets of the EU or the CEID consortium (Kwade et al., 2020) with material recycling rates of up to 95 % of e.g. nickel (Ni), aluminum (Al), cobalt (Co), and 70 % of lithium, have not yet been achieved. Compared with other countries and regions of the world, the EU sets very high target recycling quotas with the proposed Battery Directive, which are also pursued equally by China. Producers are obliged to collect the batteries brought into circulation and return them to the material cycles. Other Asian countries aim to achieve similar goals (South Korean RoHS/ELV/WEEE Act, 2007 and Japan's End-of-Life Vehicle Recycling Law).

With the help of the process steps for the LIB recycling, depending on the combination as depicted in Fig. 3, most of the valuable materials can be recovered and used for further battery applications or, if more meaningful,

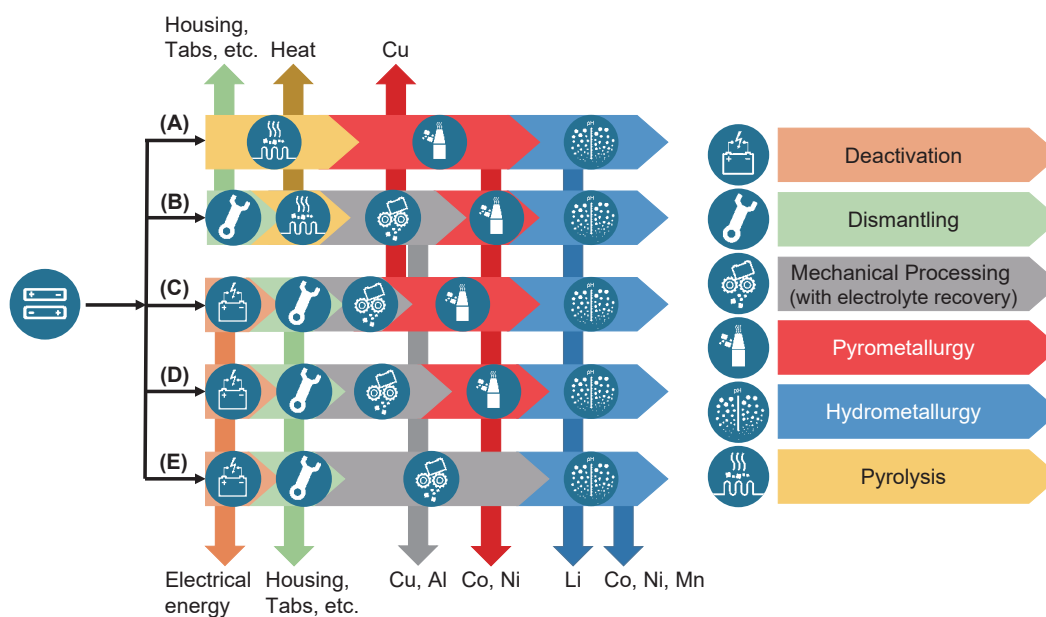


**Fig. 3** Overview of potential recycling process chains for lithium ion batteries. Reprinted from Ref. (Doose et al., 2021b) under the terms of the CC-BY 4.0 license. Copyright: (2021) The Authors, published by MDPI.

high-value application alternatives. With regard to the desired raw material-independent production sites of LIB, the process of recovery, after initial raw material supply to the producers, allows to both increase sustainability and environmental protection by decreasing the need for primary material from extraction sites, as well as to minimize the equipment required for production of the valuable metal salts for active material synthesis (Bonsu, 2020; Mathieux et al., 2017).

### 2.2.2 Potential LIB recycling processes

Today, LIBs with liquid electrolytes dominate the main market application (BEV, PHEV, portable devices and stationary energy storage). Regardless of the type of application, LIBs contain nickel, cobalt, manganese, aluminum, copper, graphite, polymeric and/or iron components, and in new technologies, silicon (Diekmann et al., 2017). From this point of view, it is clear that processes for recycling LIB's are of enormous importance.

In principle, the processes of recycling LIB have a recurring scheme, which can be described independently from the chosen processing route. The first step is to deactivate the battery cells by discharging and short-circuiting them, by treating them with saline solution or pyrolyzing them at more than 200 °C (Georgi-Maschler et al., 2012; Hanisch et al., 2015a). Subsequently, four different process types can be used and combined in different ways: mechanical, thermal, pyrometallurgical and hydrometallurgical processes. Fig. 3 shows possible different process routes that can be applied. The individual processes allow only very limited possibilities to recover the materials, which is why a combination is essential. Pure pyrometallurgical processes (see Fig. 3(A)), as with direct smelting of LIB

battery modules, are already industrially established, but allow only high recovery rates for transition metals such as nickel, cobalt and copper, whereas lithium in particular causes difficulties and is found especially within the resulting slag. To enable recovery of lithium and manganese along the way, the route has to be further linked to hydrometallurgical and undoubtedly mechanical processes as well. Other components such as graphite, organic solvents and polymers are thermally consumed as an energy source. For this reason, overall a relatively low total recovery rate can be assumed (Brückner et al., 2020).

Direct pyrometallurgical recycling can also be preceded by a mechanical crushing and sorting step, with subsequent pyrometallurgical treatment of the black mass or shredded battery material (see (C) and (D) in Fig. 3). The proportion of mechanical processing is a variable factor here. This pretreatment increases the recovery rate, as material such as polymers and aluminum can also be recovered.

Another route starts with the pyrolysis of the entire battery system to achieve safe handling in further process steps (see (B) in Fig. 3). By this route, all volatile components are removed, including a high portion of the fluorine containing components, which requires a complex gas cleaning. Afterwards, the parts of the battery system that are not burned are dismantled, and the cells are further mechanically processed using a shredder and separation devices, such as zig-zag-classifiers (more details see descriptions for route (B) in Chapter 2.2.3).

### 2.2.3 Mechanical-hydrometallurgical processing

A complex process route of LIB recycling is a combination of mechanical and hydrometallurgical steps, without an intermediate pyrometallurgical process, but



**Fig. 4** Exemplary process diagram for the LithoRec recycling process for LIB. Reprinted with permission from Ref. (Kwade and Diekmann, 2018). Copyright: (2018) Springer Nature.

with low temperature treatment or, eventually, a pyrolysis process step after shredding (Brückner et al., 2020; Georgi-Maschler et al., 2012; Kwade and Diekmann, 2018; Velázquez-Martínez et al., 2019). Upstream of mechanical processing, is a step to deactivate the modules and battery cells, which can be achieved by electrical deep discharge to 0 V and short circuiting, saline solutions, or shock freezing (Georgi-Maschler et al., 2012; Hanisch et al., 2015b; Shaw-Stewart et al., 2019). The discharged battery modules or cells are then crushed, the shredded product usually treated thermally, and the components are separated into the individual fractions in a sequence of different sorting and classification processes. The obtained black mass can be processed by hydrometallurgical processes to produce metal salts or graphite.

Two established, and largely mechanical processes for LIB recycling are the so-called LithoRec and Accurec processes. The LithoRec process was developed within the framework of public funding in Germany and subsequently commercialized within the company Duesenfeld GmbH, Wendeburg, Germany. The developed process chain, according to Fig. 3(E) and Fig. 4, combines deep mechanical process steps with subsequent hydrometallurgy (Hanisch et al., 2015b; Diekmann et al., 2017; Kwade and Diekmann, 2018). In a first process step, the battery packs are electrically deep discharged and short-circuited. Material that has already been removed, such as the casing, battery management system and cables, can be forwarded for conventional recycling. The battery modules or cells are shredded in a 4-roller shredder or a rotor shear, whereby product sizes of 10 to 20 mm have been shown to be advantageous for the subsequent process steps according to Hanisch et al. (2015b); Kwade and Diekmann (2018). Due to the presence of electrolyte components (Ethylene carbonate (EC), Ethyl methyl carbonate (EMC), Dimethyl carbonate (DMC)), which pose in example a risk of flammability, it is recommended to carry out dry crushing in a nitrogen atmosphere (Kwade and Diekmann, 2018; Diekmann et al., 2020; Doose et al., 2021a). The comminution is followed by a drying step to remove electrolyte components. At temperatures of 100–140 °C, the highly volatile components DMC and EMC can be removed and recovered from the comminuted material (Stehmann et al., 2018). Alternatively, this can also be carried out in a vacuum drying process at reduced temperature, or at evaluated temperatures of more than 200 °C under inert or vacuum atmosphere (pyrolysis). The aim is to remove as much of

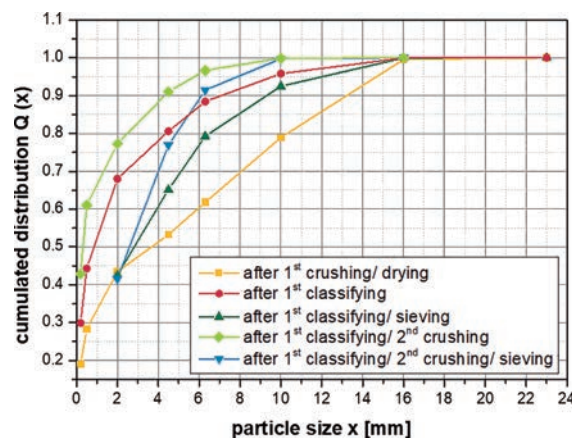


**Fig. 5** Change of the cumulated distribution of fragments of a battery module after different process steps. Reprinted from Ref. (Diekmann et al., 2017) under the terms of the CC-BY 4.0 license. Copyright: (2017) The Authors, published by Electrochemical Society.

the carbonates as possible, but to avoid the formation of reactive hydrogen fluoride (HF) from the conductive salt  $\text{LiPF}_6$  and PVDF binder. An optional mechanical mixing tool, used within the drying process, can also increase the detachment of active material from the conductor films, as well as the uniformity of thermal treatment of the material to be dried. This step is followed by mechanical separation of the present materials by way of a combination of air sifting by zig-zag-classifier, shredding and further sieving steps. In the first sifting step, components of the module and cell casings are removed from the shredded material. Subsequently, the remaining electrode foils, separator foil, polymeric components and black mass are shredded in a cutting mill to a maximum size of 10 mm. In addition, this process further promotes the detachment of black mass from the current collector foils. In a downstream air-sieving step, with sieve widths of 500  $\mu\text{m}$ , the black mass is separated from the remaining fraction. The influence of additional 2<sup>nd</sup> comminution and separation of the components can be seen in Fig. 5. As the process depth increases, the percentage of fine material increases, which is mainly due to the increasing amount of black mass detached from the electrode foils. The black mass obtained can then be fed to hydrometallurgical processing for the recovery of Co, Ni, Mn and Li. In addition, the remaining fraction is separated from separator foil in a further sifting process and de-coated aluminum and copper foil as well as plastic components can be forwarded for further commercial recycling (Diekmann et al., 2017; Kwade and Diekmann,

2018). The combination of these mechanical processes can result in more than a 90 % recovery of the black mass.

Another process already commercially established is the so-called Accurec recycling (Accurec GmbH, Krefeld, Germany) process for LIB, according to **Fig. 3(B)**. The process combines thermal (pyrolysis, pyrometallurgical), mechanical and hydrometallurgical processes to recover valuable materials from LIBs. The process begins with the separation of battery cells and casing materials, as well as BMS and cables. These are subsequently fed into the conventional recycling processes. In the next process step, the dismantled battery cells are deactivated by means of a thermal vacuum step. In this batchwise process step, the cells are safely deactivated under vacuum with up to 600 °C, in order to remove electrolyte components and volatile hydrocarbons (Brückner et al., 2020; Georgi-Maschler et al., 2012). The pyrolysis material obtained is subsequently fed into a milling process in order to separate the valuable materials from each other and make them accessible for mechanical separation processes. The processed material is separated in several separation steps with the help of vibrating sieves, magnetic separators and sifters. The exact process sequence and parameters are not described in detail in literature. With this process chain, the electrode active materials can be separated from iron, nickel, copper and aluminum components and processed separately in the following processes. The electrode active materials are subsequently pyrometallurgically processed at 800 °C under reducing conditions (e.g. regarding contained graphite from the anode) to form an alloy that may contain nickel, copper, cobalt and iron. The excess slag may contain lithium. Both fractions can subsequently be hydrometallurgically processed for high-value production, and transferred to a new application.

In addition to these two recycling process chains, there are further processes based essentially on mechanical processing that have already been developed, or are in development. For example, the Battery Resources “Closed Loop” process (Gratz et al., 2014), the OnTo Technology, and others that have already been established and whose function has been demonstrated.

#### 2.2.4 Mechanical-pyrometallurgical processing

Commercially, the pyrometallurgical process route for recycling of LIBs has been established and implemented for the longest. In this process chain, the battery modules or cells can be processed directly by the pyrometallurgical high temperature treatment (see **(A)** in **Fig. 3**), or subjected to mechanical processing beforehand (see **(C)** and **(D)** in **Fig. 3**). With regard to an increased overall recycling rate, it has been shown to be advantageous to carry out mechanical processing beforehand (Brückner et al., 2020). Mechanical processing, from removal of the casing, to comminution of the modules and cells, and separation of the valuable

materials into individual components, can be carried out analogously to the process steps used in mechanical-hydro-metallurgical processing routes. The obtained black mass can be fed to pyrometallurgical processing. Of course, whole cells can also be given for further processing after removal of the casing. Pyrometallurgical processes include high temperature processes, such as melting and roasting of the materials to obtain battery slag, alloys and kiln dust. Black mass processing in pyrometallurgy begins with a heating phase in the range of 150–500 °C, during which electrolyte, binder and other remaining polymeric constituents are removed. In the next process phase, under reducing conditions, temperatures of up to 1450 °C are reached (by decomposing graphite in the black mass, coke,  $\text{NH}_4\text{Cl}$ ,  $\text{CaCl}_2$  and/or  $\text{NaHSO}_4$ ), and the products obtained are battery slag with Li-containing components  $\text{Li}_2\text{O}$  and  $\text{Li}_2\text{O}_3$  and alloys. Ni, Co and Cu can be individually removed from the process and recovered, due to their different melting points. However, the other valuable materials (Li, Mn and Al) are contained in the kiln slag and/or the dust, and can only be recovered at high cost. The alloy, as well as the slag, and dust obtained are subsequently be processed hydrometallurgically, usually after milling.

As an industrial example, the process of Umicore Valéas<sup>TM</sup> (Bruxelles, Belgium) can be cited. The process is focused on the recovery of the metals Co and Ni from LIB and NiMH batteries, and is a combination of mechanical, pyro- and hydrometallurgical processes (Velázquez-Martínez et al., 2019). Compared to hydrometallurgical processing the pyrometallurgical processing of LIBs is very insensitive against different battery types, changing feed material and impurities. However, a subsequent hydrometallurgical treatment of the pyrometallurgical products obtained is necessary after pyrometallurgical processing, since intermediates that have no further industrial application are primarily produced (Brückner et al., 2020).

### 3. Active material production

To enable high growth in battery cell production, the availability of battery grade primary and secondary raw materials in form of metal salts, such as carbonates, sulphates and hydroxides (as basis for the cathode active materials), and graphites and silicon (as basis for the anode active materials) are essential.

#### 3.1 Cathode active material

Common cathode active materials (CAM) are lithium metal oxides (e.g.  $\text{LiNi}_{1-x-y}\text{Mn}_x\text{Co}_y\text{O}_2$  and  $\text{LiNi}_{1-x-y}\text{Co}_x\text{Al}_y\text{O}_2$ , known as NMC and NCA, respectively) or lithium iron phosphates (e.g.  $\text{LiFePO}_4$ , so-called LFP). The mean size, size distribution and morphology of CAM particles have a remarkable influence on the final structure, as well as on the resulting electrochemical performance of the lithium-ion battery (Ju and Kang, 2008; Sinha, 2009; Du et al.,



2010). In fact, lower CAM particle sizes have shown to bring advantages, such as improved charge and discharge rates due to an increased electrolyte-CAM contact area. However, there are also some disadvantages, such as the increase of undesired side reactions due to a larger specific surface area. As a consequence, the ongoing formation and development of the solid electrolyte interface can occur, leading to self-discharge of the cell and thus, unwanted safety issues (Sinha, 2009). More specifically, targeted particle design has been addressed and directed through different techniques, the most common being milling and classification processes at various stages of CAM production.

The synthesis of CAM can be performed via different techniques. For NMC materials, for example, precipitation reactions forming hydroxides (Cao H. et al., 2005) or carbonates (Guo et al., 2011; Zhang Y. et al., 2006), sol-gel syntheses (Peng et al., 1998), hydrothermal syntheses (Burukhin, 2002), syntheses via spray drying, combustion reactions (Dahbi et al., 2012) and solid-state reactions (Gan et al., 2005) have already been investigated, achieving different product qualities. In addition, there are further methods for coating (Lu et al., 2013), doping (Naghsh and Lee, 2001) and modification (Hashem et al., 2011) of the surfaces in order to enhance properties such as specific capacity, thermal stability or ionic conductivity. An overview of the process chain for the production of CAM, and the final application of milling and classification processes for precise control of particle size, is presented in Fig. 6.

Liu N. et al. (2014a) used a ball mill at the beginning of the synthesis route in order to pretreat a  $\text{LiFePO}_4$ -precursor suspension (300 rpm with zirconia grinding balls of 1 mm diameter). This led to higher homogeneity and narrower size distribution in the subsequent spray drying synthesis process, which was combined with a carbon-thermal reduction to finally produce  $\text{LiFePO}_4/\text{C}$  (carbon coating). They also demonstrated that smaller particles were cor-

related with a higher electrochemical performance. The initial discharge capacities of samples with particle sizes of about  $12 \mu\text{m}$  reached about  $158 \text{ mA h g}^{-1}$ , whereas those particles with sizes of  $1.5 \mu\text{m}$  achieved  $167.6 \text{ mA h g}^{-1}$ . They assumed that there was a decrease in the surface resistance, along with an improvement in the surface electronic conductivity, because of more homogeneous and complete carbon coating. Also, in this line of research work, Li H. et al. (2021) investigated the influence of ball milling after producing the precursor material by a co-precipitation process. After calcinating, the cathode material tailored by milling ( $\text{Li}_{1.2}\text{Ni}_{0.13}\text{Co}_{0.13}\text{Mn}_{0.54}\text{O}_2$ ) showed improved electrochemical properties.

Furthermore, ball milling is used to perform solid state synthesis by mixing and grinding all precursor materials at the same time (Cambaz et al., 2016; Kang et al., 2008; Yudha et al., 2019; Zhang Y. et al., 2006). A detailed understanding of the material manufacturing process can be found in the published studies of Kang et al. (2008) and Zhao et al. (2016), who varied the milling time in order to produce  $\text{LiFePO}_4$  and  $\text{LiFePO}_4/\text{C}$  respectively. Kang et al. demonstrated that small crystallites are achieved through longer milling periods. Based on their results, they proposed that CAM particles with very low sizes may hinder the insertion and extraction of  $\text{Li}^+$  ions, and thus decrease the electrochemical performance. Nevertheless, by finding the optimum parameters of milling, along with optimized heat-treatment parameters, they were able to produce  $\text{LiFePO}_4$ , which demonstrated a stable cycle performance and a discharge capacity of  $160 \text{ mA g}^{-1}$  at 0.1 C. Zhao et al. showed similar results, and additionally discovered that the effect is more significant at low temperatures (Zhao et al., 2016). This is caused by a hindrance of the lithium ion diffusivity, and an increment in the charge transfer resistance at the interfaces between electrode and electrolyte.

Furthermore, it has been demonstrated that calcinating the particles leads to an increase in their sizes, compared

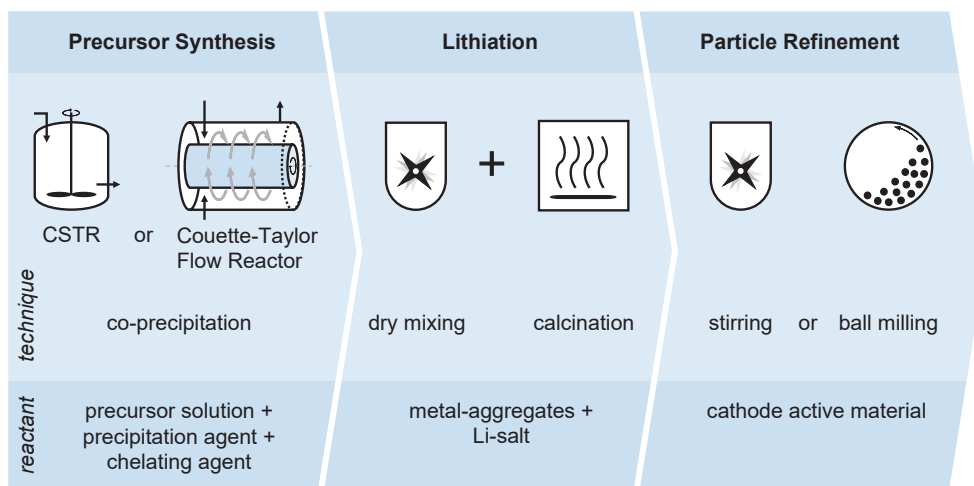


Fig. 6 Process chain for the production of cathode active materials by co-precipitation, mixing, calcination and further conditioning.

to the precursor material used, which results in a decreased specific capacity (Martha et al., 2009). Taking all these facts into consideration, controlling the final particle size distribution via a subsequent milling and classification processes is the key motivation of many studies (Ibarra-Palos et al., 2005; Kim et al., 2011; Stein IV et al., 2016). Milling parameters (e.g. process time, grinding media size and milling speed) have a direct impact on the size and morphology of the processed particles, a topic which has also been tackled by some researchers. In combination with comminution as a downstream process after synthesis, different classification processes are also used to achieve the target particle size. In particular, Stein IV et al. (2016) described the relationship between crystallite size and process parameters. Similar to the work of Kang et al. (2008), the smallest crystallite size did not lead to the best electrochemical performance, which proved to be significantly dependent on local structures within the electrode. These interdependencies between the grinding process and structural properties of active materials were thoroughly investigated by Pan et al. (2019). They varied the process times and identified relevant relationships with regard to the processing of NMC 442 cathode materials. Based on this study, it can be concluded that a reduction of the particle size can also be accompanied by structural changes in the form of a disordering of the layered structure, which then results in higher coulombic inefficiencies and capacity fading during cycling.

### 3.2 Anode active material

Graphite (natural and synthetic) is the most widely used active material on the anode side for lithium-ion batteries because of its good reversibility, stable voltage profile and good processing capabilities (Asenbauer et al., 2020). The high reversibility is due to the layered structure of graphite, in which the lithium ions can intercalate during charging and deintercalate during discharging of the battery (Yazami

and Touzain, 1983). The intercalation process takes place step-wise, which is reflected as plateaus in the voltage profile. At the fully lithiated state, the theoretical specific capacity of graphite totals  $372 \text{ mAh g}^{-1}$  (Asenbauer et al., 2020). Despite its good reversibility and high specific capacity compared to the CAM, the anode is still in the focus of interest to increase the energy density (Wh/L) and performance of the cell. The two major research topics on the anode side are the increase of the specific capacity by using new active materials, like silicon or tin, and the reduction of the initial capacity loss from the formation of the Solid Electrolyte Interface (SEI). The SEI is formed in the first charge step as a consequence of the instability of the electrolyte in the voltage window of the anode, and consumes lithium, thus, reducing the amount of active lithium in the cell and the capacity (An et al., 2016; Ng et al., 2009). This initial loss of lithium is directly correlated to the specific surface area on the anode side, which should therefore be minimized (An et al., 2016; Wang H. et al., 1999).

In order to decrease the specific surface area, two different processes are applied: surface coating and mechanical spheronization of graphite particles. By coating the graphite particles with an additional layer, the nano- and micron-sized pores can be closed, and hence the specific surface area is decreased (Yoon et al., 2001). This process is only reasonable for blocking smaller pores, otherwise the coating thickness would become too large, with negative impacts on the ion transport and energy density (Asenbauer et al., 2020; Casino et al., 2020). In order to change the particle morphology, a mechanical spheronization can be used. An overview of the mechanical treatment of anode active materials is shown in Fig. 7.

### 3.3 Spheronization of graphite

Normally, graphite exhibits a flake-like structure, consisting of multiple stacked layers of graphene with a large thickness in the horizontal direction (basal plane) and

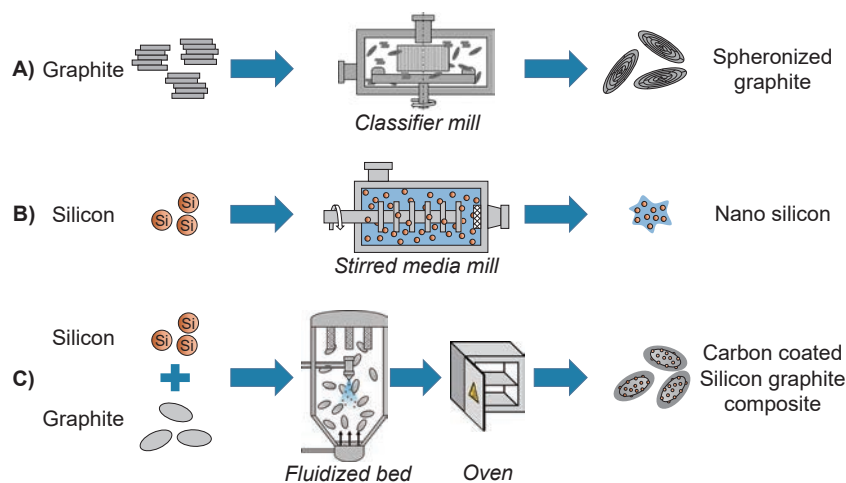


**Fig. 7** Overview of possible treatments of anode active materials; **A)** Mechanical spheronization of graphite, **B)** Nano-grinding of silicon, **C)** Preparation of silicon graphite composites. Adapted with permission from Ref. (Müller et al., 2021). Copyright: (2021) Elsevier B.V.

low thickness in the vertical direction (Lämmerer and Flachberger, 2017). By spheronization using a series of impact milling and classification process steps, the graphite morphology is modified to a more spherical shape, often referred to as “potato”-like shape (Asenbauer et al., 2020; Lämmerer and Flachberger, 2017).

This resulting structure, with a reduced specific surface area, leads to various benefits compared to the pristine graphite material, e.g. higher tap-density (Asenbauer et al., 2020; Kwon et al., 2021; Lämmerer and Flachberger, 2017), lower electrode tortuosity (Ebner et al., 2014; Müller et al., 2018) and increased energy density (Müller et al., 2018). Furthermore, the winding of the graphene layers during spheronization leads to more superficially localized edge planes, enabling new active sites at the surface for lithium ion intercalation. This facilitates faster ion transport and, thus, a higher rate capability and specific capacity for the spheronized graphite particles (Lämmerer and Flachberger, 2017; Natarajan et al., 2001; Wu et al., 2011). In addition to the reduction of specific surface area, spheronization also diminishes and narrows the particle size distribution, both enabling a better cell performance and preventing lithium plating (Bläubaum et al., 2020).

However, with increasing stressing time within the impact mills, more and more basal planes are destroyed and the highly reactive edge planes created at the surface are prone to higher SEI growth and the exfoliation of graphite by the electrolyte and, therefore, diminishes the capacity again (Wang H. et al., 1999). Moreover, it was found that the open porosity in the structure (accessible for the electrolyte) increases, but the closed porosity (not accessible for the electrolyte) decreases with increasing stressing time (Mundszinger et al., 2017). Consequently, the process parameters and stressing times have to be carefully selected for optimized particle design and cell performance. Moreover, the spheronization is often combined with subsequent carbon-coating, to further decrease the specific surface area and contact of the superficial edge planes with the electrolyte (Lämmerer and Flachberger, 2017).

The preparation of these spherical graphite particles is often carried out via impact stressing of the graphite particles in fluidized bed mills, jet mills or classifier mills. In industrial applications, a cascade of several dry-operated classifier mills, as shown in **Fig. 7 A**), is mostly used. Within these classifier mills, a disc with grinding tools in a rectangular shape, or shaped as rounded blocks, rotates around a central classifier wheel. The grinding tools can be adjusted towards the breakage or deformation of the milling feed. For the purpose of spheronization, a rounded shape is preferred so that the particles are only plastically deformed, or the edges broken off. The particle fragments are removed by the integrated classifier, and the spheronized product remains in the process chamber. In the standard type of operation, the spheronization is carried out in a

cascade of up to 20 mills. This process is, however, ineffective, because of its high operation cost, difficult scalability and low flexibility for change of product (Northern Graphite). The final yield amounts for only 30–50 %, meaning that more than half of the graphite used initially exits the process as fine powder, which cannot be used as active material anymore (Northern Graphite) (Steinrötter, 2011).

As previously discussed small particles exhibit a high specific surface area which enables on the one hand higher charging and discharging rates without lithium plating but on the other hand increases the irreversible capacity loss due to strong SEI growth (Bläubaum et al., 2020; Utsunomiya et al., 2011) and necessitates the usage of more binder leading to a decrease of energy density on electrode level due to larger inactive material content (Landesfeind et al., 2018). Furthermore, it was found that narrow particle size distributions in the single-digit micrometer range ( $x_{10} \approx 4 \mu\text{m}$ ,  $x_{50} \approx 6 \mu\text{m}$ ,  $x_{90} \approx 9 \mu\text{m}$ ) result in the best cell performance, among others highest specific capacity, cycling stability and C-rate capability (Bläubaum et al., 2020). Therefore, both mean particle size and width of particle size distribution are important factors for achieving a maximum possible cell performance.

Therefore, new classifier mills (e.g. FACULTY<sup>®</sup> S series from Hosokawa (HMC, 2021) and GyRho<sup>®</sup> from Netzsch) have been developed recently, which are able to replace these mill cascades and achieve the same throughput by reduced energy consumption and higher product yields. In contrast to the mill cascades, these mills operate in a batch or semi-batch mode.

Obrovac et al. (2020) developed a new simple method for spheronizing graphite particles by using ZrO<sub>2</sub> as host particles in a dry micro-granulation. The graphite flakes roll up around the ZrO<sub>2</sub> particles and form an additional layer with increasing thickness over time. At one point, this graphite layer becomes instable and flakes off as “potato”-shaped particles, which are then further rounded. Several other processes have been developed for the spheronization of graphite on laboratory scale, demonstrating superior characteristics of the structures obtained (Kwon et al., 2021; Lai et al., 2012; Wang H. et al., 1999).

### 3.4 Silicon: Next generation anode material

Silicon is a key material for many different application fields, because of its outstanding physical properties. It is the second most abundant element in the earth’s crust, and easily accessible. In the past ten years, the rising popularity of lithium-ion batteries (LIBs) led to growing interest in the use of silicon as an anode material, as the theoretical specific capacity of silicon (3580–4200 mAh/g) is roughly ten times higher than that of graphite (372 mAh/g) (Ashuri et al., 2016). During the charge/discharge cycles, silicon undergoes significant volume changes (up to 300 %). This leads to breakage of the silicon particles, resulting in

continuous exposure of the active silicon surface and, thus, Lithium consumption through surface reactions. Moreover, the electrode structure becomes damaged, and results in loss of connection between particles and current collector, and destruction of the SEI. In the end, a silicon based battery shows poor cycling stability (Hu et al., 2014; Sun et al., 2016a).

In order to overcome the challenge of volume expansion and particle cracking, the failure mechanisms of silicon-based electrodes need to be understood in order to create a fully functioning silicon-based anode. For this purpose, the mechanisms during cycling of the battery must be investigated (Szczech and Jin, 2011). Sun et al. (2016a) discovered that pulverization of silicon particles and electrochemical passivation of some silicon particles lead to failure of the battery cell during lithiation. Liu and Huang (2011) investigated the charge and discharge behavior of batteries using silicon possessing varying sizes and structures. They could show that a critical particle diameter of 150 nm exists, at which no cracking during volume expansion occurs. This critical particle diameter is mentioned and confirmed in other publications (Liu X.H. et al., 2012; Sun et al., 2016b; Szczech and Jin, 2011). This also leads to the design of different nano structures, such as silicon based nanowires (Zhang C. et al., 2013a), nanotubes (Wu et al., 2012), nanosheets and nanoporous Si particles. Even though nano-sized silicon is able to maintain its structure without cracking, the problems from the large volume expansion (unstable formation of the SEI and contact loss of particles) still remains, although to a lesser extent. For that reason, silicon composite materials are targeted as promising solutions. Here, a composite material, often graphite, is used as framework for nano-sized silicon particles. The goal is to allow the silicon to expand inside the composite, while the electrode structure is maintained by the composite framework. By looking at the literature, the approach of customized composites is the most promising electrode design, both in terms of the electrochemical performance, as well as the mechanical integrity of silicon-based battery cells (see [Chapter 3.5](#)).

An important challenge is the production of nano-sized silicon, which can either be achieved via bottom-up or top-down processes. Bottom-up methods usually depend on chemical approaches, and often require long reaction times, expensive chemicals, complex process control and up-scaling difficulties (Hou et al., 2015; Nilssen et al., 2020). In top-down methods, coarser materials are broken down into smaller fragments by comminution. The choice of the right comminution machine highly depends on the size of the starting material.

Silicon is a rather hard and brittle material, rendering it suitable for grinding tasks. Leblanc et al. (2015) describe a comminution process route from silicon ingots, with sizes of a couple of centimeters down to the nanometer range.

First, different silicon feedstocks, such as quartz or gravel ( $\text{SiO}_2$ ), were treated thermally in a furnace. By using a carbonaceous material, the silicon feedstock was converted to molten MG-silicon ingots. Subsequently, the ingots were crushed and ground in several dry grinding steps comprising of a jaw crusher, a roll mill and a jet mill. After these milling steps, the obtained silicon powder was in the range of a few micrometers (Leblanc et al., 2015). However, silicon in this size range is often already available from the semiconductor and photovoltaic industry, which cuts silicon wafers for their applications and produces pure micron-sized silicon dust as byproduct.

The subsequent nano-comminution is carried out in a solvent, in order to prevent agglomeration of the particles. Most commonly, stirred media mills are used for this task ([Fig.7 B](#)), and in the lab scale planetary ball mills may be employed. This type of mill was intensively investigated by researchers over the past decades (Breitung-Faes and Kwade, 2008; 2014; Knieke et al., 2010). Hou et al. (2015) applied a stirred media milling process for silicon, and investigated the structural changes and their impact on battery performance. They report that the bead milling strategy improved the battery performance because of amorphization of crystal structure, the formation of an oxidized surface ( $\text{SiO}_2$ ) and smaller particle size compared to micrometer-sized silicon. Early investigations of phase transition in silicon during bead milling were conducted by Gaffet and Harmelin (1990). A major challenge in nano-comminution is the stabilization of the ground particles. Here, the choice of an appropriate solvent is essential. Reindl et al. investigated the impact of dispersing silicon nanoparticles in different organic solvents, such as 1-butanol or toluene (Reindl et al., 2007; 2008). They found that the silicon particles have a pronounced tendency to agglomerate in organic solvents. They could stabilize the silicon nanoparticles by using fish oil as a steric stabilizing agent (Reindl et al., 2008). Nöske et al. (2019) applied a stirred media mill for the nano-comminution of silicon in ethanol. They performed an electrostatic stabilization, by preparing a sodium hydroxide solution in ethanol. The analysis of particle size and zeta-potential revealed that at  $\text{pH}^*$ -values greater than 7.5 the silicon nanoparticles can be stabilized, and do not agglomerate. As a result, they suggest a two-step grinding process and electrostatic stabilization at  $\text{pH}^* = 7.5$ . The results of their approach containing a pre- and fine grinding step can be seen in [Fig. 8](#). Considering both grinding steps, the final product, particles with a size of  $x_{50,3} = 75$  nm, is obtained after a specific energy input of  $106 \text{ MJ kg}^{-1}$  (Nöske et al., 2019).

The impact of electrostatic stabilization was also reported by Švrček et al. (2005). They claim that nano-sized silicon particles in ethanol could be stabilized by adding ammonia. Additionally, Nilssen and Kleiv (2020) investigated the impact of stabilization on the efficiency of silicon

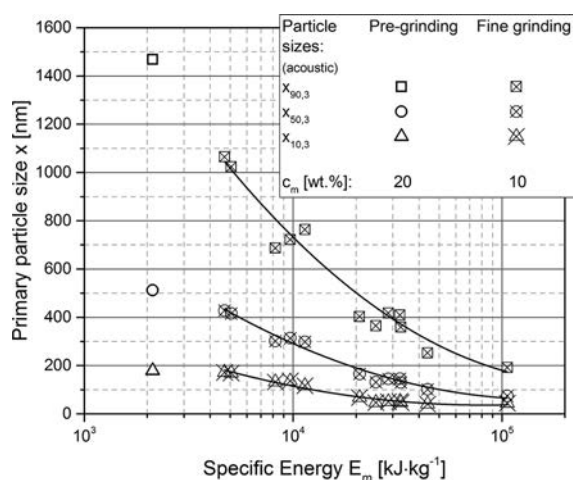


**Fig. 8** Primary particle size vs. specific energy input for the two-step grinding of silicon proposed by Nöske et al. (2019). Reprinted from Ref. (Nöske et al., 2019) under the terms of the CC-BY 4.0 license. Copyright: (2019) The Authors, published by Electrochemical Society.

nano-comminution in stirred media mills. They could show that the lack of sufficient stabilization leads to an increase in the viscosity of the slurry. However, they also report that the non-stabilized slurry did not have a significant impact on the grinding efficiency. This was attributed to the pseudoplastic rheology of the slurry and high shear rates in the grinding chamber. Moreover, they investigated the importance of optimal stress energy on the grinding of silicon by varying the stirrer tip speed and size of the grinding media. Their parameter combinations suggest that at the lowest specific energy input, an optimum exists at a point of low stress energy (Nilssen et al., 2020; Nilssen and Kleiv, 2020). From a production point of view, this means a longer overall grinding or production time, but less product contamination caused by grinding media wear. The impact of wear from silicon grinding on battery performance is still being investigated. In general, the choice of appropriate grinding parameters is a compromise between productivity and product purity (Nilssen et al., 2020).

### 3.5 Silicon composites

Even though silicon is the most promising anode material for the future, silicon has only been applied in small amounts (typically <5 wt %) in commercial cells (Choi and Aurbach, 2016). As previously discussed, this is mainly due to the challenges arising from the large volume change of silicon during lithiation (up to 300 %), whereas graphite shows only minor volume expansion of 10 %. Therefore, the combination of silicon and graphite has attracted much attention. While graphite with its high electrical conductivity, good cycling characteristics and low volume expansion provides a stable matrix, even small amounts of silicon can significantly enhance the capacity. This can be illustrated by the fact that by using 10 wt % silicon, the specific capacity of the anode can be nearly doubled.

In current commercial cell manufacturing, small silicon contents are simply blended with the graphite active material during electrode production (Choi and Aurbach, 2016). However, when using larger silicon contents, the resulting cell performance is poor and requires an optimized particle design. Therefore, multiple composite structures for silicon and silicon graphite composites have been developed, and been proven to be beneficial for capacity retention. These structures can be divided into three main approaches (Franco Gonzalez et al., 2017; He et al., 2021; Jin et al., 2017): nanostructures, porous and other 3D-structures and Si/SiO<sub>x</sub> composites.

Two different composite structures comprising silicon nanoparticles are possible: a core-shell structure with a layer of silicon nanoparticles on graphite, or the encapsulation of the nanoparticles (Li M. et al., 2014; Müller et al., 2021; Sui et al., 2018). Müller et al. demonstrated a good performance, for which silicon nanoparticles are prepared beforehand by grinding in a stirred media mill, and then coated onto coarser graphite particles by scalable fluidized bed granulation (Si@Gr). After subsequent pitch-coating (Si@Gr/C), the composite demonstrated good cycling stability and rate performance (Müller et al., 2021). The manufacturing process of these composites is shown in Fig. 7 C).

Additionally, silicon nanoparticles can be encapsulated in hollow carbon spheres. The silicon particles can expand in the highly conductive carbon matrix without any volume change of the composite particle itself. This characteristic is advantageous, because it prevents electrical isolation even after pulverization and allows for a stable SEI layer and superior cycling characteristics (Liu Y. et al., 2014b).

## 4. Electrode slurry production

The production of electrodes initially requires the classical mechanical process of dispersive mixing to obtain a coatable slurry (Kwade et al., 2018; Liu H. et al., 2021; Wenzel et al., 2015). In this context dispersive mixing means that beside a homogenization of the material mixture (i.e. a distributive mixing) material components are reduced in their size and changed in their structure by mechanical stresses and, thus, comminution of these material components. Here the fine carbon black (CB) agglomerates and aggregates have to be reduced in size by breaking off solid bridges and van der Waals based adhesion between the CB primary particles. Typically, after a dry homogenization, and an optional dry intensive, i.e. dispersive mixing, the powder components (active materials (AM), conductive agents like carbon black (CB) and polymeric binders) are mixed with a solvent and homogeneously distributed in it. During the dispersive mixing, the main objective is to fragment the carbon black agglomerates, and to comminute CB aggregates to defined sizes and structures, without damaging the other components (Bockholt et al.,

2016b; Wenzel et al., 2015). Particularly in combination with polymer binders, the size and distribution of CB defines the formation of the microstructural network in the slurry, and later the electrode (Gaikwad and Arias, 2017). This microstructure determines the resulting electrode properties and the cell performance (Bockholt et al., 2016b; Zhang C. et al., 2013a), which turns the process steps of dispersive mixing into a central and property-defining part of the knowledge-based production of high quality LIB electrodes. The type of conductive additives and binder systems used will vary depending on the electrode type (Zhang Q. et al., 2013b). For example, polyvinylidene fluoride (PVDF) binders in combination with different types of CB and conductive graphite (CG) are used in cathode slurries. According to recent literature, cathode slurries are mostly N-2-methylpyrrolidone-(NMP)-based, while anode slurries are processed with water, using a binder system of carboxymethyl cellulose (CMC) and styrene butadiene rubber (SBR) (Gordon et al., 2020; Kwade et al., 2018).

#### 4.1 State of technology

Due to the highlighted significance of size and distribution of conductive additives for the microstructural formation, the characterization of conductive additives before, during, and after mixing is of particular importance. Thus, a methodology via light diffraction and scattering for determining the size of CB particles from electrode slurries, including a sample preparation routine, was developed and tested (Dreger et al., 2017). In addition, other studies identify the condition and effects of CB via electrical, viscometric, imaging, or ultrasound scattering techniques. During dispersion, the formulation strategy and the process parameters determine the particle size and distribution (Wenzel et al., 2014). Thus, numerous publications focus on the relationship of processing and electrode slurry properties. For example, the importance, and subsequent consequences, of formulation strategies were shown. Here, optimal electrochemical rate performance was achieved due to ideal electrode porosities by utilizing moderate dispersing intensities for dry and binder type formulations (Haselrieder et al., 2014). In order to set the CB size, an additional dry mixing step prior to dispersion in a (high) intensity mixer can be applied: prolonged exposure of the components leads to a lower density of the coating due to increased deagglomeration of CB, and ultimately to increased adhesive strengths and improved discharge capacities and cycle stabilities (Bockholt et al., 2016a). These effects generally result in lower porosities and higher cohesiveness of the electrode coating. Additionally, CB attaches to the AM particle surfaces, establishing short-range electrical contacts all around the NMC particles (Bauer et al., 2015; Bockholt et al., 2016a). These CB-coated AM particles can also be achieved by dispersion processes without prior dry mixing. For example, kneading processes

in planetary mixers are suitable for high-intensity stressing of slurries at high solids contents (~80 wt % and above), favoring very small sizes of CB in the range of 100 nm, which are particularly important for the formation of short-range conductive paths (Mayer et al., 2020). Process control in batch mixers concerning the dispersing intensity is also proving to be very important for optimizing electrodes, specifically with thicker layers for high-energy applications (Kremer et al., 2020).

For the dispersive mixing, the specific energy is a key evaluation value. It can be determined by the power input of the machine, minus the no-load power consumption, summed over time, in relation to the mass of the slurry. To highlight the role of the specific energy input, Fig. 9 shows exemplary results for CB deagglomeration with a dissolver (Dispermat AE03, VMA Getzmann) and a planetary mixer (PMH10, NETZSCH) by relating the decreasing volumetric median of the typically bimodal particle size distribution of CB, determined as described by Dreger et al. (2017), to the specific energy. The influence of the dispersing machines is directly evident: In the planetary mixer, the mixing tool velocities affect the final particle sizes of CB that can be achieved. In the dissolver, however, the particle size is exclusively dependent on the specific energy. Additionally, the dissolver shows a higher energy efficiency, but is less suitable for scaling to industrial standards due to its poorer distributive mixing properties.

Based on such experimental results, model-like descriptions of the dispersion of LIB slurries can be created purely empirically (Griebl et al., 2021), or by means of classical relationships of particle stressing in slurries (approaches according to Kolmogorov (1958); Krekel (1966); Kwade (2003)). Dispersion models enable knowledge-based scaling of the process machines, and converting discontinuous

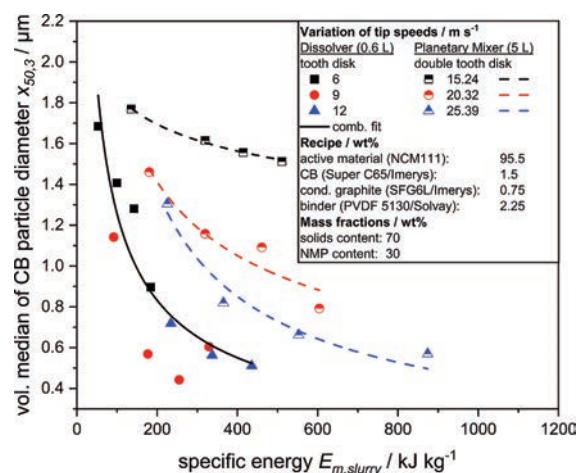


**Fig. 9** Dependence of CB size on specific energy of the dispersion process for a planetary mixer (dashed lines) and dissolver (full line). Symbols indicate the progressive dispersion time (15, 30, 45 and 60 min) for each test series from left to right.

into continuous processes, which will become increasingly important in the future.

#### 4.2 Future perspective

In order to increase the economic efficiency of the dispersion process and, thus, enable large-scale production, even at labor expensive locations, the conversion of typical batch mixers used industrially into continuous mixing processes is advised (e.g. using twin-screw extruders (Schunemann et al., 2016)). Accordingly, the application of extruders for electrode production is increasingly moving into the focus of research and process development. For instance, a laboratory-scale dissolver process was compared to a discontinuous kneading and a continuous extrusion process. The continuous production of slurries by the low-solvent extrusion processes exhibit good electrochemical performance, showing good deagglomeration and almost complete coverage of active material particles by CB (Dreger et al., 2015). Further investigations showed the decisive influence of the solids content on the extrusion-based production of cathode slurries. Higher solids contents reduce sedimentation effects and binder migration. In addition, they define the fragmentation of the conductive CB and, thus, the resulting properties of manufactured cathodes (Haarmann et al., 2020). Other works show the use, or combination, of batch and continuous processes. The powder components are prepared for a subsequent extrusion-based coating process by means of intensive mixers and kneaders, whereby the actual dispersion takes place before the extrusion process (Seeba et al., 2020). Beside extrusion, the dispersing in continuously operated stirred media mills was also reported from industry.

On the material side, due to their advantageous properties, fiber-like conductive additives, such as carbon nano tubes (CNT) and vapor-grown carbon fibers (VGCF), are increasingly used in research and industrial applications as a supplement, or a complete replacement, for conductive CB (Landi et al., 2009; Park et al., 2018; Qi et al., 2015). CNTs are only needed in small quantities, but are in some cases more expensive than CB (Bauer et al., 2015). LIB cathodes with CNTs show low initial Coulomb efficiencies and large voltage hysteresis, but exceedingly high electrical conductivity (Bauer et al., 2015). This advantage results from the ability to connect several active material particles within the electrode structure due to its length and also obtain an improved cycle stability and C-rate performance (Huang et al., 2010; Zhang Q. et al., 2013b). For the dispersing of the fiber-like conductive additives, high-pressure homogenizers are a well-suited alternative to conventional equipment. In terms of cathode active materials, adaptations will be necessary in the future for the more nickel-rich layered oxides (e.g. NCM811), which are both sensitive to moisture and mechanically more unstable (Heck et al., 2020).

## 5. Outlook—Solid electrolytes

### 5.1 Mechanochemical synthesis

In order to enable scalable production of solid-state batteries, solid electrolytes are required in sufficient quantities and with high and consistent quality. Although planetary ball mills, vibrating ball mills, and stirred media mills should all be suitable for mechanochemical syntheses of solid electrolytes, so far planetary ball mills have almost always been used on a laboratory scale (Schlem et al., 2021b).

The reasons might be the simple experimental setup, as well as the wide-spread use. As their ability for large-scale synthesis is quite poor, a transfer to continuous ball/bead mill types (e.g. stirred media mills) seems desirable. Most publications on mechanochemical routes consider the effect of processing parameters and conditions for the conversion time, instead of energy input. As this makes it difficult to distinguish between effects of energy dissipation and activation thresholds, and simply faster mechanical processing, further investigations with focus on process technology are still required.

Among solid electrolytes, thiophosphates and sulfides represent the material system considered the most promising class of materials, with very high Li ionic conductivities up to  $10^{-2}$  S/cm and beyond (Kato et al., 2016). They are usually produced by classical solid-state syntheses via dry process routes (Dietrich et al., 2017; Kraft et al., 2018), or via solvent-based processes (Ghidu et al., 2019). To ensure sufficient ionic conductivity,  $\sigma_{\text{ion}}$ , and electrochemical stability (e.g. against high-voltage cathode materials), the absence of possible impurities is especially crucial. The latter can result from solvents used in the synthesis process and necessitate thorough washing (Kudu et al., 2018). While classical solid-state synthesis in sealed quartz ampoules does not seem suitable for scalable production (Kudu et al., 2018), mechanochemical synthesis within mills is a promising approach. Compared to the alternative methods, the products have predominantly amorphous structures, due to the kinetically controlled reactions, but can often be crystallized by a subsequent annealing step (Gautam et al., 2019). Sulfide electrolytes can be prepared as pure Li-P-S phases from starting materials  $\text{Li}_2\text{S}$  and  $\text{P}_2\text{S}_5$  with different stoichiometries (Dietrich et al., 2017; Tatsumisago et al., 2002), or in combination with metals (e.g. Si or Ge), or halides (Cl, Br, I) (Zhang Z. et al., 2018). Compared to classical solid-state syntheses, mechanochemical methods allow the synthesis of additional metastable compounds and local structures (Stöffler et al., 2019). Of particular importance are the argyrodites,  $\text{Li}_6\text{PS}_5\text{Cl}$  and  $\text{Li}_6\text{PS}_5\text{Br}$ , as well as their variants with iso- and aliovalent substitutions, in whose synthesis an annealing step follows a ball-milling process (Kraft et al., 2018; Rao and Adams, 2011). A significantly poorer  $\sigma_{\text{ion}}$  is exhibited by  $\text{Li}_6\text{PS}_5\text{I}$  (Hanghofer et al., 2019), although  $\sigma_{\text{ion}}$  here can be increased by two orders

of magnitude by subsequent “soft” ball-milling of 120 min at 400 rpm (Brinek et al., 2020). This is attributed to the transition from micro- to nanocrystallinity. However, it is by no means the case that mechanochemical stress leads to an improvement of the material in every case: as shown by Dewald et al. (2021), ball-milling of  $\text{Li}_6\text{PS}_5\text{Cl}$  synthesized via classical solid-state reaction leads to a decrease in  $\sigma_{\text{ion}}$ .

Among solid electrolytes for sodium batteries,  $\text{Na}_3\text{PS}_4$  is frequently synthesized mechanochemically (Nguyen et al., 2019; Takeuchi et al., 2018). Nguyen et al. (2019) thoroughly studied the influence of milling media size, disc rotation speed, and process time in a planetary ball mill. They found that the same  $\sigma_{\text{ion}}$  can be obtained by different synthesis conditions. The mechanochemically prepared compounds mostly have higher  $\sigma_{\text{ion}}$ , which is attributed to different achievable crystal structures, as well as disorder in the structure of  $\text{Na}^+$  (Krauskopf et al., 2018). Mechanochemical methods are also well suited for introducing defects by doping, achieving  $\sigma_{\text{ion}}$  as high as 41 mS/cm (Fuchs et al., 2020; Hayashi et al., 2019). The relationship between the structure influenced by the mechanochemical processes—micro-, macrostrain, and defects—and ion transport is studied in detail by Famprikis et al. (2020).

Another class of solid electrolytes that can be produced via mechanochemical reactions are halides (Asano et al., 2018; Li X. et al., 2019). They provide high electrochemical stability against cathode active materials, as well as mechanical deformability at room temperature (Li X. et al., 2020). Schlem et al. (2020) showed that for  $\text{Li}_3\text{ErCl}_6$  and  $\text{Li}_3\text{YCl}_6$ , cation disorder induced by ball-milling leads to an increase in  $\sigma_{\text{ion}}$ . In contrast, for  $\text{Li}_3\text{YBr}_6$  the  $\sigma_{\text{ion}}$  can be increased by subsequent annealing (Schlem et al., 2021a). Recently, it was demonstrated that a halide superionic conductor without rare earth metals, namely  $\text{Li}_{2.25}\text{Zr}_{0.75}\text{Fe}_{0.25}\text{Cl}_6$ , with a  $\text{Li}^+$  conductivity up to  $\approx 1 \text{ mS cm}^{-1}$ , could be prepared in a planetary ball mill (Kwak et al., 2021).

In order to combine the advantages of different types of solid electrolytes (i.e. the high  $\sigma_{\text{ion}}$  at room temperature of inorganic electrolytes and the good processability of polymer electrolytes) so-called hybrid electrolytes are produced. For example, the reaction of  $70\text{Li}_2\text{S} \cdot 30\text{P}_2\text{S}_5$  (mol%) and different –OH group terminated oligomers in a planetary ball mill can lead to the formation of P–O–C bonds. To combine an oxide electrolyte with polymer, LLZO was mixed with an acetonitrile solution of PEO and  $\text{LiClO}_4$ , and subsequently uniformly homogenized in a low energy ball mill (Dixit et al., 2019). The slurry obtained was subsequently coated via coextrusion, demonstrating a scalable manufacturing process.

## 5.2 Conditioning

For use in composite cathodes or separators, in addition to the (electro)chemical properties, the particle size of

the solid electrolyte is crucial (Kerman et al., 2017). For example, a particle size smaller than  $1 \mu\text{m}$  allows a more uniform distribution in the cathode and, thus, a better contacting of the active material (Calpa et al., 2019). Dixit et al. (2020) conditioned the microstructure and interface between the separator and the metallic lithium anode using iodine doping, as well as ball-milling and annealing. They milled an LPS/0.5LiI mixture together with heptane for 12 h, at a rather low rotation speed of 200 rpm, to reduce the particle size.

In addition, mechanochemical methods can be used to obtain desirable cathode composite microstructures, which are crucial for the performance of all solid-state batteries (Nagao et al., 2012). A ball-milled cathode composite for Li-S solid-state batteries consisting of  $\text{Li}_6\text{PS}_5\text{Cl}$  and sulfur-carbon composite outperformed a hand-ground one with respect to initial capacity, as well as capacity retention (Ohno et al., 2019). This is attributed to the grinding of the active material, leading to intimate contact in the composite, which helps to mitigate volume changes during cycling. An alternative to the application of ball mills is dry-coating of the active material particles with the solid electrolyte by a dry blending device (Nara Machinery Co., Ltd.) to achieve a high contact area, as well as well-percolated ion transport pathways (Nakamura et al., 2020).

Graebe et al. (2017) reported the use of a centrifugal mixer for the preparation of a composite material for a solvent-free manufacture of polyethylene oxide (PEO) based solid state electrodes. This dry mixing and mechanofusion process step is the key challenging step, as it ensures a free-flowing powder, necessary to produce a dense solid-state cathode or solid-state separator. This is accomplished by coating the PEO secondary particles with  $\text{SiO}_2$  or  $\text{C}_{65}$  to prevent further agglomeration.

## 6. Conclusion and outlook

The increasing demand for lithium-ion-batteries and future types of lithium batteries, especially for the ramp-up of electromobility worldwide, requires the further development of an economically and, at the same time, ecologically sustainable supply and production chain, starting with the extraction and processing of the primary and secondary raw materials, over their refinement to battery grade intermediates, to active and passive materials in the production of the cell components, like electrodes and finally battery cells. However, sustainability can only be reached if the end-of-life battery systems are used as secondary material source for the production of new battery cells, through which the recycling of the materials and the re-synthesis or re-conditioning of the active materials, especially for the cathode, becomes mandatory. Accordingly, regulations will be issued by the governments, like the EU, to ensure very high recovery rates for the entire battery system and especially for the valuable metals. Latest by this demand



milling, dispersing and classification processes get a central role within the circular processing of lithium-ion batteries and next battery generations.

However, as shown in the review, comminution and classification is not only very central for the primary and secondary raw material processing, but also for the production of the cathode and anode active materials and, in the future, the mechanochemical synthesis of the solid electrolytes. The dry and wet mixing and dispersion of the electrode material mixture requires processes in which the particles are stressed, so that besides different types of mixers, extruders and wet operated mills are also used for the wet dispersion of components, especially in the case of nano-sized components. The mill and classifier manufacturers, the plant designers and builders, as well as the research institutions, should embrace these opportunities and develop new machinery and new processes to significantly increase the sustainability of circular battery cell production. In the near future, great attention should lie on energy efficient recycling processes, which ensure a high recycling rate of nearly 100 % and high component purity, as well as processes for dry electrode processing, where the dry pretreatment of the material mixture is a crucial process step. Moreover, the tailoring of the particle size distributions and particle morphologies, especially for new material classes like monocrystalline cathode active material and solid electrolytes, is an important task for the particle technology community.

## Acknowledgements

Many thanks to Michael Grube, Moritz Hofer and Clara Sangrós for their input to this review in the field of active materials and the production of sulphidic solid electrolytes as well as Heather Cavers for an overall review of the spelling.

## Nomenclature

Al	Aluminum
AM	Active material
ASSB	All-solid-state battery
BEV	Battery electric vehicle
BMS	Battery management system
Br	Bromine
CAM	Cathode active material
CB	Carbon black
CEID	Circular Economy Initiative Germany
CG	Conductive graphite
CMC	Carboxymethyl cellulose
CNT	Carbon nano tubes
CO <sub>2</sub>	Carbon dioxide
DMC	Dimethyl carbonate
EC	Ethylene carbonate
ELV	End of life vehicle

EMC	Ethyl methyl carbonate
$E_{m,slurry}$	Specific energy related to slurry mass
EOl	End of life
EU	European Union
Gr	Graphite
HF	Hydrogen fluoride
HPGR	High pressure grinding rolls
LFP	Lithium iron phosphate
LMNO	Lithium manganese nickel oxide
Li	Lithium
LIB	Lithium ion batteries
LiFePO <sub>3</sub>	Lithium iron phosphate
LIS	Lithium sulfur battery
LLZO	Lithium lanthanum zirconium oxide
LPS	Li <sub>3</sub> PS <sub>4</sub> (sulphidic solid electrolyte)
Mio.	Million
NCA	Lithium nickel cobalt aluminum oxide
NiMH	Nickel metal hydrate
NMC	Lithium nickel manganese cobalt oxide (LiNi <sub>1-y-z</sub> Mn <sub>y</sub> Co <sub>z</sub> O <sub>2</sub> )
NMP	N-2-methyl-pyrrolidone
PEO	Polyethylene oxide
PHEV	Plug-in hybrid electric vehicle
PVDF	Polyvinylidene fluoride
SAG	Semi-autogenous grinding
SBR	Styrene-butadiene rubber
SEI	Solid electrolyte interface
Si@Gr	Graphite with Si-nanoparticles
Si@GrC	Graphite with Si-nanoparticles and carbon coating
tph	tons per hour
VGCF	Vapor grown carbon fiber
wt	weight
$x_{50,3}$	Volumetric median particle size
$\sigma_{ion}$	ionic conductivity

## References

- Amarante M.M., Sousa A.B. de, Leite M.M., Processing a spodumene ore to obtain lithium concentrates for addition to glass and ceramic bodies, *Minerals Engineering*, 12 (1999) 433–436. DOI: 10.1016/S0892-6875(99)00023-0
- Amer A.M., The hydrometallurgical extraction of lithium from Egyptian montmorillonite-type clay, *JOM*, 60 (2008) 55–57. DOI: 10.1007/s11837-008-0137-5
- An S.J., Li J., Daniel C., Mohanty D., Nagpure S., Wood D.L., The state of understanding of the lithium-ion-battery graphite solid electrolyte interphase (SEI) and its relationship to formation cycling, *Carbon*, 105 (2016) 52–76. DOI: 10.1016/j.carbon.2016.04.008
- Arshad F., Li L., Amin K., Fan E., Manurkar N., Ahmad A., Yang J., Wu F., Chen R., A comprehensive review of the advancement in recycling the anode and electrolyte from spent lithium ion batteries, *ACS Sustainable Chemistry & Engineering*, 8 (2020) 13527–13554. DOI: 10.1021/acssuschemeng.0c04940
- Asano T., Sakai A., Ouchi S., Sakaida M., Miyazaki A., Hasegawa S., Solid halide electrolytes with high lithium-ion

- conductivity for application in 4 V class bulk-type all-solid-state batteries, *Advanced Materials*, 30 (2018) 1803075. DOI: 10.1002/adma.201803075
- Asenbauer J., Eisenmann T., Kuenzel M., Kazzazi A., Chen Z., Bresser D., The success story of graphite as a lithium-ion anode material – fundamentals, remaining challenges, and recent developments including silicon (oxide) composites, *Sustainable Energy & Fuels*, 4 (2020) 5387–5416. DOI: 10.1039/d0se00175a
- Ashuri M., He Q., Shaw L.L., Silicon as a potential anode material for Li-ion batteries: where size, geometry and structure matter, *Nanoscale*, 8 (2016) 74–103. DOI: 10.1039/c5nr05116a
- Baláz P., Mechanical activation in hydrometallurgy, *International Journal of Mineral Processing*, 72 (2003) 341–354. DOI: 10.1016/S0301-7516(03)00109-1
- Ballantyne G.R., Peukert W., Powell M.S., Size specific energy (SSE)—energy required to generate minus 75 micron material, *International Journal of Mineral Processing*, 136 (2015) 2–6. DOI: 10.1016/j.minpro.2014.09.010
- Ballantyne G.R., Powell M.S., Benchmarking comminution energy consumption for the processing of copper and gold ores, *Minerals Engineering*, 65 (2014) 109–114. DOI: 10.1016/j.mineng.2014.05.017
- Barbosa L.I., Valente G., Orsoco R.P., González J.A., Lithium extraction from  $\beta$ -spodumene through chlorination with chlorine gas, *Minerals Engineering*, 56 (2014) 29–34. DOI: 10.1016/j.mineng.2013.10.026
- Bauer W., Nötzel D., Wenzel V., Nirschl H., Influence of dry mixing and distribution of conductive additives in cathodes for lithium ion batteries, *Journal of Power Sources*, 288 (2015) 359–367. DOI: 10.1016/j.jpowsour.2015.04.081
- Bläubaum L., Röder F., Nowak C., Chan H.S., Kwade A., Krewer U., Impact of particle size distribution on performance of lithium-ion batteries, *ChemElectroChem*, 7 (2020) 4755–4766. DOI: 10.1002/celec.202001249
- Bloomberg New Energy Finance, *Electric Vehicle Outlook 2018 (summary)*, (2018). Retrieved from <https://bnf.turtl.co/story/evo2018?teaser=true> accessed 17032022.
- Bockholt H., Haselrieder W., Kwade A., Intensive powder mixing for dry dispersing of carbon black and its relevance for lithium-ion battery cathodes, *Powder Technology*, 297 (2016a) 266–274. DOI: 10.1016/j.powtec.2016.04.011
- Bockholt H., Indrikova M., Netz A., Golks F., Kwade A., The interaction of consecutive process steps in the manufacturing of lithium-ion battery electrodes with regard to structural and electrochemical properties, *Journal of Power Sources*, 325 (2016b) 140–151. DOI: 10.1016/j.jpowsour.2016.05.127
- Bonsu N.O., Towards a circular and low-carbon economy: Insights from the transitioning to electric vehicles and net zero economy, *Journal of Cleaner Production*, 256 (2020) 120659. DOI: 10.1016/j.jclepro.2020.120659
- Breitung-Faes S., Kwade A., Nano particle production in high-power-density mills, *Chemical Engineering Research and Design*, 86 (2008) 390–394. DOI: 10.1016/j.cherd.2007.11.006
- Breitung-Faes S., Kwade A., Use of an enhanced stress model for the optimization of wet stirred media milling processes, *Chemical Engineering & Technology*, 37 (2014) 819–826. DOI: 10.1002/ceat.201300686
- Brinek M., Hiebl C., Wilkening H.M.R., Understanding the origin of enhanced Li-ion transport in nanocrystalline argyrodite-type  $\text{Li}_6\text{PS}_5\text{I}$ , *Chemistry of Materials*, 32 (2020) 4754–4766. DOI: 10.1021/acs.chemmater.0c01367
- Brückner L., Frank J., Elwert T., Industrial recycling of lithium-ion batteries—a critical review of metallurgical process routes, *Metals*, 10 (2020) 1107. DOI: 10.3390/met10081107
- Burukhin A., Hydrothermal synthesis of  $\text{LiCoO}_2$  for lithium rechargeable batteries, *Solid State Ionics*, 151 (2002) 259–263. DOI: 10.1016/S0167-2738(02)00721-X
- Calpa M., Rosero-Navarro N.C., Miura A., Tadanaga K., Electrochemical performance of bulk-type all-solid-state batteries using small-sized  $\text{Li}_7\text{P}_3\text{S}_{11}$  solid electrolyte prepared by liquid phase as the ionic conductor in the composite cathode, *Electrochimica Acta*, 296 (2019) 473–480. DOI: 10.1016/j.electacta.2018.11.035
- Cambaz M.A., Anji Reddy M., Vinayan B.P., Witte R., Pohl A., Mu X., Chakravadhanula V.S.K., Kübel C., Fichtner M., Mechanical milling assisted synthesis and electrochemical performance of high capacity  $\text{LiFePO}_4$  for lithium batteries, *ACS applied materials & interfaces*, 8 (2016) 2166–2172. DOI: 10.1021/acsami.5b10747
- Cao H., Zhang Y., Zhang J., Xia B., Synthesis and electrochemical characteristics of layered  $\text{LiNi}_{0.6}\text{Co}_{0.2}\text{Mn}_{0.2}\text{O}_2$  cathode material for lithium ion batteries, *Solid State Ionics*, 176 (2005) 1207–1211. DOI: 10.1016/j.ssi.2005.02.023
- Casino S., Niehoff P., Börner M., Winter M., Protective coatings on silicon particles and their effect on energy density and specific energy in lithium ion battery cells – a model study, *Journal of Energy Storage*, 29 (2020) 101376. DOI: 10.1016/j.est.2020.101376
- Choi J.W., Aurbach D., Promise and reality of post-lithium-ion batteries with high energy densities, *Nature Reviews Materials*, 1 (2016). DOI: 10.1038/natrevmats.2016.13
- Dahbi M., Wikberg J.M., Saadouni I., Gustafsson T., Svedlindh P., Edström K., Electrochemical behavior of  $\text{LiNi}_{1-y-z}\text{Co}_y\text{Mn}_z\text{O}_2$  probed through structural and magnetic properties, *Journal of Applied Physics*, 111 (2012) 23904. DOI: 10.1063/1.3676434
- Dessemond C., Lajoie-Leroux F., Soucy G., Laroche N., Magnan J.-F., Spodumene: the lithium market, resources and processes, *Minerals*, 9 (2019) 334. DOI: 10.3390/min9060334
- Dewald G.F., Ohno S., Hering J.G.C., Janek J., Zeier W.G., Analysis of charge carrier transport toward optimized cathode composites for all-solid-state Li–S batteries, *Batteries & Supercaps*, 4 (2021) 183–194. DOI: 10.1002/batt.202000194
- Diekmann J., Doose S., Weber S., Münch S., Haselrieder W., Kwade A., Development of a new procedure for nail penetration of lithium-ion cells to obtain meaningful and reproducible results, *Journal of The Electrochemical Society*, 167 (2020) 90504. DOI: 10.1149/1945-7111/ab78ff
- Diekmann J., Hanisch C., Froböse L., Schällicke G., Loellhoeffel T., Fölster A.-S., Kwade A., Ecological recycling of lithium-ion batteries from electric vehicles with focus on mechanical processes, *Journal of The Electrochemical Society*, 164 (2017) A6184–A6191. DOI: 10.1149/2.0271701jes
- Dietrich C., Weber D.A., Sedlmaier S.J., Indris S., Culver S.P., Walter D., Janek J., Zeier W.G., Lithium ion conductivity in  $\text{Li}_2\text{S}-\text{P}_2\text{S}_5$  glasses – building units and local structure evolution during the crystallization of superionic conductors  $\text{Li}_3\text{PS}_4$ ,  $\text{Li}_7\text{P}_3\text{S}_{11}$  and  $\text{Li}_4\text{P}_2\text{S}_7$ , *Journal of Materials Chemistry A*, 5 (2017) 18111–18119. DOI: 10.1039/C7TA00607J
- Dixit M.B., Singh N., Horwath J.P., Shevchenko P.D., Jones M., Stach E.A., Arthur T.S., Hatzell K.B., In situ investigation of chemomechanical effects in thiophosphate solid electrolytes, *Matter*, 3 (2020) 2138–2159. DOI: 10.1016/j.matt.2020.09.018
- Dixit M.B., Zaman W., Bootwala Y., Zheng Y., Hatzell M.C., Hatzell K.B., Scalable manufacturing of hybrid solid electrolytes with interface control, *ACS Applied Materials & Interfaces*, 11 (2019) 45087–45097. DOI: 10.1021/acsami.9b15463

- Doose S., Haselrieder W., Kwade A., Effects of the nail geometry and humidity on the nail penetration of high-energy density lithium ion batteries, *Batteries*, 7 (2021a) 6. DOI: 10.3390/batteries7010006
- Doose S., Mayer J.K., Michalowski P., Kwade A., Challenges in ecofriendly battery recycling and closed material cycles: a perspective on future lithium battery generations, *Metals*, 11 (2021b) 291. DOI: 10.3390/met11020291
- Dreger H., Bockholt H., Haselrieder W., Kwade A., Discontinuous and continuous processing of low-solvent battery slurries for lithium nickel cobalt manganese oxide electrodes, *Journal of Electronic Materials*, 44 (2015) 4434–4443. DOI: 10.1007/s11664-015-3981-4
- Dreger H., Huelsebrock M., Froboese L., Kwade A., Method development for quality control of suspensions for lithium-ion battery electrodes, *Industrial & Engineering Chemistry Research*, 56 (2017) 2466–2474. DOI: 10.1021/acs.iecr.6b02103
- Du W., Gupta A., Zhang X., Sastry A.M., Shyy W., Effect of cycling rate, particle size and transport properties on lithium-ion cathode performance, *International Journal of Heat and Mass Transfer*, 53 (2010) 3552–3561. DOI: 10.1016/j.ijheatmasstransfer.2010.04.017
- Ebner M., Chung D.-W., García R.E., Wood V., Tortuosity anisotropy in lithium-ion battery electrodes, *Advanced Energy Materials*, 4 (2014) 1301278. DOI: 10.1002/aenm.201301278
- Famprikis T., Kudu Ö.U., Dawson J.A., Canepa P., Fauth F., Suard E., Zbiri M., Dambournet D., Borkiewicz O.J., Bouyanfif H., Emge S.P., Cretu S., Chotard J.-N., Grey C.P., Zeier W.G., Islam M.S., Masquelier C., Under pressure: mechanochemical effects on structure and ion conduction in the sodium-ion solid electrolyte  $\text{Na}_3\text{PS}_4$ , *Journal of the American Chemical Society*, 142 (2020) 18422–18436. DOI: 10.1021/jacs.0c06668
- Franco Gonzalez A., Yang N.-H., Liu R.-S., Silicon anode design for lithium-ion batteries: progress and perspectives, *The Journal of Physical Chemistry C*, 121 (2017) 27775–27787. DOI: 10.1021/acs.jpcc.7b07793
- Frausto J.J., Ballantyne G.R., Runge K., Powell M.S., Wightman E.M., Evans C.L., Gonzalez P., Gomez S., The effect of screen versus cyclone classification on the mineral liberation properties of a polymetallic ore, *Minerals Engineering*, 169 (2021) 106930. DOI: 10.1016/j.mineng.2021.106930
- Fuchs T., Culver S.P., Till P., Zeier W.G., Defect-mediated conductivity enhancements in  $\text{Na}_{3-x}\text{Pn}_{1-x}\text{W}_x\text{S}_4$  (Pn = P, Sb) using aliovalent substitutions, *ACS Energy Letters*, 5 (2020) 146–151. DOI: 10.1021/acsenenergylett.9b02537
- Gaffet E., Harmelin M., Crystal-amorphous phase transition induced by ball-milling in silicon, *Journal of the Less Common Metals*, 157 (1990) 201–222. DOI: 10.1016/0022-5088(90)90176-K
- Gaikwad A.M., Arias A.C., Understanding the effects of electrode formulation on the mechanical strength of composite electrodes for flexible batteries, *ACS applied materials & interfaces*, 9 (2017) 6390–6400. DOI: 10.1021/acsmi.6b14719
- Gan C., Hu X., Zhan H., Zhou Y., Synthesis and characterization of  $\text{Li}_{1.2}\text{Ni}_{0.6}\text{Co}_{0.2}\text{Mn}_{0.2}\text{O}_{2+\delta}$  as a cathode material for secondary lithium batteries, *Solid State Ionics*, 176 (2005) 687–692. DOI: 10.1016/j.ssi.2004.10.021
- Gautam A., Sadowski M., Prinz N., Eickhoff H., Minafra N., Ghidui M., Culver S.P., Albe K., Fässler T.F., Zobel M., Zeier W.G., Rapid crystallization and kinetic freezing of site-disorder in the lithium superionic argyrodite  $\text{Li}_6\text{PS}_5\text{Br}$ , *Chemistry of Materials*, 31 (2019) 10178–10185. DOI: 10.1021/acs.chemmater.9b03852
- Georgi-Maschler T., Friedrich B., Weyhe R., Heegn H., Rutz M., Development of a recycling process for Li-ion batteries, *Journal of Power Sources*, 207 (2012) 173–182. DOI: 10.1016/j.jpowsour.2012.01.152
- Ghidui M., Ruhl J., P. Culver S., G. Zeier W., Solution-based synthesis of lithium thiophosphate superionic conductors for solid-state batteries: a chemistry perspective, *Journal of Materials Chemistry A*, 7 (2019) 17735–17753. DOI: 10.1039/C9TA04772G
- Gordon R., Orias R., Willenbacher N., Effect of carboxymethyl cellulose on the flow behavior of lithium-ion battery anode slurries and the electrical as well as mechanical properties of corresponding dry layers, *Journal of Materials Science*, 55 (2020) 15867–15881. DOI: 10.1007/s10853-020-05122-3
- Graebe H., Netz A., Baesch S., Haerdtnr V., Kwade A., A solvent-free electrode coating technique for all solid state lithium ion batteries, *ECS Transactions*, 77 (2017) 393–401. DOI: 10.1149/07711.0393ecst
- Gratz E., Sa Q., Apelian D., Wang Y., A closed loop process for recycling spent lithium ion batteries, *Journal of Power Sources*, 262 (2014) 255–262. DOI: 10.1016/j.jpowsour.2014.03.126
- Grießl D., Huber K., Scherbauer R., Kwade A., Dispersion kinetics of carbon black for the application in lithium-ion batteries, *Advanced Powder Technology* (2021). DOI: 10.1016/j.appt.2021.05.003
- Guo S.-h., Chen G., Peng J.-h., Chen J., Li D.-b., Liu L.-j., Microwave assisted grinding of ilmenite ore, *Transactions of Nonferrous Metals Society of China*, 21 (2011) 2122–2126. DOI: 10.1016/S1003-6326(11)60983-7
- Haarmann M., Haselrieder W., Kwade A., Extrusion-based processing of cathodes: influence of solid content on suspension and electrode properties, *Energy Technology*, 8 (2020) 1801169. DOI: 10.1002/ente.201801169
- Habib K., Hansdóttir S.T., Habib H., Critical metals for electromobility: Global demand scenarios for passenger vehicles, 2015–2050, *Resources, Conservation and Recycling*, 154 (2020) 104603. DOI: 10.1016/j.resconrec.2019.104603
- Hanghofer I., Brinek M., L. Eisbacher S., Bitschnau B., Volck M., Hennige V., Hanzu I., Rettenwander D., Wilkening H.M.R., Substitutional disorder: structure and ion dynamics of the argyrodites  $\text{Li}_6\text{PS}_5\text{Cl}$ ,  $\text{Li}_6\text{PS}_5\text{Br}$  and  $\text{Li}_6\text{PS}_5\text{I}$ , *Physical Chemistry Chemical Physics*, 21 (2019) 8489–8507. DOI: 10.1039/C9CP00664H
- Hanisch C., Diekmann J., Stieger A., Haselrieder W., Kwade A., Recycling of lithium-ion batteries, in: Yan J. (Ed.), *Handbook of Clean Energy Systems*, John Wiley & Sons, Ltd, Chichester, UK, 2015a, pp. 1–24, ISBN: 9781118388587. DOI: 10.1002/9781118991978.hces221
- Hanisch C., Loellhoeffel T., Diekmann J., Markley K.J., Haselrieder W., Kwade A., Recycling of lithium-ion batteries: a novel method to separate coating and foil of electrodes, *Journal of Cleaner Production*, 108 (2015b) 301–311. DOI: 10.1016/j.jclepro.2015.08.026
- Haselrieder W., Ivanov S., Tran H.Y., Theil S., Froböse L., Westphal B., Wohlfahrt-Mehrens M., Kwade A., Influence of formulation method and related processes on structural, electrical and electrochemical properties of LMS/NCA-blend electrodes, *Progress in Solid State Chemistry*, 42 (2014) 157–174. DOI: 10.1016/j.progsolidstchem.2014.04.009
- Hashem A.M.A., Abdel-Ghany A.E., Eid A.E., Trottier J., Zaghbi K., Mauger A., Julien C.M., Study of the surface modification of  $\text{LiNi}_{1/3}\text{Co}_{1/3}\text{Mn}_{1/3}\text{O}_2$  cathode material for lithium ion battery, *Journal of Power Sources*, 196 (2011) 8632–8637. DOI: 10.1016/j.jpowsour.2011.06.039

- Hayashi A., Masuzawa N., Yubuchi S., Tsuji F., Hotehama C., Sakuda A., Tatsumisago M., A sodium-ion sulfide solid electrolyte with unprecedented conductivity at room temperature, *Nature communications*, 10 (2019) 5266. DOI: 10.1038/s41467-019-13178-2
- He S., Huang S., Wang S., Mizota I., Liu X., Hou X., Considering critical factors of silicon/graphite anode materials for practical high-energy lithium-ion battery applications, *Energy & Fuels*, 35 (2021) 944–964. DOI: 10.1021/acs.energyfuels.0c02948
- Heck C.A., Horstig M.-W. von, Huttner F., Mayer J.K., Haselrieder W., Kwade A., Review—knowledge-based process design for high quality production of NCM811 cathodes, *Journal of The Electrochemical Society*, 167 (2020) 160521. DOI: 10.1149/1945-7111/abcd11
- HMC (Hosokawa Micron Corporation), 2021, Faculty S series, F-S – spheronization, <<https://www.hosokawamicron.co.jp/en/machines/181>> accessed 09/12/2021.
- Hou X., Zhang M., Wang J., Hu S., Liu X., Shao Z., High yield and low-cost ball milling synthesis of nano-flake Si@SiO<sub>2</sub> with small crystalline grains and abundant grain boundaries as a superior anode for Li-ion batteries, *Journal of Alloys and Compounds*, 639 (2015) 27–35. DOI: 10.1016/j.jallcom.2015.03.127
- Hu R., Sun W., Chen Y., Zeng M., Zhu M., Silicon/graphene based nanocomposite anode: large-scale production and stable high capacity for lithium ion batteries, *J. Mater. Chem. A*, 2 (2014) 9118–9125. DOI: 10.1039/c4ta01013b
- Huang W., Cheng Q., Qin X., Carbon nanotubes as a conductive additive in LiFePO<sub>4</sub> cathode material for lithium-ion batteries, *Russian Journal of Electrochemistry*, 46 (2010) 175–179. DOI: 10.1134/S1023193510020084
- Ibarra-Palos A., Strobel P., Darie C., Bacia M., Soupart J.B., Nanosized manganese oxide as cathode material for lithium batteries: Influence of carbon mixing and grinding on cyclability, *Journal of Power Sources*, 146 (2005) 294–299. DOI: 10.1016/j.jpowsour.2005.03.093
- Janek J., Zeier W.G., A solid future for battery development, *Nature Energy*, 1 (2016) 1167. DOI: 10.1038/nenergy.2016.141
- Jin Y., Zhu B., Lu Z., Liu N., Zhu J., Challenges and recent progress in the development of Si anodes for lithium-ion battery, *Advanced Energy Materials*, 7 (2017) 1700715. DOI: 10.1002/aenm.201700715
- Ju S.H., Kang Y.C., Fine-sized LiNi<sub>0.8</sub>Co<sub>0.15</sub>Mn<sub>0.05</sub>O<sub>2</sub> cathode powders prepared by combined process of gas-phase reaction and solid-state reaction methods, *Journal of Power Sources*, 178 (2008) 387–392. DOI: 10.1016/j.jpowsour.2007.11.112
- Kang H.-C., Jun D.-K., Jin B., Jin E.M., Park K.-H., Gu H.-B., Kim K.-W., Optimized solid-state synthesis of LiFePO<sub>4</sub> cathode materials using ball-milling, *Journal of Power Sources*, 179 (2008) 340–346. DOI: 10.1016/j.jpowsour.2007.12.093
- Kato Y., Hori S., Saito T., Suzuki K., Hirayama M., Mitsui A., Yonemura M., Iba H., Kanno R., High-power all-solid-state batteries using sulfide superionic conductors, *Nature Energy*, 1 (2016) 16030. DOI: 10.1038/nenergy.2016.30
- Kerman K., Luntz A., Viswanathan V., Chiang Y.-M., Chen Z., Review—practical challenges hindering the development of solid state li ion batteries, *Journal of The Electrochemical Society*, 164 (2017) A1731–A1744. DOI: 10.1149/2.1571707jes
- Kim S.-B., Kim S.-J., Kim C.-H., Kim W.-S., Park K.-W., Nanostructure cathode materials prepared by high-energy ball milling method, *Materials Letters*, 65 (2011) 3313–3316. DOI: 10.1016/j.matlet.2011.07.023
- Kingman S.W., Recent developments in microwave processing of minerals, *International Materials Reviews*, 51 (2006) 1–12. DOI: 10.1179/174328006X79472
- Knieke C., Steinborn C., Romeis S., Peukert W., Breitung-Faes S., Kwade A., Nanoparticle production with stirred-media mills: opportunities and limits, *Chemical Engineering & Technology*, 33 (2010) 1401–1411. DOI: 10.1002/ceat.201000105
- Kolmogorov A.N., Die lokale Struktur der Turbulenz in einer inkompressiblen zähen Flüssigkeit bei sehr großen Reynoldsschen Zahlen, *Compt. Rend. Acad. Sc. USSR*, 30 (1958).
- Kraft M.A., Ohno S., Zinkevich T., Koerver R., Culver S.P., Fuchs T., Senyshyn A., Indris S., Morgan B.J., Zeier W.G., Inducing high ionic conductivity in the lithium superionic argyrodites Li<sub>6+x</sub>P<sub>1-x</sub>Ge<sub>x</sub>S<sub>5</sub>I for all-solid-state batteries, *Journal of the American Chemical Society*, 140 (2018) 16330–16339. DOI: 10.1021/jacs.8b10282
- Krauskopf T., Culver S.P., Zeier W.G., Local tetragonal structure of the cubic superionic conductor Na<sub>3</sub>PS<sub>4</sub>, *Inorganic Chemistry*, 57 (2018) 4739–4744. DOI: 10.1021/acs.inorgchem.8b00458
- Krekel J., Zerkleinerung von agglomeraten in scherströmungen mit besonders hoher schubspannung, *Chemie Ingenieur Technik*, 38 (1966) 229–234. DOI: 10.1002/cite.330380307
- Kremer L.S., Hoffmann A., Danner T., Hein S., Prifling B., Westhoff D., Dreer C., Latz A., Schmidt V., Wohlfahrt-Mehrens M., Manufacturing process for improved ultra-thick cathodes in high-energy lithium-ion batteries, *Energy Technology*, 8 (2020) 1900167. DOI: 10.1002/ente.201900167
- Kudu Ö.U., Famprakis T., Fleutot B., Braida M.-D., Le Mercier T., Islam M.S., Masquelier C., A review of structural properties and synthesis methods of solid electrolyte materials in the Li<sub>2</sub>S – P<sub>2</sub>S<sub>5</sub> binary system, *Journal of Power Sources*, 407 (2018) 31–43. DOI: 10.1016/j.jpowsour.2018.10.037
- Kwade A., A stressing model for the description and optimization of grinding processes, *Chemical Engineering & Technology*, 26 (2003) 199–205. DOI: 10.1002/ceat.200390029
- Kwade A., Hagelüken C., Kohl H., Buchert M., Herrmann C., Vahle T., vonWittken R., Carrara M., Daelemans S., Ehrenberg H., Fluchs S., Goldmann D. et al., *Circular Economy Initiative Deutschland (Ed.), Resource-Efficient Battery Life Cycles – Driving Electric Mobility with the Circular Economy*, acatech/SYSTEMIQ, Munich/London, 2020. DOI: 10.48669/ceid\_2021-2
- Kwade A., Haselrieder W., Leithoff R., Modlinger A., Dietrich F., Droeder K., Current status and challenges for automotive battery production technologies, *Nature Energy*, 3 (2018) 290–300. DOI: 10.1038/s41560-018-0130-3
- Kwade A., Diekmann J. *Recycling of Lithium-Ion Batteries*, Springer, Cham, 2018, ISBN: 9783319705712. DOI: 10.1007/978-3-319-70572-9
- Kwak H., Han D., Lyoo J., Park J., Jung S.H., Han Y., Kwon G., Kim H., Hong S.-T., Nam K.-W., Jung Y.S., New cost-effective halide solid electrolytes for all-solid-state batteries: mechanochemically prepared Fe<sup>3+</sup>-substituted Li<sub>2</sub>ZrCl<sub>6</sub>, *Advanced Energy Materials*, 11 (2021) 2003190. DOI: 10.1002/aenm.202003190
- Kwon H.-J., Woo S.-W., Lee Y.-J., Kim J.-Y., Lee S.-M., Achieving high-performance spherical natural graphite anode through a modified carbon coating for lithium-ion batteries, *Energies*, 14 (2021) 1946. DOI: 10.3390/en14071946
- Lai J., Guo H., Wang Z., Li X., Zhang X., Wu F., Yue P., Preparation and characterization of flake graphite/silicon/carbon spherical composite as anode materials for lithium-ion batteries, *Journal of Alloys and Compounds*, 530 (2012) 30–35. DOI: 10.1016/j.jallcom.2012.03.096

- Lämmerer W., Flachberger H., Wissenswertes zur charakterisierung und aufbereitung von rohgraphiten, BHM Berg- und Hüttenmännische Monatshefte, 162 (2017) 336–344. DOI: 10.1007/s00501-017-0651-2
- Landesfeind J., Eldiven A., Gasteiger H.A., Influence of the binder on lithium ion battery electrode tortuosity and performance, Journal of The Electrochemical Society, 165 (2018) A1122-A1128. DOI: 10.1149/2.0971805jes
- Landi B.J., Ganter M.J., Cress C.D., DiLeo R.A., Raffaele R.P., Carbon nanotubes for lithium ion batteries, Energy & Environmental Science, 2 (2009) 638. DOI: 10.1039/b904116h
- Leblanc D., Hovington P., Kim C., Guerfi A., Bélanger D., Zaghbi K., Silicon as anode for high-energy lithium ion batteries: From molten ingot to nanoparticles, Journal of Power Sources, 299 (2015) 529–536. DOI: 10.1016/j.jpowsour.2015.09.040
- Lee J., Extraction of lithium from lepidolite using mixed grinding with sodium sulfide followed by water leaching, Minerals, 5 (2015) 737–743. DOI: 10.3390/min5040521
- Li H., Rao W., Gu Z., Wang Y., Wang N., Lv X., Chen B., Jiang H., Chen L., Nano-grinding derived high-performance  $\text{Li}_{1.2}\text{Ni}_{0.13}\text{Co}_{0.13}\text{Mn}_{0.54}\text{O}_2$  cathode material: from kilogram-scale synthesis to its pouch cell, Ionics, 27 (2021) 491–506. DOI: 10.1007/s11581-020-03875-0
- Li M., Hou X., Sha Y., Wang J., Hu S., Liu X., Shao Z., Facile spray-drying/pyrolysis synthesis of core-shell structure graphite/silicon-porous carbon composite as a superior anode for Li-ion batteries, Journal of Power Sources, 248 (2014) 721–728. DOI: 10.1016/j.jpowsour.2013.10.012
- Li X., Liang J., Luo J., Banis M.N., Wang C., Li W., Deng S., Yu C., Zhao F., Hu Y., Sham T.-K., Zhang L., Zhao S., Lu S., Huang H., Li R., Adair K.R., Sun X., Air-stable  $\text{Li}_3\text{InCl}_6$  electrolyte with high voltage compatibility for all-solid-state batteries, Energy & Environmental Science, 12 (2019) 2665–2671. DOI: 10.1039/C9EE02311A
- Li X., Liang J., Yang X., Adair K.R., Wang C., Zhao F., Sun X., Progress and perspectives on halide lithium conductors for all-solid-state lithium batteries, Energy & Environmental Science, 13 (2020) 1429–1461. DOI: 10.1039/C9EE03828K
- Liu H., Cheng X., Chong Y., Yuan H., Huang J.-Q., Zhang Q., Advanced electrode processing of lithium ion batteries: a review of powder technology in battery fabrication, Particology, 57 (2021) 56–71. DOI: 10.1016/j.partic.2020.12.003
- Liu N., Lu Z., Zhao J., McDowell M.T., Lee H.-W., Zhao W., Cui Y., A pomegranate-inspired nanoscale design for large-volume-change lithium battery anodes, Nature Nanotechnology, 9 (2014) 187–192. DOI: 10.1038/nnano.2014.6
- Liu X.H., Huang J.Y., In situ TEM electrochemistry of anode materials in lithium ion batteries, Energy & Environmental Science, 4 (2011) 3844. DOI: 10.1039/c1ee01918j
- Liu X.H., Zhong L., Huang S., Mao S.X., Zhu T., Huang J.Y., Size-dependent fracture of silicon nanoparticles during lithiation, ACS nano, 6 (2012) 1522–1531. DOI: 10.1021/nn204476h
- Liu Y., Liu H., Zhao X., Wang L., Liang G., Effect of spherical particle size on the electrochemical properties of lithium iron phosphate, Journal of Wuhan University of Technology-Mater. Sci. Ed., 34 (2019) 549–557. DOI: 10.1007/s11595-019-2086-y
- Lu J., Peng Q., Wang W., Nan C., Li L., Li Y., Nanoscale coating of  $\text{LiMO}_2$  (M = Ni, Co, Mn) nanobelts with  $\text{Li}^+$ -conductive  $\text{Li}_2\text{TiO}_3$ : toward better rate capabilities for Li-ion batteries, Journal of the American Chemical Society, 135 (2013) 1649–1652. DOI: 10.1021/ja308717z
- Martha S.K., Sclar H., Szmuk Framowitz Z., Kovacheva D., Saliyski N., Gofer Y., Sharon P., Golik E., Markovsky B., Aurbach D., A comparative study of electrodes comprising nanometric and submicron particles of  $\text{LiNi}_{0.50}\text{Mn}_{0.50}\text{O}_2$ ,  $\text{LiNi}_{0.33}\text{Mn}_{0.33}\text{Co}_{0.33}\text{O}_2$ , and  $\text{LiNi}_{0.40}\text{Mn}_{0.40}\text{Co}_{0.20}\text{O}_2$  layered compounds, Journal of Power Sources, 189 (2009) 248–255. DOI: 10.1016/j.jpowsour.2008.09.090
- Mathieux F., Ardente F., Bobba S., Nuss P., Blengini G., Alves Dias P., Blagoeva D., Torres De Matos C., Wittmer D., Pavel C., Hamor T., Saveyn H., Gawlik B., Orveillon G., Huygens D. et al., Critical Raw Materials and the Circular Economy – Background Report, EUR 28832 EN, Publications Office of the European Union, Luxembourg, 2017, ISBN 978-92-79-74283-5. DOI: 10.2760/378123
- Mayer J.K., Almar L., Asylbekov E., Haselrieder W., Kwade A., Weber A., Nirschl H., Influence of the carbon black dispersing process on the microstructure and performance of Li-ion battery cathodes, Energy Technology, 8 (2020) 1900161. DOI: 10.1002/ente.201900161
- Moskvitch K., Field of dreams: the plants that love heavy metal, New Scientist, 221 (2014) 46–49. DOI: 10.1016/S0262-4079(14)60594-7
- Müller J., Abdollahifar M., Vinograd A., Nöske M., Nowak C., Chang S.-J., Placke T., Haselrieder W., Winter M., Kwade A., Wu N.-L., Si-on-graphite fabricated by fluidized bed process for high-capacity anodes of Li-ion batteries, Chemical Engineering Journal, 407 (2021) 126603. DOI: 10.1016/j.cej.2020.126603
- Müller S., Eller J., Ebner M., Burns C., Dahn J., Wood V., Quantifying inhomogeneity of lithium ion battery electrodes and its influence on electrochemical performance, Journal of The Electrochemical Society, 165 (2018) A339-A344. DOI: 10.1149/2.0311802jes
- Mundsinger M., Farsi S., Rapp M., Golla-Schindler U., Kaiser U., Wachtler M., Morphology and texture of spheroidized natural and synthetic graphites, Carbon, 111 (2017) 764–773. DOI: 10.1016/j.carbon.2016.10.060
- Nagao M., Hayashi A., Tatsumisago M., High-capacity  $\text{Li}_2\text{S}$ -nanocarbon composite electrode for all-solid-state rechargeable lithium batteries, Journal of Materials Chemistry, 22 (2012) 10015–10020. DOI: 10.1039/C2JM16802B
- Naghash A.R., Lee J.Y., Lithium nickel oxyfluoride ( $\text{Li}_{1-z}\text{Ni}_{1+z}\text{F}_y\text{O}_{2-y}$ ) and lithium magnesium nickel oxide ( $\text{Li}_{1-z}(\text{Mg}_x\text{Ni}_{1-x})_{1+z}\text{O}_2$ ) cathodes for lithium rechargeable batteries, Electrochimica Acta, 46 (2001) 2293–2304. DOI: 10.1016/S0013-4686(01)00452-2
- Nakamura H., Kawaguchi T., Masuyama T., Sakuda A., Saito T., Kuratani K., Ohsaki S., Watano S., Dry coating of active material particles with sulfide solid electrolytes for an all-solid-state lithium battery, Journal of Power Sources, 448 (2020) 227579. DOI: 10.1016/j.jpowsour.2019.227579
- Natarajan C., Fujimoto H., Mabuchi A., Tokumitsu K., Kasuh T., Effect of mechanical milling of graphite powder on lithium intercalation properties, Journal of Power Sources, 92 (2001) 187–192. DOI: 10.1016/S0378-7753(00)00528-0
- Ng S.H., Vix-Guterl C., Bernardo P., Tran N., Ufheil J., Buqa H., Dentzer J., Gadiou R., Spahr M.E., Goers D., Novák P., Correlations between surface properties of graphite and the first cycle specific charge loss in lithium-ion batteries, Carbon, 47 (2009) 705–712. DOI: 10.1016/j.carbon.2008.11.008
- Nguyen H., Banerjee A., Wang X., Tan D., Wu E.A., Doux J.-M., Stephens R., Verbist G., Meng Y.S., Single-step synthesis of highly conductive  $\text{Na}_3\text{PS}_4$  solid electrolyte for sodium all solid-state batteries, Journal of Power Sources, 435 (2019) 126623. DOI: 10.1016/j.jpowsour.2019.05.031
- Nilssen B.E., Henriksen B.R., Kleiv R.A., Effect of operation

- parameters and formulation on the submicron and nano size silicon powder properties produced by mechanical grinding, *Silicon for the Chemical and Solar Industry XV*, (2020) 295–308.
- Nilssen B.E., Kleiv R.A., Silicon powder properties produced in a planetary ball mill as a function of grinding time, Grinding Bead Size and Rotational Speed, *Silicon*, 12 (2020) 2413–2423. DOI: 10.1007/s12633-019-00340-0
- Nöske M., Breitung-Faes S., Kwade A., Electrostatic stabilization and characterization of fine ground silicon particles in ethanol, *Silicon*, 11 (2019) 3001–3010. DOI: 10.1007/s12633-019-0089-0
- Obrovac M.N., Zheng L., Garayt M.D.L., Engineered particle synthesis by dry particle microgranulation, *Cell Reports Physical Science*, 1 (2020) 100063. DOI: 10.1016/j.xcrp.2020.100063
- Ohno S., Koerver R., Dewald G., Rosenbach C., Titscher P., Steckermeier D., Kwade A., Janek J., Zeier W.G., Observation of chemomechanical failure and the influence of cutoff potentials in all-solid-state Li–S batteries, *Chemistry of Materials*, 31 (2019) 2930–2940. DOI: 10.1021/acs.chemmater.9b00282
- Palaniandy S., Powell M., Hilden M., Allen J., Kermanshahi K., Oats B., Lollback M., VertiMill® – preparing the feed within floatable regime at lower specific energy, *Minerals Engineering*, 73 (2015) 44–52. DOI: 10.1016/j.mineng.2014.11.014
- Pan T., Alvarado J., Zhu J., Yue Y., Xin H.L., Nordlund D., Lin F., Doeff M.M., Structural degradation of layered cathode materials in lithium-ion batteries induced by ball milling, *Journal of The Electrochemical Society*, 166 (2019) A1964–A1971. DOI: 10.1149/2.0091910jes
- Park B.H., Jeong J.H., Lee G.-W., Kim Y.-H., Roh K.C., Kim K.-B., Highly conductive carbon nanotube micro-spherical network for high-rate silicon anode, *Journal of Power Sources*, 394 (2018) 94–101. DOI: 10.1016/j.jpowsour.2018.04.112
- Parker T., Shi F., Evans C., Powell M., The effects of electrical comminution on the mineral liberation and surface chemistry of a porphyry copper ore, *Minerals Engineering*, 82 (2015) 101–106. DOI: 10.1016/j.mineng.2015.03.019
- Peng Z.S., Wan C.R., Jiang C.Y., Synthesis by sol–gel process and characterization of LiCoO<sub>2</sub> cathode materials, *Journal of Power Sources*, 72 (1998) 215–220. DOI: 10.1016/S0378-7753(97)02689-X
- Peters J.F., Baumann M., Zimmermann B., Braun J., Weil M., The environmental impact of Li-Ion batteries and the role of key parameters – a review, *Renewable and Sustainable Energy Reviews*, 67 (2017) 491–506. DOI: 10.1016/j.rser.2016.08.039
- Powell M.S., How our clients will drive the need to slash energy use in mining. Proc. 26th IMCET Int. Mining Congress, Antalya, Turkey, 16–19 April 2019.
- Qi C., Ma X., Ning G., Song X., Chen B., Lan X., Li Y., Zhang X., Gao J., Aqueous slurry of S-doped carbon nanotubes as conductive additive for lithium ion batteries, *Carbon*, 92 (2015) 245–253. DOI: 10.1016/j.carbon.2015.04.028
- Rao R.P., Adams S., Studies of lithium argyrodite solid electrolytes for all-solid-state batteries, *Physica Status Solidi (A)*, 208 (2011) 1804–1807. DOI: 10.1002/pssa.201001117
- Reindl A., Aldabergenova S., Altin E., Frank G., Peukert W., Dispersing silicon nanoparticles in a stirred media mill-investigating the evolution of morphology, structure and oxide formation, *Physica Status Solidi (A)*, 204 (2007) 2329–2338. DOI: 10.1002/pssa.200622557
- Reindl A., Voronov A., Gorle P.K., Rauscher M., Roosen A., Peukert W., Dispersing and stabilizing silicon nanoparticles in a low-epsilon medium, *Colloids and Surfaces A: Physicochemical and Engineering Aspects*, 320 (2008) 183–188. DOI: 10.1016/j.colsurfa.2008.01.045
- Schlem R., Banik A., Ohno S., Suard E., Zeier W.G., Insights into the lithium sub-structure of superionic conductors Li<sub>3</sub>YCl<sub>6</sub> and Li<sub>3</sub>YBr, *Chemistry of Materials*, 33 (2021a) 327–337. DOI: 10.1021/acs.chemmater.0c04352
- Schlem R., Muy S., Prinz N., Banik A., Shao-Horn Y., Zobel M., Zeier W.G., Mechanochemical synthesis: a tool to tune cation site disorder and ionic transport properties of Li<sub>3</sub>MCl<sub>6</sub> (M = Y, Er) superionic conductors, *Advanced Energy Materials*, 10 (2020) 1903719. DOI: 10.1002/aenm.201903719
- Schlem R., Burmeister C.F., Michalowski P., Ohno S., Dewald G.F., Kwade A., Zeier W.G., Energy storage materials for solid-state batteries: design by mechanochemistry, *Advanced Energy Materials*, 11 (2021b) 2101022. DOI: 10.1002/aenm.202101022
- Schönert K., A first survey of grinding with high-compression roller mills, *International Journal of Mineral Processing*, 22 (1988) 401–412. DOI: 10.1016/0301-7516(88)90075-0
- Schunemann J.-H., Dreger H., Bockholt H., Kwade A., Smart electrode processing for battery cost reduction, *ECS Transactions*, 73 (2016) 153–159. DOI: 10.1149/07301.0153ecst
- Seeba J., Reuber S., Heubner C., Müller-Köhn A., Wolter M., Michaelis A., Extrusion-based fabrication of electrodes for high-energy Li-ion batteries, *Chemical Engineering Journal*, 402 (2020) 125551. DOI: 10.1016/j.cej.2020.125551
- Shaw-Stewart J., Alvarez-Reguera A., Greszta A., Marco J., Masood M., Sommerville R., Kendrick E., Aqueous solution discharge of cylindrical lithium-ion cells, *Sustainable Materials and Technologies*, 22 (2019) e00110. DOI: 10.1016/j.susmat.2019.e00110
- Sinha N.N., The effect of particle size on performance of cathode materials of Li-ion batteries, *Journal of the Indian Institute of Science*, 89 (2009) 381–392.
- Sitando O., Crouse P.L., Processing of a Zimbabwean petalite to obtain lithium carbonate, *International Journal of Mineral Processing*, 102–103 (2012) 45–50. DOI: 10.1016/j.minpro.2011.09.014
- Stehmann F., Bradtmöller C., Scholl S., Separation of the electrolyte—thermal drying, in: Kwade A., Diekmann J. (Eds.), *Recycling of Lithium-Ion Batteries. Sustainable Production, Life Cycle Engineering and Management*, Springer, Cham., 2018, pp. 139–153, ISBN: 978-3-319-70571-2. DOI: 10.1007/978-3-319-70572-9\_8
- Stein IV M., Chen C.-F., Mullings M., Jaime D., Zaleski A., Mukherjee P.P., Rhodes C.P., Probing the effect of high energy ball milling on the structure and properties of LiNi<sub>1/3</sub>Mn<sub>1/3</sub>Co<sub>1/3</sub>O<sub>2</sub> cathodes for Li-ion batteries, *Journal of Electrochemical Energy Conversion and Storage*, 13 (2016) 031001. DOI: 10.1115/1.4034755
- Steinrötter M., Carbon based anodes – a rare earth situation? Third German Electric Vehicle Congress, Bonn, Germany, 2011.
- Stöffler H., Zinkevich T., Yavuz M., Hansen A.-L., Knapp M., Bednarčík J., Randau S., Richter F.H., Janek J., Ehrenberg H., Indris S., Amorphous versus crystalline Li<sub>3</sub>PS<sub>4</sub>: local structural changes during synthesis and li ion mobility, *The Journal of Physical Chemistry C*, 123 (2019) 10280–10290. DOI: 10.1021/acs.jpcc.9b01425
- Sui D., Xie Y., Zhao W., Zhang H., Zhou Y., Qin X., Ma Y., Yang Y., Chen Y., A high-performance ternary Si composite anode material with crystal graphite core and amorphous carbon shell, *Journal of Power Sources*, 384 (2018) 328–333. DOI:

- 10.1016/j.jpowsour.2018.03.008
- Sun F., Markötter H., Dong K., Manke I., Hilger A., Kardjilov N., Banhart J., Investigation of failure mechanisms in silicon based half cells during the first cycle by micro X-ray tomography and radiography, *Journal of Power Sources*, 321 (2016a) 174–184. DOI: 10.1016/j.jpowsour.2016.04.126
- Sun W., Hu R., Zhang M., Liu J., Zhu M., Binding of carbon coated nano-silicon in graphene sheets by wet ball-milling and pyrolysis as high performance anodes for lithium-ion batteries, *Journal of Power Sources*, 318 (2016b) 113–120. DOI: 10.1016/j.jpowsour.2016.04.016
- Švrček V., Rehspringer J.-L., Gaffet E., Slaoui A., Muller J.-C., Unaggregated silicon nanocrystals obtained by ball milling, *Journal of Crystal Growth*, 275 (2005) 589–597. DOI: 10.1016/j.jcrysgro.2004.12.012
- Szczech J.R., Jin S., Nanostructured silicon for high capacity lithium battery anodes, *Energy & Environmental Science*, 4 (2011) 56–72. DOI: 10.1039/c0ee00281j
- Takeuchi S., Suzuki K., Hirayama M., Kanno R., Sodium superionic conduction in tetragonal  $\text{Na}_3\text{PS}_4$ , *Journal of Solid State Chemistry*, 265 (2018) 353–358. DOI: 10.1016/j.jssc.2018.06.023
- Talens Peiró L., Villalba Méndez G., Ayres R.U., Lithium: sources, production, uses, and recovery outlook, *JOM*, 65 (2013) 986–996. DOI: 10.1007/s11837-013-0666-4
- Tatsumisago M., Hama S., Hayashi A., Morimoto H., Minami T., New lithium ion conducting glass-ceramics prepared from mechanochemical  $\text{Li}_2\text{S}-\text{P}_2\text{S}_5$  glasses, *Solid State Ionics*, 154–155 (2002) 635–640. DOI: 10.1016/S0167-2738(02)00509-X
- Taylor L., Skuse D., Blackburn S., Greenwood R., Stirred media mills in the mining industry: material grindability, energy-size relationships, and operating conditions, *Powder Technology*, 369 (2020) 1–16. DOI: 10.1016/j.powtec.2020.04.057
- Utsunomiya T., Hatozaki O., Yoshimoto N., Egashira M., Morita M., Influence of particle size on the self-discharge behavior of graphite electrodes in lithium-ion batteries, *Journal of Power Sources*, 196 (2011) 8675–8682. DOI: 10.1016/j.jpowsour.2011.06.070
- Velázquez-Martínez O., Valio J., Santasalo-Aarnio A., Reuter M., Serna-Guerrero R., A critical review of lithium-ion battery recycling processes from a circular economy perspective, *Batteries*, 5 (2019) 68. DOI: 10.3390/batteries5040068
- Wang H., Ikeda T., Fukuda K., Yoshio M., Effect of milling on the electrochemical performance of natural graphite as an anode material for lithium-ion battery, *Journal of Power Sources*, 83 (1999) 141–147. DOI: 10.1016/S0378-7753(99)00288-8
- Wenzel V., Moeller R.S., Nirschl H., Influence of mixing technology and the potential to modify the morphological properties of materials used in the manufacture of lithium-ion batteries, *Energy Technology*, 2 (2014) 176–182. DOI: 10.1002/ente.201300091
- Wenzel V., Nirschl H., Nötzel D., Challenges in lithium-ion-battery slurry preparation and potential of modifying electrode structures by different mixing processes, *Energy Technology*, 3 (2015) 692–698. DOI: 10.1002/ente.201402218
- Wills B.A., Napier-Munn T., Wills' Mineral Processing Technology: An Introduction to the Practical Aspects of Ore Treatment and Mineral Recovery, 7th Edition, Butterworth-Heinemann, Amsterdam, London, 2006, ISBN: 9780080479477.
- Wu H., Chan G., Choi J.W., Ryu I., Yao Y., McDowell M.T., Lee S.W., Jackson A., Yang Y., Hu L., Cui Y., Stable cycling of double-walled silicon nanotube battery anodes through solid-electrolyte interphase control, *Nature Nanotechnology*, 7 (2012) 310–315. DOI: 10.1038/nnano.2012.35
- Wu Y.S., Yeh T.S., Lee Y.H., Lee Y.C., Spheroidization modification of artificial graphite applied as anode materials for high rate lithium ion batteries, *Advanced Materials Research*, 201–203 (2011) 421–424. DOI: 10.4028/www.scientific.net/AMR.201-203.421
- Xu C., Dai Q., Gaines L., Hu M., Tukker A., Steubing B., Future material demand for automotive lithium-based batteries, *Communications Materials*, 1 (2020) 99. DOI: 10.1038/s43246-020-00095-x
- Yan Q., Li X., Wang Z., Wu X., Wang J., Guo H., Hu Q., Peng W., Extraction of lithium from lepidolite by sulfation roasting and water leaching, *International Journal of Mineral Processing*, 110–111 (2012) 1–5. DOI: 10.1016/j.minpro.2012.03.005
- Yazami R., Touzain P., A reversible graphite-lithium negative electrode for electrochemical generators, *Journal of Power Sources*, 9 (1983) 365–371. DOI: 10.1016/0378-7753(83)87040-2
- Yoon S., Kim H., Oh S.M., Surface modification of graphite by coke coating for reduction of initial irreversible capacity in lithium secondary batteries, *Journal of Power Sources*, 94 (2001) 68–73. DOI: 10.1016/S0378-7753(00)00601-7
- Yudha C.S., Muzayanha S.U., Widiyandari H., Iskandar F., Sutopo W., Purwanto A., Synthesis of  $\text{LiNi}_{0.85}\text{Co}_{0.14}\text{Al}_{0.01}\text{O}_2$  cathode material and its performance in an NCA/graphite full-battery, *Energies*, 12 (2019) 1886. DOI: 10.3390/en12101886
- Zeng X., Li J., Singh N., Recycling of spent lithium-ion battery: a critical review, *Critical Reviews in Environmental Science and Technology*, 44 (2014) 1129–1165. DOI: 10.1080/10643389.2013.763578
- Zhang C., Gu L., Kaskhedikar N., Cui G., Maier J., Preparation of silicon@silicon oxide core-shell nanowires from a silica precursor toward a high energy density Li-ion battery anode, *ACS Applied Materials & Interfaces*, 5 (2013a) 12340–12345. DOI: 10.1021/am402930b
- Zhang Q., Wang X., Lu W., Tang F., Guo J., Yu W., Qu M., Yu Z., Comparisons of short carbon nanotubes containing conductive additives of cathode for lithium ion batteries, *Materials Research Bulletin*, 48 (2013b) 2865–2870. DOI: 10.1016/j.materresbull.2013.04.010
- Zhang Z., Shao Y., Lotsch B., Hu Y.-S., Li H., Janek J., Nan C., Nazar L., Maier J., Armand M., Chen L., New horizons for inorganic solid state ion conductors, *Energy & Environmental Science*, 11 (2018) 1945–1976. DOI: 10.1039/C8EE01053F
- Zhang Y., Cao H., Zhang J., Xia B., Synthesis of  $\text{LiNi}_{0.6}\text{Co}_{0.2}\text{Mn}_{0.2}\text{O}_2$  cathode material by a carbonate co-precipitation method and its electrochemical characterization, *Solid State Ionics*, 177 (2006) 3303–3307. DOI: 10.1016/j.ssi.2006.09.008
- Zhao M., Li B.-Q., Zhang X.-Q., Huang J.-Q., Zhang Q., A perspective toward practical lithium-sulfur batteries, *ACS Central Science*, 6 (2020) 1095–1104. DOI: 10.1021/acscentsci.0c00449
- Zhao N., Li Y., Zhao X., Zhi X., Liang G., Effect of particle size and purity on the low temperature electrochemical performance of  $\text{LiFePO}_4/\text{C}$  cathode material, *Journal of Alloys and Compounds*, 683 (2016) 123–132. DOI: 10.1016/j.jallcom.2016.04.070

## Authors' Short Biographies



### Arno Kwade

Arno Kwade worked 9 years as a process engineer in leading positions in industry after finishing his doctorate in 1996. Since 2005 he is leading as Professor the Institute for Particle Technology at TU Braunschweig. His research focus lies on developing process-structure-property relationships for processes in which particles are mechanically stressed and formulated, from milling and mechanochemical synthesis over mixing to production and calendaring of electrodes for lithium-ion and all-solid-state batteries. Today he is Chairman of the Battery LabFactory Braunschweig (BLB) and the Center of Pharmaceutical Engineering (PVZ).



### Marcel Möller

Marcel Möller received his master's degree in biochemical and chemical engineering at the TU Braunschweig in 2019. After a year of industrial experience at Volkswagen AG as engineer for battery slurry production, he joined the Institute for Particle Technology. In his research, he targets high quality and low-cost production of nano-sized silicon via wet-grinding. For that purpose, he develops different formulating strategies as well as suited process conditions and evaluates the impact on the production of the silicon nanoparticles.



### Janne Müller

Janne Müller got his master's degree at the Technical University Braunschweig in 2018 and is working as a PhD student in the working group Battery Process Engineering at the Institute for Particle Technology since then. His research focuses on the scalable preparation of nano-silicon graphite composites as anode material for lithium-ion batteries. In his recent publication he demonstrated the preparation via fluidized bed granulation with subsequent carbon coating enabling high performance silicon materials.



### Jutta Hesselbach

Jutta Hesselbach studied mechanical engineering at the TU Braunschweig, where she proceeded her studies in the field of process engineering as a research associate at the Institute for Particle Technology. Within this field, she completed her doctoral thesis in July 2020 at the TU Braunschweig. Now she works at the Fraunhofer Institute for Surface Engineering and Thin Films IST within the department Process and Production Engineering for Sustainable Energy Storage Systems, where she was promoted to Head of the Group "Material and Process Development".



### Sabrina Zellmer

Sabrina Zellmer studied mechanical engineering at the TU Braunschweig, where she proceeded her studies in the field of nanomaterials as a research associate at the Institute for Particle Technology. She completed her doctoral studies in the field of particle functionalization and spray drying. During her work at the iPAT, she broadened her scientific expertise by working in the BLB, becoming the head of the junior research group "Solid-State Battery Materials and Electrodes". Since January 2019 Sabrina Zellmer is Head of Department Process and Production Engineering for Sustainable Energy Storage Systems at the Fraunhofer IST.



## Authors' Short Biographies



### Stefan Doose

Stefan Doose received his master degree in biotechnology with a focus on process engineering from TU Braunschweig in 2017. Subsequently, he started his work as a research assistant (PhD student) in the Battery Process Engineering research group at the Institute of Particle Technology of Technische Universität Braunschweig in 2017 with a focus on mechanical safety studies with accompanying online gas analysis as well as mechanical-thermal recycling processes of lithium-ion batteries.



### Julian Mayer

Julian Mayer received his Bachelor of Engineering from the University of Applied Sciences Munich in 2013 and subsequently completed his Master's degree from the Technical University of Braunschweig in 2016. Since then, he has been researching the continuous and discontinuous dispersion of lithium-ion battery slurries, with focus on the carbon black fragmentation at the Institute for Particle Technology. Since 2020, he has been deputy head of the Battery Process Engineering group.



### Peter Michalowski

Peter Michalowski studied physics at the University Jena and graduated in the field of superconductivity. Subsequently, he worked on his doctoral thesis project on cathodes for lithium ion batteries at the University Oldenburg and received his title in 2017. He joined the Institute for Particle Technology at the TU Braunschweig in 2018 and became leader of the junior research group "Solid-State Battery Materials and Electrodes" in 2019. Since the start of 2021 he has been the head of the battery processing division of the iPAT and part of the head office of the Battery LabFactory Braunschweig.



### Malcom Powell

Malcom Powell has applied fundamental comminution research to design and process improvement on over 60 mines worldwide during 35 years at Mintek, UCT, and then as Professor of comminution at the JKMRRC in Australia. Malcolm collaborates extensively, with close compatriots on 5 continents forming the Global Comminution Collaborative (GCC)—providing an expert research and consulting. Malcolm's research vision is of integrated total process simulation as a tool for innovation—linking geology, mining, energy and size reduction, gangue rejection and recovery into flexible process design and process optimization.



### Sandra Breitung-Faes

Sandra Breitung-Faes studied process engineering at TU Clausthal and received her doctoral grade in 2009 at the Institute for Particle Technology at the TU Braunschweig with the topic of wet stirred media milling of ceramic nano particles. Afterwards she had the position of a team leader for grinding, a group leader for grinding and dispersing and is now, since 2018 the division manager for powder and slurry processes at the Institute for Particle Technology of TU Braunschweig.



# Recent Research Trend in Powder Process Technology for High-Performance Rare-Earth Permanent Magnets<sup>†</sup>

Kenta Takagi\*, Yusuke Hirayama, Shusuke Okada, Akihide Hosokawa and Wataru Yamaguchi

*Magnetic Powder Metallurgy Research Center, National Institute of Advanced Industrial Science and Technology (AIST), Japan*

## Abstract

Higher performance is constantly required in rare earth permanent magnets, which are an indispensable component of the motors of electric vehicles. When producing sintered magnets, advanced structural control is necessary in the powder metallurgy process in order to achieve high performance. Especially in recent years, it has become important to develop processes for Sm-Fe-N magnets and metastable phase magnets as next-generation magnets to replace the Nd-Fe-B magnets. Because the crystal grain refinement of sintered magnets is most effective for improving coercivity, production methods for raw powders have evolved from the traditional pulverization to chemical synthesis approaches, and as a result, a submicron-sized Sm-Fe-N powder with huge coercivity has been developed. State-of-the-art physical synthesis methods have also been applied successfully to the synthesis of nanopowders. Since control of the grain boundary is very effective in Nd-Fe-B magnets, this approach has also been evolved to Sm-Fe-N magnets by nano coating. On the other hand, since technologies for crystalline orientation control and high-density sintering are indispensable for improvement of remanence, new low-thermal load consolidation techniques such as spark plasma sintering are being developed for Sm-Fe-N magnets and metastable phase magnets in order to overcome the inherent low thermal stability of these materials.

**Keywords:** rare earth permanent magnets, powder metallurgy processes, grain refinement, crystalline orientation, grain boundary control

## 1. Introduction

Rare earth permanent magnets are a typical material produced by powder metallurgy technology, and most of these products are now used in electric motors. Permanent magnet synchronous motors (PMSMs) using rare earth magnets are much more efficient than inductive motors, and were the driving force behind the industrialization of hybrid and electric vehicles in the late 1990s. More recently, higher efficiency has been required in motors in response to the growing need for global CO<sub>2</sub> reduction, and new high-performance permanent magnets are being developed from this viewpoint. Among rare earth magnets, materials based mainly on Nd-Fe-B, Sm-Co and Sm-Fe-N have been industrialized, but most magnets used in motors are Nd-Fe-B magnets. As a practical problem, the prices of the specific rare earth and heavy rare earth elements that are the raw materials for these rare earth magnets, such as the Nd and Dy used in Nd-Fe-B magnets, are easily affected by the international situation due to their strongly uneven

regional distribution (Seo Y. and Morimoto S., 2014). In particular, since the “rare earth shock” of 2010, difficult development aimed at improving magnetic characteristics while considering resource problems has been urgently needed.

Various magnetic properties must be considered when developing permanent magnet materials for motors, but the most important are the maximum energy that can be extracted from the magnet  $(BH)_{\max}$  and coercivity, which indicates the resistance to the opposite magnetic field. Although  $(BH)_{\max}$  is determined by various magnetic properties such as remanence, coercivity and rectangularity, the most influential factor is remanence. In other words, the first consideration when developing a high-performance magnet is improvement of coercivity and remanence.

The potential for improving coercivity depends on the anisotropic magnetic field, which is an intrinsic property of each magnetic compound, but coercivity very strongly depends on the crystal grain size and grain boundary structure. For example, the anisotropic magnetic field of Nd<sub>2</sub>Fe<sub>14</sub>B is about 1/3 that of Sm<sub>2</sub>Fe<sub>17</sub>N<sub>3</sub>, but the coercivity of the Nd<sub>2</sub>Fe<sub>14</sub>B bulk magnet, which is achieved by using advanced microstructural control technology, exceeds that of Sm<sub>2</sub>Fe<sub>17</sub>N<sub>3</sub>. Many studies so far have shown that the basic guidelines for developing high coercivity magnets are selection of a magnetic material with a high anisotropic

<sup>†</sup> Received 16 January 2022; Accepted 29 March 2022  
J-STAGE Advance published online 21 May 2022

\* Corresponding author: Kenta Takagi;  
Add: 2266-98 Anagahora, Shimo-Shidami, Moriyama-ku, Nagoya,  
Aichi 463-8560, Japan  
E-mail: k-takagi@aist.go.jp  
TEL: +81-52-736-7561 FAX: +81-52-736-7406



magnetic field, refinement of its microstructure and appropriate control of its grain boundary structure.

On the other hand, the guideline for high remanence is achieving remanence closer to saturation magnetization, which is an intrinsic property of the compound. The easy axis and hard axis of magnetization in a magnetic crystal are mutually orthogonal, and high magnetization is achieved in the direction of the easy axis. This means that a high crystal orientation is necessary in a magnet with a high remanence. Moreover, since the occupied volume ratio of the magnetic phase in a sintered magnet is also important, pores and non-magnetic phase should be reduced to the absolute minimum.

As described above, in the development of high-performance rare earth magnets, various factors such as grain refinement, grain boundary control, crystal orientation and high density must be achieved simultaneously. For this reason, most modern rare earth magnet materials are produced by powder metallurgy technology, which enables advanced microstructural control. However, various restrictions arise in the production process because the rare earth powders which are the constituents of the magnets are more easily oxidized than aluminum and magnesium, and thus, various restrictions arise in the process of passing through powder with an extremely large specific surface area. In order to solve this complex problem, various advanced powder processes from powder preparation to consolidation have been developed in an integrated manner. This paper describes the trends in the development of powder processes for improving coercivity and remanence, focusing on Nd-based and Sm-based magnets. The development and expectations of the powder process for metastable phase magnets and nanocomposite magnets, which are considered to be next-generation magnets, are also described.

**Fig. 1** compares the various powder processing tech-

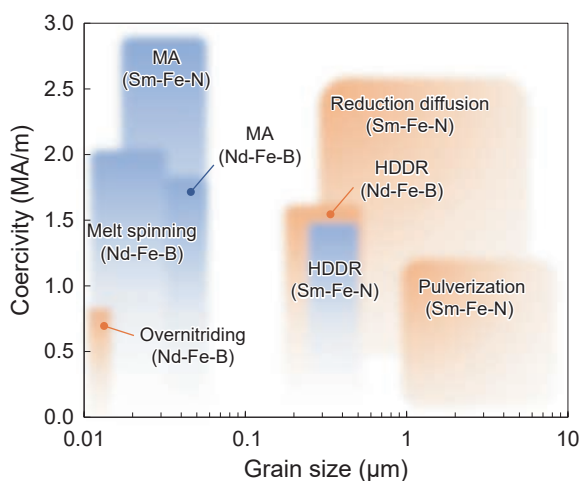


**Fig. 1** Comparison of various preparation methods of rare earth magnet powder. The blue and orange areas represent isotropic and anisotropic powders, respectively.

niques in term of coercivity. The traditional mechanical pulverization, mechanical alloying and melt spinning methods were applied in powder preparation with the aim of refining the crystal size to improve coercivity. Grain refinement made it possible to achieve high coercivity in the powders produced by these methods, and coercivity as high as 1.7 MA/m has been achieved in Nd-Fe-B magnets. Therefore, for example, Nd-Fe-B and Sm-Fe-N based powders produced by melt spinning were industrialized at an early stage. However, since these powders have a polycrystalline structure with random crystal orientations, it is difficult to orient the crystals when they are used as bulk magnets, which means they cannot be used directly in high-remanence magnets. The hydrogenation-disproportionation-desorption-recombination (HDDR) process and the reduction-diffusion (R-D) process have been developed in recent years to overcome this problem. The HDDR process is capable of producing polycrystalline powders with a crystalline orientation, and the R-D process make it possible to obtain very fine single-crystal powders. These respective processes realize anisotropic powders with high coercivity of more than 1.5 MA/m and huge coercivity of up to 4.7 MA/m, respectively. Recently, advances in mechanical pulverization methods such as ball milling and jet milling have made it possible to produce submicron-sized powders, and physical synthesis approaches such as the thermal plasma method have been applied successfully to nanopowders.

In addition, as mentioned above, the development of high coercivity magnets by grain boundary control in sintered compact is being actively carried out with Nd-Fe-B magnets. Forming Dy-Fe-B with a high anisotropic magnetic field at the grain boundaries of Nd-Fe-B magnets greatly improves coercivity. Initially, the grain boundary phase was formed by using a mixed powder (two-alloy method), but the development of the grain boundary diffusion method has made it possible to obtain high coercivity magnets. In the Sm-Fe-N magnet, high coercivity of up to 4.7 MA/m has been obtained by adding Zn to the grain boundaries, and more recently, sintered magnets with high coercivity and high remanence have been discovered by combining low oxygen powder metallurgy with powder coating.

Various powder processes have been also examined to improve remanence. Although the current-generation Nd-Fe-B magnets can be densified by liquid phase sintering under atmospheric pressure, since Sm-Fe-N magnets are thermally decomposable, high temperature sintering cannot be applied. Low thermal load sintering techniques such as spark plasma sintering (SPS) have been studied, but remanence is still limited to a low level due to insufficient densification. As a new approach, high strain rate consolidation techniques such as the shear compression method and the powder rolling method are being studied. For

Nd-Fe-B magnets, a special processing method called the hot-deformation method was developed to simultaneously achieve a high crystal orientation and grain refinement, that is, both high remanence and high coercivity at the same time. The strongest Nd-Fe-B bulk magnet to date was produced by this process.

As described above, novel powder processes are constantly being developed for high-performance rare earth magnets. The next chapter introduces the individual powder processes and powder metallurgy processes for high-performance magnets in more detail.

## 2. Powder processes for enhanced coercivity

### 2.1 Production technologies for fine powder

#### 2.1.1 Pulverization

The traditional approach to grain refinement in powder metallurgy is pulverization of the material into a fine powder. Currently, the gas flow-type pulverization method (jet milling) is often used for fine pulverization of Nd-Fe-B magnet materials. Unlike ball mills, a crushing medium is not used in jet milling, so impurities can be reduced. As an additional advantage, although the particle surface of the rare earth alloy powder is extremely active, deterioration of magnetic properties due to oxidation of the particle surface can be suppressed if the oxygen concentration of the pulverizing gas is sufficiently reduced. In general production processes for Nd-Fe-B magnets, the powder is refined to a size of several  $\mu\text{m}$  by high throughput counter-type jet milling before the sintering process. In recent years, Sagawa et al. have shown that swirling-type jet milling using helium gas, which can generate a high-speed gas flow, can refine the powder down to a size of 1  $\mu\text{m}$  (Sepahri-Amin H. et al., 2011). Nakamura et al. succeeded in producing a Nd-Fe-B magnetic powder with a size of 0.33  $\mu\text{m}$  by helium-gas jet milling using HDDR powder as the raw powder, as shown in Fig. 2 (Nakamura M. et al., 2013). By combining the ultrafine powders produced by this type of process with

grain boundary control technology, Nd-Fe-B sintered magnets with coercivity of 1.59 MA/m have been obtained (Sugimoto S. et al., 2015).

Improvement of coercivity by fine pulverization has also been attempted with other alloys. Takagi et al. applied swirling-type jet milling to a Sm-Fe-N alloy and demonstrated that it can be pulverized to 1  $\mu\text{m}$  (Takagi K. et al., 2020). However, the coercivity of the sintered magnets derived from this fine powder was only about 0.8 MA/m, which is much smaller than the coercivity expected from its huge anisotropic magnetic field. This is considered to be closely related to the mechanical damage introduced during jet milling. That is, crystals which contain defects such as dislocations have a lower anisotropic magnetic field than perfect crystals and tend to become nucleation sites for the reverse magnetic domain. As a result, coercivity is significantly reduced by surface damage in the powder. It may be noted that the coercivity of the Nd-Fe-B powder prepared by the pulverization method is actually very small, but since the Nd-Fe-B sintered magnet can be consolidated by liquid phase sintering, the surface damage can be recovered, resulting in high coercivity in the sintered magnet. However, only solid-phase sintering in the low temperature range is possible with the Sm-Fe-N magnet, as this material is a thermally-decomposable alloy, so the coercivity of the powder is inherited unchanged in the sintered magnet. Hosokawa et al. conducted a detailed TEM investigation of the  $\text{Sm}_2\text{Fe}_{17}\text{N}_3$  fine powder produced by jet milling. As shown in Fig. 3, that study revealed that numerous dislocations and nanocrystallization occur on the particle surface, and these types of damage increase as pulverization progresses (Hosokawa A. et al., 2021a). In fact, it was found that the decrease in the crystallinity of the particle surface leads not only to the above-mentioned decrease in coercivity, but also to a decrease in remanence. Although the reason for this decrease in remanence has not yet been clarified, this suggests that some solution, such as

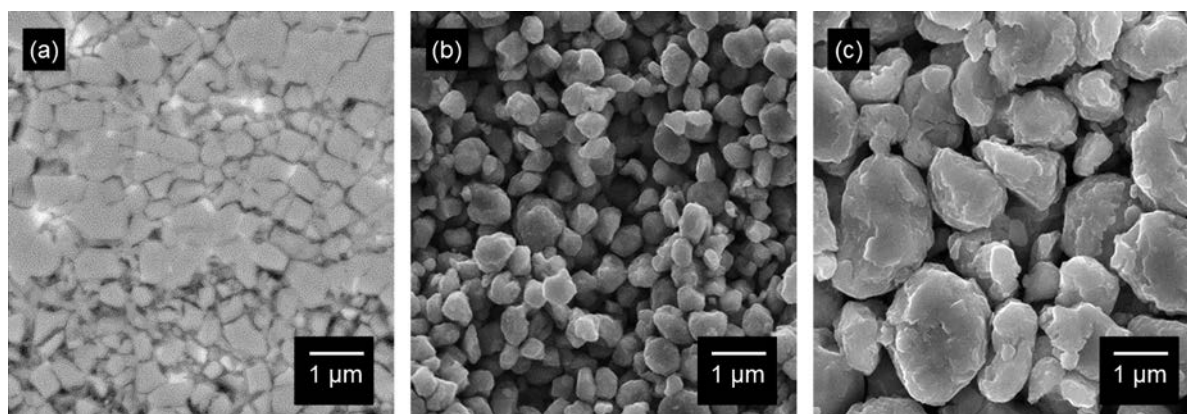


**Fig. 2** BSE image of (a) hydrogen decapitated HDDR alloy, and SE images of jet-milled powders of (b) HDDR and (c) SC alloys. The median diameter ( $d_{50}$ ) of the jet-milled powder of the HDDR alloy in (b) is about 0.33  $\mu\text{m}$ . Reprinted with permission from Ref. (Nakamura M. et al., 2013). Copyright: (2013) AIP Publishing LLC.

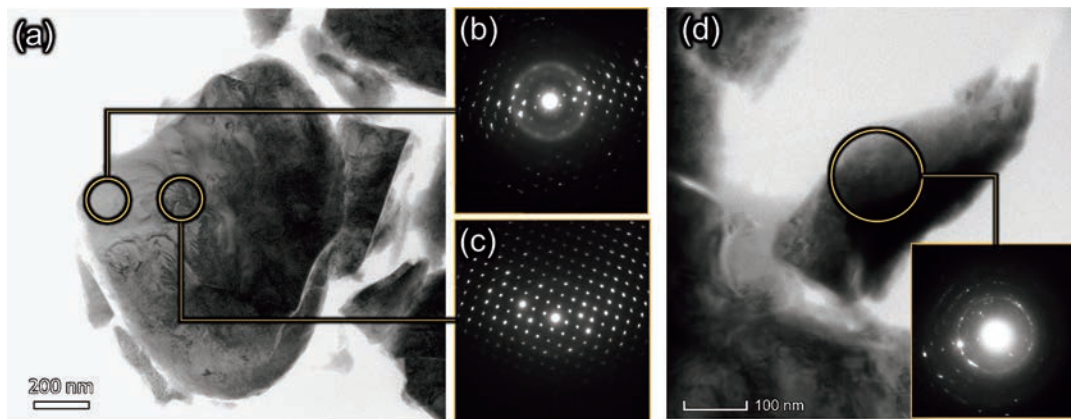


**Fig. 3** (a) TEM BF image of a jet-milled powder particle, and (b) and (c) corresponding SADPs. (d) TEM BF image of a UFP and its corresponding SADP. Reprinted with permission from Ref. (Hosokawa A. et al., 2021a). Copyright: (2021) Elsevier B.V.

heat treatment, is required in order to recover the damage.

Besides jet milling, it has often been reported that further pulverization is possible by ball milling using a surfactant. In traditional ball milling, crushing and rewelding are performed repeatedly, so particle size reduction becomes saturated, but addition of a surfactant to the solvent suppresses rewelding, allowing pulverization to progress. As a pioneering study, Chakka et al. pulverized Sm-Co and Nd-Fe-B to sizes of less than 30 nm by surfactant-assisted ball milling (Chakka V.M. et al., 2006). Akdogan et al. and Yue et al. have also produced SmCo<sub>5</sub> nanopowder with a coercivity of 1.4 MA/m and Nd-Fe-B nanopowder with 0.3 MA/m by surfactant-assisted ball milling (Akdogan N.G. et al., 2009; Yue M. et al., 2012). However, as in the case of jet milling, the high coercivity expected from the particle size has not been obtained so far, and this is thought to be the result of mechanical damage induced by the milling process.

### 2.1.2 Chemical synthesis

As mentioned in the previous section, milling methods have the problem of causing damage to the particle surface and thus are not an appropriate approach for magnetic alloys such as Sm-Fe-N which are not suitable for liquid phase sintering. Moreover, milling cannot be considered an ideal method for producing powders for bonded magnets due to the issue of reduced coercivity. Therefore, chemical powder synthesis processes which enable direct production of high coercivity fine powders have been developed recently. The most successful chemical synthesis method for rare-earth magnet fine powders is the reduction-diffusion (R-D) method, which was originally developed by Robert E. Cech of General Electric in 1969 to produce SmCo<sub>5</sub> magnetic powder (Cech R.E., 1973; 1974). In the R-D method, rare earth magnet alloy powders are produced by heating a mixture of rare earth oxide powders, transition metal powders and Ca in an inert atmosphere. During heating, the rare earth metals that are reduced by Ca diffuse into

the transition metal particles, resulting in an alloy powder. Therefore, the particle size of the alloy powder is greatly affected by the particle size of the raw transition metal powder. Conventionally, a fine alloy powder is produced by grinding the R-D powder to the order of tens of microns after synthesis from coarse transition metal and rare earth oxide raw powders. Recent research has demonstrated that micron-sized fine alloy powders can be directly synthesized by the R-D process from fine raw powders synthesized by a wet chemical method, and it has been reported that the powders synthesized by the R-D process exhibit higher coercivity than milled powders because the R-D powders are free of surface damage (Tada S. et al., 2012). Particularly, the last ten years of research have successfully shown that submicron-sized alloy powder can be synthesized by using of nano-sized oxide raw powders prepared by the pyrolysis or sol-gel method, and by using techniques to prevent necking and particle growth during Ca reduction (Ma Z.-H. et al., 2018; Zhang H. et al., 2011a). As mentioned above, the R-D method has high potential for producing fine rare earth magnetic powders and has been energetically studied, especially for Sm-Co and Sm-Fe-N alloys.

SmCo<sub>5</sub> has a large anisotropy field and has been reported to exhibit high coercivity. Fig. 4 summarizes the particle size dependency of coercivity for SmCo<sub>5</sub> fine powders. (Dong Y. et al., 2019; Li C. et al., 2018; Ma Z.-H. et al., 2018; Ma Z. et al., 2019a; Ma Z. et al., 2019c; Ma Z. et al., 2015; Shen B. et al., 2019; Tang H. et al., 2020a; 2021; Tang H. et al., 2020c; Wu Q. et al., 2020b; Zhang H. et al., 2011a). Coercivity improves as the average particle diameter becomes finer, but reaches its maximum at about 400 nm and then decreases in the smaller diameter range. This decrease is considered to be due to the more pronounced effect of particle surface oxidation as the particle size decreases, i.e., as the specific surface area increases. The highest coercive force at room temperature was 5.8 MA/m, as reported by Dong et al. (Dong Y. et al., 2019), when a hydroxide powder synthesized by

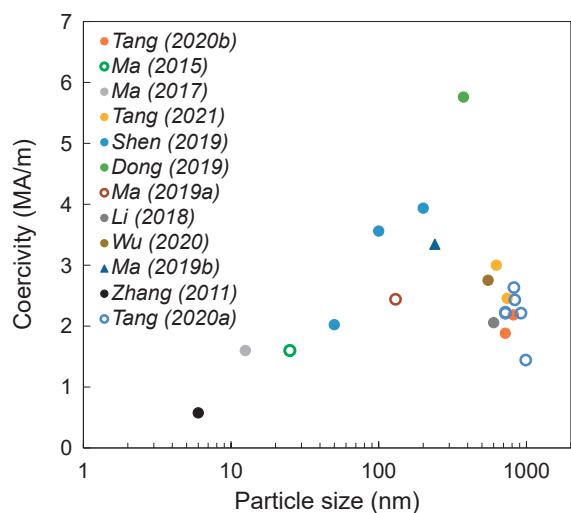


**Fig. 4** Particle size dependency of coercivity of  $\text{SmCo}_5$  powder (Dong Y. et al., 2019; Li C. et al., 2018; Ma Z.-H. et al., 2017; Ma Z. et al., 2019a; Ma Z. et al., 2019b; Ma Z. et al., 2015; Shen B. et al., 2019; Tang H. et al., 2020a; Tang H. et al., 2021; Tang H. et al., 2020b; Wu Q. et al., 2020a; Zhang H. et al., 2011b).

coprecipitation of a  $\text{SmCl}_3$ ,  $\text{CoCl}_2$  and  $\text{CaCl}_2$  aqueous solution was mixed with KCl and Ca and subjected to a R-D process at a relatively low temperature of 1 133 K. In their study, the CaO coating, which was derived from  $\text{CaCl}_2$  and dilution of Ca by KCl, prevented necking and growth between particles, resulting in an ultrafine powder with a narrow particle size distribution.

Of the rare earth magnetic powders produced by the R-D method, the  $\text{Sm}_2\text{Fe}_{17}\text{N}_3$  powder is the only raw material powder which is produced commercially for bonded magnets. **Fig. 5** shows the relationship between the particle size and coercivity of the  $\text{Sm}_2\text{Fe}_{17}\text{N}_3$  powder (Hirayama Y. et al., 2016; Okada S. et al., 2019; Okada S. et al., 2017; Okada S. and Takagi K., 2019; Dong Y. et al., 2019; Tada S. et al., 2012; Takagi K. et al., 2021). Okada et al. revealed that  $\text{Sm}_2\text{Fe}_{17}\text{N}_3$  fine powder synthesized by the R-D method exhibited high coercivity even at the submicron size, unlike powders prepared by milling. In particular, they reported that  $\text{Sm}_2\text{Fe}_{17}\text{N}_3$  with a giant coercive force of 2.5 MA/m and an average particle diameter of about 400 nm can be produced by improving various processing steps (Okada S. et al., 2019; Okada S. et al., 2017; Okada S. and Takagi K., 2019; Takagi K. et al., 2021). They employed a synthesis process in which Sm-Fe oxide powders synthesized by coprecipitation were subjected to hydrogen reduction, reduction-diffusion and nitridation. Using a different approach, Dong et al. applied a particle growth suppression technique, which was used to achieve the previously described synthesis of  $\text{SmCo}_5$  fine powder with huge coercivity, to the synthesis of  $\text{Sm}_2\text{Fe}_{17}\text{N}_3$  fine powder, and reported  $\text{Sm}_2\text{Fe}_{17}\text{N}_3$  ultrafine powder with a particle size of about 100 nm. However, the coercive force was only about 1.2 MA/m (Dong Y. et al., 2019).

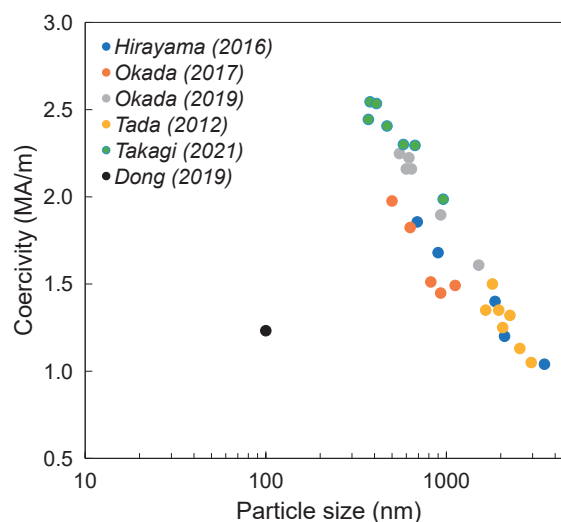


**Fig. 5** Particle size dependency of coercivity of  $\text{Sm}_2\text{Fe}_{17}\text{N}_3$  powder (Hirayama Y. et al., 2016; Okada S. et al., 2019; Okada S. et al., 2017; Dong Y. et al., 2019; Tada S. et al., 2012; Takagi K. et al., 2021).

Although there have been reports on the synthesis of Nd-Fe-B alloys, coercivity was not outstanding, being limited to around 0.5 MA/m (Jeong J.H. et al., 2016; Swaminathan V. et al., 2013). Since Nd-Fe-B is a ternary system, adjustment of the composition seems to be difficult, especially in controlling the amount of B (Guo Y. et al., 2019). Moreover, because Nd-Fe-B is more easily oxidized than Sm-based materials, decreased coercivity due to surface oxidation is considered to have a serious influence. As for  $\text{ThMn}_{12}$ -type alloys, which are expected to be a new type of magnet, Gabay et al. reported  $(\text{Sm,Zr})_1(\text{Fe,Co,Ti})_{12}$  powder with a high coercivity exceeding 1 MA/m by the R-D method using raw powders prepared by a mechanochemical process (Gabay A.M. and Hadjipanayis G.C., 2021). Although  $\text{TbCu}_7$ -type Sm-Fe-N is expected to be a next-generation magnet with high saturation magnetization, there had been no reports on production of this material by the R-D route because it is a metastable phase. However, Okada et al. recently developed a low-temperature R-D method using molten salts such as LiCl as a solvent for Ca, which enables a R-D reaction below the melting point of Ca, and succeeded in synthesizing a  $\text{TbCu}_7$ -type Sm-Fe single-crystal fine powder at an R-D reaction temperature of about 873 K (Okada S. and Takagi K., 2021).

### 2.1.3 Physical synthesis

Physical synthesis approaches for rare earth magnetic powders include, for example, vapor phase methods such as an arc discharge method and a high frequency induced thermal plasma method, as well as the cluster beam deposition method. Vapor phase methods are able to synthesize ultrafine particles much smaller than those prepared by the breakdown methods described in **Section 2.1.1**, and these ultrafine particles are also extremely pure, as they

are free of the particle surface contamination which is a drawback of the chemical synthesis processes described in [Section 2.1.2](#). Many reports on nanoparticle synthesis of rare earth-transition magnetic alloys using the gas phase method have been based on the cluster beam deposition method, in which the alloy is deposited on a substrate (Sellmyer D.J. et al., 2015). In particular, many reports have examined the synthesis of Sm-Co nanoparticles. However, while the obtained particle size was smaller than 50 nm, maximum coercivity was only about 0.6 MA/m at room temperature (Abbas N. et al., 2019; Balamurugan B. et al., 2012; Balasubramanian B. et al., 2011; He S. et al., 2013; Landi G.T. and Santos A.D., 2010; Stoyanov S. et al., 2003). Here, the high coercivity expected in nanoparticles is not obtained due to the difficulty of synthesizing nanoparticles with high crystallinity and avoiding surface oxidation due to the large surface area. Recently, Hirayama et al. energetically investigated the synthesis of these metal nanoparticles by a thermal plasma process, especially focusing on easily oxidizable metals such as Al and rare earth alloys. They newly modified a conventional thermal plasma method so that the nanoparticles can be synthesized and handled under an extremely low oxidizing atmosphere, as indicated in [Fig. 6](#). Their research demonstrated that Al nanoparticles obtained by this method form necking under low temperature heating because surface oxidation is minimized (Hirayama Y. et al., 2018; Kim D. et al., 2021), and Fe-Co alloy nanoparticles with reduced surface oxidation exhibited the same saturation magnetization as the conventional bulk alloy without a hydrogen reduction treatment (Hirayama Y. and Takagi K., 2019). In the synthesis of rare earth-transition metal nanoparticles, Hirayama et al. showed the possibility of synthesizing a TbCu<sub>7</sub>-type metastable phase in a Nd-Fe system by this process by taking advantage of its high quenching rate (Hirayama Y. et al., 2021). Synthesis of core-shell particles with a Sm-Co shell/Co core structure, which could not be obtained until now, has also been reported (Park K. et al., 2021), and is a very

noteworthy new process for raw material powders for the creation of novel permanent magnets in the future.

## 2.2 Grain refinement technologies

### 2.2.1 Rapid solidification

The previous section introduced attempts to develop single crystalline powder with the finest possible particle size for production of high coercivity fine-grained sintered magnets. On the other hand, the production methods for polycrystalline powders composed of ultrafine grains accompanied by rapid solidification have also been studied. The most common method is single roll melt spinning, and in fact, magnetic powder production by this method has already been commercialized. [Fig. 7](#) shows a schematic diagram of a melt spinning device and an image of the typical nanostructure (Mishra R.K., 1986). In the melt spinning method, a molten metal is directly poured into a rotating cold copper roll to achieve an extremely rapid quenching effect. Traditionally, this method was used in the development of amorphous and nanocrystalline materials. In the 1980s, it was reported that high coercivity could be obtained by alloying Fe with Tb, Pr, La, etc., and later, similar coercivity enhancement in Re-Fe alloys was also reported. General Motors (GM) was apparently searching for Re-Fe-based hard magnetic materials at the time, and Croat et al. at GM reported that Nd-Fe-B produced an excellent magnetic powder with coercivity of about 1.2 MA/m (Croat J.J., 1982).

The flake powder obtained by melt spinning has the advantage that extremely high coercivity due to the effect of grain refinement can be achieved because fine grains of several 10 nm to several 100 nm can be obtained without pulverization. However, since the orientation of each crystal grain is random, remanence and  $(BH)_{\max}$  are inferior to those of anisotropic magnets. In spite of this weakness, this powder has been applied practically in bonded magnets, in which the powder is kneaded with resin and molded, and melt-spun powder is also an indispensable raw material for

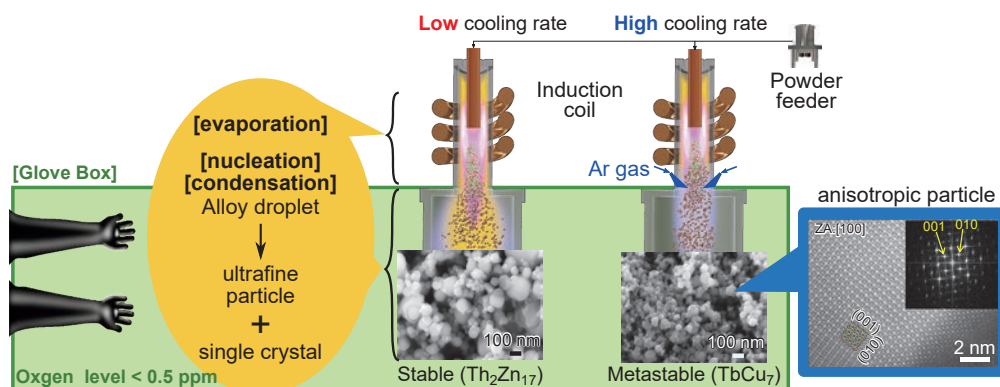


**Fig. 6** Experimental set-up of low-oxygen induction thermal plasma process. The cooling rate can be controlled by introducing extra Ar gas at the tail of the plasma, which results in differences in the formed phase. Reprinted with permission from Ref. (Hirayama Y. et al., 2021). Copyright: (2021) Elsevier B.V.

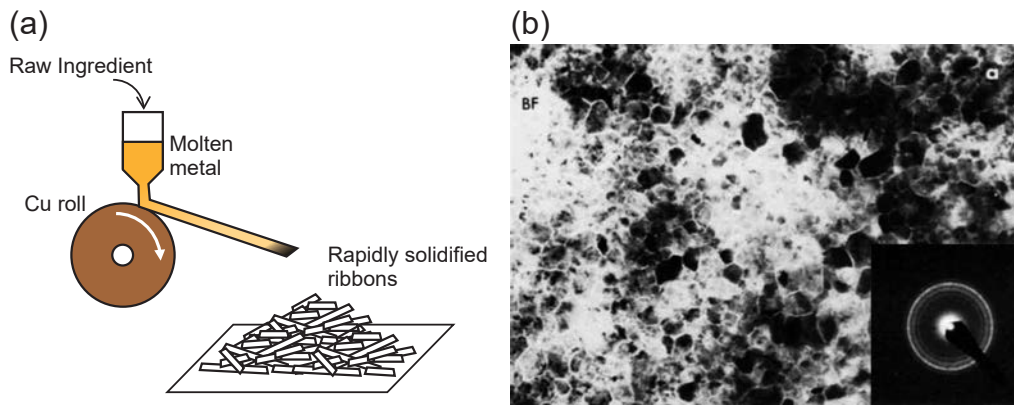


**Fig. 7** (a) Schematic illustration of melt spinning apparatus and (b) typical microstructure of as-spun ribbons. Reprinted with permission from Ref. (Mishra R.K., 1986). Copyright: (1986) Elsevier B.V.

hot-deformation magnets, which have attracted attention recently, as will be explained in detail in [Section 3.1](#).

The rapid solidification method also has the advantage of obtaining a non-equilibrium phase. For example, in the TbCu<sub>7</sub> type Sm-Fe-N alloy, it is possible to obtain a supersaturated Fe composition by melt spinning, and a high saturation magnetization of 1.7 T, which exceeds the values of Sm<sub>2</sub>Fe<sub>17</sub>N<sub>3</sub> and Nd<sub>2</sub>Fe<sub>14</sub>B, can be obtained (Katter M. et al., 1991; Sakurada S. et al., 1996). This TbCu<sub>7</sub> type Sm-Fe-N melt-spun powder was partially commercialized as a bonded magnet (Morii K. and Hasegawa F., 2008). As another example of melt-spun powders, Toshiba commercialized a 240 kJ/m<sup>3</sup> class sintered magnet using a Sm-Co-Fe-based magnet with a TbCu<sub>7</sub> structure (Horiuchi Y. et al., 2015; Horiuchi Y. et al., 2014), and this magnet is already used in the main motors of railway vehicles.

The single roll melt spinning method is also used for research on nanocomposite magnets, which are candidates for next-generation magnet materials. Nanocomposite magnets, also known as exchange spring magnets, are a new type of magnet. The original concept was first proposed by Kneller and Hawig (Kneller E.F. and Hawig R., 1991). When the hard magnetic phase and the soft magnetic phase are composited at the nano scale, the soft magnetic phase is expected to behave as if it were a hard magnetic phase due to exchange coupling at the interface. Prior to this work, Coehoorn of Philips in fact had performed an experimental work and reported a magnet similar to this concept in which nano-sized  $\alpha$ -Fe was dispersed in the Nd<sub>2</sub>Fe<sub>14</sub>B matrix by melt-spinning Nd-Fe-B powder with a Fe-rich composition (Coehoorn R. et al., 1989). Later, Skomski and Coey predicted that the combination of Sm<sub>2</sub>Fe<sub>17</sub>N<sub>3</sub> and FeCo would yield ultra-strong nanocomposite magnets with  $(BH)_{\max} = 1\,000$  kJ/m<sup>3</sup> (Skomski R. and Coey J.M.D., 1993). Following those pioneering works, nanocomposite magnets using melt-spun powder were actively investigated (e.g. (Hirosawa S. and Kanekiyo H., 1996; Hirosawa S. et al., 2003; Manaf A. et al., 1993a; Manaf A. et al., 1992; 1993b)), and Hitachi Metals later developed a new

process in which amorphous powder obtained by melt spinning is annealed to obtain a hard/soft nanocomposite structure. This class of powder was commercialized under the name Sprax<sup>®</sup>. Nevertheless, the values of  $(BH)_{\max}$  for the nanocomposite magnets reported to date have never exceeded that of the single-phase Nd<sub>2</sub>Fe<sub>14</sub>B magnet, except for a thin film reported by Cui et al. (Cui W.B. et al., 2015). The work by Zhang et al. (Zhang J. et al., 2005) is another interesting experiment with thin films, wherein the  $(BH)_{\max}$  obtained in the SmCo/Fe composite is superior to that of the SmCo hard phase. As indicated by these thin-film experiments, it is definitely important to align the crystal orientations in order to achieve the combined advantages of both the hard phase and the soft phase. Although this precise microstructural control is still difficult by methods other than the thin-film technique, thin films cannot be commercialized as permanent magnets. Thus, it is essential to develop new manufacturing processes that will potentially enable mass production of permanent magnets in a bulk form. Our group is currently energetically conducting research targeting anisotropic nanocomposite magnets by combining the melt spinning method, hot deformation method and addition of low melting point alloys (Hosokawa A. and Takagi K., 2018b; 2019; Hosokawa A. et al., 2019).

### 2.2.2 Solid synthesis

Another approach for synthesizing a powder consisting of ultrafine crystal grains is mechanical alloying (MA). In many studies on Nd-Fe-B-based, Sm-Fe-N-based and Sm-Co-based alloys, rare earth magnetic powders with crystal grain sizes of several 10 nm to several 100 nm have been synthesized for MA. For example, the mechanical-alloyed Nd-Fe-B powder produced by Zhang et al. had a high coercivity of 1.7 MA/m, which is comparable to the value obtained by the melt spinning method (Zhang Z.-D. et al., 1998), and Teresiak et al. demonstrated that Sm<sub>2</sub>Fe<sub>17</sub>N<sub>x</sub> powders produced by MA exhibited a huge coercivity of 2.8 MA/m (Teresiak A. et al., 1999). However, the MA



process has not been industrialized, as its low productivity makes it unsuitable for mass production.

MA has been used in many studies to explore metastable compounds such as  $\text{TbCu}_7$  type and  $\text{ThMn}_{12}$  type alloys because it is possible to synthesize a metastable phase by solid-phase synthesis without melting, and grain refinement is also possible. In particular, MA was actively utilized in research on  $\text{ThMn}_{12}$  type alloys, leading to clarification of the magnetic properties of  $\text{ThMn}_{12}$  type Nd-Fe-M-N alloys and Sm-Fe-M alloys (M: Ti, V, Mo) (Jin Z.-q. et al., 1997; Schultz L. et al., 1990; Shengen Z. et al., 2001). The  $\text{ThMn}_{12}$  type compound has recently been discovered to have magnetic properties superior to those of existing compounds, and has attracted renewed attention (Hirayama Y. et al., 2015; 2017). Nevertheless, MA is rarely used in current development of magnet materials because only polycrystalline powder can be obtained and as mentioned above, it is not suitable for mass production.

### 2.2.3 Gas reaction

As an epoch-making method for producing fine polycrystalline magnetic powders, approaches utilizing the reaction between solids and gases have attracted strong interest. Because rare earth transition metal alloys react with hydrogen and nitrogen to form unique microstructures, research on producing crystallographically-oriented polycrystalline powder by using gas reactions has been widely conducted. The hydrogenation-disproportionation-desorption-recombination method (HDDR) makes it possible to produce a polycrystalline powder consisting of sub-micron-sized crystal grains from single crystal powder by using the reaction between a rare earth transition metal alloy phase and hydrogen gas. For example, when an Nd-Fe-B alloy is heated in a  $\text{H}_2$  atmosphere, the alloy is temporarily decomposed into an  $\text{NdH}_2$  phase, Fe phase,  $\text{Fe}_2\text{B}$  phase, etc. (decomposition). Subsequently, when dehydrogenation is performed by heating in a reduced pressure environment, the phase returns to the Nd-Fe-B phase (recombination). In this process, the Nd-Fe-B phase forms fine crystal grains with sizes controlled in the range from 0.2 to 0.6  $\mu\text{m}$ , depending on the treatment temperature. In particular, unlike rapid solidification and MA, HDDR treatment under appropriate conditions is capable of producing crystallographically-oriented grains as shown in Fig. 8 (Takizawa R. et al., 2017). That is, although this alloy is a polycrystal, particles close to a single crystal can be produced, which means the powder can be used as a raw material for anisotropic magnets. The latest theory concerning the mechanism of microstructure refinement and crystal orientation is summarized in the literature by Hirokawa et al. (Horikawa T. et al., 2021). The maximum coercivity of the reported HDDR-processed Nd-Fe-B powder is 1.3 MA/m (Morimoto K. et al., 2003), and coercivity is improved to 1.6 MA/m by diffusing Cu at the grain boundaries in the subsequent

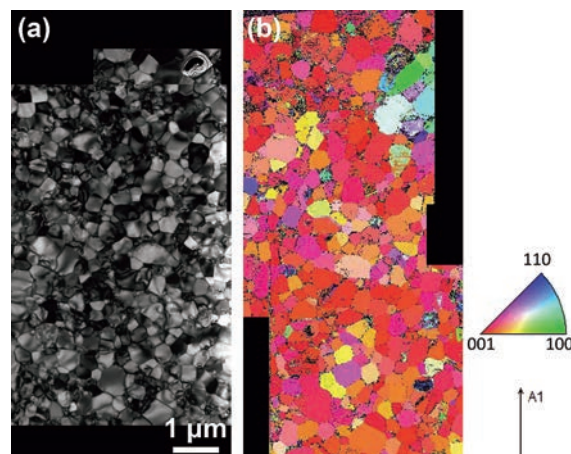


**Fig. 8** Typical microstructure of HDDR-treated Nd-Fe-B powder. (a) TEM-BF image and (b) inverse pole-figure map obtained by TEM-PED. Reprinted with permission from Ref. (Takizawa R. et al., 2017). Copyright: (2017) Elsevier B.V.

process (Sepehri-Amin H. et al., 2010).

HDDR can also be used to produce fine-grained Sm-Fe-N and Sm-Co powders with high coercivity. The internal crystal grain size of HDDR-processed  $\text{SmCo}_5$  powder has been refined to less than 100 nm, which achieved a huge coercivity exceeding 3 MA/m (Bulyk I.I. and Panasyuk V.V., 2012). While high coercivity of 1.4 MA/m has also been obtained with HDDR-processed  $\text{Sm}_2\text{Fe}_{17}\text{N}_3$  (Arlot R. et al., 1999), crystal orientation has not been realized in any of these alloy systems, and HDDR is currently effective only for Nd-Fe-B alloys. On the other hand, HDDR can also be used to synthesize fine-grained powders of  $\text{TbCu}_7$  type and  $\text{ThMn}_{12}$  type alloys (Dirba I. et al., 2019; Takagi K. et al., 2018), suggesting that it may be a very promising process, provided crystal orientation can be realized in alloys other than Nd-Fe-B in the future.

For  $\text{Sm}_2\text{Fe}_{17}\text{N}_3$ , a unique grain refinement method employing a nitrogen gas reaction is possible (Saito K. et al., 1994). When nitriding  $\text{Sm}_2\text{Fe}_{17}$  alloy powder, various  $\text{Sm}_2\text{Fe}_{17}\text{N}_x$  compound powders with different nitrogen content  $x$  can be obtained by tuning the nitriding conditions. While it is known that nitriding with a mixed gas of ammonia and hydrogen can overnitride the compound to a maximum nitrogen content of about  $x = 6$ , it is also known that the highest saturation magnetization and highest anisotropy are obtained when  $x = 3$ . Thus, optimally-nitrided  $\text{Sm}_2\text{Fe}_{17}\text{N}_3$  having a small diameter (typically, up to 3  $\mu\text{m}$ ) is used in permanent magnet applications.

Overnitriding  $\text{Sm}_2\text{Fe}_{17}\text{N}_x$  to the region of  $x > 3$  induces the interesting phenomenon of nanocrystalline cell formation. According to classical TEM results, this microstructure is composed of very fine nanocrystalline cells (30 to 100 nm) and amorphous cell walls dividing the individual cells. Several researchers have reported that this technique makes it possible to obtain reasonably high coercivity even

with coarse powders without reducing the particle size (Imaoka A. et al., 1998; Imaoka N. et al., 1995; Saito K. et al., 1994). In particular, in overnitridation treatment of Mn-added  $\text{Sm}_2\text{Fe}_{17}\text{N}_x$ , excess N and Mn were concentrated on the amorphous cell walls, resulting in the formation of domain walls. A maximum coercivity of about 0.7 MA/m was reportedly obtained by this approach. A group at Osaka University later reported that addition of Ti, V and Cr in addition to Mn had the same effect of increasing coercivity as Mn. A group at Sumitomo Metal Mining reported that a high-performance powder with  $(BH)_{\text{max}} = 175 \text{ kJ/m}^3$  was obtained with an  $\text{Sm}_2(\text{FeMn})_{17}\text{N}_x$  system by combining crushing treatment after overnitriding, and this powder was actually commercialized. Although the coercivity of the  $\text{Sm}_2\text{Fe}_{17}\text{N}_3$  powder produced by the pulverization method was drastically reduced when exposed to a high temperature environment of about 200 °C, it is noteworthy that the overnitrided coarse powder exhibited excellent thermal stability (Iseki T. et al., 2003; Ito M. et al., 2003; Ito M. et al., 2002; Majima K. et al., 1997; Ohmori K. et al., 2006).

The coercivity mechanism of optimally-nitrided  $\text{Sm}_2\text{Fe}_{17}\text{N}_3$  is normally classified as the nucleation-type, but in contrast, an analysis of the initial magnetization curves of the overnitrided  $\text{Sm}_2\text{Fe}_{17}\text{N}_x$  revealed that its coercivity mechanism is pinning-type (Imaoka et al., 1995). This viewpoint was later supported by the Lorenz microscopy, which directly captured the domain wall being pinned at the Mn- and N-enriched amorphous cell walls in the overnitrided  $\text{Sm}_2(\text{FeMn})_{17}\text{N}_x$ , as indicated in Fig. 9 (Kim J.J. et al., 2007; Yasuhara A. et al., 2005; Yasuhara A. et al., 2004).

As demonstrated above, while overnitriding method is an excellent approach for obtaining high coercivity magnetic powders, they have the disadvantage that residual magnetization decreases when the nitrogen content reaches  $x > 5$ , where coercivity increases. This decrease in remanence was originally thought to be caused by spontaneous rotation of the nanocrystalline cells after cell formation by overnitriding. Therefore, our group initially attempted to develop a new process that would make it possible to control the cell rotation during nitridation. We began by

investigating what actually occurs in  $\text{Sm}_2\text{Fe}_{17}\text{N}_x$  during overnitridation treatment. An interesting finding during this investigation was that the formation of this nanocell structure can be observed with a recent high-performance SEM which makes it possible to observe a very large field of view (Hosokawa A. and Takagi K., 2017; Hosokawa A. and Takagi K., 2018a). Coupling SEM and TEM enables multi-scale observation of the  $\text{Sm}_2\text{Fe}_{17}\text{N}_x$ , and it has been found that a large number of plate-shaped amorphous bands are generated and then form a ladder-like structure, as shown in Fig. 10. These amorphous bands eventually form a cell-like structure inside an initially single-crystalline coarse particle. Since this investigation also confirmed that the size of the cells decreases as the (local) nitrogen content increases, the degradation of residual magnetization is thought to be due simply to the increased amount of low magnetization amorphous regions (Hosokawa A. and Takagi K., 2017; Hosokawa A. and Takagi K., 2018a). This means that it is not necessary to control the rotation of the crystalline cells, and new, completely different guidelines are needed to improve this process.

## 2.3 Grain boundary engineering

### 2.3.1 Nd-Fe-B magnets

The only drawback of Nd-Fe-B magnets is their heat resistance. When used in an onboard vehicle motor, the operating temperature is as high as 150 to 200 °C, and coercivity is significantly reduced by heating. An effective solution to this problem, which will make it possible to withstand use in the high temperature automotive environment, is to increase the absolute value of coercivity or, alternatively, to reduce the temperature dependency of coercivity (temperature coefficient). Since no significant improvement in the temperature dependency of coercivity has been realized in Nd-Fe-B magnets, neodymium magnets which can withstand high-temperature use have been developed by increasing the absolute value of coercivity.

In order to increase coercivity, appropriate control in/around the grain boundary phase is required. A grain boundary diffusion method for this type of control has been

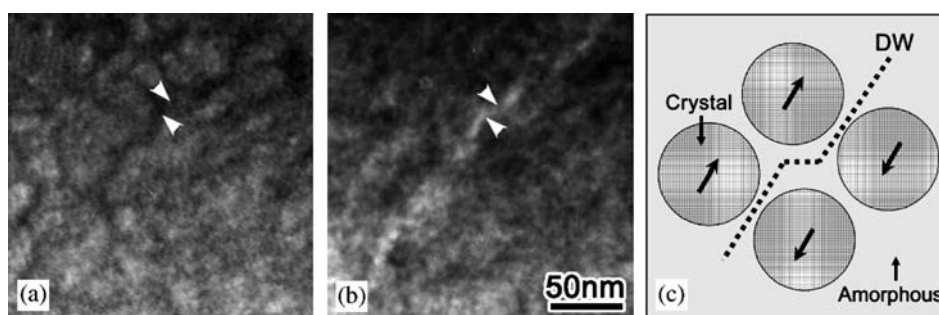
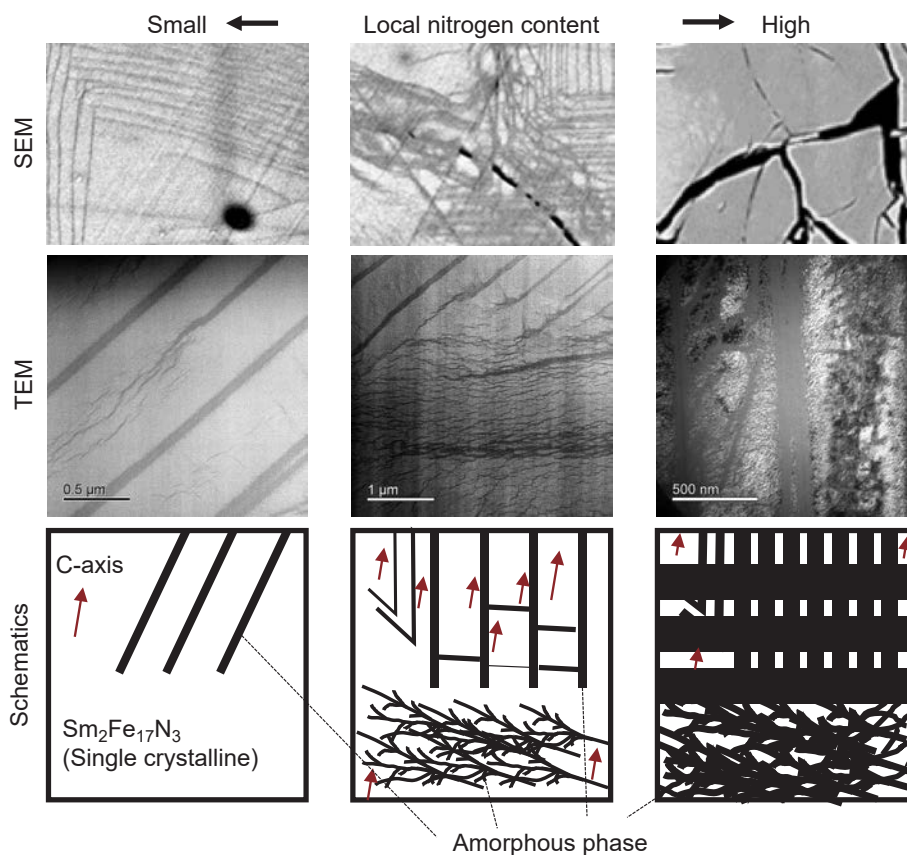


Fig. 9 (a) and (b) Domain wall pinning at amorphous boundaries captured by Lorenz microscopy and (c) schematic diagram of the pinning mechanism. Reprinted with permission from Ref. (Yasuhara A. et al., 2005). Copyright: (2005) Elsevier B.V.



**Fig. 10** Typical microstructural evolution during formation of cell structures. Reconstructed with permission from Ref. (Hosokawa A. and Takagi K., 2017). Copyright: (2017) Acta Materialia Inc. Published by Elsevier Ltd.

developed based on a report by Park et al. (Park K.T. et al., 2000). Since Nd-Fe-B magnets have a new creation-type coercivity mechanism, suppressing the formation of reverse magnetic domains on the surface of crystal particles is extremely effective for improving coercivity. Therefore, a (Nd-Dy/Tb)<sub>2</sub>Fe<sub>14</sub>B phase having a higher anisotropic magnetic field than the main Nd<sub>2</sub>Fe<sub>14</sub>B phase is formed only in the grain boundary by diffusion of Dy and Tb, resulting in a significant increase in coercivity. In particular, after preparing the sintered compact by the conventional process, metallic Dy and Tb or their oxide/fluoride are applied to the surface of the sintered compact and diffused at 800 to 900 °C. Because only the grain boundary phase becomes a liquid, diffusion of Dy and Tb is limited to the grain boundary.

Another technique for increasing coercivity is the low temperature eutectic alloy diffusion method, which can be mentioned as a method for increasing coercivity by controlling the grain boundary phase. In this method, magnetic decoupling between particles is induced by diffusing a low melting point eutectic alloy into the grain boundaries to increase the thickness of the grain boundary phase, which greatly improves coercivity. Many reports on this technology have appeared in connection with HDDR powders with fine crystal grains and heat-sensitive processed magnets, and significant improvement of coercivity has been

achieved. In particular, this method is very important for the development of high coercivity magnets which do not use the heavy rare earth elements Tb and Dy.

### 2.3.2 Sm-Fe-N magnets

The grain boundary diffusion method described in the previous section cannot be applied to Sm-Fe-N magnets because Sm-Fe-N is thermally decomposed below the diffusion treatment temperature of 800 to 900 °C. Therefore, different approaches are applied to grain boundary control of Sm-Fe-N magnets.

The oldest attempt of grain boundary control in the history of Sm-Fe-N development is the “metal-bonded magnet” proposed by Otani et al. (Otani Y. et al., 1991). Since Sm-Fe-N has a low decomposition temperature (Coe J.M.D. et al., 1991; Katter M. et al., 1992; Zhang D.T. et al., 2007), conventional sintering methods involving high temperature heating cannot be applied. Therefore, use of low melting point metals such as Sn, Bi, Zn, or Al as a binder was proposed to obtain a bulk magnet at a sufficiently low temperature (Huang M.Q. et al., 1991; Otani Y. et al., 1991). However, preparation of a metal-bonded magnet with a Zn bond led to the discovery Zn bonding significantly increases coercivity. As a result, much research has been devoted to Zn-bonded magnets as a technology for improving coercivity, but some critical problems were

discovered in the course of development. Specifically, although coercivity increases monotonically with the amount of Zn added, more than 20 wt% of Zn must be added to achieve coercivity on the order of 1 MA/m, as indicated in **Table 1** (Ito S. et al., 2004; Kuhrt C. et al., 1992; Otani Y. et al., 1991; Prabhu D. et al., 2012). However, the magnetic Sm-Fe-N phase is inevitably diluted by addition of Zn, resulting in a decrease in remanence, and it was also found that heavy Zn addition significantly deteriorates the squareness of the demagnetization curve (Kuhrt C. et al., 1992; Müller K.H. et al., 1996). Therefore, even if coercivity increases,  $(BH)_{\max}$  decreases.

The mechanism of coercivity improvement by Zn was initially attributed to soft magnetic  $\alpha$ -Fe crystallites on the particle surface, which remain as an impurity in the raw material preparation process (Kuhrt C. et al., 1992). In

addition, the non-magnetic  $\Gamma$ -FeZn reaction phase spreads to the grain boundaries and was believed to block the magnetic coupling between Sm-Fe-N grains (Wendhausen P.A.P. et al., 1993). Based on a study utilizing microstructural observation, Hiraga et al. explained that Zn reacts with the Sm-Fe-N main phase into the Sm-(Fe, Zn)-N phase on the surface of the grains, which smooths the grain surfaces, and the Sm-(Fe, Zn)-N phase isolates the by-product soft magnetic  $\alpha$ -FeZn from the main phase, thereby suppressing the formation of reverse magnetic domains (Hiraga K. et al., 1993). However, certain problems remain unsolved: In particular, this interpretation relies on the assumption that the Sm-(Fe, Zn)-N phase is non-magnetic, and it does not explain why squareness is significantly deteriorated. Recently, Matsuura et al. conducted more detailed microstructure observations (Matsuura M. et al., 2020) (**Fig. 11**),

**Table 1** Magnetic parameters of sintered samples for various heat treatment conditions. Reprinted with permission from Ref. (Prabhu D. et al., 2012). Copyright: (2012;) Elsevier B.V.

Zn conc. (wt %)	Coercivity and remanence for various heat-treatment conditions							
	As-sintered		425 °C/1 h		435 °C/1 h		450 °C/1 h	
	$\mu_0 H_c$ (T)	$B_r$ (T)	$\mu_0 H_c$ (T)	$B_r$ (T)	$\mu_0 H_c$ (T)	$B_r$ (T)	$\mu_0 H_c$ (T)	$B_r$ (T)
10	0.56	0.67	1.11	0.67	1.39	0.68	1.67	0.69
15	0.42	0.56	1.24	0.62	2.75	0.62	2.33	0.62
20	0.65	0.53	1.54	0.58	1.78	0.59	2.13	0.44

Magnetic properties of the initial SmFeN powder:  $\mu_0 H_c = 1.2$  T and  $\mu_0 M_s = 1.25$  T.

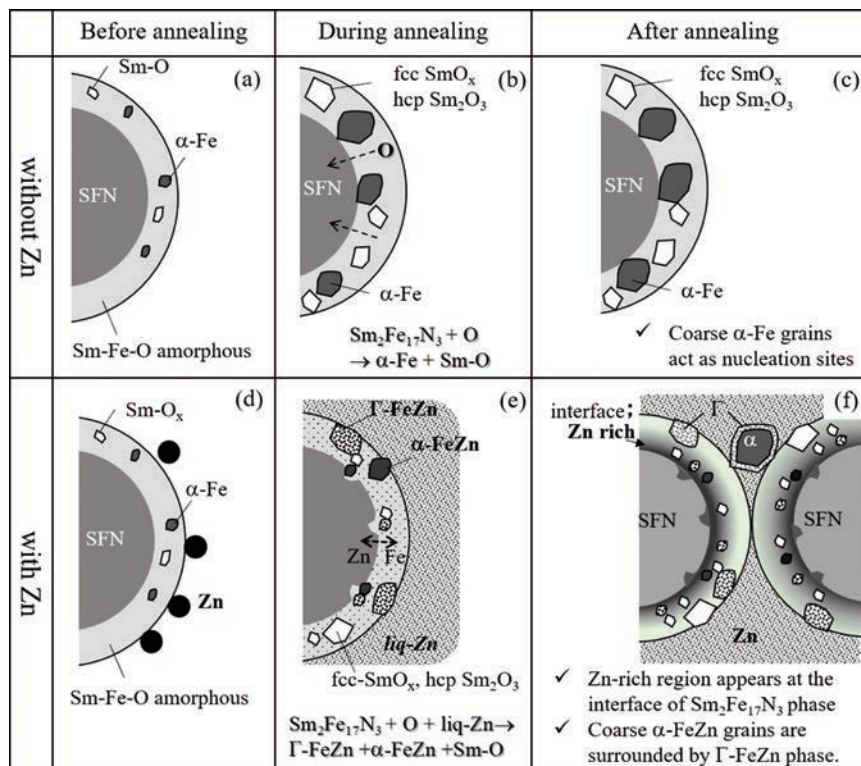


**Fig. 11** Schematic diagram of microstructural changes in Sm-Fe-N (SFN) bulk magnets during annealing. Reprinted with permission from Ref. (Matsuura M. et al., 2020). Copyright: (2020) Elsevier B.V.

and concluded that the non-magnetic  $\Gamma$ -FeZn phase surrounds the soft-magnetic  $\alpha$ -FeZn crystallites and breaks the magnetic coupling between the grains.

While the mechanism of improved coercivity by Zn is still unclear, the amount of Zn added should be reduced to suppress the harmful effects of Zn. In order to maximize the effect of Zn with limited addition, it will be necessary to form a thin layer of Zn at the grain boundaries, and this layer should be as thin and uniform as possible. Various thin-film and coating techniques such as vacuum deposition (Fukunaga H. et al., 1996; Makita K. and Hirosawa S., 1997) and photolysis of organic metal complexes (Arlot R. et al., 1997; Izumi H. et al., 1996; Machida K.-i. et al., 1995) have been applied to Sm-Fe-N powders for this purpose. Initial attempts showed meaningful improvements in thermal stability and oxidation resistance, but the improvement in coercivity was modest and coercivity remained inferior to the levels achieved by conventional processes. The problems of these thin-film approaches are considered to be two-fold: (1) Since the original purpose was metal bonding, the research target was biased toward low melting point metals. However, now that other low-temperature consolidation techniques are available, the scope of research should be extended to materials with higher melting points (Imaoka N. et al., 2008; Saito T. et al., 2017). (2) The direct effect on the Sm-Fe-N main phase could not be investigated because the added metals were not in direct contact with the magnetic phase, but were in contact with non-magnetic surface oxides. Thus, a process for forming a coating on a surface without an oxide film can be expected to have a higher coercivity improvement effect with a small amount of Zn addition.

Recent efforts to implement these two approaches simultaneously include a combination of powder coating

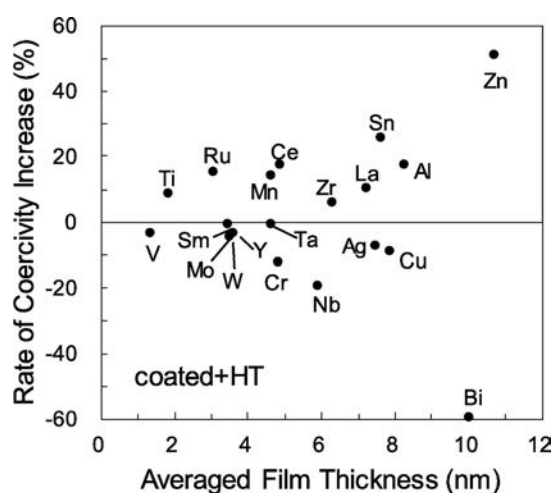


**Fig. 12** Effects of sputter coating of 20 nonmagnetic metals on surface oxide-free  $\text{Sm}_2\text{Fe}_{17}\text{N}_3$  powders on coercivity. The powders were heat treated at 500 °C for 2 min after coating. Reprinted with permission from Ref. (Yamaguchi W. and Takagi K., 2020). Copyright: (2020) Elsevier B.V.

technology with the low oxygen powder metallurgy process. Sm-Fe-N fine powder without a surface oxide film is produced by pulverization in a low oxygen atmosphere, followed by sputter-coating with continuous stirring (Yamaguchi W. et al., 2020). This is a highly versatile powder coating technique which is capable of forming a direct metal-metal interface, and it can also form a thin and uniform film even on a material with a high melting point. Yamaguchi et al. used this technique to coat Sm-Fe-N powder with 20 kinds of non-magnetic metal elements, and found that, in addition to Zn, addition of metals such as Al, Sn and Ce is also effective for improving coercivity as indicated in Fig. 12 (Yamaguchi W. and Takagi K., 2020). Matsuura et al. also succeeded in producing a Zn-added Sm-Fe-N anisotropic sintered magnet with  $(BH)_{\text{max}} = 179 \text{ kJ/m}^3$  by a similar coating technique (Matsuura M. et al., 2018).

### 3. Powder technologies for enhancement of remanence

#### 3.1 Hot deformation techniques

To produce a sintered magnet with high residual magnetization, it is important to produce a green compact in which the easy axis of magnetization of the crystal grains is aligned in one direction and to achieve the highest possible densification of the compact by sintering. In addition, as described above, it is also essential to construct a fine grain structure for high coercivity. Since all these simultaneous improvements have become saturated in the conventional powder metallurgy process consisting of magnetic-aligned compaction and atmospheric sintering, the hot deformation process has attracted attention as a new process.

Lee reported that an anisotropic magnet with the easy axis oriented in the press direction was obtained when a sintered compact produced from Nd-Fe-B melt-spun powder was upset at an elevated temperature (Lee R.W., 1985). Mishra and Lee observed hot-deformed anisotropic magnets by TEM and found that the grains were significantly flattened in shape and all the crystal grains were oriented in the  $c$ -axis // press direction (Mishra R.K. and Lee R.W., 1986; Sephiri-Amin H. et al., 2013) as shown in Fig. 13. Since that time, intensive research has been carried out, and magnets with  $(BH)_{\text{max}}$  exceeding  $350 \text{ kJ/m}^3$  have been reported (Mishra R.K., 1987; 1989; Mishra R.K. et al., 1988; Mishra R.K. et al., 1990; Mishra R.K. et al., 1993). The formation of this oriented microstructure is not the result of a deformation texture mechanism, but a unique mechanism involving liquid phase formation of an Nd-rich phase at the grain boundaries in the hot working temperature range (Grunberger W. et al., 1997). When the grain boundary phase is liquified at the hot deformation temperature, diffusion between the main phase and the liquid phase becomes extremely active. At this time, high stress is generated in the direction of uniaxial compressive stress, that is, in the

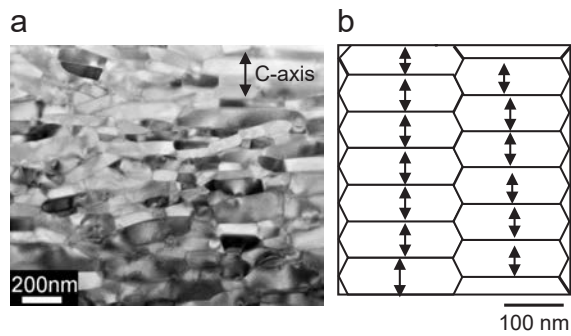


**Fig. 13** (a) Typical microstructure of highly textured nanocrystalline structure after die-upsetting and (b) schematic diagram. Reprinted with permission from Ref. (Sepehri-Amin H. et al., 2013). Copyright: (2013) Acta Materialia Inc. Published by Elsevier Ltd.

vertical direction of the crystal grains, while stress is low in the lateral direction. “Dissolution” is promoted at this high-stress location, the substance moves toward the low-stress location through the liquid phase, “reprecipitation” occurs, and as a result, the above-mentioned oriented microstructure is formed (Pharr G.M. and Ashby M.F., 1983; Raj R. and Chyung C.K., 1981; Wakai F., 1994). What is important here is that when a liquid phase grain boundary exists between  $\text{Nd}_2\text{Fe}_{14}\text{B}$  main phases with a highly anisotropic crystal structure, the rate of dissolution-reprecipitation changes greatly depending on the crystal orientation. In the Nd-Fe-B phase, it is generally thought that only specific crystal grains having an azimuth relationship of stress axis // c axis grow preferentially in the ab axis direction, and an oriented structure is obtained.

Daido Steel succeeded in commercializing hot-deformed magnets (Akiya T. et al., 2014a; b; Liu J. et al., 2014). Another advantage of hot-deformed magnets is that they tend to have improved thermal resistance since the thermal stability of coercivity increases as the crystal grain size decreases. In this connection, studies on hot-worked magnets of the  $\text{ThMn}_{12}$  type using Sm as the main raw material have been reported recently (Schonhobel A.M. et al., 2020; Schonhobel A.M. et al., 2019).

### 3.2 Low-thermal load consolidation

As mentioned in 2-3-2, Nd-Fe-B alloys and Sm-Co alloys can be sintered by high temperature heating, but Sm-Fe-N alloys are thermally decomposed at about 620 °C, making it difficult to produce bulk magnets by sintering. In addition, non-equilibrium alloys such as the  $\text{TbCu}_7$  type and  $\text{ThMn}_{12}$  type also transform to a stable phase at high temperatures, so consolidation in a low thermal load environment is considered necessary. Therefore, various low thermal load sintering techniques have been examined for these alloys. Spark plasma sintering (SPS) is a hot-pressing process with rapid heating, and has been applied to  $\text{Sm}_2\text{Fe}_{17}\text{N}_3$  alloys and metastable alloys such as  $\text{TbCu}_7$  type Sm-Fe-N alloys (Saito T., 2008; Zhang D.T.

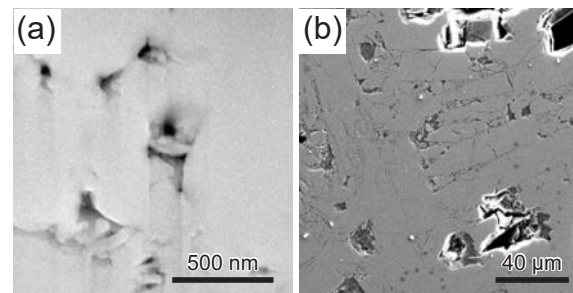


**Fig. 14** Cross-sectional SEM images of (a)  $\text{Sm}_2\text{Fe}_{17}\text{N}_3$  anisotropic sintered magnet and (b)  $\text{TbCu}_7$  type Sm-Fe-N isotropic sintered magnet produced by high-pressure current sintering. Reprinted with permission from Ref. (Takagi K. et al., 2012c; Takagi K. et al., 2020). Copyright: (2012; 2020) Elsevier B.V.

et al., 2007). Although these materials cannot be heated to high temperatures, these studies have demonstrated that sintered magnets with a relative density of more than 90 % can be obtained without degrading the magnetic properties of the powder by sintering at a high pressure exceeding 1000 MPa as shown in Fig. 14 (Nakayama H. et al., 2012; Saito T., 2008; Takagi K. et al., 2012a; Takagi K. et al., 2012b; Takagi K. et al., 2020). In particular, Matsuura et al. and Takagi et al. used a low oxygen powder metallurgy process combined with SPS to perform sintering without decreasing coercivity due to surface oxidation, and achieved  $(BH)_{\text{max}}$  exceeding 190 kJ/m<sup>3</sup>, which is the highest value reported for a  $\text{Sm}_2\text{Fe}_{17}\text{N}_3$  sintered magnet (Matsuura M. et al., 2018; Takagi K. et al., 2020).

Prototype bulk magnets using non-heat forming processes such as shear compression (Saito T. et al., 2005; Saito T. and Kitazima H., 2011; Saito T. and Sato H., 2006; Saito T. et al., 2006) and shock consolidation (Mashimo T. et al., 2000; Mashimo T. et al., 1999) have been reported, and recently, the authors also conducted research that refocuses on powder rolling (Hosokawa A. et al., 2021b). A method called high-pressure torsion processing has also attracted attention in recent years (Edalati K. and Horita Z., 2016; Valiev R.Z. et al., 2000). A schematic illustration of high-pressure torsion is shown in Fig. 15. Since permanent magnets are generally brittle, it is not possible to apply huge strain by shear deformation by ordinary methods. However, high-pressure torsion makes it possible to apply huge shear strain without breaking brittle materials thanks to hydrostatic stress (Hosokawa A. et al., 2014a; Hosokawa A. et al., 2014b). Recently, many applications of this technique to permanent magnet materials have been reported (Gorshenkov M.V. et al., 2020; Popov A.G. et al., 2006; Shchetinin I.V. et al., 2020; Straumal B.B. et al., 2015). It has also been reported that Nd-Fe-B powder can be consolidated without heating by applying a huge strain exceeding 10 in shear strain, and as a result, the internal structure of the magnet can be improved as shown in Fig. 15(b) (Hosokawa A. and Takagi K., 2018b; Hosokawa A. et al.,

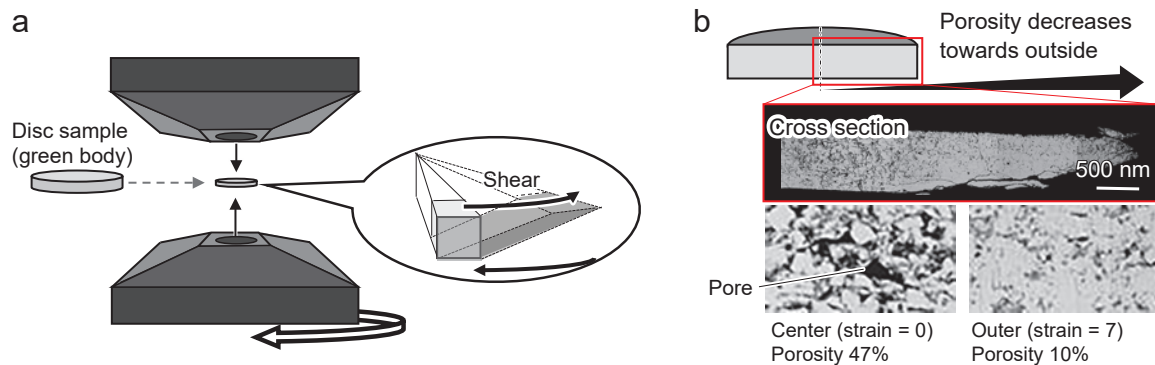


**Fig. 15** Schematic illustration of high-pressure torsion process. (a) The deformation mode at the perimeter region is essentially simple shear. (b) Example of densification by high-pressure torsion captured by SEM. Porosity decreases with the distance from the center.

2019). Although mass production cannot be expected by the high-pressure torsion route, research in this direction is needed in order to obtain clues for envisioning a new process that utilizes shear processing without relying on high-temperature heating.

#### 4. Concluding remarks

In order to improve the efficiency of electric motors, continuous improvement of the performance of the rare earth magnets which are their core component is essential. Research on conventional Nd-Fe-B magnets has provided design guidelines for control of the internal microstructure of sintered magnets, such as grain refinement, nanoscale grain boundary control and crystal orientation, to improve the performance of rare earth permanent magnets, and an advanced powder metallurgy process which can efficiently achieve these types of control is being developed. Especially in recent years, process development for Sm-Fe-N magnets and metastable phase magnets as next-generation magnets has become important. In order to improve coercivity, it is necessary to refine the crystal grain size, and for that purpose, refinement of the raw powder is being studied. Research on pulverization is evolving from traditional pulverization approaches such as jet milling to chemical/physical synthesis methods such as the reduction diffusion (R-D) method and the thermal plasma method, and the submicron- and nano-sized Sm-Fe-N powder obtained by these methods have achieved huge coercivity of 2.5 MA/m. Methods for synthesizing nanopolycrystalline powders using gas reactions such as the HDDR method and the overnitriding method have also been examined, and crystal-oriented ultrafine polycrystalline powders have been synthesized successfully. In Nd-Fe-B magnets, it has been found that, in addition to grain refinement, grain boundary phase control is also very effective in improving coercivity. Recently, grain boundary control of Sm-Fe-N sintered magnets by sputter coating on the powder surface has been investigated, and a new grain boundary phase has been proposed. To improve remanence, uniaxial orientation technology for crystal grains and high-density sintering

technology are indispensable. Especially for Sm-Fe-N magnets and metastable phase magnets, which have low thermal stability, new low thermal load consolidation techniques such as rapid hot pressing and large-strain consolidation are being developed. However, for practical use of next-generation magnets, it will be necessary to develop a powder consolidation technique that enables higher densification.

#### References

- Abbas N., Li Y., Ding J.-z., Liu J.P., Luo H.-b., Du J., Xia W.-x., Yan A., Wang F., Zhang J., A facile synthesis of directly gas-phase ordered high anisotropic SmCo based non-segregated nanoalloys by cluster beam deposition method, *Materials & Design*, 181 (2019) 108052. DOI: 10.1016/j.matdes.2019.108052
- Akdogan N.G., Hadjipanayis G.C., Sellmyer D.J., Anisotropic Sm-(Co,Fe) nanoparticles by surfactant-assisted ball milling, *Journal of Applied Physics*, 105 (2009). DOI: 10.1063/1.3067851
- Akiya T., Liu J., Sepehri-Amin H., Ohkubo T., Hioki K., Hattori A., Hono K., High-coercivity hot-deformed Nd-Fe-B permanent magnets processed by Nd-Cu eutectic diffusion under expansion constraint, *Scripta Materialia*, 81 (2014a) 48–51. DOI: 10.1016/j.scriptamat.2014.03.002
- Akiya T., Liu J., Sepehri-Amin H., Ohkubo T., Hioki K., Hattori A., Hono K., Low temperature diffusion process using rare earth-Cu eutectic alloys for hot-deformed Nd-Fe-B bulk magnets, *Journal of Applied Physics*, 115 (2014b) 17a766. DOI: 10.1063/1.4869062
- Arlot R., de Rango P., Fruchart D., Soubeyroux J.L., de la Bathie R.P., High coercive Sm-Fe-Co-N powder prepared by applying the HDDR process, *International Journal of Hydrogen Energy*, 24 (1999) 661–664. DOI: 10.1016/S0360-3199(98)00116-5
- Arlot R., Izumi H., Machida K., Fruchart D., Adachi G., Particle size dependence of the magnetic properties for zinc-coated  $\text{Sm}_2(\text{Fe}_{0.9}\text{Co}_{0.1})_{17}\text{N}_{2.9}$  powders, *Journal of Magnetism and Magnetic Materials*, 172 (1997) 119–127. DOI: 10.1016/S0304-8853(97)00105-4
- Balamurugan B., Skomski R., Li X.Z., Hadjipanayis G.C., Sellmyer D.J., Magnetism of directly ordered Sm-Co clusters, *Journal of Applied Physics*, 111 (2012) 07B527. DOI: 10.1063/1.3677668
- Balasubramanian B., Skomski R., Li X., Valloppilly S.R., Shield J.E., Hadjipanayis G.C., Sellmyer D.J., Cluster synthesis

- and direct ordering of rare-earth transition-metal nanomagnets, *Nano Letters*, 11 (2011) 1747–1752. DOI: 10.1021/nl200311w
- Bulyk I.I., Panasyuk V.V., Hydrogen as a technological medium for the formation of nanostructures in Sm–Co ferromagnetic alloys, *Materials Science*, 48 (2012) 1–11. DOI: 10.1007/s11003-012-9466-1
- Cech R.E., Rare earth intermetallic compounds by a calcium hydride reduction-diffusion process, US Patent, (1973) US 3748193.
- Cech R.E., Cobalt-rare earth intermetallic compounds produced by calcium hydride reduction of oxides, *JOM*, 26 (1974) 32–35. DOI: 10.1007/BF03355863
- Chakka V.M., Altuncevahir B., Jin Z.Q., Li Y., Liu J.P., Magnetic nanoparticles produced by surfactant-assisted ball milling, *Journal of Applied Physics*, 99 (2006). DOI: 10.1063/1.2170593
- Coehoorn R., Demooij D.B., Dewaard C., Meltspun permanent-magnet materials containing Fe<sub>3</sub>B as the main phase, *Journal of Magnetism and Magnetic Materials*, 80 (1989) 101–104. DOI: 10.1016/0304-8853(89)90333-8
- Coey J.M.D., Lawler J.F., Sun H., Allan J.E.M., Nitrogenation of R<sub>2</sub>Fe<sub>17</sub> compounds: R=rare earth, *Journal of Applied Physics*, 69 (1991) 3007–3010. DOI: 10.1063/1.348614
- Croat J.J., Permanent-magnet properties of rapidly quenched rare earth-iron alloys, *IEEE Transactions on Magnetics*, 18 (1982) 1442–1447. DOI: 10.1109/Tmag.1982.1061972
- Cui W.B., Sepehri-Amin H., Takahashi Y.K., Hono K., Hard magnetic properties of spacer-layer-tuned NdFeB/Ta/Fe nanocomposite films, *Acta Materialia*, 84 (2015) 405–412. DOI: 10.1016/j.actamat.2014.10.008
- Dirba I., Sepehri-Amin H., Ohkubo T., Hono K., Development of ultra-fine grain sized SmFe<sub>12</sub>-based powders using hydrogenation disproportionation desorption recombination process, *Acta Materialia*, 165 (2019) 373–380. DOI: 10.1016/j.actamat.2018.11.065
- Dong Y., Zhang T., Xia Z., Wang H., Ma Z., Liu X., Xia W., Coey J.M.D., Jiang C., Dispersible SmCo<sub>5</sub> nanoparticles with huge coercivity, *Nanoscale*, 11 (2019) 16962–16967. DOI: 10.1039/c9nr06653e
- Edalati K., Horita Z., A review on high-pressure torsion (HPT) from 1935 to 1988, *Materials Science and Engineering: A*, 652 (2016) 325–352. DOI: 10.1016/j.msea.2015.11.074
- Fukunaga H., Aikawa T., Nagaoka S., Kanai Y., Improvement in hard magnetic properties of rapidly quenched Sm–Fe–N flakes by Zn-coating, *Journal of Magnetism and Magnetic Materials*, 157–158 (1996) 105–106. DOI: 10.1016/0304-8853(95)01074-2
- Gabay A.M., Hadjipanayis G.C., High-coercivity ThMn<sub>12</sub>-type monocrystalline Sm–Zr–Fe–Co–Ti particles by high-temperature reduction diffusion, *Scripta Materialia*, 196 (2021) 113760. DOI: 10.1016/j.scriptamat.2021.113760
- Gorshenkov M.V., Karpenkov D.Y., Sundeev R.V., Cheverikin V.V., Shchetinin I.V., Magnetic properties of Mn–Al alloy after HPT deformation, *Materials Letters*, 272 (2020) 127864. DOI: 10.1016/j.matlet.2020.127864
- Grunberger W., Hinz D., Kirchner A., Muller K.H., Schultz L., Hot deformation of nanocrystalline Nd–Fe–B alloys, *IEEE Transactions on Magnetics*, 33 (1997) 3889–3891. DOI: 10.1109/20.619605
- Guo Y., You J., Pei W., Qu Y., Zhao D., Yang Z., Effect of (C<sub>2</sub>H<sub>5</sub>)<sub>3</sub>NBH<sub>3</sub> content on microstructure and properties of Nd–Fe–B nanoparticles prepared by chemical and reduction-diffusion method, *Journal of Alloys and Compounds*, 777 (2019) 850–859. DOI: 10.1016/j.jallcom.2018.10.398
- He S., Jing Y., Wang J.-P., Direct synthesis of large size ferromagnetic SmCo<sub>5</sub> nanoparticles by a gas-phase condensation method, *Journal of Applied Physics*, 113 (2013) 134310. DOI: 10.1063/1.4798475
- Hiraga K., Okamoto K., Iriyama T., Microstructure of zinc-bonded Sm<sub>2</sub>Fe<sub>17</sub>N<sub>3</sub> permanent magnet studied by transmission and analytical electron microscopy, *Materials Transactions, JIM*, 34 (1993) 569–571. DOI: 10.2320/matertrans1989.34.569
- Hirayama Y., Panda A.K., Ohkubo T., Hono K., High coercivity Sm<sub>2</sub>Fe<sub>17</sub>N<sub>3</sub> submicron size powder prepared by polymerized-complex and reduction–diffusion process, *Scripta Materialia*, 120 (2016) 27–30. DOI: 10.1016/j.scriptamat.2016.03.028
- Hirayama Y., Shigeta M., Liu Z., Yodoshi N., Hosokawa A., Takagi K., Anisotropic Nd–Fe ultrafine particles with stable and metastable phases prepared by induction thermal plasma, *Journal of Alloys and Compounds*, 873 (2021) 159724. DOI: 10.1016/j.jallcom.2021.159724
- Hirayama Y., Suzuki K., Yamaguchi W., Takagi K., Cold welding behavior of fine bare aluminum powders prepared by new low oxygen induction thermal plasma system, *Journal of Alloys and Compounds*, 768 (2018) 608–612. DOI: 10.1016/j.jallcom.2018.07.275
- Hirayama Y., Takagi K., Evaluation of compositional homogeneity of Fe–Co alloy nanoparticles prepared by thermal plasma synthesis, *Journal of Alloys and Compounds*, 792 (2019) 594–598. DOI: 10.1016/j.jallcom.2019.04.083
- Hirayama Y., Takahashi Y.K., Hirosawa S., Hono K., NdFe<sub>12</sub>N hard-magnetic compound with high magnetization and anisotropy field, *Scripta Materialia*, 95 (2015) 70–72. DOI: 10.1016/j.scriptamat.2014.10.016
- Hirayama Y., Takahashi Y.K., Hirosawa S., Hono K., Intrinsic hard magnetic properties of Sm(Fe<sub>1-x</sub>Co<sub>x</sub>)<sub>12</sub> compound with the ThMn<sub>12</sub> structure, *Scripta Materialia*, 138 (2017) 62–65. DOI: 10.1016/j.scriptamat.2017.05.029
- Hirosawa S., Kanekiyo H., Nanostructure and magnetic properties of chromium-doped Fe<sub>3</sub>B–Nd<sub>2</sub>Fe<sub>14</sub>B exchange-coupled permanent magnets, *Materials Science and Engineering: A*, 217 (1996) 367–370. DOI: 10.1016/S0921-5093(96)10284-7
- Hirosawa S., Shigemoto Y., Miyoshi T., Kanekiyo H., Direct formation of Fe<sub>3</sub>B/Nd<sub>2</sub>Fe<sub>14</sub>B nanocomposite permanent magnets in rapid solidification, *Scripta Materialia*, 48 (2003) 839–844. DOI: 10.1016/S1359-6462(02)00620-6
- Horikawa T., Yamazaki M., Matsuura M., Sugimoto S., Recent progress in the development of high-performance bonded magnets using rare earth–Fe compounds, *Science and Technology of Advanced Materials*, 22 (2021) 729–747. DOI: 10.1080/14686996.2021.1944780
- Horiuchi Y., Hagiwara M., Endo M., Sanada N., Sakurada S., Influence of intermediate-heat treatment on the structure and magnetic properties of iron-rich Sm(CoFeCuZr)(Z) sintered magnets, *Journal of Applied Physics*, 117 (2015) 17c704. DOI: 10.1063/1.4906757
- Horiuchi Y., Hagiwara M., Okamoto K., Kobayashi T., Endo M., Kobayashi T., Sanada N., Sakurada S., Effect of pre-aging treatment on the microstructure and magnetic properties of Sm(Co,Fe,Cu,Zr)<sub>7,8</sub> sintered magnets, *Materials Transactions*, 55 (2014) 482–488. DOI: 10.2320/matertrans.MBW201325
- Hosokawa A., Ii S., Tsuchiya K., Work hardening and microstructural development during high-pressure torsion in pure iron, *Materials Transactions*, 55 (2014a) 1097–1103. DOI: 10.2320/matertrans.M2013462
- Hosokawa A., Ohtsuka H., Li T.T., Ii S., Tsuchiya K., Microstructure and magnetic properties in nanostructured Fe



- and Fe-based intermetallics produced by high-pressure torsion, *Materials Transactions*, 55 (2014b) 1286–1291. DOI: 10.2320/matertrans.M2014119
- Hosokawa A., Takagi K., The formation mechanism of the nano-crystalline cells in  $\text{Sm}_2\text{Fe}_{17}\text{N}_x$  powder during overnitridation, *Acta Materialia*, 136 (2017) 366–377. DOI: 10.1016/j.actamat.2017.07.019
- Hosokawa A., Takagi K., Multi-scale electron microscopy of overnitrided Sm-Fe-Mn-N powder, *AIP Advances*, 8 (2018a) 055031. DOI: 10.1063/1.5036670
- Hosokawa A., Takagi K., Powder consolidation of Nd-Fe-B/ $\alpha$ -Fe nanocomposite materials by cold deformation process, *AIP Advances*, 8 (2018b) 095019. DOI: 10.1063/1.5045797
- Hosokawa A., Takagi K., Anisotropic nanocomposite Nd-Fe-B magnets produced by hot deformation with assistance of Nd-Cu, *Journal of Magnetism and Magnetic Materials*, 489 (2019) 165453. DOI: 10.1016/j.jmmm.2019.165453
- Hosokawa A., Takagi K., Kuriwa T., Inoue Y., Ozaki K., Severe plastic deformation of Nd-Fe-B nanocomposite magnets at room temperature, *Journal of Magnetism and Magnetic Materials*, 473 (2019) 51–60. DOI: 10.1016/j.jmmm.2018.10.032
- Hosokawa A., Yamaguchi W., Suzuki K., Takagi K., Influences of microstructure on macroscopic crystallinity and magnetic properties of Sm-Fe-N fine powder produced by jet-milling, *Journal of Alloys and Compounds*, 869 (2021a). DOI: 10.1016/j.jallcom.2021.159288
- Hosokawa A., Yoneyama N., Nakanowatari I., Eguchi H., Takagi K., Production of anisotropic Sm-Fe-N magnet sheets by modified powder rolling, *Materials Letters*, 294 (2021b) 129815. DOI: 10.1016/j.matlet.2021.129815
- Huang M.Q., Zhang L.Y., Ma B.M., Zheng Y., Elbicki J.M., Wallace W.E., Sankar S.G., Metal-bonded  $\text{Sm}_2\text{Fe}_{17}\text{-N}$ -type magnets, *Journal of Applied Physics*, 70 (1991) 6027–6029. DOI: 10.1063/1.350082
- Imaoka A., Okamoto A., Kato H., Ohsuna T., Hiraga K., Motokawa M., Magnetic properties and microstructure of Mn-substituted  $\text{Sm}_2(\text{Fe},\text{Mn})_{17}\text{N}_x$ , *Journal of the Magnetism Society of Japan*, 22 (1998) 353–356.
- Imaoka N., Iriyama T., Itoh S., Okamoto A., Katsumata T., Effect of Mn addition to Sm-Fe-N magnets on the thermal-stability of coercivity, *Journal of Alloys and Compounds*, 222 (1995) 73–77. DOI: 10.1016/0925-8388(94)04920-3
- Imaoka N., Koyama Y., Nakao T., Nakaoka S., Yamaguchi T., Kakimoto E., Tada M., Nakagawa T., Abe M., High electrical resistance composite magnets of  $\text{Sm}_2\text{Fe}_{17}\text{N}_3$  powders coated with ferrite layer for high frequency applications, *Journal of Applied Physics*, 103 (2008) 07E129. DOI: 10.1063/1.2832864
- Iseki T., Ishikawa T., Kawamoto A., Omori K., Study of SmFeMn magnets, *Journal of the Japan Society of Powder and Powder Metallurgy*, 50 (2003) 633–635. DOI: 10.2497/jjspm.50.633
- Ito M., Majima K., Shimuta T., Katsuyama S., Effects of partial substitution of V and Ti for Fe on nitrogenation rate and magnetic properties of  $\text{Sm}_2\text{Fe}_{17}\text{N}_x$  anisotropic coarse powders, *Journal of Alloys and Compounds*, 349 (2003) 334–340. DOI: 10.1016/s0925-8388(02)00913-1
- Ito M., Majima K., Shimuta T., Katsuyama S., Nagai H., Magnetic properties of  $\text{Sm}_2(\text{Fe}_{0.95}\text{M}_{0.05})_{17}\text{N}_x$  (M=Cr and Mn) anisotropic coarse powders with high coercivity, *Journal of Applied Physics*, 92 (2002) 2641. DOI: 10.1063/1.1498880
- Ito S., Kikuchi M., Fujii T., Ishikawa T., HIP sintering and magnetic properties of  $\text{Sm}_2\text{Fe}_{17}\text{N}_3$  with Zn additive, *Journal of Magnetism and Magnetic Materials*, 270 (2004) 15–21. DOI: 10.1016/j.jmmm.2003.07.003
- Izumi H., Machida K.-i., Shiomi A., Iguchi M., Adachi G.-y., High-performance characteristics of bonded magnets produced using  $\text{Sm}_2\text{Fe}_{17}\text{N}_x$  powder stabilized by photoinduced zinc metal coating, *Japanese Journal of Applied Physics*, 35 (1996) L894–L896. DOI: 10.1143/jjap.35.L894
- Jeong J.H., Ma H.X., Kim D., Kim C.W., Kim I.H., Ahn J.W., Kim D.S., Kang Y.S., Chemical synthesis of  $\text{Nd}_2\text{Fe}_{14}\text{B}$  hard phase magnetic nanoparticles with an enhanced coercivity value: effect of  $\text{CaH}_2$  amount on the magnetic properties, *New Journal of Chemistry*, 40 (2016) 10181–10186. DOI: 10.1039/C6NJ02436J
- Jin Z.-q., Sun X.K., Liu W., Zhao X.-g., Xiao Q.-f., Sui Y.-c., Zhang Z.-d., Wang Z.-g., Qin H.-x., Dependence of magnetic properties on microstructure in mechanically alloyed Nd-Fe-Ti-N, *Journal of Magnetism and Magnetic Materials*, 169 (1997) 135–144. DOI: 10.1016/s0304-8853(96)00732-9
- Katter M., Wecker J., Kuhrt C., Schultz L., Grossinger R., Magnetic-properties and thermal-stability of  $\text{Sm}_2\text{Fe}_{17}\text{N}_3$  with intermediate nitrogen concentrations, *Journal of Magnetism and Magnetic Materials*, 117 (1992) 419–427. DOI: 10.1016/0304-8853(92)90099-a
- Katter M., Wecker J., Schultz L., Structural and hard magnetic-properties of rapidly solidified Sm-Fe-N, *Journal of Applied Physics*, 70 (1991) 3188–3196. DOI: 10.1063/1.349302
- Kim D., Hirayama Y., Liu Z., Kwon H., Kobashi M., Takagi K., Highly conductive Al/Al interfaces in ultrafine grained Al compact prepared by low oxygen powder metallurgy technique, *Nanomaterials*, 11 (2021) 1182. DOI: 10.3390/nano11051182
- Kim J.J., Park H.S., Shindo D., Iseki T., Oshimura N., Ishikawa T., Ohmori K., Magnetic domain structure and magnetic hardening in Sm-Fe-Mn-N coarse powder, *Materials Transactions*, 48 (2007) 2606–2611. DOI: 10.2320/matertrans.MD200702
- Kneller E.F., Hawig R., The exchange-spring magnet—a new material principle for permanent-magnets, *IEEE Transactions on Magnetics*, 27 (1991) 3588–3600. DOI: 10.1109/20.102931
- Kuhrt C., O'Donnell K., Katter M., Wecker J., Schnitzke K., Schultz L., Pressure-assisted zinc bonding of microcrystalline  $\text{Sm}_2\text{Fe}_{17}\text{N}_x$  powders, *Applied Physics Letters*, 60 (1992) 3316–3318. DOI: 10.1063/1.106678
- Landi G.T., Santos A.D., High-density gas aggregation nanoparticle gun applied to the production of SmCo clusters, *Journal of Materials Science*, 45 (2010) 4906–4911. DOI: 10.1007/s10853-010-4271-4
- Lee R.W., Hot-pressed neodymium-iron-boron magnets, *Applied Physics Letters*, 46 (1985) 790. DOI: 10.1063/1.95884
- Li C., Wu Q., Ma Z., Xu H., Cong L., Yue M., A novel strategy to synthesize anisotropic  $\text{SmCo}_5$  particles from  $\text{Co/Sm(OH)}_3$  composites with special morphology, *Journal of Materials Chemistry C*, 6 (2018) 8522–8527. DOI: 10.1039/c8tc02048e
- Liu J., Sepehri-Amin H., Ohkubo T., Hioki K., Hattori A., Hono K., Microstructure evolution of hot-deformed Nd-Fe-B anisotropic magnets, *Journal of Applied Physics*, 115 (2014) 17A744. DOI: 10.1063/1.4867960
- Ma Z.-H., Zhang T.-L., Wang H., Jiang C.-B., Synthesis of  $\text{SmCo}_5$  nanoparticles with small size and high performance by hydrogenation technique, *Rare Metals*, 37 (2017) 1021–1026. DOI: 10.1007/s12598-016-0873-6
- Ma Z.-H., Zhang T.-L., Wang H., Jiang C.-B., Synthesis of  $\text{SmCo}_5$  nanoparticles with small size and high performance by hydrogenation technique, *Rare Metals*, 37 (2018) 1021–1026. DOI: 10.1007/s12598-016-0873-6

- Ma Z., Liang J., Ma W., Cong L., Wu Q., Yue M., Chemically synthesized anisotropic  $\text{SmCo}_5$  nanomagnets with a large energy product, *Nanoscale*, 11 (2019a) 12484–12488. DOI: 10.1039/C9NR03412A
- Ma Z., Tian H., Cong L., Wu Q., Yue M., Sun S., A flame-reaction method for the large-scale synthesis of high-performance  $\text{Sm}_x\text{Co}_y$  nanomagnets, *Angewandte Chemie, International Edition in English*, 58 (2019b) 14509–14512. DOI: 10.1002/anie.201907763
- Ma Z., Tian H., Cong L., Wu Q., Yue M., Sun S., A flame-reaction method for the large-scale synthesis of high-performance  $\text{Sm}_x\text{Co}_y$  nanomagnets, *Angewandte Chemie International Edition*, 58 (2019c) 14509–14512. DOI: 10.1002/anie.201907763
- Ma Z., Zhang T., Jiang C., A facile synthesis of high performance  $\text{SmCo}_5$  nanoparticles, *Chemical Engineering Journal*, 264 (2015) 610–616. DOI: 10.1016/j.cej.2014.11.138
- Machida K.-i., Nakamoto A., Nakatani Y., Adachi G.-y., Onodera A., New processing routes for the preparation of  $\text{Sm}_2\text{Fe}_{17}\text{M}_x$  ( $\text{M} \equiv \text{C}$  and/or  $\text{N}$ ) materials, *Journal of Alloys and Compounds*, 222 (1995) 18–22. DOI: 10.1016/0925-8388(94)04905-x
- Majima K., Ito M., Katsuyama S., Nagai H., Structure and magnetic properties of  $\text{Sm}_2(\text{Fe,Mn})_{17}\text{N}_x$  coarse powders with high coercivity, *Journal of Applied Physics*, 81 (1997) 4530. DOI: 10.1063/1.364942
- Makita K., Hirose S., Coercivity of Zn evaporation-coated  $\text{Sm}_2\text{Fe}_{17}\text{N}_x$  fine powder and its bonded magnets, *Journal of Alloys and Compounds*, 260 (1997) 236–241. DOI: 10.1016/S0925-8388(97)00155-2
- Manaf A., Buckley R.A., Davies H.A., New nanocrystalline high-remnance Nd-Fe-B alloys by rapid solidification, *Journal of Magnetism and Magnetic Materials*, 128 (1993a) 302–306. DOI: 10.1016/0304-8853(93)90475-H
- Manaf A., Leonowicz M., Davies H.A., Buckley R.A., Nanocrystalline Fe-Nd-B type permanent magnet materials with enhanced remanence, *Materials Letters*, 13 (1992) 194–198. DOI: 10.1016/0167-577x(92)90219-a
- Manaf A., Leonowicz M., Davies H.A., Buckley R.A., High-energy-product rapidly solidified Fe–Nd–B alloys with additions of Nb and Si, *Journal of Applied Physics*, 73 (1993b) 6473–6475. DOI: 10.1063/1.352584
- Mashimo T., Huang X., Hirose S., Makita K., Kato Y., Mitsudo S., Motokawa M., Magnetic properties of fully dense  $\text{Sm}_2\text{Fe}_{17}\text{N}_x$  magnets prepared by shock compression, *Journal of Magnetism and Magnetic Materials*, 210 (2000) 109–120. DOI: 10.1016/S0304-8853(99)00762-3
- Mashimo T., Huang X., Hirose S., Makita K., Mitsudo S., Motokawa M., Effects of decomposition on the magnetic property of shock-consolidated  $\text{Sm}_2\text{Fe}_{17}\text{N}_x$  bulk magnets, *Journal of Materials Processing Technology*, 85 (1999) 138–141. DOI: 10.1016/S0924-0136(98)00278-7
- Matsuura M., Nishijima Y., Tezuka N., Sugimoto S., Shoji T., Sakuma N., Increase of energy products of Zn-bonded Sm-Fe-N magnets with low oxygen content, *Journal of Magnetism and Magnetic Materials*, 467 (2018) 64–68. DOI: 10.1016/j.jmmm.2018.07.064
- Matsuura M., Yamamoto K., Tezuka N., Sugimoto S., Microstructural changes in high-coercivity Zn-bonded Sm-Fe-N magnets, *Journal of Magnetism and Magnetic Materials*, 510 (2020) 166943. DOI: 10.1016/j.jmmm.2020.166943
- Mishra R.K., Microstructure of melt-spun Nd-Fe-B magnequench magnets, *Journal of Magnetism and Magnetic Materials*, 54-7 (1986) 450–456. DOI: 10.1016/0304-8853(86)90660-8
- Mishra R.K., Microstructure of hot-pressed and die-upset NdFeB magnets, *Journal of Applied Physics*, 62 (1987) 967. DOI: 10.1063/1.339709
- Mishra R.K., Crystallographic and magnetic alignment in die-upset Nd-Fe-B magnets, *Journal of Materials Engineering*, 11 (1989) 87–93. DOI: 10.1007/bf02833758
- Mishra R.K., Brewer E.G., Lee R.W., Grain growth and alignment in hot deformed Nd-Fe-B magnets, *Journal of Applied Physics*, 63 (1988) 3528. DOI: 10.1063/1.340731
- Mishra R.K., Chu T.-Y., Rabenberg L.K., The development of the microstructure of die-upset Nd-Fe-B magnets, *Journal of Magnetism and Magnetic Materials*, 84 (1990) 88–94. DOI: 10.1016/0304-8853(90)90168-p
- Mishra R.K., Lee R.W., Microstructure, domain walls, and magnetization reversal in hot-pressed Nd-Fe-B magnets, *Applied Physics Letters*, 48 (1986) 733. DOI: 10.1063/1.96704
- Mishra R.K., Panchanathan V., Croat J.J., The microstructure of hot formed neodymium–iron–boron magnets with energy product 48 MG Oe, *Journal of Applied Physics*, 73 (1993) 6470–6472. DOI: 10.1063/1.352583
- Morii K., Hasegawa F., Data sheet of Sm-Fe-N isotropic bonded magnet, *Denki-Seiko [Electric Furnace Steel]*, 79 (2008) 149–155. DOI: 10.4262/denkiseiko.79.149
- Morimoto K., Niizuma E., Igarashi K., Mori K., Watanabe M., Nakayama R., Preparation of fully dense Nd-Fe-B magnets using semi-processed HDDR powders, *Journal of Magnetism and Magnetic Materials*, 265 (2003) 345–351. DOI: 10.1016/S0304-8853(03)00286-5
- Müller K.H., Cao L., Dempsey N.M., Wendhausen P.A.P.,  $\text{Sm}_2\text{Fe}_{17}$  interstitial magnets (invited), *Journal of Applied Physics*, 79 (1996) 5045–5050. DOI: 10.1063/1.361568
- Nakamura M., Matsuura M., Tezuka N., Sugimoto S., Une Y., Kubo H., Sagawa M., Preparation of ultrafine jet-milled powders for Nd-Fe-B sintered magnets using hydrogenation–disproportionation–desorption–recombination and hydrogen decrepitation processes, *Applied Physics Letters*, 103 (2013) 022404. DOI: 10.1063/1.4813399
- Nakayama H., Takagi K., Ozaki K., Kobayashi K., Correlation between microstructure and magnetic properties in  $\text{Sm}_2\text{Fe}_{17}\text{N}_3$  magnet prepared by pulsed current sintering, *Materials Transactions*, 53 (2012) 1962–1966. DOI: 10.2320/matertrans.M2012169
- Ohmori K., Oshimura N., Iseki T., Ishikawa T., Structure analysis of  $\text{Sm}_2(\text{Fe,Mn})_{17}\text{N}_x$  magnet, *Journal of Iron and Steel Research, International*, 13 (2006) 268–272. DOI: 10.1016/S1006-706x(08)60192-2
- Okada S., Node E., Takagi K., Fujikawa Y., Enokido Y., Moriyoshi C., Kuroiwa Y., Synthesis of  $\text{Sm}_2\text{Fe}_{17}\text{N}_3$  powder having a new level of high coercivity by preventing decrease of coercivity in washing step of reduction-diffusion process, *Journal of Alloys and Compounds*, 804 (2019) 237–242. DOI: 10.1016/j.jallcom.2019.06.385
- Okada S., Suzuki K., Node E., Takagi K., Ozaki K., Enokido Y., Preparation of submicron-sized  $\text{Sm}_2\text{Fe}_{17}\text{N}_3$  fine powder with high coercivity by reduction-diffusion process, *Journal of Alloys and Compounds*, 695 (2017) 1617–1623. DOI: 10.1016/j.jallcom.2016.10.306
- Okada S., Takagi K., Development of synthesis method for highly heat-resistant rare earth magnet powder without heavy rare earths, *AIST*, 2019.
- Okada S., Takagi K., Novel synthesis of single-crystalline  $\text{TbCu}_7$ -type Sm-Fe powder by low-temperature reduction-diffusion process using molten salt, *Journal of Rare Earths*, (2021). DOI: 10.1016/j.jre.2021.05.017
- Otani Y., Moukarika A., Sun H., Coey J.M.D., Devlin E., Harris I.R., Metal bonded  $\text{Sm}_2\text{Fe}_{17}\text{N}_{3-\delta}$  magnets, *Journal of Applied*

- Physics, 69 (1991) 6735–6737. DOI: 10.1063/1.348900
- Park K., Hirayama Y., Shigeta M., Liu Z., Kobashi M., Takagi K., Anisotropic Sm-Co nanopowder prepared by induction thermal plasma, *Journal of Alloys and Compounds*, 882 (2021) 160633. DOI: 10.1016/j.jallcom.2021.160633
- Park K.T., Hiraga K., Sagawa M., Effect of metal-coating and consecutive heat treatment on coercivity of thin Nd-Fe-B sintered magnets, *Proceedings of 16th International Workshop on Rare Earth Magnets and Their Applications*, (2000) 257–264.
- Pharr G.M., Ashby M.F., On creep enhanced by a liquid phase, *Acta Metallurgica*, 31 (1983) 129–138. DOI: 10.1016/0001-6160(83)90072-x
- Popov A.G., Gaviko V.S., Shchegoleva N.N., Shreder L.A., Gunderov D.V., Stolyarov V.V., Li W., Li L.L., Zhang X.Y., Effect of high-pressure torsion deformation and subsequent annealing on structure and magnetic properties of over-quenched melt-spun Nd<sub>9</sub>Fe<sub>85</sub>B<sub>6</sub> alloy, *Journal of Iron and Steel Research, International*, 13 (2006) 160–165. DOI: 10.1016/s1006-706x(08)60175-2
- Prabhu D., Sepehri-Amin H., Mendis C.L., Ohkubo T., Hono K., Sugimoto S., Enhanced coercivity of spark plasma sintered Zn-bonded Sm-Fe-N magnets, *Scripta Materialia*, 67 (2012) 153–156. DOI: 10.1016/j.scriptamat.2012.04.001
- Raj R., Chyung C.K., Solution-precipitation creep in glass-ceramics, *Acta Metallurgica*, 29 (1981) 159–166. DOI: 10.1016/0001-6160(81)90096-1
- Saito K., Nakamura H., Sugimoto S., Okada M., Homma M., Microstructural changes with N content in Sm-Fe-N alloys, *Journal of the Magnetism Society of Japan*, 18 (1994) 201–204.
- Saito T., Magnetic properties of anisotropic Sm-Fe-N bulk magnets produced by spark plasma sintering method, *Journal of Magnetism and Magnetic Materials*, 320 (2008) 1893–1897. DOI: 10.1016/j.jmmm.2008.02.155
- Saito T., Deguchi T., Yamamoto H., Magnetic properties of Sm-Fe-N bulk magnets produced from Cu-plated Sm-Fe-N powder, *AIP Advances*, 7 (2017) 056204. DOI: 10.1063/1.4973396
- Saito T., Fukui M., Takeishi H., Sm-Fe-N bulk magnets produced by compression shearing method, *Scripta Materialia*, 53 (2005) 1117–1121. DOI: 10.1016/j.scriptamat.2005.07.025
- Saito T., Kitazima H., Hard magnetic properties of anisotropic Sm-Fe-N magnets produced by compression shearing method, *Journal of Magnetism and Magnetic Materials*, 323 (2011) 2154–2157. DOI: 10.1016/j.jmmm.2011.03.022
- Saito T., Sato H., Magnetic properties of Sm-Fe-N thick films produced by compression shearing, *Applied Physics Letters*, 89 (2006) 042508. DOI: 10.1063/1.2245375
- Saito T., Sato H., Takeishi H., Nakayama N., Anisotropic Sm-Fe-N magnets produced by compression shearing method, *Applied Physics Letters*, 89 (2006) 162511. DOI: 10.1063/1.2362589
- Sakurada S., Tsutai A., Hirai T., Yanagida Y., Sahashi M., Abe S., Kaneko T., Structural and magnetic properties of rapidly quenched (R,Zr)(Fe,Co)<sub>10</sub>N<sub>x</sub> (R=Nd,Sm), *Journal of Applied Physics*, 79 (1996) 4611–4613. DOI: 10.1063/1.361679
- Schonhobel A.M., Madugundo R., Barandiaran J.M., Hadjipanayis G.C., Palanisamy D., Schwarz T., Gault B., Raabe D., Skokov K., Gutfleisch O., Fischbacher J., Schrefl T., Nanocrystalline Sm-based 1:12 magnets, *Acta Materialia*, 200 (2020) 652–658. DOI: 10.1016/j.actamat.2020.08.075
- Schonhobel A.M., Madugundo R., Gabay A.M., Barandiaran J.M., Hadjipanayis G.C., The Sm-Fe-V based 1:12 bulk magnets, *Journal of Alloys and Compounds*, 791 (2019) 1122–1127. DOI: 10.1016/j.jallcom.2019.03.249
- Schultz L., Schnitzke K., Wecker J., Magnetic hardening of Sm-Fe-Mo, Sm-Fe-V and Sm-Fe-Ti magnets, *Journal of Magnetism and Magnetic Materials*, 83 (1990) 254–256. DOI: 10.1016/0304-8853(90)90506-1
- Sellmyer D.J., Balamurugan B., Das B., Mukherjee P., Skomski R., Hadjipanayis G.C., Novel structures and physics of nanomagnets (invited), *Journal of Applied Physics*, 117 (2015) 172609. DOI: 10.1063/1.4914339
- Seo Y., Morimoto S., Comparison of dysprosium security strategies in Japan for 2010–2030, *Resources Policy*, 39 (2014) 15–20. DOI: 10.1016/j.resourpol.2013.10.007
- Sepehri-Amin H., Ohkubo T., Nagashima S., Yano M., Shoji T., Kato A., Schrefl T., Hono K., High-coercivity ultrafine-grained anisotropic Nd-Fe-B magnets processed by hot deformation and the Nd-Cu grain boundary diffusion process, *Acta Materialia*, 61 (2013) 6622–6634. DOI: 10.1016/j.actamat.2013.07.049
- Sepehri-Amin H., Ohkubo T., Nishiuchi T., Hirotsawa S., Hono K., Coercivity enhancement of hydrogenation-disproportionation-desorption-recombination processed Nd-Fe-B powders by the diffusion of Nd-Cu eutectic alloys, *Scripta Materialia*, 63 (2010) 1124–1127. DOI: 10.1016/j.scriptamat.2010.08.021
- Sepehri-Amin H., Une Y., Ohkubo T., Hono K., Sagawa M., Microstructure of fine-grained Nd-Fe-B sintered magnets with high coercivity, *Scripta Materialia*, 65 (2011) 396–399. DOI: 10.1016/j.scriptamat.2011.05.006
- Shchetinin I.V., Bordyuzhin I.G., Sundeev R.V., Menushenkov V.P., Kamynin A.V., Verbetsky V.N., Savchenko A.G., Structure and magnetic properties of Sm<sub>2</sub>Fe<sub>17</sub>N<sub>x</sub> alloys after severe plastic deformation by high pressure torsion, *Materials Letters*, 274 (2020) 127993. DOI: 10.1016/j.matlet.2020.127993
- Shen B., Yu C., Baker A.A., McCall S.K., Yu Y., Su D., Yin Z., Liu H., Li J., Sun S., Chemical synthesis of magnetically hard and strong rare earth metal based nanomagnets, *Angewandte Chemie International Edition*, 58 (2019) 602–606. DOI: 10.1002/anie.201812007
- Skomski R., Coey J.M.D., Giant energy product in nanostructured 2-phase magnets, *Physical Review B*, 48 (1993) 15812–15816. DOI: 10.1103/PhysRevB.48.15812
- Stoyanov S., Skumryev V., Zhang Y., Huang Y., Hadjipanayis G., Nogués J., High anisotropy Sm-Co nanoparticles: Preparation by cluster gun technique and their magnetic properties, *Journal of Applied Physics*, 93 (2003) 7592–7594. DOI: 10.1063/1.1544503
- Straumal B.B., Kilmametov A.R., Mazilkin A.A., Protasova S.G., Kolesnikova K.I., Straumal P.B., Baretzky B., Amorphization of Nd-Fe-B alloy under the action of high-pressure torsion, *Materials Letters*, 145 (2015) 63–66. DOI: 10.1016/j.matlet.2015.01.041
- Sugimoto S., Nakamura M., Matsuura M., Une Y., Kubo H., Sagawa M., Enhancement of coercivity of Nd-Fe-B ultrafine powders comparable with single-domain size by the grain boundary diffusion process, *IEEE Transactions on Magnetics*, 51 (2015). DOI: 10.1109/tmag.2015.2434889
- Swaminathan V., Deheri P.K., Bham S.D., Ramanujan R.V., Novel microwave assisted chemical synthesis of Nd<sub>2</sub>Fe<sub>14</sub>B hard magnetic nanoparticles, *Nanoscale*, 5 (2013) 2718–2725. DOI: 10.1039/C3NR33296A
- Tada S., Tomimoto T., Kume M., High-coercivity anisotropic SmFeN magnetic materials, *Proceedings of the 22nd International Workshop on Rare-Earth Permanent Magnets and Their Application*, (2012) 48–53.

- Takagi K., Hirayama Y., Okada S., Yamaguchi W., Ozaki K., Novel powder processing technologies for production of rare-earth permanent magnets, *Science and Technology of Advanced Materials*, 22 (2021) 150–159. DOI: 10.1080/14686996.2021.1875791
- Takagi K., Jinno M., Ozaki K., Preparation of TbCu<sub>7</sub>-type Sm-Fe powders by low-temperature HDDR treatment, *Journal of Magnetism and Magnetic Materials*, 454 (2018) 170–175. DOI: 10.1016/j.jmmm.2018.01.092
- Takagi K., Nakayama H., Ozaki K., Microstructural behavior on particle surfaces and interfaces in Sm<sub>2</sub>Fe<sub>17</sub>N<sub>3</sub> powder compacts during low-temperature sintering, *Journal of Magnetism and Magnetic Materials*, 324 (2012a) 2336–2341. DOI: 10.1016/j.jmmm.2012.02.021
- Takagi K., Nakayama H., Ozaki K., Kobayashi K., Fabrication of high-performance Sm-Fe-N isotropic bulk magnets by a combination of high-pressure compaction and current sintering, *Journal of Magnetism and Magnetic Materials*, 324 (2012b) 1337–1341. DOI: 10.1016/j.jmmm.2011.11.035
- Takagi K., Nakayama H., Ozaki K., Kobayashi K., Fabrication of high-performance Sm-Fe-N isotropic bulk magnets by a combination of high-pressure compaction and current sintering, *Journal of Magnetism and Magnetic Materials*, 324 (2012c) 1337–1341. DOI: 10.1016/j.jmmm.2011.11.035
- Takagi K., Soda R., Jinno M., Yamaguchi W., Possibility of high-performance Sm<sub>2</sub>Fe<sub>17</sub>N<sub>3</sub> sintered magnets by low-oxygen powder metallurgy process, *Journal of Magnetism and Magnetic Materials*, 506 (2020) 166811. DOI: 10.1016/j.jmmm.2020.166811
- Takizawa R., Itakura M., Katayama N., Morimoto K., Crystallographic orientation analysis in HDDR process of anisotropic Nd-Fe-B magnet powders, *Journal of Magnetism and Magnetic Materials*, 433 (2017) 187–194. DOI: 10.1016/j.jmmm.2017.03.014
- Tang H., Mamakhel M.A.H., Christensen M., Enhancing the coercivity of SmCo<sub>5</sub> magnet through particle size control, *Journal of Materials Chemistry C*, 8 (2020a) 2109–2116. DOI: 10.1039/c9tc06137a
- Tang H., Mamakhel M.A.H., Christensen M., High coercivity SmCo<sub>5</sub> synthesized with assistance of colloidal SiO<sub>2</sub>, *Scientific Reports*, 11 (2021) 4682. DOI: 10.1038/s41598-021-83826-5
- Tang H., Wang Z., Mamakhel M.A.H., Dong M., Christensen M., Combustion assisted preparation of high coercivity Sm-Co hard magnet with stable single-domain size, *Journal of Alloys and Compounds*, 816 (2020b). DOI: 10.1016/j.jallcom.2019.152527
- Tang H., Wang Z., Mamakhel M.A.H., Dong M., Christensen M., Combustion assisted preparation of high coercivity Sm-Co hard magnet with stable single-domain size, *Journal of Alloys and Compounds*, 816 (2020c) 152527. DOI: 10.1016/j.jallcom.2019.152527
- Teresiak A., Kubis M., Mattern N., Wolf M., Gruner W., Müller K.H., Influence of nitrogenation on structure development and magnetic properties of mechanically alloyed and annealed Sm-Fe powders, *Journal of Alloys and Compounds*, 292 (1999) 212–220. DOI: 10.1016/s0925-8388(99)00297-2
- Valiev R.Z., Islamgaliev R.K., Alexandrov I.V., Bulk nanostructured materials from severe plastic deformation, *Progress in Materials Science*, 45 (2000) 103–189.
- Wakai F., Step model of solution-precipitation creep, *Acta Metallurgica et Materialia*, 42 (1994) 1163–1172. DOI: 10.1016/0956-7151(94)90133-3
- Wendhausen P.A.P., Eckert D., Handstein A., Müller K.H., Leitner G., Skomski R., On the role of Zn in Sm<sub>2</sub>Fe<sub>17</sub>N<sub>x</sub> permanent magnets, *Journal of Applied Physics*, 73 (1993) 6044–6046. DOI: 10.1063/1.353464
- Wu Q., Cong L., Yue M., Li C., Ma Z., Ma X., Wang Y., A unique synthesis of rare-earth-Co-based single crystal particles by “self-aligned” Co nano-arrays, *Nanoscale*, 12 (2020a) 13958–13963. DOI: 10.1039/d0nr00490a
- Wu Q., Cong L., Yue M., Li C., Ma Z., Ma X., Wang Y., A unique synthesis of rare-earth-Co-based single crystal particles by “self-aligned” Co nano-arrays, *Nanoscale*, 12 (2020b) 13958–13963. DOI: 10.1039/D0NR00490A
- Yamaguchi W., Soda R., Takagi K., Metal-coated Sm<sub>2</sub>Fe<sub>17</sub>N<sub>3</sub> magnet powders with an oxide-free direct metal-metal interface, *Journal of Magnetism and Magnetic Materials*, 498 (2020) 166101. DOI: 10.1016/j.jmmm.2019.166101
- Yamaguchi W., Takagi K., Effects of nonmagnetic overlay metals on coercivity of Sm<sub>2</sub>Fe<sub>17</sub>N<sub>3</sub> magnet powders, *Journal of Magnetism and Magnetic Materials*, 516 (2020). DOI: 10.1016/j.jmmm.2020.167327
- Yasuhara A., Park H.S., Shindo D., Iseki T., Oshimura N., Ishikawa T., Ohmori K., Microstructures and magnetic domain structures in Sm<sub>2</sub>(Fe,Mn)<sub>17</sub>N<sub>8</sub> powders studied by analytical electron microscopy and Lorentz microscopy, *Journal of Magnetism and Magnetic Materials*, 295 (2005) 1–6. DOI: 10.1016/j.jmmm.2004.12.032
- Yasuhara A., Shindo D., Tobise M., Analysis of microstructure and magnetic domain structure in Sm-Fe-N particles by transmission electron microscopy, *Journal of the Japan Institute of Metals*, 68 (2004) 320–325. DOI: 10.2320/jinstmet.68.320
- Yue M., Pan R., Liu R.M., Liu W.Q., Zhang D.T., Zhang J.X., Zhang X.F., Guo Z.H., Li W., Crystallographic alignment evolution and magnetic properties of Nd-Fe-B nanoflakes prepared by surfactant-assisted ball milling, *Journal of Applied Physics*, 111 (2012). DOI: 10.1063/1.3679414
- Zhang D.T., Yue M., Zhang J.X., Study on bulk Sm<sub>2</sub>Fe<sub>17</sub>N<sub>x</sub> sintered magnets prepared by spark plasma sintering, *Powder Metallurgy*, 50 (2007) 215–218. DOI: 10.1179/174329007x169128
- Zhang H., Peng S., Rong C.-b., Liu J.P., Zhang Y., Kramer M.J., Sun S., Chemical synthesis of hard magnetic SmCo nanoparticles, *Journal of Materials Chemistry*, 21 (2011a) 16873–16876. DOI: 10.1039/C1JM11753J
- Zhang H., Peng S., Rong C.-b., Liu J.P., Zhang Y., Kramer M.J., Sun S., Chemical synthesis of hard magnetic SmCo nanoparticles, *Journal of Materials Chemistry*, 21 (2011b). DOI: 10.1039/c1jm11753j
- Zhang J., Takahashi Y.K., Gopalan R., Hono K., Sm(Co,Cu)<sub>7</sub>/Fe exchange spring multilayer films with high energy product, *Applied Physics Letters*, 86 (2005). DOI: 10.1063/1.1889238
- Zhang S.G., Li D.P., Ying Q.M., Zhou M.L., Zuo T.Y., High magnetic performance NdFe<sub>10.5</sub>Mo<sub>1.5</sub>N<sub>x</sub> prepared by mechanical alloying, *Journal of Materials Science*, 36 (2001) 107–111. DOI: 10.1023/A:1004855228269
- Zhang Z.-D., Liu W., Sun X.K., Zhao X.-g., Xiao Q.-f., Sui Y.-c., Zhao T., Structure and magnetic properties of Nd-Fe-B-Ti prepared by mechanical alloying, *Journal of Magnetism and Magnetic Materials*, 184 (1998) 101–105. DOI: 10.1016/s0304-8853(97)01111-6

## Authors' Short Biographies



### **Kenta Takagi**

Kenta Takagi is a senior researcher at the National Institute of Advanced Industrial Science and technology. He obtained his bachelor's degree and master's degree in Materials Science from Tohoku University in 1995 and 1997, respectively. Later he obtained his Doctor of Engineering from Tohoku University in 2003. His latest research interests revolve around permanent magnets. In particular, he is motivated in studying on powder processing for low-sinterable and metastable magnetic alloys.



### **Yusuke Hirayama**

Yusuke Hirayama is a senior researcher at the National Institute of Advanced Industrial Science and technology. He obtained his Doctor of Engineering from Osaka University in 2012. His latest research is focused on magnetic materials. He is now working on the development of the physical process of metal nanoparticle.



### **Shusuke Okada**

Shusuke Okada is a senior researcher at the National Institute of Advanced Industrial Science and technology. He obtained his Doctor of Engineering from Osaka University in 2013. His latest research is synthesis of magnetic material powder by wet-chemical process.



### **Akihide Hosokawa**

Akihide Hosokawa is a senior research scientist at the National Institute of Advanced Industrial Science and technology. He obtained his Ph.D. degree 2010 at McMaster University (Hamilton, ON, Canada). His research interest is to develop new generation ultrastrong permanent magnets through development of novel microstructural control techniques.



### **Wataru Yamaguchi**

Wataru Yamaguchi is a senior research scientist at the National Institute of Advanced Industrial Science and Technology. He received his doctorate from the University of Tokyo in 1997. He is currently working on methods to improve the performance of a group of rare-earth magnets through grain boundary engineering.

# Morphology Control of Transition Metal Oxides by Liquid-Phase Process and Their Material Development<sup>†</sup>

Shu Yin<sup>1,2\*</sup> and Takuya Hasegawa<sup>1</sup>

<sup>1</sup> Institute of Multidisciplinary Research for Advanced Materials (IMRAM), Tohoku University, Japan

<sup>2</sup> Advanced Institute for Materials Research (WPI-AIMR), Tohoku University, Japan

## Abstract

It is well known that the functionality of inorganic materials strongly depends on the chemical composition, morphology, particle size, crystal facet, etc., which are strongly influenced by the synthesis process. The precise control of the synthesis process is expected to lead to the discovery of new functionality and improvement of the functionality of materials. For example, in a high-temperature solid-phase reaction, it is difficult to control the morphology of nanocrystals. On the other hand, synthesizing functional materials using solution processes, such as hydrothermal and solvothermal reactions, makes it possible to control the morphology and particle size precisely. Usually, the solution process is strongly related to the dissolution reprecipitation mechanism. Therefore, the material composition can be strictly controlled and is suitable for forming fine particles with high crystallinity. In this review paper, the role of the solvent in the solution process, its effect on particle size and morphology of the transition metal oxide, and the related functional improvement will be focused. Furthermore, the direct formation of functional thin films by the solution process and the morphology control by non-oxide materials by the topotactic reaction will also be introduced.

**Keywords:** morphological control, liquid phase synthesis, transition metal oxides, thin films, IR light response

## 1. Introduction

It is known that the functionality of inorganic materials strongly depends on the chemical composition of the materials, particle morphology and size, specific surface area, crystal structure, crystal facet, etc. In order to realize functional control of inorganic materials, precise control of the synthesis process is important. Until now, while there are many materials synthesis processes, liquid phase reaction uses liquid solvent as a reaction medium and carries out the reaction in a sealed pressure reaction vessel (autoclave) is called a hydrothermal or solvothermal reaction. Not only the temperature but also the pressure control of the reaction system, together with the use of additives, the particle morphology and size of the product, crystal structure, crystal plane, crystallinity, etc. can be efficiently controlled. Therefore, it has been accepted that the hydrothermal or solvothermal processes show great potential for improving the functionality of various materials, and offer many applications such as non-toxic pigments, photocatalysts, ultraviolet rays, and infrared shielding materials etc. (Cao et al., 2022; Guo et al., 2010; Hermawan et al., 2021; Taufik et

al., 2020; Xue and Yin, 2022; Yin, 2015; Yin and Asakura, 2019). The liquid phase reactions proceed under mild conditions compared to high-temperature methods such as solid-phase reactions, which are environmentally friendly. They are expected to be effective for the industrial synthesis of materials. Usually, electric furnace heating is used for traditional hydrothermal and solvothermal reactions. Using a microwave irradiation heating method becomes a complex chemical reaction field, resulting in a quickly synthesizing process for nano / micro functional materials, generating a metastable crystal phase, suppressing crystal growth, etc. (Liu et al., 2012). In addition, for oxide materials, elements replaced by cations and anions in the material will significantly change their physical and chemical properties, and it is expected that new functionality of the material will be discovered, and the functionality of materials will be dramatically improved (Cao et al., 2022; Kageyama et al., 2018; Zhao et al., 2017). It is possible to synthesize oxides and nitrides with different morphologies and sizes via a topotactic method, using the precursors with controllable morphology and particle size synthesized from the solution process. It is expected that some novel material functionality could be found because of their unique morphologies (Hermawan et al., 2018b; 2020; Yin et al., 2012). Furthermore, the liquid phase method could directly prepare powder materials and functional thin films (Yin and Sato, 2005). In this review paper, some examples

<sup>†</sup> Received 29 June 2022; Accepted 25 July 2022  
J-STAGE Advance published online 10 September 2022

\* Corresponding author: Shu Yin;  
<sup>1,2</sup> Add: 2-1-1, Katahira, Aoba-ku, Sendai 980-8577, Japan  
E-mail: yin.shu.b5@tohoku.ac.jp  
TEL: +81-22-217-5597 FAX: +81-22-217-5597

will be introduced in detail from the viewpoint of particle morphology control and functionality control.

## 2. Composition, morphology, and functional control by a solution reaction process

### 2.1 Hydrothermal and solvothermal reactions

A chemical reaction that occurs in the presence of hot water at a temperature above 100 °C and high pressure of more than 1 atm is called a hydrothermal reaction. It is said that it was initially developed by geology-related scientists in the former Soviet Union to study the mechanism of mineral formation, and to imitate the high-temperature, high-pressure reaction environment similar to that of underground magma. Since the 1980s, it has been used as a new method for synthesizing inorganic functional materials, and has made remarkable progress. Depending on the type of chemical reaction, the hydrothermal process is divided into five categories: hydrothermal oxidation, hydrothermal synthesis, hydrothermal precipitation, hydrothermal decomposition, and hydrothermal crystallization (Somiya, 1984). In recent years, hydrothermal reactions have come to be used not only for inorganic materials but also for organic synthesis. Instead of a water solvent, various organic solvents can be used as reaction solvents for the mentioned liquid-phase reactions. Among them, when liquid ammonia is used as a solvent, it is called amonothermal (Hertrampf et al., 2018). When using glycol or ionic liquid as a solvent, it was called glycothermal (Zhu et al., 2020) or ionothermal (Jaleel et al., 2022). A liquid phase reaction using various solvents containing water is universally referred to as a solvothermal reaction. Compared to high-temperature methods such as solid-phase reactions, many solvothermal reactions can synthesize materials in a relatively low-temperature range of around 200 °C and a low-pressure range with little energy consumption. In addition, some post-processing processes such as calcination or pulverization can be omitted after the solvothermal treatment. So, it is an environmentally friendly synthesis method and could be classified as a soft chemical process (Byrappa and Yoshimura, 2012).

Many solvents in solvothermal reactions have change-

able physical and chemical properties due to temperature and pressure changes, resulting in different reaction environments by simple condition changing (such as temperature, pressure, pH, additives, etc.). In general, solvothermal reactions produce particles by a dissolution-reprecipitation mechanism, in which the existence of water molecules significantly affects the crystalline growth of the products (Sato et al., 1998).

Fig. 1 shows the dependence of the dissolution reprecipitation mechanism in the liquid phase reaction and the particle size dependence of oxides material synthesized in water or organic solvents. The water solvent has a high dielectric constant of 78.3, resulting in an environment with a low supersaturation and the particles tend to grow larger. In contrast, in organic solvents such as ethanol (EtOH), the dielectric constant is low as 23.8, the dissolution ability of the solvent is limited, and the supersaturation degree is high. In this case, instead of particle growth, nuclei are easy to generate, and many fine particles tend to be produced simultaneously, leading to the formation of fine particles with less agglomeration. When water is used as a solvent, the particle size grows relatively large, and hard agglomeration can be observed because of hydrogen bonding in the solution. On the other hand, when the organic solvent methanol or ethanol is used, less agglomeration could be observed. As the proportion of water in the water-ethanol mixture solvent increases, a tendency can be observed that the particle size of the oxide to be produced tends to increase. This behavior is strongly related to the existence of water, which can be reasonably explained by the dissolution-reprecipitation mechanism (Sato et al., 1998).

### 2.2 Composition, crystal phase control, and functionality of titanium dioxide

Semiconductor titanium oxide photocatalytic materials can effectively utilize solar energy and realize environmental purification, self-cleaning, etc. Generally, oxide semiconductor photocatalysts have a large band gap and can only be excited by ultraviolet rays. Therefore, it is essential to provide a visible light response from the viewpoint of improving the efficiency of solar energy. In order to realize

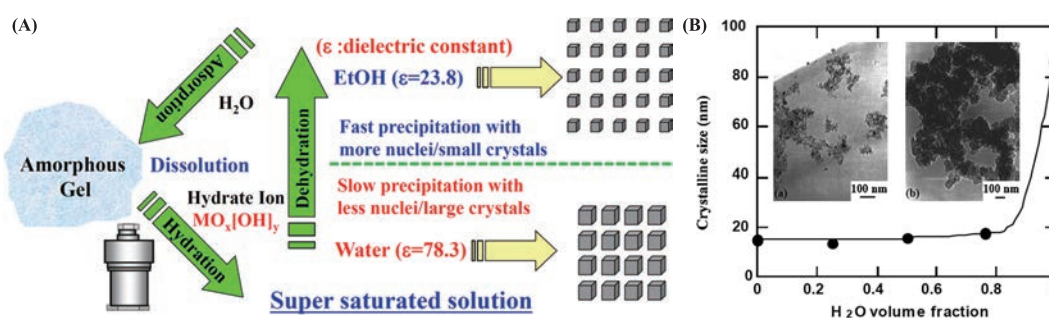
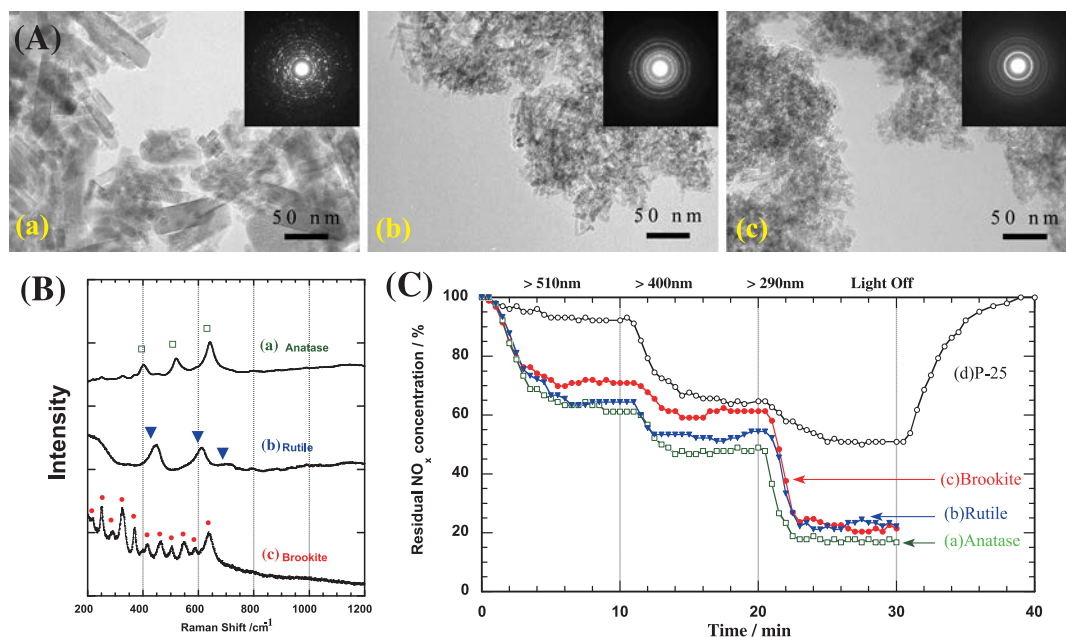


Fig. 1 (A) Dissolution reprecipitation mechanism in liquid phase reaction system, (B) Water-methanol ratio and particle size dependence of produced oxide (inserted TEM photographs: oxides produced by (a) solvothermal reaction, and (b) hydrothermal reaction).



**Fig. 2** (A) TEM images, (B) Raman spectra and (C) photocatalytic deNO<sub>x</sub> photocatalytic activity of TiO<sub>2-x</sub>N<sub>y</sub> powders with different phase compositions selectively synthesized by solvothermal reaction at 190 °C for 2 h in (a) TiCl<sub>3</sub>–HMT aqueous solution at pH 1, (b) TiCl<sub>3</sub>–HMT aqueous solution at pH 9, (c) TiCl<sub>3</sub>–HMT methanol solution at pH 9; (a) anatase (□); (b) rutile (▼); (c) brookite (●); (d) P-25, standard photocatalyst Degussa P-25). [Part of the figure is reproduced from Ref. (Yin et al., 2005) with permission from the RSC]

the visible light activity of titanium oxide-based photocatalysts, anion-doping is an effective way (Asahi et al., 2001; Kageyama et al., 2018; Zhao et al., 2017), and so far, RF (high frequency) magnetron sputtering, ion implantation, partial oxidation of non-oxide titanium compounds are utilized as the methods for doping anions on titanium oxide. Usually, it requires high-temperature treatment, expensive precursors synthesized in a high-temperature atmosphere, large-scale equipment, etc., and it cannot necessarily be said that they are environmentally friendly. The synthesis of anion-doped oxides by solvothermal reactions can be realized in a solution around 200 °C. Various crystal phases can be selectively synthesized, and no post-treatment is required, and anion dopants or dopants such as nitrogen, sulfur, and fluorine can be realized in one step (Cao et al., 2022; Yin et al., 2005; Yin and Asakura, 2019). In a typical synthesis process, a titanium compound (TiCl<sub>3</sub>) is introduced in urea or hexamethylenetetramine (HMT) aqueous solution, followed by hydrothermal/solvothermal treatment at 190 °C. By controlling the reaction temperature, solvent and pH, it is possible to selectively synthesize three representative nitrogen-doped polymorphs of titanium oxide, i.e., anatase, rutile, and brookite phases as a single phase. All the nitrogen-doped titanium oxides possessed excellent light absorption and excellent NO<sub>x</sub> removal (deNO<sub>x</sub>) photocatalytic activity under ultraviolet and visible light irradiation (see Fig. 2) (Yin et al., 2005).

In general, titanium oxide is widely used as a photocatalyst and white pigment. Adding various transition metal elements is usually utilized to improve the functionality

of the photocatalyst and realize the coloring of inorganic white pigments. However, in many cases, crystalline defects are produced due to metal ion doping, hindering photocatalytic activity improvement. In addition, due to the toxicity of transition metal ions, safety risks are concerned when they are used as raw materials for cosmetics, etc. Applying mixed ions doping makes it possible to synthesize colorful titanium oxide without using transition metals except for titanium (Cao et al., 2022). It is known that titania possesses yellow color when nitrogen is doped at the oxygen site of the titania and shows gray color when the boron element is doped. When nitrogen and boron are co-doped, the band gap is further reduced, and absorption in visible light becomes remarkable. At that time, various colors can be realized by changing their crystal phase. The presence of slight differences in the levels of the original valence bands of anatase, rutile, and brookite results in the formation of the colorful titanium oxide, such as red, cyan, and yellow-green can be realized. This result indicates that titanium oxide can be used as a colorful inorganic pigment, which is non-toxic without any other transition metal addition (Cao et al., 2022).

### 2.3 Morphology and functional control of zinc oxide

Zinc oxide possesses a hexagonal structure and has piezoelectric properties. Z.L. Wang et al. reported the morphology control of zinc oxide by a high-temperature sublimation method and various unique morphologies such as nanowires, nano-plates, nano-combs, nano-rings,



nano-springs, etc. can be synthesized (Wang, 2005; Wang and Song, 2006). In particular, the concept of nanogenerators using piezoelectric ZnO nanowires significantly impacted the world. On the other hand, in the high-temperature sublimation method, since the generated morphology differs depending on the temperature of the substrate in the electric furnace, it is difficult to ensure complete uniformity of the morphology because the substrate temperature changes a little with their position in the furnace. Therefore, it is challenging to realize the scale-up of the products. On the other hand, the solution process can cover the disadvantages of the high-temperature sublimation method and is also suitable for product scale-up. When slowly crystallized in a low-concentration solution, zinc oxide tends to grow according to the *c*-axis direction. While, when the ion concentration increases, nucleus formation accelerates and tends to become fine particles. Therefore, it is usually challenging to synthesize spherical microparticles with low anisotropy. In the solution process, various factors such as solvent, precursor type and concentration, reaction temperature and time, and various additives significantly affect the zinc oxide crystal growth and particle morphology.

When various alcohol solvents were utilized, zinc oxide with different microstructures, such as symbiotic nanorods, radial symbiotic nano-screws, and incomplete crystals, was obtained. It seems to be because solvents with different dielectric constants have different solubilities on zinc ions, affecting the precipitation rate in the dissolution-reprecipitation process. **Fig. 3** shows the SEM photographs of various representative particle morphologies that successfully synthesized the solution process under

different synthesis conditions. The ZnO tends to produce rod-like particles by growing in the *c*-axis direction (**Fig. 3(a)(b)(f)(j)** etc.) (Long et al., 2009a; Yin and Sato, 2005). When ethylene glycol was used, the morphology was significantly different from that obtained in ordinary alcohols. A mono dispersion rod-like structure with a low aspect ratio is successfully obtained. In all cases, the size of the particles was relatively uniform. By controlling the amount of ethylene glycol additive, it was possible to get the rod-like morphology with a precisely controlled aspect ratio. Furthermore, using different precursors makes it possible to realize a significant change in morphology. For example, when zinc chloride is used, plate-like zinc oxide can be synthesized (**Fig. 3-(c)**). It is because zinc oxide particles (**Fig. 3-(c,d)**) exhibiting plate-like or nut-like morphologies are generated through layered structure precursors such as simoncholate, by taking in chloride ions and acetate ions into the products. The plate-like precursor can be decomposed by heat treatment while their morphology remains maintained, and converted to oxide with a similar morphology by the topotactic reaction (Long et al., 2009b). Spherical particles are ordinarily difficult to synthesize with high yields (Long et al., 2010a; 2010b). As an additive, the triethanolamine could be utilized to synthesize uniform spherical microparticles (**Fig. 3(e)**). Also, the as-prepared zinc oxide particles are further annealed in hexamethylenediamine (HMT) solution for more than 72 h. In that case, the microstructure of the particle surface is significantly changed by the dissolution reprecipitation reaction, resulting in the formation of developed unique surface morphologies, such as screw-shaped, hollow nut,

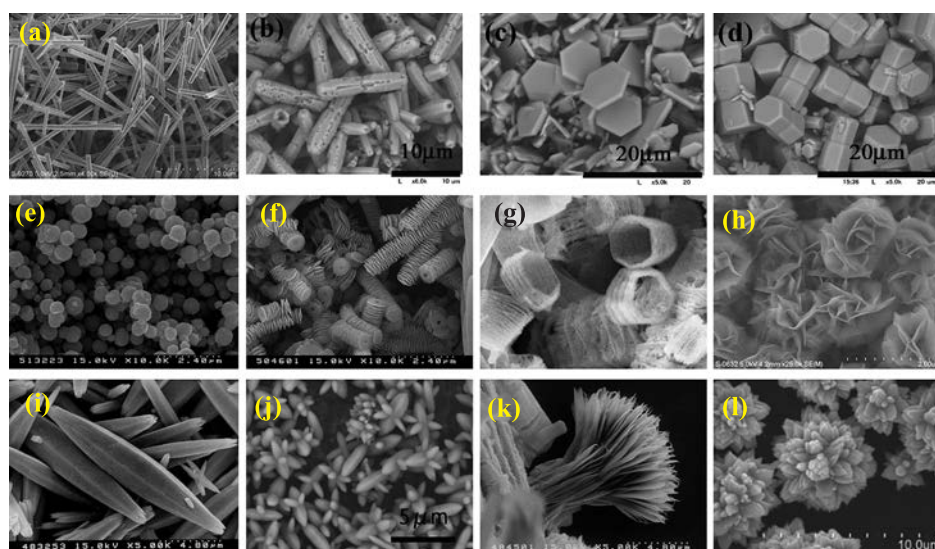


**Fig. 3** SEM images of the zinc oxide particles with various morphologies synthesized by solution reaction process. **(a)** 0.01 M ZnNO<sub>3</sub>-HMT (95 °C, 3 h), **(b)** 0.05 M ZnNO<sub>3</sub>-50 %EG-HMT (95 °C, 12 h), **(c)** 0.05 M ZnCl<sub>2</sub>-50 %EG-HMT (95 °C, 12 h), **(d)** 0.05 M Zn(CH<sub>3</sub>COO)<sub>2</sub>-50 %EG-HMT (95 °C, 12 h), **(e)** 0.025 M ZnNO<sub>3</sub>-Diethanolamine-HMT (95 °C, 3 h), **(f)** post heat-treatment **(a)** in HMT solution for 72 h, **(g)** post heat-treatment of **(d)** in HMT solution for 72 h, **(h)** post heat-treatment of **(e)** in HMT solution for 72 h **(i)** 0.025 M ZnNO<sub>3</sub>-50 %EG-HMT (95 °C, 3 h), **(j)** 0.001 M ZnNO<sub>3</sub>-75 %EG-HMT (95 °C, 24 h), **(k)** 0.001 M ZnNO<sub>3</sub>-Urea (95 °C, 3 h), **(l)** microwave-hydrothermal reaction at 190 °C for 10 min, with monoethylamine additive. [Part of the figure is reproduced from Ref. (Long et al., 2010a) with permission from Springer Nature]

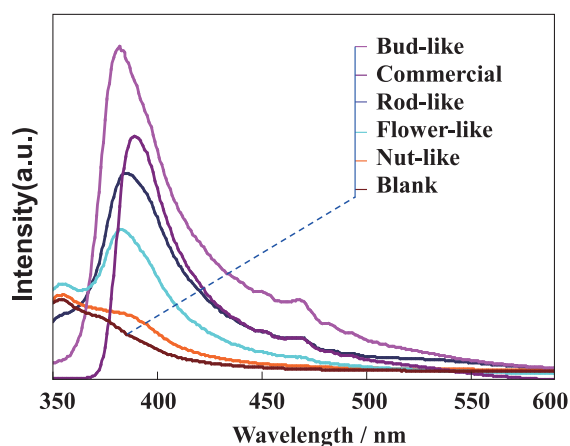


**Fig. 4** Photoluminescence spectra of ZnO crystals with different morphologies.

rose-shaped, with a large specific surface area (**Fig. 3(f–h)**) (Long et al., 2010a; 2010b). In addition, when urea was used as a precipitating agent, the effect of CO<sub>2</sub> gas produced by hydrolysis reaction resulted in the formation of unique flower-shaped particles (**Fig. 3(k)**).

In the microwave-assisted hydrothermal and solvothermal process, instead of the electric furnace heating, irradiating a microwave with a frequency of 2.45 GHz equivalent to that of a microwave oven is utilized. The products can be obtained in a short period of heating. In the reaction field to which 2.45 GHz microwave irradiation is applied, a large amount of crystal nuclei are produced rapidly due to the fast temperature rise affecting the reaction product generation behavior. Also, it is possible to synthesize metastable crystal phase and unique morphologies of products that are difficult to be obtained by normal hydrothermal reaction (Liu et al., 2012). As shown in **Fig. 3(i)**, zinc oxide synthesized by microwave-assisted hydrothermal reaction has a petal-like morphology with uniform particle size.

The morphology and microstructure of zinc oxide particles change significantly in the solution. It depends on the solubility of zinc ions in the solvent, the rate of reprecipitation, and differences in ion adsorption ability on the surface of zinc oxide crystals. Therefore, some physicochemical properties related to their particle morphology are expected. For example, all the ZnO can be excited by 325 nm light irradiation, and a peak of near-ultraviolet emission of 390 nm can be observed. It was also observed that different particle morphology results in different luminescence properties with a clear morphological dependence (Long T. et al., 2010a; 2010b), and the emission intensity shows the sequence of bud-like > rod-like > flower-like > nut-like (see **Fig. 4**) (Long et al., 2010b).

#### 2.4 Homogeneous particle morphology and functional control of cerium oxide

Similar to the plate-like zinc oxide synthesis process, pre-

cursors' topotactic morphological transcription techniques can be used to control the morphology of other inorganic compounds. For example, in the case of cerium oxide, spherical-like, rod-like, and plate-like cerium compound precursors can be successfully synthesized by applying a room-temperature aging process before a normal homogeneous precipitation reaction at 70 °C. Then, the precursors are decomposed to produce cerium oxide by heat treatment. As a result, the topotactic reaction can successfully synthesize a spherical, rod-like, plate-like cerium oxide. Under typical synthetic conditions, a 0.008 M aqueous solution of cerium (III) nitrate is mixed with a 0.5 M aqueous urea solution and aged at room temperature (25 °C) for 0 h, 72 h, 144 hours, followed by heating the aged solution at 70 °C for 2 hours. The cerium carbonate-based precursors with different morphology, spherical-like, rod-shaped, and plate-like, were obtained under different room temperature aging times. The size of the seed crystal generated at the initial stage changed depending on the room temperature aging time, thereby changing the shape of the grown crystal at the evaluated temperature process. Finally, similar morphologies of cerium oxides could be obtained by the following heat treatment at 400 °C (Yin et al., 2010).

It has also been found that cerium carbonate precursors having a larger plate-like size can be synthesized at room temperature by a simple solution process (Yin et al., 2012). In a typical thesis process, 5 mL of 1.0 M trivalent cerium nitrate solution was slowly added into a 45 mL 0.33 M–0.45 M sodium hydrogen carbonate/sodium carbonate mixed solution. Then, the precipitate slurry is kept in a constant temperature water bath of 25 °C for 24 hours, followed by filtration and washing, then drying at 60 °C overnight to obtain a single crystal of plate-like cerium carbonate octahydrate. After calcination at 400 °C for 1 h, the plate-like cerium oxide particles could be synthesized with similar plate-like morphology to that of the cerium carbonate single crystal. **Fig. 5** shows the SEM, TEM images, crystal structure, and morphologies changing process of the plate-like cerium carbonate octahydrate precursor. Since cerium carbonate octahydrate precursor has a layered structure, plate-like morphology is easy to be formed. In the early stages of the reaction, nucleation is first carried out, then the crystal growth proceeds to create the plate-like morphology, and the plate-like particles gradually become larger. At about 30 min of reaction time, an apparent plate-like crystal is formed. As the time is further extended, tiny crystals coexisting dissolve progressively, and the cerium ions gather on the surface of the large crystals and gradually become larger, because of the Ostwald ripening mechanism. The spiral growth of crystals was also observed in some cases. The as-prepared plate-like cerium oxide particles possess high gloss derived from their large plate-like particle size and also show good slipperiness and suppressed oxidation catalytic activity, indicating its

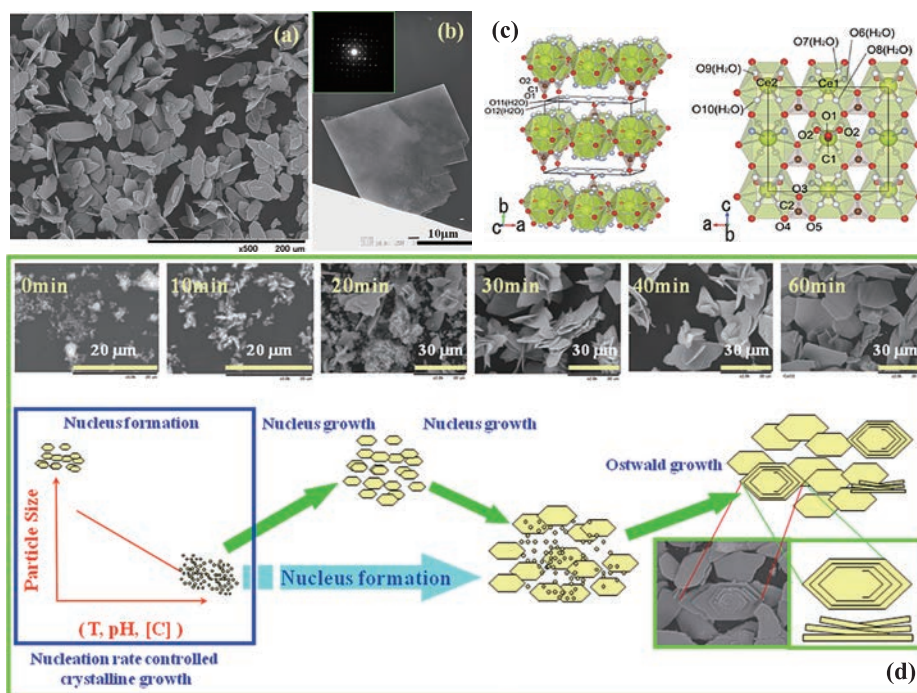


**Fig. 5** Typical (a) SEM and (b) TEM image (insert SED pattern) and (c) the layered structure of  $\text{Ce}_2(\text{CO}_3)_3 \cdot 8\text{H}_2\text{O}$  projected on the a–b and a–c planes of the plate-like cerium carbonate hydrate single crystal synthesized in 0.1 M  $\text{Ce}(\text{NO}_3)_3$  and 0.3 M  $\text{NaHCO}_3$  mixed solution. (d) Mechanism of crystalline formation and crystalline growth. [Reproduced from Ref. (Yin et al., 2012) with permission from the RSC]

potential applications as new functional cosmetics (Minamidate et al., 2010; Yin et al., 2012).

### 2.5 Novel water molecule control release solvothermal process (WCRSP) for the synthesis of uniform nanomaterials

Usually, a simple solvent such as water or alcohol is used in the conventional solvothermal reaction. In this case, particle growth and agglomeration are easy to occur. By controlling the dielectric constant of the solvent and introducing some additives, it is possible to control the number of crystal nuclei and the crystal growth rate of particle formation, which is effective for synthesizing fine particles with good dispersibility. Also, the particle morphology can be precisely controlled by using a surface surfactant as an additive. Since the slight amount of water in the solvent significantly affects crystal growth, further precise control of the synthesis process is required to synthesize monodispersed nano-sized uniform particles. Here, a novel solvothermal process, denoted “Water Controlled-Release Solvothermal Process (WCRSP)” is designed to synthesize the particle with homogeneous morphologies.

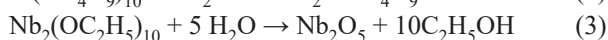
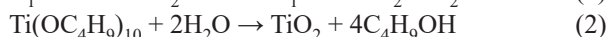
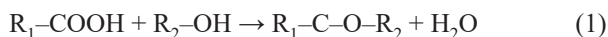
The WCRSP uses a mixture of alcohol and carboxylic acid as a reaction solvent and skillfully utilizes the water produced by the esterification reaction between alcohol and carboxylic acid at high temperatures. The released water molecules amount in the reaction solvent can be precisely controlled by changing the ratio of the starting alcohol and carboxylic acid solvents. The released water amount

significantly affects the crystal growth of the products. In principle, changing the composition of solvents will result in different water amounts in the reaction system, finally affecting the particle size and morphology of the products. Therefore, the WCRSP process can be utilized for controlling particle size and morphology because the water molecular is slowly released, and the reaction environment can be kept in a constant state, resulting in the formation of homogeneous particles size and morphology (Guo et al., 2010; 2011d; 2013a).

**Fig. 6** shows the principle and reaction mechanism of the WCRSP process. There are three key points in the WCRSP process. First, water is not the starting solvent in the reaction, but carboxylic acids and alcohols are used. At high temperatures, the esterification reactions proceed, and water molecules are produced and released in the reaction system; Second, the number of water molecules can be previously controlled by controlling the solvent composition; Third, the subsequent reaction should be a hydrolysis reaction. In some cases, the release of water molecules is also possible by etherification between various alcohol molecules. Still, in the case of esterification using carboxylic acids and alcohols, the control of water molecules is efficient. When the reaction temperature rises, the reaction between or among the liquid solvents such as ethanol ( $\text{C}_2\text{H}_5\text{OH}$ ), n-butanol ( $\text{C}_4\text{H}_9\text{OH}$ ), and acetic acid ( $\text{CH}_3\text{COOH}$ ) is carried out. The self-dehydration of ethanol, n-butanol and the cross-dehydration between different organic molecules are carried out. Also, the reaction

with acetic acid produces ethyl acetate ( $\text{CH}_3\text{COOC}_2\text{H}_5$ ) or *n*-butyl acetate ( $\text{CH}_3\text{COOC}_4\text{H}_9$ ), at the same time releasing a certain amount of water molecular (Gao et al., 2019). Therefore, an increase in the reaction temperature benefits the formation of ether.

In the case of titanium oxide formation, tetra-*n*-butyl titanate ( $\text{Ti}(\text{OC}_4\text{H}_9)_4$ ) or titanium tetraisopropoxide ( $\text{Ti}(\text{OC}_3\text{H}_7)_4$ ) are utilized as a titanium source, acetic acid ( $\text{CH}_3\text{COOH}$ ) and various alcohols are used as a solvent. The mixture is sealed in a 100 ml Teflon-lined stainless autoclave and reacted under a hydrothermal reaction at 200–240 °C for 24 h. The typical chemical reactions are shown in Eqns. (1) & (2):



The esterification reaction of carboxylic acids and alcohols produces esters and water molecules. The water

molecule produced by Eqn. (1) is utilized in the hydrolysis reaction with tetra-*n*-butyl titanate of Eqn. (2), and finally, titanium oxide is synthesized. The number of water molecules produced can be controlled by controlling the ratio of carboxylic acids and alcohols. Furthermore, using various alkoxides makes precise composition control of the products possible. For example, the Nb-doped titanium oxide (NTO) can be synthesized by introducing the desired amount of a niobium alkoxide ( $\text{Nb}_2(\text{OC}_2\text{H}_5)_{10}$ ) into the titanium alkoxide to realize the composition control, as shown in the reaction of Eqn. (3) (Asakura et al., 2018).

Fig. 7 shows the TEM images of the 15 % Nb-doped  $\text{TiO}_2$  particles (NTO) synthesized in the solvents with various ethanol: acetic acid (*x*:*y*) ratios. The produced and released water amount increases with the acetic acid amount increment in the solvent. As mentioned in Fig. 1, during the dissolution-precipitation process, water as a solvent with a large dielectric constant prefers to enhance crystalline growth, resulting in large particle size. As a result, less

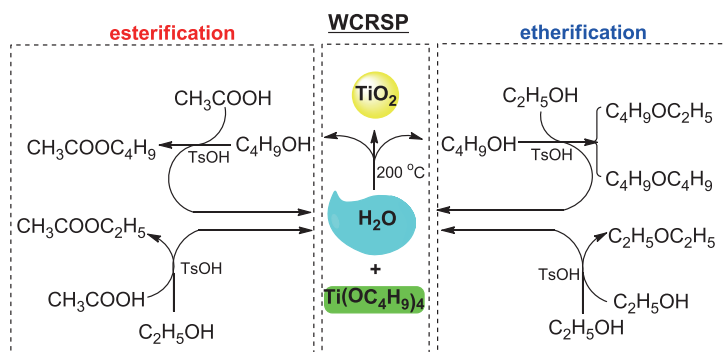


**Fig. 6** Principle and reaction mechanism of the WCRSP for  $\text{TiO}_2$  formation in ethanol and acetic acid solution (TsOH (*p*-toluenesulfonic acid) is an acid catalyst that acts as a reaction-promoting catalyst, and the reaction can proceed without using it.) [Reproduced from Ref. (Gao et al., 2019) with permission from the IOP].

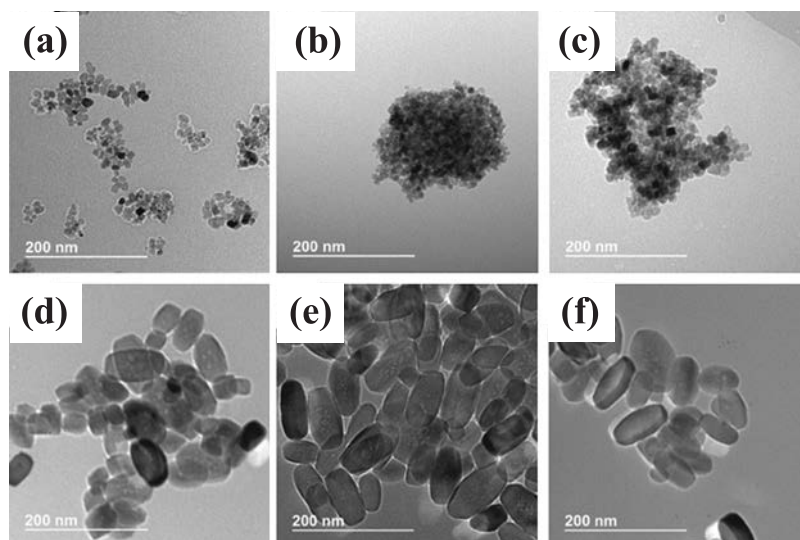
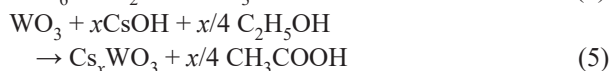


**Fig. 7** TEM image of 15 % Nb-doped titanium oxide particles (NTO (*x*:*y*), *x*:ethanol (ml); *y*:acetic acid (ml)) synthesized by WCRSP in an acetic acid-ethanol mixed solvent. (a) NTO(60:0), (b) NTO(55:5), (c) NTO(50:10), (d) NTO(40:20), (e) NTO(35:25), (f) NTO(30:30). [Reproduced from Ref. (Asakura et al., 2018) with permission from the IOP]

acetic acid in the WCRSP produces less water, leading to the formation of the tiniest particles, as shown in **Fig. 7(a)**. When the ethanol: acetic acid ratio reaches 30:30 (i.e., 1:1), the most significant amount of water is produced, leading to the formation of the large particles, as shown in **Fig. 7(f)**.

Another example is the mixed-valence state tungsten bronze structure  $M_xWO_3$  ( $x = 0.33$ ,  $M = Cs, Na, K$ , etc.), in which alkali metal ions are doped into the W site tungsten. The mixed-valence state tungsten base compound possesses high free electron density. It is expected to be applied to various new functional materials such as infrared shielding materials, transparent conductive materials, etc. Conventionally,  $M_xWO_3$  is synthesized by solid-state reaction, and a high temperature of above 1000 °C is required. Usually, high reaction temperature results in a large product particle size. Also, morphological control is quite challenging. (Takeda and Adachi, 2007). Similar to that of Nb–TiO<sub>2</sub>, the influence of the solvent is also obvious for the synthesis of  $M_{0.33}WO_3$ . **Fig. 8** shows the SEM images of the  $M_xWO_3$  ( $M = Cs, K, Na$ ) obtained by the solution process. The Cs ion has a large ionic radius and is difficult to dope with high concentration. The maximum Cs doping amount is about 1/3, forming a tunnel structure with a hexagonal phase ( $x = 0.33$ ). In a traditional hydrothermal synthesis process, a single phase of  $Cs_{0.33}WO_3$  can be successfully produced; however, the particle growth is remarkable, and the particle size reaches large than 500 nm (**Fig. 8(a)**) (Liu et al., 2010).



On the other hand, by using the WCRSP process under the esterification reaction, the number of released water molecules can be precisely controlled. As a result, the single phase of  $M_xWO_3$  with rod-like uniform morphology

can be successfully obtained. Eqn. (4) shows that tungsten oxide is first generated, tungsten oxide further reacts with CsOH, the presence of alcohol also serves as a reducing agent. Finally, a part of tungsten is reduced, and the mixed-valence state  $Cs_xWO_3$  is generated (Eqn. (5)). Because of the continuously released small amount of water in the reaction system, the particle growth due to the dissolution reprecipitation is suppressed. As a result, the particle size can remain small, producing  $Cs_{0.33}WO_3$  nanorods with a length of 90 nm and a diameter of 10 nm (**Fig. 8(b)**) (Guo et al., 2010; 2011d), which is about 1/5 or less of the size of that prepared by normal hydrothermal process (500 nm) (Liu et al., 2010). The tungsten bronze structure  $Cs_xWO_3$  has a hexagonal phase structure shown in **Fig. 8(c)**. In the cases of smaller ions such as sodium and potassium being utilized instead of cesium, the nanowire morphology (Guo et al., 2010; 2011a; 2011c; 2011d) with long length and tetragonal structure will be produced (see **Fig. 8(d–f)**). The small particle size of the mixed-valence state possesses many benefits such as excellent IR shielding properties, less light scattering resulting in high transparency, and ease of being introduced in cells for bio-applications. The related results will be introduced in the following.

Similarly, in the WCRSP process utilizing alcohols and carboxylic acids as solvents, it is possible to synthesize and control the morphology of various other oxide particles. **Fig. 9** shows various successful synthesized examples with unique particle morphologies. By using the WCRSP process, TiO<sub>2</sub> spherical particles with different sizes (Guo et al., 2013a), unique octahedron attached (Ta,N)-TiO<sub>2</sub> fibers, SnO spherical/hollow particles, plate-like, Moyatto ball-like, and tailed-shaped  $W_{18}O_{49}$  particles, etc. are successfully synthesized by using different precursors (Guo et al., 2012a; 2012d; Yin et al., 2018). All the particles possess uniform and unique morphology. Therefore, the WCRSP method can be used as a general-purpose synthesis way. In

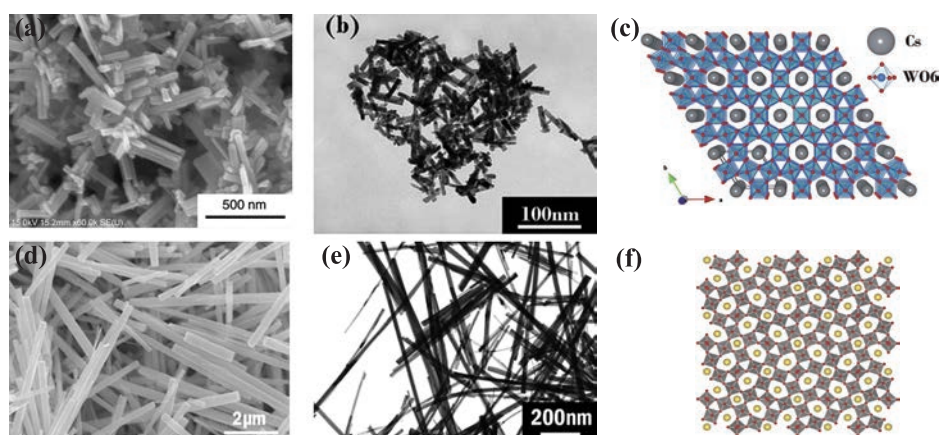


**Fig. 8** (a) SEM photograph of  $M_{0.33}WO_3$  by traditional solvothermal reaction, (b) TEM image of monodisperse  $Cs_{0.33}WO_3$  nanorods synthesized by WCRSP process using ethanol and 10 % acetic acid as reaction solvents (90 nm in length, 5–10 nm in diameter); (c) Hexagonal crystal structure of  $Cs_{0.33}WO_3$  (d) SEM image of  $Na_xWO_3$ , (e) TEM image of  $K_xWO_3$  nanowire; (f) crystal structure of tetragonal  $M_xWO_3$ , ( $M = K, Na$ ). [Reproduced from Ref. (Guo et al., 2011a; 2011d, Liu et al., 2010) with permission from the RSC, Elsevier, ACS]

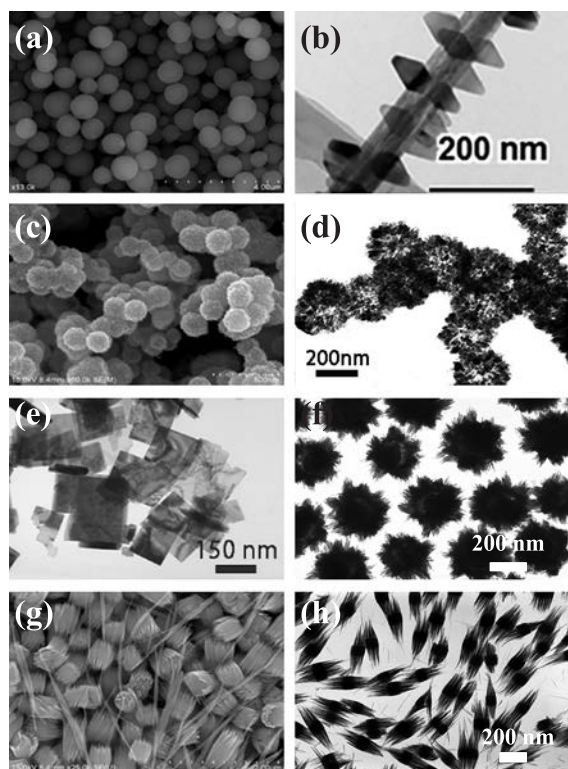


**Fig. 9** Uniform oxide particles with controllable morphology synthesized by WCRSP. (a)  $\text{TiO}_2$  spherical particles, (b) Fibrous (Ta, N)– $\text{TiO}_2$  with the octahedral structure on the surface together with high specific surface area; (c)  $\text{SnO}$  spherical particles; (d)  $\text{SnO}$  hollow particles; (e) Plate-like  $\text{WO}_3$  particles, (f) Mo-atom ball-like  $\text{W}_{18}\text{O}_{49}$  particles (using  $\text{W}(\text{CO})_6$  as a precursor), (g)  $\text{W}_{18}\text{O}_{49}$  (using  $\text{W}(\text{EtO})_6$  as a precursor), (h)  $\text{W}_{18}\text{O}_{49}$  (using  $\text{WCl}_6$  as a precursor). [Part of photos are reproduced from Ref. (Guo C. et al., 2012a; 2012d; 2013a; Yin S. et al., 2018) with permission from the RSC, ACS]

addition to ethanol, a series of higher alcohols such as butanol, ethylene glycol, and higher carboxylic acids such as acetic acid, butanoic acid, hexanoic acid, and octanoic acid is available as a reaction solvent and expected to be applied for the synthesis of various kinds of uniform inorganic functional particles with unique morphologies.

**Fig. 10** shows the schematic illustrations of the simulated experiment and temperature increment during the halogen lamp irradiation, together with the transmittance and reflectance spectra of  $\text{Cs}_x\text{WO}_3$  nanorods and ITO glass. Again, the  $\text{Cs}_x\text{WO}_3$  film shows a better temperature depress effect than those of ITO. The mixed-valence state tungsten bronze compounds  $\text{M}_x\text{WO}_3$  ( $\text{M} = \text{Cs}, \text{Na}, \text{K}, \text{etc.}$ ) have high free electron density. The free electrons move back and forth between  $\text{W}^{5+}$  and  $\text{W}^{6+}$ , resulting in an absorption of light corresponding to the vibration of electrons, leading to infrared light absorption. The tungsten bronze  $\text{M}_x\text{WO}_3$  is comparable with tin-doped indium (ITO) transparent conductive oxide film. The  $\text{M}_x\text{WO}_3$  can cover a more comprehensive infrared shielding range, realize excellent IR light-shielding properties over a broad infrared region than ITO conductive thin films, and show great potential as a smart window.

In order to improve visible light transparency and functionality of thin films, it is effective to reduce light scattering by using nanosize particles. The  $\text{M}_x\text{WO}_3$  particles synthesized by the WCRSP show a tiny size of about 20 nm, and light scattering is suppressed when a thin film is formed, resulting in high transparency. Furthermore, the resistance of the pressed powder reached 0.03–0.96 ( $\Omega \cdot \text{cm}$ ), suggesting its potential as a conductive material (Guo et al., 2012c). In addition, the nanowire morphology

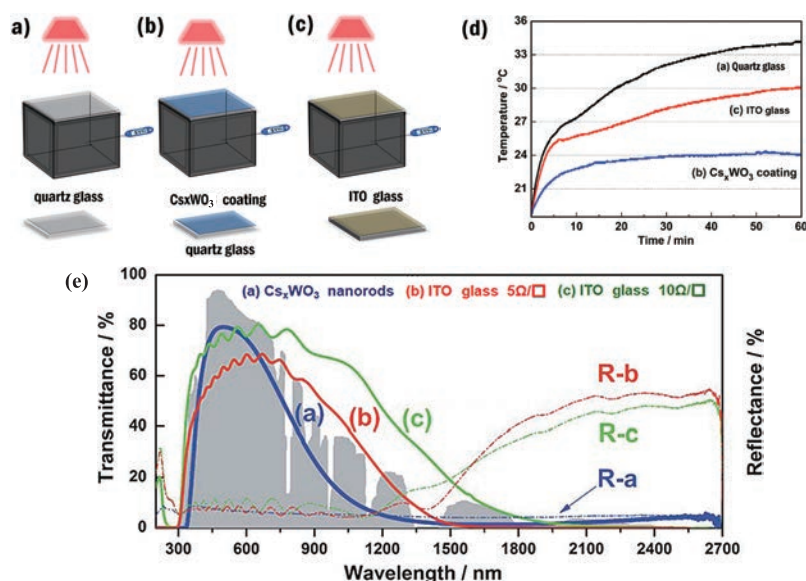


**Fig. 10** (a–c) Schematic illustrations of simulated experiment and (d) temperature increment during the halogen lamp irradiation for 1 h. Sealed boxes were covered by quartz glass,  $\text{Cs}_x\text{WO}_3$  coated quartz glass, and ITO glass ( $10 \Omega/\text{sq}$ ). (e) Transmittance and reflectance (R-a, R-b, R-c) spectra of  $\text{Cs}_x\text{WO}_3$  nanorods and ITO glass ( $5 \Omega/\text{sq}$  and  $10 \Omega/\text{sq}$ ). The background shows the relative energy wavelength distribution of solar spectrum on the sea level. [Reproduced from Ref. (Guo et al., 2011b; 2011d) with permission from the RSC]

of  $M_x\text{WO}_3$  ( $M = \text{K}, \text{Na}$ ) shown in Fig. 8(c,d) possesses a low interparticle resistance so that it can realize better conductivity than nanoparticles (Guo et al., 2011c; 2012c). Some other tungsten bronze materials, such as  $(\text{NH}_4)_x\text{WO}_3$  and  $\text{W}_{18}\text{O}_{49}$  with a reduced tungsten valence state, also consist of mixed-valence state of  $\text{W}^{5+}$  and  $\text{W}^{6+}$ . These compounds also contain free electrons and excellent infrared light-shielding properties (Guo et al., 2012b; 2012d; 2013b).

Fig. 11 shows the correlation between the particle size of  $\text{W}_{18}\text{O}_{49}$  and the infrared shielding property. The  $\text{W}_{18}\text{O}_{49}$  is also one of the mixed-valence state tungsten-based materials with a monoclinic crystal structure. As the particle size decreases, it can be confirmed that the infrared light-shielding property has been improved. It is thought to be due to the polaron effect on the surface of the  $\text{W}_{18}\text{O}_{49}$  particles. In the  $\text{W}_{18}\text{O}_{49}$ ,  $\text{W}^{5+}$  and  $\text{W}^{6+}$  are reversed due to the electrons' movement. It leads to the surface charge

revision of tungsten ions next to each other. As a result, free electrons cause plasmon oscillations on the surface of tungsten in the mixed-valence state, shielding light with energies lower than the infrared wavelength without passing through. The larger the surface of the particles, the stronger the polaron effect is considered to appear (Guo et al., 2012d). On the other hand, since  $\text{WO}_3$  is not a mixed-valence state substance, it cannot cover the light in the infrared region and has no infrared shielding property.

In addition, uniform  $\text{Cs}_{0.33}\text{WO}_3$  nanoparticles can successfully be introduced into cancer cells by hydrophilic surface treatment using a PEG-silane coupling agent. The effect of the temperature rise under irradiation with a 980 nm infrared laser ( $0.07 \text{ Wcm}^{-2}$ ) is confirmed, suggesting that  $\text{Cs}_{0.33}\text{WO}_3$  nanoparticles may be utilized as a new hyperthermia treatment material for cancer cells (Guo et al., 2013b). Fig. 12 shows the temperature increment effect under IR light irradiation, with and without hydrophilic

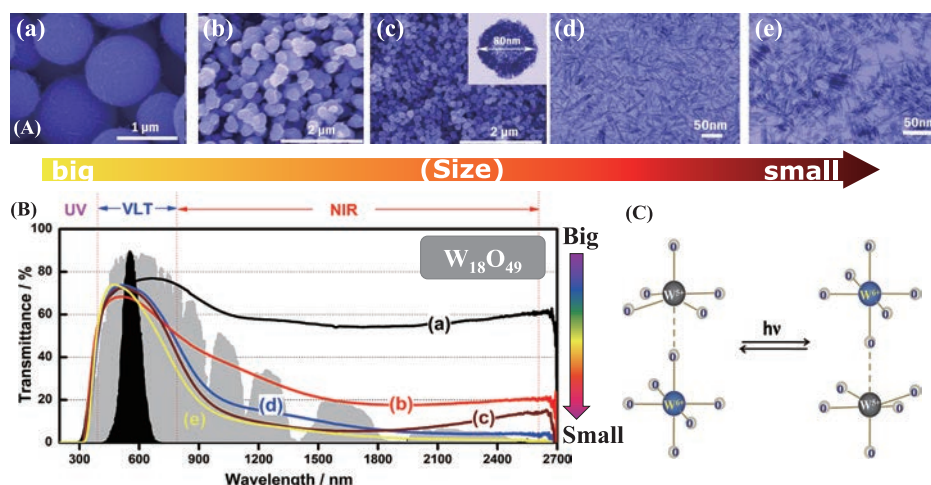


**Fig. 11** (A) SEM image of spherical  $\text{W}_{18}\text{O}_{49}$  with different particle sizes; (B) Transmission spectrum (infrared shielding characteristics) of  $\text{W}_{18}\text{O}_{49}$  samples; (C) Infrared light shielding mechanism of  $\text{W}^{5+}$ - $\text{W}^{6+}$  mixed-valence state tungsten-based compounds. [Reproduced from Ref. (Guo et al., 2012d) with permission from the ACS]

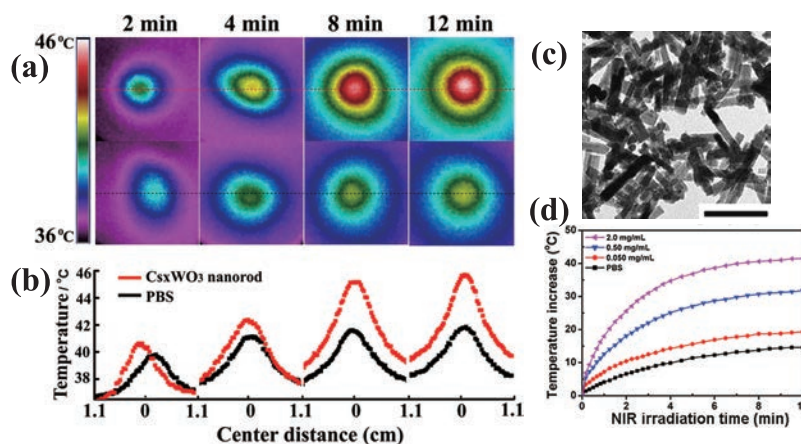


**Fig. 12** (a) Temperature increment thermographic images and (b) temperature distribution profile with/without  $\text{Cs}_{0.33}\text{WO}_3$  nanorods ((c) TEM image) dispersed in simulated culture solution PBS, under infrared light irradiation for 2–12 min. (d) Efficient temperature increment by controlling the concentration of nanoparticles and irradiation time. [Reproduced from Ref. (Guo et al., 2013b) with permission from RSC]

$\text{Cs}_{0.33}\text{WO}_3$  nanoparticles introduced in the pseudo-culture medium PBS. An efficient temperature increment effect can be observed by controlling the concentration of  $\text{Cs}_{0.33}\text{WO}_3$  nanoparticles and the IR light irradiation time. The cancer cells take in excess nutrition, and blood vessels are often incomplete. It is difficult to transport decomposed products in blood; therefore, lactic acid accumulates and shows the property of being vulnerable to temperature. As a result, the cancer cells are more susceptible to heat than normal cells.

IR light possesses a deep reach distance in the human body and causes minor damage to normal cell tissues. By incorporating  $\text{Cs}_{0.33}\text{WO}_3$  nanoparticles into cancer cells and exposing them to infrared light irradiation, it is possible to selectively kill cancer cells that can reach a temperature range above  $42^\circ\text{C}$  under IR light irradiation. In order to efficiently introduce the nanoparticles that absorb infrared rays into the cancer cell, it is necessary to produce a uniform morphology and small particle size, so the WCRSP process shows its effectiveness and great potential for practice bio-applications.

## 2.6 Direct formation of functional thin films by solution reaction

Some vapor synthesis methods, such as vapor deposition, CVD, sputtering, etc., are usually used for thin-film formation. In the above cases, external energy such as high vacuum, high frequency, and a high electric field is required for these synthesis processes. On the other hand, as a method of forming a thin film starting from a powder material, pressure molding method, doctor blade method, spin coating method, or using the powders sintering body or powder casting body as a target for sputtering are

widely utilized. Furthermore, as a novel thin-film synthesis method, the direct film formation of oxides is also possible using a solution process. Here, an example of the direct formation of a zinc oxide particle film is introduced.

In **Section 2.3**, it was introduced that the zinc oxide particles with various morphologies can be synthesized in the aqueous zinc nitrate solution with the addition of a specific concentration of hexamethylenetetramine ( $\text{C}_6\text{H}_{12}\text{N}_4$ , HMT). A glass substrate was introduced into the reaction system during the synthesis process. Not only the zinc oxide particles are produced in the solution, but a uniform thin film could also be precipitated on the surface of the glass substrate directly. The mentioned liquid-phase reaction can synthesize a relatively durable oxide particle film. Furthermore, the nanostructure of the zinc oxide particle film changed significantly by a long-term aging process treatment, similar to that of the formation process of rose-like particles. **Fig. 13** shows the hydrophilicity evaluation results and surface morphology of particle films synthesized by the solution process. The contact angle of water drop on the surface of the zinc oxide single crystal (001) plane was  $93^\circ$ . However, the zinc oxide particle film with nanorod morphology shows a contact angle of  $165^\circ$ , indicating a super-water repellency of the surface. In contrast, the ZnO particle thin film with developed nano-screw morphology shows a complete opposite property. The water drop on the ZnO surface shows a contact angle of  $0^\circ$ , showing super hydrophilicity. Interestingly, the same material of ZnO with quite different morphologies can achieve the opposite super hydrophilicity and superhydrophobicity (Long et al., 2010b; Yin and Sato, 2005). The unique microstructure of zinc oxide thin films is thought to depend on the solubility

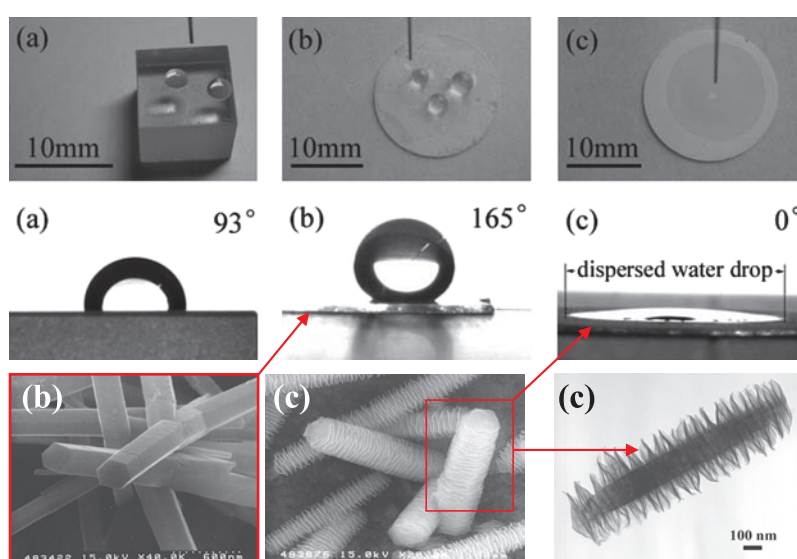


**Fig. 13** (Upper) Top view CCD image of water drop on various surfaces. (a) ZnO single crystal (001) surface; (b) superhydrophobic surface of ZnO film with nanorod superstructure; (c) super hydrophilic surface of ZnO film with the nano-screw superstructure; (Middle) Side view CCD images (Evaluation of contact angle / hydrophilicity); (Bottom) SEM and TEM images of (b) nanorods and (c) nano-screws. [Reproduced from Ref. (Yin and Sato, 2005) with permission from the RSC]



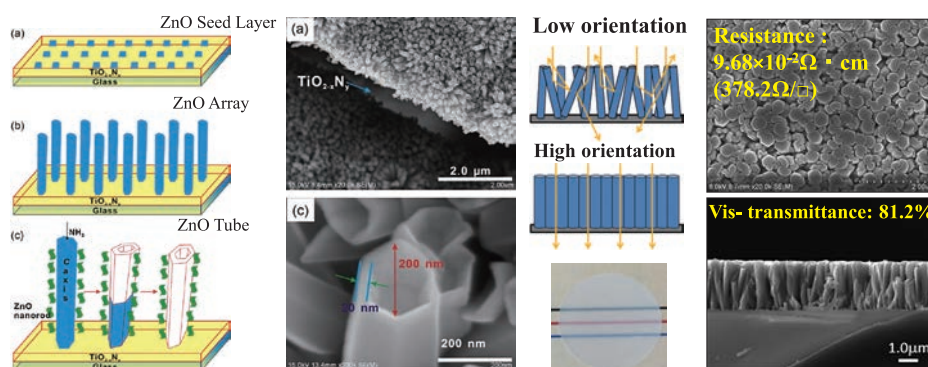


**Fig. 14** (Left) Formation process and SEM image of  $\text{TiO}_{2-x}\text{N}_y/\text{ZnO}$  oriented tube structure composite thin film; (Right) Excellent transparency and conductivity of ZnO film consisting of hexagonal nanorods oriented on the substrate.

of zinc ions in the solvent, the dissolution-precipitation rate, differences in ion adsorption capacity at different zinc oxide crystal surfaces, etc.

This zinc oxide morpho-regulatory method can also be used to realize new functionality by combining it with other functional materials. Combining high photocatalytic active nitrogen-doped titanium oxide with developed nanostructured zinc oxide particle thin film is an exciting combination. The thin film of  $\text{TiO}_{2-x}\text{N}_y$  on a glass substrate is prepared by a spin coating method at first, and then the film is set in a  $\text{Zn}(\text{NO}_3)_2$ -HMT solution to precipitate a ZnO complex film at  $95^\circ\text{C}$ . In another case, orientated ZnO nanorods are grown on the  $\text{TiO}_{2-x}\text{N}_y$  surface, then leached by alkali solution to produce a complex tubular ZnO structure (Fig. 14 (left)). The complex structure of ZnO or tubular ZnO possesses excellent adsorption properties, which can accelerate the photocatalytic reaction on  $\text{TiO}_{2-x}\text{N}_y$ . The complex structures of the ZnO / tubular ZnO thin films also have a fantastic light-limiting effect. The irradiated light can be reflected inside the complex structure or tubular structure to achieve multiple irradiations on the  $\text{TiO}_{2-x}\text{N}_y$  photocatalytic surface (Huang et al., 2012; Yin et al., 2008).

In addition, in order to get a high-quality and dense ZnO thin film, another seed crystalline method is utilized. At first, ZnO nanoparticles less than 10 nm are prepared and coated in advance on the surface of a glass substrate by a spin coating method. Then, the as-prepared thin film is introduced in a  $\text{Zn}(\text{NO}_3)_2$ -HMT solution to precipitate a ZnO complex film at  $95^\circ\text{C}$ . The nano-sized crystals on the substrate act as seeds during the following precipitation process. It is found that zinc oxide-oriented dense film that grew uniformly in the *c*-axis direction can be synthesized perfectly (Fig. 14 (right)). The hexagonal columnar rods are arranged in the same direction, making it possible to be a dense ZnO thin film in which only the {002} surface of zinc oxide is exposed. Because of the highly orientated crystal growth with high density and less porosity, such high transparency of 81.2% and excellent conductivity of  $9.68 \times 10^{-2} \Omega \cdot \text{cm}$  are successfully realized, indicating

its potential applications on transparent oxide conductive thin film.

## 2.7 Morphological control and functional improvement of non-oxide by topotactic reaction

Transition metal nitrides and oxynitrides have been focused on their novel functionality, and their importance has been recognized. By replacing the oxygen site of oxides with an anion having a different electronegativity, the material's electronic structure will be significantly changed, and the discovery of some novel physical and chemical properties is expected (Kageyama et al., 2018). Usually, the synthesis of transition metal nitride and oxynitride requires a high temperature, and its morphology control is difficult. As mentioned above, the solution process has the merits of particle size and morphological controllability so that the oxide could be utilized for the synthesis of the morphology controllable nitrides and oxynitrides. At first, hydrothermal or solvothermal reactions synthesize morphologically controlled metal oxides or hydroxide precursors. Then, these precursors are utilized to synthesize the non-oxide materials with similar particle morphologies and sizes by topotactic reactions under relatively low and mild reaction conditions. This method provides a possibility to synthesize nitrides and oxynitrides with controllable morphologies. For example, under hydrothermal conditions, aluminum hydroxide  $\gamma\text{-AlOOH}$  (boehmite) with a nest-like or plate shape morphologies can be synthesized by controlling the reaction temperature, pH, and adding a surfactant. By using these aluminum hydroxides as the precursor, it is possible to synthesize aluminum nitride with different morphologies such as plates, fibers, nanosize, etc., by treating the mentioned precursors in ammonia gas. However, if the nitridation temperature is too high, the morphologies of the oxide precursor may collapse. During the nitridation treatment, a small amount of hydrazine addition can accelerate the nitridation reaction and reduce the nitridation temperature and time (Hermawan et al., 2020).

Fig. 15 shows the SEM photographs of boehmite and

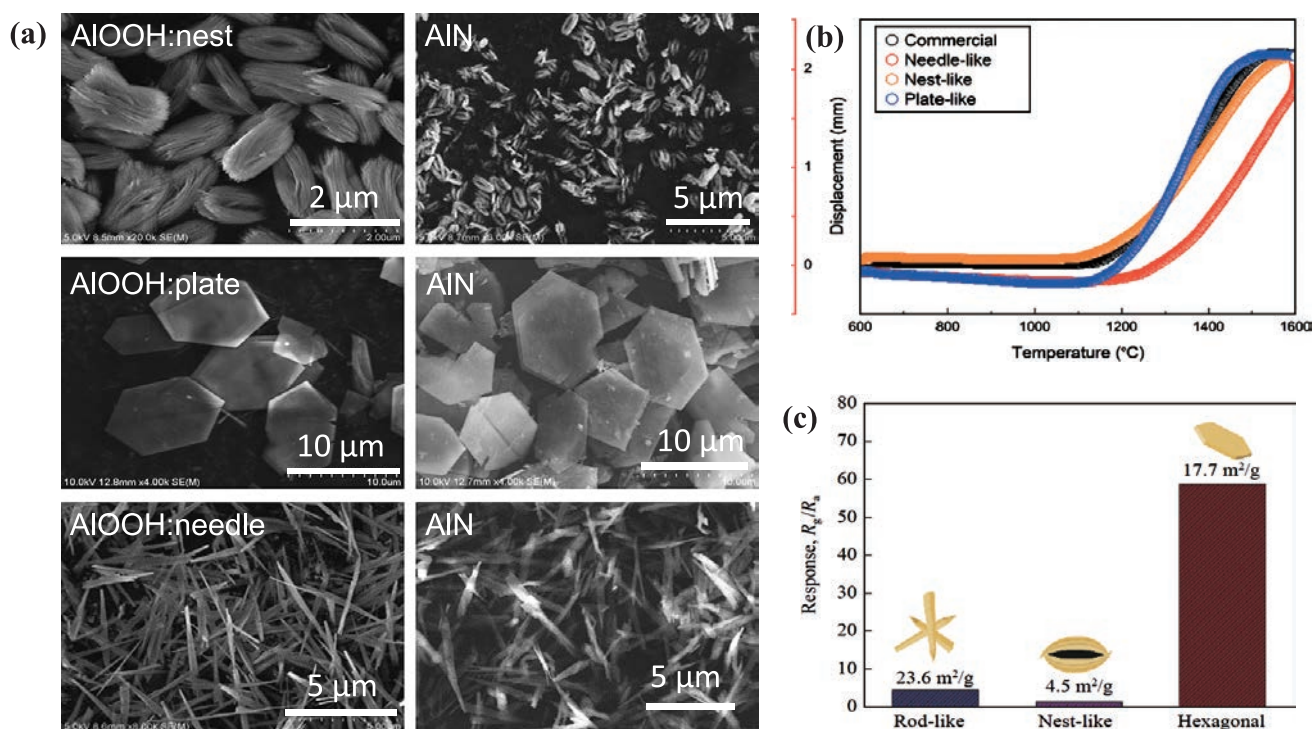


**Fig. 15** (a) Topotactic morphology conversion from AlOOH (left column) to AlN (right column); (b) sintering behavior of AlN particles with different morphology; (c) Hydrogen gas response properties of morphologically controlled AlN. [Reproduced from Ref. (Hermawan et al., 2018b; 2020) with permission from the Springer & Taylor]

nitrides with various morphologies. The sintering performance and hydrogen gas sensing properties of nitrides with various morphologies are also characterized. It is suggested that such topotactic reaction could realize the morphology control of non-oxides materials. Furthermore, the morphological dependence of functionality of the nitrides is observed. As shown in Fig. 15(b), the sintering properties of nitrides with different particle morphologies are significantly changed. However, the plate-like particles are easily arranged in the same direction and could be sintered at relatively low temperatures. Furthermore, aluminum nitride having a plate-like morphology, showed a superior hydrogen gas sensing functionality compared to aluminum nitride with other morphologies (Hermawan et al., 2018b). Also, in the case of  $\alpha$ -GaOOH precursor, the same topotactic reaction enables the synthesis of nitrides (GaN) with the same morphology of oxides ( $\beta$ -Ga<sub>2</sub>O<sub>3</sub>). Therefore, it is found that the GaN possesses better hydrogen gas sensing sensitivity than that of  $\beta$ -Ga<sub>2</sub>O<sub>3</sub> with the same morphology (Hermawan et al., 2018a).

### 3. Future outlook

The morphology control of various transition metal oxide materials and their functionality development are reviewed. This paper focuses on the synthesis process and the relationship between morphologies and their functionalities. Hydrothermal and solvothermal processes are environmentally friendly processes that provide the possibility

for morphologies and particle size control. Water molecules are essential in promoting the dissolution–reprecipitation process and significantly affect the particle morphologies and size. The utilization of esterification reactions between various alcohols and carboxylic acids (WCRSP process) allows uniform morphologies and controllable particle size. Furthermore, the effectiveness of morphological control using the topotactic reaction is confirmed. The oxides and non-oxides with unique morphologies show many applications, such as photocatalysts, ultraviolet/heat ray shielding, cancer cell hyperthermia treatment, hydrophilic/hydrophobic thin films, and gas sensor, etc. Different novel functionality can be realized by morphological control, material design, and the optimization of their synthesis processes, and further research and progress are expected in the future.

### Acknowledgements

This scientific work was partly financed from the JSPS Grant-in-Aid for Scientific Research on Innovative Areas “Mixed anion” (No. 16H06439, Grant-in-Aid for Scientific Research (20H00297)).

### References

- Asahi R., Morikawa T., Ohwaki T., Aoki K., Taga Y., Visible-light photocatalysis in nitrogen-doped titanium oxides, *Science*, 293 (2001) 269–271. DOI: 10.1126/science.1061051
- Asakura Y., Anada Y., Hamanaka R., Sato T., Katsumata K.-I., Wu X., Yin S., Multifunctionality in coating films including

- Nb-doped TiO<sub>2</sub> and Cs<sub>x</sub>WO<sub>3</sub>: near infrared shielding and photocatalytic properties, *Nanotechnology*, 29 (2018) 224001. DOI: 10.1088/1361-6528/aab600
- Byrappa K., Yoshimura M., *Handbook of Hydrothermal Technology*, 2nd ed, William Andrew Inc., New York, 2012, ISBN: 9780123750907. DOI: 10.1016/C2009-0-20354-0
- Cao J., Hasegawa T., Asakura Y., Sun P., Yang S., Li B., Cao W., Yin S., Synthesis and color tuning of titanium oxide inorganic pigment by phase control and mixed-anion co-doping, *Advanced Powder Technology*, 33 (2022) 103576. DOI: 10.1016/j.apt.2022.103576
- Gao X., Chang H., Asakura Y., Zhao Z., Gao W., Qiao Y., Yin S., Influence of water-controlled release process on the physical and chemical property of nanosize TiO<sub>2</sub> particles, *Materials Research Express*, 6 (2019) 066208. DOI: 10.1088/2053-1591/ab0d67
- Guo C., Wu X., Yan M., Dong Q., Yin S., Sato T., Liu S., The visible-light driven photocatalytic destruction of NO<sub>x</sub> using mesoporous TiO<sub>2</sub> spheres synthesized *via* a “water-controlled release process”, *Nanoscale*, 5 (2013a) 8184–8191. DOI: 10.1039/c3nr02352d
- Guo C., Yin S., Dong Q., Sato T., The near infrared absorption properties of W<sub>18</sub>O<sub>49</sub>, *RSC Advances*, 2 (2012a) 5041–5043. DOI: 10.1039/c2ra01366e
- Guo C., Yin S., Dong Q., Sato T., Simple route to (NH<sub>4</sub>)<sub>x</sub>WO<sub>3</sub> nanorods for near infrared absorption, *Nanoscale*, 4 (2012b) 3394–3398. DOI: 10.1039/c2nr30612c
- Guo C., Yin S., Huang L., Sato T., Synthesis of one-dimensional potassium tungsten bronze with excellent near-infrared absorption property, *ACS Applied Materials & Interfaces*, 3 (2011a) 2794–2799. DOI: 10.1021/am200631e
- Guo C., Yin S., Huang L., Yang L., Sato T., Discovery of an excellent IR absorbent with a broad working waveband: Cs<sub>x</sub>WO<sub>3</sub> nanorods, *Chemical Communications*, 47 (2011b) 8853–8855. DOI: 10.1039/c1cc12711j
- Guo C., Yin S., Sato T., Synthesis of one-dimensional hexagonal sodium tungsten oxide and its near-infrared shielding property, *Nanoscience and Nanotechnology Letters*, 3 (2011c) 413–416. DOI: 10.1166/nml.2011.1182
- Guo C., Yin S., Sato T., Effects of crystallization atmospheres on the near-infrared absorption and electroconductive properties of tungsten bronze type M<sub>x</sub>WO<sub>3</sub> (M = Na,K), *Journal of the American Ceramic Society*, 95 (2012c) 1634–1639. DOI: 10.1111/j.1551-2916.2011.05039.x
- Guo C., Yin S., Yan M., Kobayashi M., Kakihana M., Sato T., Morphology-controlled synthesis of W<sub>18</sub>O<sub>49</sub> nanostructures and their near-infrared absorption properties, *Inorganic Chemistry*, 51 (2012d) 4763–4771. DOI: 10.1021/ic300049j
- Guo C., Yin S., Yan M., Sato T., Facile synthesis of homogeneous Cs<sub>x</sub>WO<sub>3</sub> nanorods with excellent low-emissivity and NIR shielding property by a water controlled-release process, *Journal of Materials Chemistry*, 21 (2011d) 5099–5105. DOI: 10.1039/c0jm04379f
- Guo C., Yin S., Yu H., Liu S., Dong Q., Goto T., Zhang Z., Li Y., Sato T., Photothermal ablation cancer therapy using homogeneous Cs<sub>x</sub>WO<sub>3</sub> nanorods with broad near-infrared absorption, *Nanoscale*, 5 (2013b) 6469–6478. DOI: 10.1039/c3nr01025b
- Guo C., Yin S., Zhang P., Yan M., Adachi K., Chonan T., Sato T., Novel synthesis of homogenous Cs<sub>x</sub>WO<sub>3</sub> nanorods with excellent NIR shielding properties by a water controlled-release solvothermal process, *Journal of Materials Chemistry*, 20 (2010) 8227–8229. DOI: 10.1039/c0jm01972k
- Hermawan A., Amrillah T., Riapanitra A., Ong W.J., Yin S., Prospects and challenges of MXenes as emerging sensing materials for flexible and wearable breath-based biomarker diagnosis, *Advanced Healthcare Materials*, 10 (2021) 2100970. DOI: 10.1002/adhm.202100970
- Hermawan A., Asakura Y., Kobayashi M., Kakihana M., Yin S., High temperature hydrogen gas sensing property of GaN prepared from α-GaOOH, *Sensors and Actuators B: Chemical*, 276 (2018a) 388–396. DOI: 10.1016/j.snb.2018.08.021
- Hermawan A., Asakura Y., Yin S., Morphology control of aluminum nitride (AlN) for a novel high-temperature hydrogen sensor, *International Journal of Minerals, Metallurgy and Materials*, 27 (2020) 1560–1567. DOI: 10.1007/s12613-020-2143-8
- Hermawan A., Son H., Asakura Y., Mori T., Yin S., Synthesis of morphology controllable aluminum nitride by direct nitridation of γ-AlOOH in the presence of N<sub>2</sub>H<sub>4</sub> and their sintering behavior, *Journal of Asian Ceramic Societies*, 6 (2018b) 63–69. DOI: 10.1080/21870764.2018.1439611
- Hertrampf J., Becker P., Widenmeyer M., Weidenkaff A., Schlücker E., Niewa R., Ammonothermal crystal growth of indium nitride, *Crystal Growth and Design*, 18 (2018) 2365–2369. DOI: 10.1021/acs.cgd.7b01776
- Huang Y., Wei Y., Wu J., Guo C., Wang M., Yin S., Sato T., Low temperature synthesis and photocatalytic properties of highly oriented ZnO/TiO<sub>2-x</sub>N<sub>y</sub> coupled photocatalysts, *Applied Catalysis B: Environmental*, 123–124 (2012) 9–17. DOI: 10.1016/j.apcatb.2012.04.010
- Jaleel A., Haider A., Nguyen C. Van, Lee K.R., Choung S., Han J.W., Baek S.H., Shin C.H., Jung K.D., Structural effect of nitrogen/carbon on the stability of anchored Ru catalysts for CO<sub>2</sub> hydrogenation to formate, *Chemical Engineering Journal*, 433 (2022) 133571. DOI: 10.1016/j.cej.2021.133571
- Kageyama H., Hayashi K., Maeda K., Atfield J.P., Hiroi Z., Rondinelli J.M., Poeppelmeier K.R., Expanding frontiers in materials chemistry and physics with multiple anions, *Nature Communications*, 9 (2018) 772. DOI: 10.1038/s41467-018-02838-4
- Liu B., Wang Y., Huang Y., Dong P., Yin S., Morphological control and photocatalytic activities of nitrogen-doped titania nanoparticles by microwave-assisted solvothermal process, *Journal of the Australian Ceramic Society*, 48 (2012) 249–252. <http://www.scopus.com/inward/record.url?scp=84865266242&partnerID=8YFLogxK>
- Liu J.-X., Ando Y., Dong X.-L., Shi F., Yin S., Adachi K., Chonan T., Tanaka A., Sato T., Microstructure and electrical–optical properties of cesium tungsten oxides synthesized by solvothermal reaction followed by ammonia annealing, *Journal of Solid State Chemistry*, 183 (2010) 2456–2460. DOI: 10.1016/j.jssc.2010.08.017
- Long T., Dong X., Liu X., Liu J., Yin S., Sato T., Synthesis of ZnO crystals with unique morphologies by a low-temperature solvothermal process and their photocatalytic deNO<sub>x</sub> properties, *Research on Chemical Intermediates*, 36 (2010a) 61–67. DOI: 10.1007/s11164-010-0114-9
- Long T., Takabatake K., Yin S., Sato T., Mild solvothermal synthesis and characterization of ZnO crystals with various morphologies on borosilicate glass substrate, *Journal of Crystal Growth*, 311 (2009a) 576–579. DOI: 10.1016/j.jcrysgro.2008.09.048
- Long T., Yin S., Sato T., Soft solution synthesis of ZnO films with developed superstructures, *Journal of Nanoscience and Nanotechnology*, 10 (2010b) 4619–4623. DOI: 10.1166/jnn.2010.1681
- Long T., Yin S., Takabatake K., Zhnag P., Sato T., Synthesis and characterization of ZnO nanorods and nanodisks from zinc chloride aqueous solution, *Nanoscale Research Letters*, 4

- (2009b) 247. DOI: 10.1007/s11671-008-9233-2
- Minamidate Y., Yin S., Sato T., Synthesis and characterization of plate-like ceria particles for cosmetic application, *Materials Chemistry and Physics*, 123 (2010) 516–520. DOI: 10.1016/j.matchemphys.2010.05.007
- Sato T., Inoue Y., Yin S., Fujishiro Y., Odashima T., Crystallisation of ceria-doped tetragonal zirconia in methanol, n-hexane and water at elevated temperatures, *Ceramic Transactions*, 81 (1998) 29–34.
- Somiya S., Preparation of ultrafine powders by hydrothermal reactions, *Journal of the Japan Society of Colour Material (in Jpn)*, 57 (1984) 403–408. DOI: 10.4011/shikizai1937.57.403
- Takeda H., Adachi K., Near infrared absorption of tungsten oxide nanoparticle dispersions, *Journal of the American Ceramic Society*, 90 (2007) 4059–4061. DOI: 10.1111/j.1551-2916.2007.02065.x
- Taufik A., Asakura Y., Kato H., Kakihana M., Saleh R., Sekino T., Yin S., 1T/2H-MoS<sub>2</sub> engineered by in-situ ethylene glycol intercalation for improved toluene sensing response at room temperature, *Advanced Powder Technology*, 31 (2020) 1868–1878. DOI: 10.1016/j.apt.2020.02.022
- Wang Z.L., Self-assembled nanoarchitectures of polar nanobelts/nanowires, *Journal of Materials Chemistry*, 15 (2005) 1021–1024. DOI: 10.1039/b414550j
- Wang Z.L., Song J., Piezoelectric nanogenerators based on zinc oxide nanowire arrays, *Science*, 312 (2006) 242–246. DOI: 10.1126/science.1124005
- Xue Y., Yin S., Element doping: a marvelous strategy to pioneering the smart applications of VO<sub>2</sub>, *Nanoscale*, (2022) 11054–11097. DOI: 10.1039/d2nr01864k
- Yin S., Creation of advanced optical responsive functionality of ceramics by green processes, *Journal of the Ceramic Society of Japan*, 123 (2015) 823–834. DOI: 10.2109/jcersj2.123.823
- Yin S., Aita Y., Komatsu M., Wang J., Tang Q., Sato T., Synthesis of excellent visible-light responsive TiO<sub>2-x</sub>N<sub>y</sub> photocatalyst by a homogeneous precipitation-solvothermal process, *Journal of Materials Chemistry*, 15 (2005) 674–682. DOI: 10.1039/b413377c
- Yin S., Asakura Y., Recent research progress on mixed valence state tungsten based materials, *Tungsten*, 1 (2019) 5–18. DOI: 10.1007/s42864-019-00001-0
- Yin S., Chang H., Asakura Y., Sato T., Creation of functional inorganic nanoparticles by esterification reaction, *Ceramics Japan (in Jpn)*, 53 (2018) 722–725.
- Yin S., Ihara K., Li R., Sato T., Soft solution synthesis of a zinc oxide nano-screw superstructure and its composite with nitrogen-doped titania, *Research on Chemical Intermediates*, 34 (2008) 393–402. DOI: 10.1163/156856708784040641
- Yin S., Minamidate Y., Sato T., Synthesis and morphological control of monodispersed micro size ceria particles, *Surface Review and Letters*, 17 (2010) 147–152. DOI: 10.1142/s0218625x10013552
- Yin S., Minamidate Y., Tonouchi S., Goto T., Dong Q., Yamane H., Sato T., Solution synthesis of homogeneous plate-like multifunctional CeO<sub>2</sub> particles, *RSC Advances*, 2 (2012) 5976–5982. DOI: 10.1039/c2ra20280h
- Yin S., Sato T., Mild solution synthesis of zinc oxide films with superhydrophobicity and superhydrophilicity, *Journal of Materials Chemistry*, 15 (2005) 4584–4587. DOI: 10.1039/b512239b
- Zhao Z., Fan J., Chang H., Asakura Y., Yin S., Recent progress on mixed-anion type visible-light induced photocatalysts, *Science China Technological Sciences*, 60 (2017) 1447–1457. DOI: 10.1007/s11431-016-9022-9
- Zhu H., Zhang Z., Jiang X., Glycothermal synthesis of VO<sub>2</sub>(B) nanoparticles for gas sensing application, *Journal of Nano-science and Nanotechnology*, 20 (2020) 1946–1954. DOI: 10.1166/jnn.2020.17167

## Authors' Short Biographies



**Shu Yin**

Dr. Shu Yin received a Ph.D. in applied chemistry from Tohoku University in 1999. After that, he became a research assistant, lecturer, Associate Professor, and then a Full Professor at the Institute of Multidisciplinary Research for Advanced Materials (IMRAM), Tohoku University. Now he is also a Professor at the Advanced Institute for Materials Research (WPI-AIMR), Tohoku University. His research interests include morphological control, photocatalysts, UV-IR shielding, smart window, gas sensor, hydrothermal/solvothermal process, etc. He had won some scientific awards such as the 69<sup>th</sup> CerSJ Awards for Academic Achievements in Ceramic Science and Technology, and the APT Distinguished Paper Award etc.



**Takuya Hasegawa**

Dr. Takuya Hasegawa received a Ph.D. degree in engineering from Niigata University in 2016. He joined at Kochi University, Japan as an Assistant Professor in 2016, and then transferred to the Institute of Multidisciplinary Research for Advanced Materials (IMRAM), Tohoku University as Assistant Professor in 2019. His research topics are the development, including the synthesis, structural characterization and discovery of functionalities, of new photo-functional inorganic materials.

# Cellulose Nanofibrils Pulverized from Biomass Resources: Past, Present, and Future Perspectives<sup>†</sup>

Tetsuo Kondo

<sup>1</sup> Graduate School of Bioresource and Bioenvironmental Sciences, Kyushu University, Japan

<sup>2</sup> Enviro-Sustainable Materials Science Lab, Institute of Agriculture, Tokyo University of Agriculture and Technology, Japan

## Abstract

Advances in nanotechnology have changed conventional concepts in materials science. This has also strongly influenced natural biomass products with hierarchically built-up structures. In general, hierarchical structures in bio-based materials are built up by molecular self-assembly, followed by nanoassembly to form higher-level structures. Key to each step is the formation of interactions at each individual scale. Nature usually achieves such fabrication through a bottom-up process. However, fabrication can also be achieved through a top-down process, with various such downsizing methods now in development. This review article aims to describe trends in nanofiber technology among downsizing processes applied to cellulose as a representative biomass, ranging from fundamentals to recent techniques. The advantages of our recently developed technique, nanopulverization by aqueous counter collision, are also discussed. This method successfully decomposes interactions selectively without damaging the molecular structure, finally liberating components of various sizes into water to provide a transparent and homogeneous component–water system. As nanocellulose research is a broad area involving various fields, the cited references are limited to the scope of the author’s knowledge.

**Keywords:** cellulose nanofibril, cellulose nanocrystal, nanocellulose, aqueous counter collision (ACC), TEMPO-oxidized cellulose nanofibril, amphiphilicity, Janus-type nanofibril surface

## 1. Introduction

Nanotechnology, which is based on clarification of the surface structure of substances on the nanoscale and their interface interactions, has changed conventional concepts in materials science. Nanotechnology has also been extended to living organisms, known as nanobiotechnology. Furthermore, nanometer-scale interactions between macromolecules and organisms have the potential to create new structures (Drexler, 1992; Taton, 2003).

Regarding nanofiber technology in the field of textiles, the US government was quick to recognize the innovative effects of nanofibrils and consider them a strategically important technology. Japan has fallen behind in nanofibril development, information technology (IT), and human genome decoding owing to the absence of a national strategy. However, Japan shows great potential regarding fiber technology owing to its long history of cultivating fiber and textile industries. In the 21st century, evaluating the characteristics of practical fibers and controlling their structure at the nanoscale have become important. This can lead

to light high-strength structural materials for optical and electronic devices, drug discovery, regenerative medicine, and environmental purification.

This review article focuses on cellulose as a representative natural fiber. A brief history of cellulose is provided, and then nanocellulose manufacturing methods are outlined, covering the nature of cellulose nanofibers and difficulties in their manufacture. Future perspectives on nanofibrils are also described.

Herein, the term “nanocellulose” represents nanosized cellulose materials with a fiber width of 100 nm or less, which are generally categorized as cellulose nanofibrils (CNFs) with high-aspect ratios ( $\geq 100$ ) and cellulose nanocrystals (CNCs) with low-aspect ratios ( $< 100$ ).

## 2. History of cellulose and nanocellulose

### 2.1 Brief history of cellulose materials

Cellulose, the most abundant natural fiber, is a  $\beta$ -1,4-glucan-linked carbohydrate polymer discovered in 1838 by French chemist Anselme Payen (1795–1871). After graduating from École Polytechnique, Payen became manager of a borax-refining factory in the suburbs of Paris and developed new methods for refining sugar and refining starch and alcohol from potatoes. In 1835, Payen became a professor of applied chemistry at École Centrale Paris, where he separated the components of wood by

<sup>†</sup> Received 29 August 2021; Accepted 6 December 2021

J-STAGE Advance published online 16 February 2022

<sup>1</sup> Add: West 5th, 744, Motooka, Nishi-ku, Fukuoka 819-0395, Japan

<sup>2</sup> Current Add: 3-5-8 Saiwai-cho, Fuchu-shi, Tokyo 183-8509, Japan

E-mail: tekondo@agr.kyushu-u.ac.jp; tuat-tekondo@go.tuat.ac.jp

TEL/FAX: +81-42-367-5588

treating various woods with nitric acid. He discovered that a fibrous substance could be obtained, with elemental analysis revealing a chemical formula of  $C_6H_{10}O_5$ , that he named “cellulose” in an 1838 publication in *Comptes Rendus* (Payen, 1838). Today, the Anselme Payen Award is an annual prize awarded by the Cellulose and Renewable Materials Division of the American Chemical Society (ACS) to researchers that have made a major contribution to cellulose-related research.

Although cellulose has been known for around 180 years, its nanofibril has only recently become considered as a new biomaterial. As shown in **Fig. 1**, wood cell walls are composed of fiber bundles of cellulose at the microscale, which are constructed from a minimum aggregate (elementary fibril at the nanoscale) to form a higher order microfibril. Cellulose forms a complex hierarchical structure from the nanoscale to macroscale through lamination, resulting in the formation of a layered structure of lamellae as cell walls.

With advances in nanotechnology, cellulose nanofibrils or nanocrystals (known collectively as nanocellulose) with nanometer-scale widths have been developed. Furthermore, owing to its sustainability and wide-ranging applications, the use of nanocellulose will contribute to the conservation and maintenance of the global environment. In this context, technology for the preparation of nanocellulose has rapidly developed in the last 10–15 years, as described below.

## 2.2 Advantages of nanocellulose

Nanocellulose obtained by various preparation processes has exhibited specific gravity that is one-fifth that of steel and specific strength (1–3 GPa; Saito et al., 2013) more than five times that of steel. Nanocellulose also shows thermal expansion deformation that is only approximately

one-fiftieth that of glass from  $-200\text{ }^{\circ}\text{C}$  to  $200\text{ }^{\circ}\text{C}$ , and is a high-performance material with a specific surface area of  $\geq 250\text{ m}^2/\text{g}$  (Klemm et al., 2018). The advantages of nanocellulose are listed in **Table 1**.

## 2.3 Global research trends in nanocellulose

A proposal submitted by Canada for deliberation of the international standardization of nanocellulose has been accepted by the International Organization for Standardization (ISO/TS21346). In this proposal, the main target is cellulose nanocrystals, which are formed by treating cellulose microfibrils with sulfuric acid.

Historically, Nickerson and Habrle (1947) first showed that crystalline cellulose of a certain size (degree of polymerization, approx. 200–250) can be obtained by refluxing with cellulose with 2.5 N sulfuric acid. Mukherjee and Woods (1953) confirmed that this material was nanosized crystalline cellulose (cellulose nanocrystals) by transmission electron microscopy. In Canada, Marchessault et al. (1959) reported that the dispersed water suspension became a gel-like substance at a concentration of  $\geq 13\text{ wt}\%$ , indicating a nematic-order sequence, while Revol et al. (1992) confirmed the formation of a chiral nematic structure during evaporation of this dispersion. This historical research is closely related to the aforementioned Canadian ISO proposal.

Research on nanocellulose in the USA started late compared with Canada, Scandinavia, and Japan. However, in recent years, collaboration among industry, academia, and government has been promoted in the USA, with universities and research institutes providing samples without restrictions such as intellectual property rights. In addition to accelerated open innovation, the USA also plays a central role in the ISO.

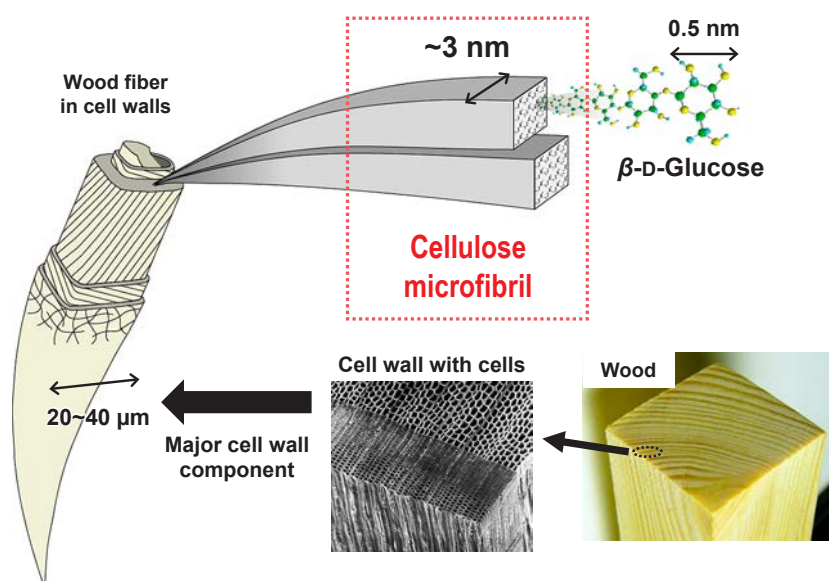


**Fig. 1** Hierarchical structure of natural cellulose containing nanocellulose.

**Table 1** Common advantages in cellulose nanofibrils (CNFs) produced by various procedures.

Properties	Reference Value
[Nanocellulose having width less than 50 nm: sustainable, light weight, high strength]	
-Plants are sustainable and abundant resources up to 1 trillion [t] = 6 x (oil deposits)	
-Plant cell walls comprise CNF as a basic skeletal component	
-CNF is a high-performance green nanofiber as the essential of a wood	
-CNFs, a microcrystal, are built up of cellulose molecules having extended polymer chain	
Properties	Reference Value
Fiber size	Length: > 1 $\mu\text{m}$ Width : < 20 nm
Density	$\cong 1.6 \text{ g/cm}^3$
Strength (7–8 $\times$ steel)	Elastic modulus: 140 Gpa Tensile strength: 3 Gpa
Liner thermal expansion ( $\cong$ Quartz glass)	0.1 ppm/K (longitude)
Thermal stability in elastic modulus	-200 $^{\circ}\text{C}$ – +200 $^{\circ}\text{C}$
Highly thermal conductivity ( $\cong$ Glass)	0.8 W/mK

In Europe, the EU has conducted large-scale nanocellulose projects in recent years, centered in laboratories in Finland and Sweden (Finland National Technology Center (VTT) and Sweden Wallenberg Wood Science Center (WWSC)), which are now working toward practical use.

In Japan, companies such as Nisshinbo Holdings Inc., Daicel Co., and Asahi Kasei Co. have proposed patents on the miniaturization of natural cellulose fibers using a stone mill-type grinder. To our knowledge, Taniguchi was the first to prepare nanofibrils with a width of 20–90 nm, which is considered the beginning of nanocellulose research (Taniguchi and Okamura, 1998). When a suspension undergoes ultrafine defibrillation between two rotating desks with a shear force applied in a direction perpendicular to the long axis of the fiber, the fiber width ranges from a few nanometers to several tens of nanometers. Subsequently, various methods for nanocellulose production have been proposed, with Japan contributing to diverse methods worldwide. The Japan Revitalization Strategy, revised in June 2014, stated that the use of nanocellulose materials should be promoted. Subsequently, the Nanocellulose Forum centered on industry, government, and academia under an all-Japan system was founded. The Nanocellulose Forum was recently succeeded by Nanocellulose Japan (NCJ), a private-sector organization launched in 2020.

Accordingly, the production of cellulose nanofibrils and cellulose nanocrystals has been facilitated, and research and development sites are now considering how to use such nanosized natural materials in society. The practical application of nanocellulose is rapidly gaining momentum.

### 3. Nanocellulose production—Correlation between nanocellulose manufacturing method and chemical characteristics—

#### 3.1 General aspects

In the last two decades, various technologies have been developed for isolating cellulose nanofibrils derived from biomass raw materials (Kondo, 2008; Thomas et al., 2020; Isogai, 2021; Heise et al., 2021). Three typical methods proposed in Japan early on are compared in Fig. 2. The first is a chemical method, TEMPO (2,2,6,6-tetramethylpiperidine-1-oxy radical) catalytic oxidation, that has been applied to natural cellulose (Fig. 2, right) (Saito and Isogai, 2004). The second is nanofibril preparation by a stone mill-type grinder, which is a chemical-free process that does not chemically modify the cellulose surface (Fig. 2, center) (Yano and Nakahara, 2004; Nakagaito and Yano, 2005a; Uetani and Yano, 2011). Furthermore, we have proposed an aqueous counter collision (ACC) method involving the collision of opposing high-pressure water jet streams of aqueous suspension samples. ACC can be applied not only to cellulose materials, but also to the nanominiaturization of biomass (Fig. 2, left) (Kondo et al., 2005; 2014a; Kose et al., 2011c).

Notably, nanocellulose exhibits different characteristics depending on the production method used. As shown in Figs. 2 and 3, the nanocellulose surface obtained by TEMPO oxidation and the grinder method exhibit high hydrophilicity similar to that of conventional natural cellulose fibers. In contrast, the nanocellulose surface obtained by the ACC method is more hydrophobic and amphiphilic (Kondo and Kasai, 2015; Tsuboi et al., 2014; Tsuji et al., 2021).

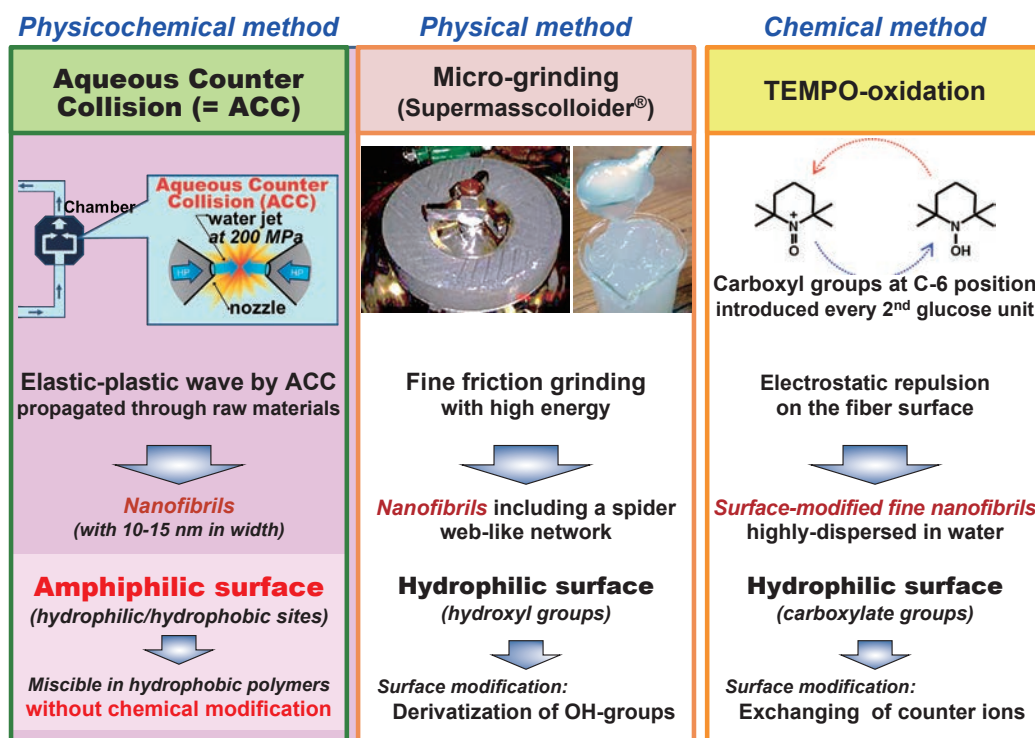


Fig. 2 Comparison of the three main cellulose nanofiber manufacturing methods proposed at an early stage in Japan.

## 3.2 Typical production methods for cellulose nanofibrils

### 3.2.1 Production of cellulose nanofibrils by chemical treatment

Chemical processes for the preparation of cellulose nanofibrils mostly involve initial loosening of the crystalline domains and interfibril interactions in cellulose raw materials before facile mechanical separation into nanofibrils.

#### 3.2.1.1 Cellulose nanocrystals (CNCs) prepared by sulfuric acid treatment

Generally, CNCs are rod-like cellulose fibers that have been hydrolyzed to remove noncrystalline fibers by treatment with sulfuric acid (952 g/L) at 30 °C or 40 °C for 24 h, as described in Section 2.3. The degree of polymerization is almost constant, at approximately 200–250 (Nickerson and Habrle, 1947). CNCs are also known as cellulose nanowhiskers. In 1959, Marchessault et al. reported that acid-treated cellulose and chitin microcrystal (microfibril) gels at concentrations of >13 wt% exhibited birefringence, which was derived from the nematic order sequence, while Revol et al. (1992) reported that a chiral nematic structure was formed by a CNC dispersion through evaporation. CNCs are considered to be stably dispersed in water owing to electrostatic repulsion between the sulfuric acid groups partially introduced on the fiber surfaces. Based on this study, the self-assembly of cellulose (Araki et al., 1998; 1999) or grafted CNC (Araki et al., 2001; Heux et al., 2000; Gousse et al., 2002; Zhou et al., 2005; Lönnberg

et al., 2006) dispersions has been developed (Trache et al., 2017). Furthermore, the use of cellulose nanowhiskers or nanofibers with a high axial ratio (aspect ratio) as a reinforcing agent for composite materials has received attention (Oksman and Sain, 2006; also see the recent review by Shojaeiarani et al., 2021).

#### 3.2.1.2 Cellulose nanofibrils prepared by TEMPO catalytic oxidation (TOCNFs)

Shibata and Isogai (2003) found that TEMPO (2,2,6,6-tetramethylpiperidin-1-oxyl) catalytic oxidation selectively oxidized the primary hydroxyl group at the C6 position of regenerated cellulose (viscose rayon) to an aldehyde under mild conditions, as shown in Fig. 3A. This reaction occurs in an aqueous medium at pH 10–11 and consumes sodium hypochlorite, but the catalytic amounts of TEMPO and sodium bromide can be recycled. Furthermore, Saito and Isogai (2004) showed that, when this TEMPO-catalyzed oxidation was applied to natural cellulose, specific surface modification occurred, introducing carboxyl groups and aldehyde groups at a high density only on the surface of crystalline cellulose microfibrils. When TEMPO-oxidized natural cellulose was subjected to simple mechanical treatment in water using a mixer or similar apparatus, a highly viscous transparent dispersion could be obtained by increasing the amount of carboxyl groups introduced. Transmission electron microscopy showed that a transparent dispersion of isolated cellulose single microfibrils with a width of approx. 3 nm was obtained by mechanical treatment of TEMPO-oxidized



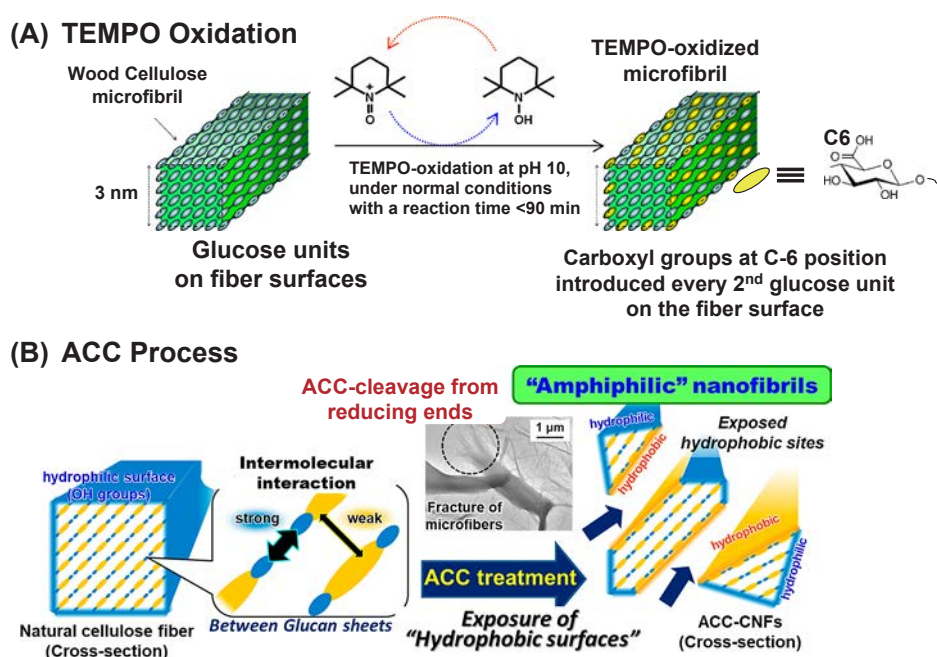


**Fig. 3** Schematic diagrams of (A) chemical characteristics of nanocellulose obtained by TEMPO oxidation (Courtesy of Prof. Isogai at University of Tokyo) and (B) the ACC process, which is likely to expose hydrophobic van der Waals (200) faces normally hidden inside the native crystalline cellulose fibers to the surface.

wood cellulose (Saito et al., 2006). They also indicated that TEMPO-catalyzed oxidation does not oxidize the inside of crystalline microfibrils, meaning that C6 hydroxyl groups on the surface are selectively oxidized to the corresponding sodium carboxylate salt, which causes charge repulsion between the nanofibrils.

### 3.2.1.3 Nanoelements prepared by enzymatic hydrolysis

Using an enzyme derived from *Trichoderma*, Hayashi et al. attempted to hydrolyze microbial cellulose crystalline nanofibrils with a width of 40–60 nm secreted from *Gluconacetobacter* bacteria and natural cellulose fibers derived from seaweeds, which have both crystalline forms of cellulose (I $\alpha$  and I $\beta$ ). Crystalline phase I $\alpha$  has been reported to be more susceptible to enzymatic degradation (Hayashi et al., 1997a, b). Furthermore, the residue of a short elements (width, 10 nm; length, 350 nm) obtained by hydrolysis with an enzyme of the same *Trichoderma* origin was found to mainly comprise highly crystalline I $\beta$  phase by wide-angle X-ray diffraction, electron diffraction, and FTIR measurements (Hayashi et al., 2005). This material has potential applications as an additive, especially in food and cosmetics.

### 3.2.1.4 CNFs prepared by mechanochemical treatment

Mechanochemistry using planetary ball milling (Endo et al., 1999; Takai-Yamashita et al., 2021) is a sustainable method for the synthesis of functionalized cellulose nanofi-

bers (CNFs). In this process, changes in the microstructure of a CNF aqueous sol under planetary ball milling were investigated in terms of its rheological behavior, crystallinity, and diameter distribution. A decreased thixotropy hysteresis loop observed in the ball mill-treated CNFs indicated a weaker interaction among the fibers, but with a three-dimensional structure retained.

### 3.2.2 Production of cellulose nanofibrils (CNFs) by mechanical treatment

Mechanical processes for the preparation of cellulose nanofibrils mostly involve shear stress, where pulp is dispersed in water, pre-crushed using a Supermasscollider® grinder (Masuko Sangyo Co. Ltd., Saitama, Japan), and further micro-/nano-fibrillated using a high-pressure homogenizer (M110P Microfluidizer, Microfluidics Corp., Newton, MA) (Yano and Nakahara, 2004; Nakagaito and Yano, 2005a; Uetani and Yano, 2011). Under typical treatment conditions, the pulp fibers are first processed under high shear in a Masuko Supermasscollider grinder for three passes, and then further fluidized using a microfluidizer equipped with 200- and 100- $\mu$ m chambers at 2000 psi for 10–12 passes (Huan et al., 2017).

As a result, cellulose nanofibrils with a spider web-like network can be obtained. Additional compounding and dehydrating with a phenol resin, oxidized starch, and polylactic acid in a mold, followed by heat-pressing, allows a high-strength composite molded product to be obtained. Instead of the cellulose nanofiber network, when the bacterial nanocellulose pellicle (gel-like membrane produced

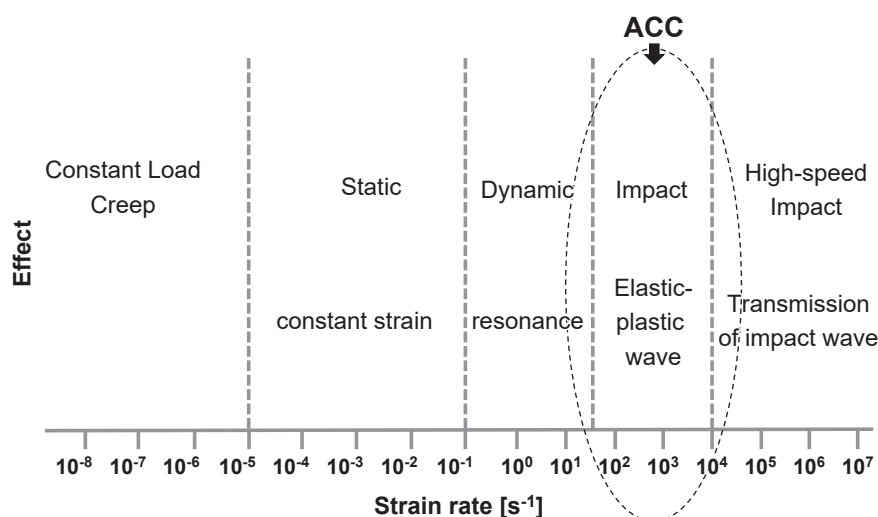


**Fig. 4** Classification of energy loading effects vs strain rate onto materials (Yu and Qiu, 2018). Typically, ACC process provides both interfacial peeling and a thermodynamic effect onto samples. Adapted with permission from Ref. (Yu and Qiu, 2018). Copyright: 2018 Tsinghua University.

by *Gluconacetobacter* bacteria) composed of a three-dimensional nanofibril network was subjected to heat-pressing treatment, the resulting high-strength composite material had a Young's modulus of approx. 30 GPa, which was 1.5 times higher than that of the material obtained using wood cellulose nanofibrils (Nakagaito et al., 2005b).

This difference was attributed to the dense network in the bacterial cellulose pellicle, which was uniform at a scale of a few tens of nanometers (Yano et al., 2005). To our knowledge, this result was the starting point for subsequent research on resin nanocomposites with high tensile strength using nanocellulose. Nanocellulose being lightweight, more than five times stronger than steel, and having a low linear expansion (one-fiftieth that of glass) could lead to a reduction in weight of car bodies to encourage better gas mileage, especially through its use in automobile parts. This matches the current global direction of realizing a low-carbon society. Recently, Kitagawa and Yano proposed the “Kyoto Process” for integrated production of cellulose nanofiber materials (Kitagawa and Yano, 2012; Igarashi et al., 2018). Such research on developing resin materials with excellent strength per unit weight is being conducted extensively worldwide. Numerous studies on nanocomposites containing nanocellulose have been published to date. For coverage of literature in this area beyond the scope of this review, please see other recent reviews (Oksman et al., 2016; Klemm et al., 2018; Shojaeiarani et al., 2021).

### 3.2.3 Production of cellulose nanofibrils by physicochemical treatment

The key phenomenon in physicochemical processes for the preparation of CNFs is selective interfacial cleavage among weak intermolecular interactions by a propagating elastic–plastic wave (as shown in Figs. 3B and 4), which is attributed to shockwaves generated by impact dynamics

depending on the strain rate ( $s^{-1}$ ) through impact energy transmission (Yu and Qiu, 2018). Namely, loading as total mechanical energy / areas induces impact energy transmission to cause an effect in materials that relates to strain rate. When heterogeneous interface of the material is suffered by such concentrated loading energy, interfacial peeling within it is likely to occur.

Our aqueous counter collision (ACC) method for the nanopulverization of bio-based materials is a typical physicochemical process without any chemical modification (Kondo et al., 2005; 2014a; Kose 2011c). The ACC method relies on the impingement of two high-speed jets of aqueous suspension of raw materials expelled through a pair of opposing nozzles. Typically, the ejection pressure of 200 MPa generates a supersonic flow of dual water jets at Mach 2. Schematic diagram is shown in Figs. 3B and 4.

The calculated kinetic energy generated by impingement of the water jets in the ACC method is up to 14.3 kJ/mol at an ejection pressure of 200 MPa (Kondo et al., 2014a). The relationship between water ejection pressure and calculated kinetic energy of water molecules in the ACC process is shown in Table 2, together with a summary of typical bonding energies. Regardless of dissipative energy loss during the ACC process, the kinetic energy, which can be converted into elastic–plastic waves, remains higher than the van der Waals forces and weak hydrogen bonds at an ejection pressure of 200 MPa (Kondo et al., 2014a). The width and size distribution of the nano-pulverized samples are dependent on the ACC ejection pressure and number of repeat cycles/passes, respectively. The propagation of shock waves resulting from ACC occurs through elastic crystalline domains to cleave the hydrophobic van der Waals (200) planes normally hidden inside native crystalline cellulose fibers (Cousins and Brown, 1995) with these hydrophobic planes eventually being exposed on the

**Table 2** Energy barrier capable of being overcome by ACC.**(A) Calculated potential energy of a water molecule in ACC process**

Ejecting pressure /MPa	Kinetic energy /kJ mol <sup>-1</sup>
50	3.6
100	7.2
150	10.8
200	14.3

**(B) Hydrogen bonding energies**

O–H···O Hydrogen-bonded compound	–ΔE(kJ mol <sup>-1</sup> Hydrogen bonds)	
	Dimer (gas)	Liquid
CH <sub>3</sub> COOH	29.3	24.3
H <sub>2</sub> O	21.0	14.2
CH <sub>3</sub> OH	16.8–18.9	19.7
C <sub>2</sub> H <sub>5</sub> OH	16.8	17
C <sub>3</sub> H <sub>7</sub> OH		25

**(C) Various bonding energies**

Type of bond	Bonding energy /kJ mol <sup>-1</sup>
H–OH (covalent bond)	499
H–H (covalent bond)	436
Ion–ion	250
Medium hydrogen bond	21–62
Weak hydrogen bond	4.2 × 10 <sup>-1</sup> –4.2
London dispersion force	2
Dipole–dipole	0.6–2

surface (Li and Renneckar, 2011) (see Fig. 3B). The resulting ACC–CNFs have a Janus-type amphiphilic surface composed of both hydrophobic and hydrophilic planes in an aqueous system (Tsuji et al., 2021). Kose et al. (2011c) reported that ACC provides a single CNF from bacterial nanocellulose (BNC) pellicles, denoted ACC–BNC herein, which are nanofibers engaged in a 3D network secreted by *Gluconacetobacter* bacteria, that exhibited amphiphilic properties (Kose et al., 2011a). In BNC, which is already highly crystalline, shock waves are simply propagated through the elastic crystalline domains from the initial stage, resulting in the direct cleavage of certain interfaces.

Later, Kondo et al. (2014a) reported ACC pulverization steps for microcrystalline cellulose (MCC) containing 30 % noncrystalline domains derived from wood-based cellulose fiber (pulp). Regarding the nanopulverization behavior of MCC in the ACC method, initially, a shear stress is mainly generated through the ACC flow system to pulverize the

MCC microfibrils into fibers with widths of a few hundred nanometers. Highly crystalline domains remain in the cellulosic samples after the effects of shear stress. A drastic decrease in fiber width then occurs, presumably due to the cleavage of weak hydrogen bonds between crystalline domains of CNFs. Accordingly, ACC nanopulverization is considered to be an effective synergistic process that generates shear stress and propagating shock waves in various biomass resources (Kose and Kondo, 2011b; Kondo et al., 2014b; Jiang et al., 2016; Tsujita and Kondo, 2019; Ye et al., 2021).

Additionally, Kawano and Kondo (2014) reported that carbon materials without dissociative functional groups treated using the ACC method exhibited negative zeta potentials and dispersed in an aqueous system, which might be due to water molecules present on the surface. Therefore, the resulting ACC–CNFs might disperse in an aqueous system, even if hydrophobic planes are exposed on the CNF surfaces.

Recently, the ACC method afforded CNFs with different surface properties from various cellulosic raw materials comprising different hierarchical structures depending on the species present, as described later (Tsuji et al., 2021).

Nanocellulose is usually considered to comprise symmetrical nanofibrils, nanorods, or fibrillated nanofibrils, regardless of asymmetric effects caused by the presence of one reducing end. Asymmetrical nanocellulose would have considerably extended utility in new applications. We have produced an asymmetric cellulose nanofibril with a shape that changes from a thick nanobarrel at one end to a thinner cylinder with a few flourishes towards the reducing end. The “cellulose nanoanemone” fibrils, named after sea anemones, were fabricated by the ACC of bacterial cellulose pellicles cultured under dissolved oxygen conditions (see Fig. 5) (Utsunomiya et al. 2022; Nagashima et al., 2015). The cellulose I $\alpha$  crystalline phase located on the fiber surface was transformed into cellulose I $\beta$  crystalline phase owing to propagation of the collision energy of high-speed water jets in this treatment (Kose et al., 2011c).

## 4. Characteristic advantages of the ACC process

### 4.1 Amphiphilic Janus-type surface properties of ACC–CNFs

ACC–CNFs are likely to exhibit specific phenomena owing to their two anisotropic faces in aqueous media (Tsuji et al., 2021). Kose et al. (2011a) reported that the wettability of solid substrates, regardless of whether the surface was hydrophilic or hydrophobic, can be switched by spray-coating with ACC–CNFs. Tsuboi et al. (2014) reported that ACC–CNFs can be used as emulsifiers and/or emulsion stabilizers without a surfactant. The properties of the obtained emulsions differed depending on the starting raw materials used (Yokota et al., 2019). Recently, Kondo

et al. reported that the preferential adsorption of ACC–CNFs to hydrophobic polymer surfaces results in hydrophilic properties (Kondo et al., 2017; Ishikawa et al., 2021).

As mentioned above, ACC–CNFs are assumed to exhibit two distinct physicochemical properties (amphiphilicity) due to being composed of hydrophobic planes and the initial hydrophilic planes in aqueous systems. Therefore, a novel concept regarding the physicochemical surface properties of ACC–CNFs, namely, amphiphilic Janus-type fibers, is introduced, in which two anisotropic faces are present along the entire fiber axis that exhibit different physicochemical properties on the surface. An analogous concept, Janus particles, has been studied extensively. Janus particles, named after the two-faced ancient Roman god, have two anisotropic faces with different physicochemical properties owing to a half-and-half surface struc-

ture (Walther and Müller, 2008; Yabu et al., 2013; Jiang et al., 2010). However, such unique surface characteristics have yet to be reported in fibers. Therefore, the surface characteristics of ACC–CNFs are defined differently to typical Janus particles.

Amphiphilic Janus-type fibers are described as fibers with two types of surface bearing hydrophilic and hydrophobic faces that are individually present along the entire single fiber axis in aqueous systems (Kose et al., 2011a; Tsuboi et al., 2014; Yokota et al., 2019). Accordingly, amphiphilic Janus-type fibers can also be described as Janus-type faces along a single fiber axis, which is different to typical Janus particles with a half-and-half structure.

Recently, the surface characteristics of single ACC–CNFs have been visualized at the nanoscale using fluorescence microscopy (FM) observation with fluorescence probes (Tagawa et al., 2021). Fluorescent-probe carbohydrate-binding modules (CBMs), Congo red (CR), and Calcofluor white (CFW) have been employed as reagents for the qualitative and quantitative evaluation of surface characteristics in ACC–CNFs, focusing on their hydrophobic and hydrophilic planes (Tsuji et al., 2021). CBMs are included in cellulase as a binding domain that anchors selectively to the hydrophobic phase of cellulose (Linder and Teeri, 1996), CR adsorbs onto cellulose crystalline surfaces as a monolayer (Hubbe et al., 2012; Nge et al., 2013; Mazeau and Wyszomirski, 2012), and CFW has been used to detect plant hydrophilic cellulose structures (Hughes and McCully, 1975) and CNFs (Peretz et al., 2019). The three-dimensional structure of CBM, and chemical structures of direct dyes CR and CFW, are shown in Fig. 6.

According to the fluorescence microscopy images, CNFs stained with CFW were approximately 10 times wider than those observed by field emission scanning electron microscopy (Tagawa et al., 2021). Therefore, the surface

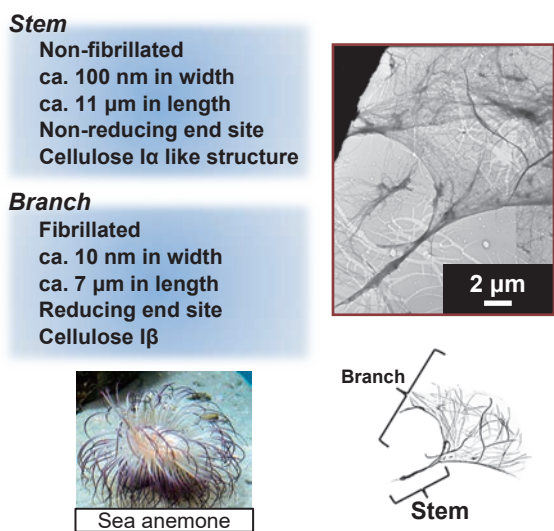
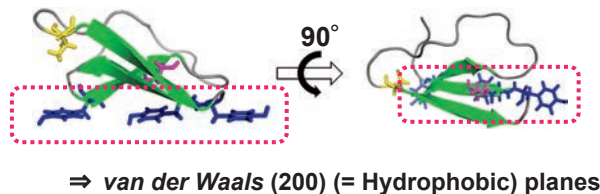
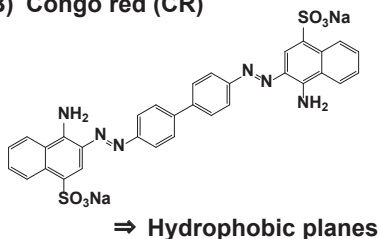


**Fig. 5** Images of a typical asymmetric “cellulose nanoanemone”. The TEM and schematic images (bottom of figure) define the “stem” and “branch” of the cellulose nanoanemone.

**(A) Carbohydrate-binding modules fused to green fluorescence protein (CBM-GFP)**



**(B) Congo red (CR)**



**(C) Calcofluor White (CFW)**

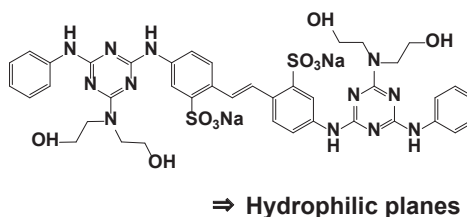


**Fig. 6** Site-specific fluorescence probes for CNF surfaces.

characteristics of CNFs can be visualized by confocal laser microscopy (CLMS) using site-specific fluorescence probes and a highly sensitive fluorescence detector.

The localization of hydrophobic and hydrophilic planes on the ACC–BNC surface was visualized by staining with typical site-selective fluorescent probes CFW, CBM fused with green fluorescent protein (CBM–GFP), and CR. ACC–BNC is a suitable model material for investigating ACC–CNFs because BNC is a pure cellulose sample. Nanofibrils cannot be observed by optical microscopy owing to resolution limitations. However, fluorescence-stained nanofibrils were visible by CLSM, as shown in Fig. 7, owing to the spread of fluorescence emissions with similar shapes. The width magnification achieved by fluorescence emission was approximately 13 times that achieved by transmission electron microscopy (TEM). The same fiber was observed separately by fluorescence staining, using CFW for hydrophilic surfaces or CBM–GFP for hydrophobic surfaces (Figs. 7a and 7b). Each fluorescent emission of CFW and CBM–GFP was distinguished in most fibers. When images (a) and (b) in Fig. 7 were merged, the hydrophobic areas (b) were fixed empty areas surrounded by hydrophilic areas (a) in the merged image (c) of Fig. 7. Therefore, ACC–BNCs can be concluded to have hydrophobic and hydrophilic faces on a single ACC–BNC surface. This result reflects the concept that, in ACC nanopulverization, shockwaves propagate through highly crystalline domains, samples are chopped into individual nanofibrils, and the resulting hydrophobic faces might be similar to exposed van der Waals (200) planes from the native cellulose crystals (Li and Rennecker, 2011).

In the visualization described above, the ACC–BNC surface had an amphiphilic Janus-type fiber structure with hydrophobic and hydrophilic faces in aqueous systems, and

CR was found to be a substitute for CBM in hydrophobic face evaluation. Therefore, CR can be used to quantitatively evaluate the hydrophobic face, partly because a CBM–GFP calibration curve by weight is difficult to prepare and some CNFs might aggregate in the acetate buffer. The hydrophobic and hydrophilic faces of ACC–BNC were determined by quantitative measurement of the amounts of CR and CFW adsorbed on a Langmuir monolayer. The maximum monolayer adsorption amounts of CR and CFW on ACC–CNFs were calculated from the Langmuir isotherms, as shown in Table 3. CR and CFW were adsorbed on all ACC–CNFs. Fig. 8 shows the relative occupied area (OA) ratio of CR to CFW on ACC–CNFs as a function of CR occupancy for the surface area of ACC–CNFs. The results indicated that the degree of hydrophobicity of the ACC–CNFs was in the order of BNC > BBKP > HBKP  $\approx$  MCC. Therefore, the surface hydrophobicity of ACC–CNFs depends on their origin (Tsuji et al., 2021). Considering the recent damage of bamboo as an unnecessary resource, despite this natural material containing various active ingredients, the above results are of interest and potential importance regarding the development of a functional biomass nanofibrous material.

## 4.2 Specific adsorption phenomena caused by two anisotropic faces in amphiphilic Janus-type ACC–CNFs

### 4.2.1 ACC-assisted oil-in-water Pickering emulsions

The characteristic surface of ACC–CNFs can be expected to expand common understanding of nanocelluloses. First, the amphiphilicity is promising for applications as emulsifiers and stabilizers. Oil-in-water Pickering emulsions with long-term stability are readily prepared by ultrasonic mixing of aqueous ACC–CNF dispersions with

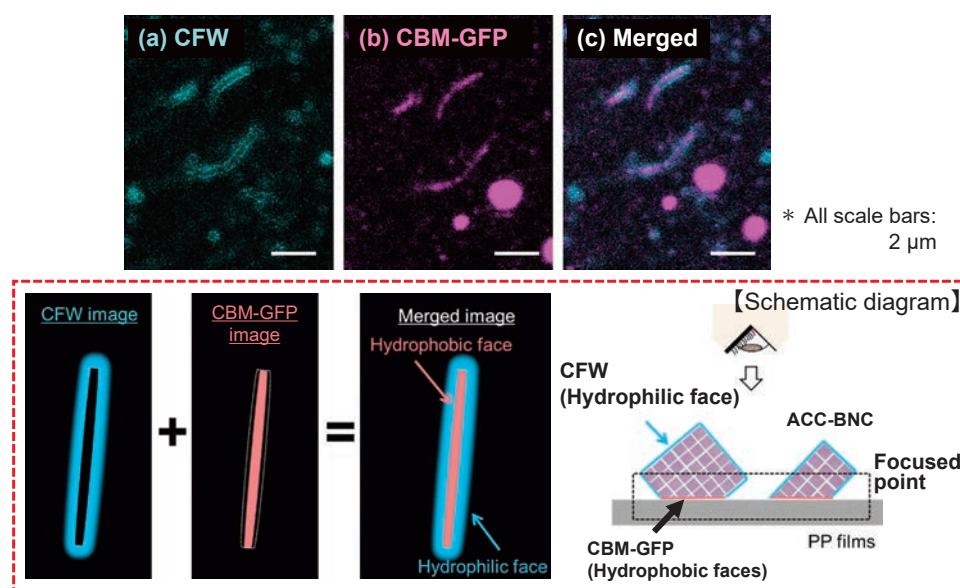


Fig. 7 Hydrophilic and hydrophobic faces on the ACC–BNC surfaces stained separately with CFW and CBM–GFP.

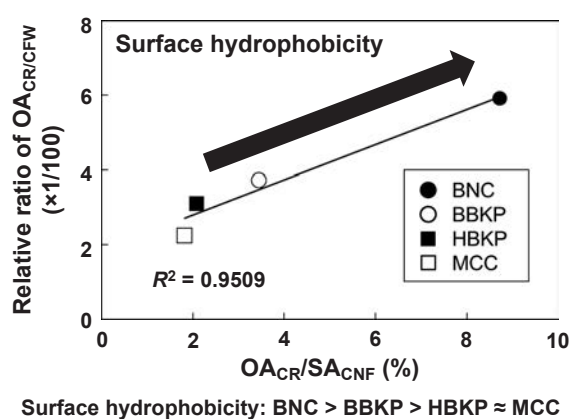
**Table 3** Characteristic values for individual ACC–CNFs from different origins.

(A) Maximum monolayer adsorption amounts of dyes onto CNFs based on the Langmuir adsorption isotherms and zeta potentials of individual CNFs.

Derivation	CR adsorption (mg/g CNF)	CFW adsorption (mg/g CNF)	Zeta potential (mV)
BNC	7.5 ± 0.9	87.0 ± 8.5	−18.8 ± 2.1
BBKP	7.1 ± 0.6	131.5 ± 10.2	−36.7 ± 2.1
HBKP	4.7 ± 0.6	103.7 ± 18.3	−44.7 ± 1.2
MCC	4.1 ± 0.8	119.1 ± 7.6	−29.3 ± 2.1

(B) Average height, width, and SSA values for ACC–CNFs based on AFM observation of the samples. Adapted with permission from Ref. (Tsuji et al., 2021) Copyright 2021 American Chemical Society.

Derivation	Height (nm)	Width (nm) (Data from TEM)	SSA (m <sup>2</sup> /g)
BNC	12.1 ± 5.5	50.5 ± 15.9 (34 ± 13)	127.9
BBKP	4.8 ± 2.8	25.2 ± 7.1 (20.7 ± 8.3)	307.8
HBKP	4.2 ± 2.9	31.8 ± 11.8 (22.3 ± 12.4)	338.5
MCC	4.4 ± 1.9	22.4 ± 6.1 (15 ± 6)	337.4



Surface hydrophobicity: BNC > BBKP > HBKP ≈ MCC

**Fig. 8** Relative occupied area (OA) ratio of CR to CFW on ACC–CNFs as a function of CR occupancy for the surface area of ACC–CNFs, indicating surface hydrophobicity depending on the origin.

Note: BNC: Bacterial nanocellulose pellicle; BBKP: Bamboo-derived bleached kraft pulp; HBKP: Hardwood-derived bleached kraft pulp; MCC: Microcrystalline cellulose (from wood kraft pulp). Longitudinal axis corresponds to relative ratio of OA of CR to CFW. Horizontal axis corresponds to OA of CR per surface area of CNFs based on AFM data.

nonpolar solvents. The emulsification abilities of ACC–CNFs for stable Pickering emulsions have been proven to be significantly greater than those of CNFs prepared by high-pressure homogenization or other chemical preparation methods. This is attributed to ACC exposing inherently hydrophobic surface planes of CNFs. Furthermore, the emulsification and stability of the Pickering emulsions were sensitive to solvent properties, such as permittivity, density and viscosity (Yokota et al., 2019).

In a stable emulsion prepared from a water dispersion of 0.1 wt% ACC–CNFs derived from bamboo pulp, hollow particles, similar to colloidosomes (Thompson et al., 2015),

were formed from the bamboo-based emulsion droplets by carefully washing the excess nanocellulose with water and then freeze-drying, as shown in Fig. 9 (left). The spherical particles were covered with a stable thin layer composed of ACC–CNFs and were completely hollow inside (Fig. 9b left), while fluffy fibrous objects (Yokota et al., 2019; Tsuboi et al., 2014) between spherical particles were negligible. By removing the unanchored CNF, the thin layer around droplets could be observed in higher magnification images. This thin layer contained pores approximately 10–500 nm in size, as shown in Figs. 9c and d (left). This suggested that the obtained emulsion droplets were fabricated and stabilized by adsorption of ACC–CNFs onto the oil surface to form an oil-in-water emulsion. Therefore, colloidosome microcapsules were formed in this Pickering emulsion without requiring further stabilization treatment.

To control the surface properties of ACC–CNFs, their surfaces at the oil–water interfaces of a Pickering emulsion can be selectively acetylated (Ishida et al., 2021). To achieve this, ACC–CNFs adsorbed on the surfaces of oil droplets containing the reaction reagents undergo localized interfacial reactions. Such acetylation reactions occur while maintaining the crystallinity and fibrous morphology of the original CNFs. The surfaces of films cast from these acetylated ACC–CNFs had unique self-aggregation properties (Ishida et al., 2021) that contrasted markedly with those of films cast from acetylated ACC–CNFs prepared in homogenous dispersions (Yokota et al., 2021).

#### 4.2.2 Adsorption of Janus-type amphiphilic ACC–CNFs onto microparticles of semi-crystalline polymers

As a further development of the above research, ACC–

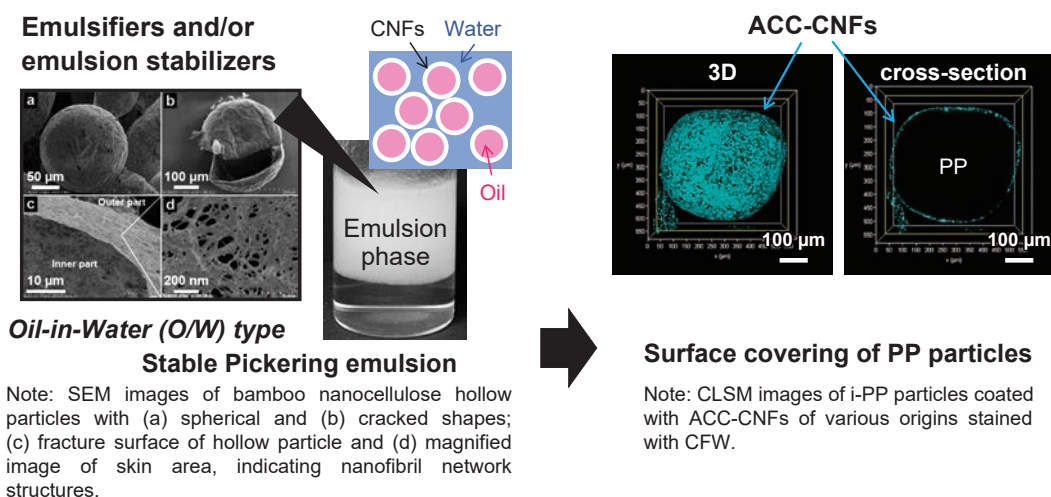


**Fig. 9** Specific adsorption properties of ACC–CNFs: Pickering emulsion formation (**left**) and adsorption onto i-polypropylene (i-PP: **right**). Left: adapted with permission from Ref. (Yokota et al., 2019). Copyright 2019 Elsevier; adapted with permission from Ref. (Tsuboi et al., 014). Copyright 2014 De Gruyter. Right: adapted with permission from Ref. (Ishikawa et al., 2021) Copyright 2021 American Chemical Society.

CNFs tend to preferentially adsorb onto hydrophobic isotactic polypropylene (i-PP) microparticles (see **Fig. 9, right**) and linear low-density polyethylene (LLDPE), which demonstrates their characteristic amphiphilicity. This is achieved by simply mixing the components together in aqueous media (Ishikawa et al., 2021). The surface-covered products were confirmed by visualization using CLMS. Furthermore, thermodynamics measurements obtained by differential scanning calorimetry (DSC) showed that the melting points of i-PP/ACC–CNFs and LLDPE/ACC–CNFs were lower than those of the untreated polymers, indicating interactions between the ACC–CNFs and polymer surfaces. Therefore, coating the polymer particles with the ACC–CNFs, as confirmed by CLMS, reduced their melting points. This demonstrated the possibility of a novel fusion between synthetic polymeric materials and biomass nano-objects (Kondo et al., 2021).

Prior to the CLSM observations, the i-PP particles were mixed with Janus-type amphiphilic ACC–CNFs in an aqueous medium, fully dried, and stained with CFW. As described earlier, nanoscale fibers can be observed by CLSM, even below the level of microscopic resolution, owing to scattering of the fluorescence emission.

**Fig. 9 (right)** shows a dark field fluorescent image of a particle coated with the ACC–CNFs. The bright spots indicate fluorescence due to stained ACC–CNFs on the surface of i-PP particles, showing that the i-PP spheres were completely covered by the ACC–CNFs. These images also indicated that, during the process of washing away excess CFW, the CNFs remained attached to the i-PP particle surface, demonstrating that interfacial interactions existed between the i-PP and ACC–CNF surfaces after adsorption had occurred by shaking in water.

Particles of other polymers, namely, high-density polyethylene (HDPE), linear low-density polyethylene

(LLDPE), and polyethylene terephthalate (PET), were also treated with an aqueous suspension of ACC–CNFs using the same method as for i-PP. The CLSM images indicated that more ACC–CNFs were present on the surface of LLDPE microparticles than on those of HDPE and PET particles (Ishikawa et al., 2021). Accounting for the self-fluorescence for PET showed that ACC–CNFs were not necessarily adsorbed on the PET surface. Furthermore, the high-magnification CLSM images suggested that i-PP and LLDPE particles were more efficiently coated with ACC–CNFs than HDPE and PET particles.

Among the materials tested, i-PP particles had the greatest affinity for ACC–CNFs. When the i-PP/ACC–CNFs were heated from 20 to 200 °C at 10 °C/min, they exhibited a small but typical endothermic shoulder peak at 142.6 °C after fusion commenced at approximately 113 °C and before the melting peak at approximately 162 °C. This indicated that coating with ACC–CNFs reduced the i-PP melting point in some areas (presumably surface areas coated with ACC–CNFs) and therefore the reduction probably occurred on the surface (skin side) of the microparticles. In agreement with the CLMS data, DSC analysis showed that ACC–CNFs coated the i-PP particles as a monolayer.

The effect of the origin of ACC–CNFs on their affinity for i-PP particles was also examined. ACC–CNFs from BBKPs and ACC–BNC derived from bacterial cellulose pellicles exhibited strong interfacial interactions with i-PP, while relatively hydrophilic ACC–MCC derived from microcrystalline wood cellulose had a lower affinity. A better understanding of the interfacial interactions between various polymer particles and ACC–CNFs will lead to the novel fusion of bio-based materials and synthetic polymer materials at the nanoscale (Kondo and Kasai, 2015; Kondo et al., 2017; Ishikawa et al., 2021).

## 5. Conclusions and future perspectives

Nanocellulose is a lightweight material, more than five times stronger than steel, and with a low linear expansion of one-fiftieth that of glass. Accordingly, Yano (2016) has proposed using this material to reduce car body weight, especially through its use in automobile parts. Therefore, a stream of resin materials with excellent strength per unit weight is undergoing vigorous development.

Our research group at Kyushu University, in collaboration with Chuetsu Pulp & Paper Co., Ltd., developed the Janus-type amphiphathic ACC–CNFs described herein, which are more hydrophobic than other nanocellulose materials, and also proposed a novel fusion of bio-based materials and synthetic polymer materials at the nanoscale. Therefore, this section will discuss future perspectives and trends for the preparation of nanocomposites containing CNFs.

Various additives have been widely used to improve the production performance of tailor-made polymeric products. These include plasticizers, flame retardants, impact modifiers, antioxidants, antimicrobials, and UV stabilizers (Hahladakis et al., 2018). The global additives market expanded steadily to over 50.0 billion USD by the end of the last decade, with the total weight of additives anticipated to reach 17 megatons by 2020 (Marturano et al., 2017). As additives are often more expensive than resins, two different production designs are considered to counterbalance usage and cost, namely, “high-price and low-loading” or “low-price and high-loading”. Inorganic materials, such as calcium carbonate, silica, glass fiber, and talc, which are relatively inexpensive, have usually been used in high volumes as fillers to improve the mechanical properties of polyolefins.

In recent years, nanoscale fillers, such as nanocarbon particles, various inorganic/organic nanoclays, and metal oxide nanoparticles, have been used at low loading levels (Winey and Vaia, 2007). Wood flour has been successfully mixed with various polyolefins to form wood–plastic composites for use as organic fillers (Clemons, 2002). Furthermore, in the last two decades, nanocelluloses (NCs) (Klemm et al., 2018; Nechyporchuk et al., 2016), including cellulose nanofibrils (CNFs), microfibrillated cellulose (MFC), and cellulose nanocrystals (CNCs), which are believed to be predominantly hydrophilic, have been extensively studied for use as fillers (Kargarzadeh et al., 2017). This results from their large surface areas of  $>50 \text{ m}^2/\text{g}$  (Kose et al., 2011c; Klemm et al., 2018), high mechanical strength (Saito et al., 2013), and low thermal expansion in the direction of the fiber axis (Nishino et al., 2004).

As described herein, NCs can be manufactured using the following three methods, each of which has a different effect on the surface characteristics, dispersibility, and compatibility of the NCs regarding mixing with commodity polymers: (i) Mechanical processes, mostly involving

shear stress; (ii) chemical processes that loosen crystalline domains and interfibril interactions; and (iii) physicochemical processes that selectively cleave weak intermolecular interactions by propagating generated shockwaves. Methods (i) and (ii) provide polar hydrophilic nanofibrils. Therefore, when such hydrophilic CNFs are added as fillers to polyolefins, their surfaces must either be chemically modified to render them hydrophobic, or they must be used in conjunction with a compatibilizer (Oksman et al., 2016; Nodera et al., 2016). Alternatively, chemically treated raw cellulose materials can be nano-pulverized and compounded with the polymer matrix in a parallel or sequential manner (Igarashi et al., 2018).

In contrast, aqueous counter collision (ACC) is a physicochemical process involving the impact-induced nanopulverization of bio-based materials using a pair of high-speed jets containing micro-sized target materials in aqueous media. The CNFs produced by ACC exhibit unique characteristics owing to the pulverization mechanism, as described herein.

Many plasticizers, which are used for solvation in matrix polymers, reduce intermolecular forces and decrease the relaxation temperature. Therefore, an evaluation of the affinity between matrix polymers and secondary ingredients is important for understanding their mutual contribution to the properties of the material, and the design of novel and sustainable multicomponent polymeric products. Regarding the use of nanocellulose in nanocomposites, such a study is still required.

Furthermore, applications to electronic devices (Kasuga et al., 2021) and other fields (Apelgren et al., 2019; Hai et al., 2020; Halim et al., 2019; Kim et al., 2021) appear feasible for practical use. From a future perspective, the expansion of nanocellulose research worldwide means that describing all potential application fields for nanocellulose is currently almost impossible.

## Acknowledgments

The author thanks Dr. Simon Partridge from Edanz for editing a draft of this manuscript.

## References

- Apelgren P., Karabulut E., Amoroso M., Mantas A., Martínez Ávila H., Kölby L., Kondo T., Toriz G., Gatenholm P., In vivo human cartilage formation in three-dimensional bioprinted constructs with a novel bacterial nanocellulose bioink, *ACS Biomaterials Science & Engineering*, 5 (2019) 2482–2490. DOI: 10.1021/acsbomaterials.9b00157
- Araki J., Wada M., Kuga S., Okano T., Flow properties of microcrystalline cellulose suspension prepared by acid treatment of native cellulose, *Colloids and Surfaces A: Physicochemical and Engineering Aspects*, 142 (1998) 75–82. DOI: 10.1016/S0927-7757(98)00404-X
- Araki J., Wada M., Kuga S., Okano T., Influence of surface charge on viscosity behavior of cellulose microcrystal suspension, *Journal of Wood Science*, 45 (1999) 258–261. DOI: 10.1007/



- BF01177736
- Araki J., Wada M., Kuga S., Steric stabilization of a cellulose microcrystal suspension by poly(ethylene glycol) grafting, *Langmuir*, 17 (2001) 21–27. DOI: 10.1021/la001070m
- Clemons C., Wood-plastic composites in the United States—the interfacing of two industries, *Forest Products Journal*, 52 (2002) 10–18. <https://www.fs.usda.gov/treearch/pubs/8778>
- Cousins S.K., Brown R.M., Cellulose I microfibril assembly: computational molecular mechanics energy analysis favours bonding by van der Waals forces as the initial step in crystallization, *Polymer*, 36 (1995) 3885–3888. DOI: 10.1016/0032-3861(95)99782-P
- Drexler K.E., *Nanosystems: Molecular Machinery, Manufacturing, and Computation*, Wiley, 1992, ISBN: 978-0-471-57518-4.
- Endo T., Kitagawa R., Zhang F., Hirotsu T. Hisokawa J., Mechanochemical preparation of novel cellulose-poly(ethylene glycol) composite, *Chemistry Letters*, 28 (1999) 1155–1156. DOI: 10.1246/cl.1999.1155
- Goussé C., Chanzy H., Excoffier G., Soubeyrand L., Fleury E., Stable suspensions of partially silylated cellulose whiskers dispersed in organic solvents, *Polymer*, 43 (2002) 2645–2651. DOI: 10.1016/S0032-3861(02)00051-4
- Hahladakis J.N., Velis C.A., Weber R., Iacovidou E., Purnell P., An overview of chemical additives present in plastics: migration, release, fate and environmental impact during their use, disposal and recycling, *Journal of Hazardous Materials*, 344 (2018) 179–199. DOI: 10.1016/j.jhazmat.2017.10.014
- Hai L.V., Zhai L., Kim H.C., Panicker P.S., Pham D.H., Kim J., Chitosan nanofiber and cellulose nanofiber blended composite applicable for active food packaging, *Nanomaterials*, 10 (2020) 1752. DOI: 10.3390/nano10091752
- Halim A., Xu Y., Lin K.-H., Kobayashi M., Kajiyama M., Enomae T., Fabrication of cellulose nanofiber-deposited cellulose sponge as an oil-water separation membrane, *Separation and Purification Technology*, 224 (2019) 322–331. DOI: 10.1016/j.seppur.2019.05.005
- Hayashi N., Kondo T., Ishihara M., Enzymatically produced nano-ordered short elements containing cellulose I<sub>β</sub> crystalline domains, *Carbohydrate Polymers*, 61 (2005) 191–197. DOI: 10.1016/j.carbpol.2005.04.018
- Hayashi N., Sugiyama J., Okano T., Ishihara M., Selective degradation of the cellulose I<sub>α</sub> component in *Cladophora* cellulose with *Trichoderma viride* cellulase, *Carbohydrate Research*, 305 (1997a) 109–116. DOI: 10.1016/S0008-6215(97)00281-4
- Hayashi N., Sugiyama J., Okano T., Ishihara M., The enzymatic susceptibility of cellulose microfibrils of the algal-bacterial type and the cotton-ramie type, *Carbohydrate Research*, 305 (1997b) 261–269. DOI: 10.1016/S0008-6215(97)10032-5
- Heise K., Kontturi E., Allahverdiyeva Y., Tammelin T., Linder M.B., Nonappa, Ikkala O., Nanocellulose: recent fundamental advances and emerging biological and biomimicking applications, *Advanced Materials*, 33 (2021) 2004349. DOI: 10.1002/adma.202004349
- Heux L., Chauve G., Bonini C., Nonfloculating and chiral-nematic self-ordering of cellulose microcrystals suspensions in nonpolar solvents, *Langmuir*, 16 (2000) 8210–8212. DOI: 10.1021/la9913957
- Huan S., Yokota S., Bai L., Ago M., Borghei M., Kondo T., Rojas O.J., Formulation and composition effects in phase transitions of emulsions costabilized by cellulose nanofibrils and an ionic surfactant, *Biomacromolecules*, 18 (2017) 4393–4404. DOI: 10.1021/acs.biomac.7b01452
- Hubbe M.A., Beck K.R., O’Neal W.G., Sharma Y.C., Cellulosic substrates for removal of pollutants from aqueous systems: a review. 2. Dyes, *BioResources*, 7 (2012) 2592–2687. [https://bioresources.cnr.ncsu.edu/wp-content/uploads/2016/06/BioRes\\_07\\_2\\_2592\\_Hubbe\\_Cell\\_Remov\\_Pt2\\_Dyes.pdf](https://bioresources.cnr.ncsu.edu/wp-content/uploads/2016/06/BioRes_07_2_2592_Hubbe_Cell_Remov_Pt2_Dyes.pdf)
- Hughes J., McCully M.E., The use of an optical brightener in the study of plant structure, *Stain Technology*, 50 (1975) 319–329. DOI: 10.3109/10520297509117082
- Igarashi Y., Sato A., Okumura H., Nakatsubo F., Yano H., Manufacturing process centered on dry-pulp direct kneading method opens a door for commercialization of cellulose nanofiber reinforced composites, *Chemical Engineering Journal*, 354 (2018) 563–568. DOI: 10.1016/j.cej.2018.08.020
- Ishida K., Yokota S., Kondo T., Localized surface acetylation of aqueous counter collision cellulose nanofibrils using a Pickering emulsion as an interfacial reaction platform, *Carbohydrate Polymers*, 261 (2021) 117845. DOI: 10.1016/j.carbpol.2021.117845
- Ishikawa G., Tsuji T., Tagawa S., Kondo T., Adsorption of Janus-type amphiphilic cellulose nanofibrils onto microspheres of semicrystalline polymers, *Macromolecules*, 54 (2021) 9393–9400. DOI: 10.1021/acs.macromol.1c01163
- Isogai A., Emerging nanocellulose technologies: recent developments, *Advanced Materials*, 33 (2021) 2000630. DOI: 10.1002/adma.202000630
- Jiang F., Kondo T., Hsieh Y.-L., Rice straw cellulose nanofibrils via aqueous counter collision and differential centrifugation and their self-assembled structures, *ACS Sustainable Chemistry & Engineering*, 4 (2016) 1697–1706. DOI: 10.1021/acssuschemeng.5b01653
- Jiang S., Chen Q., Tripathy M., Luijten E., Schweizer K.S., Granick S., Janus particle synthesis and assembly, *Advanced Materials*, 22 (2010) 1060–1071. DOI: 10.1002/adma.200904094
- Kargarzadeh H., Mariano M., Huang J., Lin N., Ahmad I., Dufresne A., Thomas S., Recent developments on nanocellulose reinforced polymer nanocomposites: a review, *Polymer*, 132 (2017) 368–393. DOI: 10.1016/j.polymer.2017.09.043
- Kasuga T., Yagyu H., Uetani K., Koga H., Nogi M., Cellulose nanofiber coatings on Cu electrodes for cohesive protection against water-induced short-circuit failures, *ACS Applied Nano Materials*, 4 (2021) 3861–3868. DOI: 10.1021/acsanm.1c00267
- Kawano Y., Kondo T., Preparation of aqueous carbon material suspensions by aqueous counter collision, *Chemistry Letters*, 43 (2013) 483–485. DOI: 10.1246/cl.131046
- Kim J.-K., Choi B., Jin J., Transparent, water-stable, cellulose nanofiber-based packaging film with a low oxygen permeability, *Carbohydrate Polymers*, 249 (2020) 116823. DOI: 10.1016/j.carbpol.2020.116823
- Kitagawa K., Yano H., Microfibrillated cellulose composite resin and method for producing the same, JP Patent (2012) JP5030667B2. <https://patents.google.com/patent/JP5030667B2/en>
- Klemm D., Cranston E.D., Fischer D., Gama M., Kedzior S.A., Kralisch D., Kramer F., Kondo T., Lindström T., Nietzsche S., Petzold-Welcke K., Rauchfuß F., Nanocellulose as a natural source for groundbreaking applications in materials science: today’s state, *Materials Today*, 21 (2018) 720–748. DOI: 10.1016/j.mattod.2018.02.001
- Kondo T., New aspects of cellulose nanofibers, *Mokuzai Gakkaishi*, 54 (2008) 107–115. DOI: 10.2488/jwrs.54.107
- Kondo T., Kasai W., Method for imparting water repellency and oil resistance using cellulose nanofibers, JP Patent (2015) JP5690387B2. <https://patents.google.com/patent/JP5690387B2/en>

- Kondo T., Kose R., Naito H., Kasai W., Aqueous counter collision using paired water jets as a novel means of preparing bio-nanofibers, *Carbohydrate Polymers*, 112 (2014a) 284–290. DOI: 10.1016/j.carbpol.2014.05.064
- Kondo T., Kumon D., Mieno A., Tsujita Y., Kose R., Preparation and characterization of two types of separate collagen nanofibers with different widths using aqueous counter collision as a gentle top-down process, *Materials Research Express*, 1 (2014b) 045016. DOI: 10.1088/2053-1591/1/4/045016
- Kondo T., Morita M., Hayakawa K., Onda, Y., Wet pulverizing of polysaccharides, US Patent (2005) US7357339B2. <https://patents.google.com/patent/US7357339B2>
- Kondo T., Tanaka H., Yokota S., Nanocomposite and manufacturing method of nanocomposite, JP Patent (2021) JP6979083B2. <https://patents.google.com/patent/JP6979083B2/en>
- Kose R., Kasai W., Kondo T., Switching surface properties of substrates by coating with a cellulose nanofiber having a high adsorbability, *Sen'i Gakkaishi*, 67 (2011a) 163–167. DOI: 10.2115/fiber.67.163
- Kose R., Kondo T., Favorable 3D-network formation of chitin nanofibers dispersed in water prepared using aqueous counter collision, *Sen'i Gakkaishi*, 67 (2011b) 91–95. DOI: 10.2115/fiber.67.91
- Kose R., Mitani I., Kasai W., Kondo T., “Nanocellulose” as a single nanofiber prepared from pellicle secreted by *Gluconacetobacter xylinus* using aqueous counter collision, *Biomacromolecules*, 12 (2011c) 716–720. DOI: 10.1021/bm1013469
- Li Q., Rennecker S., Supramolecular structure characterization of molecularly thin cellulose I nanoparticles, *Biomacromolecules*, 12 (2011) 650–659. DOI: 10.1021/bm101315y
- Linder M., Teeri T.T., The cellulose-binding domain of the major cellobiohydrolase of *Trichoderma reesei* exhibits true reversibility and a high exchange rate on crystalline cellulose, *Proceedings of the National Academy of Sciences*, 93 (1996) 12251–12255. DOI: 10.1073/pnas.93.22.12251
- Lönnerberg H., Zhou Q., Brumer H., Teeri T.T., Malmström E., Hult A., Grafting of cellulose fibers with poly( $\epsilon$ -caprolactone) and poly(L-lactic acid) via ring-opening polymerization, *Biomacromolecules*, 7 (2006) 2178–2185. DOI: 10.1021/bm060178z
- Marchessault R.H., Morehead F.F., Walter N.M., Liquid crystal systems from fibrillar polysaccharides, *Nature*, 184 (1959) 632–633. DOI: 10.1038/184632a0
- Marturano V., Cerruti P., Ambrogi V., Polymer additives, *Physical Sciences Reviews*, 2 (2017) 20160130. DOI: 10.1515/psr-2016-0130
- Mazeau K., Wyszomirski M., Modelling of Congo red adsorption on the hydrophobic surface of cellulose using molecular dynamics, *Cellulose*, 19 (2012) 1495–1506. DOI: 10.1007/s10570-012-9757-6
- Mukherjee S.M., Woods H.J., X-ray and electron microscope studies of the degradation of cellulose by sulphuric acid, *Biochimica et Biophysica Acta*, 10 (1953) 499–511. DOI: 10.1016/0006-3002(53)90295-9
- Nagashima A., Tsuji T., Kondo T., A uniaxially oriented nanofibrous cellulose scaffold from pellicles produced by *Gluconacetobacter xylinus* in dissolved oxygen culture, *Carbohydrate Polymers*, 135 (2016) 215–224. DOI: 10.1016/j.carbpol.2015.08.077
- Nakagaito A.N., Iwamoto S., Yano H., Bacterial cellulose: the ultimate nano-scalar cellulose morphology for the production of high-strength composites, *Applied Physics A*, 80 (2005b) 93–97. DOI: 10.1007/s00339-004-2932-3
- Nakagaito A.N., Yano H., Novel high-strength biocomposites based on microfibrillated cellulose having nano-order-unit web-like network structure, *Applied Physics A*, 80 (2005a) 155–159. DOI: 10.1007/s00339-003-2225-2
- Nechyporchuk O., Belgacem M.N., Bras J., Production of cellulose nanofibrils: a review of recent advances, *Industrial Crops and Products*, 93 (2016) 2–25. DOI: 10.1016/j.indcrop.2016.02.016
- Nge T.T., Lee S.-H., Endo T., Preparation of nanoscale cellulose materials with different morphologies by mechanical treatments and their characterization, *Cellulose*, 20 (2013) 1841–1852. DOI: 10.1007/s10570-013-9962-y
- Nickerson R.F., Habrle J.A., Cellulose intercrystalline structure, *Industrial & Engineering Chemistry*, 39 (1947) 1507–1512. DOI: 10.1021/ie50455a024
- Nishino T., Matsuda I., Hirao K., All-cellulose composite, *Macromolecules*, 37 (2004) 7683–7687. DOI: 10.1021/ma049300h
- Nodera A., Hashiba H., Tanaka H., Polyolefin resin composition, JP Patent, (2016) JP2016079311A. <https://patents.google.com/patent/JP2016079311A/en>
- Oksman K., Aitomäki Y., Mathew A.P., Siqueira G., Zhou Q., Butylina S., Tanpichai S., Zhou X., Hooshmand S., Review of the recent developments in cellulose nanocomposite processing, *Composites Part A: Applied Science and Manufacturing*, 83 (2016) 2–18. DOI: 10.1016/j.compositesa.2015.10.041
- Oksman K., Sain M., Cellulose Nanocomposites, Processing, Characterization and Properties, ACS Symposium Series, 938, American Chemical Society, Washington, DC, 2006, ISBN: 9780841239807. DOI: 10.1021/bk-2006-0938
- Payen A., Mémoire sur la composition du tissu propre des plantes et du ligneux, *Comptes Rendus*, 7 (1838) 1052–1056.
- Peretz R., Mamane H., Sterenzon E., Gerchman Y., Rapid quantification of cellulose nanocrystals by Calcofluor White fluorescence staining, *Cellulose*, 26 (2019) 971–977. DOI: 10.1007/s10570-018-2162-z
- Revol J.F., Bradford H., Giasson J., Marchessault R.H., Gray D.G., Helicoidal self-ordering of cellulose microfibrils in aqueous suspension, *International Journal of Biological Macromolecules*, 14 (1992) 170–172. DOI: 10.1016/S0141-8130(05)80008-X
- Saito T., Isogai A., TEMPO-mediated oxidation of native cellulose. The effect of oxidation conditions on chemical and crystal structures of the water-insoluble fractions, *Biomacromolecules*, 5 (2004) 1983–1989. DOI: 10.1021/bm0497769
- Saito T., Kuramae R., Wohler J., Berglund L.A., Isogai A., An ultrastrong nanofibrillar biomaterial: the strength of single cellulose nanofibrils revealed via sonication-induced fragmentation, *Biomacromolecules*, 14 (2013) 248–253. DOI: 10.1021/bm301674e
- Saito T., Nishiyama Y., Putaux J.-L., Vignon M., Isogai A., Homogeneous suspensions of individualized microfibrils from TEMPO-catalyzed oxidation of native cellulose, *Biomacromolecules*, 7 (2006) 1687–1691. DOI: 10.1021/bm060154s
- Shibata I., Isogai A., Nitroxide-mediated oxidation of cellulose using TEMPO derivatives: HPSEC and NMR analyses of the oxidized products, *Cellulose*, 10 (2003) 335–341. DOI: 10.1023/A:1027330409470
- Shojaeirani J., Bajwa D.S., Chanda S., Cellulose nanocrystal based composites: a review, *Composites Part C: Open Access*, 5 (2021) 100164. DOI: 10.1016/j.jcomc.2021.100164
- Tagawa S., Ishida K., Tsuji T., Kondo T., Facile size evaluation of cellulose nanofibrils adsorbed on polypropylene substrates using fluorescence microscopy, *Cellulose*, 28 (2021) 2917–2929. DOI: 10.1007/s10570-021-03759-0
- Takai-Yamashita C., Mabuchi Y., Ikeda J., Fuji M., Senna M., Ohya Y., Physicochemical effects and surface activity of

- cellulose nanofiber sols induced by a planetary ball milling treatment, *Journal of the Society of Powder Technology, Japan*, 58 (2021) 164–169. DOI: 10.4164/sptj.58.164
- Taniguchi T., Okamura K., New films produced from microfibrillated natural fibres, *Polymer International*, 47 (1998) 291–294. DOI: 10.1002/(SICI)1097-0126(199811)47:3<291::AID-PI11>3.0.CO;2-1
- Taton T.A., Two-way traffic, *Nature Materials*, 2 (2003) 73–74. DOI: 10.1038/nmat824
- Thomas P., Duolikun T., Rumjit N.P., Moosavi S., Lai C.W., Bin Johan M.R., Fen L.B., Comprehensive review on nanocellulose: recent developments, challenges and future prospects, *Journal of the Mechanical Behavior of Biomedical Materials*, 110 (2020) 103884. DOI: 10.1016/j.jmbbm.2020.103884
- Thompson K.L., Williams M., Armes S.P., Colloidosomes: synthesis, properties and applications, *Journal of Colloid and Interface Science*, 447 (2015) 217–228. DOI: 10.1016/j.jcis.2014.11.058
- Trache D., Hussin M.H., Haafiz M.K.M., Thakur V.K., Recent progress in cellulose nanocrystals: sources and production, *Nanoscale*, 9 (2017) 1763–1786. DOI: 10.1039/C6NR09494E
- Tsuboi K., Yokota S., Kondo T., Difference between bamboo- and wood-derived cellulose nanofibers prepared by the aqueous counter collision method, *Nordic Pulp & Paper Research Journal*, 29 (2014) 69–76. DOI: 10.3183/npprj-2014-29-01-p069-076
- Tsuji T., Tsuboi K., Yokota S., Tagawa S., Kondo T., Characterization of an amphiphilic Janus-type surface in the cellulose nanofibril prepared by aqueous counter collision, *Biomacromolecules*, 22 (2021) 620–628. DOI: 10.1021/acs.biomac.0c01464
- Tsujita Y., Kondo T., A building block of collagen fibrils demonstrated by sequential aqueous counter collision process, *Journal of Fiber Science and Technology*, 75 (2019) 112–118. DOI: 10.2115/fiberst.2019-0014
- Uetani K., Yano H., Nanofibrillation of wood pulp using a high-speed blender, *Biomacromolecules*, 12 (2011) 348–353. DOI: 10.1021/bm101103p
- Utsunomiya H., Tsujita Y., Kondo T., Cellulose nanoanemone: an asymmetric form of nanocellulose, *Cellulose*, 29 (2022) 2899–2916. DOI: 10.1007/s10570-021-04231-9
- Walther A., Müller A.H.E., Janus particles, *Soft Matter*, 4 (2008) 663–668. DOI: 10.1039/B718131K
- Winey K.I., Vaia R.A., Polymer nanocomposites, *MRS Bulletin*, 32 (2011) 314–322. DOI: 10.1557/mrs2007.229
- Yabu H., Kanahara M., Shimomura M., Arita T., Harano K., Nakamura E., Higuchi T., Jinnai H., Polymer Janus particles containing block-copolymer stabilized magnetic nanoparticles, *ACS Applied Materials & Interfaces*, 5 (2013) 3262–3266. DOI: 10.1021/am4003149
- Yano H., Nakahara S., Bio-composites produced from plant microfiber bundles with a nanometer unit web-like network, *Journal of Materials Science*, 39 (2004) 1635–1638. DOI: 10.1023/B:JMISC.0000016162.43897.0a
- Yano H., Nano Cellulose Vehicle Project, Ministry of the Environment of Japan (2016–2019). <https://www.env.go.jp/press/103177.html>
- Yano H., Sugiyama J., Nakagaito A.N., Nogi M., Matsuura T., Hikita M., Handa K., Optically transparent composites reinforced with networks of bacterial nanofibers, *Advanced Materials*, 17 (2005) 153–155. DOI: 10.1002/adma.200400597
- Ye W., Yokota S., Fan Y., Kondo T., A combination of aqueous counter collision and TEMPO-mediated oxidation for doubled carboxyl contents of  $\alpha$ -chitin nanofibers, *Cellulose*, 28 (2021) 2167–2181. DOI: 10.1007/s10570-021-03676-2
- Yokota S., Kamada K., Sugiyama A., Kondo T., Pickering emulsion stabilization by using amphiphilic cellulose nanofibrils prepared by aqueous counter collision, *Carbohydrate Polymers*, 226 (2019) 115293. DOI: 10.1016/j.carbpol.2019.115293
- Yokota S., Tagawa S., Kondo T., Facile surface modification of amphiphilic cellulose nanofibrils prepared by aqueous counter collision, *Carbohydrate Polymers*, 255 (2021) 117342. DOI: 10.1016/j.carbpol.2020.117342
- Yu T., Qiu X., Chapter 2 Elastic-Plastic Waves, in: Yu T. and Qiu X. (eds), *Introduction to Impact Dynamics*, Tsinghua University Press, 2018, pp. 19–38, ISBN: 9781118929841. DOI: 10.1002/9781119113133.ch2
- Zhou Q., Greffe L., Baumann M.J., Malmström E., Teeri T.T., Brumer H., Use of xyloglucan as a molecular anchor for the elaboration of polymers from cellulose surfaces: a general route for the design of biocomposites, *Macromolecules*, 38 (2005) 3547–3549. DOI: 10.1021/ma047712k

## Author's Short Biography



### Tetsuo Kondo

Tetsuo Kondo is the Full Professor of both laboratories of Biomacromolecular Materials Lab, and Biomaterial Design Lab at Graduate School of Bioresource and Bioenvironmental Sciences, Kyushu University. Recently, he has joined Tokyo University of Agriculture and Technology as an endowed chair of Enviro-Sustainable Materials Science Lab. He graduated BSc, MS and Ph.D. from The University of Tokyo. He obtained his second Ph.D of Engineering from Kyoto University. For more than 35 years, Dr. Kondo has been contributing extensively to the interdisciplinary interfaces between chemistry and biology of cellulose, based on cellulose physical chemistry through basic and applied research using various cellulose from different origins.



# Functionalized Graphitic Carbon Nitrides for Photocatalytic $\text{H}_2\text{O}_2$ Production: Desired Properties Leading to Rational Catalyst Design †

Zhengyuan Teng, Wenan Cai and Teruhisa Ohno\*

*Department of Applied Chemistry, Faculty of Engineering, Kyushu Institute of Technology, Japan*

## Abstract

Photocatalytic  $\text{H}_2\text{O}_2$  production based on graphitic carbon nitride (g- $\text{C}_3\text{N}_4$ ) materials has been attracting increasing attention. However, it is difficult to reveal the inner relationships among the structure, properties and performance of a g- $\text{C}_3\text{N}_4$ -based photocatalyst by simply summarizing preparation methods, properties and performances in previous works. In this review, the three most important issues for improving  $\text{H}_2\text{O}_2$  generation based on the band diagram and physicochemical properties of pristine g- $\text{C}_3\text{N}_4$  are proposed. Improvement of the charge separation, promotion of the light absorption and introduction of active sites for  $2\text{e}^-$  oxygen reduction reaction to suppress side reactions are the most three attractive strategies for enhancing the activities. Following discussion of these strategies, representative functionalization methods are summarized on the basis of the most desired properties for improving the photocatalytic activities for  $\text{H}_2\text{O}_2$  production. Other influence factors for improving  $\text{H}_2\text{O}_2$  production such as addition of electron donors and adjustment of pH value of the solution are also discussed. Future challenges for photocatalytic  $\text{H}_2\text{O}_2$  based on g- $\text{C}_3\text{N}_4$  materials are also summarized to provide future directions in this field.

**Keywords:** carbon nitride, photocatalysis, functionalization,  $\text{H}_2\text{O}_2$

## 1. Introduction

$\text{H}_2\text{O}_2$  has been recognized as one of the 100 most important chemicals worldwide (Jones C.W., 1999; Pesterfield L., 2009). The reactive oxygen content in  $\text{H}_2\text{O}_2$  (47.1 % w/w) is the highest among all chemicals. No toxic by-products are produced from  $\text{H}_2\text{O}_2$ , making  $\text{H}_2\text{O}_2$  a highly efficient and environmental-friendly oxidant.  $\text{H}_2\text{O}_2$  has been widely applied for disinfection and sterilization (McDonnell G., 2014; Teng Z. et al., 2019), organic synthesis (Zhan W. et al., 2018) and wastewater treatment (Zhang M.-h. et al., 2019). A one-compartment fuel cell using  $\text{H}_2\text{O}_2$  in which  $\text{H}_2\text{O}_2$  is used as both an oxidant and a reductant has recently been developed (Mousavi Shaegh S.A. et al., 2012). Studies on this fuel cell showed that the theoretical output potential is 1.09 V, which is comparable to that of a conventional hydrogen ( $\text{H}_2$ ) fuel cell (1.23 V) (Mousavi Shaegh S.A. et al., 2012; Kim D. et al., 2015; Yamada Y. et al., 2013). Compared to  $\text{H}_2$ ,  $\text{H}_2\text{O}_2$  showed a promising prospect as a water-soluble solar fuel ( $\text{H}_2\text{O}_2$ , 3.0 MJL<sup>-1</sup>, in an aqueous solution higher than the intensity of compressed  $\text{H}_2$  gas, 2.8 MJL<sup>-1</sup>, 35 MPa) (Kim D. et al., 2015). Unlike

hydrogen,  $\text{H}_2\text{O}_2$  is fully soluble in water and is easily transportable, making it an ideal energy carrier alternative to  $\text{H}_2$ . The anthraquinone (AQ) method for  $\text{H}_2\text{O}_2$  production is the main process used in industry (more than 95 % of total production, Fig. 1) (Campos-Martin J.M. et al., 2006). The AQ process includes the following four steps: (i) in an organic solvent, hydrogenation of anthraquinone (AQ) is firstly catalyzed on an Ni/Pd catalyst; (ii) hydrogenated anthraquinone (HAQ) is oxidized with the aid of a catalyst; (iii)  $\text{H}_2\text{O}_2$  is extracted by pure water, and HAQ is used to reproduce AQ; and iv) the as-prepared  $\text{H}_2\text{O}_2$  is purified and concentrated for following commercial use. These hydrogenation and oxidation reactions consume a lot of energy. Additionally, the AQ process is not environmental-friendly because large amounts of wastes are generated (Campos-Martin J.M. et al., 2006).

Efforts have been made to develop new methods for  $\text{H}_2\text{O}_2$  production under more moderated reaction conditions with less waste production. (Yi Y. et al., 2016). Direct synthesis from  $\text{H}_2$  and  $\text{O}_2$  in the presence of a Pd catalyst or a bimetallic Au–Pd catalyst is a possible alternative route for  $\text{H}_2\text{O}_2$  production based on the reaction of  $\text{H}_2 + \text{O}_2 = \text{H}_2\text{O}_2$ . Typical reaction conditions mainly include  $\text{H}_2/\text{O}_2$  mixture gas catalyzed by noble metal catalysts (Xia C. et al., 2019; Freakley S.J. et al., 2016). The ratio of the  $\text{H}_2/\text{O}_2$  mixture needs to be precisely controlled in the process to avoid the risk of explosions (Xia C. et al., 2019; Freakley S.J. et al.,

† Received 22 December 2021; Accepted 6 February 2022  
J-STAGE Advance published online 2 April 2022  
Add: 1-1 Sensuicho, Tobata Ward, Kitakyushu, Fukuoka 804-8550, Japan  
E-mail: tohno@che.kyutech.ac.jp  
TEL: +81-093-884-3318 FAX: +81-72-867-1658



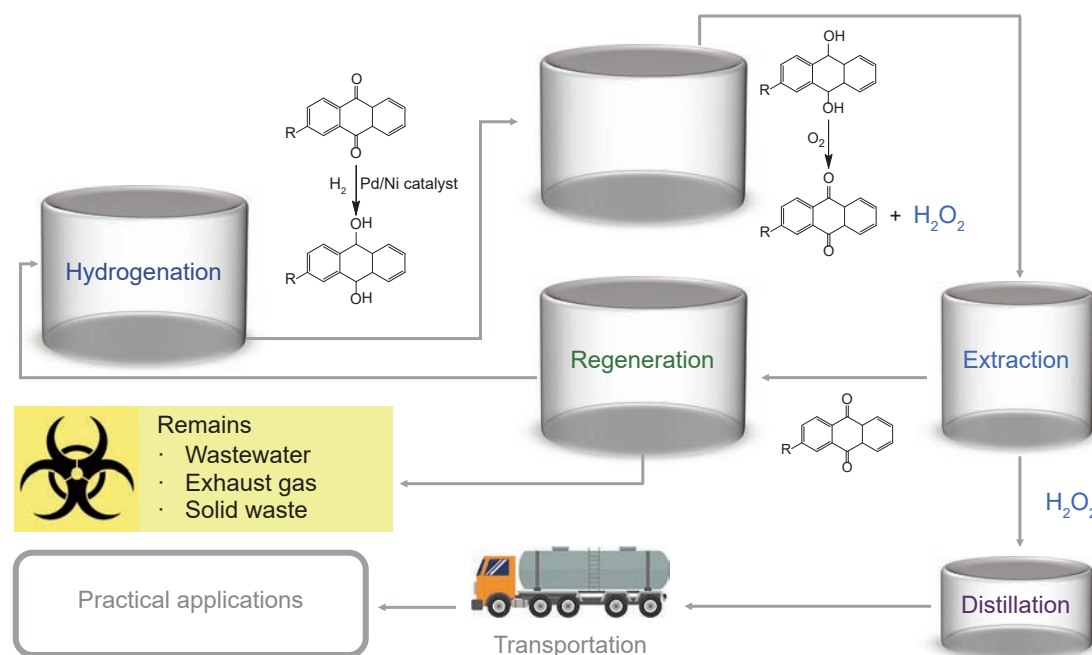


Fig. 1 Schematic of the anthraquinone oxidation (AQ) process.

2016). Recently, much attention has been given to the possibility of efficient  $\text{H}_2\text{O}_2$  production by a photocatalytic reaction process, which would be a significant breakthrough in  $\text{H}_2\text{O}_2$  chemistry. A photocatalytic approach would enable the use of explosive  $\text{H}_2$  gas to be avoided and it would only need light,  $\text{O}_2$  and water, with no pollutant generated in the overall process. Much interest has therefore been shown in photocatalytic strategies for  $\text{H}_2\text{O}_2$  production.

In past one decade, many kinds of semiconductors including metal oxides, metal sulfides, metal organic compounds and organic semiconductors have been prepared for photocatalytic  $\text{H}_2\text{O}_2$  production (Hou H. et al., 2020). Among these photocatalysts, graphite-like carbon nitride ( $\text{g-C}_3\text{N}_4$ ), also named polymeric carbon nitride (PCN), as a metal-free polymer semiconductor (n-type), possesses a stacked two-dimensional (2D) structure of tri-*s*-triazine connected via tertiary amines (Wang X. et al., 2009). Because of its unique electrical, optical, structural and physicochemical properties,  $\text{g-C}_3\text{N}_4$  has been recognized as a new class of cost-efficient multifunctional materials for electronic, catalytic and energy applications (Banerjee T. et al., 2021). Shiraishi and co-workers first found in 2014 that pristine  $\text{g-C}_3\text{N}_4$  showed some photocatalytic activity for  $\text{H}_2\text{O}_2$  production with the addition of ethanol as an electron donor (Shiraishi Y. et al., 2014b). Since then, more than 80 studies on photocatalytic  $\text{H}_2\text{O}_2$  production based on  $\text{g-C}_3\text{N}_4$  materials have been published. Several reviews summarizing some of the recent progress in photocatalytic  $\text{H}_2\text{O}_2$  production have also been published (Hou H. et al., 2020; Zhang G. et al., 2020). Most of those reviews focused on how the various protocols for preparation of functionalized  $\text{g-C}_3\text{N}_4$  influenced the photocatalytic activity (Hou H. et

al., 2020; Zhang G. et al., 2020). However, it is difficult to reveal the inner relationships among the structure, properties and performance of a  $\text{g-C}_3\text{N}_4$ -based photocatalyst by simply summarizing preparation methods, properties and performances (Zhang G. et al., 2020; Torres-Pinto A. et al., 2019). Generally, the structure of a photocatalyst defines its properties, and the properties of the photocatalyst determine its performance. Thus, it is necessary to determine the desired properties of a  $\text{g-C}_3\text{N}_4$ -based photocatalyst for  $\text{H}_2\text{O}_2$  production. Determination of the desired properties would lead to a comprehensive understanding of the photocatalyst from rational structure design to good performance.

In this review, we firstly show the principles of photocatalytic  $\text{H}_2\text{O}_2$  production. Then the three most important issues for improving  $\text{H}_2\text{O}_2$  generation based on the band diagram and physicochemical properties of pristine  $\text{g-C}_3\text{N}_4$  are proposed. By combining the fundamental principles with preparation strategies and possible influencing factors in liquid-phase photocatalytic systems, future challenges and possible directions for  $\text{H}_2\text{O}_2$  production using functionalized  $\text{g-C}_3\text{N}_4$  catalysts are presented in this review with the hope that they will inspire design and preparation strategies for not only carbon nitrides but also a variety of photocatalysts with good performance.

## 2. Principles of photocatalytic $\text{H}_2\text{O}_2$ generation

Since solar energy is renewable and sustainable, photocatalysis using power systems has received much attention in the past few years and it has been applied to various fields including water splitting for  $\text{H}_2$  and  $\text{O}_2$  production

(Wang X. et al., 2009; Wang Q. and Domen K., 2020), CO<sub>2</sub> reduction (Liu R. et al., 2020), nitrogen fixation (Zhang G. et al., 2020), degradation of pollutants (Koe W.S. et al., 2020) and disinfections (Teng Z. et al., 2019), organic synthesis and H<sub>2</sub>O<sub>2</sub> production (Hou H. et al., 2020). Photocatalytic power systems are cost-efficient and easy to operate compared with photo-electrochemical systems and photovoltaic-electrochemical systems (Hisatomi T. and Domen K., 2019). There are three typical steps in a photocatalytic process (Fig. 2) (Nosaka Y. and Nosaka A., 2016). Sufficient light absorption, efficient charge separation, and surface reactions are crucial properties for typical efficient photocatalysts.

Photocatalytic production of H<sub>2</sub>O<sub>2</sub> follows the photocatalytic reaction principles. H<sub>2</sub>O<sub>2</sub> can be generated through either oxygen reduction reaction (ORR) or water oxidation reaction (WOR) (Fan W. et al., 2020) as shown by a schematic diagram of photocatalytic H<sub>2</sub>O<sub>2</sub> production in Fig. 3. The light-driven 2e<sup>-</sup> WOR pathway (Eqn. (3), Table 1) is difficult to be achieved because of the uphill thermodynamics (1.76 V vs. a reversible hydrogen electrode, simplified as RHE, Table 1), i.e., the decomposition of as-produced H<sub>2</sub>O<sub>2</sub> will occur at this potential (1.76 V) because H<sub>2</sub>O<sub>2</sub>

is an excellent hole scavenger (Shi X. et al., 2017). In the case of the ORR pathway, H<sub>2</sub>O<sub>2</sub> can be produced by either a 2e<sup>-</sup> direct oxygen reduction (O<sub>2</sub> → H<sub>2</sub>O<sub>2</sub>) route or a sequential 1e<sup>-</sup> indirect reduction (O<sub>2</sub> → •O<sub>2</sub><sup>-</sup> → H<sub>2</sub>O<sub>2</sub>). For h<sup>+</sup> in consumption, the most effective reaction route is to oxidize H<sub>2</sub>O into O<sub>2</sub> and H<sup>+</sup> via a 4e<sup>-</sup> pathway (Eqn. (1)). Eqn. (7) to Eqn. (10) in Table 1 show production of H<sub>2</sub>O<sub>2</sub> via the two-step 1e<sup>-</sup> reduction pathway. First, superoxide radicals (•O<sub>2</sub><sup>-</sup>) are formed (Eqn. (7)) and further produce HO<sub>2</sub>• radicals with the reaction of H<sup>+</sup> (Eqn. (8)). Then, the HO<sub>2</sub>• radicals could produce HO<sub>2</sub><sup>-</sup> anions by undergoing another 1e<sup>-</sup> reduction (Eqn. (9)). Finally, HO<sub>2</sub><sup>-</sup> reacts with H<sup>+</sup> to generate H<sub>2</sub>O<sub>2</sub>. Eqn. (2) shows the one-step 2e<sup>-</sup> direct reduction for H<sub>2</sub>O<sub>2</sub> production. In this process, O<sub>2</sub> directly reacts with two protons to form an H<sub>2</sub>O<sub>2</sub> product via two-electron photoreduction. It should be noted that the back reaction of WOR via a 4e<sup>-</sup> pathway is the ORR process via a 4e<sup>-</sup> pathway (Eqn. (1)), which could also be a competitive reaction for H<sub>2</sub>O<sub>2</sub> production via 2e<sup>-</sup> ORR. The most ideal situation would be for photocatalytic production of H<sub>2</sub>O<sub>2</sub> to be generated from H<sub>2</sub>O and O<sub>2</sub> via 4e<sup>-</sup> WOR and 2e<sup>-</sup> ORR, which is an uphill reaction (ΔG<sub>0</sub> = 117 kJ mol<sup>-1</sup>).

### 3. Desired physicochemical properties of polymeric carbon nitride for photocatalytic H<sub>2</sub>O<sub>2</sub> production

Since Wang and his co-workers first discovered the photocatalytic activities of g-C<sub>3</sub>N<sub>4</sub> (Wang X. et al., 2009), g-C<sub>3</sub>N<sub>4</sub>-based particulate photocatalysts have attracted much interest. The band gap of g-C<sub>3</sub>N<sub>4</sub> (Carbon nitrides produced by thermal treatment at 500~550 °C with nitrogen-rich precursors have various names as polymeric carbon nitride (PCN), graphitic carbon nitride (GCN), and melon) is ~2.7 eV, corresponding to an optical wavelength of ~460 nm, which makes it a promising visible-light-response photocatalyst with an appropriate band structure (Fig. 4) (Ong W.-J. et al., 2016; Hou H. et al., 2020). Additionally, the conjugated heptazine ring in the PCN matrix can provide active sites for 2e<sup>-</sup> ORR (Shiraishi Y.

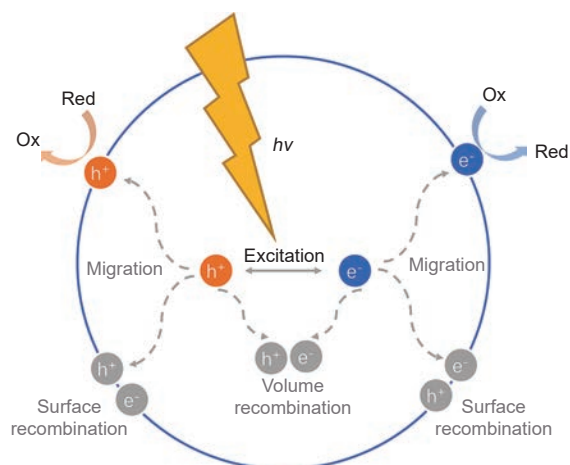


Fig. 2 Photoexcitation and charge decay pathway.

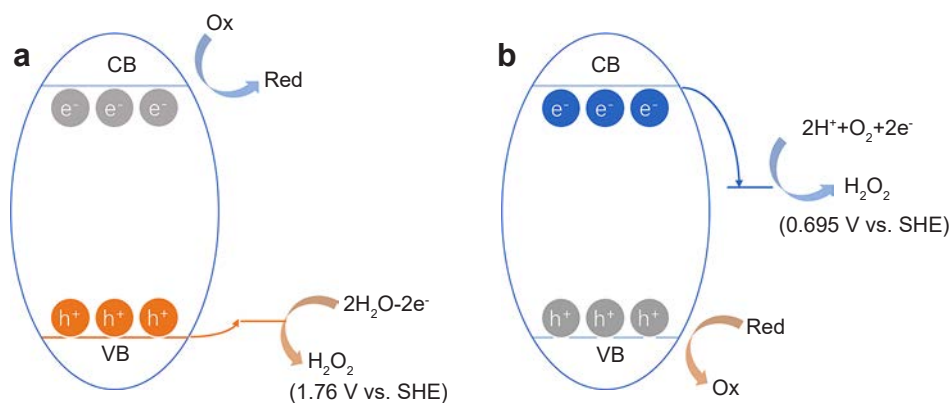


Fig. 3 Schematic diagram for photocatalytic H<sub>2</sub>O<sub>2</sub> production. (a) Photocatalytic H<sub>2</sub>O<sub>2</sub> production via water oxidation reaction. (b) Photocatalytic H<sub>2</sub>O<sub>2</sub> production via oxygen reduction. CB is the abbreviation for conduction band. VB is the abbreviation for valence band.

**Table 1** Standard electrode potentials for aqueous ORR half-reactions (Gao J. and Liu B., 2020). Reprinted with permission from Ref. (Gao J. and Liu B., 2020). Copyright: (2020) American Chemical Society.

Eqn. No.	Half-reactions	$E^0$ (V vs. SHE*)	$E^0$ (V vs. RHE**)
(1)	$O_2(g) + 4H^+ + 4e^- \leftrightarrow 2H_2O$	1.229	1.229
(2)	$O_2(g) + 2H^+ + 2e^- \leftrightarrow H_2O_2$	0.695	0.695
(3)	$H_2O_2 + 2H^+ + 2e^- \leftrightarrow 2H_2O$	1.763	1.763
(4)	$O_2(g) + 2H_2O + 4e^- \leftrightarrow 4OH^-$	0.401	1.229
(5)	$O_2 + H_2O + 2e^- \leftrightarrow HO_2^- + OH^-$	-0.065	0.764
(6)	$HO_2^- + H_2O + 2e^- \leftrightarrow 3OH^-$	0.867	1.696
(7)	$O_2(g) + e^- \leftrightarrow O_2^-$	-0.33	-0.33
(8)	$O_2(g) + H^+ + e^- \leftrightarrow HO_2^\bullet$	-0.05	-0.05
(9)	$HO_2^\bullet + e^- \leftrightarrow HO_2^-$	0.76	0.76
(10)	$HO_2^\bullet + H^+ + e^- \leftrightarrow H_2O_2$	1.44	1.44
(11)	$H_2O_2 + H^+ + e^- \leftrightarrow H_2O + \bullet OH$	0.793	0.793
(12)	$\bullet OH + e^- \leftrightarrow OH^-$	1.89	2.72

\*SHE: Standard hydrogen electrode.

\*\*RHE: Reversible hydrogen electrode.

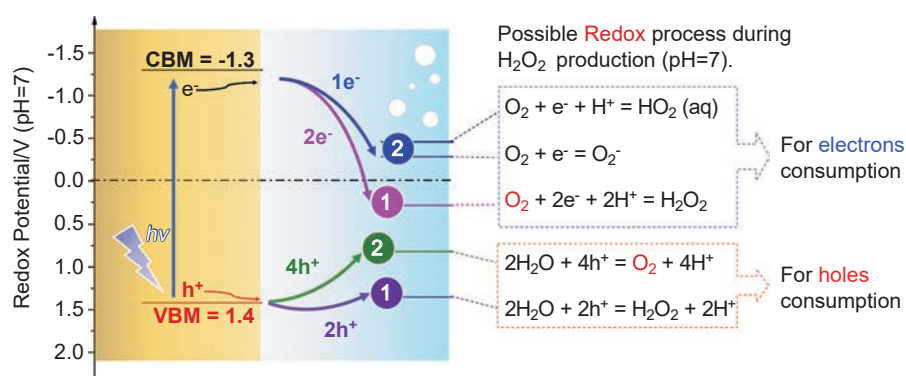


**Fig. 4** Band diagrams of  $g-C_3N_4$  and summary of potentials for redox reactions during  $H_2O_2$  production by using  $O_2$  and/or  $H_2O$ . CBM is the abbreviation for conduction band minimum and VBM is the abbreviation for valence band maximum.

et al., 2014a; Shiraishi Y. et al., 2014b), which is similar to the catalytic properties of graphene for  $2e^-$  ORR (Kim H.W. et al., 2018; Lu Z. et al., 2018). As such,  $g-C_3N_4$  has emerged as a star material in the field of photocatalytic  $H_2O_2$  production.

However, the activity of  $g-C_3N_4$  for photocatalytic  $H_2O_2$  production is still restricted by low efficiency because of some drawbacks of pristine  $g-C_3N_4$ . Firstly, a large concentration of defects is inevitably introduced into  $g-C_3N_4$  during thermal polymerization (Kim D. et al., 2015; Ong W.-J. et al., 2016). This means that the inner-plane structure of  $g-C_3N_4$  is not completely composed of covalent bonds, i.e., the interactions are hydrogen bonds between melons ( $[C_6N_9H_3]_n$ ) (Fig. 5) (Kessler F.K. et al., 2017). As a result, the charge separation and charge migration are significantly hindered, resulting in a high charge recombination rate of PCN. Secondly, the large band gap (2.7 eV) and

small absorption of visible light (Kubelka-Munk absorbance usually less than 2,  $\lambda = 420$  nm) result in insufficient visible-light harvesting. Thirdly, although the side-on adsorption of molecular oxygen on the  $\pi$ -conjugated heptazine ring enables  $g-C_3N_4$  (Shiraishi Y. et al., 2014b) to have some selectivity for  $2e^-$  ORR, it is difficult for the stepwise  $1e^-$  to  $1e^-$  ORR reaction to be prevented since signals of superoxide radicals can still be detected during the photocatalytic reactions with electron spin resonance during the photocatalytic reactions (Li S. et al., 2016). In this case, reaction sites with higher selectivity for  $2e^-$  ORR have to be constructed for improving the overall activity. To overcome these drawbacks, many protocols including tuning morphologies, defect engineering, loading co-catalysts, copolymerization of semiconductors, doping elements and hybridization have been developed. Each of these functionalization strategies overcome one or two

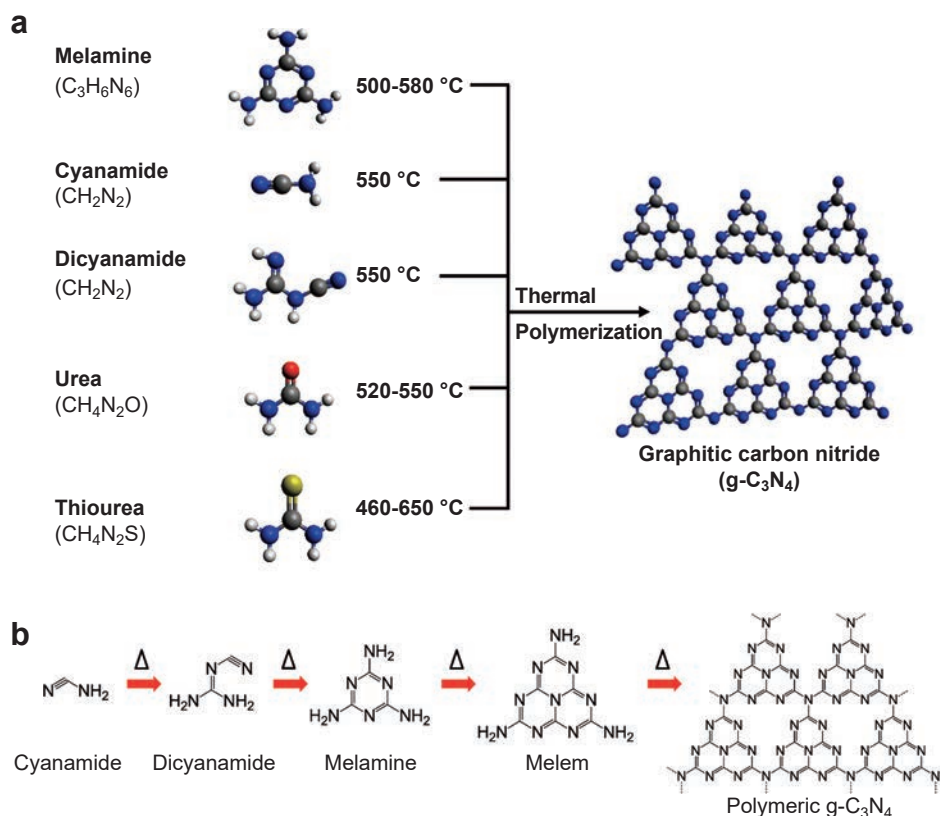


**Fig. 5** (a) Schematic illustration of the synthesis process of g-C<sub>3</sub>N<sub>4</sub> by thermal polymerization of different precursors such as melamine, cyanamide, dicyanamide, urea, and thiourea. The black, blue, white, red, and yellow balls denote C, N, H, O, and S atoms, respectively. (b) Reaction pathway for the development of g-C<sub>3</sub>N<sub>4</sub> using cyanamide as the precursor. Reprinted with permission from Ref. (Ong W.-J. et al., 2016). Copyright: (2016) American Chemical Society.

drawbacks by changing the following properties of pristine PCN: (i) suppressing charge recombination, (ii) narrowing the bandgap or/and promoting light absorbance, and (iii) introducing active sites for selective 2e<sup>-</sup> ORR (**Fig. 6**). Based on the improved physicochemical properties, functionalization strategies for improvement in the activity for photocatalytic H<sub>2</sub>O<sub>2</sub> production can also be divided into three parts, which provide a comprehensive understanding from material preparation to physicochemical properties, thus providing the insight into the relationships among structure, properties and performance.

### 3.1 Suppressing charge recombination

#### 3.1.1 Hybridization

##### 3.1.1.1 Hybridization with carbon-based materials

Carbonaceous nanomaterials are promising modifiers for photocatalysts because of their sp<sup>2</sup>-hybridized electronic structures (Shiraishi Y. et al., 2014a; Kim H.W. et al., 2018; Lu Z. et al., 2018; Yang S. et al., 2018). These materials usually work as electron transfer materials and photosensitizers to broaden the adsorption edge and improve the charge migration (Yang S. et al., 2018; Thakur S. et al., 2017; Zeng X. et al., 2017).

Carbon nanotubes (CNTs) with a π-conjugative structure are capable of accepting, transporting and storing electrons

for g-C<sub>3</sub>N<sub>4</sub> (Tasis D. et al., 2006). An amination reaction process was developed by Zhao and co-workers to introduce CNTs into nanosheets of g-C<sub>3</sub>N<sub>4</sub>, in which g-C<sub>3</sub>N<sub>4</sub> was covalently combined with CNTs (**Fig. 7a, b**) (Zhao S. et al., 2018a). The CNTs covalently combined with g-C<sub>3</sub>N<sub>4</sub> promoted charge migration by shifting the CB level to enhance the single-electron reduction of O<sub>2</sub> to ·O<sub>2</sub><sup>-</sup>, thus leading to enhanced ORR activity (Zhao S. et al., 2018a). As shown in **Fig. 7c**, the photocurrent of g-C<sub>3</sub>N<sub>4</sub>/CNTs was significantly increased compared with that pristine PCN. Shiraishi and co-workers also used reduced graphene oxide (rGO) for hybridization with a g-C<sub>3</sub>N<sub>4</sub>/perylene diimide (PDI) catalyst for further activity improvement (**Fig. 7d, e**). The improved activity may due to the ultra-thin two-dimensional nature of rGO (g-C<sub>3</sub>N<sub>4</sub>/PDI/rGO<sub>0.05</sub>) with high charge carrier mobility (Kofuji Y. et al., 2016a). As shown in **Fig. 7f**, the photocurrent of g-C<sub>3</sub>N<sub>4</sub>/PDI/rGO<sub>0.05</sub> is significantly larger than that of g-C<sub>3</sub>N<sub>4</sub>/PDI. However, no current response is found by using a rGO electrode, indicating a synergic effect of g-C<sub>3</sub>N<sub>4</sub>/PDI and rGO. It should be noted that the formation of tight junctions between the g-C<sub>3</sub>N<sub>4</sub>-based photocatalyst and carbon-based material is extremely important for the formation of electron transfer pathways since the photocurrent intensity of the physical mixture of rGO and g-C<sub>3</sub>N<sub>4</sub>/PDI is 20 % smaller than



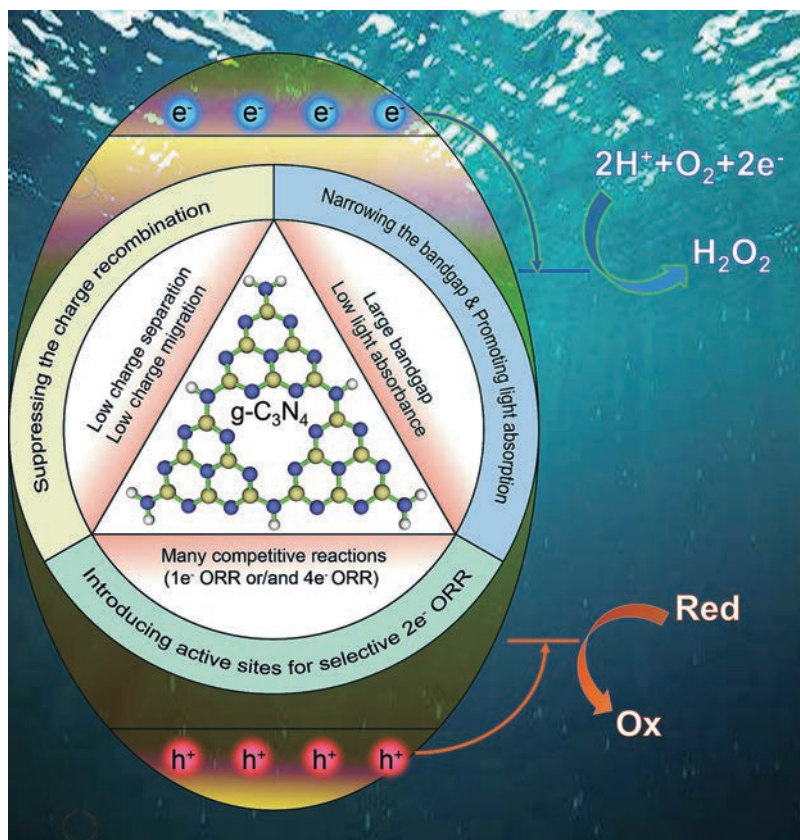


Fig. 6 Solutions for overcoming the disadvantages of pristine g-C<sub>3</sub>N<sub>4</sub> by manipulating physicochemical properties via 2e<sup>-</sup> ORR.

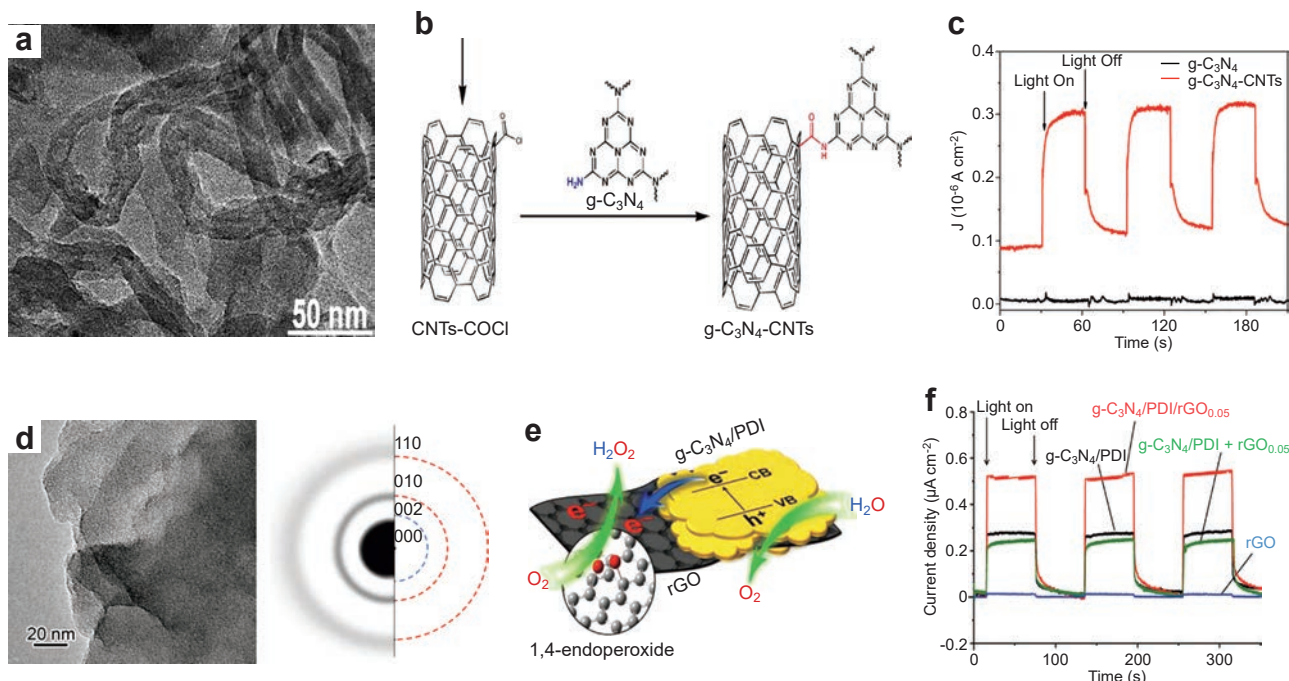
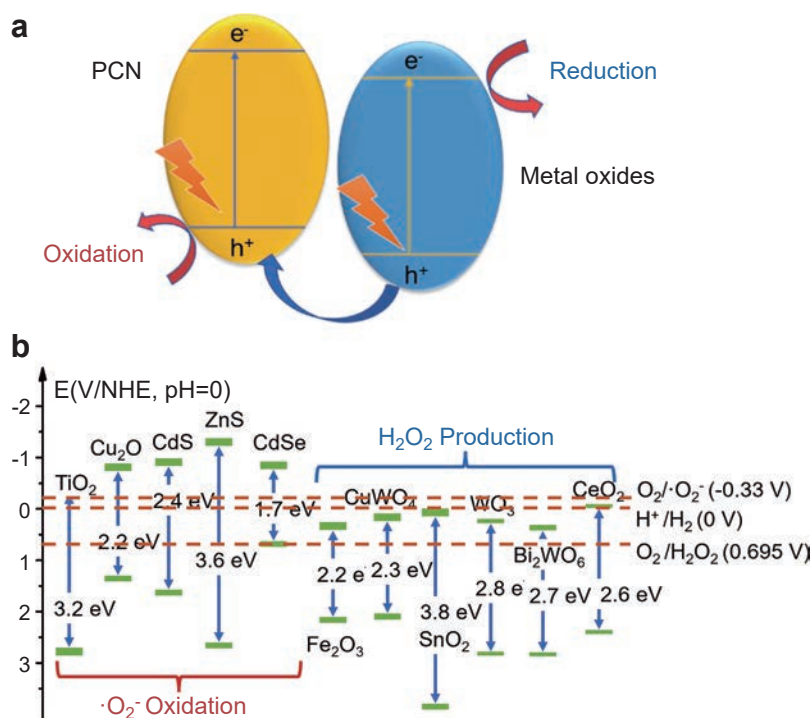


Fig. 7 Hybridization with a carbon-based material for improved charge separation. (a) TEM images of g-C<sub>3</sub>N<sub>4</sub>-CNTs. (b) Process for preparation of g-C<sub>3</sub>N<sub>4</sub>-CNTs. (c) Photocurrent response of g-C<sub>3</sub>N<sub>4</sub>-CNTs or g-C<sub>3</sub>N<sub>4</sub>-loaded electrodes under light at a bias of 0.25 V vs. SCE ( $\lambda \geq 400$  nm). (d) TEM image of g-C<sub>3</sub>N<sub>4</sub>/PDI/rGO<sub>0.05</sub> and its SAED pattern (inverse contrast) with indexed graphite pattern. (e) Schematic illustration of the proposed mechanism for photocatalytic H<sub>2</sub>O<sub>2</sub> production on g-C<sub>3</sub>N<sub>4</sub>/PDI/rGO. (f) Photocurrent responses of g-C<sub>3</sub>N<sub>4</sub>/PDI/rGO<sub>0.05</sub> and other g-C<sub>3</sub>N<sub>4</sub>-based catalysts measured on FTO in 0.1 M Na<sub>2</sub>SO<sub>4</sub> solution under visible light ( $\lambda > 420$  nm) at a bias of 0.5 V (vs Ag/AgCl). SCE is an abbreviation for saturated calomel electrode, SAED is an abbreviation for selected area electron diffraction, and FTO is an abbreviation for fluorine-doped tin oxide. Reprinted with permission from Ref. (Zhao S. et al., 2018a; Kofuji Y. et al., 2016a). Copyright: (2018) Elsevier and (2016) American Chemical Society.



**Fig. 8** Schematic diagram of (a) semiconductor heterojunctions and (b) diagram of band positions based on experimental results for common metal-based photocatalysts. NHE is an abbreviation for normal hydrogen electrode.

the photocurrent density of g-C<sub>3</sub>N<sub>4</sub>/PDI (Kofuji Y. et al., 2016a).

### 3.1.1.2 Hybridization with metal and metal compounds

Fabrication of metal compounds to form a Schottky barrier between metal-based semiconductors and PCN material has been proved to be an efficient approach for enhancing the photocatalytic efficiency for several reactions (Ong W.-J. et al., 2016; Teixeira I.F. et al., 2018). The nature of the formation of Schottky barriers in PCN/metal compounds is due to the differences between the charge potentials of metal compounds and PCN under light irradiation (Zhang Z. and Yates J.T., 2012). The electrons tend to migrate to semiconductors that have more positive potentials, while holes tend to migrate to those with negative potentials (Nosaka Y. and Nosaka A., 2016). Although the overall redox potential of the photocatalyst is decreased, the charge separation of charge carriers is significantly improved, thus leading to a significantly improved charge separation (Fig. 8a). However, there are very few reports on the promotion of photocatalytic efficiency for H<sub>2</sub>O<sub>2</sub> production by construction of heterojunctions based on PCN/metal compounds. There are two possible reasons. On the one hand, the potential of the conduction band minimum (0.9–1.3 V vs. SHE) of PCN (Fig. 4) is more negative than that of common metal compounds. In this case, the photoelectrons tend to accumulate on the metal oxides. Thus, the potential of the metal compounds determines

the reduction potential of the heterojunction materials. As shown in Fig. 8b, the photocatalytic reduction potential of TiO<sub>2</sub>, Cu<sub>2</sub>O, CdS and ZnS can hardly facilitate 2e<sup>-</sup> ORR because of the kinetically favored 1e<sup>-</sup> ORR to form •O<sub>2</sub><sup>-</sup>, thus resulting in a stepwise ORR to generate H<sub>2</sub>O<sub>2</sub>. For other metal compound semiconductors, 1e<sup>-</sup> ORR can be prevented because of the positively shifted CBM. However, the potential differences between the redox potentials of O<sub>2</sub>, 2H<sup>+</sup>/H<sub>2</sub>O<sub>2</sub> and CBM of Fe<sub>2</sub>O<sub>3</sub>, CuWO<sub>4</sub>, SnO<sub>2</sub>, WO<sub>3</sub>, etc. are quite small, which may lead to a poor thermodynamic driving force for 2e<sup>-</sup> ORR. On the other hand, formed H<sub>2</sub>O<sub>2</sub> can be decomposed by metal compounds by disproportionation or photoreaction (Li X. et al., 2001). Therefore, the formation of heterojunctions by contact of PCN with one metal compound may be an unacceptable strategy unless a unique electron transfer pathway between PCN and metal compounds is formed, such as in Z-scheme catalysts, so that reduction will occur on the surface of PCN (Wang S. et al., 2020a).

Loading active noble metal nanoparticles (NPs) is one of the effective approaches for boosting the photocatalytic activity of a photocatalyst for H<sub>2</sub>O<sub>2</sub> production (Hirakawa H. et al., 2016; Tsukamoto D. et al., 2012). Zuo and co-workers observed a similar improvement in the activity of an Au/C<sub>3</sub>N<sub>4</sub> photocatalyst for H<sub>2</sub>O<sub>2</sub> production (Zuo G. et al., 2019). In that study, the effects of different noble-metal cocatalysts on g-C<sub>3</sub>N<sub>4</sub> for H<sub>2</sub>O<sub>2</sub> production were also compared, and the results showed that g-C<sub>3</sub>N<sub>4</sub> loaded with Au nanoparticles (NPs) had the highest activity for H<sub>2</sub>O<sub>2</sub>

production (Zuo G. et al., 2019). The enhancement of  $H_2O_2$  production was attributed to the efficient separation of photogenerated electrons and holes between Au NPs and  $g-C_3N_4$  (Zuo G. et al., 2019). The function of Au NPs on PCN for charge separation is similar to that of carbon materials. The Au NPs can improve the carrier mobility of photoelectrons so that the charge recombination can be suppressed.

### 3.1.1.3 Hybridization with metal-free semiconductors and molecules

The advantages of cost efficiency, mechanical flexibility and easy operation makes organic semiconductors promising alternatives for inorganic materials to improve the charge separation (Chung D.D.L., 2019). Triazine (Jiang X. et al., 2015) and aromatic diimides have been used as modifiers for  $g-C_3N_4$  based photocatalysts (Shiraishi Y. et al., 2014a; Kofuji Y. et al., 2016a; Kofuji Y. et al., 2018; Kofuji Y. et al., 2017; Kofuji Y. et al., 2016b). Shiraishi and co-workers incorporated several aromatic diimides (Shiraishi Y. et al., 2014a; Kofuji Y. et al., 2018; Kofuji Y. et al., 2016b; Kofuji Y. et al., 2017) into the  $g-C_3N_4$  matrix by thermal condensation (Fig. 9a). All of the  $g-C_3N_4$ /PDI,  $g-C_3N_4$ /biphenyl diimide (BDI) and  $g-C_3N_4$ /mellitic triimide (MTI) catalysts successfully produced  $H_2O_2$  (millimolar level) in pure water with  $O_2$  (Shiraishi Y. et al., 2014a; Kofuji Y. et al., 2016a; Kofuji Y. et al., 2018; Kofuji Y. et al., 2017; Kofuji Y. et al., 2016b). The photocurrent showed

a significant improvement after the copolymerization of aromatic diimides. It should be noted that the introduction of more C=O groups significantly improved the photocurrent (Fig. 9b) (Kofuji Y. et al., 2017). The C=O groups in these aromatic diimides may accumulate negative charges and then increase the thickness of the space-charge region, which might improve the separation efficiency of charge carriers (Koe W.S. et al., 2020) and disinfections (Teng Z. et al., 2019). Based on this phenomenal result from the properties of C=O groups, Ohno and co-workers prepared C=O functionalized PCN by copolymerization of 2,5,8-triamino-tri-s-triazine (melem) and barbituric acid (BA) (PCNBA, Fig. 9c) (Teng Z. et al., 2020). In the photoluminescence (PL) spectra (Fig. 9d), there was a significant decrease in intensity together with a notable increase in photocurrent intensity (Teng Z. et al., 2020). The copolymerization of BA significantly suppressed recombination and accelerated the charge separation.

In the case of incorporation with semiconductors, Shiraishi and co-workers combined PCN/PDI with boron nitride (BN) to separate holes since BN has a relatively negative VBM (Kofuji Y. et al., 2018). In the system of  $g-C_3N_4$ -PDI-BN<sub>0.2</sub>-rGO, the photocurrent increased about 20 % (Kofuji Y. et al., 2018). It is notable that the oxygen evolution of  $g-C_3N_4$ -PDI-BN<sub>0.2</sub>-rGO was increased by more than 15 % compared with that of  $g-C_3N_4$ -PDI-rGO (Kofuji Y. et al., 2016a), further confirming that the charge separation introduced by BN separated photogenerated holes, leading to

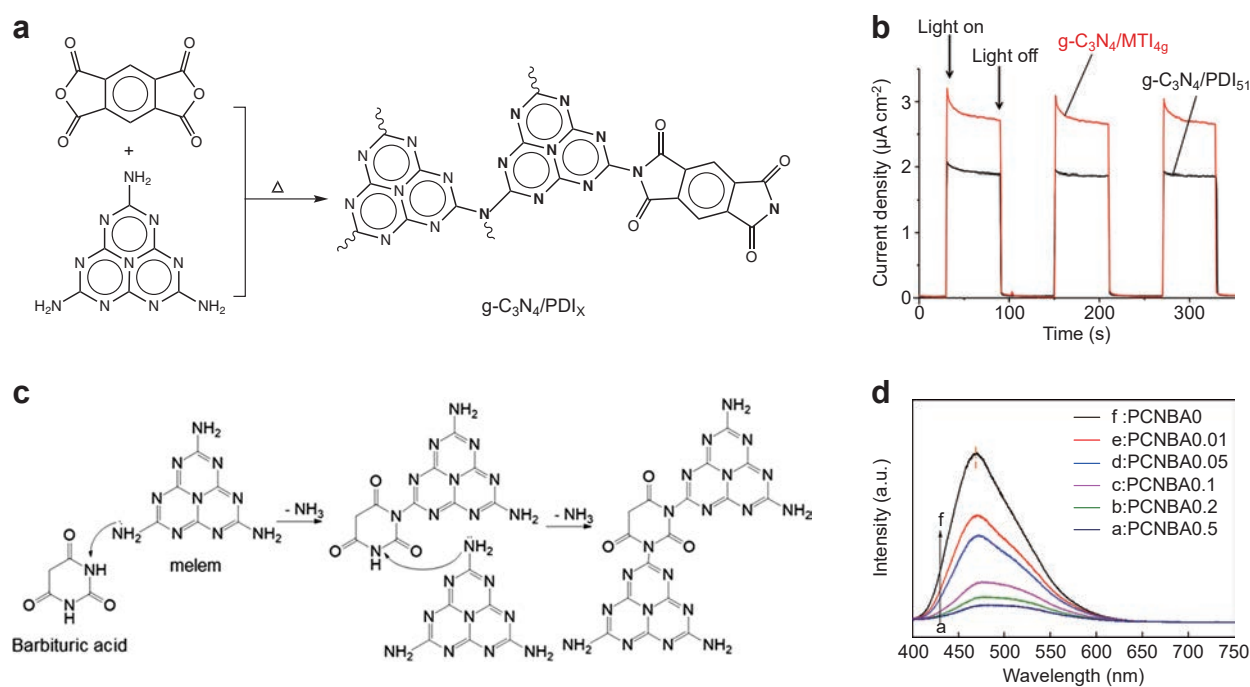


**Fig. 9** Hybridization with electron-deficient organic semiconductors for improved charge separation. (a) Scheme of the synthesis of  $g-C_3N_4$  hybridized by aromatic diimide using  $g-C_3N_4/PDI_x$  as an example. (b) Photocurrent responses of  $g-C_3N_4/MTI_{49}$  and  $g-C_3N_4/PDI_{51}$  in 0.1 M  $Na_2SO_4$  (bias: 0.5 V vs Ag/AgCl). (c) Process for polymerization of PCNBA with barbituric acid and melem as precursors. (d) Photoluminescence spectra of PCN and PCNBA samples. Reprinted with permission from Ref. (Kofuji Y. et al., 2017; Teng Z. et al., 2020). Copyright: (2017) American Chemical Society and (2020) Elsevier.

an improved charge separation. Perylene imides (PIs) were modified on  $g\text{-C}_3\text{N}_4$  nanosheets (Yang L. et al., 2017) to fabricate a Z-scheme configuration for promotion of charge separation. As a result, more electrons from the CB of the  $g\text{-C}_3\text{N}_4$  part efficiently generated  $\text{H}_2\text{O}_2$ , while the holes of  $g\text{-C}_3\text{N}_4$ /PI oxidized  $\text{OH}^-$  to  $\text{OH}$  (Yang L. et al., 2017), which also subsequently reacted to produce  $\text{H}_2\text{O}_2$ .

### 3.1.2 Doping

#### 3.1.2.1 Metal and non-metal doping

Optical, electronic and other physical properties of  $g\text{-C}_3\text{N}_4$  materials could be manipulated by doping strategies that introduce additional elements and impurities into the framework (Liu X. et al., 2020). In the case of charge separation, one of the most efficient strategies is to incorporate alkaline metal ions. Alkaline metal ions were used in several works to functionalize PCN, leading to a promoted charge separation for organic synthesis (Qiu C. et al., 2018) (Fig. 10a). Hydrogen evolution reduction (HER) (Sun S. et al., 2019), carbon dioxide reduction (COR) (Wang S. et al., 2020b), and nitrogen fixation, (Li X. et al., 2018a) can all be facilitated by incorporation of alkaline metal ions into PCN. Moon and co-workers incorporated potassium (K),

phosphorus (P), and oxygen (O) elements into a  $g\text{-C}_3\text{N}_4$  matrix by thermal calcination of melamine with potassium phosphate (KPD,  $\text{K}_2\text{HPO}_4$ ) (Moon G.-h. et al., 2017). The charge separation of KPD was significantly improved because of the significantly decreased PL intensity (Fig. 10b). The hetero-elements in the  $g\text{-C}_3\text{N}_4$  matrix increased the carrier lifetime to a picosecond range. Consequently, the generation rate of  $\text{H}_2\text{O}_2$  by K-P-O-doped  $g\text{-C}_3\text{N}_4$  was notably promoted compared to that by pure  $g\text{-C}_3\text{N}_4$  (Moon G.-h. et al., 2017) (Fig. 10c). Halogen (Br or Cl)-doped  $g\text{-C}_3\text{N}_4$  nanorods could also accelerate  $\text{H}_2\text{O}_2$  production (Zhang C. et al., 2018). The charge carrier transfer in the matrix of  $g\text{-C}_3\text{N}_4$  was promoted by the introduction of heteroatoms (Zhang C. et al., 2018). Kim et al. studied the co-doping of metal (K) and nonmetal ions (P and F) into the  $g\text{-C}_3\text{N}_4$  framework (Kim S. et al., 2018). The co-doped  $g\text{-C}_3\text{N}_4$  also significantly promoted charge separation. Under visible light irradiation, the co-doped  $g\text{-C}_3\text{N}_4$  exhibited higher activity for photocatalytic production of  $\text{H}_2\text{O}_2$  than that of bare  $g\text{-C}_3\text{N}_4$  (Fig. 10d).

Zhang et al. used density functional theory (DFT) calculation to reveal how the incorporated alkaline ions change the charge distribution over different atoms (Zhang

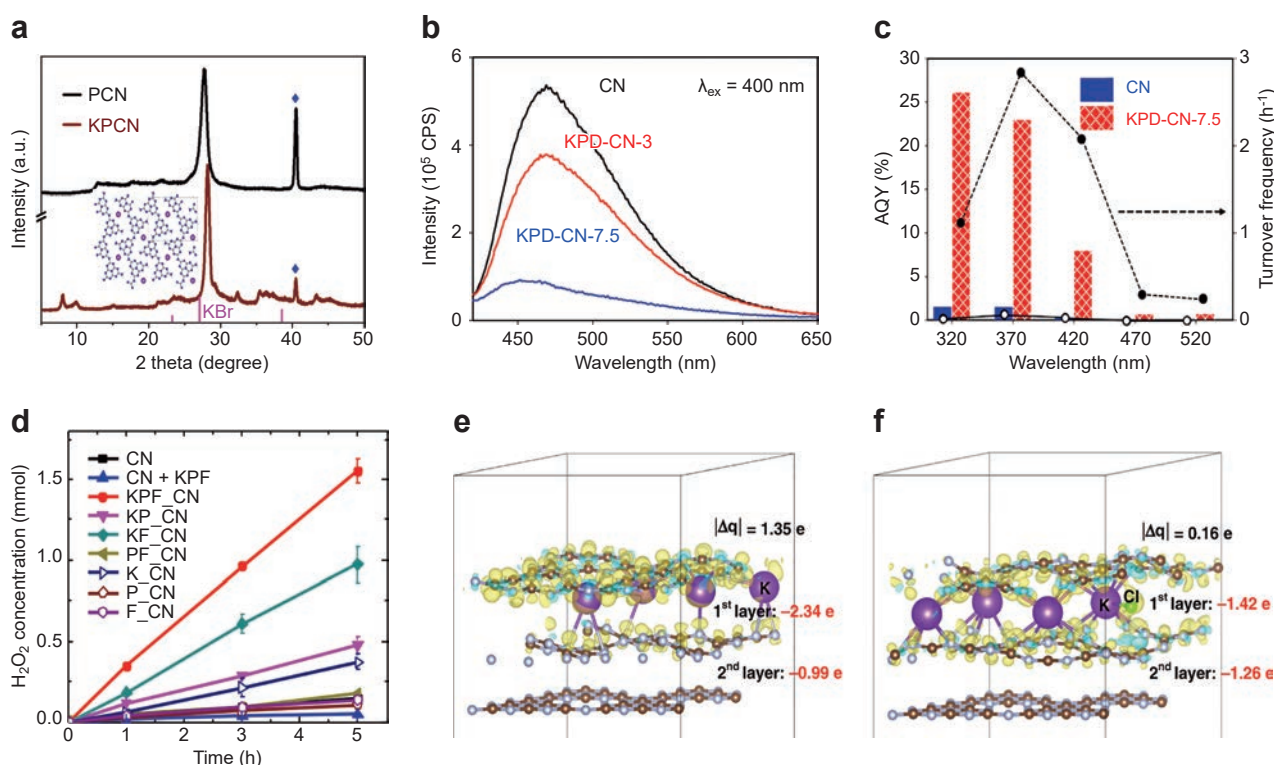


**Fig. 10** Metal and/or non-metal doping for improving the charge separation. (a) XRD patterns of pristine PCN and  $\text{K}^+$ -incorporated PCN. (b) PL emission spectra ( $\lambda = 400 \text{ nm}$ ) of bare carbon nitride (CN), KPD-CN-3, and KPD-CN-7.5. (c) Apparent quantum yield (AQY, left axis) and turnover frequency (right axis) of bare CN and those of KPD-CN-7.5 for  $\text{H}_2\text{O}_2$  production with monochromatic light irradiation. (d) Time profiles of photocatalytic  $\text{H}_2\text{O}_2$  generation using CN samples modified with various dopants and a control sample of a physical mixture of CN and  $\text{KPF}_6$  (CN + KPF). The experimental conditions were  $0.5 \text{ g L}^{-1}$  photocatalyst, 10 vol% ethanol, pH 3, continuously purged with  $\text{O}_2$  and polychromatic light through a long pass filter ( $k > 420 \text{ nm}$ ). Charge distributions of (e) K-GCN and (f) KCl-GCN obtained from density functional theory (DFT) calculations. Reprinted with permission from Ref. (Qiu C. et al., 2018; Moon G.-h. et al., 2017; Kim S. et al., 2018; Zhang P. et al., 2019). Copyright: (2018) The Authors (Qiu C. et al.), published by John Wiley & Sons, (2017) American Chemical Society, (2018) Elsevier and (2019) Springer Nature Ltd.

P. et al., 2019). The introduction of incorporated potassium species resulted in an accumulation on the first PCN layer. With the further assistance of Cl atoms, the electron distribution between the layers was more balanced (Fig. 10e and 10f), thus leading to a significantly improved interlayer charge transfer (Zhang P. et al., 2019).

Non-metal doping of PCN also enables manipulation of the electronic configuration of PCN with significantly improved charge separation (Zhang P. et al., 2020). Wei et al. developed an oxygen-enriched g-C<sub>3</sub>N<sub>4</sub> (OCN) photocatalyst that achieved enhanced H<sub>2</sub>O<sub>2</sub> production (Wei Z. et al., 2018). Compared to g-C<sub>3</sub>N<sub>4</sub>, the OCN samples achieved significantly enhanced no-sacrificial H<sub>2</sub>O<sub>2</sub> production efficiency. Electrochemical impedance spectroscopy (EIS) and photoluminescence (PL) spectra all proved that charge separation efficiency was significantly promoted after the O element had been introduced into the PCN matrix.

### 3.1.2.2 Doping with polyoxometalates and their derivatives

Polyoxometalates (POMs) are composed of cations and polyanion clusters with high structural diversity (Han X.-B. et al., 2015). Under light irradiation, a charge transfer from O<sup>2-</sup> to M<sup>n+</sup> ( $n = 5, 6$ ) usually occurred in these catalysts and lead to the formation of a hole center (O<sup>-</sup>) and trapped electron center (M<sup>(n-1)+</sup>) pair. POMs in the PCN matrix can serve as electron donor-acceptor pairs, which could significantly promote the charge separation or/and serve as co-catalysts (Han X.-B. et al., 2015). Zhao and coworkers synthesized a series of POMs clusters-modified g-C<sub>3</sub>N<sub>4</sub> samples for efficient photocatalytic H<sub>2</sub>O<sub>2</sub> evolution by the thermal condensation method (Zhao S. et al., 2017; Zhao S. and Zhao X., 2019; Zhao S. et al., 2018b). The amount of H<sub>2</sub>O<sub>2</sub> formed by g-C<sub>3</sub>N<sub>4</sub>/PW<sub>11</sub> reached 3.5 μmol within 60 min, while the catalytic performance of pure g-C<sub>3</sub>N<sub>4</sub> was only 1.3 μmol (Zhao S. et al., 2017). That research group also used other POM clusters, including [SiW<sub>11</sub>O<sub>39</sub>]<sup>8-</sup> (SiW<sub>11</sub>), (NH<sub>4</sub>)<sub>3</sub>PW<sub>12</sub>O<sub>40</sub> (NH<sub>4</sub>-PW<sub>12</sub>) and (NH<sub>4</sub>)<sub>8</sub>Co<sub>2</sub>W<sub>12</sub>O<sub>42</sub> (NH<sub>4</sub>-Co<sub>2</sub>W<sub>12</sub>), for covalent combination with g-C<sub>3</sub>N<sub>4</sub> (Zhao S. and Zhao X., 2019). All of the clusters significantly improved the charge separation of pristine PCN. Action spectra measurements revealed that the band excitation results in the generation of H<sub>2</sub>O<sub>2</sub> in both g-C<sub>3</sub>N<sub>4</sub> and g-C<sub>3</sub>N<sub>4</sub>-CoWO systems (Han X.-B. et al., 2015; Zhao S. et al., 2017; Zhao S. and Zhao X., 2019), indicating that the function of POM incorporation may be as the same as that of ion doping since POM clusters are all well dispersed in the PCN matrix. The inner-panel charge transfer and the charge transfer between the layers may be significantly promoted by the introduction of highly dispersed POM clusters.

### 3.1.3 Defect engineering

Recently, it was found that defects in semiconductors

enhance photocatalytic activity if they are precisely controlled (Pei Z. et al., 2013; Xiong J. et al., 2018; Meng A. et al., 2020). Introduction of carbon vacancies (Li S. et al., 2016; Goelcon J. and Winkler K., 2018) and introduction of nitrogen vacancies are usually defect engineering used in a g-C<sub>3</sub>N<sub>4</sub> photocatalyst (Li X. et al., 2018b; Qu X. et al., 2018; Shi L. et al., 2018; Zhu Z. et al., 2018). These strategies can change the electronic configuration and reactant molecules to promote H<sub>2</sub>O<sub>2</sub> production. For example, Li et al. synthesized g-C<sub>3</sub>N<sub>4</sub> functionalized carbon vacancies (Cv-g-C<sub>3</sub>N<sub>4</sub>) through thermal annealing in an oxygen-deficient environment (Ar flow) (Li S. et al., 2016). This Cv-g-C<sub>3</sub>N<sub>4</sub> was also functionalized with a large number of amino groups with the formation of carbon vacancies (Li S. et al., 2016). Under visible light irradiation (Kessler F.K. et al., 2017), the H<sub>2</sub>O<sub>2</sub> yield of Cv-g-C<sub>3</sub>N<sub>4</sub> was much higher than that of pure g-C<sub>3</sub>N<sub>4</sub> (Li S. et al., 2016). The improved photocatalytic activity of Cv-g-C<sub>3</sub>N<sub>4</sub> for H<sub>2</sub>O<sub>2</sub> production can be ascribed to the promoted charge separation and alteration of the H<sub>2</sub>O<sub>2</sub> production pathway from a stepwise 1e<sup>-</sup> to 1e<sup>-</sup> pathway to a 2e<sup>-</sup> pathway.

Nitrogen vacancies in g-C<sub>3</sub>N<sub>4</sub> can also boost the photocatalytic activity for H<sub>2</sub>O<sub>2</sub> production (Zhu Z. et al., 2018). Li et al. (Li X. et al., 2018b) and Qu et al. (Qu X. et al., 2018) showed that nitrogen vacancies can be introduced in the matrix of g-C<sub>3</sub>N<sub>4</sub> by dielectric barrier discharge (DBD) plasma treatment. Their results showed that H<sub>2</sub>O<sub>2</sub> evolution can be improved by up to 10 times compared with that produced by pristine PCN (Li X. et al., 2018b). In another related study, Shi et al. created a holey defective C<sub>3</sub>N<sub>4</sub> photocatalyst with nitrogen vacancies via a hydrazine photoreduction method. The transfer of charge carriers from the bulk to the surface was significantly improved, as confirmed by PL measurements (Shi L. et al., 2018). The introduced nitrogen vacancies narrowed the bandgap and the formation of defect states within the bandgap together with a notably suppressed electron-hole recombination. Therefore, the holey defective g-C<sub>3</sub>N<sub>4</sub> photocatalyst showed much higher photocatalytic activity for visible light-driven H<sub>2</sub>O<sub>2</sub> production than that of pristine g-C<sub>3</sub>N<sub>4</sub>.

In summary, the functionalization strategies of doping and defect engineering for improving the charge separation for PCN-based materials used for the 2e<sup>-</sup> ORR process are similar to the functionalization strategies for other reactions such as HER, COR, and ORR. However, the hybridization of PCN-based materials, especially hybridization with electron-deficient semiconductors, provides a PCN-based photocatalyst with unique electronic properties for improving the charge separation. We believe that copolymerization strategies to introduce other electron-deficient groups with higher charge separation efficiency might enable the generation of π-conjugated and π-stacked donor-acceptor couples (Shiraishi Y. et al., 2019) in the PCN matrix, leading to a higher efficiency for photocatalytic H<sub>2</sub>O<sub>2</sub> synthesis.

### 3.2 Improving light harvesting

Although pristine PCN can use visible light for a photocatalytic reaction, the large band gap (2.7 eV) results in insufficient visible light harvesting for further efficiency improvement (Ong W.-J. et al., 2016). Thus, improving the light absorbance of a g-C<sub>3</sub>N<sub>4</sub>-based photocatalyst and narrowing the band gap are two practical strategies for H<sub>2</sub>O<sub>2</sub> production.

Copolymerization of PCN with other organic molecules/semiconductors, such as triazine, barbituric acid and aromatic diimides, not only improves the light absorbance of the photocatalyst but also narrows the bandgap. As mentioned in Section 3.1.1.3, Shiraishi and co-workers prepared a series of PCN samples hybridized with atomic diimides with a significantly narrowed band gap from 2.7 eV of pristine PCN to 2.4 eV of PCN/PDI (Shiraishi Y. et al., 2014a; Kofuji Y. et al., 2017; Kofuji Y. et al., 2016a). The light absorbance of PCN samples hybridized with aromatic diimides improved to about ~20 % at  $\lambda = 400$  nm, indicating improved light absorption. Additionally, Ohno and co-workers co-polymerized melem with barbituric acid to expand the light absorption edge from 445 nm (2.76 eV) of pristine PCN to ~550 nm (2.18 eV) of PCNBA0.5 (Fig. 11a) (PCNBA is an abbreviation for polymetric carbon nitride doped by barbituric acid, 0.5 means calcination of 3 g melamine and 0.5 g barbituric acid) (Teng Z. et al., 2020). The absorbance of PCNBA0.2 at 420 nm was also

increased by 200 % compared with that of pristine PCN (Fig. 11b) (Teng Z. et al., 2020).

Doping of alkaline metal ions can also expand the light absorption to a small extent (0.1 eV~0.3 eV) combined with significantly light improved absorbance (50 %). Alkaline metal doping and non-metal doping were also proved to be efficient strategies for improving light absorbance (Moon G.-h. et al., 2017; Kim S. et al., 2018; Zhang P. et al., 2020). Choi and co-workers found that the light absorption ability of CN samples was gradually promoted by increasing the amount of KPF<sub>6</sub>, even though KPF<sub>6</sub> alone did not exhibit any visible-light absorption (Moon G.-h. et al., 2017) (Fig. 11c). A very recent work using K and S-co-doped PCN with functionalization of the -OH group (AKMT) also showed significant improvement in both light absorption and narrowing of the bandgap (Zhang P. et al., 2020). The light absorption edge expanded from ~450 nm of pristine PCN to ~520 nm of AKMT (Zhang P. et al., 2020) (Fig. 11d). With the addition of a sacrificial reagent, AKMT showed apparent quantum yields (AQYs) of 76 % and 40 % at 480 nm and 500 nm for H<sub>2</sub>O<sub>2</sub> production, respectively. By comparison, pristine PCN exhibited negligible activities at the same wavelengths.

Defect engineering can also slightly improve the light absorption of photocatalysts, especially for semiconductor-based materials (Li S. et al., 2016) and Zhu et al. (Zhu Z. et al., 2018) reported that the UV-vis absorption spectra of

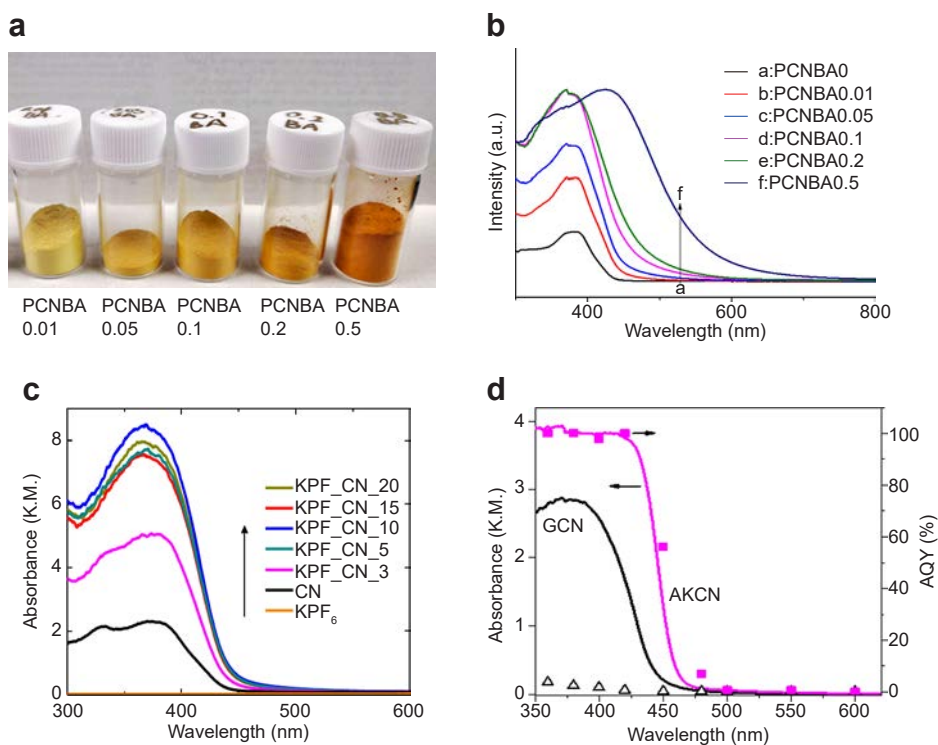


**Fig. 11** Typical strategies for improving light harvesting. (a) Photographs show the corresponding powders of PCNBA samples. (b) UV-vis spectra of PCN and PCNBA samples: absorbance spectra. (c) Diffuse reflectance UV-vis spectra (DR-UVS) of modified CN samples prepared with various KPF<sub>6</sub> contents. (d) UV-vis spectra and apparent quantum yield (AQY) of H<sub>2</sub>O<sub>2</sub> production as a function of irradiation wavelength with 10 % EtOH (v/v) under visible light irradiation ( $\lambda \geq 420$  nm) and  $T = 25$  °C. Reprinted with permission from Ref. (Teng Z. et al., 2020; Zhang P. 2019). Copyright: (2019) Springer Nature Ltd. and (2020) Elsevier.

g-C<sub>3</sub>N<sub>4</sub> and carbon vacancy-functionalized g-C<sub>3</sub>N<sub>4</sub> showed a red shift of absorption edges compared with that of pristine ones. Nitrogen vacancies also significantly improve light absorption (Li X. et al., 2018b; Qu X. et al., 2018; Shi L. et al., 2018). Ye and co-workers compared the optical properties of bulk PCN (BCN) and those of N-defected CN samples (DCN) (Shi L. et al., 2018). The absorption edges of the samples showed red shifts of ~40 nm compared with that of pristine g-C<sub>3</sub>N<sub>4</sub> samples without thermal treatment (Shi L. et al., 2018). They also revealed that the electrons could be accommodated by forming defect states in BCN, which greatly promoted light harvesting (Shi L. et al., 2018). Compared with the copolymerization of an electron-deficient semiconductor and metal/non-metal doping, the influence of defect engineering is relatively small because defect states are usually located just below the CBM. In this case, the extent of narrowing of the band-gap by introducing defects is limited. Copolymerization of electron-deficient semiconductors seems to be the most promising functionalization strategy for both improving light absorbance and expanding the absorption edge.

### 3.3 Introduction of active sites for selective 2e<sup>-</sup> ORR

Introduction of active sites with specific physicochemical properties can significantly improve both selectivity and activities (Bo Y. et al., 2020). To give a systematic review for this topic, three dominant strategies for introducing active sites for photocatalytic H<sub>2</sub>O<sub>2</sub> production are presents as follows.

#### 3.3.1 Increasing the surface area

PCN prepared by the thermal polymerization method is usually quite small (<15 m<sup>2</sup> g<sup>-1</sup>) (Teng Z. et al., 2017). As previously mentioned, the conjugated heptazine ring in the PCN matrix can provide active sites for 2e<sup>-</sup> ORR (Shiraishi Y. et al., 2014a). A plausible strategy for increasing the number of active sites for 2e<sup>-</sup> ORR is to increase the surface area (Mohamed N.A. et al., 2019; Ou H. et al., 2017; Liao G. et al., 2019). However, there is still some controversy about whether the overall 2e<sup>-</sup> ORR rate can be improved by increasing the specific surface area of PCN. Shiraishi and co-workers investigated the photocatalytic production of H<sub>2</sub>O<sub>2</sub> with the existence of O<sub>2</sub> and Et-OH. A series of mesoporous g-C<sub>3</sub>N<sub>4</sub> catalysts having different specific surface areas (SSA) were prepared by a hard template (silica nanoparticles with different diameters) method (Fig. 12a) (Shiraishi Y. et al., 2015). In these systems, photogenerated holes oxidize Et-OH and the conduction band electrons localized at the melem unit reduce O<sub>2</sub> to form H<sub>2</sub>O<sub>2</sub>. This g-C<sub>3</sub>N<sub>4</sub> catalysts exhibit significant higher SSA of 56 and 160 m<sup>2</sup> g<sup>-1</sup> compared with that of pristine g-C<sub>3</sub>N<sub>4</sub> (10 m<sup>2</sup> g<sup>-1</sup>) and higher activity for H<sub>2</sub>O<sub>2</sub> production (Shiraishi Y. et al., 2015). However, g-C<sub>3</sub>N<sub>4</sub> with the

largest SSA (228 m<sup>2</sup> g<sup>-1</sup>) showed significantly decreased activity and selectivity for H<sub>2</sub>O<sub>2</sub> formation (Fig. 12b) (Shiraishi Y. et al., 2015). Mesoporous g-C<sub>3</sub>N<sub>4</sub> with the largest surface area inherently contains the largest number of primary amine moieties (Shiraishi Y. et al., 2015). The H<sub>2</sub>O<sub>2</sub> selectivity was significantly suppressed since these defects can also serve as active sites for 4e<sup>-</sup> reduction of O<sub>2</sub> (Fig. 12c) (Shiraishi Y. et al., 2015). These defects also further decomposed the formed H<sub>2</sub>O<sub>2</sub>, leading to significantly suppressed activity. Results of density function theory (DFT) calculations confirmed (i) a large distribution of lowest unoccupied molecular orbital (LUMO) electrons onto the primary amine moieties and (ii) a decrease in H<sub>2</sub>O<sub>2</sub> selectivity with an increase in the amount of primary amine moieties, strongly suggesting that the primary amine moieties on the surfaces of mesopores behave as the active sites for four-electron reduction (Fig. 12d–f) (Shiraishi Y. et al., 2015). However, the specific types of those defects were not described in their reports. Specification of the types and fine structures of defects is important to further improvement by defect engineering strategies.

#### 3.3.2 Copolymerization with electron-deficient semiconductors

Copolymerization with electron-deficient semiconductors such as PDI, BDI and MTI has also been proved to be one of the most efficient strategies for promoting the selectivity of a photocatalyst (Shiraishi Y. et al., 2014a; Kofuji Y. et al., 2017; Kofuji Y. et al., 2016a). Calculations based on the density functional theory (DFT) were investigated to clarify the influence of the PDI unit on the electronic structure of the g-C<sub>3</sub>N<sub>4</sub> framework (Shiraishi Y. et al., 2014a). Time-dependent results showed that the main transitions are S<sub>0</sub>→S<sub>1</sub> (highest occupied molecular orbitals, HOMO→LUMO and HOMO→LUMO+2). The iso-surfaces showed that electron distributions of the melem-PDI model (main transitions HOMO→LUMO+2) are located mainly at the melem units with partial distribution to the PDI units (Shiraishi Y. et al., 2014a). The high electron affinity of the PDI units in g-C<sub>3</sub>N<sub>4</sub>/PDI may significantly improve the polarization of the whole frameworks.

Being specific, the electrons on HOMO are concentrated at the N2 and N6 atom positions of the melem unit, and those on LUMO+2 are located at the C1 and N4 atoms (Shiraishi Y. et al., 2014a). The Raman spectra of g-C<sub>3</sub>N<sub>4</sub>/PDI and g-C<sub>3</sub>N<sub>4</sub> confirmed that the side-on adsorption of O<sub>2</sub> was significantly promoted on g-C<sub>3</sub>N<sub>4</sub>/PDI, indicating a crucial role of copolymerization of electron-deficient semiconductors.

#### 3.3.3 Doping/Heteroatom incorporation

Incorporation of metal species or no-metal species in the PCN matrix can both improve the charge separation and introduce active sites for specific reactions (Hu S.

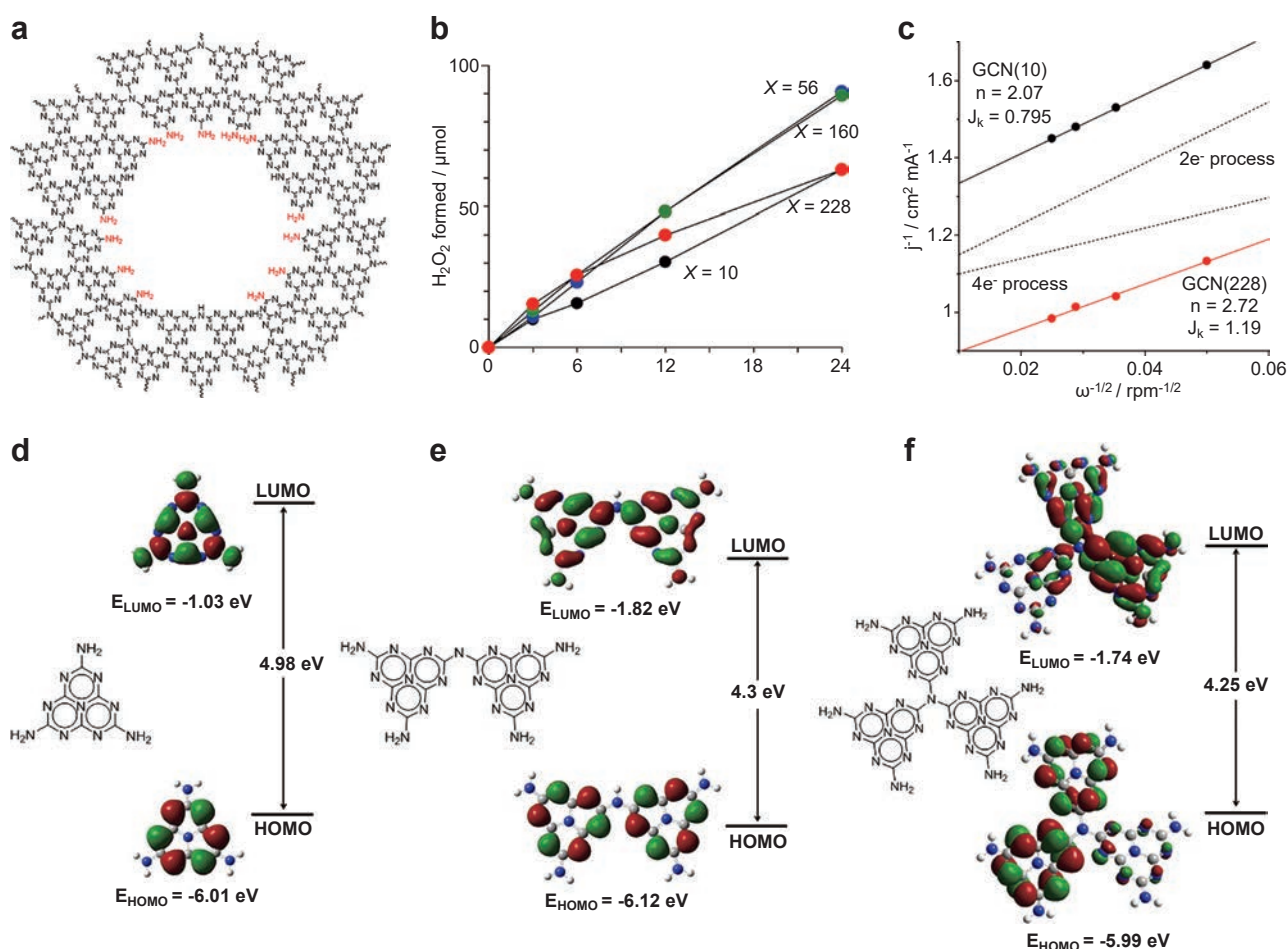


**Fig. 12** Influence of surface defects on H<sub>2</sub>O<sub>2</sub> production by using a PCN-based material. (a) Different N atoms of PCN. (b) Time-dependent change in the amounts of H<sub>2</sub>O<sub>2</sub> during photoreaction on the respective GCN(x) catalysts. (c) Electron transfer numbers during the photocatalytic H<sub>2</sub>O<sub>2</sub> production. Interfacial plots of the main orbitals for (d) single, (e) double, and (f) triple melem-conjugated models, calculated by the function of B3LYP at the 6-31G (d) level. Reprinted with permission from Ref. (Shiraishi Y. et al., 2015). Copyright: (2015) American Chemical Society.

et al., 2018; Zhang Z. et al., 2022). By the template-assisted method, Hu and co-workers fabricated hollow copper-doped g-C<sub>3</sub>N<sub>4</sub> microspheres. The g-C<sub>3</sub>N<sub>4</sub> with copper incorporation showed a much higher H<sub>2</sub>O<sub>2</sub> production ability (~4.8 mmol·L<sup>-1</sup>) than that of pristine g-C<sub>3</sub>N<sub>4</sub> (0.45 mmol·L<sup>-1</sup>). DFT simulations showed that the Cu(I)-N sites work as reactive sites to activate molecular O<sub>2</sub> (Hu S. et al., 2018). The OCN proposed by Zhu and co-workers was proven to show a high selectivity for 2e<sup>-</sup> ORR for photocatalytic H<sub>2</sub>O<sub>2</sub> production, which is attributed to the functionalized C-O-C groups on OCNs (Wei Z. et al., 2018). Choi and co-workers revealed by DFT calculations that the K incorporation could result in improved adsorption for O<sub>2</sub> molecules (Zhang P. et al., 2019) (Fig. 13a, b). They also investigated whether electrons on S-doped g-C<sub>3</sub>N<sub>4</sub> can be donated to the antibonding π\* orbital of adsorbed \*O<sub>2</sub> (with -0.40 |e|) for forming efficient ORR sites, as well as AQ doping as cocatalysts (Fig. 13c). The strong electron pushing effect between carbon and oxygen facilitates subsequent protonation in ORR kinetics (Chu C. et al., 2020). Both the activity and selectivity of ORR

can be changed by manipulating the properties of metallic sites (Kulkarni A. et al., 2018). As elaborated in several electrochemical catalysts, the end-on O<sub>2</sub> adsorption usually lead to highly selective 2e<sup>-</sup> ORR. It is difficult to prevent the splitting of O-O bond breaking on surface of metal particles since end-on O<sub>2</sub> molecular adsorption and side-on O<sub>2</sub> molecular adsorption occur on metal particles (Choi C.H. et al., 2014; Chu C. et al., 2019). Benefiting from the desirable features of a single atom catalyst (SAC) (Sun H. et al., 2021), the adsorption of O<sub>2</sub> molecules on atomically isolated sites is often end-on type, which could reduce the possibility of O-O bond splitting (Kulkarni A. et al., 2018; Wang A. et al., 2018). For example, SACs with Pt<sup>2+</sup> (Shen R. et al., 2019) and Co-N<sub>4</sub> (Gao J. et al., 2020; Jung E. et al., 2020) centers could electrochemically reduce O<sub>2</sub> to H<sub>2</sub>O<sub>2</sub> via a 2e<sup>-</sup> ORR pathway with ultrahigh selectivity (>96 %). However, it is difficult for Pt<sup>2+</sup> and Co-N<sub>4</sub> sites to be coupled in the photocatalytic system due to their high charge recombination characteristics, which originate from the intermediate band formed by the half-filled d electrons (Teng Z. et al., 2021a). Very recently, Ohno and co-workers



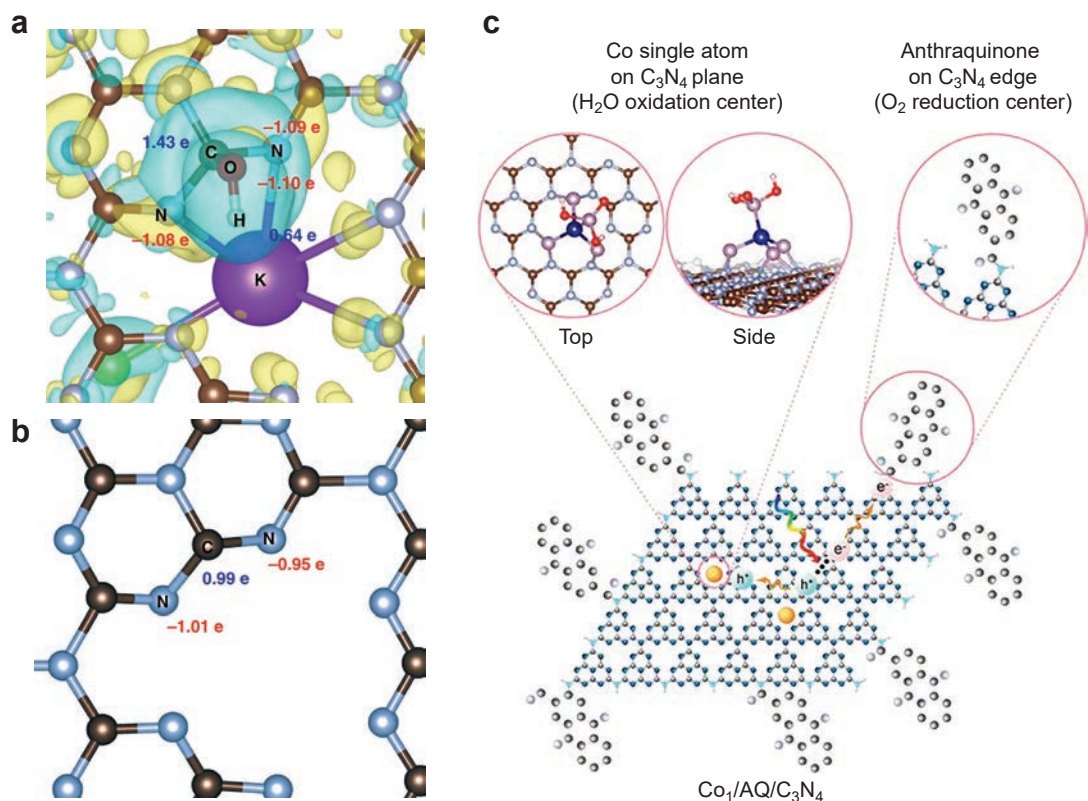


**Fig. 13** Typical strategies for introducing active sites for efficient  $2e^-$  ORR. (a) An enlarged top view of KCl-OH-GCN, and (b) an enlarged top view of pristine GCN. The yellow and blue colors represent electron accumulation and depletion at an isosurface value of  $0.002 \text{ \AA}^{-3}$ . The brown, gray, and violet colors represent carbon, nitrogen, and potassium, respectively. (c) Spatial separation of Co single atom (as an oxidation center) and AQ (as a reduction center) cocatalysts by anchoring them in the center (i.e., pyridinic N) and on the edge (i.e., primary/secondary amine N) of 2D ultrathin C<sub>3</sub>N<sub>4</sub>. Reprinted with permission from Ref. (Zhang P. et al., 2019; Chu C. et al., 2020). Copyright: (2019) Springer Nature Ltd. and (2020) The Authors (Chu C. et al.), published by National Academy of Science.

developed an Sb single atom photocatalyst (Sb-SAPC) for non-sacrificial photocatalytic H<sub>2</sub>O<sub>2</sub> synthesis in a water and oxygen mixture under visible light irradiation (Teng Z. et al., 2021a). The Sb-SAPC was prepared by a wet chemical method using NaSbF<sub>6</sub> and melamine as precursors. As shown in the image acquired from high-angle annular dark field scanning TEM (HAADF-STEM) measurement, the bright spots with high density are uniformly dispersed in the entire carbon nitride matrix (Fig. 14a). Electron energy loss spectroscopy (EELS) (Fig. 14b) measurement revealed bright spots corresponding to Sb atoms, in which the oxidation state of Sb is regulated to +3 with a  $4d^{10}5s^2$  electron configuration (Fig. 14c, d). The results of experimental and theoretical investigations indicated that the adsorption of O<sub>2</sub> on isolated Sb atomic sites is end-on type, which promotes the formation of Sb- $\mu$ -peroxide (Sb-OOH), leading to an efficient  $2e^-$  ORR pathway for H<sub>2</sub>O<sub>2</sub> production (Fig. 14e). The  $2e^-$  ORR efficiency of Sb species improved by almost one magnitude in the presence of 2-propanol (Fig. 14f). The apparent charge recombination of Sb-SAPC was significantly suppressed by introducing Sb species into the PCN matrix (Fig. 14g, h). With highly concentrated holes, this catalyst also achieved non-sacrificial H<sub>2</sub>O<sub>2</sub> production using water as an electronic donor.

### 3.3.4 Cocatalyst loading

Cocatalyst loading is a traditional strategy for introducing active sites for specific reactions (Nosaka Y. and Nosaka A, 2016). For instance, pristine PCN shows quite low efficiency in photocatalytic hydrogen production, and loading of platinum species on PCN usually significantly improves the HER performance (Wang Q. and Domen K., 2020). The reason for loading a cocatalyst to boost the photocatalytic reactions is usually the decreased overpotential of the reactions on the co-catalyst surface compared with that on pristine photocatalysts (Hirakawa H. et al., 2016; Tsukamoto D. et al., 2012; Peng Y. et al., 2017). AQ species can enhance the selectivity of O<sub>2</sub> reduction to H<sub>2</sub>O<sub>2</sub> based on the mechanism of the current industrial H<sub>2</sub>O<sub>2</sub> production process (Kim H.-i. et al., 2018; Chu C. et al., 2020). Kim and co-workers prepared several AQ-modified PCN samples with significantly improved selectivity for  $2e^-$  ORR (Chu C. et al., 2020). Loading an AQ cocatalyst onto ultrathin g-C<sub>3</sub>N<sub>4</sub> significantly improved the selectivity of H<sub>2</sub>O<sub>2</sub> production, combined with a 1.9-fold enhancement of the amount of H<sub>2</sub>O<sub>2</sub> production (Chu C. et al., 2020). Several works in which Au nanoparticles were loaded onto the C<sub>3</sub>N<sub>4</sub> matrix all showed significantly improved  $2e^-$  ORR efficiency (Chang X. et al., 2018; Zuo G. et al., 2019). This

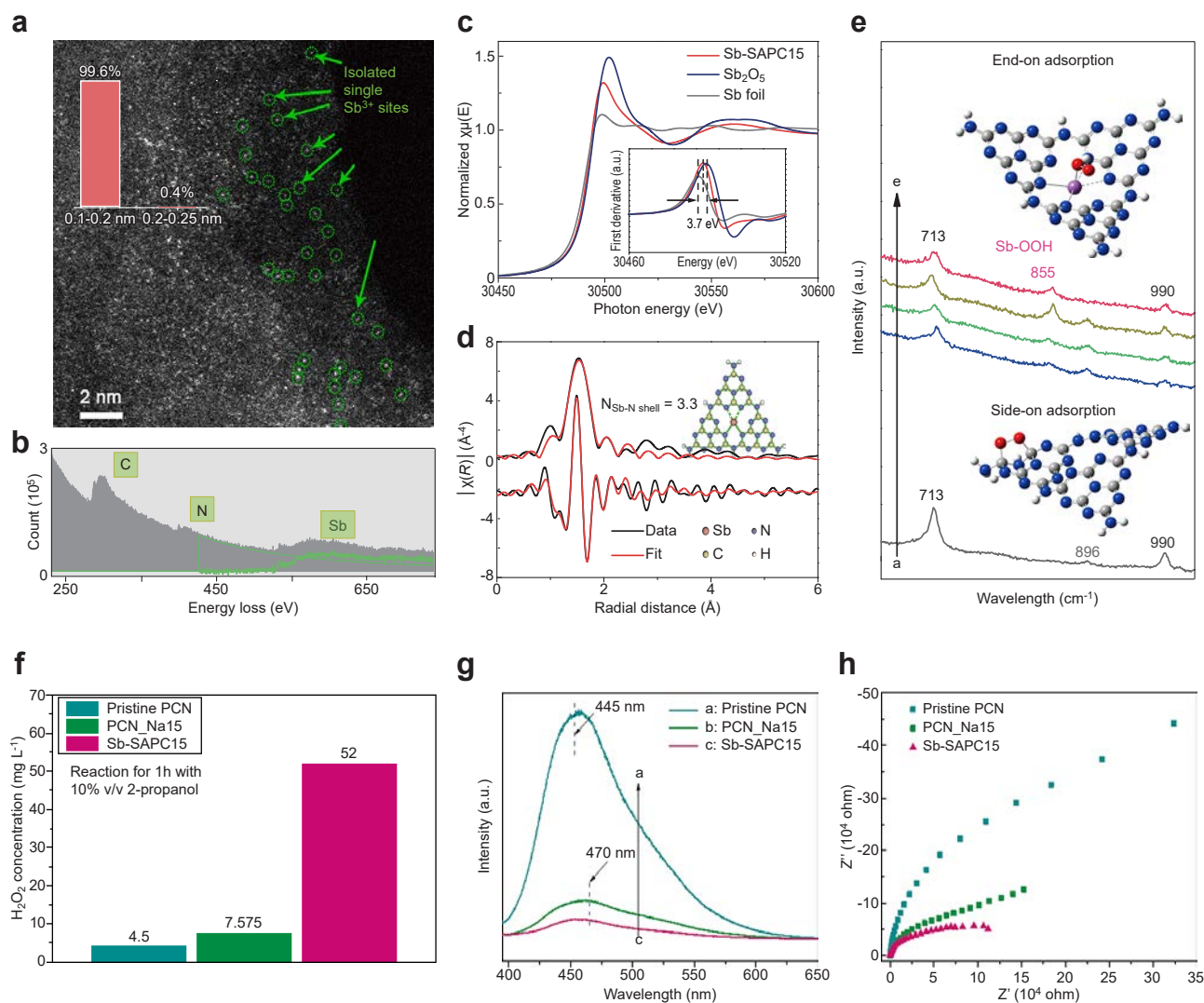


**Fig. 14** Single atomic sites for efficient ORR. **(a)** High-magnification HAADF-STEM image of Sb-SAPC15. The insert shows size distribution of the bright spots. **(b)** Electron energy-loss spectroscopy (EELS) spectrum of Sb-SAPC15. **(c)** Sb-K edge X-ray absorption near edge structure (XANES) of Sb foil, Sb<sub>2</sub>O<sub>5</sub> and Sb-SAPC15. **(d)** Fitting of the extended X-ray absorption fine structure (EXAFS) data for Sb-SAPC15 based on the model obtained from DFT optimization. Inserted figures: optimized molecular models based on DFT for EXAFS fitting. **(e)** Experimental Raman spectra recorded during the photoreaction in a 2-propanol aqueous solution with saturated oxygen. Spectra a, b, c and d: PCN, Sb-SAPC1, Sb-SAPC5 and Sb-SAPC15 in 10% (v/v) 2-propanol aqueous solutions. Spectrum e: Sb-SAPC15 in pure water. **(f)** Comparison of H<sub>2</sub>O<sub>2</sub> production in 10% (v/v) 2-propanol aqueous solutions catalyzed by pristine PCN, PCN\_Na15 and Sb-SAPC15. **(g)** Photoluminescence spectra of PCN, PCN\_Na15 and Sb-SAPC15 at an excitation wavelength of 380 nm **(h)** Electrochemical impedance spectroscopy (EIS) spectra (Nyquist plots) of pristine PCN and Sb-SAPC15 in the frequency range from 100 kHz to 0.01 Hz at 0.6 V (vs. Ag/AgCl) under visible light irradiation. Reprinted with permission from Ref. (Teng Z. et al., 2021b). Copyright: (2021) Springer Nature Ltd.

phenomenon may be attributed to the cocatalytic effects of the Au surface on the photocatalytic 2e<sup>-</sup> ORR, which has already been proved by investigating other photocatalysts and photocathodes (Hirakawa H. et al., 2016).

In summary, there are two fundamental strategies for introducing active sites for the improvement of 2e<sup>-</sup> ORR of a PCN-based photocatalyst. One is to manipulate the electronic configurations of the functionalized PCN catalyst so that the selectivity and activity of the  $\pi$ -conjugated heptazine ring for boosting H<sub>2</sub>O<sub>2</sub> production can be significantly enhanced. Similar strategies have also been used in some other carbon-based materials for promoting selective H<sub>2</sub>O<sub>2</sub> production. On the contrary, the nature of melem

sites is side-on adsorption of oxygen (Shiraishi Y. et al., 2015), which might result in unexpected splitting of O-O bonds, thus leading to the possible 4e<sup>-</sup> ORR process and a limited selectivity for 2e<sup>-</sup> ORR (Siahrostami S. et al., 2013; Verdaguer-Casadevall A. et al., 2014). The other strategy is to introduce active sites beyond the  $\pi$ -conjugated heptazine ring for selective 2e<sup>-</sup> ORR. Up to now, only a few cocatalysts have been developed for selective ORR (Section 3.3.4). Further development of 2e<sup>-</sup> ORR sites beyond the  $\pi$ -conjugated heptazine rings may overcome the disadvantage of side-on O<sub>2</sub> adsorption and shed light on further improvement for H<sub>2</sub>O<sub>2</sub> production.

## 4. Other factors for boosting photocatalytic efficiency for H<sub>2</sub>O<sub>2</sub> production

### 4.1 Adding electron donors or not

Sacrificial reagents are commonly used to consume the photogenerated electrons or holes so that half of the reaction can be significantly boosted (Schneider J. and Bahnemann D.W., 2013). In the case of g-C<sub>3</sub>N<sub>4</sub>-based photocatalysts, most researchers used electron donors so that reduction reactions could be maximized in a certain photocatalytic system since an electron donor prevents the photogenerated electrons from recombining with holes (Wang Y. et al., 2019; Wang M. et al., 2017). g-C<sub>3</sub>N<sub>4</sub> has shown promising prospects for catalyzing several photochemical reduction reactions with the existence of electron donors. The reason may be as follows: the CBM of pristine PCN (−1.3 V) is quite negative, thus resulting in significantly larger redox potentials of hydrogen evolution reaction (HER), nitrogen reduction reaction (NRR), carbon dioxide reduction reaction (CRR) and 2e<sup>−</sup> ORR (0.695 V vs. SHE) (Wang Y. et al., 2019). Combined with the merits of the side-on O<sub>2</sub> adsorption on melem units (forming 1-4 endoperoxide species) as acceptable 2e<sup>−</sup> reduction sites, PCN satisfied the thermodynamic potential for 2e<sup>−</sup> ORR with the existence of alcohol. However, a green and sus-

tainable process for photocatalytic H<sub>2</sub>O<sub>2</sub> synthesis requires the use of earth-abundant water as an electron donor, i.e., water oxidation reaction instead of alcohol oxidation should occur for hole consumption.

There have been several studies in which mechanisms for photoreduction reactions were systematically investigated by using g-C<sub>3</sub>N<sub>4</sub> (Wang Y. et al., 2019). Since the functions of electron donors were clarified in those works, we will focus on the crucial properties and functionalization strategies for achieving H<sub>2</sub>O<sub>2</sub> production with water and oxygen (Fig. 15a). Typically, water oxidation via a 4e<sup>−</sup> pathway is usually recognized as an oxygen evolution reaction (OER) that is usually needed to overcome the large overpotential. VBMs of photocatalysts for OER usually have quite positive potentials (VBM<sub>TiO<sub>2</sub>-rutile</sub> ~2.9 V vs. SHE, VBM<sub>BiVO<sub>4</sub></sub> ~2.53 V) (Fan W. et al., 2020; Hirakawa H. et al., 2016). As shown in Fig. 15b, pristine PCN is unable to generate H<sub>2</sub>O<sub>2</sub> in the presence of water and O<sub>2</sub> because the valence band maximum (VBM) lies at approximately 1.4 V, which shows an insufficient thermodynamic driving force for OER (ca. 0.8 V versus RHE, pH 7) (Shiraishi Y. et al., 2014a). To overcome this obstacle, band engineering and the use of a cocatalyst are two effective strategies.

The bandgap position of PCN can be easily manipulated

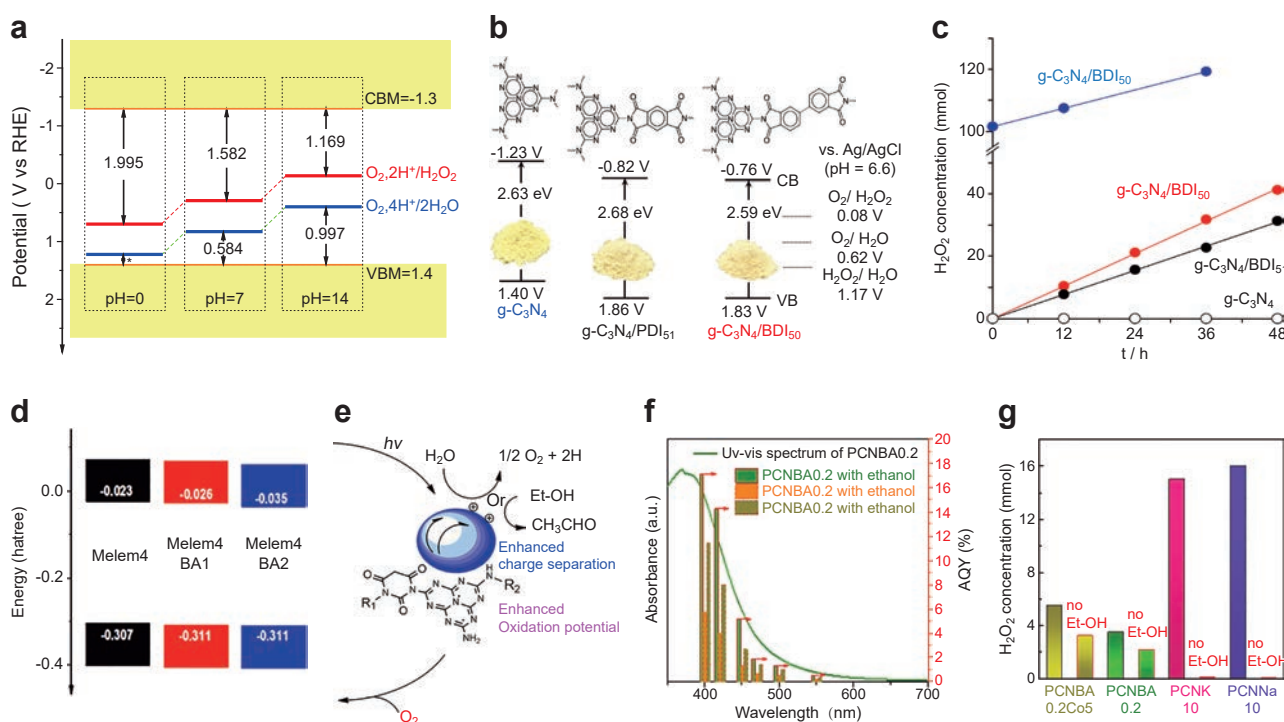


**Fig. 15** Typical strategies for preparation of a g-C<sub>3</sub>N<sub>4</sub>-based catalyst for photocatalytic H<sub>2</sub>O<sub>2</sub> production with water and O<sub>2</sub>. (a) Real hydrogen electrode potentials of 2e<sup>−</sup> ORR and 4e<sup>−</sup> WOR compared with the band diagram of PCN. (b) Electronic band structures of pristine PCN and g-C<sub>3</sub>N<sub>4</sub>/BDI<sub>x</sub>. (c) Changes in the amounts of H<sub>2</sub>O<sub>2</sub> formed during photoreaction with respective catalysts. For the reaction in (c), 100 mg of catalyst was used. The irradiance at 420–500 nm is 27.3 W m<sup>−2</sup>. Blue points show the results of photoreaction with water containing ca. 100 μmol of H<sub>2</sub>O<sub>2</sub>. (d) Calculated HOMO and LUMO of Melem<sub>4</sub> model (representing PCN), Melem<sub>4</sub>BA1 (representing PCNBA with a low motif concentration) and Melem<sub>4</sub>BA2 (representing PCNBA with a high motif concentration). (e) Schematic diagram of PCNBA<sub>x</sub>CO<sub>x</sub> for accelerating water oxidation. (f) Absorption spectrum of PCNBA0.2 and action spectra for H<sub>2</sub>O<sub>2</sub> formation on the respective catalysts. (g) Time course of O<sub>2</sub> evolution measured under Ar pressure of 0.6-kPa and 300-W xenon lamp irradiation with 0.5 g L<sup>−1</sup> of the catalyst, 1 g L<sup>−1</sup> La<sub>2</sub>O<sub>3</sub>, and 20 mM AgNO<sub>3</sub> in 100 mL of water. Reprinted with permission from Ref. (Kofuji Y. et al., 2016b; Teng Z. et al., 2020). Copyright: (2016) American Chemical Society and (2020) Elsevier.

by functionalization. Shiraishi and co-workers successfully manipulate the band positions of a PCN-based photocatalyst by copolymerized melamine with electron-deficient aromatic diimide (Shiraishi Y. et al., 2014a; Shiraishi Y. et al., 2014b; Kofuji Y. et al., 2016a; Kofuji Y. et al., 2017; Kofuji Y. et al., 2016b). The valence band of the as-prepared co-polymerized PCN is about 1.8–2.4 V (vs. NHE). Taking g-C<sub>3</sub>N<sub>4</sub>/PDI as an example, the activity results revealed a significant role of band engineering. Pristine g-C<sub>3</sub>N<sub>4</sub> (VBM = 1.40 V vs. NHE) barely produces H<sub>2</sub>O<sub>2</sub>, and g-C<sub>3</sub>N<sub>4</sub>/BDI51 (VBM = 1.86 V vs. NHE) produces 31 μmol of H<sub>2</sub>O<sub>2</sub> after photocatalytic reaction for 48 h (Kofuji Y. et al., 2016b) (**Fig. 15c**). g-C<sub>3</sub>N<sub>4</sub>/BDI50 (VBM = 1.83 V vs. NHE) shows a higher performance (41 μmol) (Kofuji Y. et al., 2016b). With the addition of electron acceptors, O<sub>2</sub> can be detected by GC, which further confirmed that water oxidation to generate oxygen consumed the generated holes during the photocatalytic reactions (Kofuji Y. et al., 2016b). Introduction of boron nitride (BN) can further improve the activity of the g-C<sub>3</sub>N<sub>4</sub>/PDI-rGO photocatalyst because of the enhanced charge separation efficiency (Kofuji Y. et al., 2018). Following those works, Ohno and co-workers further revealed by analysis of the density of states that the copolymerization of electron-deficient units results in the introduction of O 2p states (Teng Z. et al., 2020). The introduced O 2p states compose the valence band with the states of N 2p and C 2p, resulting in a more positive potential than that of pristine PCN for which the VB is only composed of the states of N 2p and C 2p (**Fig. 15d**) (Teng Z. et al., 2020). Thus, the OER activity is significantly promoted (**Fig. 15e**). Additionally, preparation of POM-incorporated PCN samples with ideal electronic configurations and band positions also played similar roles (shifting the VBM to a more oxidative potential) for boosting the OER, which successfully achieved the H<sub>2</sub>O<sub>2</sub> production via ORR and WOR (Zhao S. et al., 2018b; Zhao S. et al., 2017; Zhao S. and Zhao X., 2019). Another strategy for improving the OER activity of PCN is loading a cocatalyst for OERs. Ohno and co-workers loaded Na<sub>2</sub>CoP<sub>2</sub>O<sub>7</sub> on the band-engineered PCNBA0.2 by a simple ball milling method (**Fig. 15e**) (Teng Z. et al., 2020). The time-dependent H<sub>2</sub>O<sub>2</sub> production and action spectra confirmed the cocatalytic effects of Na<sub>2</sub>CoP<sub>2</sub>O<sub>7</sub> (Teng Z. et al., 2020). The action spectra showed that its bandgap excitation produces H<sub>2</sub>O<sub>2</sub> (Teng Z. et al., 2020). The apparent quantum yield (AQY) of PCNBA with loading of 5 % Na<sub>2</sub>CoP<sub>2</sub>O<sub>7</sub> (PCNBA0.2Co5 %) at 420 nm (8.0 %) was two-times higher than that of PCNBA0.2 (4.0 %) (**Fig. 15f**) (Teng Z. et al., 2020). Additionally, no H<sub>2</sub>O<sub>2</sub> was produced at the light-irradiation wavelengths between 550 nm and 650 nm, indicating that Na<sub>2</sub>CoP<sub>2</sub>O<sub>7</sub> works as a cocatalyst and does not work as a photocatalyst for production of H<sub>2</sub>O<sub>2</sub> (Teng Z. et al., 2020). More recently, Chu and co-workers prepared single-atom dispersed

Co as a co-catalyst for OER (Chu C. et al., 2020). X-ray absorption fine-structure spectroscopy (FT-EXAFS) showed that the oxidation state of the Co single atoms coordinated by P atoms is close to +2 (Chu C. et al., 2020). The OER activity of g-C<sub>3</sub>N<sub>4</sub> was significantly increased (8.4-fold) by the introduction of Co single atomic sites (**Fig. 15g**). The chemical states of P-coordinated Co atoms are close to +2, indicating that the unique electronic configuration of Co(II)-P may provide active sites for OER during solar H<sub>2</sub>O<sub>2</sub> synthesis (Chu C. et al., 2020). It is notable that the VBM of this single-Co dispersed PCN (~1.4 V vs. SHE) (Chu C. et al., 2020), quite close to that of PCN, is significantly more positive than that of metal oxides (>2.3 V vs. SHE). Thus, the Co(II)-P single atomic sites may significantly boost the kinetic process of water oxidation. Very recently, the Sb-SAPC proposed by Ohno and co-workers also showed good activity based on non-sacrificial photocatalytic H<sub>2</sub>O<sub>2</sub> activities. Based on the results detailed characterizations and analyses, the following reaction mechanism (**Fig. 16**) of Sb-SAPC for photocatalytic H<sub>2</sub>O<sub>2</sub> production is proposed. Firstly, efficient charge separation occurs on Sb-SAPC under visible light irradiation, resulting in the generation of photoexcited electrons and holes for ORR and WOR, respectively. Then water molecules are oxidized to evolve O<sub>2</sub> by photogenerated holes localized at the N atoms near the single Sb atoms. Simultaneously, O<sub>2</sub> dissolved in water and that generated from the WOR both participate in the ORR process to produce H<sub>2</sub>O<sub>2</sub>. It is notable that the efficient charge separation, ideal single atomic sites for end-on type O<sub>2</sub> adsorption and close spatial distribution of active sites boost both the 2e<sup>-</sup> ORR and 4e<sup>-</sup> WOR for efficient H<sub>2</sub>O<sub>2</sub> production.

In summary, accelerating the photocatalytic oxygen evolution reaction by using a PCN-based photocatalyst is the most crucial challenge for achieving photocatalytic H<sub>2</sub>O<sub>2</sub> production with water and O<sub>2</sub>. Band engineering and loading cocatalyst for OER may respectively improve the oxidation potential and promote the kinetics for 4e<sup>-</sup> OER.

## 4.2 pH value

It is difficult for the light-driven 2e<sup>-</sup> WOR pathway to be achieved because of the uphill thermodynamics (1.76 V vs. NHE), i.e., the as-synthesized H<sub>2</sub>O<sub>2</sub> will decompose at this highly oxidative potential because H<sub>2</sub>O<sub>2</sub> is an excellent hole scavenger (Fuku K. and Sayama K., 2016). Therefore, we will focus on the 2e<sup>-</sup> ORR pathway. Substantial efforts have been devoted to the 2e<sup>-</sup> ORR concept with the aim of achieving high-yield production of H<sub>2</sub>O<sub>2</sub> in basic, neutral, and acidic media (Gao J. and Liu B., 2020; Kim H.W. et al., 2018; Lu Z. et al., 2018; Iglesias D. et al., 2018). The acid dissociation constant of H<sub>2</sub>O<sub>2</sub> (H<sub>2</sub>O<sub>2</sub> ↔ H<sup>+</sup> + HO<sub>2</sub><sup>-</sup>,  $K_a = \frac{[H^+][HO_2^-]}{[H_2O_2]}$ , pK<sub>a</sub> = 11.7) suggests that the main form of H<sub>2</sub>O<sub>2</sub> would be HO<sub>2</sub><sup>-</sup> in an alkaline

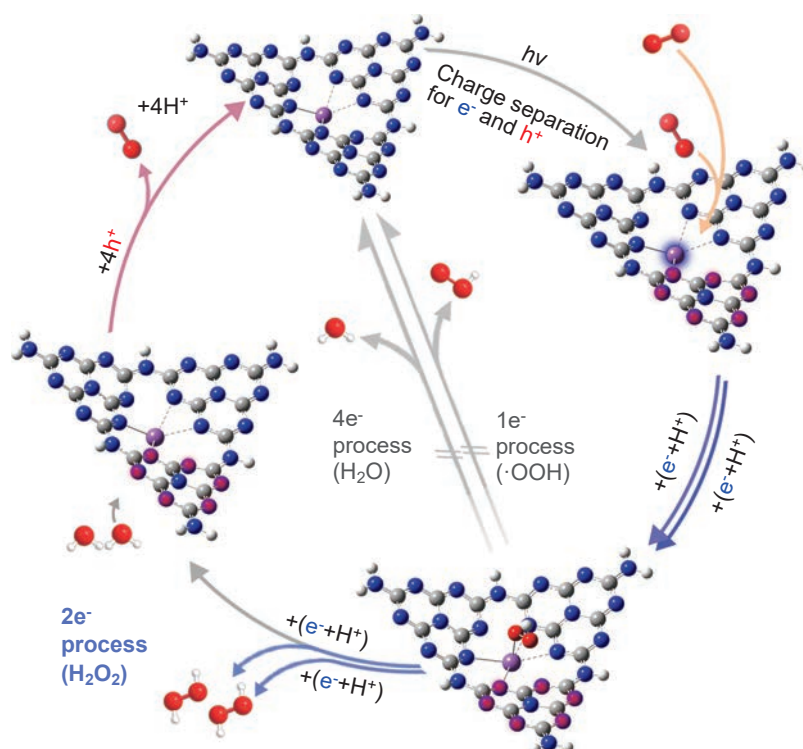


**Fig. 16** Mechanism of photocatalytic H<sub>2</sub>O<sub>2</sub> production. (White, gray, blue, red and magenta spheres indicate hydrogen, carbon, nitrogen, oxygen and Sb atoms, respectively.) After shining visible light, the photogenerated electrons are localized at the Sb sites (with a blue glow), and the photogenerated holes are localized at the N atoms at the melem units (with a red glow). Subsequently, the dissolved O<sub>2</sub> molecules are adsorbed (orange arrows) onto the Sb sites and then become reduced (blue arrows) via a 2e<sup>-</sup> transfer pathway through the formation of an electron μ-peroxide as the intermediate. Simultaneously, water molecules are oxidized (pink arrows) to generate O<sub>2</sub> by the highly concentrated holes on the melem units. Reprinted with permission from Ref. (Teng Z. et al., 2021b). Copyright: (2021) Springer Nature Ltd.

water solution (pH > 11.7). Alkaline H<sub>2</sub>O<sub>2</sub> is widely used in the pulp bleaching industry. However, the production of H<sub>2</sub>O<sub>2</sub> in basic media has the following two limitations: (1) H<sub>2</sub>O<sub>2</sub> is less stable and can self-decompose in an alkaline condition (especially at pH > 9), and it therefore needs to be consumed in a short time (Gao J. and Liu B., 2020; Qiang Z. et al., 2002) and (2) H<sub>2</sub>O<sub>2</sub> is more widely used in natural or acidic media with stronger oxidation ability than in an alkaline solution. For instance, Fenton's reagent, which is widely used in effluent treatment and organic synthesis, has a favorable pH range of 2.5–3.5 (Gao J. and Liu B., 2020; Kuo W.G. et al., 1992). Therefore, improving H<sub>2</sub>O<sub>2</sub> production in acidic or neutral media by photocatalysts has attracted much attention for industrial applications. Over the past few years, although various g-C<sub>3</sub>N<sub>4</sub> catalysts have been developed for H<sub>2</sub>O<sub>2</sub> production via the 2e<sup>-</sup> ORR process (Shiraishi Y. et al., 2014b), there have been very few works in which the optimized pH conditions were investigated.

Kim and co-workers found that photocatalytic activity for H<sub>2</sub>O<sub>2</sub> production was higher at lower pH values (Fig. 17a) with the existence of an electron donor. This is probably due to proton conduction within the CN framework and is much more facilitated in KPF\_CN. The proton conduction of KPF\_CN was greatly enhanced when

PF<sub>6</sub><sup>-</sup> anions was introduced into the structure of the g-C<sub>3</sub>N<sub>4</sub> framework (Kim S. et al., 2018). The higher charge carrier density in KPF\_CN might be favorable for facilitating proton conduction. The higher proton conductivity within the KPF\_CN framework promotes the production of H<sub>2</sub>O<sub>2</sub>, particularly when the reaction between O<sub>2</sub> and protons occurs within the interlayer space (Kim S. et al., 2018). Ohno and co-workers also investigated the optimal pH conditions by measuring the amount of H<sub>2</sub>O<sub>2</sub> produced by the photocatalytic reaction using PCNBA0.2 (Fig. 17b) (Teng Z. et al., 2020). When ethanol was introduced into the system, the amount of produced H<sub>2</sub>O<sub>2</sub> remained almost constant when the pH value was increased from 1 to 9 and then decreased drastically (Teng Z. et al., 2020). When the pH value was lower than 7, the concentration of protons had almost no effect on the pH value (Teng Z. et al., 2020). This phenomenon revealed that protonation plays a less essential role in the PCNBA system, indicating that incorporation of BA units further improved the proton conductivity compared with that of KPF\_CN. They also found that the lowest [H<sup>+</sup>] is 10<sup>-9</sup> mol L<sup>-1</sup> for O<sub>2</sub> reduction to H<sub>2</sub>O<sub>2</sub> production. When no sacrificial agent was added to the system, the amount of H<sub>2</sub>O<sub>2</sub> rapidly increased before the pH value reached 7 and then gradually decreased, indicating that a low concentration of OH<sup>-</sup> also restricts the generation

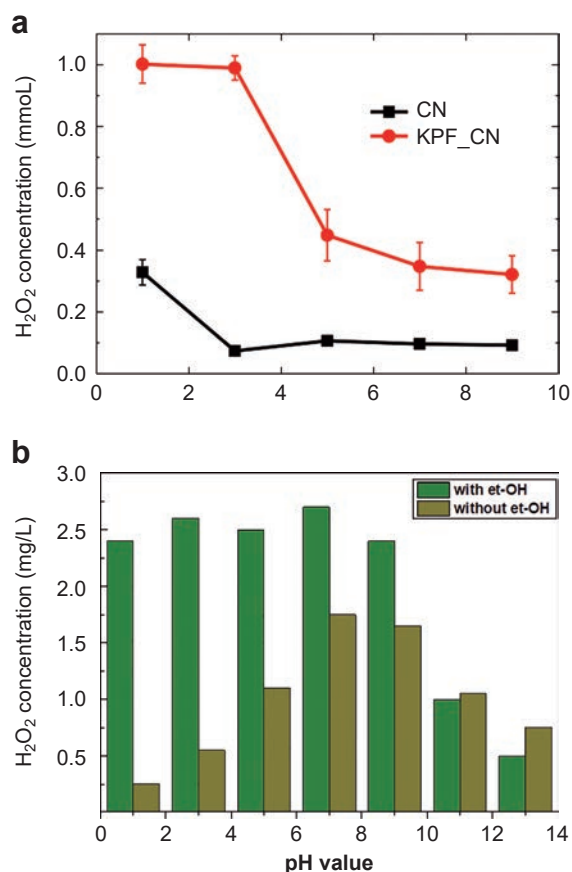


**Fig. 17** Influence of pH values during H<sub>2</sub>O<sub>2</sub> production by using a PCN-based photocatalyst. (a) H<sub>2</sub>O<sub>2</sub> production in an irradiated suspension of bare CN and KPF\_CN<sub>15</sub> at different pH values. (b) Optimization of the pH condition for H<sub>2</sub>O<sub>2</sub> production when PCNBA0.2 was used as a photocatalyst. Reprinted with permission from (Kim S. et al., 2018) and (Teng Z. et al., 2020). Copyright: (2018, 2020) Elsevier.

of O<sub>2</sub> from water (Wang Q. and Domen K., 2020). Therefore, the optimal pH condition for H<sub>2</sub>O<sub>2</sub> production from O<sub>2</sub> and water using PCNBA is 7-9. The production of H<sub>2</sub>O<sub>2</sub> significantly decreased in both of the works when pH was larger than 9, being consistent with the fact that H<sub>2</sub>O<sub>2</sub> self-decomposes in alkaline conditions. Although there have been only few works in which the influence of pH on the amount of H<sub>2</sub>O<sub>2</sub> generated was investigated, it was shown that the pH value did play an essential role during the photosynthesis process. Additionally, the pH value of the interfaces between materials and reaction solution might be even more important compared with the pH value of the whole solution. The rational design of Helmholtz layer by the manipulation of the surface properties are extremely important for improving the H<sub>2</sub>O<sub>2</sub> production (Zeng X. et al., 2020). We believe that systematic investigations of the effects of pH on the amount of H<sub>2</sub>O<sub>2</sub>, surface properties and electronic configurations should be carried out to reveal the mechanisms of ORR and WOR during the photosynthesis of H<sub>2</sub>O<sub>2</sub>.

## 5. Summary and perspectives

Photocatalytic H<sub>2</sub>O<sub>2</sub> production by using a PCN-based material has shown a promising prospective in environmental and energy-related realms. We have summarized the principles for photocatalytic H<sub>2</sub>O<sub>2</sub> production, especially for the photocatalytic H<sub>2</sub>O<sub>2</sub> production using g-C<sub>3</sub>N<sub>4</sub>. Advantages and disadvantages for H<sub>2</sub>O<sub>2</sub> production and the most favorable properties of PCN for photocatalytic H<sub>2</sub>O<sub>2</sub> production were briefly summarized. Based on the intrinsic properties of pristine g-C<sub>3</sub>N<sub>4</sub>, the most urgent issue for overcoming the drawbacks was focused on. Notably, current PCN-based photocatalysts still suffer from relatively low H<sub>2</sub>O<sub>2</sub> yield. Due to the low activity, g-C<sub>3</sub>N<sub>4</sub>-based photocatalysts are far from the requirements for industrial applications. Improving the charge separation, promoting the light absorption and introducing active sites for 2e<sup>-</sup> ORR to suppress the side reaction are three attractive strategies for boosting the activities. Following discussion of these strategies, the most representative functionalization method was summarized on the basis of the most desired properties for improving the photocatalytic activities for H<sub>2</sub>O<sub>2</sub> production. Other factors for improving H<sub>2</sub>O<sub>2</sub> production such as addition of electron donors and pH value of the solution were also discussed.

There are several outlooks and suggestions for further improvement of photocatalysts. First of all, further improvement in the charge separation of the PCN is necessary. New species of elements or organic semiconductors for incorporation are highly recommended. Secondly, the absorption edge of the functionalized PCN can hardly be extended to >550 nm with a reasonable AQY for H<sub>2</sub>O<sub>2</sub> production (Teng Z. et al., 2020). Further narrowing of band gap is therefore still of great importance. It is notable that the narrowing of the bandgap could reduce the thermodynamic driving force, leading to weakened capability for reduction reactions and oxidation reactions. Thus, reducing the overpotential for 2e<sup>-</sup> ORR and oxidation reactions on the PCN surface is of great importance. Exploring new reaction sites with higher performance beyond the heptazine rings in the PCN matrix for 2e<sup>-</sup> ORR efficiency is also of great importance for further improvement of photocatalytic activity and selectivity for H<sub>2</sub>O<sub>2</sub> production. Recently, single-atom catalysts (SACs) have shown excellent selectivity for H<sub>2</sub>O<sub>2</sub> production with Pt<sup>2+</sup> (Shen R. et al., 2019; Gao J. et al., 2020; Jung E. et al., 2020) via a 2e<sup>-</sup> ORR pathway. In the case of PCN, anchoring single-atom catalysts that have large amounts of nitrogen atoms with lone electron pairs is easy to perform. However, Pt<sup>2+</sup> and Co-N<sub>4</sub> sites can hardly be utilized for photocatalytic systems due to poor charge separation, which origin form the half-filled d electrons of Pt<sup>2+</sup> and Co-N<sub>4</sub> may result in a high bulk-recombination rate of PCN. The preparation of photocatalysts having atomically dispersed atoms with a d<sup>0</sup> or d<sup>10</sup> electronic configuration usually introduce intermediate bands with

energetic levels that are slightly more negative than that of CBM, which can promote electron mobility, thus leading to a boosted performance (Inoue Y., 2009). It should be mentioned that measurement of  $\text{H}_2\text{O}_2$  production was carried out in most studies with the addition of an organic sacrificial electron donor to consume the photogenerated holes and inhibit the recombination of photogenerated carries, which is energy-consuming and cost-inefficient. Despite of band engineering and cocatalyst loading, the construction of an all-solid-state Z-scheme photocatalytic system is another recommended strategy for achieving non-sacrificial  $\text{H}_2\text{O}_2$  production with water and oxygen (Xu Q. et al., 2018). Additionally, it is necessary to develop approaches other than optimization of pH conditions to prevent decomposition of the generated  $\text{H}_2\text{O}_2$ . The stability of organic semiconductors during photocatalytic  $\text{H}_2\text{O}_2$  production should also be investigated (Liu L. et al., 2021). Last not but least, attention should be given to precise determination of the amount of  $\text{H}_2\text{O}_2$  generated because the species in the solution can influence the accuracy for determination (Wei Y. et al., 2021).

To optimize the design of functionalized PCN with maximized photocatalytic  $\text{H}_2\text{O}_2$  production, a comprehensive understanding of the photocatalytic mechanism for  $\text{H}_2\text{O}_2$  production is necessary. Both experimental and theoretical investigations should be simultaneously carried out. In situ measurements by Kelvin probe microscopy (Zhu J. et al., 2015) and X-ray absorption fine structure analysis (Yang H. et al., 2018) could be used to study the dynamic behavior of photogenerated carriers on the surface and the changes of oxidized states in a photocatalyst (Hou H. et al., 2020). In situ Raman spectroscopy may reveal the process from the adsorption of  $\text{O}_2$  to dissociation of  $\text{H}_2\text{O}_2$ , thus leading to a more precise understanding of the mechanism. In the case of fundamental calculations and simulations for investigation of the mechanism, ground state properties such as density of states, adsorption energy, and the structural and electronic properties have been widely used for explanation of physicochemical properties for the design of an ideal photocatalyst for  $\text{H}_2\text{O}_2$  production (Dong J.-C. et al., 2020). However, investigation of the excitation properties of PCN materials has not been sufficient to obtain a fundamental understanding of the excitation behavior of a photocatalyst. We suggest that excitation properties of the functionalized PCN, such as transition densities based on time-dependent DFT calculations (Laurent A.D. et al., 2013; Teng Z. et al., 2021b; Che H. et al., 2021), should be investigated in future studies in order to establish a satisfactory blueprint for designing a PCN catalyst for  $\text{H}_2\text{O}_2$  production. Last but not least, since  $\text{H}_2\text{O}_2$  production is a green oxidant for many chemical reactions, the development of highly value-added chemicals based on the photocatalytic systems is needed. Using the in-situ generated  $\text{H}_2\text{O}_2$  for synthesis of chemicals could also be achieved on

the basis of previous work using  $\text{D}_2\text{O}$  to produce deuterated chemicals (Zhang B. et al., 2021). We believe that better design strategies and guidelines for not only PCN-based materials but also other efficient photocatalysts can be established for  $\text{H}_2\text{O}_2$  formation if the above-mentioned properties can be achieved.

## Acknowledgements

The authors acknowledge the financial support of Mitsubishi Chemical Corporation, JSPS Grant-in-Aid for Scientific Research (B, No. 20H02847), and Grant-in-Aid for JSPS Fellows (DC2, 20J13064).

## References

- Banerjee T., Podjaski F., Kröger J., Biswal B.P., Lotsch B.V., Polymer photocatalysts for solar-to-chemical energy conversion, *Nature Reviews Materials*, 6 (2021) 168–190. DOI: 10.1038/s41578-020-00254-z
- Bo Y., Gao C., Xiong Y., Recent advances in engineering active sites for photocatalytic  $\text{CO}_2$  reduction, *Nanoscale*, 12 (2020) 12196–12209. DOI: 10.1039/D0NR02596H
- Campos-Martin J.M., Blanco-Brieva G., Fierro J.L.G., Hydrogen peroxide synthesis: an outlook beyond the anthraquinone process, *Angewandte Chemie International Edition*, 45 (2006) 6962–6984. DOI: 10.1002/anie.200503779
- Chang X., Yang J., Han D., Zhang B., Xiang X., He J., Enhancing light-driven production of hydrogen peroxide by anchoring Au onto  $\text{C}_3\text{N}_4$  catalysts, *Catalysts*, 8 (2018) 147. DOI: 10.3390/catal8040147
- Che H., Gao X., Chen J., Hou J., Ao Y., Wang P., Iodide-induced fragmentation of polymerized hydrophilic carbon nitride for high-performance quasi-homogeneous photocatalytic  $\text{H}_2\text{O}_2$  production, *Angewandte Chemie International Edition*, 60 (2021) 25546–25550. DOI: 10.1002/anie.202111769
- Choi C.H., Kwon H.C., Yook S., Shin H., Kim H., Choi M., Hydrogen peroxide synthesis via enhanced two-electron oxygen reduction pathway on carbon-coated Pt surface, *The Journal of Physical Chemistry C*, 118 (2014) 30063–30070. DOI: 10.1021/jp5113894
- Chu C., Huang D., Zhu Q., Stavitski E., Spies J.A., Pan Z., Mao J., Xin H.L., Schmuttenmaer C.A., Hu S., Kim J.-H., Electronic tuning of metal nanoparticles for highly efficient photocatalytic hydrogen peroxide production, *ACS Catalysis*, 9 (2019) 626–631. DOI: 10.1021/acscatal.8b03738
- Chu C., Zhu Q., Pan Z., Gupta S., Huang D., Du Y., Weon S., Wu Y., Muhich C., Stavitski E., Domen K., Kim J.-H., Spatially separating redox centers on 2D carbon nitride with cobalt single atom for photocatalytic  $\text{H}_2\text{O}_2$  production, *Proceedings of the National Academy of Sciences of the United States of America*, 117 (2020) 6376. DOI: 10.1073/pnas.1913403117
- Chung D.D.L., *Carbon Materials: Science and Applications*, World Scientific Publishing Company, 2019, ISBN: 9789811200939.
- Dong J.-C., Su M., Briega-Martos V., Li L., Le J.-B., Radjenovic P., Zhou X.-S., Feliu J.M., Tian Z.-Q., Li J.-F., Direct in situ Raman spectroscopic evidence of oxygen reduction reaction intermediates at high-index Pt(hkl) surfaces, *Journal of the American Chemical Society*, 142 (2020) 715–719. DOI: 10.1021/jacs.9b12803
- Fan W., Zhang B., Wang X., Ma W., Li D., Wang Z., Dupuis M., Shi J., Liao S., Li C., Efficient hydrogen peroxide synthesis by metal-free polyterthiophene via photoelectrocatalytic

- dioxygen reduction, *Energy & Environmental Science*, 13 (2020) 238–245. DOI: 10.1039/C9EE02247C
- Freakley S.J., He Q., Harry J.H., Lu L., Crole D.A., Morgan D.J., Ntainjua E.N., Edwards J.K., Carley A.F., Borisevich A.Y., Kiely C.J., Hutchings G.J., Palladium-tin catalysts for the direct synthesis of H<sub>2</sub>O<sub>2</sub> with high selectivity, *Science*, 351 (2016) 965. DOI: 10.1126/science.aad5705
- Fuku K., Sayama K., Efficient oxidative hydrogen peroxide production and accumulation in photoelectrochemical water splitting using a tungsten trioxide/bismuth vanadate photoanode, *Chemical Communications*, 52 (2016) 5406–5409. DOI: 10.1039/C6CC01605G
- Gao J., Liu B., Progress of electrochemical hydrogen peroxide synthesis over single atom catalysts, *ACS Materials Letters*, 2 (2020) 1008–1024. DOI: 10.1021/acsmaterialslett.0c00189
- Gao J., Yang H.b., Huang X., Hung S.-F., Cai W., Jia C., Miao S., Chen H.M., Yang X., Huang Y., Zhang T., Liu B., Enabling direct H<sub>2</sub>O<sub>2</sub> production in acidic media through rational design of transition metal single atom catalyst, *Chem*, 6 (2020) 658–674. DOI: 10.1016/j.chempr.2019.12.008
- Goclon J., Winkler K., Computational insight into the mechanism of O<sub>2</sub> to H<sub>2</sub>O<sub>2</sub> reduction on amino-groups-containing g-C<sub>3</sub>N<sub>4</sub>, *Applied Surface Science*, 462 (2018) 134–141. DOI: 10.1016/j.apsusc.2018.08.070
- Han X.-B., Li Y.-G., Zhang Z.-M., Tan H.-Q., Lu Y., Wang E.-B., Polyoxometalate-based nickel clusters as visible light-driven water oxidation catalysts, *Journal of the American Chemical Society*, 137 (2015) 5486–5493. DOI: 10.1021/jacs.5b01329
- Hirakawa H., Shiota S., Shiraishi Y., Sakamoto H., Ichikawa S., Hirai T., Au nanoparticles supported on BiVO<sub>4</sub>: effective inorganic photocatalysts for H<sub>2</sub>O<sub>2</sub> production from water and O<sub>2</sub> under visible light, *ACS Catalysis*, 6 (2016) 4976–4982. DOI: 10.1021/acscatal.6b01187
- Hisatomi T., Domen K., Reaction systems for solar hydrogen production via water splitting with particulate semiconductor photocatalysts, *Nature Catalysis*, 2 (2019) 387–399. DOI: 10.1038/s41929-019-0242-6
- Hou H., Zeng X., Zhang X., Production of hydrogen peroxide by photocatalytic processes, *Angewandte Chemie International Edition*, 59 (2020) 17356–17376. DOI: 10.1002/anie.201911609
- Hu S., Qu X., Li P., Wang F., Li Q., Song L., Zhao Y., Kang X., Photocatalytic oxygen reduction to hydrogen peroxide over copper doped graphitic carbon nitride hollow microsphere: the effect of Cu(I)-N active sites, *Chemical Engineering Journal*, 334 (2018) 410–418. DOI: 10.1016/j.cej.2017.10.016
- Iglesias D., Giuliani A., Melchionna M., Marchesan S., Criado A., Nasi L., Bevilacqua M., Tavagnacco C., Vizza F., Prato M., Fornasiero P., N-doped graphitized carbon nanohorns as a forefront electrocatalyst in highly selective O<sub>2</sub> Reduction to H<sub>2</sub>O<sub>2</sub>, *Chem*, 4 (2018) 106–123. DOI: 10.1016/j.chempr.2017.10.013
- Inoue Y., Photocatalytic water splitting by RuO<sub>2</sub>-loaded metal oxides and nitrides with d<sup>0</sup>- and d<sup>10</sup>-related electronic configurations, *Energy & Environmental Science*, 2 (2009) 364–386. DOI: 10.1039/B816677N
- Jiang X., Wang P., Zhao J., 2D covalent triazine framework: a new class of organic photocatalyst for water splitting, *Journal of Materials Chemistry A*, 3 (2015) 7750–7758. DOI: 10.1039/C4TA03438D
- Jones C.W., Applications of hydrogen peroxide and derivatives, Royal Society of Chemistry, 1999, ISSN: 978-0-85404-536-5
- Jung E., Shin H., Lee B.-H., Efremov V., Lee S., Lee H., Kim J., Antink W., Park S., Lee K.-S., Cho S.-P., Yoo J.S., Sung Y.-E., Hyeon T., Atomic-level tuning of Co–N–C catalyst for high-performance electrochemical H<sub>2</sub>O<sub>2</sub> production, *Nature Materials*, 19 (2020) 1–7. DOI: 10.1038/s41563-019-0571-5
- Kessler F.K., Zheng Y., Schwarz D., Merschjann C., Schnick W., Wang X., Bojdys M.J., Functional carbon nitride materials—design strategies for electrochemical devices, *Nature Reviews Materials*, 2 (2017) 17030. DOI: 10.1038/natrevmats.2017.30
- Kim D., Sakimoto K.K., Hong D., Yang P., Artificial photosynthesis for sustainable fuel and chemical production, *Angewandte Chemie International Edition*, 54 (2015) 3259–3266. DOI: 10.1002/anie.201409116
- Kim H.-i., Choi Y., Hu S., Choi W., Kim J.-H., Photocatalytic hydrogen peroxide production by anthraquinone-augmented polymeric carbon nitride, *Applied Catalysis B: Environmental*, 229 (2018) 121–129. DOI: 10.1016/j.apcatb.2018.01.060
- Kim H.W., Ross M.B., Kornienko N., Zhang L., Guo J., Yang P., McCloskey B.D., Efficient hydrogen peroxide generation using reduced graphene oxide-based oxygen reduction electrocatalysts, *Nature Catalysis*, 1 (2018) 282–290. DOI: 10.1038/s41929-018-0044-2
- Kim S., Moon G.-h., Kim H., Mun Y., Zhang P., Lee J., Choi W., Selective charge transfer to dioxygen on KPF<sub>6</sub>-modified carbon nitride for photocatalytic synthesis of H<sub>2</sub>O<sub>2</sub> under visible light, *Journal of Catalysis*, 357 (2018) 51–58. DOI: 10.1016/j.jcat.2017.10.002
- Koe W.S., Lee J.W., Chong W.C., Pang Y.L., Sim L.C., An overview of photocatalytic degradation: photocatalysts, mechanisms, and development of photocatalytic membrane, *Environmental Science and Pollution Research*, 27 (2020) 2522–2565. DOI: 10.1007/s11356-019-07193-5
- Kofuji Y., Isobe Y., Shiraishi Y., Sakamoto H., Ichikawa S., Tanaka S., Hirai T., Hydrogen peroxide production on a carbon nitride–boron nitride-reduced graphene oxide hybrid photocatalyst under visible light, *ChemCatChem*, 10 (2018) 2070–2077. DOI: 10.1002/cctc.201701683
- Kofuji Y., Isobe Y., Shiraishi Y., Sakamoto H., Tanaka S., Ichikawa S., Hirai T., Carbon nitride–aromatic diimide–graphene nanohybrids: Metal-free photocatalysts for solar-to-hydrogen peroxide energy conversion with 0.2 % efficiency, *Journal of the American Chemical Society*, 138 (2016a) 10019–10025. DOI: 10.1021/jacs.6b05806
- Kofuji Y., Ohkita S., Shiraishi Y., Sakamoto H., Ichikawa S., Tanaka S., Hirai T., Mellitic triimide-doped carbon nitride as sunlight-driven photocatalysts for hydrogen peroxide production, *ACS Sustainable Chemistry & Engineering*, 5 (2017) 6478–6485. DOI: 10.1021/acssuschemeng.7b00575
- Kofuji Y., Ohkita S., Shiraishi Y., Sakamoto H., Tanaka S., Ichikawa S., Hirai T., Graphitic carbon nitride doped with biphenyl diimide: efficient photocatalyst for hydrogen peroxide production from water and molecular oxygen by sunlight, *ACS Catalysis*, 6 (2016b) 7021–7029. DOI: 10.1021/acscatal.6b02367
- Kulkarni A., Siahrostami S., Patel A., Nørskov J.K., Understanding catalytic activity trends in the oxygen reduction reaction, *Chemical Reviews*, 118 (2018) 2302–2312. DOI: 10.1021/acs.chemrev.7b00488
- Kuo W.G., Decolorizing dye wastewater with Fenton’s reagent., *Water Research*, 26 (1992) 881–886. DOI: 10.1016/0043-1354(92)90192-7
- Laurent A.D., Jacquemin D., TD-DFT benchmarks: a review, *International Journal of Quantum Chemistry*, 113 (2013) 2019–2039. DOI: 10.1002/qua.24438
- Li S., Dong G., Hailili R., Yang L., Li Y., Wang F., Zeng Y., Wang C., Effective photocatalytic H<sub>2</sub>O<sub>2</sub> production under visible light irradiation at g-C<sub>3</sub>N<sub>4</sub> modulated by carbon vacancies,



- Applied Catalysis B: Environmental, 190 (2016) 26–35. DOI: 10.1016/j.apcatb.2016.03.004
- Li X., Chen C., Zhao J., Mechanism of photodecomposition of H<sub>2</sub>O<sub>2</sub> on TiO<sub>2</sub> surfaces under visible light irradiation, Langmuir, 17 (2001) 4118–4122. DOI: 10.1021/la010035s
- Li X., Sun X., Zhang L., Sun S., Wang W., Efficient photocatalytic fixation of N<sub>2</sub> by KOH-treated g-C<sub>3</sub>N<sub>4</sub>, Journal of Materials Chemistry A, 6 (2018a) 3005–3011. DOI: 10.1039/C7TA09762J
- Li X., Zhang J., Zhou F., Zhang H., Bai J., Wang Y., Wang H., Preparation of N-vacancy-doped g-C<sub>3</sub>N<sub>4</sub> with outstanding photocatalytic H<sub>2</sub>O<sub>2</sub> production ability by dielectric barrier discharge plasma treatment, Chinese Journal of Catalysis, 39 (2018b) 1090–1098. DOI: 10.1016/S1872-2067(18)63046-3
- Liao G., Gong Y., Zhang L., Gao H., Yang G.-J., Fang B., Semiconductor polymeric graphitic carbon nitride photocatalysts: the “holy grail” for the photocatalytic hydrogen evolution reaction under visible light, Energy & Environmental Science, 12 (2019) 2080–2147. DOI: 10.1039/C9EE00717B
- Liu L., Gao M.-Y., Yang H., Wang X., Li X., Cooper A.L., Linear conjugated polymers for solar-driven hydrogen peroxide production: the importance of catalyst stability, Journal of the American Chemical Society, 143 (2021) 19287–19293. DOI: 10.1021/jacs.1c09979
- Liu R., Chen Z., Yao Y., Li Y., Cheema A.W., Wang D., Zhu S., Recent advancements in g-C<sub>3</sub>N<sub>4</sub>-based photocatalysts for photocatalytic CO<sub>2</sub> reduction: a mini review, RSC Advances, 10 (2020) 29408–29418. DOI: 10.1039/D0RA05779G
- Liu X., Ma R., Zhuang L., Hu B., Chen J., Liu X., Wang X., Recent developments of doped g-C<sub>3</sub>N<sub>4</sub> photocatalysts for the degradation of organic pollutants, Critical Reviews in Environmental Science and Technology, (2020) 1–40. DOI: 10.1080/10643389.2020.1734433
- Lu Z., Chen G., Siahrostami S., Chen Z., Liu K., Xie J., Liao L., Wu T., Lin D., Liu Y., Jaramillo T.F., Nørskov J.K., Cui Y., High-efficiency oxygen reduction to hydrogen peroxide catalysed by oxidized carbon materials, Nature Catalysis, 1 (2018) 156–162. DOI: 10.1038/s41929-017-0017-x
- McDonnell G., The use of hydrogen peroxide for disinfection and sterilization applications, PATAI’S Chemistry of Functional Groups, (2014) 1–34. DOI: 10.1002/9780470682531.pat0885
- Meng A., Teng Z., Zhang Q., Su C., Intrinsic defects in polymeric carbon nitride for photocatalysis applications, Chemistry—An Asian Journal, 15 (2020) 3405–3415. DOI: 10.1002/asia.202000850
- Mohamed N.A., Safaei J., Ismail A.F., Jailani M.F.A.M., Khalid M.N., Noh M.F.M., Aadenan A., Nasir S.N.S.N., Sagu J.S., Teridi M.S.M., The influences of post-annealing temperatures on fabrication graphitic carbon nitride, (g-C<sub>3</sub>N<sub>4</sub>) thin film, Applied Surface Science, (2019) 92–100. DOI: 10.1016/j.apsusc.2019.05.312.
- Moon G.-h., Fujitsuka M., Kim S., Majima T., Wang X., Choi W., Eco-friendly photochemical production of H<sub>2</sub>O<sub>2</sub> through O<sub>2</sub> reduction over carbon nitride frameworks incorporated with multiple heteroelements, ACS Catalysis, 7 (2017) 2886–2895. DOI: 10.1021/acscatal.6b03334
- Mousavi Shaegh S.A., Nguyen N.-T., Mousavi Ehteshami S.M., Chan S.H., A membraneless hydrogen peroxide fuel cell using Prussian Blue as cathode material, Energy & Environmental Science, 5 (2012) 8225–8228. DOI: 10.1039/C2EE21806B
- Nosaka Y., Nosaka A., Introduction to Photocatalysis: From Basic Science to Applications, 1st edition, Royal Society of Chemistry, 2016, ISBN: 1782623205.
- Ong W.-J., Tan L.-L., Ng Y.H., Yong S.-T., Chai S.-P., Graphitic carbon nitride (g-C<sub>3</sub>N<sub>4</sub>)-based photocatalysts for artificial photosynthesis and environmental remediation: are we a step closer to achieving sustainability?, Chemical Reviews, 116 (2016) 7159–7329. DOI: 10.1021/acs.chemrev.6b00075
- Ou H., Yang P., Lin L., Anpo M., Wang X., Carbon nitride aerogels for the photoredox conversion of water, Angewandte Chemie International Edition, 56 (2017) 10905–10910. DOI: 10.1002/anie.201705926
- Pei Z., Ding L., Hu J., Weng S., Zheng Z., Huang M., Liu P., Defect and its dominance in ZnO films: a new insight into the role of defect over photocatalytic activity, Applied Catalysis B: Environmental, 142–143 (2013) 736–743. DOI: 10.1016/j.apcatb.2013.05.055
- Peng Y., Wang L., Liu Y., Chen H., Lei J., Zhang J., Visible-light-driven photocatalytic H<sub>2</sub>O<sub>2</sub> production on g-C<sub>3</sub>N<sub>4</sub> loaded with CoP as a noble metal free cocatalyst, European Journal of Inorganic Chemistry, 2017 (2017) 4797–4802. DOI: 10.1002/ejic.201700930
- Pesterfield L., The 100 most important chemical compounds: a reference guide (by Richard L. Myers), Journal of Chemical Education, 86 (2009) 1182. DOI: 10.1021/ed086p1182
- Qiang Z., Chang J.-H., Huang C.P., Electrochemical generation of hydrogen peroxide from dissolved oxygen in acidic solutions, Water Research, 36 (2002) 85–94. DOI: 10.1016/S0043-1354(01)00235-4
- Qiu C., Xu Y., Fan X., Xu D., Tandiana R., Ling X., Jiang Y., Liu C., Yu L., Chen W., Su C., Highly crystalline k-intercalated polymeric carbon nitride for visible-light photocatalytic alkenes and alkynes deuterations, Advanced Science, 6 (2019) 1801403. DOI: 10.1002/advs.201801403
- Qu X., Hu S., Li P., Li Z., Wang H., Ma H., Li W., The effect of embedding N vacancies into g-C<sub>3</sub>N<sub>4</sub> on the photocatalytic H<sub>2</sub>O<sub>2</sub> production ability via H<sub>2</sub> plasma treatment, Diamond and Related Materials, 86 (2018) 159–166. DOI: 10.1016/j.diamond.2018.04.027
- Schneider J., Bahnemann D.W., Undesired role of sacrificial reagents in photocatalysis, The Journal of Physical Chemistry Letters, 4 (2013) 3479–3483. DOI: 10.1021/jz4018199
- Shen R., Chen W., Peng Q., Lu S., Zheng L., Cao X., Wang Y., Zhu W., Zhang J., Zhuang Z., Chen C., Wang D., Li Y., High-concentration single atomic Pt sites on hollow CuSx for selective O<sub>2</sub> reduction to H<sub>2</sub>O<sub>2</sub> in acid solution, Chem, 5 (2019) 2099–2110. DOI: 10.1016/j.chempr.2019.04.024
- Shi L., Yang L., Zhou W., Liu Y., Yin L., Hai X., Song H., Ye J., Photoassisted construction of holey defective g-C<sub>3</sub>N<sub>4</sub> photocatalysts for efficient visible-light-driven H<sub>2</sub>O<sub>2</sub> production, Small, 14 (2018) 1703142. DOI: 10.1002/smll.201703142
- Shi X., Siahrostami S., Li G.-L., Zhang Y., Chakthranont P., Studt F., Jaramillo T.F., Zheng X., Nørskov J.K., Understanding activity trends in electrochemical water oxidation to form hydrogen peroxide, Nature Communications, 8 (2017) 701. DOI: 10.1038/s41467-017-00585-6
- Shiraishi Y., Kanazawa S., Kofuji Y., Sakamoto H., Ichikawa S., Tanaka S., Hirai T., Sunlight-driven hydrogen peroxide production from water and molecular oxygen by metal-free photocatalysts, Angewandte Chemie International Edition, 53 (2014a) 13454–13459. DOI: 10.1002/anie.201407938
- Shiraishi Y., Kanazawa S., Sugano Y., Tsukamoto D., Sakamoto H., Ichikawa S., Hirai T., Highly selective production of hydrogen peroxide on graphitic carbon nitride (g-C<sub>3</sub>N<sub>4</sub>) photocatalyst activated by visible light, ACS Catalysis, 4 (2014b) 774–780. DOI: 10.1021/cs401208c
- Shiraishi Y., Kofuji Y., Sakamoto H., Tanaka S., Ichikawa S., Hirai T., Effects of surface defects on photocatalytic H<sub>2</sub>O<sub>2</sub>

- production by mesoporous graphitic carbon nitride under visible light irradiation, *ACS Catalysis*, 5 (2015) 3058–3066. DOI: 10.1021/acscatal.5b00408
- Shiraishi Y., Takii T., Hagi T., Mori S., Kofuji Y., Kitagawa Y., Tanaka S., Ichikawa S., Hirai T., Resorcinol–formaldehyde resins as metal-free semiconductor photocatalysts for solar-to-hydrogen peroxide energy conversion, *Nature Materials*, 18 (2019) 985–993. DOI: 10.1038/s41563-019-0398-0
- Siahrostami S., Verdaguier-Casadevall A., Karamad M., Deiana D., Malacrida P., Wickman B., Escudero-Escribano M., Paoli E.A., Frydendal R., Hansen T.W., Chorkendorff I., Stephens I.E.L., Rossmesl J., Enabling direct H<sub>2</sub>O<sub>2</sub> production through rational electrocatalyst design, *Nature Materials*, 12 (2013) 1137–1143. DOI: 10.1038/nmat3795
- Sun H., Ma Y., Zhang Q., Su C., Engineering the local coordination environment of single-atom catalysts and their applications in photocatalytic water splitting: a review, *Transactions of Tianjin University*, 27 (2021) 313–330. DOI: 10.1007/s12209-021-00295-7
- Sun S., Li J., Cui J., Gou X., Yang Q., Jiang Y., Liang S., Yang Z., Simultaneously engineering K-doping and exfoliation into graphitic carbon nitride (g-C<sub>3</sub>N<sub>4</sub>) for enhanced photocatalytic hydrogen production, *International Journal of Hydrogen Energy*, 44 (2019) 778–787. DOI: 10.1016/j.ijhydene.2018.11.019
- Tasis D., Tagmatarchis N., Bianco A., Prato M., Chemistry of carbon nanotubes, *Chemical Reviews*, 106 (2006) 1105–1136. DOI: 10.1021/cr050569o
- Teixeira I.F., Barbosa E.C.M., Tsang S.C.E., Camargo P.H.C., Carbon nitrides and metal nanoparticles: from controlled synthesis to design principles for improved photocatalysis, *Chemical Society Reviews*, 47 (2018) 7783–7817. DOI: 10.1039/C8CS00479J
- Teng Z., Cai W., Liu S., Wang C., Zhang Q., Chenliang S., Ohno T., Bandgap engineering of polymetric carbon nitride copolymerized by 2,5,8-triamino-tri-s-triazine (melem) and barbituric acid for efficient nonsacrificial photocatalytic H<sub>2</sub>O<sub>2</sub> production, *Applied Catalysis B: Environmental*, 271 (2020) 118917. DOI: 10.1016/j.apcatb.2020.118917
- Teng Z., Cai W., Sim W., Zhang Q., Wang C., Su C., Ohno T., Photoexcited single metal atom catalysts for heterogeneous photocatalytic H<sub>2</sub>O<sub>2</sub> production: Pragmatic guidelines for predicting charge separation, *Applied Catalysis B: Environmental*, 282 (2021a) 119589. DOI: 10.1016/j.apcatb.2020.119589
- Teng Z., Lv H., Wang C., Xue H., Pang H., Wang G., Bandgap engineering of ultrathin graphene-like carbon nitride nanosheets with controllable oxygenous functionalization, *Carbon*, 113 (2017) 63–75. DOI: 10.1016/j.carbon.2016.11.030
- Teng Z., Yang N., Lv H., Wang S., Hu M., Wang C., Wang D., Wang G., Edge-functionalized g-C<sub>3</sub>N<sub>4</sub> nanosheets as a highly efficient metal-free photocatalyst for safe drinking water, *Chem*, 5 (2019) 664–680. DOI: 10.1016/j.chempr.2018.12.009
- Teng Z., Zhang Q., Yang H., Kato K., Yang W., Lu Y.-R., Liu S., Wang C., Yamakata A., Su C., Liu B., Ohno T., Atomically dispersed antimony on carbon nitride for the artificial photosynthesis of hydrogen peroxide, *Nature Catalysis*, 4 (2021b) 374–384. DOI: 10.1038/s41929-021-00605-1
- Thakur S., Kshetri T., Kim N.H., Lee J.H., Sunlight-driven sustainable production of hydrogen peroxide using a CdS-graphene hybrid photocatalyst, *Journal of Catalysis*, 345 (2017) 78–86. DOI: 10.1016/j.jcat.2016.10.028
- Torres-Pinto A., Sampaio M.J., Silva C.G., Faria J.L., Silva M.T.A., Recent strategies for hydrogen peroxide production by metal-free carbon nitride photocatalysts, *Catalysts*, 9 (2019) 990. DOI: 10.3390/catal9120990
- Tsukamoto D., Shiro A., Shiraishi Y., Sugano Y., Ichikawa S., Tanaka S., Hirai T., Photocatalytic H<sub>2</sub>O<sub>2</sub> production from ethanol/O<sub>2</sub> system using TiO<sub>2</sub> loaded with Au–Ag bimetallic alloy nanoparticles, *ACS Catalysis*, 2 (2012) 599–603. DOI: 10.1021/cs2006873
- Verdaguier-Casadevall A., Deiana D., Karamad M., Siahrostami S., Malacrida P., Hansen T.W., Rossmesl J., Chorkendorff I., Stephens I.E.L., Trends in the electrochemical synthesis of H<sub>2</sub>O<sub>2</sub>: enhancing activity and selectivity by electrocatalytic site engineering, *Nano Letters*, 14 (2014) 1603–1608. DOI: 10.1021/nl500037x
- Wang A., Li J., Zhang T., Heterogeneous single-atom catalysis, *Nature Reviews Chemistry*, 2 (2018) 65–81. DOI: 10.1038/s41570-018-0010-1
- Wang M., Shen S., Li L., Tang Z., Yang J., Effects of sacrificial reagents on photocatalytic hydrogen evolution over different photocatalysts, *Journal of Materials Science*, 52 (2017) 5155–5164. DOI: 10.1007/s10853-017-0752-z
- Wang Q., Domen K., Particulate photocatalysts for light-driven water splitting: mechanisms, challenges, and design strategies, *Chemical Reviews*, 120 (2020) 919–985. DOI: 10.1021/acs.chemrev.9b00201
- Wang S., Teng Z., Xu Y., Yuan M., Zhong Y., Liu S., Wang C., Wang G., Ohno T., Defect as the essential factor in engineering carbon-nitride-based visible-light-driven Z-scheme photocatalyst, *Applied Catalysis B: Environmental*, 260 (2020a) 118145. DOI: 10.1016/j.apcatb.2019.118145
- Wang S., Zhan J., Chen K., Ali A., Zeng L., Zhao H., Hu W., Zhu L., Xu X., Potassium-doped g-C<sub>3</sub>N<sub>4</sub> achieving efficient visible-light-driven CO<sub>2</sub> Reduction, *ACS Sustainable Chemistry & Engineering*, 8 (2020b) 8214–8222. DOI: 10.1021/acssuschemeng.0c01151
- Wang X., Maeda K., Thomas A., Takane K., Xin G., Carlsson J.M., Domen K., Antonietti M., A metal-free polymeric photocatalyst for hydrogen production from water under visible light, *Nature Materials*, 8 (2009) 76–80. DOI: 10.1038/nmat2317
- Wang Y., Vogel A., Sachs M., Sprick R.S., Wilbraham L., Moniz S.J.A., Godin R., Zwijnenburg M.A., Durrant J.R., Cooper A.I., Tang J., Current understanding and challenges of solar-driven hydrogen generation using polymeric photocatalysts, *Nature Energy*, 4 (2019) 746–760. DOI: 10.1038/s41560-019-0456-5
- Wei Y., Zhang J., Zheng Q., Miao J., Alvarez P.J., Long M., Quantification of photocatalytically-generated hydrogen peroxide in the presence of organic electron donors: interference and reliability considerations, *Chemosphere*, 279 (2021) 130556. DOI: 10.1016/j.chemosphere.2021.130556
- Wei Z., Liu M., Zhang Z., Yao W., Tan H., Zhu Y., Efficient visible-light-driven selective oxygen reduction to hydrogen peroxide by oxygen-enriched graphitic carbon nitride polymers, *Energy & Environmental Science*, 11 (2018) 2581–2589. DOI: 10.1039/C8EE01316K
- Xia C., Xia Y., Zhu P., Fan L., Wang H., Direct electrosynthesis of pure aqueous H<sub>2</sub>O<sub>2</sub> solutions up to 20 % by weight using a solid electrolyte, *Science*, 366 (2019) 226. DOI: 10.1126/science.aay1844
- Xiong J., Di J., Xia J., Zhu W., Li H., Surface defect engineering in 2D nanomaterials for photocatalysis, *Advanced Functional Materials*, 28 (2018) 1801983. DOI: 10.1002/adfm.201801983
- Xu Q., Zhang L., Yu J., Wageh S., Al-Ghamdi A.A., Jaroniec M., Direct Z-scheme photocatalysts: principles, synthesis, and

- applications, *Materials Today*, 21 (2018) 1042–1063. DOI: 10.1016/j.mattod.2018.04.008
- Yamada Y., Yoneda M., Fukuzumi S., A robust one-compartment fuel cell with a polynuclear cyanide complex as a cathode for utilizing  $H_2O_2$  as a sustainable fuel at ambient conditions, *Chemistry – A European Journal*, 19 (2013) 11733–11741. DOI: 10.1002/chem.201300783
- Yang H.B., Hung S.-F., Liu S., Yuan K., Miao S., Zhang L., Huang X., Wang H.-Y., Cai W., Chen R., Gao J., Yang X., Chen W., Huang Y., Chen H.M., et al., Atomically dispersed Ni(i) as the active site for electrochemical  $CO_2$  reduction, *Nature Energy*, 3 (2018) 140–147. DOI: 10.1038/s41560-017-0078-8
- Yang L., Dong G., Jacobs D.L., Wang Y., Zang L., Wang C., Two-channel photocatalytic production of  $H_2O_2$  over g- $C_3N_4$  nanosheets modified with perylene imides, *Journal of Catalysis*, 352 (2017) 274–281. DOI: 10.1016/j.jcat.2017.05.010
- Yang S., Verdager-Casadevall A., Arnarson L., Silvioli L., Čolić V., Frydendal R., Rossmeisl J., Chorkendorff I., Stephens I.E.L., Toward the decentralized electrochemical production of  $H_2O_2$ : a focus on the catalysis, *ACS Catalysis*, 8 (2018) 4064–4081. DOI: 10.1021/acscatal.8b00217
- Yi Y., Wang L., Li G., Guo H., A review on research progress in the direct synthesis of hydrogen peroxide from hydrogen and oxygen: noble-metal catalytic method, fuel-cell method and plasma method, *Catalysis Science and Technology*, 6 (2016) 1593–1610. DOI: 10.1039/C5CY01567G
- Zeng X., Liu Y., Kang Y., Li Q., Xia Y., Zhu Y., Hou H., Uddin M.H., Gengenbach T.R., Xia D., Sun C., Mccarthy D.T., Deletic A., Yu J., Zhang X., Simultaneously tuning charge separation and oxygen reduction pathway on graphitic carbon nitride by polyethylenimine for boosted photocatalytic hydrogen peroxide production, *ACS Catalysis*, 10 (2020) 3697–3706. DOI: 10.1021/acscatal.9b05247
- Zeng X., Wang Z., Meng N., McCarthy D.T., Deletic A., Pan J.-h., Zhang X., Highly dispersed  $TiO_2$  nanocrystals and carbon dots on reduced graphene oxide: ternary nanocomposites for accelerated photocatalytic water disinfection, *Applied Catalysis B: Environmental*, 202 (2017) 33–41. DOI: 10.1016/j.apcatb.2016.09.014
- Zhan W., Ji L., Ge Z.-m., Wang X., Li R.-t., A continuous-flow synthesis of primary amides from hydrolysis of nitriles using hydrogen peroxide as oxidant, *Tetrahedron*, 74 (2018) 1527–1532. DOI: 10.1016/j.tet.2018.02.017
- Zhang B., Qiu C., Wang S., Gao H., Yu K., Zhang Z., Ling X., Ou W., Su C., Electrocatalytic water-splitting for the controllable and sustainable synthesis of deuterated chemicals, *Science Bulletin*, 66 (2021) 562–569. DOI: 10.1016/j.scib.2020.09.016
- Zhang C., Bai J., Ma L., Lv Y., Wang F., Zhang X., Yuan X., Hu S., Synthesis of halogen doped graphite carbon nitride nanorods with outstanding photocatalytic  $H_2O_2$  production ability via saturated  $NH_4X$  ( $X = Cl, Br$ ) solution-hydrothermal post-treatment, *Diamond and Related Materials*, 87 (2018) 215–222. DOI: 10.1016/j.diamond.2018.06.013
- Zhang G., Yang X., He C., Zhang P., Mi H., Constructing a tunable defect structure in  $TiO_2$  for photocatalytic nitrogen fixation, *Journal of Materials Chemistry A*, 8 (2020) 334–341. DOI: 10.1039/C9TA10471B
- Zhang M.-h., Dong H., Zhao L., Wang D.-x., Meng D., A review on Fenton process for organic wastewater treatment based on optimization perspective, *Science of the Total Environment*, 670 (2019) 110–121. DOI: 10.1016/j.scitotenv.2019.03.180
- Zhang P., Sun D., Cho A., Weon S., Lee S., Lee J., Han J.W., Kim D.-P., Choi W., Modified carbon nitride nanozyme as bifunctional glucose oxidase-peroxidase for metal-free bioinspired cascade photocatalysis, *Nature Communications*, 10 (2019) 940. DOI: 10.1038/s41467-019-08731-y
- Zhang P., Tong Y., Liu Y., Vequizo J.J.M., Sun H., Yang C., Yamakata A., Fan F., Lin W., Wang X., Heteroatom dopants promote two-electron  $O_2$  reduction for photocatalytic production of  $H_2O_2$  on polymeric carbon nitride, *Angewandte Chemie*, 132 (2020) 16343–16351. DOI: 10.1002/ange.202006747
- Zhang Z., Xu Y., Zhang Q., Fang S., Sun H., Ou W., Su C. Semi-heterogeneous photo-Cu-dual-catalytic cross-coupling reactions using polymeric carbon nitrides. *Science Bulletin*, 67 (2022) 71–78. DOI: 10.1016/j.scib.2021.08.001
- Zhang Z., Yates J.T., Band bending in semiconductors: Chemical and physical consequences at surfaces and interfaces, *Chemical Reviews*, 112 (2012) 5520–5551. DOI: 10.1021/cr3000626
- Zhao S., Guo T., Li X., Xu T., Yang B., Zhao X., Carbon nanotubes covalent combined with graphitic carbon nitride for photocatalytic hydrogen peroxide production under visible light, *Applied Catalysis B: Environmental*, 224 (2018a) 725–732. DOI: 10.1016/j.apcatb.2017.11.005
- Zhao S., Zhao X., Insights into the role of singlet oxygen in the photocatalytic hydrogen peroxide production over polyoxometalates-derived metal oxides incorporated into graphitic carbon nitride framework, *Applied Catalysis B: Environmental*, 250 (2019) 408–418. DOI: 10.1016/j.apcatb.2019.02.031
- Zhao S., Zhao X., Ouyang S., Zhu Y., Polyoxometalates covalently combined with graphitic carbon nitride for photocatalytic hydrogen peroxide production, *Catalysis Science and Technology*, 8 (2018b) 1686–1695. DOI: 10.1039/C8CY00043C
- Zhao S., Zhao X., Zhang H., Li J., Zhu Y., Covalent combination of polyoxometalate and graphitic carbon nitride for light-driven hydrogen peroxide production, *Nano Energy*, 35 (2017) 405–414. DOI: 10.1016/j.nanoen.2017.04.017
- Zhu J., Fan F., Chen R., An H., Feng Z., Li C., Direct imaging of highly anisotropic photogenerated charge separations on different facets of a single  $BiVO_4$  photocatalyst, *Angewandte Chemie International Edition*, 54 (2015) 9111–9114. DOI: 10.1002/anie.201504135
- Zhu Z., Pan H., Murugananthan M., Gong J., Zhang Y., Visible light-driven photocatalytically active g- $C_3N_4$  material for enhanced generation of  $H_2O_2$ , *Applied Catalysis B: Environmental*, 232 (2018) 19–25. DOI: 10.1016/j.apcatb.2018.03.035
- Zuo G., Liu S., Wang L., Song H., Zong P., Hou W., Li B., Guo Z., Meng X., Du Y., Wang T., Roy V.A.L., Finely dispersed Au nanoparticles on graphitic carbon nitride as highly active photocatalyst for hydrogen peroxide production, *Catalysis Communications*, 123 (2019) 69–72. DOI: 10.1016/j.catcom.2019.02.011

## Authors' Short Biographies



### Zhenyuan Teng

Dr. Zhenyuan Teng is currently a JSPS Research Fellow (PD) in the Research Initiative for Supra-Materials (RISM), Interdisciplinary Cluster for Cutting Edge Research, Shinshu University. He obtained his B.S. degree in 2016 and then acquired the Master degree (2018) from Yangzhou University. He obtained his Doctoral degree from Kyushu Institute of Technology in 2021 under the supervision of Prof. Teruhisa Ohno. His research interest focuses on the design and synthesis of single-atom organic-inorganic photocatalytic systems for energetic and environmental applications.



### Wenan Cai

Wenan Cai received his B.S. in Beijing Institute of Petrochemical Technology in 2016. Currently, he is a Ph.D. student under the supervision of Prof. Ohno Teruhisa in Kyushu Institute of Technology. His research interest is the development and design of long-wavelength response photocatalysts for H<sub>2</sub>O<sub>2</sub> production.



### Teruhisa Ohno

Prof. Teruhisa Ohno is currently the dean of faculty of engineering in Kyushu Institute of Technology. He obtained his Doctoral degree in Kyushu University in 1988. He worked as an Associate Professor in Kyushu University from 1992 to 1994 and in Osaka University from 1994–2003. Then he moved to Kyushu Institute of Technology as a Full Professor. From 2016 to 2021, He published 57 SCI papers. Field-Weighted Citation Impact: 2.04, Citation Count: 1,108, h-index: 48, h5-index: 15. A number of papers have published on influential periodical, such as Applied Catalysis B: Environmental, ACS catalysis and Nature Catalysis. From 1983 to now, published about 202 SCI papers, these papers were totally quoted more than 11,763 times and h-index is 49 (Scopus Data). His research interests are: 1. Development of visible light sensitive photocatalysts; 2. Nanoscale surface structure control of TiO<sub>2</sub> photocatalysts; 3. Development of photocatalyst and photoelectrode system for CO<sub>2</sub> reduction; 4. Visible light responsive photocatalyst and photoelectrode for H<sub>2</sub>O<sub>2</sub> production.

# Mechanistic Formulation Design of Spray-Dried Powders<sup>†</sup>

Mani Ordoubadi\*, Hui Wang and Reinhard Vehring

*Department of Mechanical Engineering, University of Alberta, Canada*

## Abstract

Spray drying is gaining traction in the pharmaceutical industry as one of the processing methods of choice for the manufacture of solid dosage forms intended for pulmonary, oral, and parenteral delivery. This process is particularly advantageous because of its ability to produce engineered particles with improved efficacy and stability by combining active pharmaceutical ingredients or biologics with appropriate excipients. Moreover, due to its high throughput, continuous operation, and ability to produce thermostable solid powders, spray drying can be a manufacturing method of choice in the production of drugs and other formulations, including vaccines, for global distribution. Formulation design based on a mechanistic understanding of the different phenomena that occur during the spray drying of powders is complicated and can therefore make the use of available particle formation models difficult for the practitioner. This review aims to provide step-by-step guidance accompanied by critical background information for the successful formulation design of spray-dried microparticles. These include discussion of the tools needed to estimate the surface concentration of each solute during droplet drying, their times and modes of solidification, and the amount of glass stabilizers and shell formers required to produce stable and dispersible powders.

**Keywords:** spray drying, powders, formulation design, particle formation, pharmaceutical particles, pulmonary delivery

## 1. Introduction

Among the different industrial methods employed in the manufacture of pharmaceutical powders and solid dosage forms, spray drying has attracted considerable interest as a fast, scalable, and continuous process (Baumann et al., 2021; Carrigy and Vehring, 2019). By readily allowing a formulator to control or predict many of the physical properties of particles such as size distribution, density, solid-state, and radial spread of different components inside the particle, spray drying offers significant advantages over milling, the current industrial processing method of choice for the large-scale production of microparticles (Alhajj et al., 2021). The importance of glass-stabilized spray-dried products has also gained increasing appreciation due to the growing demand for thermostable platforms containing vaccines or other biologics in the battle against global pandemics and infectious diseases (Capua and Giaquinto, 2021; Gomez and Vehring, 2022; Kristensen et al., 2016). Moreover, spray-dried powders containing low-water-soluble therapeutics show improved bioavailability due to their usually achieved amorphous state as compared with

the crystalline state of the raw material, especially when formulated in the form of amorphous solid dispersions (Davis and Walker, 2018; Huang et al., 2016; Ma and Williams, 2019).

In addition to the aforementioned pharmaceutical applications, spray drying was originally invented for and is still widely employed in the food industry to produce powder products such as dried milk, instant coffee, and encapsulated food ingredients (Woo, 2019). Such powders have increased shelf life, maintain flavor, and expedite global food distribution (Mohammed et al., 2020).

The process of spray drying, as shown schematically in **Fig. 1**, begins with the atomization of a liquid feed solution or suspension into a fine spray in a drying chamber, where it is then subjected to a large quantity of a hot drying gas made up of either nitrogen or dry air, depending on the solvent. The liquid spray is consequently rapidly evaporated, leaving behind solid particles that are then separated from the gas flow, most commonly through cyclonic separation (Pinto et al., 2021). Through evaporative cooling, the atomized droplets maintain a relatively low temperature for most of their drying history, making this process ideal for the production of temperature-sensitive powders (Ordoubadi et al., 2019).

Through a mechanistic understanding of the diverse phenomena that occur during spray drying, a particle engineer can design process and formulation parameters to meet a set of predefined production objectives and goals.

<sup>†</sup> Received 6 May 2022; Accepted 31 May 2022  
J-STAGE Advance published online 9 July 2022

\* Corresponding author: Mani Ordoubadi;  
Add: 10-203 Donadeo Innovation Centre for Engineering, 9211  
116th Street NW, Edmonton, Alberta T6G 1H9, Canada  
E-mail: ordoubad@ualberta.ca  
TEL: +1-780-492-3446 FAX: +1-780-492-2200

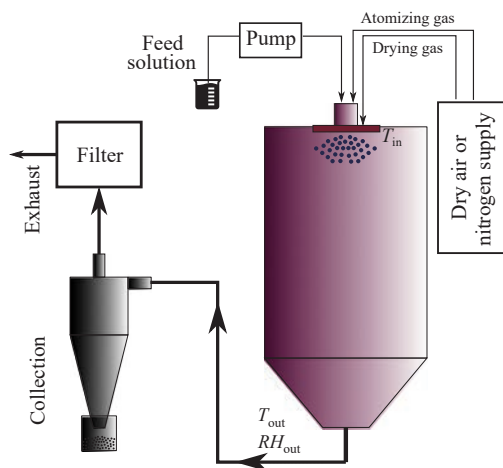


**Fig. 1** A typical open-cycle spray dryer showing the key stages of atomization, drying, and collection.

Spray drying process conditions, including inlet and outlet temperatures, drying gas flow rate, feed flow rate, and atomizing pressure, predominantly influence the size distribution of the particles, the outlet conditions of the dryer, and the production yield (Carrigy and Vehring, 2019), while spray drying formulation parameters, including total feed concentrations, choice of excipients, and feed composition, influence properties such as the radial distribution of each material inside the dried particles, their physico-chemical properties, and their general morphology (Alhajj et al., 2021). Hence, careful design of both the process and formulation parameters can significantly reduce the initial research and development stage of product development, thereby decreasing production time, costs, and associated risks (Boraey and Vehring, 2014; Vehring, 2008; Vehring et al., 2007).

Many studies have succeeded in developing particle formation models (Boraey and Vehring, 2014; Ivey and Vehring, 2010; Ordoubadi et al., 2019; 2021a; 2021b) and process models (Carrigy and Vehring, 2019) that can be used during the formulation design of spray-dried powders. These models are frequently not easily accessible as their use requires knowledge of different branches of science and engineering, including mechanical, chemical, and materials engineering. In this study, we aim to reduce these challenges by reviewing the different stages of the design of engineered spray-dried particles and providing sufficient background information to make this process accessible to a broader group of scientists and researchers.

## 2. Formulation and process design

Like most design problems, the design of spray-dried microparticles is an iterative process. During each iteration, the formulation and process parameters are selected based on particle formation models or previous experience. This includes the estimation of the surface concentration of each component and the specific moment during the

evaporation process at which they solidify. Using these data, the next logical step in the formulation design is choosing the total solids concentration and feed fractions of the active pharmaceutical ingredients (APIs), biologics, and excipients to meet the design objectives based on other factors such as the required drug loading, producibility, stability considerations, and regulatory matters. For example, the feed fractions of a shell-forming excipient and a glass stabilizer can be selected so that the former solidifies first and the latter increases the glass transition temperature above the required limit. Afterward, sample batches are spray dried and characterized to assess their performance. In case of unsatisfactory properties, the formulation and process parameters are modified until the requirements are satisfied. The different stages of such a proposed design process are shown in Fig. 2.

### 2.1 The choice of the solvent system

One of the first problems a formulator faces in the product development of spray-dried pharmaceutical powders is the question of which solvent system to use. Depending on solubility constraints, the answer can be as straightforward as plain water or as complicated as a multi-solvent system with correct solvent ratios. For the spray drying of biologics and APIs with adequate aqueous solubility, water is the solvent of choice because it is safe, inexpensive, and requires no capture of the evaporated water vapor at the exhaust (Davis and Walker, 2018; Selvamuthukumar, 2019). However, more than 60 % of newly discovered chemical entities and 40 % of currently marketed drugs exhibit poor water solubility (Davis and Walker, 2018; Paredes et al., 2021). Hence, it is inevitable that a particle engineer will face the task of formulating a spray-dried platform for a hydrophobic active, especially when striving for significant enhancement in bioavailability after spray drying into an amorphous powder (Ojarinta et al., 2017; Salama, 2020). For such compounds, an organic solvent or a mixture of cosolvents can be selected after a thorough solubility screening. Solubility limitations are of significance only when the API is intended to be dissolved in the feed liquid, as opposed to applications in which one or more of the components are emulsified or dispersed, in which case there should be negligible solubility of the suspended material to avoid instability in the feedstock during manufacturing (Gomez et al., 2021a; Maniyar and Kokare, 2019; Wang H. et al., 2022). A handful of organic solvents have been considered as solvents or cosolvents for feed preparation, with only a limited number of these deemed safe for inhaled product development. The solvents most encountered in the literature are water, acetone, ethanol, methanol, ethyl acetate, dichloromethane, and tetrahydrofuran (Shepard et al., 2020; Vasconcelos et al., 2016).

Formulation design becomes most complicated when the solubility of the active ingredient is not high enough

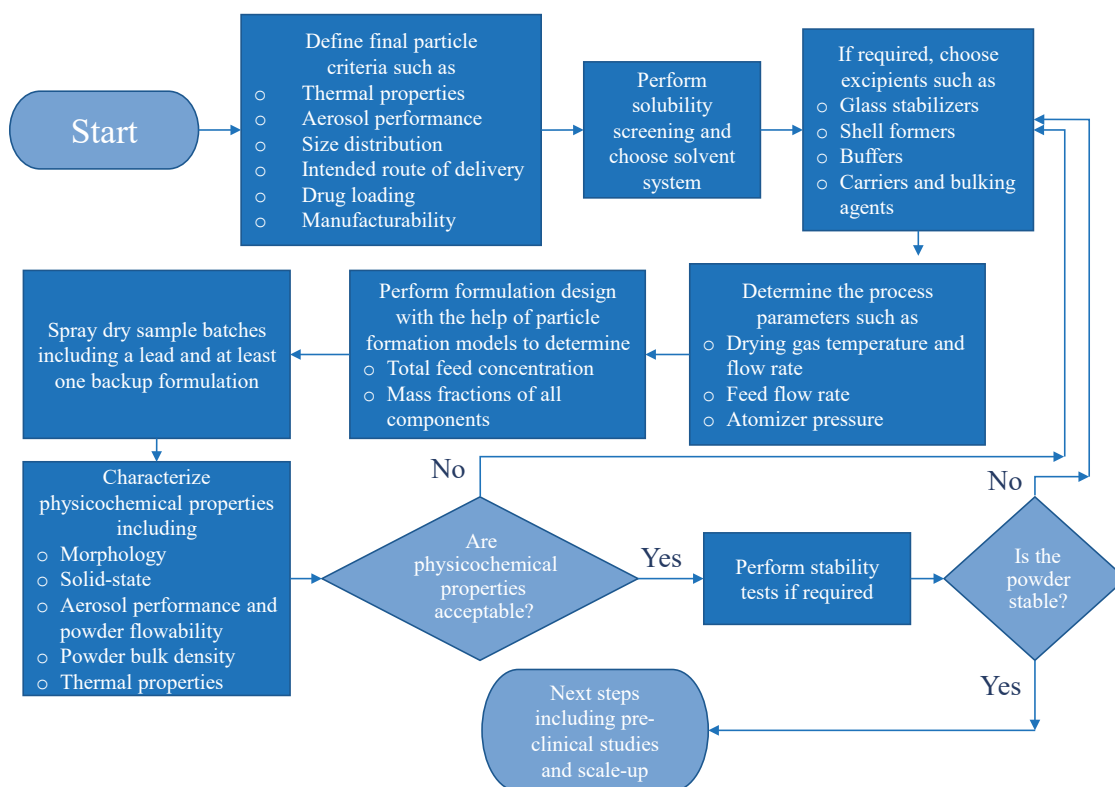


**Fig. 2** The process of formulation design of spray-dried powders.

in a single solvent system and is instead higher at specific fractions in a multi-solvent system, or when the compound has a high solubility in a specific solvent but is not stable or dispersible on its own and therefore requires to be spray dried in conjunction with appropriate excipients that are soluble in another solvent, for example, budesonide, with its higher solubility in ethanol, and leucine, with its greater solubility in water (Boraey et al., 2013). For such cases, as shown schematically in **Fig. 3**, specific alterations can be made to the formulation or process design; for example, a cosolvent system can be used during feed preparation (Alhajj et al., 2021; Boraey et al., 2013; Mishra et al., 2018), or a 3-fluid atomizer can be incorporated (Focaroli et al., 2020; Kauppinen et al., 2018; Shetty et al., 2020; Sunderland et al., 2015).

For cosolvent systems, solubility data can be used in conjunction with advanced particle formation models to choose the optimal solvent ratios. It has previously been shown that, due to non-ideal vapor-liquid equilibria, multi-solvent droplets might have an azeotrope-like state during evaporation at which no change in the solvent composition can occur (Bader et al., 2013; Ordoubadi et al., 2019). For example, it was found that a microdroplet composed of 24 % w/w water and 76 % w/w ethanol evaporating in dry air at different temperatures, maintains a constant evaporation rate and droplet composition (Ordoubadi et al., 2019). When the ethanol content is increased (above 76 % w/w) during evaporation, the droplets will lose their

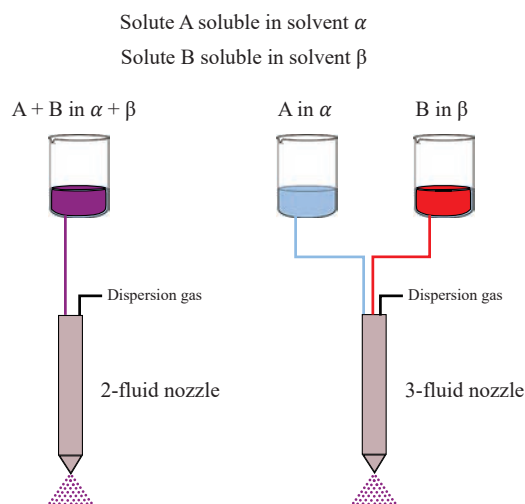


**Fig. 3** The use of a 2-fluid nozzle for a cosolvent system and a 3-fluid nozzle to handle issues of solubility incompatibility between different components and solvents.

water content first (ethanol enrichment), but when the ethanol content is reduced (below 76 % w/w) they will lose their ethanol content first (water enrichment). A formulator should be aware of such reversals in the drying behavior because, for example, they might cause the sensitive active to precipitate first on the surface of the droplet instead of the intended shell former.

## 2.2 The choice of excipients

Upon spray drying, most APIs and biologics are dried into an amorphous solid (Baumann et al., 2021; Chang et al., 2020; Chiou and Langrish, 2007). Amorphous spray-dried powders can be hygroscopic (Li L. et al., 2016; Momin et al., 2018), show poor long-term stability due to the possibility of recrystallization (Singh and Van den Mooter, 2016), and exhibit low glass transition temperatures (Červinka and Fulem, 2021). They can also be cohesive, resulting in poor powder and aerosol performance (Alhajj et al., 2021; Jüptner and Scherließ, 2019). Furthermore, some of these adverse properties can exacerbate the others, as in the case of plasticization due to moisture uptake. To overcome these problems, biologically inert compounds or excipients can be formulated with active ingredients to act as carriers, bulking agents, buffers, dispersibility enhancers, and glass stabilizers (Lechuga-Ballesteros et al., 2019; Weers and Miller, 2015). Two such excipients frequently used for pulmonary applications and having the most impact on the particle formation process, i.e. glass stabilizers and shell formers, are discussed in detail next.

### 2.2.1 Glass stabilizers

Amorphous materials are in a metastable thermodynamic state and may eventually crystallize due to their microscopic molecular mobility (Kawakami, 2019; Singh and Van den Mooter, 2016). For spray-dried powders, the rate of this transition depends on the residual solvent content, ambient humidity, and storage temperature (Chiou and Langrish, 2007). It has previously been shown that storing pharmaceutical glasses at about 50 °C below their glass transition temperature prevents significant molecular mobility during their lifetime (Hancock et al., 1995). This approach has been used to design and assess spray-dried platforms containing different pharmaceutical ingredients and biological entities (Chan and Chang, 2021; Hoe et al., 2014; Shepard et al., 2021). Accordingly, for a powder product to be room-temperature-stable (assuming a storage temperature of 25 °C), its glass transition temperature,  $T_g$ , needs to be more than 75 °C. The climate of the product's intended market should also be considered. For example, for global health applications such as vaccine development for the developing and least developed countries more stringent conditions need to be accounted for (WHO Expert Committee on Biological Standardization, 2016). Hence, during formulation design, the particle engineer can aim for a predicted glass transition temperature so that  $T_g > T_{st} + 50$  K, where  $T_{st}$  is the storage temperature. If the glass transition temperature of the amorphous drug is less than this value, then a glass stabilizer is required in the formulation to improve the thermostability of the product. A number of saccharides and polymers such as trehalose, sucrose, pullulan, and inulin are some of the glass formers that have been studied for the stabilization of spray-dried

products (Carrigy et al., 2019c; Gomez and Vehring, 2022; Weers and Miller, 2015).

The prediction of the glass transition temperature is complicated since spray-dried powders may contain residual solvent that can act as a plasticizer (Patel et al., 2015; Shepard et al., 2020). The amount of the residual solvent itself is a function of the solvent-uptake properties of the powder, the outlet vapor activity (relative humidity in the case of aqueous systems), and the outlet temperature of the dryer (Carrigy and Vehring, 2019). Hence, to determine the required mass fraction of the glass-forming excipient,  $Y_{exp}$ , the amount of residual solvent can be neglected initially and the Fox equation (Fox, 1956) can be rearranged to give

$$1 > Y_{exp} > \frac{\frac{1}{T_{st} + 50K} - \frac{1}{T_{g,act}}}{\frac{1}{T_{g,exp}} - \frac{1}{T_{g,act}}} \quad (1)$$

where,  $T_{st}$ ,  $T_{g,act}$ , and  $T_{g,exp}$ , all in Kelvin, are the long-term storage temperature, active glass transition temperature, and the stabilizing excipient glass transition temperature, respectively. Eqn. (1) can only be used when  $T_{g,exp} > T_{g,act}$  and  $T_{g,exp} > T_{st} + 50$  K. For example, if trehalose is to be used as a glass-forming excipient with a dry  $T_{g,exp}$  of 390 K (~117 °C) (Drake et al., 2018) to stabilize an active with a  $T_{g,act}$  of 323.15 K (50 °C), more than 42 % w/w of the formulation should be composed of trehalose for the product to be stable at a storage temperature,  $T_{st}$ , of 298.15 K (25 °C). For storage at a temperature of 313.15 K (40 °C), more than 65 % of the system should be composed of trehalose, and for storage at a temperature of 343.15 K (70 °C), the product cannot be stabilized with trehalose at all.

In addition to their anti-plasticizing effect, some glass-forming excipients can be used to stabilize sensitive biologics such as bacteriophages, vaccines, and proteins in spray-dried platforms (Carrigy et al., 2019a; Gomez et al., 2021a). The reasons for this protective property are believed to be twofold: first, the hydrogen bonds formed between water and protein molecules are replaced with new bonds formed during drying between the hydroxyl groups of the stabilizers and the proteins, and second, the immobilization of the proteins in a glassy matrix significantly reduces the risk of different forms of denaturation (Hinrichs et al., 2001; Mensink et al., 2017). The required mass fraction of the glass former is believed to depend on the stabilizer and the biological entity, but a minimum mass ratio of 1:1 was shown to result in acceptable physical stability in several studies (Massant et al., 2020; Shepard et al., 2021).

### 2.2.2 Dispersibility enhancers and shell formers

As mentioned before, and as shown in Fig. 4, spray-dried particles (in particular, those made of small-molecule



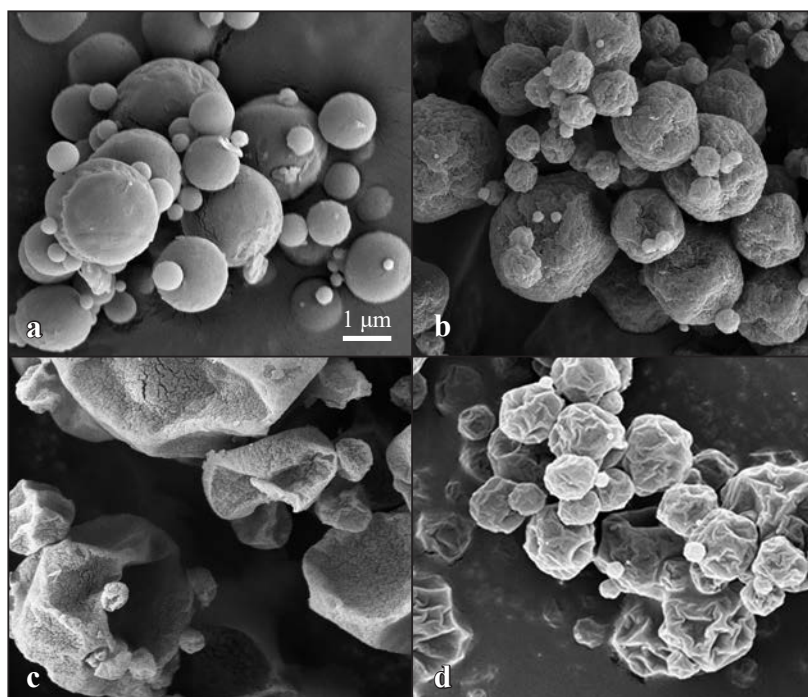


**Fig. 4** Micrographs of spray-dried trehalose and different shell formers: (a) trehalose; (b) trehalose and 20 % w/w L-leucine; (c) trehalose and 5 % w/w trileucine; (d) trehalose and 3 % w/w Eudragit. (Reproduced from Bin Karim et al., 2021 with the permission of Elsevier.)

compounds) are usually amorphous with smooth surfaces and high surface energies (Alhajj et al., 2021). When combined with the small size of the particles, especially those intended for pulmonary delivery, these properties result in cohesiveness that causes poor powder flowability and undesirable aerosol properties (Jüptner and Scherließ, 2019). To diminish these problems, another class of excipients, usually called shell formers or dispersibility enhancers, are included in the spray-dried formulations. The shell formers are intended to precipitate first on the surface of the dried particles and improve the aerosol properties of the powders via two mechanisms: first, they increase surface rugosity and hence decrease the contact area with the surrounding particles or external surfaces (Baldelli and Vehring, 2016); second, they decrease surface energies (Jong et al., 2016; Zhou et al., 2015). Both of these mechanisms reduce the cohesive (interparticle) and adhesive (extra particle) forces. Because it forms solid shells around the interior core of the particles, this kind of excipient might also protect the valuable actives or biologics from different surface-mediated degradation mechanisms (Carrigy et al., 2019b; Gomez et al., 2021b) or in some cases provide short-term protection against moisture-induced interparticle fusion (Li L. et al., 2016; Wang Z. et al., 2021b).

For maximized encapsulation, all shell formers need to precipitate or solidify before other components on the surface of the droplets during evaporation. Certain properties, such as low crystalline or amorphous solubility, large molecular size, and high surface activity can cause early shell formation. For instance, materials with low solubili-

ties can solidify first during drying and tend to accumulate on the surface of the droplet until a solid shell is formed, while large molecules enrich the surface and reach their precipitation limit faster than smaller compounds. For example, some of the polysaccharides and other polymeric compounds, such as pullulan, Eudragit, and maltodextrin, produce a shell early during the evaporation process and can act as a shell former by increasing the surface rugosity (Bin Karim et al., 2021; Carrigy et al., 2019d; Zhang et al., 2018). Surface activity is another important attribute that can cause surface accumulation of excipients. The interfacial adsorption of surface-active molecules decreases the surface energy of the dried particles because of the outward orientation of their hydrophobic tails (Jong et al., 2016; Vartiainen et al., 2016). Furthermore, some surface-active shell formers, like trileucine (Carrigy et al., 2019b; Lechuga-Ballesteros et al., 2008; Ordoubadi et al., 2021a), undergo early phase-separation near the droplet surface resulting in highly rugose particles with decreased contact area (Wang H. et al., 2019). Some of the most effective shell formers have two or more of these properties. For example, both leucine and trileucine are surface-active and have low solubilities resulting in surface adsorption as well as early solidification during droplet evaporation (Lechuga-Ballesteros et al., 2008; Ordoubadi et al., 2021a; 2021b).

## 2.3 Process parameters

### 2.3.1 Feedstock preparation

Spray drying is essentially a method of desiccating liquid

feedstocks into a dry powder form composed of microparticles. A typical spray drying process involves feedstock preparation, atomization of the feedstock to form droplets, desiccation of the atomized droplets in a drying chamber, and separation of the dried particles from the drying gas (Cal and Sollohub, 2010). Carefully designed formulations intended for spray drying need to be presented in a liquid form before they can undergo subsequent atomization and drying processes. The feedstock preparation process for actives or excipients that are soluble in the selected solvent system is relatively straightforward and usually involves mixing the solid and liquid phases at appropriate conditions with additional agitation if needed. Despite the simplicity of preparation for solution-based feedstocks, spray drying from a homogeneous solution can have many variations and, if properly designed, can produce particles with multifunctional structures, such as layered, hollow, dimpled, porous, etc. (Vehring, 2008). A more in-depth discussion on this topic will be provided in the particle formation section.

Because a large proportion of all new drug candidates entering the development pipeline face various problems due to their poor aqueous solubility (Nagarwal et al., 2011), suspensions have become a popular dosage form of medication in drug delivery applications (Rabinow, 2004). For the same reason, the preparation of a stabilized suspension or emulsion feedstock is the most common modification to the simple solution-based spray drying process (Chaubal and Popescu, 2008; Dollo et al., 2003; Kumar et al., 2014; Soottitantawat et al., 2003). These two-phase systems are sometimes also employed to transfer some of their pre-existing structural properties onto the final dry particles. Two typical examples are the hybrid large porous nanoparticle aggregates reported by Tsapis et al. (Lintingre et al., 2016; Tsapis et al., 2002) and the porous PulmoSphere™ lipid particles summarized by Weers et al. (Weers and Tarara, 2014). Careful selection of surfactants assisted by a powered mixing process such as high shear mixing or high-pressure homogenization is usually needed to produce stable suspension feedstocks for the production of consistent products throughout the spray drying process (Chaubal and Popescu, 2008; Dollo et al., 2003; Singh and Van den Mooter, 2016; Verma et al., 2011).

More complex multi-phase systems with more than two dispersed phases such as feedstocks with multiple suspended solid materials, feedstocks with multiple emulsions, and emulsion-based feedstocks with additional suspended solids have been explored to meet more specific formulation design targets. For instance, feedstocks consisting of calcium salts dispersed in an aqueous Eudragit polymeric suspension were spray dried to produce microencapsulated particles for a controlled gastrointestinal release profile (Oneda and Ré, 2003). A complex dispersion of polymeric nanocapsules containing an oil core was spray dried with colloidal silica to form nanoparticle-coated microparticles

(Tewa-Tagne et al., 2006; 2007). Orange oil was encapsulated in the inner compartment of another double emulsion by spray drying for better protection of the inner material (Edris and Bergnstahl, 2001). Micronized drug particles such as budesonide, ciprofloxacin, and amphotericin B were suspended within an oil (perflubron)-in-water emulsion feedstock and spray dried to produce drug-loaded composite particles for inhalation (Weers et al., 2019). Many of the studies referenced here employed multi-step feedstock preparation processes in which precursors were manufactured prior to the preparation of the final feedstock, an approach that is being increasingly used in complex formulations (Vehring, 2008).

### 2.3.2 Atomization, drying, and collection

Atomization of feedstocks into liquid sprays significantly increases the specific surface areas of the liquid phase that are exposed to the drying gas, thereby effectively facilitating rapid heat transfer from the heated drying gas to the atomized droplets and mass transfer of volatile solvents to the gas phase (Cal and Sollohub, 2010). Various atomizer designs based on different liquid disintegration mechanisms have been used to break up liquid feedstocks for the formation of dried particles with the desired physicochemical and morphological attributes. The most commonly used atomizer types can be generally categorized into rotary atomizers, hydraulic nozzles, pneumatic nozzles, and ultrasonic nozzles (Cal and Sollohub, 2010; Santos et al., 2018).

Among these, pneumatic nozzles, also known as multi-fluid nozzles, are the most popular atomizer for pharmaceutical applications (Cal and Sollohub, 2010). The most common configuration of such devices is based on a two-fluid nozzle atomizer in which the liquid feedstock is supplied to the nozzle, met by compressed atomizing gas, and atomized due to the high frictional forces between the two mixing fluids. Pneumatic atomizers are known for their ease of operation, good control over resulting particle size, applicability to different types of feedstocks, and wide range of throughput, all of which characteristics make them suitable for various applications from lab-scale research to industrial mass production (Santos et al., 2018). In terms of size coverage, which is a critical specification for atomizers, pneumatic nozzles can usually produce droplets in the 5–200  $\mu\text{m}$  diameter range. The exact droplet size distribution for each atomizer can be affected by multiple parameters including the atomizer design, feedstock properties, and liquid and gas supply rate, etc. (Santos et al., 2018) and therefore needs to be calibrated for a better prediction of the final particle properties (Hoe et al., 2014).

As a rapid process of energy and mass exchange between the atomized droplets and the surrounding drying gas in a controlled environment, the drying process is where the liquid formulation eventually solidifies into solid particles. Many critical parameters are involved in this process

(Baumann et al., 2021). Temperature and vapor activity inside the drying chamber are two of the main parameters that need to be carefully controlled and monitored: the temperature affects the particle formation process and the resultant particle morphology and structure, while vapor activities can have a major impact on the long-term physicochemical stability of the final powder product (Carrigy and Vehring, 2019). Thermodynamic modeling of the drying process has been used to predict the outlet temperature and relative humidity for different inlet conditions (Carrigy and Vehring, 2019; Ivey and Vehring, 2010); the concepts underlying this approach can be equally applied to different systems for an expedited formulation and spray drying process development (Carrigy et al., 2018; Wang H. et al., 2020).

A particle separation procedure needs to be implemented to collect dried particles seeded in the drying gas at the end of the drying process. The device most commonly employed for such purposes, the cyclone separator, uses centrifugal forces to collect particles from the gas flow supplied into a cylindrical chamber tangentially (Baumann et al., 2021). Fine particles smaller than the cut-off aerodynamic diameter of a specific cyclone operated at the corresponding gas flow rate will be expelled from the cyclone in an inner counterflow vortex to the exhaust, while larger particles will be collected (Santos et al., 2018). Bag filters based on fabric filtration technologies are another particle separation method used extensively in spray drying processes and feature high collection efficiency even for submicron particles, especially when a series of filters with gradually downsized pores are used (Cal and Sollohub, 2010). Other techniques such as scrubbers and electrostatic precipitators are also used for particle collection in various spray drying applications (Dobrowolski et al., 2018).

The initial studies and research on new formulations are frequently performed on small-scale or laboratory-scale spray dryers, which, compared to pilot-scale and production-scale dryers, generally have lower production rates and yields due to their smaller drying chambers and smaller production batches (Poozesh and Bilgili, 2019). The transition to larger dryers requires an informed methodology development that involves process scale-up, relating to the thermodynamic aspects, and formulation scale-up, relating to the particle formation mechanisms (Gil et al., 2010).

### 3. Particle formation theory

#### 3.1 Generation of solid particles during solvent evaporation

The primary size distribution of spray-dried particles is an important parameter that should be considered carefully during process and formulation design in accordance with the intended application of the powder. For example, for oral lung delivery it is customary to spray dry particles with aerodynamic diameters in the range of one to five

micrometers (Dabbagh et al., 2018; El-Gendy et al., 2011), whereas larger particles are acceptable for nasal (Calmet et al., 2019; Kiaee et al., 2018) and other routes of delivery (Ferreira et al., 2020; LeClair et al., 2018). Assuming they are roughly spherical in shape, the mass median aerodynamic diameter (MMAD) of the spray-dried particles can be approximated by Vehring (2008)

$$\text{MMAD} = \text{MMD}_0 \sqrt[6]{\frac{\rho_p}{\rho^*}} \sqrt[3]{\frac{C_F}{\rho^*}} \quad (2)$$

Here  $\text{MMD}_0$ , a process parameter, is the mass median diameter of the atomized droplets (equal to the initial droplet diameter,  $d_0$ , for monodisperse sprays), which is a function of atomization parameters such as the atomizing pressure and the liquid feed flow rate for a twin-fluid atomizer (Hoe et al., 2014; Ivey et al., 2018);  $\rho_p$  and  $\rho^*$  are the density of the solid particles and the reference density of 1 mg/mL, respectively; and  $C_F$  is the total feed concentration, a formulation parameter. It is evident from Eqn. (2) that the size distribution of the dried particles is strongly influenced by the atomized droplet distribution, with weaker sensitivity to the other variables, such as the commonly unknown particle density for which only a rough estimate is required due to the sixth root dependence. This relatively simple but practical equation does not describe the internal distribution of different components and does not consider their instants of solidification, for which the diffusion equations inside the evaporating droplets need to be solved (Gac, 2022).

Upon atomization into the drying chamber, the droplets may cool down or heat up depending on the initial feed temperature and the wet-bulb temperature of the solvent system (Chen X.D., 2008), with possible collision and coalescence of the droplets (Boel et al., 2020). After the brief initial transient stage, the temperature and evaporation rate of each droplet are stabilized and the constant-rate drying starts based on the  $d^2$ -law (Baumann et al., 2021; Vehring et al., 2007). The recession of the droplet surface due to rapid evaporation causes the concentration of solutes to rise near the surface. This induced concentration gradient causes a radially inward movement of the solutes in accordance with Fick's law of diffusion. The constant-rate evaporation continues until the start of solidification, when the solvent can no longer evaporate unhindered. At this point, the temperature inside the droplet rises rapidly based on the local temperature and vapor activity inside the drying chamber, and solidification is completed with further loss of the solvent. The actual shape and morphology of the final dried product are related mostly to the rheological and physical properties of the solids, the process conditions, and the solvent system, which, in some cases, can cause inflation, deflation, or rupture of the particles (Baumann et al., 2021; Ordoubadi et al., 2021b; Vehring, 2008; Walton, 2000).

The mass transfer equations governing the diffusion

of solutes can only be solved straightforwardly for the constant-rate portion of the droplet drying. The mass transfer in the initial transient stage requires a full numerical simulation (Ordoubadi et al., 2019), while the modeling of the hindered evaporation of water due to the semi-solid crust on the surface during the later stages of solidification is generally impractical and also requires computational analysis (Mezhericher et al., 2008; 2010). It can be assumed that the initial transient stage is only a small fraction of the total drying time because of the very small size of the atomized droplets and the high heat diffusivity of the solution. Furthermore, during the formulation design, the main objective is to uncover the component that solidifies first, not the exact kinetics of the subsequent crystallization or glass formation. Therefore, the solution of the mass transfer equations during the constant-rate evaporation period is essential during formulation design and will be discussed next.

### 3.2 Diffusion inside evaporating droplets

As previously explained, the rapid evaporation of the solvents causes surface accumulation of solutes which in turn results in solute diffusion from the surface towards the center (Boraey and Vehring, 2014; Nandiyanto and Okuyama, 2011). Because of the small size of the droplets, it can be assumed that during the constant-rate evaporation stage the droplets are already moving with minimal relative velocity with respect to the drying medium, and the effects of shear stresses on the internal convective circulation can be neglected. Therefore, the mass transfer equations can be solved in a spherically symmetric manner in the radial direction only (Ordoubadi et al., 2019). Based on this assumption, the governing mass transfer equation for solute  $i$  inside an evaporating droplet is as follows:

$$\frac{\partial C_i}{\partial t} = \frac{4D_i}{d^2} \left( \frac{\partial^2 C_i}{\partial R^2} + \frac{2}{R} \frac{\partial C_i}{\partial R} \right) - \frac{\kappa R}{2d^2} \frac{\partial C_i}{\partial R} \quad (3)$$

where  $C_i$  is the temporal concentration of the solute at the dimensionless radial coordinate  $R = 2r/d$ ,  $r$  is the radial coordinate here, and  $d$  is the time-dependent droplet diameter, while  $D_i$  and  $\kappa$  are the diffusion coefficient of the solute and the evaporation rate of the droplet, respectively. The evaporation rate is a measure of the rate of the decrease of the droplet surface area or

$$\kappa = -\frac{dd^2}{dt} \quad (4)$$

The parabolic partial differential equation for the mass diffusion (Eqn. (3)) can be solved numerically through integration in time using the initial condition  $C_i = C_{0,i}$  and boundary conditions  $\partial C_i / \partial R = 0$  at  $R = 0$  and  $D_i \partial C_i / \partial R - (\kappa / 8) C_i = 0$  at  $R = 1$  (Ordoubadi et al., 2019). Here,  $C_{0,i}$  is the initial concentration of the solute  $i$  in the feed solution. The solution of Eqn. (3) for each solute gives the concen-

tration of that component for each instance and at each radial location that can be used to predict their moments of solidification.

The behavior of different components under different drying conditions was previously quantified by the Péclet number as defined below (Vehring et al., 2007):

$$Pe_i = \frac{\kappa}{8D_i} \quad (5)$$

This dimensionless number illustrates the relative significance of the recession of the droplet surface due to evaporation and the diffusion of the solutes. A very large Péclet number ( $Pe_i \gg 1$ ) means that the evaporation rate is so rapid that the solute molecules do not have enough time to diffuse towards the center and the result will be a very sharp concentration gradient near the surface, with the interior concentration values being close to the initial mean concentration for most of the evaporation period. A small Péclet number ( $Pe_i \ll 1$ ) denotes the fact that the evaporation is slow and the solute molecules can freely diffuse away from the interface, resulting in a rather constant radial distribution, approximately equal to the bulk concentration, that increases with time due to the decrease of the droplet volume. For a moderate Péclet number ( $0.1 \leq Pe_i \leq 20$ ) there will be a smooth transition from a maximum concentration on the surface to a minimum at the center of the droplet. These three different conditions are shown schematically in Fig. 5. This discussion of the internal diffusion based on Eqn. (3) is true for non-surface-active components in molecular form. In the case of surface-active materials, Eqn. (3) needs to be modified to account for surface adsorption (Ordoubadi et al., 2021a; 2021c).

Spray drying at high Péclet numbers usually results in hollow particles such as those of polysaccharides, proteins, and other macromolecules (Bin Karim et al., 2021; Carrigy et al., 2019c; Hu et al., 2017; Shepard et al., 2021), while spray drying at low Péclet numbers usually results in solid spherical particles, such as spray-dried trehalose (Mah et al., 2019; Ordoubadi et al., 2019) and lactose particles (Wu L. et al., 2014). Besides the Péclet number, the moment and mechanism of phase separation and solidification also play an important role in the final morphology of the dried

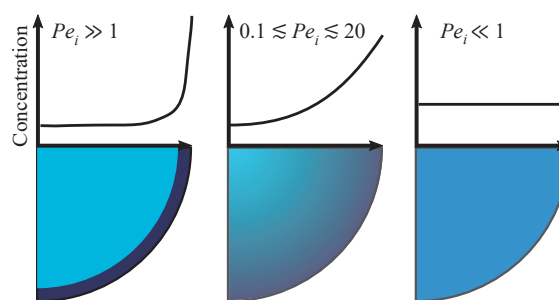


Fig. 5 The effect of the Péclet number on the internal solute distribution during droplet evaporation at a specific time.

particles, as will be discussed later.

During the formulation design of multicomponent systems, especially amorphous solid dispersions and glass stabilized systems, special attention should be paid to the Péclet numbers of individual solutes, since a very large difference in their interior distribution might result in separate solidification of each component as opposed to co-amorphization into a uniform glassy matrix (Carrigy et al., 2019c; Li N. et al., 2020; Ousset et al., 2018).

As mentioned before, regardless of the Péclet number, each solute will have a maximum concentration near the droplet surface. Hence, it has been customary to provide solutions to the diffusion equations in the form of the surface enrichment,  $E_{s,i}$ , defined as the surface concentration,  $C_{s,i}$ , divided by the mean concentration of that solute inside the droplet,  $C_{m,i}$ . Generally, the surface and mean concentrations change with time, while the surface enrichment asymptotically converges to a constant steady-state value,  $E_{ss,i}$ , during the constant-rate drying period. This asymptotic value can be approximated for different Péclet number regimes as (Boraey and Vehring, 2014)

$$E_{ss,i} = \frac{C_{s,i}}{C_{m,i}} \approx \begin{cases} \text{If } Pe_i < 20: & 1 + Pe_i / 5 + Pe_i^2 / 100 - Pe_i^3 / 4000 \\ \text{If } Pe_i \geq 20: & Pe_i / 3 + 0.363 \end{cases} \quad (6)$$

It has previously been shown that for Péclet numbers larger than 0.5 the time to reach steady-state surface enrichment might be a significant portion of the total droplet drying time,  $t_d$  (Boraey and Vehring, 2014). Therefore, for these conditions ( $Pe_i > 0.5$ ) the transient evolution of the surface enrichment needs to be approximated to accurately predict the diffusion-controlled particle formation during spray drying. Through correlation to numerical data, cer-

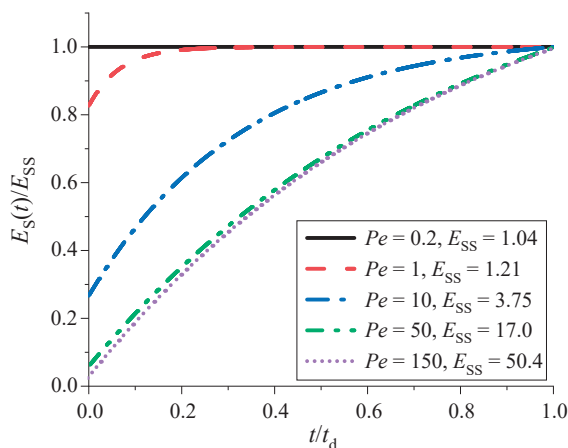


**Fig. 6** The time evolution of surface enrichment,  $E_s(t)$ , normalized by the steady-state surface enrichment,  $E_{ss}$  (Eqn. (6)), versus the normalized time for different Péclet numbers, obtained from the correlations given in Eqn. (7). Here,  $t_d = d_0^2 / \kappa$  is the droplet drying time.

tain relationships have been suggested as a way to estimate the transient surface enrichment of solutes,  $E_{s,i}(t)$ , during droplet evaporation as shown below (Boraey and Vehring, 2014):

$$E_{s,i}(t) = \frac{C_{s,i}(t)}{C_{m,i}(t)} \approx \begin{cases} \text{If } Pe_i < 0.5: & E_{ss,i} \\ \text{If } 0.5 < Pe_i < 25: & \frac{E_{ss,i} - \exp(-n_1)}{1 - \exp(-n_1)} - \frac{E_{ss,i} - 1}{1 - \exp(-n_1)} \exp(-n_1 t / t_d) \\ \text{If } 25 < Pe_i < 200: & \frac{E_{75,i} - \exp(-n_2)}{1 - \exp(-n_2)} - \frac{E_{75,i} - 1}{1 - \exp(-n_2)} \exp(-n_2 4t / 3t_d) \end{cases} \quad (7)$$

Here  $n_1 = 15Pe_i^{-0.7}$ ,  $n_2 = 0.95$ ,  $E_{75,i} = 0.858E_{ss,i}$ , and  $t_d = d_0^2 / \kappa$  is the droplet drying time based on the constant-evaporation assumption, while  $d_0$  is the initial droplet diameter and  $\kappa$  is the evaporation rate defined in Eqn. (4) and provided for some of the solvents in Fig. 7. The relationships in Eqn. (7) can be used for Péclet numbers ranging from zero to two hundred, which span a broad array of conditions for spray drying applications ranging from small molecules to large suspended nanodroplets. For example, the Péclet numbers of trehalose dissolved in water (an example of a small-molecule excipient or active) and an aqueous nanoemulsion with an average droplet size of 100 nm (an example of a very large aggregate or

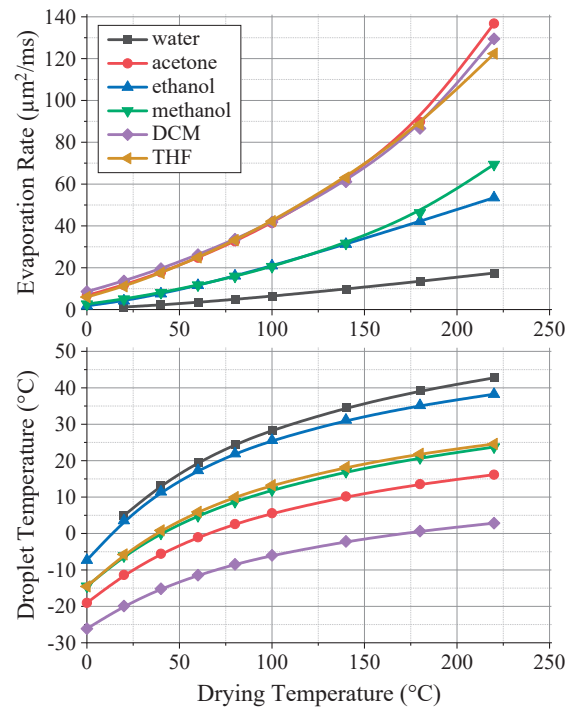


**Fig. 7** The evaporation rates and droplet temperatures of several solvents frequently used in pharmaceutical spray drying at different drying temperatures. The values were calculated using a full numerical model.

biologic) both drying at a temperature of 100 °C (in a typical range of drying temperatures for the spray drying of pharmaceutical particles) are 1.25 and 153, respectively. These numbers were calculated using Eqn. (5); the numerical values for the evaporation rate and diffusion coefficients will be discussed in the next two subsections.

The evolution of surface enrichment with time for a range of Péclet numbers is shown in Fig. 6. It is apparent from these profiles that for larger Péclet numbers corresponding to the spray drying of larger solutes or at higher temperatures, the transient behavior of surface enrichment is more significant than for smaller Péclet numbers. For such conditions, the use of the correlations given in Eqn. (7) is the most accessible and practical method for approximating the surface concentration of each solute.

After the calculation of surface enrichment with the help of Eqn. (7), the actual surface concentration of each solute at each time,  $C_{s,i}(t)$ , can be obtained from

$$C_{s,i}(t) = E_{s,i}(t)C_{m,i}(t) \quad (8)$$

in which  $C_{m,i}(t)$  is the mean concentration of solute  $i$  inside the droplet, which can be obtained from a mass balance equation compared to the initial state of the atomized droplet as follows:

$$C_{m,i}(t) = C_{0,i} \left(1 - \frac{t}{t_d}\right)^{-3/2} \quad (9)$$

Here,  $C_{0,i}$  is the initial feed concentration of solute  $i$  and, as mentioned before,  $t_d = d_0^2 / \kappa$  is the drying time of the droplet assuming a constant evaporation rate.

During the actual formulation design, the surface concentration of all excipients and actives can be calculated for  $0 \leq t \leq t_d$  and compared to their respective solidification thresholds to determine which component is expected to precipitate first, as will be discussed in later sections.

### 3.3 Evaporation rates

As seen in Eqn. (3), the evaporation rate of the droplets is one of the determining factors of particle formation and solidification. For single-solvent systems, the evaporation rate can be assumed to be constant throughout the drying stage, neglecting the initial stabilization of the droplet temperature and the final decrease due to solute enrichment (Boel et al., 2020). On the other hand, solvent composition and evaporation rate vary with time for multi-solvent systems due to the different volatility of the solvents and any non-ideal effects (Ordoubadi et al., 2019). For this reason, the evaporation rates of multi-solvent systems should be predicted using full numerical methods and algorithms as explained elsewhere (Ordoubadi et al., 2019). In this subsection, the evaporation rates and the droplet temperatures of some of the solvents most frequently used in the spray drying of pharmaceuticals and biologics are presented. To this end, a numerical model, verified and

validated previously (Gregson et al., 2019; Ordoubadi et al., 2019), was used to calculate the evaporation behaviors of microdroplets composed of water, acetone, ethanol, methanol, dichloromethane (DCM), and tetrahydrofuran (THF). The evaporation rates, defined as  $-dd^2/dt$ , and the droplet temperatures of these solvents drying at different drying temperatures and zero vapor activity (dry condition) are shown in Fig. 7. The equilibrium droplet temperature, which is close to the wet-bulb temperature, is important in determining the temperature-dependent properties of the solutes, such as the diffusivity coefficient and the solubility. This temperature is also of significance in choosing the optimal process conditions so as not to subject temperature-sensitive biologics to conditions outside of their tolerance. The drying temperature can be conservatively approximated as the inlet temperature of the spray dryer, even though the actual temperatures and vapor activities in the vicinity of a spray plume inside a spray dryer vary significantly and are generally unknown for all the possible processing conditions (Longest et al., 2020). It can be seen from Fig. 7 that the equilibrium temperatures of these solvents drying at temperatures as hot as 200 °C barely reach 40 °C, pointing to the inherent advantage of the spray drying process in protecting sensitive molecules and biological entities from elevated temperatures due to the evaporative cooling effect.

### 3.4 The diffusion coefficients

In the absence of any experimental data for the diffusion coefficients of the solutes in the solvent of interest, which is usually the case for newly discovered drugs or biologics, the Stokes-Einstein equation can be used as an approximation, as shown below (Bird et al., 2006; Zmpitas and Gross, 2021),

$$D_{i,j} = \frac{k_B T_d}{3\pi\mu_j d_i} \quad (10)$$

where  $D_{i,j}$  is the diffusion coefficient of solute  $i$  in solvent  $j$  at infinite dilution,  $k_B \cong 1.38 \times 10^{-23} \text{ m}^2 \cdot \text{kg} \cdot \text{s}^{-2} \cdot \text{K}^{-1}$  is the Boltzmann constant,  $T_d$  is the droplet temperature in Kelvin, which can be obtained from Fig. 7,  $\mu_j$  is the dynamic viscosity of the solvent at the droplet temperature in Pa·s, presented in Fig. 8, and  $d_i$  is the hydrodynamic spherical diameter of the molecule or particle of interest in m obtained from  $\sqrt[3]{6V_i / \pi}$ . Here,  $V_i$  is the molecular volume in  $\text{m}^3$  that can be obtained via different methods (Bird et al., 2006; Edward, 1970; Kooijman, 2002; Zmpitas and Gross, 2021), for example, by using the Van der Waals volumes obtained from the atomic and group incremental volumes (Blokhina et al., 2017; Bondi, 1964; Edward, 1970). The hydrodynamic diameters of some of the excipients and APIs used in the formulation of pharmaceutical solid particles were calculated based on their Van der Waals volumes (Edward, 1970) and are presented in Table 1. The

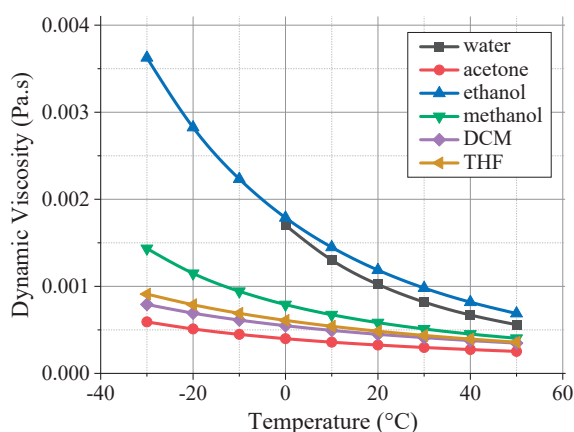


**Fig. 8** The dynamic viscosity values of several solvents frequently used in pharmaceutical spray drying at different droplet temperatures (Yaws, 2010).

**Table 1** The hydrodynamic diameters of some small-molecule excipients and actives typically used in the formulation of spray-dried particles as obtained from their approximate Van der Waals volumes.

Molecule	Hydrodynamic Diameter (nm)
Lactose/Trehalose/Sucrose	0.82
Mannitol	0.68
Raffinose	0.93
Leucine	0.64
Trileucine	0.89
Glycine	0.51
DSPC	1.17
DPPC	1.14
Salmeterol	0.93
Fluticasone	0.90
Beclometasone	0.97
Salbutamol	0.77
Formoterol	0.85
Budesonide	0.92
Vilanterol	0.94
Etravirine	0.86

molecular volumes of these compounds were determined based on their neutral and anhydrous forms.

The Stokes-Einstein equation should be used with the knowledge that it gives accurate results only for dilute solutions and for solute molecules that are relatively spherical and much larger than the solvent molecules. The concentration-dependency of the diffusion coefficient becomes significant only near the end of droplet evaporation and hence can be neglected for practical uses of particle formation theory. It should be noted that the use of the

molecular diameters in Eqn. (10) is not reasonable when the solutes are not in molecular solution form. For example, when the solutes or actives are present in the form of liposomes, micelles, emulsions, nanoparticles, or nanocrystals, the approximate size of these larger aggregates should be used to estimate their diffusion and surface enrichment inside the evaporating droplets.

The use of atomic and group contribution methods in determining the size of macromolecules, such as proteins and polymers, is not straightforward. For such compounds, the use of available correlations and relationships of molecular volume versus molar mass is recommended. For example, the following correlation was obtained via nano-electrospray gas-phase electrophoretic mobility molecular analysis for proteins (Weiss et al., 2018):

$$d_{\text{prt}} = 1.61(M_{\text{prt}})^{0.343} \quad (11)$$

Here,  $d_{\text{prt}}$  is the molecular diameter of a protein in nm and  $M_{\text{prt}}$  is the molar mass in kDa.

### 3.5 The onset of solidification or crystallization

The solution of the mass transfer equations inside an evaporating droplet results in the concentration of each component at different times at each radial coordinate, but as soon as one of the components starts to solidify, either due to crystallization or amorphous phase separation, the concentrations are suspected to change rapidly. This is because the evaporation rate is expected to decrease upon shell formation (Boel et al., 2020) and the local sites of solidification can act as source points that result in concentration profiles with sharp gradients (Douglass and Harrowell, 2018; Fukui and Maeda, 1998) unlike those predicted by Eqn. (3). Based on these complications, one straightforward method of predicting the surface composition of the spray-dried particles is to determine which component solidifies first and assume that this solute will have the highest amount of surface coverage on the final particles. To this end, the time evolution of surface concentrations of all solutes can be compared to a critical concentration for each material. Once this concentration is reached the solidification is expected to commence for that solute. The compound that reaches its critical concentration earlier than the other solutes is then expected to be the dominant component on the surface of the particles. The exact prediction of the actual surface compositions is complicated and requires knowledge of the phase diagram of the system including all of the solutes and solvents, which is difficult to obtain for newly discovered drugs and biologics.

The estimation of the solidification thresholds depends on the ability of the material to form a crystal or glass during drying; hence, APIs and excipients can be characterized by their tendency to crystallize during spray drying. The crystallization tendency is related to many factors, including glass transition and melting temperatures,

solubility, the solvent system used, processing conditions, molecular size, and crystal structure (Kawakami, 2019); hence, the prediction of the final solid phase of spray-dried material is complicated. In the absence of any literature data, the ability of a material to crystallize during spray drying can be measured via powder X-ray diffraction or Raman spectroscopy on an initial spray-dried batch of the excipient or active of interest during the early stages of formulation development.

The critical concentrations that can be used as a threshold to compare with the instantaneous solute concentrations depend on the predicted mechanism of solidification or dissolution as will be explained below.

### 3.5.1 Crystallizing compounds

For crystallizing compounds, crystalline solubility has frequently been regarded as the concentration after which nucleation and crystal growth commence (Vehring, 2008). However, based on the classical nucleation theory, a certain level of supersaturation is required for any system to undergo crystal growth due to the nucleation barrier (Karthika et al., 2016). When the concentrations are increased above this minimum supersaturated value, the time of nucleation decreases until crystallization can be assumed to be instantaneous (He G. et al., 2006). Considering the very high rate of the evaporation of droplets during spray drying, this critical supersaturated concentration, rather than the solubility, can be deemed a threshold of nucleation and crystal growth in the formulation design of spray-dried particles (Ordoubadi et al., 2021b; Z. Wang Z. et al., 2021a).

By measuring the nucleation times of a variety of materials dissolved in several evaporating microdroplets at different conditions, He et al. proposed a semi-analytical method of calculating the critical supersaturation ratio at which nucleation would be instantaneous (He G. et al., 2006). Such methods still require the measurement or approximation of certain properties that are not readily available, such as the water activity coefficient at saturation. Hence, the actual crystalline solubility can still be used as a first approximation in the particle formation models in the absence of these data.

### 3.5.2 Glass formers

Most of the newly discovered drugs and biologics do not crystallize during spray drying but instead phase separate into glasses or amorphous materials (Baumann et al., 2021; Wang B. et al., 2021). The precipitation of a material into an amorphous state rather than a crystalline form takes place when the metastable region (between the crystalline solubility and spinodal curves) is traversed fast enough not to permit nucleation and growth (Zallen, 1998). Shown schematically in Fig. 9, this phenomenon starts immediately after atomization from the initial solute concentration,  $C_0$ , at the droplet temperature,  $T_d$ , and moves isothermally

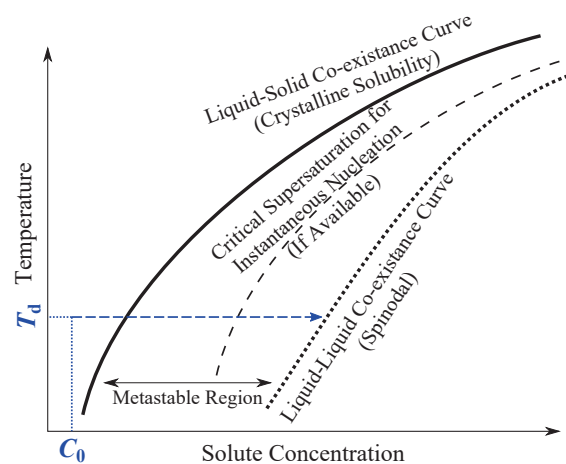


Fig. 9 Phase diagram of a compound and the isothermal route it takes from atomization to glass formation.

into the supersaturated and unstable regions due to evaporation. Note that the initial temperature stabilization of the droplet is ignored in this figure. Upon reaching the spinodal point, precipitation commences based on glass-liquid phase separation (solute-rich glass and solvent-rich liquid) or liquid-liquid phase separation (solute-rich gel and solvent-rich liquid) depending on the plasticization behavior of the system (Douglass and Harrowell, 2019). At this point, the droplet temperature increases due to the decrease in evaporation rate, and eventually the solid particle forms, making a mixture with the remaining residual solvent (Charlesworth and Marshall, 1960).

The presence of multiple glass-forming compounds in the formulation introduces complexities that require multi-phase analysis to model the co-amorphization of all components in a manner similar to the studies conducted for the preparation of amorphous solid dispersions (Davis et al., 2017; Ziaee et al., 2017). For simplicity, during the early stages of formulation design of such systems, it can be assumed that each solute precipitates in the solvent system independently, with the effects of the other components being neglected.

Particle engineers and formulators can use the concept of amorphous solubility for each glass former in the system to determine which component precipitates first. Compared to crystalline solubility, the amorphous solubility, especially of small molecules, is more difficult to determine experimentally because of the precipitation of the excess dissolved material as crystals (Douglass and Harrowell, 2018). Based on thermodynamic considerations, the amorphous solubility of a material,  $C_a$ , at temperature  $T$  can be obtained from its crystalline solubility,  $C_c$ , using Eqn. (12) (Almeida E Sousa et al., 2015; Ilevbare and Taylor, 2013),

$$C_a = C_c \cdot \exp[-I(a_2)] \cdot \exp\left(\frac{\Delta G_{a-c}}{RT}\right) \quad (12)$$

where  $\Delta G_{a-c}$  is the difference in free energy of crystalline



and amorphous states,  $I(a_2)$  is related to the activity of the amorphous state saturated with the solvent, and  $R$  is the universal gas constant. The free energy difference can be obtained from (Almeida E Sousa et al., 2015; Hoffman, 1958),

$$\Delta G_{a-c} = \frac{\Delta_f H \cdot (T_m - T) \cdot T}{T_m^2} \quad (13)$$

in which  $\Delta_f H$  is the enthalpy of melting and  $T_m$  is the melting temperature of the crystal, both of which are obtainable from differential scanning calorimetry (DSC). The activity term,  $I(a_2)$ , can be obtained from the integration of the water sorption isotherm of the amorphous solid, which can itself be obtained from dynamic vapor sorption (DVS) measurements as explained in the literature (Murdande et al., 2010).

Alternatively, the instant of phase separation of glass formers in evaporating microdroplets can be directly measured via single-particle measurements, as was previously done for trehalose (Ordoubadi et al., 2021b).

### 3.5.3 Surface-active compounds

Some excipients and biopharmaceutical actives are amphiphilic, meaning that they possess a hydrophobic tail as well as a hydrophilic head group, making them a surface-active agent, or simply a surfactant, with a tendency to be adsorbed on air-water interfaces (Rosen and Kunjappu, 2012). This adsorption on the interface is observed macroscopically via the decrease in surface tension of the solution. During spray drying and droplet shrinkage, the internal diffusion of surface-active materials is different from that shown in Eqn. (3) for non-surface-active solutes. The exact mechanisms of particle formation and diffusion of surface-active molecules have been discussed previously (Ordoubadi et al., 2021a). In short, immediately after atomization, the surface of the droplets acts as a sink for such molecules. These molecules are then adsorbed into a monolayer on the interface causing a drop in local free concentration underneath the surface. This decrease in solution concentration causes an outward radial flux of the surface-active molecules towards the interface. The surface adsorption continues until the monolayer becomes saturated with these molecules, after which further evaporation might cause the adsorbed molecules to dissolve back into the solution to maintain stability.

For surface-active excipients or APIs, the time to form a saturated monolayer on the surface can be counted a design criterion and compared to the precipitation thresholds of other components. This is because a surface-active dispersibility enhancer needs to make a saturated monolayer on the surface before the precipitation of other components so that the final dried particle will contain a fully packed hydrophobic shell. This shell can potentially decrease the surface energy of the particles and possibly

result in wrinkled surfaces, which would in turn improve aerosol properties (Mangal et al., 2015; 2019; Wang H. et al., 2019). It should be noted that besides making the monolayer, the surface-active molecules will eventually either crystallize or phase separate into a glass based on the previous discussions. For example, trileucine is expected to make a monolayer first and then solidify into an amorphous material at a later stage during droplet evaporation (Ordoubadi et al., 2021a).

The surface adsorption of surface-active compounds is kinetically controlled by two sequential phenomena: 1) diffusion of the molecules towards the surface, and 2) adsorption and reconfiguration of the molecules into the monolayer (Eastoe and Dalton, 2000; Jayasundera et al., 2009). Hence, the calculation of the instant of monolayer formation on the surface of a droplet is related to the diffusion coefficient of the surface-active compound, its maximum surface excess concentration,  $\Gamma_{max}$ , and its size and complexity. The maximum surface excess concentration, with the dimension of  $\text{kg/m}^2$  or  $\text{mol/m}^2$ , is the maximum amount of surfactant molecules that can become adsorbed on an interface and is a measure of surface activity (Rosen and Kunjappu, 2012). This property can be obtained from static surface tension measurements at different solute concentrations. Such a measurement, usually done using Wilhelmy plate, du Nouy ring, or pendant drop techniques results in a correlation between the static surface tension,  $\sigma$ , and the solute bulk concentration,  $C_b$  (Ebnesajjad, 2011). By fitting an appropriate empirical isotherm to this data, the maximum surface excess concentration of each solute can be determined. For example,  $\Gamma_{max}$  in conjunction with the Langmuir adsorption constant,  $K_L$ , are the two fit parameters in the Szyszkowski surface equation of state as seen below (Eastoe and Dalton, 2000):

$$\sigma = \sigma_0 - nRT\Gamma_{max} \ln(1 + K_L C_b) \quad (14)$$

Here,  $n$  is equal to 1 for non-ionic or zwitterionic solutes and is equal to 2 for one-by-one ionic solutes, while  $R$  is the Universal gas constant,  $T$  is the solution temperature in Kelvin,  $\sigma$  is the surface tension in  $\text{N/m}$ , and  $\sigma_0$  is the static surface tension of the solvent in the absence of any solutes. The maximum surface tension obtained directly from fitting Eqn. (14) to surface tension measurements has a unit of  $\text{mol/m}^2$  that can be simply converted to other units such as  $\text{mg/m}^2$  using the molar mass of the solute molecules. A typical surface tension measurement with a Szyszkowski fit to determine the maximum surface excess concentration is shown in Fig. 10. The critical micelle concentration (CMC) shown in this figure is a property of surfactant solutions and is the concentration above which no further decrease in surface tension is possible due to the formation of micelles.

As an example, and based on available tensiometry data at 25 °C (Gliński et al., 2000; Lechuga-Ballesteros et

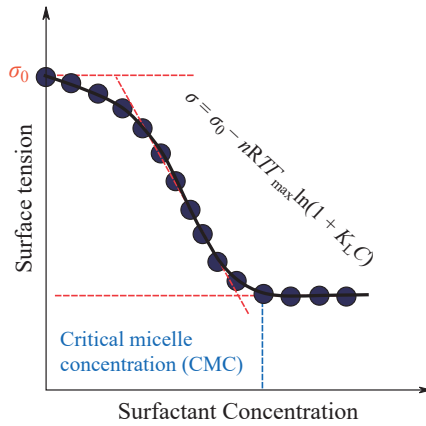


**Fig. 10** A characteristic surface tension-versus-concentration measurement and a fit based on the Szyszkowski equation of state to determine the maximum surface excess,  $\Gamma_{\max}$ .

al., 2008), the maximum surface excess concentrations of trileucine and leucine were approximated to be 0.99 and 0.15 mg/m<sup>2</sup>, respectively. These numbers partially explain the better shell-forming capabilities of trileucine compared to leucine (Ordoubadi et al., 2021a; 2021b).

Assuming that the incorporation of the surface-active molecules into the monolayer occurs instantaneously (diffusion-controlled process), the time required to saturate a semi-infinite surface,  $t_{\Gamma,i}$ , was calculated to be (He Y. et al., 2015; Ward and Tordai, 1946)

$$t_{\Gamma,i} = \frac{\pi \Gamma_{\max,i}^2}{4D_i C_{b,i}^2} \quad (15)$$

where  $\Gamma_{\max,i}^2$ ,  $D_i$ , and  $C_{b,i}$  are the maximum surface excess concentration of the surface-active solute  $i$ , its diffusion coefficient, and its bulk concentration, respectively. This rough estimate for the time to monolayer formation was used previously to explain the particle formation of spray-dried formulations containing surface-active components (Adler and Lee, 1999; Kawakami et al., 2010; Landström et al., 2000) and can be used in the formulation design of such systems. The limitations of using this equation are that it does not account for the resistance to surface adsorption due to the already adsorbed molecules, nor does it take into consideration the delay in surface adsorption due to the reorientation of the molecules. Furthermore, as explained previously (Ordoubadi et al., 2021a), this simplified method cannot model the increase in solute bulk concentration during droplet evaporation or the possible depletion of the molecules for very small droplets. Regardless of these shortcomings, the use of Eqn. (15) is simple and practical for most formulation design applications.

### 3.5.4 Nanostructures

Research into the inclusion of nanostructures in spray-dried solid powders has grown in the last couple of decades (Johnson et al., 2020; Malamatarı et al., 2020). This kind

of formulation is possible through the preparation of a feed nanoemulsion or nanosuspension by dispersing liposomes (Maniyar and Kokare, 2019), nanodroplets (Gomez et al., 2019), nanoparticles (Tsapis et al., 2002; 2005), and other forms of immiscible nanostructures (Malamatarı et al., 2020; Saallah and Lenggoro, 2018; Wang Z. et al., 2022). For such structures, the instant of close packing on the surface becomes the critical point during the drying stage since this is the point at which a shell can begin to form as these nanostructures come into close contact with each other. What happens after this point depends mostly on the interfacial forces between these nanostructures: the shell either collapses or maintains its rigidity and forms a hollow sphere (Ahumada-Lazo and Chen, 2022; Bahadur et al., 2011; Minoshima et al., 2001). The time of this close packing is important during the formulation design, regardless of what ensues afterward. As an example, a shell-forming excipient acts best if it makes a shell before the nanodroplets containing a biological entity do. To this end, the critical time of close packing for nanostructures can be calculated assuming a critical volume fraction of ~0.6 (Ahumada-Lazo and Chen, 2022; Minoshima et al., 2001). This value can be converted to mass fraction to result in a critical surface value for shell formation,  $Y_{nc}$ , as

$$Y_{nc} = \frac{3\rho_{liq}}{2\rho_n + 3\rho_{liq}} \quad (16)$$

where  $\rho_{liq}$  and  $\rho_n$  are the density values of the liquid feed and nanostructures, respectively. The critical concentration,  $C_{nc}$ , in mg/mL, can then be obtained from

$$C_{nc} = Y_{nc} \left( \frac{Y_{nc}}{\rho_n} + \frac{1 - Y_{nc}}{\rho_{liq}} \right)^{-1} \quad (17)$$

Here the densities should have the same units as the concentration. The surface concentration of the nanostructures obtained from Eqn. (7) can then be compared to this critical value to obtain their time of shell formation, while their average diameter can be used in Eqn. (10) to find their diffusion coefficient.

## 4. The characterization techniques

As mentioned previously, the sample spray-dried powders need to be characterized to be assessed against certain predefined criteria. Depending on the specific formulation, these assessments might include both physical and chemical characterizations such as size distribution, morphology, solid phase, bulk density, and composition (Barona et al., 2021; Frank et al., 2022; Mangal et al., 2019; Nicholas et al., 2020). Some of the physical characterization techniques will be reviewed here.

### 4.1 Morphology characterization

Frequently, the morphology of the spray-dried powders is the first factor to be studied. By looking at the

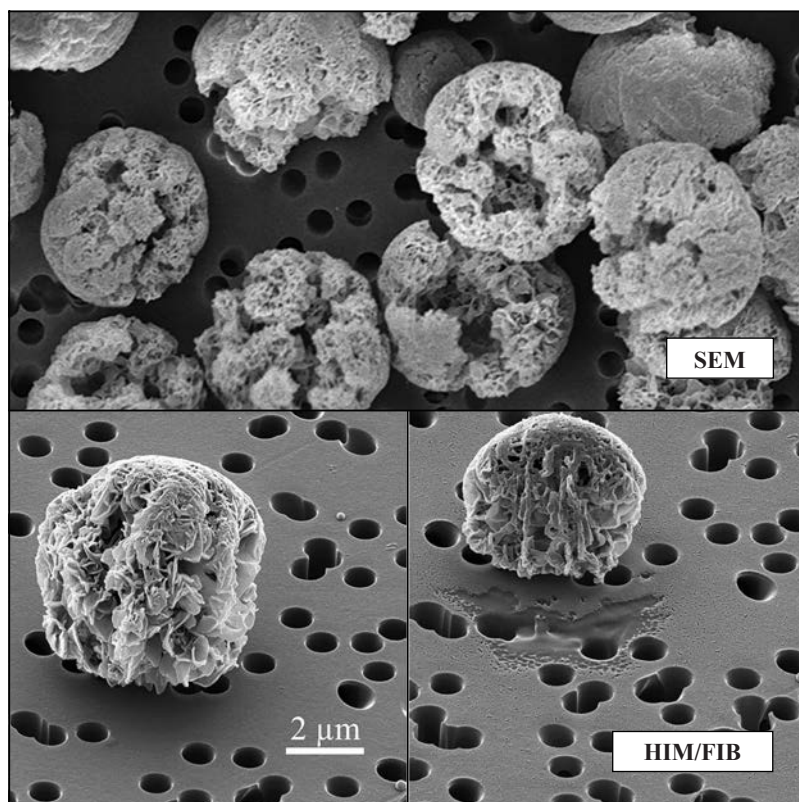


**Fig. 11** Scanning electron microscopy (SEM) and helium ion microscopy (HIM) micrographs of leucine particles collected from a monodisperse droplet chain instrument (Ordoubadi et al., 2019). The particle at the bottom was also cut using focused ion beam (FIB) milling to study the interior morphology. All micrographs are reproduced with the permission of Springer Publishing.

micrographs of the particles, for example, one can determine qualitatively if the product is dispersible or flowable based on the surface rugosity; one can also detect individual particles as opposed to an agglomerate of fused particles. The instruments of choice for such observations are scanning electron microscopes (SEMs), which provide a surface topology by scanning the sample with an electron beam. The interaction of the electron beam with the sample results in the scattering and emission of electrons that are then collected on different detectors to result in a micrograph (Leonard et al., 2012). Ion microscopy can also be used in cases where much higher resolutions are required, coating of the samples needs to be avoided, or single particles are to be cut using focused ion beam milling to study the internal morphology (Heng et al., 2007; Ordoubadi et al., 2019). Sample micrographs of some batches of dried particles obtained from these methods are shown in **Fig. 11**.

The rugosity of the spray-dried powders can also be quantified through the measurement of the specific surface area via Brunauer–Emmett–Teller (BET) analysis relative to the geometric specific surface area, as was shown previously (Wang Z. et al., 2022).

#### 4.2 Surface composition characterization

The surface composition of spray-dried engineered particles is critical to the validity of the formulation design.

As an example, a shell former needs to contribute to most of the composition on the surface of spray-dried particles to have maximum benefits, while the valuable payload, whether biologics or APIs, should typically have minimal presence on the surface.

For surface characterization, two kinds of instruments are frequently used for spray-dried microparticles: time-of-flight secondary ion mass spectrometry (ToF-SIMS) and X-ray photoelectron spectroscopy (XPS). Fundamentally, ToF-SIMS detects ion fragments, while XPS is an elemental analysis. Both methods require relatively complicated post-processing procedures for quantification (Mangal et al., 2019; Nicholas et al., 2020; Wu X. et al., 2010); however, compared to XPS analysis, ToF-SIMS has a better lateral resolution and lower analysis depths (~1–3 nm for ToF-SIMS compared to ~5–10 nm for XPS) (Alhadj et al., 2021; Nicholas et al., 2020).

Energy-dispersive X-ray spectroscopy (EDX) has also been used to map the surface elemental compositions of microparticles (Eedara et al., 2016). This elemental method has a typical penetration depth of up to 1 μm, which makes the surface characterization of microparticles more difficult (Alhadj et al., 2021).

#### 4.3 Solid-state characterization

Besides morphology, the solid phase of spray-dried

powders is one of their most important characteristics requiring in-depth study. This is because solid phase properties have substantial effects on the long-term stability of such powders and can also point to instability during storage (Edueng et al., 2019). The methodology most frequently used to assess these properties for spray-dried powders is powder X-ray diffraction (PXRD), which gives crystallinity information for the bulk powder (Bianco et al., 2012; Lu et al., 2019; Shetty et al., 2022). Microcrystals in the samples cause diffraction of an incident X-ray, translating into peaks in the obtained diffractograms that can be used to determine the crystal structure of the known material inside the powder (Brittain, 2003). The quantification of the fractions of different polymorphs is not easily achievable using PXRD, and the diffractograms are frequently used in a qualitative capacity to detect the presence of any crystalline peaks for usually amorphous spray-dried powders (Li L. et al., 2016; Wu L. et al., 2014). However, the detection of crystallinity of a component in the powder might not be possible at all if it has a low fraction in the formulation, as the crystalline peaks can be shadowed behind the stronger amorphous background (Khanal et al., 2022).

Bulk Raman spectroscopy is another analytical tool widely used to assess both the composition and the solid phase of powders that also allows the characterization of individual components through deconvolution of the Raman spectra (Frank et al., 2022; Wang H. et al., 2014). Through careful method development, the fractions of different phases of each component, either crystalline or amorphous, can be quantified with very high sensitivity (Feng et al., 2011; Wang H. et al., 2017).

Other spectroscopic techniques have also been used for the characterization of powders, including solid-state nuclear magnetic resonance (ssNMR) and Fourier-transform infrared spectroscopy (FTIR), both of which produce results complementary to the previously discussed methods (Chang et al., 2020; Chen Y. et al., 2021; French et al., 2004; Suihko et al., 2005).

#### 4.4 Characterization of thermal properties

Thermal properties, such as the wet and dry glass transition temperatures, moisture content, and moisture uptake, are important characteristics of powders that need to be studied to determine the long-term stability of the product. The glass transition temperature, melting point, decomposition point, and other thermal properties of spray-dried powders, all of which directly influence their physical stability, are usually measured via differential scanning calorimetry (DSC) (Clas et al., 1999; Leyva-Porras et al., 2019). Thermogravimetric analysis (TGA) provides complementary information that also includes the quantity of residual solvents and moisture levels (Eedara et al., 2018; Yu et al., 2017).

Moisture absorption is another important property that

quantifies the ability of the dry powder to withstand humid conditions and is frequently measured by dynamic vapor sorption (DVS), which can also be used to indirectly measure the amorphous content of the sample (Sheokand et al., 2014).

The water content of spray-dried powders influences their stability and flowability and needs to be measured during the product characterization, as high water content can decrease the glass transition temperature through plasticization of the amorphous content of the powder (Shepard et al., 2020; Shetty et al., 2018). Karl Fischer titration is usually employed to measure the water content present in the powders either when it remains as residual solvent or is absorbed during storage and handling (Carrigy and Vehring, 2019).

### 5. Summary and conclusions

Spray drying can address many of the current and future challenges in the preparation of solid dosage forms and is the ideal manufacturing process for thermostable global health products. The mechanistic formulation design of spray-dried engineered microparticles is complex, with most of the available particle formation models requiring prior knowledge of the fundamental sciences behind them. Necessary information was provided to make the use of these models more straightforward and also to assist in the selection of appropriate excipients. Using such predictive tools during the early stages of product development can significantly reduce the number of experimental iterations and thus save time and effort. Several challenges remain that require in-depth studies and cannot be predicted via simplified theoretical analysis, such as the exact coprecipitation kinetics of glass mixtures or crystalline components, the final morphology of the particles, or the long-term stability of the product at different storage conditions. These emphasize the need for complementary experimentation.

### References

- Adler M., Lee G., Stability and surface activity of lactate dehydrogenase in spray-dried trehalose, *Journal of Pharmaceutical Sciences*, 88 (1999) 199–208. DOI: 10.1021/js980321x
- Ahumada-Lazo J.A., Chen R., Effects of nanoparticle concentration and Peclet number on nanofluid droplet evaporation behavior, *International Journal of Thermal Sciences*, 178 (2022) 107582. DOI: 10.1016/j.ijthermalsci.2022.107582
- Alhaji N., O'Reilly N.J., Cathcart H., Designing enhanced spray dried particles for inhalation: a review of the impact of excipients and processing parameters on particle properties, *Powder Technology*, 384 (2021) 313–331. DOI: 10.1016/j.powtec.2021.02.031
- Almeida E. Sousa L., Reutzel-Edens S.M., Stephenson G.A., Taylor L.S., Assessment of the amorphous “solubility” of a group of diverse drugs using new experimental and theoretical approaches, *Molecular Pharmaceutics*, 12 (2015) 484–495. DOI: 10.1021/mp500571m
- Bader A., Keller P., Hasse C., The influence of non-ideal

- vapor–liquid equilibrium on the evaporation of ethanol/iso-octane droplets, *International Journal of Heat and Mass Transfer*, 64 (2013) 547–558. DOI: 10.1016/j.ijheatmasstransfer.2013.04.056
- Bahadur J., Sen D., Mazumder S., Bhattacharya S., Frielinghaus H., Goerigk G., Origin of buckling phenomenon during drying of micrometer-sized colloidal droplets, *Langmuir*, 27 (2011) 8404–8414. DOI: 10.1021/la200827n
- Baldelli A., Vehring R., Analysis of cohesion forces between monodisperse microparticles with rough surfaces, *Colloids and Surfaces A: Physicochemical and Engineering Aspects*, 506 (2016) 179–189. DOI: 10.1016/j.colsurfa.2016.06.009
- Barona D., Shamsaddini A., Aisenstat M., Thalberg K., Lechuga-Ballesteros D., Damadzadeh B., Vehring R., Modulated uniaxial compression analysis of respirable pharmaceutical powders, *KONA Powder and Particle Journal*, 38 (2021) 209–225. DOI: 10.14356/kona.2021014
- Baumann J.M., Adam M.S., Wood J.D., Engineering advances in spray drying for pharmaceuticals, *Annual Review of Chemical and Biomolecular Engineering*, 12 (2021) 217–240. DOI: 10.1146/annurev-chembioeng-091720-034106
- Bianco S., Caron V., Tajber L., Corrigan O.I., Nolan L., Hu Y., Healy A.M., Modification of the solid-state nature of sulfathiazole and sulfathiazole sodium by spray drying, *AAPS PharmSciTech*, 13 (2012) 647–660. DOI: 10.1208/s12249-012-9792-5
- Bin Karim S., Ordoubadi M., Wang H., Gomez M., Vehring R., On the feasibility of spray-dried Eudragit-trehalose microparticles for enteric drug delivery, *International Journal of Pharmaceutics*, 610 (2021) 121264. DOI: 10.1016/j.ijpharm.2021.121264
- Bird R.B., Stewart W.E., Lightfoot E.N., *Transport Phenomena*, Revised 2nd Edition, John Wiley & Sons, New York, 2006, ISBN: 978-0-470-11539-8.
- Blokhina S.V., Volkova T.V., Golubev V.A., Perlovich G.L., Understanding of relationship between phospholipid membrane permeability and self-diffusion coefficients of some drugs and biologically active compounds in model solvents, *Molecular Pharmaceutics*, 14 (2017) 3381–3390. DOI: 10.1021/acs.molpharmaceut.7b00401
- Boel E., Koekoekx R., Dedroog S., Babkin I., Vetrano M.R., Clasen C., Van den Mooter G., Unraveling particle formation: from single droplet drying to spray drying and electrospraying, *Pharmaceutics*, 12 (2020) 625. DOI: 10.3390/pharmaceutics12070625
- Bondi A., Van der Waals volumes and radii, *The Journal of Physical Chemistry*, 68 (1964) 441–451. DOI: 10.1021/j100785a001
- Boraey M.A., Hoe S., Sharif H., Miller D.P., Lechuga-Ballesteros D., Vehring R., Improvement of the dispersibility of spray-dried budesonide powders using leucine in an ethanol–water cosolvent system, *Powder Technology*, 236 (2013) 171–178. DOI: 10.1016/j.powtec.2012.02.047
- Boraey M.A., Vehring R., Diffusion controlled formation of microparticles, *Journal of Aerosol Science*, 67 (2014) 131–143. DOI: 10.1016/j.jaerosci.2013.10.002
- Brittain H.G., X-Ray diffraction of pharmaceutical materials, in: Brittain H.G. (Ed.), *Profiles of Drug Substances, Excipients and Related Methodology*, Academic Press, 2003, pp. 271–319. DOI: 10.1016/S0099-5428(03)30010-3
- Cal K., Sollohub K., Spray drying technique. I: hardware and process parameters, *Journal of Pharmaceutical Sciences*, 99 (2010) 575–586. DOI: 10.1002/jps.21886
- Calmet H., Inthavong K., Eguzkitza B., Lehmkuhl O., Houzeaux G., Vázquez M., Nasal sprayed particle deposition in a human nasal cavity under different inhalation conditions, *PLoS ONE*, 14 (2019) 1–27. DOI: 10.1371/journal.pone.0221330
- Capua I., Giaquinto C., The unsung virtue of thermostability, *The Lancet*, 397 (2021) 1346–1347. DOI: 10.1016/S0140-6736(21)00526-2
- Carrigy N., Vehring R., Engineering stable spray-dried biologic powder for inhalation, in: Hickey A.J., da Rocha S.R. (Eds.), *Pharmaceutical Inhalation Aerosol Technology*, CRC Press, Boca Raton, Florida, 2019, pp. 291–236, ISBN: 9780429055201. DOI: 10.1201/9780429055201
- Carrigy N.B., Liang L., Wang H., Kariuki S., Nagel T.E., Connerton I.F., Vehring R., Mechanistic modeling expedites the development of spray dried biologics, *Proceedings of 21th International Drying Symposium*, 2018.
- Carrigy N.B., Liang L., Wang H., Kariuki S., Nagel T.E., Connerton I.F., Vehring R., Spray-dried anti-Campylobacter bacteriophage CP30A powder suitable for global distribution without cold chain infrastructure, *International Journal of Pharmaceutics*, 569 (2019a) 118601. DOI: 10.1016/j.ijpharm.2019.118601
- Carrigy N.B., Liang L., Wang H., Kariuki S., Nagel T.E., Connerton I.F., Vehring R., Trileucine and pullulan improve anti-campylobacter bacteriophage stability in engineered spray-dried microparticles, *Annals of Biomedical Engineering*, (2019b). DOI: 10.1007/s10439-019-02435-6
- Carrigy N.B., Ordoubadi M., Liu Y., Melhem O., Barona D., Wang H., Milburn L., Ruzycki C.A., Finlay W.H., Vehring R., Amorphous pullulan trehalose microparticle platform for respiratory delivery, *International Journal of Pharmaceutics*, 563 (2019c) 156–168. DOI: 10.1016/j.ijpharm.2019.04.004
- Carrigy N.B., Ordoubadi M., Liu Y., Melhem O., Barona D., Wang H., Milburn L., Ruzycki C.A., Finlay W.H., Vehring R., Amorphous pullulan trehalose microparticle platform for respiratory delivery, in: *American Association for Aerosol Research 37th Annual Conference*, Portland, 2019d.
- Červinka C., Fulem M., Structure and glass transition temperature of amorphous dispersions of model pharmaceuticals with nucleobases from molecular dynamics, *Pharmaceutics*, 13 (2021) 1253. DOI: 10.3390/pharmaceutics13081253
- Chan H.-K., Chang R.Y.K., Inhaled delivery of anti-pseudomonal phages to tackle respiratory infections caused by superbugs, *Journal of Aerosol Medicine and Pulmonary Drug Delivery*, 35 (2021) 73–82. DOI: 10.1089/jamp.2021.0045
- Chang R.Y.K., Chen L., Chen D., Chan H.-K., Overcoming challenges for development of amorphous powders for inhalation, *Expert Opinion on Drug Delivery*, 17 (2020) 1583–1595. DOI: 10.1080/17425247.2020.1813105
- Charlesworth D.H., Marshall W.R., Evaporation from drops containing dissolved solids, *AIChE Journal*, 6 (1960) 9–23. DOI: 10.1002/aic.690060104
- Chaubal M.V., Popescu C., Conversion of nanosuspensions into dry powders by spray drying: a case study, *Pharmaceutical Research*, 25 (2008) 2302–2308. DOI: 10.1007/s11095-008-9625-0
- Chen X.D., The basics of a reaction engineering approach to modeling air-drying of small droplets or thin-layer materials, *Drying Technology*, 26 (2008) 627–639. DOI: 10.1080/07373930802045908
- Chen Y., Ling J., Li M., Su Y., Arte K.S., Mutukuri T.T., Taylor L.S., Munson E.J., Topp E.M., Zhou Q.T., Understanding the impact of protein–excipient interactions on physical stability of spray-dried protein solids, *Molecular Pharmaceutics*, 18 (2021) 2657–2668. DOI: 10.1021/acs.molpharmaceut.1c00189
- Chiou D., Langrish T.A.G., Crystallization of amorphous

- components in spray-dried powders, *Drying Technology*, 25 (2007) 1427–1435. DOI: 10.1080/07373930701536718
- Clas S.-D., Dalton C.R., Hancock B.C., Differential scanning calorimetry: applications in drug development, *Pharmaceutical Science & Technology Today*, 2 (1999) 311–320. DOI: 10.1016/S1461-5347(99)00181-9
- Dabbagh A., Abu Kasim N.H., Yeong C.H., Wong T.W., Abdul Rahman N., Critical parameters for particle-based pulmonary delivery of chemotherapeutics, *Journal of Aerosol Medicine and Pulmonary Drug Delivery*, 31 (2018) 139–154. DOI: 10.1089/jamp.2017.1382
- Davis M., Walker G., Recent strategies in spray drying for the enhanced bioavailability of poorly water-soluble drugs, *Journal of Controlled Release*, 269 (2018) 110–127. DOI: 10.1016/J.JCONREL.2017.11.005
- Davis M.T., Potter C.B., Mohammadpour M., Albadarin A.B., Walker G.M., Design of spray dried ternary solid dispersions comprising itraconazole, Soluplus and HPMCP: effect of constituent compositions, *International Journal of Pharmaceutics*, 519 (2017) 365–372. DOI: 10.1016/j.ijpharm.2017.01.043
- Dobrowolski A., Strob R., Nietfeld J., Pieloth D., Wiggers H., Thommes M., Preparation of spray dried submicron particles: part B – Particle recovery by electrostatic precipitation, *International Journal of Pharmaceutics*, 548 (2018) 237–243. DOI: 10.1016/j.ijpharm.2018.06.069
- Dollo G., Le Corre P., Guérin A., Chevanne F., Burgot J.L., Leverage R., Spray-dried redispersible oil-in-water emulsion to improve oral bioavailability of poorly soluble drugs, *European Journal of Pharmaceutical Sciences*, 19 (2003) 273–280. DOI: 10.1016/S0928-0987(03)00134-9
- Douglass I., Harrowell P., Kinetics of dissolution of an amorphous solid, *The Journal of Physical Chemistry B*, 122 (2018) 2425–2433. DOI: 10.1021/acs.jpcc.7b12243
- Douglass I., Harrowell P., Formation of ultrastable glasses via precipitation: a modeling study, *Physical Review Letters*, 122 (2019) 088003. DOI: 10.1103/PhysRevLett.122.088003
- Drake A.C., Lee Y., Burgess E.M., Karlsson J.O.M., Eroglu A., Higgins A.Z., Effect of water content on the glass transition temperature of mixtures of sugars, polymers, and penetrating cryoprotectants in physiological buffer, *PLoS ONE*, 13 (2018) e0190713. DOI: 10.1371/journal.pone.0190713
- Eastoe J., Dalton J., Dynamic surface tension and adsorption mechanisms of surfactants at the air–water interface, *Advances in Colloid and Interface Science*, 85 (2000) 103–144. DOI: 10.1016/S0001-8686(99)00017-2
- Ebnesajjad S., 3 - Surface tension and its measurement, in: Ebnesajjad S. (Ed.), *Handbook of Adhesives and Surface Preparation*, William Andrew Publishing, Oxford, 2011, pp. 21–30. DOI: 10.1016/B978-1-4377-4461-3.10003-3
- Edris A., Bergnstahl B., Encapsulation of orange oil in a spray dried double emulsion, *Nahrung*, 45 (2001) 133–137. DOI: 10.1002/1521-3803(20010401)45:2<133::AID-FOOD133>3.0.CO;2-C
- Edueng K., Bergström C.A.S., Gråsjö J., Mahlin D., Long-term physical (in)stability of spray-dried amorphous drugs: relationship with glass-forming ability and physicochemical properties, *Pharmaceutics*, 11 (2019) 425. DOI: 10.3390/pharmaceutics11090425
- Edward J.T., Molecular volumes and the Stokes-Einstein equation, *Journal of Chemical Education*, 47 (1970) 261. DOI: 10.1021/ed047p261
- Eedara B.B., Rangnekar B., Doyle C., Cavallaro A., Das S.C., The influence of surface active L-leucine and 1,2-dipalmitoyl-sn-glycero-3-phosphatidylcholine (DPPC) in the improvement of aerosolization of pyrazinamide and moxifloxacin co-spray dried powders, *International Journal of Pharmaceutics*, 542 (2018) 72–81. DOI: 10.1016/j.ijpharm.2018.03.005
- Eedara B.B., Tucker I.G., Das S.C., Phospholipid-based pyrazinamide spray-dried inhalable powders for treating tuberculosis, *International Journal of Pharmaceutics*, 506 (2016) 174–183. DOI: 10.1016/j.ijpharm.2016.04.038
- El-Gendy N., Bailey M.M., Berkland C., Particle engineering technologies for pulmonary drug delivery, in: Smyth H.D.C., Hickey A.J. (Eds.), *Controlled Pulmonary Drug Delivery*, Springer New York, New York, NY, 2011, pp. 283–312. DOI: 10.1007/978-1-4419-9745-6\_13
- Feng A.L., Boraey M.A., Gwin M.A., Finlay P.R., Kuehl P.J., Vehring R., Mechanistic models facilitate efficient development of leucine containing microparticles for pulmonary drug delivery, *International Journal of Pharmaceutics*, 409 (2011) 156–163. DOI: 10.1016/j.ijpharm.2011.02.049
- Ferreira M.P.A., Martins J.P., Hirvonen J., Santos H.A., Chapter 9—Spray-drying for the formulation of oral drug delivery systems, in: Martins J.P., Santos H.A. (Eds.), *Nanotechnology for Oral Drug Delivery*, Academic Press, 2020, pp. 253–284, ISBN: 978-0-12-818038-9. DOI: 10.1016/B978-0-12-818038-9.00007-7
- Focaroli S., Jiang G., O’Connell P., Fahy J. V., Healy A.-M., The use of a three-fluid atomising nozzle in the production of spray-dried theophylline/salbutamol sulphate powders intended for pulmonary delivery, *Pharmaceutics*, 12 (2020) 1116. DOI: 10.3390/pharmaceutics12111116
- Fox T.G., Influence of diluent and of copolymer composition on the glass temperature of a polymer system, *Bulletin of the American Physical Society*, 1 (1956) 123–128.
- Frank U., Uttinger M.J., Wawra S.E., Lübbert C., Peukert W., Progress in multidimensional particle characterization, *KONA Powder and Particle Journal*, 39 (2022) 3–28. DOI: 10.14356/kona.2022005
- French D.L., Arakawa T., Li T., Fourier transform infrared spectroscopy investigation of protein conformation in spray-dried protein/trehalose powders, *Biopolymers*, 73 (2004) 524–531. DOI: 10.1002/bip.10558
- Fukui K., Maeda K., Distribution of solute at solid–liquid interface during solidification of melt, *The Journal of Chemical Physics*, 109 (1998) 7468–7473. DOI: 10.1063/1.477369
- Gac J.M., Numerical modelling of formation of highly ordered structured micro- and nanoparticles – a review, *KONA Powder and Particle Journal*, 39 (2022) 45–61. DOI: 10.14356/kona.2022019
- Gil M., Vicente J., Gaspar F., Scale-up methodology for pharmaceutical spray drying, *Chimica Oggi/Chemistry Today*, 28 (2010) 18–22.
- Gliński J., Chavepeyer G., Platten J.-K., Surface properties of aqueous solutions of l-leucine, *Biophysical Chemistry*, 84 (2000) 99–103. DOI: 10.1016/S0301-4622(99)00150-7
- Gomez M., Archer M., Barona D., Wang H., Ordoubadi M., Bin Karim S., Carrigy N.B., Wang Z., McCollum J., Press C., Gerhardt A., Fox C.B., Kramer R.M., Vehring R., Microparticle encapsulation of a tuberculosis subunit vaccine candidate containing a nanoemulsion adjuvant via spray drying, *European Journal of Pharmaceutics and Biopharmaceutics*, 163 (2021a) 23–37. DOI: 10.1016/j.ejpb.2021.03.007
- Gomez M., McCollum J., Barona D., Jar C., Ordoubadi M., Carrigy N.B., Gerhardt A., Press C., Archer M., Kramer R.M., Fox C.B., Vehring R., Spray drying adjuvanted tuberculosis vaccine encapsulates nano-emulsions within a dry powder inhalable product, in: 5th International TB Meeting, Groningen, 2019.

- Gomez M., McCollum J., Wang H., Bachchhav S., Tetreau I., Gerhardt A., Press C., Kramer R.M., Fox C.B., Vehring R., Evaluation of the stability of a spray-dried tuberculosis vaccine candidate designed for dry powder respiratory delivery, *Vaccine*, 39 (2021b) 5025–5036. DOI: 10.1016/j.vaccine.2021.07.002
- Gomez M., Vehring R., Spray drying and particle engineering in dosage form design for global vaccines, *Journal of Aerosol Medicine and Pulmonary Drug Delivery*, 35 (2022) 1–18. DOI: 10.1089/jamp.2021.0056
- Gregson F.K.A., Ordoubadi M., Miles R.E.H., Haddrell A.E., Barona D., Lewis D., Church T., Vehring R., Reid J.P., Studies of competing evaporation rates of multiple volatile components from a single binary-component aerosol droplet, *Physical Chemistry Chemical Physics*, 21 (2019) 9709–9719. DOI: 10.1039/C9CP01158G
- Hancock B.C., Shamblin S.L., Zografi G., Molecular mobility of amorphous pharmaceutical solids below their glass transition temperatures, *Pharmaceutical Research*, 12 (1995) 799–806. DOI: 10.1023/a:1016292416526
- He G., Bhamidi V., Tan R.B.H., Kenis P.J.A., Zukoski C.F., Determination of critical supersaturation from microdroplet evaporation experiments, *Crystal Growth & Design*, 6 (2006) 1175–1180. DOI: 10.1021/cg050681f
- He Y., Yazhgur P., Salonen A., Langevin D., Adsorption–desorption kinetics of surfactants at liquid surfaces, *Advances in Colloid and Interface Science*, 222 (2015) 377–384. DOI: 10.1016/j.cis.2014.09.002
- Heng D., Tang P., Cairney J.M., Chan H.-K., Cutler D.J., Salama R., Yun J., Focused-ion-beam milling: a novel approach to probing the interior of particles used for inhalation aerosols, *Pharmaceutical Research*, 24 (2007) 1608–1617. DOI: 10.1007/s11095-007-9276-6
- Hinrichs W.L., Prinsen M., Frijlink H., Inulin glasses for the stabilization of therapeutic proteins, *International Journal of Pharmaceutics*, 215 (2001) 163–174. DOI: 10.1016/S0378-5173(00)00677-3
- Hoe S., Ivey J.W., Boraey M.A., Shamsaddini-Shahrbabak A., Javaheri E., Matinkhoo S., Finlay W.H., Vehring R., Use of a fundamental approach to spray-drying formulation design to facilitate the development of multi-component dry powder aerosols for respiratory drug delivery, *Pharmaceutical Research*, 31 (2014) 449–465. DOI: 10.1007/s11095-013-1174-5
- Hoffman J.D., Thermodynamic driving force in nucleation and growth processes, *The Journal of Chemical Physics*, 29 (1958) 1192–1193. DOI: 10.1063/1.1744688
- Hu S., Zhao G., Zheng Y., Qu M., Jin Q., Tong C., Li W., Effect of drying procedures on the physicochemical properties and antioxidant activities of polysaccharides from *Crassostrea gigas*, *PLoS ONE*, 12 (2017) e0188536. DOI: 10.1371/journal.pone.0188536
- Huang S., Mao C., Williams R.O., Yang C.-Y., Solubility advantage (and disadvantage) of pharmaceutical amorphous solid dispersions, *Journal of Pharmaceutical Sciences*, 105 (2016) 3549–3561. DOI: 10.1016/j.xphs.2016.08.017
- Ilevbare G.A., Taylor L.S., Liquid–liquid phase separation in highly supersaturated aqueous solutions of poorly water-soluble drugs: implications for solubility enhancing formulations, *Crystal Growth & Design*, 13 (2013) 1497–1509. DOI: 10.1021/cg301679h
- Ivey J.W., Barona D., Gomez M., Kuan L., Mcallister R., Oberhagemann L., Sa D.D., Lechuga-ballesteros D., Ajmera A., Gracin S., Vehring R., Isokinetic in-line sampling enables rapid characterization of atomizers and cyclones for spray drying process development, *Respiratory Drug Delivery*, 2 (2018) 551–556.
- Ivey J.W., Vehring R., The use of modeling in spray drying of emulsions and suspensions accelerates formulation and process development, *Computers & Chemical Engineering*, 34 (2010) 1036–1040. DOI: 10.1016/j.compchemeng.2010.02.031
- Jayasundera M., Adhikari B., Aldred P., Ghandi A., Surface modification of spray dried food and emulsion powders with surface-active proteins: a review, *Journal of Food Engineering*, 93 (2009) 266–277. DOI: 10.1016/j.jfoodeng.2009.01.036
- Johnson L.M., Mecham J.B., Quinn F., Hickey A.J., Nanoparticle technology for respiratory tract mucosal vaccine delivery, *KONA Powder and Particle Journal*, 37 (2020) 97–113. DOI: 10.14356/kona.2020013
- Jong T., Li J., Morton D.A.V., Zhou Q. (Tony), Larson I., Investigation of the changes in aerosolization behavior between the jet-milled and spray-dried colistin powders through surface energy characterization, *Journal of Pharmaceutical Sciences*, 105 (2016) 1156–1163. DOI: 10.1016/S0022-3549(15)00189-6
- Jüptner A., Scherließ R., Spray dried formulations for inhalation—meaningful characterisation of powder properties, *Pharmaceutics*, 12 (2019) 14. DOI: 10.3390/pharmaceutics12010014
- Karthika S., Radhakrishnan T.K., Kalaichelvi P., A review of classical and nonclassical nucleation theories, *Crystal Growth & Design*, 16 (2016) 6663–6681. DOI: 10.1021/acs.cgd.6b00794
- Kauppinen A., Broekhuis J., Grasmeijer N., Tonnis W., Ketolainen J., Frijlink H.W., Hinrichs W.L.J., Efficient production of solid dispersions by spray drying solutions of high solid content using a 3-fluid nozzle, *European Journal of Pharmaceutics and Biopharmaceutics*, 123 (2018) 50–58. DOI: 10.1016/J.EJPB.2017.11.009
- Kawakami K., Crystallization tendency of pharmaceutical glasses: relevance to compound properties, impact of formulation process, and implications for design of amorphous solid dispersions, *Pharmaceutics*, 11 (2019) 202. DOI: 10.3390/pharmaceutics11050202
- Kawakami K., Sumitani C., Yoshihashi Y., Yonemochi E., Terada K., Investigation of the dynamic process during spray-drying to improve aerodynamic performance of inhalation particles, *International Journal of Pharmaceutics*, 390 (2010) 250–259. DOI: 10.1016/j.ijpharm.2010.02.018
- Khanal D., Ke W.-R., Chan H., Raman spectroscopic evaluation of crystallinity, chemical composition and stability of pharmaceutical powder aerosols, *International Journal of Pharmaceutics*, 611 (2022) 121341. DOI: 10.1016/j.ijpharm.2021.121341
- Kiaee M., Wachtel H., Noga M.L., Martin A.R., Finlay W.H., Regional deposition of nasal sprays in adults: a wide ranging computational study, *International Journal for Numerical Methods in Biomedical Engineering*, 34 (2018) 1–13. DOI: 10.1002/cnm.2968
- Kooijman H.A., A modification of the Stokes–Einstein equation for diffusivities in dilute binary mixtures, *Industrial & Engineering Chemistry Research*, 41 (2002) 3326–3328. DOI: 10.1021/ie010690v
- Kristensen D.D., Lorenson T., Bartholomew K., Villadiego S., Can thermostable vaccines help address cold-chain challenges? Results from stakeholder interviews in six low- and middle-income countries, *Vaccine*, 34 (2016) 899–904. DOI: 10.1016/j.vaccine.2016.01.001

- Kumar S., Gokhale R., Burgess D.J., Quality by Design approach to spray drying processing of crystalline nanosuspensions, *International Journal of Pharmaceutics*, 464 (2014) 234–242. DOI: 10.1016/j.ijpharm.2013.12.039
- Landström K., Alsins J., Bergenståhl B., Competitive protein adsorption between bovine serum albumin and  $\beta$ -lactoglobulin during spray-drying, *Food Hydrocolloids*, 14 (2000) 75–82. DOI: 10.1016/S0268-005X(99)00047-8
- Lechuga-Ballesteros D., Charan C., Stults C.L.M., Stevenson C.L., Miller D.P., Vehring R., Tep V., Kuo M., Trileucine improves aerosol performance and stability of spray-dried powders for inhalation, *Journal of Pharmaceutical Sciences*, 97 (2008) 287–302. DOI: 10.1002/jps.21078
- Lechuga-Ballesteros D., Hoe S., Maynor B.W., Particle engineering technology for inhaled therapies, in: Hickey A.J., da Rocha S.R.P. (Eds.), *Pharmaceutical Inhalation Aerosol Technology*, CRC Press, Boca Raton, Florida, 2019, pp. 349–361, ISBN9780429055201. DOI: 10.1201/9780429055201
- LeClair D.A., Cranston E.D., Lichty B.D., Xing Z., Thompson M.R., Consecutive spray drying to produce coated dry powder vaccines suitable for oral administration, *ACS Biomaterials Science & Engineering*, 4 (2018) 1669–1678. DOI: 10.1021/acsbmaterials.8b00117
- Leonard D.N., Chandler G.W., Seraphin S., Scanning electron microscopy, in: *Characterization of Materials*, John Wiley & Sons, Inc., Hoboken, NJ, USA, 2012, pp. 1–35, ISBN: 978-1-118-11074-4. DOI: 10.1002/0471266965.com081.pub2
- Leyva-Porras C., Cruz-Alcantar P., Espinosa-Solis V., Martínez-Guerra E., Piñón-Balderrama C.I., Compean Martínez I., Saavedra-Leos M.Z., Application of differential scanning calorimetry (DSC) and modulated differential scanning calorimetry (MDSC) in food and drug industries, *Polymers*, 12 (2019) 5. DOI: 10.3390/polym12010005
- Li L., Sun S., Parumasivam T., Denman J.A., Gengenbach T., Tang P., Mao S., Chan H.-K., l -Leucine as an excipient against moisture on in vitro aerosolization performances of highly hygroscopic spray-dried powders, *European Journal of Pharmaceutics and Biopharmaceutics*, 102 (2016) 132–141. DOI: 10.1016/j.ejpb.2016.02.010
- Li N., Cape J.L., Mankani B.R., Zemlyanov D.Y., Shepard K.B., Morgen M.M., Taylor L.S., Water-induced phase separation of spray-dried amorphous solid dispersions, *Molecular Pharmaceutics*, 17 (2020) 4004–4017. DOI: 10.1021/acsmolpharmaceut.0c00798
- Lintingre E., Lequeux F., Talini L., Tsapis N., Control of particle morphology in the spray drying of colloidal suspensions, *Soft Matter*, 12 (2016) 7435–7444. DOI: 10.1039/C6SM01314G
- Longest P.W., Farkas D., Hassan A., Hindle M., Computational fluid dynamics (CFD) simulations of spray drying: linking drying parameters with experimental aerosolization performance, *Pharmaceutical Research*, 37 (2020) 101. DOI: 10.1007/s11095-020-02806-y
- Lu W., Rades T., Rantanen J., Yang M., Inhalable co-amorphous budesonide-arginine dry powders prepared by spray drying, *International Journal of Pharmaceutics*, 565 (2019) 1–8. DOI: 10.1016/j.ijpharm.2019.04.036
- Ma X., Williams R.O., Characterization of amorphous solid dispersions: an update, *Journal of Drug Delivery Science and Technology*, 50 (2019) 113–124. DOI: 10.1016/j.jddst.2019.01.017
- Mah P.T., O’Connell P., Focaroli S., Lundy R., O’Mahony T.F., Hastedt J.E., Gitlin I., Oscarson S., Fahy J. V., Healy A.M., The use of hydrophobic amino acids in protecting spray dried trehalose formulations against moisture-induced changes, *European Journal of Pharmaceutics and Biopharmaceutics*, 144 (2019) 139–153. DOI: 10.1016/j.ejpb.2019.09.014
- Malamataris M., Charisi A., Malamataris S., Kachrimanis K., Nikolakakis I., Spray drying for the preparation of nanoparticle-based drug formulations as dry powders for inhalation, *Processes*, 8 (2020) 788. DOI: 10.3390/pr8070788
- Mangal S., Meiser F., Tan G., Gengenbach T., Denman J., Rowles M.R., Larson I., Morton D.A.V., Relationship between surface concentration of l-leucine and bulk powder properties in spray dried formulations, *European Journal of Pharmaceutics and Biopharmaceutics*, 94 (2015) 160–169. DOI: 10.1016/j.ejpb.2015.04.035
- Mangal S., Park H., Nour R., Shetty N., Cavallaro A., Zemlyanov D., Thalberg K., Puri V., Nicholas M., Narang A.S., Zhou Q. (Tony), Correlations between surface composition and aerosolization of jet-milled dry powder inhaler formulations with pharmaceutical lubricants, *International Journal of Pharmaceutics*, 568 (2019) 118504. DOI: 10.1016/j.ijpharm.2019.118504
- Maniyar M.G., Kokare C.R., Formulation and evaluation of spray dried liposomes of lopinavir for topical application, *Journal of Pharmaceutical Investigation*, 49 (2019) 259–270. DOI: 10.1007/s40005-018-0403-7
- Massant J., Fleurime S., Batens M., Vanhaerents H., Van den Mooter G., Formulating monoclonal antibodies as powders for reconstitution at high concentration using spray-drying: Trehalose/amino acid combinations as reconstitution time reducing and stability improving formulations, *European Journal of Pharmaceutics and Biopharmaceutics*, 156 (2020) 131–142. DOI: 10.1016/j.ejpb.2020.08.019
- Mensink M.A., Frijlink H.W., van der Voort Maarschalk K., Hinrichs W.L.J., How sugars protect proteins in the solid state and during drying (review): Mechanisms of stabilization in relation to stress conditions, *European Journal of Pharmaceutics and Biopharmaceutics*, 114 (2017) 288–295. DOI: 10.1016/j.ejpb.2017.01.024
- Mezhericher M., Levy A., Borde I., Modelling of particle breakage during drying, *Chemical Engineering and Processing: Process Intensification*, 47 (2008) 1404–1411. DOI: 10.1016/j.ccep.2007.06.018
- Mezhericher M., Levy A., Borde I., Spray drying modelling based on advanced droplet drying kinetics, *Chemical Engineering and Processing: Process Intensification*, 49 (2010) 1205–1213. DOI: 10.1016/j.ccep.2010.09.002
- Minoshima H., Matsushima K., Liang H., Shinohara K., Basic model of spray drying granulation, *Journal of Chemical Engineering of Japan*, 34 (2001) 472–478. DOI: 10.1252/jcej.34.472
- Mishra J., Rades T., Löbmann K., Grohganz H., Influence of solvent composition on the performance of spray-dried co-amorphous formulations, *Pharmaceutics*, 10 (2018) 47. DOI: 10.3390/pharmaceutics10020047
- Mohammed N.K., Tan C.P., Manap Y.A., Muhiyaldin B.J., Hussin A.S.M., Spray drying for the encapsulation of oils—a review, *Molecules*, 25 (2020) 3873. DOI: 10.3390/molecules25173873
- Momin M.A.M., Tucker I.G., Doyle C.S., Denman J.A., Das S.C., Manipulation of spray-drying conditions to develop dry powder particles with surfaces enriched in hydrophobic material to achieve high aerosolization of a hygroscopic drug, *International Journal of Pharmaceutics*, 543 (2018) 318–327. DOI: 10.1016/j.ijpharm.2018.04.003
- Murdande S.B., Pikal M.J., Shanker R.M., Bogner R.H., Solubility advantage of amorphous pharmaceuticals: I. A thermodynamic analysis, *Journal of Pharmaceutical Sciences*, 99 (2010) 1254–1264. DOI: 10.1002/jps.21903



- Nagarwal R.C., Kumar R., Dhanawat M., Das N., K. Pandit J., Nanocrystal technology in the delivery of poorly soluble drugs: an overview, *Current Drug Delivery*, 8 (2011) 398–406. DOI: 10.2174/156720111795767988
- Nandiyanto A.B.D., Okuyama K., progress in developing spray-drying methods for the production of controlled morphology particles: from the nanometer to submicrometer size ranges, *Advanced Powder Technology*, 22 (2011) 1–19. DOI: 10.1016/j.apt.2010.09.011
- Nicholas M., Josefson M., Fransson M., Wilbs J., Roos C., Boissier C., Thalberg K., Quantification of surface composition and surface structure of inhalation powders using TOF-SIMS, *International Journal of Pharmaceutics*, 587 (2020) 119666. DOI: 10.1016/j.ijpharm.2020.119666
- Ojarinta R., Lermiaux L., Laitinen R., Spray drying of poorly soluble drugs from aqueous arginine solution, *International Journal of Pharmaceutics*, 532 (2017) 289–298. DOI: 10.1016/j.ijpharm.2017.09.015
- Oneda F., Ré M., The effect of formulation variables on the dissolution and physical properties of spray-dried microspheres containing organic salts, *Powder Technology*, 130 (2003) 377–384. DOI: 10.1016/S0032-5910(02)00239-5
- Ordoubadi M., Gregson F.K.A., Melhem O., Barona D., Miles R.E.H., D'Sa D., Gracin S., Lechuga-Ballesteros D., Reid J.P., Finlay W.H., Vehring R., Multi-solvent microdroplet evaporation: modeling and measurement of spray-drying kinetics with inhalable pharmaceuticals, *Pharmaceutical Research*, 36 (2019) 100. DOI: 10.1007/s11095-019-2630-7
- Ordoubadi M., Gregson F.K.A., Wang H., Carrigy N.B., Nicholas M., Gracin S., Lechuga-Ballesteros D., Reid J.P., Finlay W.H., Vehring R., Trileucine as a dispersibility enhancer of spray-dried inhalable microparticles, *Journal of Controlled Release*, 336 (2021a) 522–536. DOI: 10.1016/j.jconrel.2021.06.045
- Ordoubadi M., Gregson F.K.A., Wang H., Nicholas M., Gracin S., Lechuga-Ballesteros D., Reid J.P., Finlay W.H., Vehring R., On the particle formation of leucine in spray drying of inhalable microparticles, *International Journal of Pharmaceutics*, 592 (2021b) 120102. DOI: 10.1016/j.ijpharm.2020.120102
- Ordoubadi M., Wang H., Nicholas M., Carrigy N.B., Gracin S., Lechuga-Ballesteros D., Finlay W.H., Vehring R., How does trileucine act as a dispersibility enhancer in the spray drying of microparticles?, *Respiratory Drug Delivery*, 1 (2021c) 307–310.
- Ousset A., Chavez P.-F., Meeus J., Robin F., Schubert M., Somville P., Dodou K., Prediction of phase behavior of spray-dried amorphous solid dispersions: assessment of thermodynamic models, standard screening methods and a novel atomization screening device with regard to prediction accuracy, *Pharmaceutics*, 10 (2018) 29. DOI: 10.3390/pharmaceutics10010029
- Paredes A.J., McKenna P.E., Ramöller I.K., Naser Y.A., Volpe-Zanutto F., Li M., Abbate M.T.A., Zhao L., Zhang C., Abu-Ershaid J.M., Dai X., Donnelly R.F., Microarray patches: poking a hole in the challenges faced when delivering poorly soluble drugs, *Advanced Functional Materials*, 31 (2021) 2005792. DOI: 10.1002/adfm.202005792
- Patel B.B., Patel J.K., Chakraborty S., Shukla D., Revealing facts behind spray dried solid dispersion technology used for solubility enhancement, *Saudi Pharmaceutical Journal*, 23 (2015) 352–365. DOI: 10.1016/j.jsps.2013.12.013
- Pinto J.T., Faulhammer E., Dieplinger J., Dekner M., Makert C., Nieder M., Paudel A., Progress in spray-drying of protein pharmaceuticals: literature analysis of trends in formulation and process attributes, *Drying Technology*, 39 (2021) 1415–1446. DOI: 10.1080/07373937.2021.1903032
- Poozesh S., Bilgili E., Scale-up of pharmaceutical spray drying using scale-up rules: a review, *International Journal of Pharmaceutics*, 562 (2019) 271–292. DOI: 10.1016/j.ijpharm.2019.03.047
- Rabinow B.E., Nanosuspensions in drug delivery, *Nature Reviews Drug Discovery*, 3 (2004) 785–796. DOI: 10.1038/nrd1494
- Rosen M.J., Kunjappu J.T., *Surfactants and Interfacial Phenomena*, fourth edition, John Wiley & Sons, 2012, ISBN: 9780470541944. DOI: 10.1002/9781118228920
- Saallah S., Lenggono I.W., Nanoparticles carrying biological molecules: recent advances and applications, *KONA Powder and Particle Journal*, 35 (2018) 89–111. DOI: 10.14356/kona.2018015
- Salama A.H., Spray drying as an advantageous strategy for enhancing pharmaceuticals bioavailability, *Drug Delivery and Translational Research*, 10 (2020) 1–12. DOI: 10.1007/s13346-019-00648-9
- Santos D., Mauricio A.C., Sencadas V., Santos J.D., Fernandes M.H., Gomes P.S., Spray drying: an overview, in: Mauricio A.C. (Ed.), *Biomaterials-Physics and Chemistry—New Edition*, InTech, Rijeka, 2018, pp. 9–36. DOI: 10.5772/intechopen.72247
- Selvamuthukumaran M., *Handbook on Spray Drying Applications for Food Industries*, CRC Press, 2019, ISBN: 9780429055133. DOI: 10.1201/9780429055133
- Sheokand S., Modi S.R., Bansal A.K., Dynamic vapor sorption as a tool for characterization and quantification of amorphous content in predominantly crystalline materials, *Journal of Pharmaceutical Sciences*, 103 (2014) 3364–3376. DOI: 10.1002/jps.24160
- Shepard K.B., Dower A.M., Ekdahl A.M., Morgen M.M., Baumann J.M., Vodak D.T., Solvent-assisted secondary drying of spray-dried polymers, *Pharmaceutical Research*, 37 (2020) 156. DOI: 10.1007/s11095-020-02890-0
- Shepard K.B., Vodak D.T., Kuehl P.J., Revelli D., Zhou Y., Pluntze A.M., Adam M.S., Oddo J.C., Switala L., Cape J.L., Baumann J.M., Banks M., Local treatment of non-small cell lung cancer with a spray-dried bevacizumab formulation, *AAPS PharmSciTech*, 22 (2021) 230. DOI: 10.1208/s12249-021-02095-7
- Shetty N., Hau J., Yanez E., Shur J., Cheng J., Sun C.C., Nagapudi K., Narang A., Effect of lipidic excipients on the particle properties and aerosol performance of high drug load spray dried particles for inhalation, *Journal of Pharmaceutical Sciences*, 111 (2022) 1152–1163. DOI: 10.1016/j.xphs.2021.09.004
- Shetty N., Zeng L., Mangal S., Nie H., Rowles M.R., Guo R., Han Y., Park J.H., Zhou Q., Effects of moisture-induced crystallization on the aerosol performance of spray dried amorphous ciprofloxacin powder formulations, *Pharmaceutical Research*, 35 (2018) 7. DOI: 10.1007/s11095-017-2281-5
- Shetty N., Zhang Y., Park H., Zemlyanov D., Shah D., He A., Ahn P., Mutukuri T.T., Chan H.-K., Zhou Q., Surface composition and aerosolization stability of an inhalable combinational powder formulation spray dried using a three-fluid nozzle, *Pharmaceutical Research*, 37 (2020) 219. DOI: 10.1007/s11095-020-02937-2
- Singh A., Van den Mooter G., Spray drying formulation of amorphous solid dispersions, *Advanced Drug Delivery Reviews*, 100 (2016) 27–50. DOI: 10.1016/j.addr.2015.12.010
- Soottitantawat A., Yoshii H., Furuta T., Ohkawara M., Linko P., Microencapsulation by spray drying: influence of emulsion size on the retention of volatile compounds, *Journal of*

- Food Science, 68 (2003) 2256–2262. DOI: 10.1111/j.1365-2621.2003.tb05756.x
- Suihko E.J., Forbes R.T., Apperley D.C., A solid-state NMR study of molecular mobility and phase separation in co-spray-dried protein–sugar particles, *European Journal of Pharmaceutical Sciences*, 25 (2005) 105–112. DOI: 10.1016/j.ejps.2005.02.002
- Sunderland T., Kelly J.G., Ramtoola Z., Application of a novel 3-fluid nozzle spray drying process for the microencapsulation of therapeutic agents using incompatible drug–polymer solutions, *Archives of Pharmacal Research*, 38 (2015) 566–573. DOI: 10.1007/s12272-013-0261-9
- Tewa-Tagne P., Briançon S., Fessi H., Spray-dried microparticles containing polymeric nanocapsules: formulation aspects, liquid phase interactions and particles characteristics, *International Journal of Pharmaceutics*, 325 (2006) 63–74. DOI: 10.1016/j.ijpharm.2006.06.025
- Tewa-Tagne P., Degobert G., Briançon S., Bordes C., Gauvrit J.-Y., Lanteri P., Fessi H., Spray-drying nanocapsules in presence of colloidal silica as drying auxiliary agent: formulation and process variables optimization using experimental designs, *Pharmaceutical Research*, 24 (2007) 650–661. DOI: 10.1007/s11095-006-9182-3
- Tsapis N., Bennett D., Jackson B., Weitz D.A., Edwards D.A., Trojan particles: large porous carriers of nanoparticles for drug delivery, *Proceedings of the National Academy of Sciences*, 99 (2002) 12001–12005. DOI: 10.1073/pnas.182233999
- Tsapis N., Dufresne E.R., Sinha S.S., Riera C.S., Hutchinson J.W., Mahadevan L., Weitz D.A., Onset of buckling in drying droplets of colloidal suspensions, *Physical Review Letters*, 94 (2005) 018302. DOI: 10.1103/PhysRevLett.94.018302
- Vartiainen V., Bimbo L.M., Hirvonen J., Kauppinen E.I., Raula J., Drug permeation and cellular interaction of amino acid-coated drug combination powders for pulmonary delivery, *International Journal of Pharmaceutics*, 504 (2016) 89–97. DOI: 10.1016/j.ijpharm.2016.03.052
- Vasconcelos T., Marques S., das Neves J., Sarmiento B., Amorphous solid dispersions: rational selection of a manufacturing process, *Advanced Drug Delivery Reviews*, 100 (2016) 85–101. DOI: 10.1016/j.addr.2016.01.012
- Vehring R., Pharmaceutical particle engineering via spray drying, *Pharmaceutical Research*, 25 (2008) 999–1022. DOI: 10.1007/s11095-007-9475-1
- Vehring R., Foss W.R., Lechuga-Ballesteros D., Particle formation in spray drying, *Journal of Aerosol Science*, 38 (2007) 728–746. DOI: 10.1016/j.jaerosci.2007.04.005
- Verma S., Kumar S., Gokhale R., Burgess D.J., Physical stability of nanosuspensions: investigation of the role of stabilizers on Ostwald ripening, *International Journal of Pharmaceutics*, 406 (2011) 145–152. DOI: 10.1016/j.ijpharm.2010.12.027
- Walton D.E., The morphology of spray-dried particles a qualitative view, *Drying Technology*, 18 (2000) 1943–1986. DOI: 10.1080/07373930008917822
- Wang B., Liu F., Xiang J., He Y., Zhang Z., Cheng Z., Liu W., Tan S., A critical review of spray-dried amorphous pharmaceuticals: synthesis, analysis and application, *International Journal of Pharmaceutics*, 594 (2021) 120165. DOI: 10.1016/j.ijpharm.2020.120165
- Wang H., Barona D., Oladepo S., Williams L., Hoe S., Lechuga-Ballesteros D., Vehring R., Macro-Raman spectroscopy for bulk composition and homogeneity analysis of multi-component pharmaceutical powders, *Journal of Pharmaceutical and Biomedical Analysis*, 141 (2017) 180–191. DOI: 10.1016/j.jpba.2017.04.003
- Wang H., Boraey M.A., Williams L., Lechuga-Ballesteros D., Vehring R., Low-frequency shift dispersive Raman spectroscopy for the analysis of respirable dosage forms, *International Journal of Pharmaceutics*, 469 (2014) 197–205. DOI: 10.1016/j.ijpharm.2014.04.058
- Wang H., Gomez M., Carrigy N.B., Ordoubadi M., Vehring R., Expedited biologic formulation and spray drying process development via mechanistic modeling, in: *Respiratory Drug Delivery 2020*, 3 (2020) 527–532.
- Wang H., Nobes D.S., Vehring R., Particle surface roughness improves colloidal stability of pressurized pharmaceutical suspensions, *Pharmaceutical Research*, 36 (2019) 43. DOI: 10.1007/s11095-019-2572-0
- Wang H., Ordoubadi M., Connaughton P., Lachacz K., Carrigy N., Tavernini S., Martin A.R., Finlay W.H., Lechuga-Ballesteros D., Vehring R., Spray dried rugose lipid particle platform for respiratory drug delivery, *Pharmaceutical Research*, 39 (2022) 805–823. DOI: 10.1007/s11095-022-03242-w
- Wang Z., Ordoubadi M., Wang H., Vehring R., Morphology and formation of crystalline leucine microparticles from a co-solvent system using multi-orifice monodisperse spray drying, *Aerosol Science and Technology*, 55 (2021a) 901–919. DOI: 10.1080/02786826.2021.1904129
- Wang Z., Wang H., Vehring R., Leucine enhances the dispersibility of trehalose-containing spray-dried powders on exposure to a high-humidity environment, *International Journal of Pharmaceutics*, 601 (2021b) 120561. DOI: 10.1016/j.ijpharm.2021.120561
- Ward A.F.H., Tordai L., Time-dependence of boundary tensions of solutions I. The role of diffusion in time-effects, *The Journal of Chemical Physics*, 14 (1946) 453–461. DOI: 10.1063/1.1724167
- Weers J., Tarara T., The PulmoSphere™ platform for pulmonary drug delivery, *Therapeutic Delivery*, 5 (2014) 277–295. DOI: 10.4155/tde.14.3
- Weers J.G., Miller D.P., Formulation design of dry powders for inhalation, *Journal of Pharmaceutical Sciences*, 104 (2015) 3259–3288. DOI: 10.1002/jps.24574
- Weers J.G., Miller D.P., Tarara T.E., Spray-dried PulmoSphere™ formulations for inhalation comprising crystalline drug particles, *AAPS PharmSciTech*, 20 (2019) 103. DOI: 10.1208/s12249-018-1280-0
- Weiss V.U., Golesne M., Friedbacher G., Alban S., Szymanski W.W., Marchetti-Deschmann M., Allmaier G., Size and molecular weight determination of polysaccharides by means of nano electrospray gas-phase electrophoretic mobility molecular analysis (nES GEMMA), *Electrophoresis*, 39 (2018) 1142–1150. DOI: 10.1002/elps.201700382
- WHO Expert Committee on Biological Standardization, Annex 5 Guidelines on the stability evaluation of vaccines for use under extended controlled temperature conditions, WHO Technical Report Series No. 999, 2016, ISBN: 9789240695634. <<https://apps.who.int/iris/handle/10665/208900>> accessed 08.06..2022.
- Woo M.W., Advances in production of food powders by spray drying, in: *Advanced Drying Technologies for Foods*, 1st edition, CRC Press, 2019, pp. 107–130, ISBN: 9780367262037. DOI: 10.1201/9780367262037
- Wu L., Miao X., Shan Z., Huang Y., Li L., Pan X., Yao Q., Li G., Wu C., Studies on the spray dried lactose as carrier for dry powder inhalation, *Asian Journal of Pharmaceutical Sciences*, 9 (2014) 336–341. DOI: 10.1016/j.ajps.2014.07.006
- Wu X., Li X., Mansour H.M., Surface analytical techniques in solid-state particle characterization for predicting performance in dry powder inhalers, *KONA Powder and Particle*

- Journal, 28 (2010) 3–19. DOI: 10.14356/kona.2010005
- Yaws C.L., 2010, Yaws' thermophysical properties of chemicals and hydrocarbons (electronic edition), <app.knovel.com/hotlink/toc/id:kpYTPCHE02/yaws-thermophysical-properties/yaws-thermophysical-properties> accessed 14.11.2019.
- Yu J., Chan H.-K., Gengenbach T., Denman J.A., Protection of hydrophobic amino acids against moisture-induced deterioration in the aerosolization performance of highly hygroscopic spray-dried powders, *European Journal of Pharmaceutics and Biopharmaceutics*, 119 (2017) 224–234. DOI: 10.1016/j.ejpb.2017.06.023
- Zallen R., *The Physics of Amorphous Solids*, Wiley, 1998, ISBN: 9780471299417. DOI: 10.1002/9783527617968
- Zhang L., Zeng X., Fu N., Tang X., Sun Y., Lin L., Maltodextrin: a consummate carrier for spray-drying of xylooligosaccharides, *Food Research International*, 106 (2018) 383–393. DOI: 10.1016/j.foodres.2018.01.004
- Zhou Q.T., Leung S.S.Y., Tang P., Parumasivam T., Loh Z.H., Chan H.-K., Inhaled formulations and pulmonary drug delivery systems for respiratory infections, *Advanced Drug Delivery Reviews*, 85 (2015) 83–99. DOI: 10.1016/j.addr.2014.10.022
- Ziaee A., Albadarin A.B., Padrela L., Faucher A., O'Reilly E., Walker G., Spray drying ternary amorphous solid dispersions of ibuprofen – An investigation into critical formulation and processing parameters, *European Journal of Pharmaceutics and Biopharmaceutics*, 120 (2017) 43–51. DOI: 10.1016/j.ejpb.2017.08.005
- Zmpitas J., Gross J., Modified Stokes–Einstein equation for molecular self-diffusion based on entropy scaling, *Industrial & Engineering Chemistry Research*, 60 (2021) 4453–4459. DOI: 10.1021/acs.iecr.0c06090

## Authors' Short Biographies



### Mani Ordoubadi

Dr. Ordoubadi is a postdoctoral fellow in the Department of Mechanical Engineering at the University of Alberta. He holds a PhD from the University of Alberta focused on developing predictive tools to assist in the formulation design of spray-dried inhalable microparticles to reduce costs and risks during the early stages of product development of emerging therapeutics in solid dosage form. He is also experienced in using numerical simulations and computational fluid dynamics related to heat and mass transfer, multiphase flows, and aerosol mechanics.



### Hui Wang

Dr. Wang obtained his BSc in Materials Science and Engineering from Southeast University in Nanjing, China. During his MSc and PhD studies with the Particle Engineering Group at the University of Alberta, he focused on designing and applying advanced characterization techniques, including cascade impaction, Raman spectroscopy, and shadowgraphic imaging, for the testing and optimization of inhalation formulations for pressurized metered dose inhalers (pMDIs) and dry powder inhalers (DPIs). He has rich experience in design, production, testing, and pulmonary delivery of medicinal microparticles. He is currently a research scientist in the group, working on various projects related to respiratory drug delivery. His research interests include inhalation formulation development, pharmaceutical particle engineering, and microparticle encapsulation of biologics.



### Reinhard Vehring

Dr. Vehring is a Professor in the Mechanical Engineering Department at the University of Alberta and holds the George Ford Chair in Materials Engineering. He graduated with a diploma in Mechanical Engineering from the Gerhard Mercator University in Duisburg, Germany, and received a doctorate from the University of Bochum in the field of molecular spectroscopy on microparticles. Dr. Vehring has held positions in academia and industry advancing aerosol science and particle technology for more than 28 years. Before returning to academia, he worked on pulmonary delivery of peptides, proteins, and small molecules at Nektar Therapeutics and was part of the team developing Exubera, the first inhalable insulin. Subsequently, he developed solid dosage forms for virus vaccines, monoclonal antibodies, and oncology therapeutics at Medimmune, and supported FluMist, the first nasally administered live attenuated influenza vaccine. Dr. Vehring was the lead inventor for the co-suspension formulation technology which is used by AstraZeneca to develop metered-dose inhaler-based therapeutics for respiratory diseases. At the University of Alberta, Dr. Vehring directs the Particle Engineering facility focusing on advanced micro and nanoparticle design and analysis.

# Performance Testing for Dry Powder Inhaler Products: Towards Clinical Relevance<sup>†</sup>

Sara E. Maloney, Jeffrey B. Mecham and Anthony J. Hickey\*

*RTI International, Research Triangle Park, USA*

## Abstract

It is well established that the critical performance metrics for aerosol products are aerodynamic particle size distribution (APSD) and delivered dose uniformity (DDU). In broad terms, these performance characteristics dictate the efficiency and reproducibility with which an aerosol is administered clinically. However, these properties alone do not support in-vitro, in-vivo correlations. There have been numerous publications attempting to more directly link product performance testing to physiological relevance or further to draw direct correlations of relevance to bioequivalence testing for the development of generic products. While these novel methods have been employed in product development activity, their suitability for compendial testing has yet to be established. This paper explores the potential to establish biologically relevant compendial standards for dry powder inhaler products while maintaining accuracy and reproducibility of data collected to support the quality and performance of the product.

**Keywords:** dry powder inhaler, therapeutic aerosol, aerodynamic particle size distribution, cascade impaction, in vitro/in vivo correlation, bioequivalence

## 1. Introduction

Modern pharmaceutical aerosol products have been available for the treatment of pulmonary diseases, such as asthma, chronic obstructive pulmonary disease (COPD), and cystic fibrosis (CF), since the middle of the last century (Cheng Y.S., 2014). Attention was given to the control of the quality of these products by the manufacturing industry and government regulators. The importance of accurately and reproducibly controlling the dose of the active pharmaceutical ingredient (API) and key properties that influence therapeutic effect, notably aerodynamic particle size distribution (APSD), was seen as the key to assuring the desired therapeutic outcomes while minimizing any adverse effects. To demonstrate the quality of the product, which underpins its safety and efficacy, various tools were required for sampling. These tools, when combined with instruments in analytical chemistry, could support the specifications to which process controls could be tuned to assure the quality of these products.

There are several major categories of pharmaceutical aerosol products, namely pressurized metered dose inhalers (MDIs), dry powder inhalers (DPIs), nebulizers, and soft

mist inhalers (Cheng Y.S., 2014), which consist of an aerosol formulation and device. Each product presents unique requirements for establishing quality and performance specifications (Uddin S. et al., 2016). The development and use of DPIs over the last three decades was largely driven by the global phase-out of chlorofluorocarbon propellants in medical products due to their deleterious effects on the ozone layer (Wu X. et al., 2010) and by the need for an alternative dosage form and route of administration for the products of biotechnology. Dry powder inhalers offer many advantages, such as their propellant-free dispersal mechanisms, product stability, portability, and ease of use. The characterization of quality and performance of DPIs will therefore be the focus of this review.

### 1.1 Development tools

Development tools for solid state products include those that measure the physicochemical properties of the materials incorporated in the formulation, establishing the quality foundation. For DPI formulations, analysis of these physicochemical properties via analytical methods is imperative, as the dispersion of powders, and therefore efficiency of the DPI product, is highly influenced by such properties. These properties, such as particle size, crystallinity, surface roughness, shape factor, moisture content, and chemical composition, all contribute to interparticulate forces (e.g., electrostatic, capillary, and van der Waals forces), which correlate to particle flow and dispersion behavior (Hickey A.J., 2018a). Beyond physicochemical properties, the

<sup>†</sup> Received 29 April 2022; Accepted 9 June 2022  
J-STAGE Advance published online 3 September 2022

\* Corresponding author: Anthony J. Hickey;  
Add: 3040 Cornwallis Road, Research Triangle Park, NC 27709,  
USA  
E-mail: [ahickey@rti.org](mailto:ahickey@rti.org)  
TEL: +1 (919) 541-6771

performance of the product must be established in the final form, which includes formulation, metering system, and device (Uddin S. et al., 2016).

## 1.2 Regulatory considerations

To establish the quality and performance of inhaled drug products, a variety of considerations are required. The drug formulation must be controlled according to ICH Q1 and Q2 which govern the components (Q1) and their quantitative proportion (Q2) in the preparation. The device is accompanied by a drug master file establishing specifications and controls on its manufacture. Critical quality attributes of DPI formulations as specified by the United States Food and Drug Administration (US FDA) include assay, impurities and degradants, leachables, foreign particulate matter, moisture content, net content, microbial load, and device characteristics (US-FDA, 2018). The drug product (formulation and device) is also subject to performance testing to evaluate the APSD and delivered dose uniformity (DDU) as described in compendia (United States Pharmacopeia [USP], European Pharmacopeia [EP], and Japanese Pharmacopoeia [JP]) and regulatory guidance documents, such as those promulgated by the United States FDA (Kuribayashi R. et al., 2017; 2019).

## 1.3 Dry powder inhaler products

It is generally accepted that particles with an aerodynamic size of 1–5  $\mu\text{m}$  can enter the lungs (Adams W.P. et al., 2007; Alagusundaram M. et al., 2010; Hickey A.J., 2018a). However, the way that the particles are prepared affect their performance characteristics (Hickey A.J., 2018a). High energy processes used to prepare micron-sized particles, such as jet milling, lead to the formation of particles with high specific surface areas (i.e., surface area with respect to mass) and surface energies. These attributes generally result in poor flow, fluidization, and deaggregation (Alagusundaram M. et al., 2010; Chaurasiya B. and Zhao Y.-Y., 2021; Hickey A.J., 2018a). Formulation strategies, such as those described below, aim to mitigate these issues.

### 1.3.1 Lactose blends

Drug products intended for the treatment of asthma and COPD are primarily lactose blends. These products include  $\alpha$ -lactose monohydrate, a monoclinic crystalline substance, as a large carrier particle onto which respirable drug particles are attached at very low concentrations. The drug is prepared in respirable sizes, often by jet milling, and is predominantly crystalline. The drug is then uniformly distributed in the lactose powder using a tertiary blending process (Hickey A.J., 2018a). The large carrier particles occupy the high energy sites of the drug, reducing drug cohesiveness and improving disaggregation and dispersal (Hickey A.J., 2018b; Wu X. et al., 2010). When the formulation is released from the device by patient inhalation, the

drug detaches from the lactose and enters the lungs. The lactose (typically 50–150  $\mu\text{m}$ ) is too large to be inhaled (Hickey A.J., 2016). This process of detachment occurs through shear, turbulence, and impacts with the walls of the mouthpiece of the device (Hickey A.J., 2018a; b). Of note, while lactose is most common, alternative carrier molecules, such as mannitol, glucose, trehalose, erythritol, and sorbitol have all been proposed as large carrier particles to serve a similar purpose (Rahimpour Y. et al., 2014; Wu X. et al., 2010).

### 1.3.2 Spray dried formulations

Spray dried formulations of drug, accomplished by atomizing a liquid drug-containing solution or suspension into a hot drying medium, have been used for high dose dry powder formulations (Hickey A.J., 2018a). Notably, tobramycin, a drug used to treat *Pseudomonas aeruginosa* infection, is delivered at a dose of 112 mg (VanDevanter D.R. and Geller D.E., 2011), a dose not easily achievable through lactose blending. The spray drying process allows for manipulation of the drug into particles of pure or near pure drug content that are amorphous in nature with lower densities than a crystalline solid particle (Hickey A.J., 2018b; Wu X. et al., 2010). It is also possible to prepare hollow particles or particles with very low density and high roughness (Gradon L. and Sosnowski T.R., 2014). These attributes confer lower interparticulate forces than those observed with milled particles, and the powder requires much less energy input from the patient for high efficiency dispersion.

### 1.3.3 Other formulations

Jet milling/lactose blending and spray drying represent the most common techniques for developing DPI formulations. However, a variety of alternative methods have been considered for the preparation of dry powder formulations. Particles prepared through thin film formation occur through dropwise deposition of the drug solution or suspension onto a frozen surface to form a thin film, which is then subject to lyophilization for solvent removal. The result is a porous, brittle, interconnected matrix that can be dispersed to small particles upon aerosolization (Hufnagel S. et al., 2022). This process has been used to prepare various aerosol particles containing both small and large molecules, including tacrolimus, lactate dehydrogenase, and lysozyme (Engstrom J.D. et al., 2008; Sahakijijam S. et al., 2020). Controlled aggregation of carrier-free microparticles following jet milling, such that dispersion is efficient and reproducible, has been utilized to prepare clofazimine particles (Brunaugh A.D. et al., 2017) and ibuprofen particles (Yazdi A.K. and Smyth H.D.C., 2016) and has also been employed in the Mometasone Furoate Twisthaler product (Yang T.T. et al., 2001). Heat-sensitive biological formulations can be prepared using either spray

freeze drying or supercritical fluid drying in methods that avoid high critical temperatures. Both methods are more complicated and expensive and are typically only used when necessary for bioactive molecules (Chaurasiya B. and Zhao Y.-Y., 2021; Graddon L. and Sosnowski T.R., 2014; Wu X. et al., 2010).

## 2. Data generation

Characterization of dry powder aerosol formations includes aspects of both quality and performance. Quality evaluation, including composition and physicochemical characteristics, is performed on the dry powder formulation to monitor properties that are known to contribute to aerosol dispersion efficiency, stability, and potency. In combination with the device and metering system, performance characterizations are then investigated to monitor the aerodynamic properties of the combined product.

### 2.1 Qualitative and quantitative composition

To establish quality measures of the drug formulation, it is important to note the nature of the drug and any additives that are employed. In the first instance, this relates to the form in which each of the components is supplied with measures of purity (Hickey A.J., 2018b). Once the nature of the components has been established, the amounts employed must be defined and specifications set to assure accuracy and reproducibility of the drug dose. The quantity of each drug should be reported both in terms of concentration (amount of ingredient per unit formulation) and net content in each blister or capsule (US-FDA, 2018). Analytical instrumentation and techniques, such as X-ray microanalysis, X-ray photoelectron spectroscopy (XPS), and inverse gas chromatography (IGC) can be utilized to determine composition and evaluate homogeneity of the composition throughout the formulation (Hickey A.J., 2018b; Hickey A.J. et al., 2007; Wu X. et al., 2010). The US FDA defines composition metrics as Q1, or qualitative composition, and Q2, or quantitative composition. These metrics are used when defining bioequivalence for the contents of a drug formulation, where Q1 would inform whether two formulations contained the same active and inactive ingredients, and Q2 would inform whether those ingredients were in the same concentration for each formulation (Hickey A.J., 2018b).

### 2.2 Physicochemical characteristics

Since the drug and any additives for a DPI formulation will be in the solid state, the structure and morphology must be defined to allow for replication of the formulation by adopting adequate controls. The typical properties that must be measured include morphology and particle size, crystallinity, polymorphism, and moisture content (Dunbar C.A. et al., 1998). Dispersion of powders is highly influenced by the size distribution of the particles as well as

their shape, surface rugosity, hardness, and porosity due to the role of these properties on interparticulate interactions, as noted above (Hickey A.J., 2018a). Particle morphology and geometric size is often visualized using scanning electron microscopy (SEM), where size is manually measured from images and gives rise to a size distribution in terms of number of particles. In contrast, laser diffraction is a population-based method that is typically representative of the true geometric particle size of regularly shaped particles, and the size distribution can be reported as a function of particle volume (Hickey A.J., 2018b). Surface geometries can be visualized with both SEM and atomic force microscopy (AFM), where AFM can also provide information on specific particle interactions between drug and carrier particles or between two drug particles (Hickey A.J. et al., 2007; Wu X. et al., 2010). Surface roughness, such as that associated with corrugated particles, is often reported to increase surface dispersibility due to decreased van der Waals forces (Chaurasiya B. and Zhao Y.-Y., 2021; Wu X. et al., 2010). However, there is also a drawback to surface irregularities, as they can promote interlocking between particles (Wu X. et al., 2010). The effect of these properties must be evaluated to determine an optimal surface roughness and shape.

Bulk crystallinity properties are often evaluated using X-ray powder diffraction analysis (XRPD). The resulting diffractogram shows a series of peaks, corresponding to crystalline structural features; the absence of such features indicates that the material is amorphous (Hickey A.J., 2018b). Crystalline solids exhibit long-range molecular order, whereas amorphous solids show no long-range molecular order. Polymorphism refers to the ability of a crystalline material to exhibit more than one crystal system. To quantify the extent to which polymorphism is present, thermal analysis using differential scanning calorimetry (DSC) can be employed, as polymorphs exhibit different melting points (Hickey A.J., 2018b). Due to their lack of order, amorphous solids often exhibit greater solubility, molecular mobility, and bioavailability, as well as faster degradation kinetics (Wu X. et al., 2010). As a consequence, amorphous materials readily take up small amounts of water vapor. This moisture can induce solid-state phase transitions, chemical degradation, and physical instability due to capillary forces and can alter the bulk density of the particles, surface charge, and aerodynamic properties (Chaurasiya B. and Zhao Y.-Y., 2021; Hickey A.J., 2016; Wu X. et al., 2010). As a result, it is necessary to monitor moisture content using either Karl Fischer titrimetric analysis or thermogravimetric analysis (TGA) (Hickey A.J., 2018b). Further, the FDA recommends evaluating the effect of storage on moisture content, including storage at 25 °C/60 % relative humidity (RH) and 30 °C/65 % RH (Lyapustina S., 2018; US-FDA, 2018). Lack of change in moisture content is considered a measure of stability.

## 2.3 Performance

Once the foundational quality of the formulation has been established, the performance of the drug should be assured. However, the product must be assembled (formulation and device) and testing performed to establish performance uniformity, as it cannot be assumed. Current compendial standards include evaluating performance via monitoring the aerodynamic particle size distribution of the resulting aerosol and delivered dose uniformity. However, additional methodologies have been proposed to increase physiological relevance and thus clinical translation.

### 2.3.1 Aerodynamic particle size distribution

The aerodynamic particle size distribution (APSD) is the property that defines the performance of inhaled products. As lung deposition is a function of the APSD, it is clear that the proportion of the distribution in the desired size range dictates the dose delivered, and thereby, safe and efficacious treatment (Hickey A.J., 2018b). Generally, it is proposed that large particles (>5 μm) are deposited via inertial impaction in the oropharynx and large airways. Smaller particles (2–5 μm) are likely deposited in the bronchioles by gravitational sedimentation, and the smallest particles (< 2 μm) are deposited by diffusion in the terminal bronchioles and alveolar region (Chaurasiya B. and Zhao Y.-Y., 2021; Hickey A.J., 2016; Lee S.L. et al., 2009). By determining the APSD, particle deposition in the lungs can be speculated. However, it is important to note that this is not a direct indicator of lung deposition, as the methodologies employed to determine APSD utilize a uniform flow rate rather than varying time-flow profiles such as those exhibited in vivo (Mitchell J. et al., 2007; Mitchell J.P. and Roberts D.L., 2013).

The APSD is determined by sampling the aerosol generated by the product using a calibrated cascade impactor. Particles released from an inhaler device are subjected to changes in flow direction under laminar conditions, where the inertia of small particles causes them to stay in the flow stream upon directional change and particles of a greater size impact on the surface. Several stages are sequentially arranged in a cascade impactor, with each stage collecting particles of a progressively smaller size (Mitchell J. et al., 2007). The US FDA accepted methods for APSD via cascade impaction include the 8-stage Anderson cascade impactor operated at 28.3 L/min, the 5-stage Marple-Miller impactor operated at 60 L/min, and the 7-stage next generation impactor (NGI) with pre-separator in place operated at 60 or 100 L/min (Frohlich E., 2019; US-FDA, 2018). The cutoff diameters for each stage of the three listed methods are presented in **Table 1**. The length of collection should be adjusted based on the flow rate to allow for the collection of 4 L of air (US-FDA, 2018). Of note, the flow utilized for analysis via NGI affects the stage diameter cutoffs, and this must be considered (Weers J. and Clark

**Table 1** Stage cutoff diameters for common cascade impactor types. <sup>a</sup>

Stage	Stage Cutoff Diameter ( $D_{50}$ ) (μm)		
	Anderson Cascade Impactor <sup>b</sup>	Marple-Miller Impactor <sup>c</sup>	Next Generation Impactor <sup>c</sup>
Stage 0	—	—	—
Stage 1	9.0	—	—
Stage 2	5.8	10.0	8.06
Stage 3	4.7	5.0	4.46
Stage 4	3.3	2.5	2.82
Stage 5	2.1	1.25	1.66
Stage 6	1.1	—	0.94
Stage 7	0.7	—	0.55
Filter	0.4	0.625	0.34

<sup>a</sup> Stage cutoff diameters are reported according to USP General Chapter <601>. <sup>b</sup> Cutoff diameters are valid at a flow rate of 28.3 L/min. <sup>c</sup> Cutoff diameters are valid at a flow rate of 60 L/min.

A., 2017). Once the aerosol has been sampled, data can be depicted as mass collected on each stage according to the cutoff diameter for that stage from calibration. Importantly, the APSD can be presented as a mass distribution, where mass relates directly to the dose of the drug and is the most relevant metric, rather than a number distribution (from SEM) or volume distribution (from laser diffraction) (Hickey A.J., 2018b).

### 2.3.2 Delivered dose uniformity

A separate technique is utilized to monitor delivered dose uniformity (DDU) to minimize analytical errors resulting from dividing the dose into recovered fractions and summing measurements, as would be done with cascade impaction. Contrarily, DDU is established by sampling aerosol from the drug product into a Teflon tube with a filter under vacuum (Hickey A.J., 2018b). The delivered dose, or emitted dose, refers to the proportion of the nominal dose that leaves the mouthpiece of the inhaler (Hickey A.J., 2018b). This sampling technique will allow the amount delivered to be measured, as well as the amount remaining in the device or metering system (e.g., capsule, blister). Importantly, as the resistance varies highly between inhaler devices, the compendial standard specifies a 4 kPa pressure drop rather than a specific flow rate. Further, the time of collection should be set to not exceed a 2-L collected volume at a constant flow rate (Hickey A.J., 2018b; US-FDA, 2018).

### 2.3.3 Aerosol delivery rate

Dry powder inhalers are unique among pulmonary drug

delivery devices in that the aerosol is administered on the inspiratory flow of the patient. Consequently, the release of the drug from the device depends on the response of the formulation and device to the energy imparted by the inspiratory flow. The temporal response resulting from this sequence of events gives rise to the aerosol being delivered at a particular rate with respect to the inspiratory flow, which in turn, can affect the site of deposition in the lungs. Multiple studies have compared parameters such as aerodynamic diameter and emitted dose as a function of flow rate. For example, Louey M.D. et al (2006) compared the response of powder dispersion released from a standardized entrainment tube with a flow rate of 28.3 and 60 L/min. The greater flow rate (i.e., 60 L/min) produced increased delivered doses and fine particle fractions (i.e., percentage of particles  $< 5 \mu\text{m}$ ) and decreased mass median aerodynamic diameters (MMAD) (Louey M.D. et al., 2006). Similarly, Coates M.S. et al. (2005) discovered that powder dispersion and throat deposition increased with increasing air flow. Recently, 25 healthy volunteers were chosen to use an inhaler to provide data for the development of idealized inspiratory waveforms. Using a numerical statistical model, Kugler Sz. et al. (2019) determined that peak inhalation flow and total volume inhaled were the main factors that affect the efficiency of deposition. In another study, flow rates of 30, 40, 60, and 90 L/min were

compared across multiple dry powder inhalers (Buttini F. et al., 2016). Here, the differences found due to flow rate were suggested to be inhaler dependent. NEXThaler<sup>®</sup> and Diskus<sup>®</sup> inhaler devices were relatively unaffected by flow rate, whereas the Turbohaler<sup>®</sup> demonstrated a large decrease in emitted dose when the device was operated at 30 or 40 L/min (Buttini F. et al., 2016). The specific resistance of an inhaler is known to control the inspiratory flow rate and dispersion (Clark A.R. and Hollingworth A.M., 1993), which likely causes these discrepancies between different inhaler models.

Due to its important influence in APSD and lung deposition, the aerosol delivery rate can be studied using light obscuration methods that are designed specifically for this purpose or can employ existing methods such as laser diffraction. Ziffels S. et al. (2015) reported a methodology for monitoring aerosol release through a cascade impaction inlet via light obscuration. Briefly, the inlet of the cascade impactor was equipped with a clear tube, a photodiode (940 nm), and a phototransistor (Fig. 1). While air flowed through the tube, reductions in voltage between the diode and transistor resulted from obscuration by particles (Fig. 1A–D). It was determined that the aerosol transit time through the tube, amplitude of obscuration, and area under the response curve were all influenced by shear conditions (i.e., 1.41 and 4.34 N/m<sup>2</sup>) and carrier (Fig. 1E–F). These

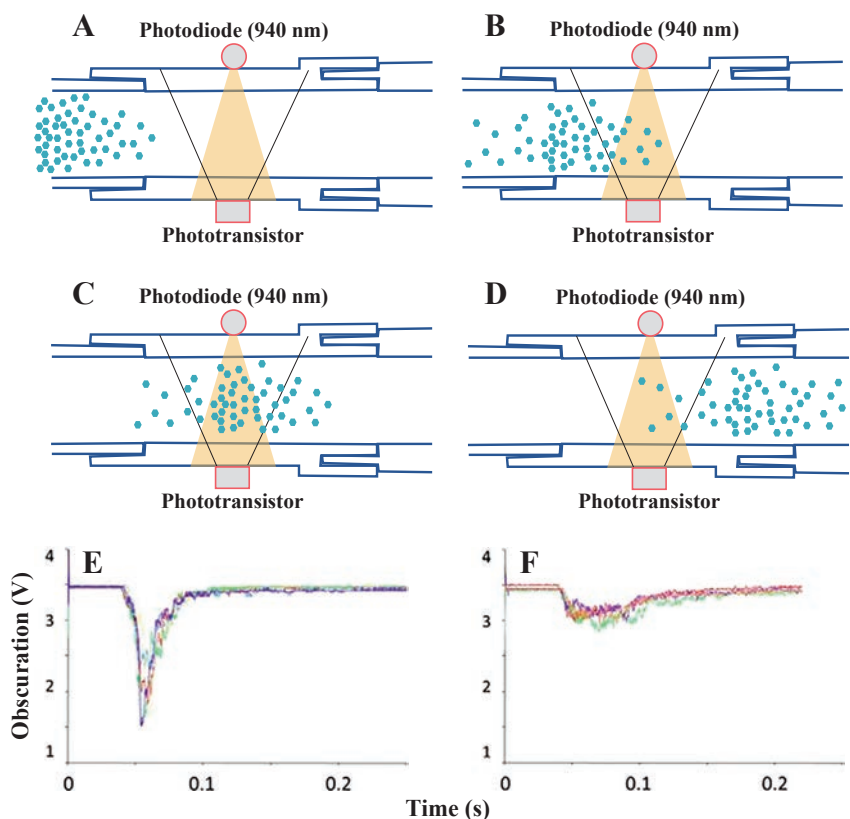


**Fig. 1** Schematic of obscuration of the phototransistor by the powder upon (A) initial generation, (B) entry to, (C) peak powder density in, and (D) departure from the optical sensing volume. Obscuration of the photodetector by albuterol sulfate delivered with lactose carrier with shear conditions of (E) 1.41 N/m<sup>2</sup> and (F) 4.34 N/m<sup>2</sup>. Figure adapted with permission from Ref. (Ziffels S. et al., 2015). Copyright: (2015) Elsevier.



same variables (i.e., shear conditions and carrier) did not affect the MMAD (Ziffels S. et al., 2015). By only evaluating metrics of APSD and DDU, the role of shear conditions and carrier would be lost, even though they may exhibit an effect in vivo. In a different approach, de Boer A.H. et al. (2002) presented the use of laser diffraction to monitor aerosol dispersion. When the apparatus was combined with a pre-separator to remove large carrier materials, dry powder inhaler formulations were able to be analyzed rapidly with high accuracy and reproducibility. Importantly, it is possible using this method to follow the size distribution in the aerosol cloud as a function of time, facilitating aerosol delivery rate measurements (de Boer A.H. et al., 2002). As the rate of delivery is likely to affect the lung deposition dose as well as the site of deposition, these methodologies allow for in vitro evaluation of aerosol delivery rate.

### 2.3.4 Physiologically relevant measures

Interest has increased in linking traditional quality measures to predictions of lung deposition as it applies to bioequivalence. Initial observations found that the fine particle fraction of drug aerosol below 3  $\mu\text{m}$  correlated to lung deposition as monitored by gamma scintigraphy (Newman S.P. and Chan H.-K., 2008). This method has since been superseded by sampling through anatomically correct inlets to the cascade impactor and/or physiologically accurate inspiratory flow cycles representing healthy and diseased lung function.

The USP sampling inlet for a cascade impactor, as is described in USP General Chapter <601>, was the first standardized inlet and allowed for meaningful comparisons between labs. However, the USP sampling inlet is a right-angled tube that does not accurately mimic airway geometry (Kaviratna A. et al., 2019). Several approaches have been used to develop realistic mouth-throat models as a sampling inlet to a cascade impactor, including geometries based on cadaver casts or CT/MRI data or idealized geometries using critical airway dimensions (Newman S.P. and Chan H.-K., 2020). Zhang Y. et al. (2007) reported a comparison on mouth-throat deposition from a DPI between the USP sampling inlet, an idealized mouth-throat model, and a highly idealized mouth-throat model. Following analysis, it was discovered that the USP inlet had the lowest mouth-throat deposition ( $57.3 \pm 4.5\%$ ), showing that both the idealized and highly idealized models, whose depositions ( $67.8 \pm 2.2\%$  and  $69.3 \pm 1.1\%$ , respectively) were much closer to the reported in vivo deposition ( $65.8 \pm 10.1\%$ ), improved accuracy of predicting in vivo deposition from in vitro analyses (Zhang Y. et al., 2007). From this study, it was realized that additional factors must be considered when developing and testing mouth-throat models, namely age, peak inspiratory flow, and disease state.

A study reported by Below A. et al. (2013) considered the role of age on mouth-throat geometry. An idealized

pediatric upper airway model, approximating age 4–5, was used to evaluate DPI performance comparing three inspiratory flow rates (28–75 L/min). High quantities of drug, up to 80 %, were deposited in the airway model, facilitating potential pulmonary doses of 29 % and 8–12 % for Easyhaler<sup>®</sup> and Novolizer<sup>®</sup> devices, respectively (Below A. et al., 2013). With a USP sampling inlet, it is likely that the potential pulmonary dose would be overestimated. Dolovich M.B. et al. (2019) evaluated three mouth-throat models specifically designed from CT scans of three COPD patients using constant inspiratory flow rates of 30, 60, 90, and 120 L/min. In this study, anatomical differences between the three patient models were found to be a major source of variability in lung deposition. The lung dose for each model was relatively consistent across all flow rates with the exception of a slight decrease in delivery at the higher inspiratory flow rates (Dolovich M.B. et al., 2019). These reports highlight the influence of mouth-throat geometry on predicting lung deposition, describing the need for more realistic sampling inlets than the current USP standard. However, an additional factor not considered in these evaluations includes the reality that the inspiratory flow is not a constant value but instead increases and then decreases in rate for each breath.

This dynamic nature of the inspiratory flow is likely to affect lung deposition, necessitating the incorporation of time-dependent breathing profiles to current in vitro analyses (Dorosz A. et al., 2020). In combining the roles of anatomy and breathing profile, Olsson B. et al. (2013) evaluated three throat models, including high, medium, and low filtering efficiency, and three inspiratory profiles. The three profiles were chosen to represent the 5<sup>th</sup>, 50<sup>th</sup>, and 95<sup>th</sup> percentiles from 74 inspiratory flow patterns from healthy adults (Fig. 2B). For APSD measurements, the mouth-throat model was utilized as a sampling inlet to a cascade impactor, which was complete with a mixing inlet connecting to both a pressurized air source (to maintain a constant flow across the cascade impactor) and a breath profile generator (to simulate an inspiratory flow cycle for the inhaler) (Fig. 2A). Three DPIs were investigated, and it was determined that the mouth-throat geometry had a significant effect for all devices, with smaller throat models facilitating less drug penetrating the model. Further, the flow profile was found to significantly affect two out of three DPIs, where the amount of drug penetrating the model, an estimate of potential lung deposition, was lower for weaker flow profiles (Olsson B. et al., 2013). In another comprehensive analysis, Wei X. et al. (2018) compared eight mouth-throat models, including small, medium, and large Virginia Commonwealth University (VCU) models, small, medium, and large Oropharyngeal Consortium (OPC) models, a medium adult Alberta Idealized Throat, and a USP sampling inlet, as displayed in Fig. 3. In addition to the many models, weak, medium, and strong

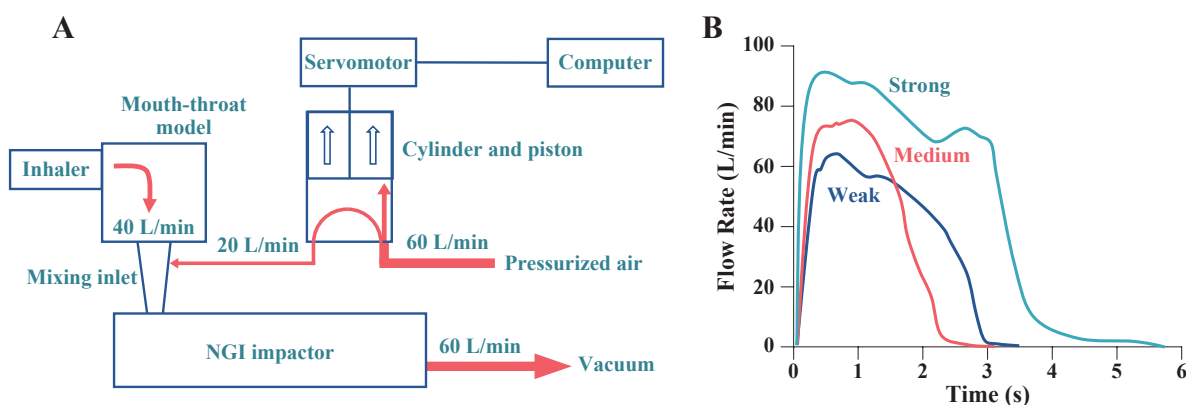


**Fig. 2** (A) Schematic demonstrating mixing inlet, breath profile generator, and impactor setup. Piston movement allows for flow through inhaler as set using the breath profile generator but holds flow in impactor constant. (B) Approximate flow profiles representing weak, medium, and strong flow. Figure adapted with permission from Ref. (Olsson B. et al., 2013). Copyright (2013) Mary Ann Liebert Inc.

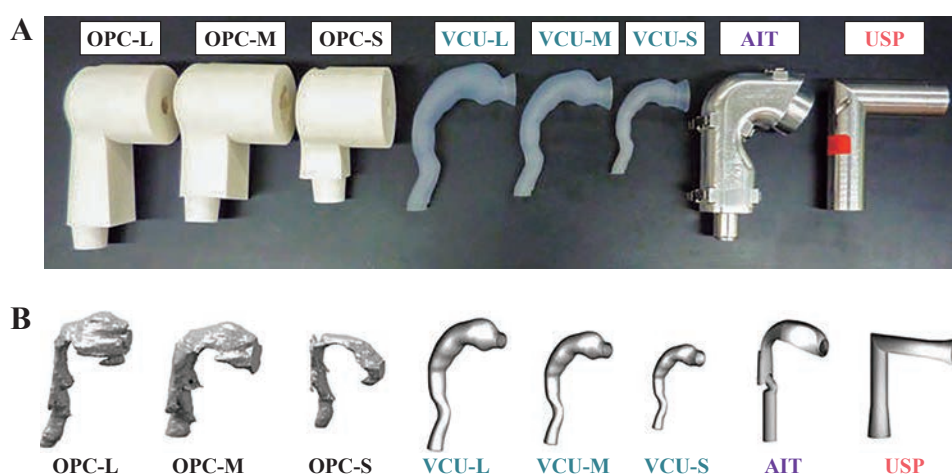


**Fig. 3** Realistic mouth-throat models developed for inhaler in vitro testing: OPC large (OPC-L), OPC medium (OPC-M), OPC small (OPC-S), VCU large (VCU-L), VCU medium (VCU-M), VCU small (VCU-S), Alberta Idealized Throat (AIT), and USP sampling inlet. (A) side view; (B) internal geometry. Figure adapted with permission from Ref. (Wei X. et al., 2018). Copyright (2018) Mary Ann Liebert Inc.

inspiratory flow profiles were included using a breath simulator. Both the model geometry and flow condition had significant effects on mouth-throat deposition; however, the effect of flow condition was stronger than that of the geometry. Consistent with previous reports, the USP throat retained the least amount of drug (Wei X. et al., 2018). In all described studies, it is noted that the mouth-throat geometry and inspiratory flow cycle affect mouth-throat and lung depositions. To enhance correlation between in vitro analyses and in vivo outcomes, the incorporation of these variables into in vitro analyses is essential.

### 3. Data analysis

Following the collection of data through the methods presented above, further analysis must be performed to extract meaningful conclusions. Further, analytical methods for comparing these results between different formulations and devices, such as in the case of preparing generic versions of brand-name drugs, must be implemented. These necessities give rise to statistical descriptors for under-

standing the data and profile comparison techniques, such as the chi-square comparison and multivariate statistical analysis techniques, as described below.

#### 3.1 Statistical descriptors

Historically, cascade impactor data was described in terms of population statistics. Each particle deposits according to its aerodynamic diameter, which is defined as a unit density sphere with the same terminal settling velocity as the real particle according to Stokes' Law. This aerodynamic diameter encompasses particle attributes including shape, density, and physical size (Hickey A.J., 2004). However, particles exist in populations, powders, that can be described in terms of a central tendency of the distribution and its breadth. Many distributions conform to a log-normal mathematical function and consequently can be described by a median according to the mass deposited on each stage, thereby giving rise to a MMAD. The MMAD also represents a degree of deaggregation, where smaller MMAD values (i.e., decreased median aerodynamic diameter)

represent greater particle deaggregation (Louey M.D. et al., 2006). As the MMAD is calculated using the logarithm of particle size in a geometric rather than arithmetic function, the geometric standard deviation (GSD) represents the variance of the distribution as a unitless dimension. The relationship between GSD and MMAD is as follows:

$$\text{GSD} = \frac{\text{MMAD}}{d_{16}} = \frac{d_{84}}{\text{MMAD}} = \sqrt{\frac{d_{84}}{d_{16}}} \quad (1)$$

Where  $d_{16}$  represents the aerodynamic diameter one standard deviation below the median (at the 16<sup>th</sup> percentile) and  $d_{84}$  represents the aerodynamic diameter one standard deviation above the median (at the 84<sup>th</sup> percentile) (Chaurasiya B. and Zhao Y.-Y., 2021; Finlay W.H. and Darquenne C., 2020; Hickey A.J., 2004). Aerosols with a GSD greater than 1.15 are considered to be polydisperse, where larger values indicate greater levels of heterogeneity in the size distribution (Chaurasiya B. and Zhao Y.-Y., 2021; Pleasants R.A. and Hess D.R., 2018). Most therapeutic aerosols exhibit GSDs in the range of 2–3 (Pleasants R.A. and Hess D.R., 2018).

Oftentimes, conversion of the APSD to something that may indicate potential lung deposition is beneficial. In these cases, the fine particle dose (FPD) and fine particle fraction (FPF) are defined. While exact cutoffs vary, the FPD is generally referred to as the total dose of dry powder, in terms of mass, that is below 3–5  $\mu\text{m}$  (Chaurasiya B. and Zhao Y.-Y., 2021; Dunbar C.A. et al., 1998). The FPF normalizes the FPD to the total emitted dose (Pleasants R.A. and Hess D.R., 2018). Further, this metric represents a degree of drug deaggregation, where a higher FPF indicates greater deaggregation (Louey M.D. et al., 2006).

### 3.2 Profile comparisons

While statistical descriptors as described above are useful for data interpretation, the US FDA advises that it is inadequate to characterize the APSD only in terms of MMAD, GSD, and FPD/FPF (US-FDA, 2018), especially when trying to compare profiles for bioequivalence determinations. As such, multiple techniques in comparing APSD profiles have been investigated. The major goals of a profile comparison test, as specified by the Product Quality Research Institute (PQRI) and Orally Inhaled and Nasal Drug Products Technical Committee (OINDP-TC) include: (1) the test is sensitive to differences at each impactor deposition site; (2) the test is based on a single metric that incorporates all differences at all sites to minimize the number of in vitro tests that must be performed; (3) the test is applicable to all inhalation products; and, (4) the test is independent of impactor type (Adams W.P. et al., 2007). With these goals in mind, multiple approaches have been presented.

#### 3.2.1 Stage-by-stage and stage-grouping comparison

The most straightforward method of profile comparisons involves comparing the mass of drug deposited on each stage individually or as groups of stages (EMA, 2009; Taki M. et al., 2011). This methodology is based on the premise that by comparing only MMAD, GSD, and FPD/FPF, changes to the distribution in the 1–5  $\mu\text{m}$  range may be overlooked in vitro but could affect the drug deposition site in the lungs. The European Medicines Agency (EMA) specified that two products must be within 15 % of each other at each deposition stage, or at 4 justified grouped stages, when tested at all flow rates to be considered equivalent (EMA, 2009). While this method is sensitive to differences in mass at each impactor stage, it does not provide a single metric for testing equivalence and does not allow for comparisons between different impactor configurations or types.

#### 3.2.2 Chi-square comparison

The chi-square ratio test does not ascribe meaning to the data under consideration but does allow comparison of two data sets which historically were considered the test and reference profile. The chi-square statistic, calculated as the sum of the squared differences in deposition at each impaction site between the two profiles, scaled by the average deposition on that site, provides a measure of distance between two profiles (Adams W.P. et al., 2007). The developed singular test metric is a comparison of the chi-square statistics characterizing both products (Adams W.P. et al., 2007). However, both products must be tested the same way with the same impactor configuration. This test allows statistical inferences to be drawn but requires subjective input to assure that meaning ascribed to the particle size distribution (i.e., two profiles are the same), is correct by observation.

The PQRI working group conducted an assessment in which they separated the impactor sized mass from the fine particle fraction and applied chi-square analysis. Subsequently, experts in the field were asked to observe the profile being compared to confirm that the chi-square ratio test was predicting similarity as would be defined by simply comparing the data. The goal of this assessment was to determine a critical value of the chi-square ratio that would separate identical profiles from those that are different (Adams W.P. et al., 2007). Unfortunately, it was discovered that choosing a singular value to separate equivalent from different profile pairs was difficult (Christopher D. et al., 2007b). Proposed critical values included 7.66 and 2.75. While 2.75 provided better discriminatory power, it resulted in less consistency when compared to the judgment of experts in the working group. While a promising method, no guidelines have been set at this time for evaluating using this test (Christopher D. et al., 2007a).

### 3.2.3 Multivariate analysis

Cascade impaction data is complicated by the fact that deposition on each stage is accompanied by variability from each replicate, while the distribution itself represents information on the variability of particle sizes, carrying the consequences for the behavior of the aerosol when inhaled. Multivariate analysis techniques, such as principal component analysis (PCA), allow the simplification of data while retaining as much information as possible. PCA is an orthogonal linear transformation that transforms the data to a new coordinate system, where the largest variance is accounted for on the first coordinate, the second greatest variance is accounted for on the second coordinate, and so on (Christopher J.D. et al., 2013). This process reduces the number of variables that must be considered by developing principal components through a purely statistical model. The threshold for equivalence using this method is related to a specified confidence interval (Christopher J.D. et al., 2013).

Another method based on multivariate analysis involves orthogonal partial least squares analysis (OPLS). While PCA is an unsupervised statistical method and is generally used as a pattern recognition tool prior to OPLS, OPLS itself is a supervised method (Shi S. and Hickey A.J., 2009). Importantly, OPLS is not a statistical test but is an analytical tool. The resulting OPLS score plot provides a visual representation of the comparison between a test and reference profile. The larger the visual difference, the further they are separated based on principal components. However, this is a qualitative test; to derive a semi-quantitative parameter,  $R^2$  can be employed. Two identical profiles would give an  $R^2$  value of one whereas two completely different profiles would give an  $R^2$  value of zero (Shi S. and Hickey A.J., 2009). The defined equivalence parameter as reported by Shi S. and Hickey A.J. (2009) is termed Eq, where one subtracted by the  $R^2$  value gives this measure of equivalence. While not a purely statistical method, this proposed metric allows for semi-quantitative analysis when comparing two APSD profiles.

### 3.3 Efficient data analysis

Full APSD evaluations from a cascade impactor require time and resources that may not be necessary for formulation and device optimization as well as routine quality control analyses. While these evaluations need to be accurate and precise, it is highly desired that throughput be increased compared to full cascade impactor and data analyses (Tougas T.P. et al., 2011). Two concepts have been introduced to expedite data acquisition and subsequent analysis: the abbreviated impactor measurement (AIM) concept and the efficient data analysis (EDA) concept.

The AIM concept involves altering the configuration of the cascade impactor to streamline analysis. Rather than provide each stage’s measurement, unnecessary stages

are removed depending on the goal of the analysis. For example, a configuration for quality control (AIM-QC) to monitor the MMAD includes a sampling inlet and initial stage, an intermediate stage near the MMAD, and a final filter. The intermediate stage as a boundary should split the powder in half to a small particle mass (SPM) and large particle mass (LPM). If the SPM and LPM portions do not each contain 50 % of the impactor-sized powder mass, it can be determined that the MMAD has shifted (Tougas T.P. et al., 2011). A different configuration has been proposed for predicting human respiratory tract deposition (AIM-pHRT), containing two intermediate stages in addition to a sampling inlet and final filter. With this method, the first stage sets a boundary at approximately 5  $\mu\text{m}$ , where the mass deposited after that stage is referred to as the fine particle mass, or FPM. The second stage is set at a boundary of approximately 1  $\mu\text{m}$ , where the mass of particles deposited after that stage denotes the extra-fine particle mass (EPM) (Tougas T.P. et al., 2011). Quantification of the EPM may be desired as this portion may be related to systemic absorption or may be exhaled before deposition can occur, especially if one’s breath is not held following inhalation (Tougas T.P. et al., 2011). However, at a minimum for the AIM-pHRT configuration, it is necessary to distinguish the FPM, which describes the mass of particles with the potential to carry drug into the respiratory tract, from the coarse particle mass, which will likely not penetrate past the oropharyngeal region (Mitchell J.P. and Tougas T.P., 2013).

Efficient data analysis represents a way to simplify AIM data as well as full-resolution cascade impaction data. Two EDA metrics are defined: (1) the large and small particle mass (LPM + SPM), and (2) their ratio (LPM/SPM) (Tougas et al., 2011). These metrics signify the amplitude of the mass distribution profile and the position of the

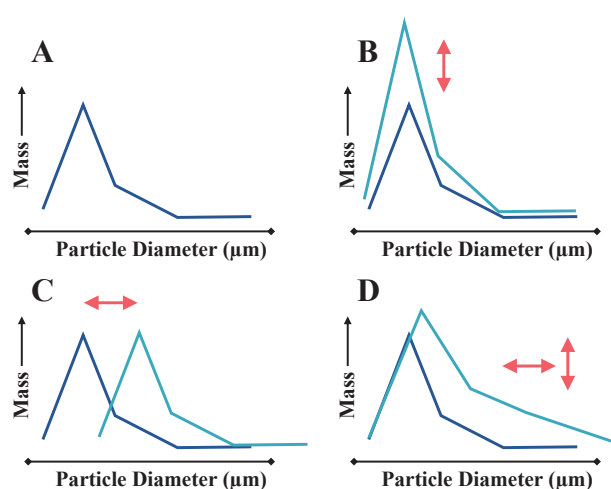


**Fig. 4** Changes in aerodynamic particle size distribution. (A) Nominal APSD, (B) shift in area under the curve (C) shift in central tendency (i.e., mean), and (D) shift in both mean and area. Figure adapted with permission from Ref. (Tougas T.P. et al., 2009). Copyright (2009) Springer Nature.

profile on the size scale and can detect changes in position or total area independently of each other (Fig. 4) (Tougas T.P. et al., 2009). When EDA is combined with an AIM approach, the time per measurement is drastically reduced, increasing throughput, and sensitivity to APSD shifts is enhanced (Mitchell J.P. and Tougas T.P., 2013). A general recommendation proposed by Mitchell J.P. and Tougas T.P. (2013) includes full resolution cascade impaction for initial screening and developing, AIM-QC for quality control measures on a smaller list of candidates; and AIM-pHRT with an anatomically correct sampling inlet for in vitro equivalence comparisons.

#### 4. Data interpretation

The implications of data obtained from in vitro testing for safety and efficacy in vivo is an important potential application, but so far, a true in vitro/in vivo correlation has been difficult to establish. The following sections describe some considerations that have been given to this topic and illustrate the significance that success in this endeavor would have for pharmaceutical product development.

##### 4.1 Inhaled biopharmaceutical classification system

The gastro-intestinal biopharmaceutical classification system (giBCS), which defines the desirability of developing a drug for oral delivery based on its solubility and permeability, has been a working guide for drug discovery and delivery since the 1990s (Hastedt J.E. et al., 2016). The approach is usually depicted as a quadrant schematic in which drugs that are highly soluble and permeable are logical candidates for further development, drugs that have low solubility and high permeability, or vice versa, may be considered candidates for formulation development to improve their properties, and those with low solubility and permeability are considered poor candidates for further development (Hickey A.J., 2018b). Using these criteria, candidate selection can be addressed early in the discovery process where many analogues are available for consideration.

In 2015, a workshop cosponsored by the American Association of Pharmaceutical Sciences (AAPS), US FDA, and USP was held to address the possibility of developing an inhaled biopharmaceutical classification system (iBCS) (Bäckman P. et al., 2022; Hastedt J.E. et al., 2016; 2022). It is important to recognize that the majority of inhaled pharmaceutical agents are intended for localized action. Consequently, permeability as defined for the giBCS may not be relevant. In addition, unlike the gastro-intestinal tract that is essentially a tube through which substances pass by entry and exit, the lungs are a closed container in which clearance mechanisms are required to remove any deposited substances. These differences suggest that alternate or additional metrics must be adopted when

developing an iBCS. Considerations for developing an iBCS include lung physiology, regional aerosol deposition, clearance mechanisms, particle dissolution, permeability, and absorption (Bäckman P. et al., 2022; Frohlich E., 2019; Hastedt J.E. et al., 2016; 2022). From this workshop, it was determined that there is an opportunity in creating this model, and additional work on this topic is forthcoming.

##### 4.2 Bioequivalence and in vitro/in vivo correlation

The goal of predicting in vivo deposition from in vitro data has been an objective of pharmaceutical scientists for decades. With the significant increase in new products over the last 20 years and the desire to bring forward generic versions, this objective has taken on urgency. When performing a comparison for bioequivalence, the goal is to demonstrate equivalent performance (i.e., not better, not worse) (Lyapustina S., 2018). However, the complexity of aerosol dosage forms makes them difficult to mimic and raises many questions about what defines equivalence (Adams W.P. et al., 2010; Apiou-Sbirlea G. et al., 2013). In oral formulations, the main way to analyze bioequivalence is through serum concentration over time; however, with inhaled formulations, the lung is the target and systemic absorption is typically not desired. One metric that has been suggested for inhaled drug bioequivalence studies is to look at the concentration of drug in exhaled breath condensate (Khoubnasabjafari M. et al., 2019). Though no direct guidance has been placed forward as of yet for inhaled therapeutics bioequivalence comparisons (Apiou-Sbirlea G. et al., 2013), profile comparisons based on cascade impactor data have garnered the most interest, as described above. However, regulatory statures for comparing inhaled drugs for bioequivalence both in vitro and in vivo are urgently needed.

From the foregoing discussion, it can be seen that in vitro methods have evolved from standards that would establish therapeutic aerosol quality in terms of accuracy and reproducibility of performance to physiologically relevant methods that would produce data predictive of lung deposition and disposition. Current compendial in vitro standards have not consistently correlated with pharmacokinetics and efficacy in vivo (Hickey A.J., 2018b). However, if physiologically relevant advances can be made to these standards, then there is the possibility that in vivo studies can be limited to the first instance of drug testing and perhaps, in the future, eliminated as a requirement for regulatory approval.

For dry powder inhalers, physiologically relevant measures of APSD and DDU would seem to be the first step towards in vitro/in vivo correlation (IVIVC). The goal of IVIVC is to construct a model that can be used to predict in vivo outcomes, such as lung deposition and peripheral-to-central deposition ratio, from in vitro cascade impactor data (Chow M.Y.T. et al., 2021). In vivo, peripheral-to-central deposition ratios have been shown to

qualitatively deviate between healthy patients and those with asthma or COPD, where patients with lung diseases exhibit slightly less drug deposition in the lung periphery. It was also proposed that differences in peripheral-to-central deposition ratios in vivo may be due to intersubject variability caused by differences in airway dimensions, which occurred to a stronger extent than variability resulting from flow rate or delivery modality (Clark A.R., 2012). As such, additional parameters incorporated within cascade impaction analysis, such as physiological throat models and representative inspiratory flow cycles of healthy and diseased individuals, may prove beneficial in such correlations. As noted above, since the point at which the aerosol is dispersed on the inspiratory flow may also affect deposition, a measure of the aerosol delivery rate should be considered as an additional in vitro analysis for the prediction of in vivo outcomes.

## 5. Conclusions

Pharmaceutical inhalation aerosols are widely used to treat diseases, notably asthma, COPD, infectious diseases, and rare diseases, such as cystic fibrosis. Dry powder inhaler products represent a significant proportion of the market. To assure safety and efficacy of these products, their quality and performance must be assured in terms of the accuracy and reproducibility of drug delivery. Since the effective dose depends on efficient aerosol generation and deposition in the lungs, properties that guarantee these outcomes must be measured. Standardized methods have been available for decades to define properties that establish quality, but recent efforts have focused on rendering these quality measures relevant to in vivo deposition and link to safety and efficacy. As these methods emerge, the role of compendial methods and regulatory guidance may progress towards in vivo relevance. Ultimately, this may support considerations of an inhaled biopharmaceutical classification system, which can be extrapolated to bioequivalence testing in a manner similar to drugs delivered by the gastro-intestinal route of administration.

## Acknowledgements

The authors would like to thank the RTI Fellow Program for their financial support.

## Nomenclature

AAPS	American Association of Pharmaceutical Sciences
AFM	Atomic force microscopy
AIM	Abbreviated impactor measurement
API	Active pharmaceutical ingredient
APSD	Aerodynamic particle size distribution
CF	Cystic fibrosis
COPD	Chronic obstructive pulmonary disease
CT	Computed tomography

DDU	Delivered dose uniformity
DPI	Dry powder inhaler
DSC	Differential scanning calorimetry
EDA	Efficient data analysis
EP	European Pharmacopeia
EPM	Extra-fine particle mass ( $\mu\text{g}$ , mg)
Eq	Equivalence parameter
FPD	Fine particle dose ( $\mu\text{g}$ , mg)
FPF	Fine particle fraction (%)
FPM	Fine particle mass ( $\mu\text{g}$ , mg)
giBCS	Gastro-intestinal biopharmaceutical classification system
GSD	Geometric standard deviation
iBCS	Inhaled biopharmaceutical classification system
ICH	International Conference on Harmonization
IGC	Inverse gas chromatography
JP	Japanese Pharmacopeia
LPM	Large particle mass ( $\mu\text{g}$ , mg)
MDI	Metered dose inhaler
MMAD	Mass median aerodynamic diameter ( $\mu\text{m}$ )
MRI	Magnetic resonance imaging
NGI	Next generation impactor
OINDP	Orally inhaled and nasal drug products
OPC	Oropharyngeal Consortium
OPLS	Orthogonal partial least squares analysis
PCA	Principal component analysis
PQRI	Product Quality Research Institute
RH	Relative humidity (%)
SEM	Scanning electron microscopy
SPM	Small particle mass ( $\mu\text{g}$ , mg)
TGA	Thermogravimetric analysis
US FDA	United States Food and Drug Administration
USP	United States Pharmacopeia
VCU	Virginia Commonwealth University
XPS	X-ray photoelectron spectroscopy
XRPD	X-ray powder diffraction

## References

- Adams W.P., Ahrens R.C., Chen M.-L., Christopher D., Chowdhury B.A., Conner D.P., Dalby R., Fitzgerald K., Hendeles L., Hickey A.J., Hochhaus G., Laube B.L., Lucas P., Lee S.L., Lyapustina S., et al., Demonstrating bioequivalence of locally acting orally inhaled drug products (OIPs): workshop summary report, *Journal of Aerosol Medicine and Pulmonary Drug Delivery*, 23 (2010) 1–29. DOI: 10.1089/jamp.2009.0803
- Adams W.P., Christopher D., Lee D.S., Morgan B., Pan Z., Singh G.J.P., Tsong Y., Lyapustina S., Product quality research institute evaluation of cascade impactor profiles of pharmaceutical aerosols, part 1: background for a statistical method, *AAPS PharmSciTech*, 8 (2007) E1–E6. DOI: 10.1208/pt0801004
- Alagusundaram M., Deepthi N., Ramkanth S., Angalapameswari S., Saleem T.S.M., Gnanaprakash K., Thiruvengadarajan V.S., Chetty C.M., Dry powder inhalers—an overview,

- International Journal of Research in Pharmaceutical Sciences, 1 (2010) 34–42.
- Apiou-Sbirlea G., Newman S., Fleming J., Siekmeier R., Ehrmann S., Scheuch G., Houchhaus G., Hickey A., Bioequivalence of inhaled drugs: fundamentals, challenges and perspectives, *Therapeutic Delivery*, 4 (2013) 343–367. DOI: 10.4155/tde.12.161
- Bäckman P., Cabal A., Clark A., Ehrhardt C., Forbes B., Hastedt J., Hickey A., Hochhaus G., Jiang W., Kassinos S., Kuehl P.J., Prime D., Son Y.-J., Teague S.P., Tehler U., et al., iBCS: 2. Mechanistic modeling of pulmonary availability of inhaled drugs versus critical product attributes, *Molecular Pharmaceutics*, 19 (2022) 2040–2047. DOI: 10.1021/acs.molpharmaceut.2c00112
- Below A., Bickmann D., Breitreutz J., Assessing the performance of two dry powder inhalers in preschool children using an idealized pediatric upper airway model, *International Journal of Pharmaceutics*, 444 (2013) 169–174. DOI: 10.1016/j.ijpharm.2013.01.007
- Brunaugh A.D., Jan S.U., Ferrati S., Smyth H.D.C., Excipient-free pulmonary delivery and macrophage targeting of clofazimine via air jet micronization, *Molecular Pharmaceutics*, 14 (2017) 4019–4031. DOI: 10.1021/acs.molpharmaceut.7b00690
- Buttini F., Brambilla G., Copelli D., Sisti V., Balducci A.G., Bettini R., Pasquali I., Effect of flow rate on in vitro aerodynamic performance of NEXThaler(R) in comparison with Diskus(R) and Turbohaler(R) dry powder inhalers, *Journal of Aerosol Medicine and Pulmonary Drug Delivery*, 29 (2016) 167–178. DOI: 10.1089/jamp.2015.1220
- Chaurasiya B., Zhao Y.-Y., Dry powder for pulmonary delivery: a comprehensive review, *Pharmaceutics*, 13 (2021) 31. DOI: 10.3390/pharmaceutics13010031
- Cheng Y.S., Mechanisms of pharmaceutical aerosol deposition in the respiratory tract, *AAPS PharmSciTech*, 15 (2014) 630–640. DOI: 10.1208/s12249-014-0092-0
- Chow M.Y.T., Tai W., Chang R.Y.K., Chan H.-K., Kwok P.C.L., In vitro-in vivo correlation of cascade impactor data for orally inhaled pharmaceutical aerosols, *Advanced Drug Delivery Reviews*, 177 (2021) 113952. DOI: 10.1016/j.addr.2021.113952
- Christopher D., Adams W., Amann A., Bertha C., Byron P.R., Doub W., Dunbar C., Hauck W., Lyapustina S., Mitchell J., Morgan B., Nichols S., Pan Z., Pal Singh G.J., Tougas T., et al., Product quality research institute evaluation of cascade impactor profiles of pharmaceutical aerosols, part 3: final report on a statistical procedure for determining equivalence, *AAPS PharmSciTech*, 8 (2007a) 65. DOI: 10.1208/pt0804090
- Christopher D., Adams W.P., Lee D.S., Morgan B., Pan Z., Singh G.J.P., Tsong Y., Lyapustina S., Product Quality Research Institute evaluation of cascade impactor profiles of pharmaceutical aerosols: part 2—evaluation of a method for determining equivalence, *AAPS PharmSciTech*, 8 (2007b) E39–E48. DOI: 10.1208/pt0801005
- Christopher J.D., Strickland H., Morgan B., Dey M., Silcock A., Tougas T.P., Mitchell J.P., Lyapustina S.A., Performance characterization of EDA and its potential to improve decision making in product batch release, in: Tougas T.P., Mitchell J.P., Lyapustina S.A. (Eds.), *Good Cascade Impactor Practices, AIM and EDA for Orally Inhaled Products*, Springer US, Boston, MA, 2013, pp. 173–249, ISBN: 978-1-4614-6296-5. DOI: 10.1007/978-1-4614-6296-5\_8
- Clark A.R., Understanding penetration index measurements and regional lung targeting, *Journal of Aerosol Medicine and Pulmonary Drug Delivery*, 25 (2012) 179–187. DOI: 10.1089/jamp.2011.0899
- Clark A.R., Hollingworth A.M., The relationship between powder inhaler resistance and peak inspiratory conditions in healthy volunteers—implications for in vitro testing, *Journal of Aerosol Medicine*, 6 (1993) 99–110. DOI: 10.1089/jam.1993.6.99
- Coates M.S., Chan H.-K., Fletcher D.F., Raper J.A., Influence of air flow on the performance of a dry powder inhaler using computational and experimental analyses, *Pharmaceutical Research*, 22 (2005) 1445–1453. DOI: 10.1007/s11095-005-6155-x
- de Boer A.H., Gjaltema D., Frijlink P.H.H.W., Characterization of inhalation aerosols: a critical evaluation of cascade impactor analysis and laser diffraction technique, *International Journal of Pharmaceutics*, 249 (2002) 219–231. DOI: 10.1016/S0378-5173(02)00526-4
- Dolovich M.B., Kuttler A., Dimke T.J., Usmani O.S., Biophysical model to predict lung delivery from a dual bronchodilator dry-powder inhaler, *International Journal of Pharmaceutics*, X, 1 (2019) 100018. DOI: 10.1016/j.ijpx.2019.100018
- Dorosz A., Cánovas P.M., Moskal A., Cascade impactor study of aerosolization process during passive dry powder inhaler performance under unsteady versus steady flow conditions, in: Marek Ochowiak S.W., Piotr Tomasz Mitkowski, Michal Doligalski (Ed.) *Practical Aspects of Chemical Engineering, PAIC 2019*, Springer, Switzerland, 2020, pp. 47–57, ISBN: 978-3-030-39866-8. DOI: 10.1007/978-3-030-39867-5\_6
- Dunbar C.A., Hickey A.J., Holzner P., Dispersion and characterization of pharmaceutical dry powder aerosols, *KONA Powder and Particle Journal*, 16 (1998) 7–45. DOI: 10.14356/kona.1998007
- EMA (European Medicines Agency), Pre-authorisation evaluation of medicines for human use, European Medicines Agency, London, 2009. <[https://www.ema.europa.eu/en/documents/scientific-guideline/guideline-requirements-clinical-documentation-orally-inhaled-products-oip-including-requirements\\_en.pdf](https://www.ema.europa.eu/en/documents/scientific-guideline/guideline-requirements-clinical-documentation-orally-inhaled-products-oip-including-requirements_en.pdf)> accessed 20.07.2022.
- Engstrom J.D., Lai E.S., Ludher B.S., Chen B., Milner T.E., III R.O.W., Kitto G.B., Johnston K.P., Formation of stable submicron protein particles by thin film freezing, *Pharmaceutical Research*, 25 (2008) 1334–1346. DOI: 10.1007/s11095-008-9540-4
- Finlay W.H., Darquenne C., Particle size distributions, *Journal of Aerosol Medicine and Pulmonary Drug Delivery*, 33 (2020) 178–180. DOI: 10.1089/jamp.2020.29028.whf
- Frohlich E., Biological obstacles for identifying in vitro-in vivo correlations of orally inhaled formulations, *Pharmaceutics*, 11 (2019) 316. DOI: 10.3390/pharmaceutics11070316
- Gradon L., Sosnowski T.R., Formation of particles for dry powder inhalers, *Advanced Powder Technology*, 25 (2014) 43–55. DOI: 10.1016/j.apt.2013.09.012
- Hastedt J.E., Bäckman P., Cabal A., Clark A., Ehrhardt C., Forbes B., Hickey A.J., Hochhaus G., Jiang W., Kassinos S., Kuehl P.J., Prime D., Son Y.-J., Teague S., Tehler U., et al., iBCS: 1. Principles and framework of an inhalation-based biopharmaceutics classification system, *Molecular Pharmaceutics*, 19 (2022) 2032–2039. DOI: 10.1021/acs.molpharmaceut.2c00113
- Hastedt J.E., Bäckman P., Clark A.R., Doub W., Hickey A., Hochhaus G., Kuehl P.J., Lehr C.-M., Mauser P., McConville J., Niven R., Sakagimi M., Weers J.G., Scope and relevance of a pulmonary biopharmaceutical classification system AAPS/FDA/USP Workshop March 16–17th, 2015 in Baltimore, MD, *AAPS Open*, 2 (2016) 1(20pp). DOI: 10.1186/s41120-015-0002-x
- Hickey A.J., Methods of aerosol particle size characterization, in:

- Hickey A.J. (Ed.) *Pharmaceutical Inhalation Aerosol Technology*, Marcel Dekker, Inc., New York, NY, 2004, pp. 345–384, ISBN: 9780429223464. DOI: 10.1201/9780203912898
- Hickey A.J., *Pulmonary drug delivery: pharmaceutical chemistry and aerosol technology*, in: Wang B., Hu L., Siahaan T.J. (Eds.), *Drug Delivery: Principles and Applications* (Second Edition), John Wiley & Sons, Inc., Hoboken, NJ, 2016, pp. 186–206, ISBN: 9781118833360. DOI: 10.1002/9781118833322.ch10
- Hickey A.J., *Fundamentals of dry powder inhaler technology*, in: Merkus H.G., Meesters G.M.H., Oostra W. (Eds.), *Particles and Nanoparticles in Pharmaceutical Products: Design, Manufacturing, Behavior and Performance*, Springer International Publishing, Cham, 2018a, pp. 213–232, ISBN: 978-3-319-94174-5. DOI: 10.1007/978-3-319-94174-5\_5
- Hickey A.J., *Inhaled Pharmaceutical Product Development Perspectives: Challenges and Opportunities*, Elsevier Science, 2018b, ISBN: 9780128123362.
- Hickey A.J., Mansour H.M., Telko M.J., Xu Z., Smyth H.D.C., Mulder T., McLean R., Langridge J., Papadopoulos D., *Physical characterization of component particles included in dry powder inhalers. I. strategy review and static characteristics*, *Journal of Pharmaceutical Sciences*, 96 (2007) 1282–1301. DOI: 10.1002/jps.20916
- Hufnagel S., Sahakijpiparn S., Moon C., Cui Z., III R.O.W., *The development of thin-film freezing and its application to improve delivery of biologics as dry powder aerosols*, *KONA Powder and Particle Journal*, 39 (2022) 176–192. DOI: 10.14356/kona.2022010
- Kaviratna A., Tian G., Liu X., Delvadia R., Lee S., Guo C., *Evaluation of bio-relevant mouth-throat models for characterization of metered dose inhalers*, *AAPS PharmSciTech*, 20 (2019) 130. DOI: 10.1208/s12249-019-1339-6
- Khoubnasabjafari M., Rahimpour E., Samini M., Jouyban-Gharamaleki V., Chen L., Chen D., Chan H.-K., Jouyban A., *A new hypothesis to investigate bioequivalence of pharmaceutical inhalation products*, *DARU Journal of Pharmaceutical Sciences*, 27 (2019) 517–524. DOI: 10.1007/s40199-019-00250-x
- Kugler Sz., Nagy A., Kerekes A., Veres M., Rigó I., Czitrovsky A., *Determination of emitted particle characteristics and upper airway deposition of Symbicort® Turbuhaler® dry powder inhaler*, *Journal of Drug Delivery Science and Technology*, 54 (2019) 101229. DOI: 10.1016/j.jddst.2019.101229
- Kuribayashi R., Myoenzono A., Takagi K., Hirota M., *Current understanding of the equivalence evaluations for in vitro tests on generic dry powder inhaler drug products in Japan*, *European Journal of Drug Metabolism and Pharmacokinetics*, 44 (2019) 743–745. DOI: 10.1007/s13318-019-00561-z
- Kuribayashi R., Yamaguchi T., Sako H., Takishita T., Takagi K., *Bioequivalence evaluations of generic dry powder inhaler drug products: similarities and differences between Japan, USA, and the European Union*, *Clinical Pharmacokinetics*, 56 (2017) 225–233. DOI: 10.1007/s40262-016-0438-8
- Lee S.L., Adams W.P., Li B.V., Conner D.P., Chowdhury B.A., Yu L.X., *In vitro considerations to support bioequivalence of locally acting drugs in dry powder inhalers for lung diseases*, *The AAPS Journal*, 11 (2009) 414–423. DOI: 10.1208/s12248-009-9121-4
- Louey M.D., Oort M.V., Hickey A.J., *Standardized entrainment tubes for the evaluation of pharmaceutical dry powder dispersion*, *Journal of Aerosol Science*, 37 (2006) 1520–1531. DOI: 10.1016/j.jaerosci.2006.04.002
- Lyapustina S., *Regulatory pitfalls and opportunities when repurposing for inhalation therapy*, *Advanced Drug Delivery Reviews*, 133 (2018) 57–65. DOI: 10.1016/j.addr.2018.04.013
- Mitchell J., Newman S., Chan H.-K., *In vitro and in vivo aspects of cascade impactor tests and inhaler performance: a review*, *AAPS PharmSciTech*, 8 (2007) E1–E12. DOI: 10.1208/pt0804110
- Mitchell J.P., Roberts D.L., *Current Approaches to APSD Measurements of OIPs Based on Inertial Impaction*, in: Tougas T.P., Mitchell J.P., Lyapustina S.A. (Eds.), *Good Cascade Impactor Practices, AIM and EDA for Orally Inhaled Products*, Springer US, Boston, MA, 2013, pp. 15–55, ISBN: 978-1-4614-6296-5. DOI: 10.1007/978-1-4614-6296-5\_2
- Mitchell J.P., Tougas T.P., *The AIM and EDA Concepts: Why they are needed and how they fit together*, in: Tougas T.P., Mitchell J.P., Lyapustina S.A. (Eds.), *Good Cascade Impactor Practices, AIM and EDA for Orally Inhaled Products*, Springer US, Boston, MA, 2013, pp. 119–133, ISBN: 978-1-4614-6296-5. DOI: 10.1007/978-1-4614-6296-5\_5
- Newman S.P., Chan H.-K., *In vitro/in vivo comparisons in pulmonary drug delivery*, *Journal of Aerosol Medicine and Pulmonary Drug Delivery*, 21 (2008) 77–84. DOI: 10.1089/jamp.2007.0643
- Newman S.P., Chan H.-K., *In vitro-in vivo correlations (IVIVCs) of deposition for drugs given by oral inhalation*, *Advanced Drug Delivery Reviews*, 167 (2020) 135–147. DOI: 10.1016/j.addr.2020.06.023
- Olsson B., Borgström L., Lundbäck H., Svensson M., *Validation of a general in vitro approach for prediction of total lung deposition in healthy adults for pharmaceutical inhalation products*, *Journal of Aerosol Medicine and Pulmonary Drug Delivery*, 26 (2013) 355–369. DOI: 10.1089/jamp.2012.0986
- Pleasant R.A., Hess D.R., *Aerosol delivery devices for obstructive lung diseases*, *Respiratory Care*, 63 (2018) 708–733. DOI: 10.4187/respcare.06290
- Rahimpour Y., Kouhsoltani M., Hamishehkar H., *Alternative carriers in dry powder inhaler formulations*, *Drug Discovery Today*, 19 (2014) 618–626. DOI: 10.1016/j.drudis.2013.11.013
- Sahakijpiparn S., Moon C., Ma X., Su Y., Koleng J.J., Dolocan A., Williams III R.O., *Using thin film freezing to minimize excipients in inhalable tacrolimus dry powder formulations*, *International Journal of Pharmaceutics*, 586 (2020) 119490. DOI: 10.1016/j.ijpharm.2020.119490
- Shi S., Hickey A.J., *Multivariate data analysis as a semi-quantitative tool for interpretive evaluation of comparability or equivalence of aerodynamic particle size distribution profiles*, *AAPS PharmSciTech*, 10 (2009) 1113–1120. DOI: 10.1208/s12249-009-9303-5
- Taki M., Ahmed S., Marriott C., Zeng X.-M., Martin G.P., *The ‘stage-by-stage’ deposition of drugs from commercial single-active and combination dry powder inhaler formulations*, *European Journal of Pharmaceutical Sciences*, 43 (2011) 225–235. DOI: 10.1016/j.ejps.2011.04.014
- Tougas T.P., Christopher D., Mitchell J., Lyapustina S., Van Oort M., Bauer R., Glaab V., *Product lifestyle approach to cascade impactor measurements*, *AAPS PharmSciTech*, 12 (2011) 312–322. DOI: 10.1208/s12249-011-9590-5
- Tougas T.P., Christopher D., Mitchell J.P., Strickland H., Wyka B., Van Oort M., Lyapustina S., *Improved quality control metrics for cascade impactor measurements of orally inhaled drug products (OIPs)*, *AAPS PharmSciTech*, 10 (2009) 1276–1285. DOI: 10.1208/s12249-009-9312-4
- Uddin S., Hossain M., Al Mamun A., Zaman S., Asaduzzaman, Rashid M., *Pharmacopoeial standards and specifications for pharmaceutical aerosols: in-process and finished products*



- quality control tests, *Advances in Research*, 6 (2016) 22442 (12pp). DOI: 10.9734/AIR/2016/22442
- US-FDA, Metered Dose Inhaler (MDI) and Dry Powder Inhaler (DPI) Drug Products—Quality Considerations: Guidance for Industry, US Food and Drug Administration, Silver Spring, MD, 2018, FDA-2018-D-1098. <<https://www.fda.gov/media/70851/download>> accessed 20.07.2022.
- VanDevanter D.R., Geller D.E., Tobramycin administered by the TOBI(R) Podhaler(R) for persons with cystic fibrosis: a review, *Medical Devices: Evidence and Research*, 4 (2011) 179–188. DOI: 10.2147/MDER.S16360
- Weers J., Clark A., The impact of inspiratory flow rate on drug delivery to the lungs with dry powder inhalers, *Pharmaceutical Research*, 34 (2017) 507–528. DOI: 10.1007/s11095-016-2050-x
- Wei X., Hindle M., Kaviratna A., Huynh B.K., Delvadia R.R., Sandell D., Byron P.R., In vitro tests for aerosol deposition. VI: realistic testing with different mouth-throat models and in vitro-in vivo correlations for a dry powder inhaler, metered dose inhaler, and soft mist inhaler, *Journal of Aerosol Medicine and Pulmonary Drug Delivery*, 31 (2018) 358–371. DOI: 10.1089/jamp.2018.1454
- Wu X., Li X., Mansour H.M., Surface analytical techniques in solid-state particle characterization for predicting performance in dry powder inhalers, *KONA Powder and Particle Journal*, 28 (2010) 3–18. DOI: 10.14356/kona.2010005
- Yang T.T., Li S., Wyka B., Kenyon D., Drug delivery performance of the mometasone furoate dry powder inhaler, *Journal of Aerosol Medicine*, 14 (2001) 487–494. DOI: 10.1089/08942680152744695
- Yazdi A.K., Smyth H.D.C., Carrier-free high-dose dry powder inhaler formulation of ibuprofen: physicochemical characterization and in vitro aerodynamic performance, *International Journal of Pharmaceutics*, 511 (2016) 403–414. DOI: 10.1016/j.ijpharm.2016.06.061
- Zhang Y., Gilbertson K., Finlay W.H., In vivo-in vitro comparison of deposition in three mouth-throat models with Qvar(R) and Turbuhaler(R) inhalers, *Journal of Aerosol Medicine*, 20 (2007) 227–235. DOI: 10.1089/jam.2007.0584
- Ziffels S., Bemelmans N.L., Durham P.G., Hickey A.J., In vitro dry powder inhaler formulation performance considerations, *Journal of Controlled Release*, 199 (2015) 45–52. DOI: 10.1016/j.jconrel.2014.11.035

## Authors' Short Biographies



**Sara E. Maloney**

Dr. Sara Maloney is currently a postdoctoral fellow at RTI International in Research Triangle Park, NC. She obtained her B.S. in chemistry and forensic chemistry from Towson University and her Ph.D. in analytical chemistry from the University of North Carolina at Chapel Hill under the direction of Dr. Mark H. Schoenfish. Her current research interests include therapeutic aerosol formulation, characterization, and delivery as well as development of antibacterial biomaterials for lung infections.



**Jeffrey B. Mecham**

Dr. Mecham is a Research Chemist in RTI International's Center for Engineered systems, in the Technology Advancement and Commercialization Division. In this capacity, he is responsible for the design and synthesis of monomers, polymers, and nanoparticles (at the micro- and nano-scale) with targeted performance capabilities for a wide array of applications. His team are contributors to the Center's successful development of particle-based controlled release technologies for triggered release of therapeutics and chemistries for environmental remediation. The development of such materials over the last several years at RTI has resulted in IP that has been licensed by interested parties for further development and subsequent commercialization of particles with controlled release properties.



**Anthony J. Hickey**

Dr. Hickey is a Distinguished Fellow at RTI International, Professor Emeritus of Pharmaco-engineering and Molecular Pharmaceutics, and Adjunct Professor of Biomedical Engineering at the University of North Carolina at Chapel Hill. He obtained Ph.D. and D.Sc. degrees in pharmaceutical sciences from Aston University, Birmingham, UK. He is a Fellow of the American Association for the Advancement of Science, the American Association of Pharmaceutical Scientists, the Royal Society of Biology, and the Royal Society of Medicine, and member of the Pharmaceutical Dosage Forms Expert Committee (DFEC) and Aerosols Sub-Committee of the DFEC of the United States Pharmacopeia. Dr. Hickey is a highly published (over 300 papers) and cited author having edited or authored 16 books on pharmaceutical aerosols, particulates, manufacturing and complex systems. He holds over 25 patents and conducts multidisciplinary research programs in the field of pulmonary drug and vaccine delivery for the treatment and prevention of a variety of diseases.

# Environmentally Friendly Green Synthesis of Fine Particles by Dry Mechanical Processes Toward SDGs: A Review<sup>†</sup>

Tomohiro Iwasaki

Department of Chemical Engineering, Osaka Metropolitan University, Japan

## Abstract

The United Nations Sustainable Development Goals (SDGs) have attracted much attention due to increasing interest in global social, energy and environmental problems. The immediate contribution to the achievement of the SDGs is required in all individual and industrial activities. The industries dealing with fine particles are also no exception to the demand and have actively worked on the contribution. Conventionally, fine particles have been industrially synthesized in gas, liquid and solid phases using top-down and bottom-up approaches. Among them, dry synthesis processes are promising from a viewpoint of the SDGs due to the solvent-free and simplicity, which can lead to energy saving, efficient resource utilization, waste management, etc. This review describes dry mechanical processes for synthesis of fine particles, particularly focusing on grinding and mechanochemical treatment.

**Keywords:** SDGs, particle synthesis, dry grinding, mechanical activation, mechanochemical effect, mechanochemically assisted method

## 1. Introduction

### 1.1 Spread of SDGs

The United Nations Sustainable Development Goals (SDGs) consisting of 17 goals with 169 targets require to solve serious global problems relating to, for example, health, education, safety and human rights as well as resource, energy and environment. The SDGs have been widely spread through various media and many people recognize the importance. At present, contributions to the achievement of the SDGs cannot be avoided in all human activities ranging from individual to global level. In particular, business activities considering the SDGs are becoming more active according to corporate image-building (branding) strategy which can affect the sales of products due to high consumer recognition. Under such circumstances, we frequently see and hear the SDGs everywhere.

### 1.2 SDGs in powder processing

Powder handling and processing, such as storage, conveying, mixing, reaction, crystallization, grinding, compaction, granulation, classification, separation, and surface modification, are also required to work diligently on the contribution to the achievement of the SDGs without exception. To do so, conventional powder processes may be modified to eco- and environment-friendly (green) pro-

cesses by applying various advanced technologies (**Fig. 1**). Examples of possible future contribution of powder processes are listed in **Table 1**. In **Fig. 1** and **Table 1**, 9 goals which are expected to be achieved in the near future are selected as an example. Some powder processes and products considering the SDGs have been reviewed: e.g., food (Bartolucci et al., 2020), pharmaceutical (Assali and Zaid, 2022), agricultural material (Swoboda et al., 2022), catalyst (Nawaz et al., 2021), antibacterial material (Bhardwaj et al., 2021; Parmar et al., 2022), environmental improvement material (Nnadozie and Ajibade, 2020; Rehman et al., 2021). The use of fine particles in the processes shows many merits such as uniformity and reactivity; however, some serious demerits such as safety, labor environment and air pollution are latent. Although attempts for removing the demerits have been conducted, there are still few cases emphasizing clearly the contribution to the achievement of



### Contribution to SDGs

#### Eco- and Environment-Friendly (Green) Processes

Energy Saving, Efficient Resource Utilization, Waste Management  
Production of Food, Pharmaceutical, Catalyst, Energy-Relating Material, etc.

#### Advanced Technologies

Nanoscience, Bioscience, Data Science, etc.

#### Conventional Powder Processes

**Fig. 1** Contribution of powder processes to SDGs.

<sup>†</sup> Received 29 June 2022; Accepted 22 July 2022  
J-STAGE Advance published online 3 September 2022  
Add: 1-1 Gakuen-cho, Nakaku, Sakai, Osaka 599-8531, Japan  
E-mail: tomohiro.iwasaki@omu.ac.jp  
TEL: +81-72-254-9307 FAX: +81-72-254-9911

**Table 1** Examples of possible future contribution of powder processes.

Goal (Target)	Example
2 (2.1, 2.4, 2.c)	Improvement of productivity, processability and functionality of foods
	Stabilization of foods for long-term storage
	Development of functional fertilizers with high performance
3 (3.8, 3.9)	Development of functional pharmaceuticals with high performance
	Improvement of productivity and stability of pharmaceuticals
	Environmental purification
6 (6.3, 6.a)	Purification and conservation of water environment
	Treatment of waste and polluted water
	Recycling and reuse of water
7 (7.2, 7.3, 7.a)	Generation of clean energy (hydrogen production)
	Energy saving
8 (8.3)	Improvement working environment
	Reduction of working hours
9 (9.4, 9.5, 9.b)	Effective use of resources
	Innovation in powder processing technologies
	Development of processes for synthesis of functional particles
12 (12.2, 12.4, 12.5)	Effective use of fossil fuels by energy saving
	Reduction and utilization of wastes
14 (14.1, 14.3)	Removal of marine pollutants
	Improvement of ocean acidification by immobilization of atmospheric CO <sub>2</sub>
15 (15.3)	Restraint of expansion of cultivated acreage by improvement of food production efficiency

the SDGs; the technology development in this field seems to fall behind. Therefore, various improvements can be made in the powder processes. In particular, energy saving and/or process simplifying should be immediately realized in all processes, which can lead to the reduction of process costs and environmental impacts.

### 1.3 Contributions in fine particle synthesis

#### 1.3.1 Bottom-up approach

In general, fine particles can be synthesized by various wet and dry processes using bottom-up (build up) and top-down (break down) approaches. In bottom-up methods, monomers form via assembly of atoms and molecules and then particles are obtained by growing them. The formation process is described by the LaMer diagram. The particle synthesis processes are operated in gas, liquid and solid

phases, and the particle formation progresses according to almost the same mechanism regardless of the type of phases. However, the growth rate of particles greatly varies in the phases depending strongly on the diffusion velocity of atoms and molecules. When the growth rate is higher, the productivity of particles also becomes larger; in contrast, the control of particle size distribution is difficult.

Usually, the bottom-up processes using gas (Kerminen et al., 2018; Khitab et al., 2018) and liquid (Jadoun et al., 2021; Khitab et al., 2018; Mastalska-Popławska et al., 2020; Shaikh et al., 2021; Wichaita et al., 2019) phases are employed. However, liquid-phase methods have some weak points: e.g., additional post-treatments, such as solid-liquid separation, liquid waste treatment, drying and disintegration of aggregates, which leads to the increase in the energy consumption and process cost. Accordingly, gas-phase methods without any post liquid treatments, such as physical vapor deposition (PVD) and chemical vapor deposition (CVD) with heating by chemical flame, plasma, laser and high frequency induction, may be slightly advantageous, although they are low versatility and need high temperatures. In any case, bottom-up processes seem to be unsuitable to the contribution to meeting the SDGs. However, as technologies of measurement and analysis progress, dry mechanochemical processes using solid-state reactions have been recognized as a useful bottom-up method.

#### 1.3.2 Top-down approach

On the other hand, in top-down methods, the raw feed is broken (ground) into small pieces by applying the mechanical energy. Powder grinding has been traditionally used in home and industries due to the simple operation. Although technical problems in grinding, such as the mechanical work (energy) for obtaining fine particles with a desired size, the prediction and control of the size distribution of products, and the analysis of grinding kinetics, have been studied, they are still not completely solved. For contributing to the SDGs, such problems must be solved by using new technologies (e.g., machine learning).

The grinding processes are classified roughly into dry and wet methods and various types of machines are used for dry and wet grinding. The particle formation mechanism is complicated regardless of the methods because the particle breaking is caused by various kinds of loads induced by compression, tension, shear, bending, friction, and so on. However, the grinding processes have some merits which can lead to the contribution to meeting the SDGs: e.g., simple process, high throughput, low cost, etc. The particle breaking occurs according to two mechanisms: volume grinding and surface grinding. For producing fine particles, the latter is effective. In dry grinding processes, newly formed fine particles tend to aggregate each other during grinding. When the particle size reaches

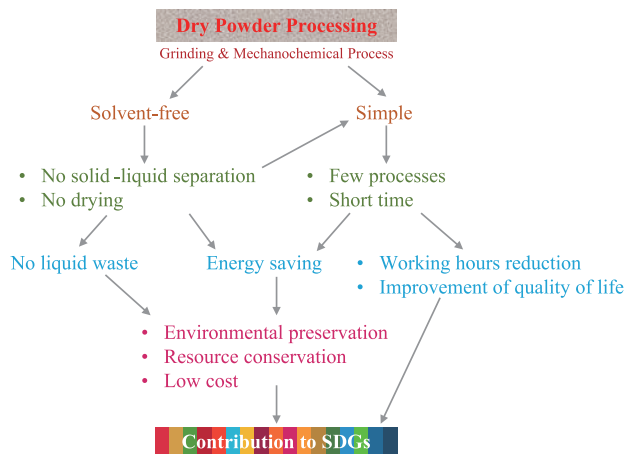


**Fig. 2** Overview of connections between dry processing and SDGs.

a few micrometers, the grinding can often be in an apparent equilibrium state. Further size reduction often requires wet grinding, which can provide nanometer-sized particles. For the production of dry powder, however, dry grinding processes do not need additional post-treatments, such as solid-liquid separation and drying, and are conventionally recognized as a green process with low environmental impact. Therefore, dry grinding is contributable to the achievement of the SDGs (Fig. 2).

### 1.3.3 Dry fine particle synthesis

For bulk synthesis of fine particles under dry conditions, not only dry grinding as a top-down method but also dry mechanochemical process as a bottom-up method are an effective choice. In both cases, the improvement of energy consumption and productivity is a very important problem and the efficiencies must be sufficiently increased. In addition, the functionalization and/or enhancement of properties should be made through the processes. These progress may contribute to many SDGs.

There are still few papers describing dry particle synthesis with an emphasis on the contribution to meeting the SDGs. This article reviews recent studies on dry mechanical processing for particle formation, which pay attention to SDGs and are published mainly in the last decade. In particular, dry grinding and mechanochemical processes are focused.

## 2. Dry grinding process

### 2.1 Relationship between dry grinding and SDGs

Grinding (including comminution and pulverization) of particulate materials under dry conditions have been conventionally used in many industrial fields for various purposes such as enhancement of the reactivity due to increase in the specific surface area and improvement of the processability and handling. Conventional dry grinding processes with older technologies can often consume large energy and cause the reduction of the productivity and the

discharge of large amounts of waste. Technological innovation in the dry grinding can solve the serious problems. Therefore, recent dry grinding processes substantially contribute to meeting SDGs, in particular, waste management. Soni et al. (2022) mentioned a role of grinding process in solid waste management for effective utilization of mineral resources waste as building construction materials in India.

Many researchers have also devoted to the reduction of energy consumption in the grinding processes. For increasing the energy efficiency leading to achievement of SDGs 7, 9, 12 and 13, García et al. (2021) analyzed in detail the results of the Bond grindability test to elucidate the influence of particle size distribution of feed and ground products on the Bond work index using an experimental design approach. As a result, the mesh size of a sieve used to close the grinding circuit and the 80 % passing size of feed were found to be the important parameters via the ANOVA test. As a contribution to SDGs relating to food problems, Raheem et al. (2022) refer to the grinding of corn, which is one of the most important crops in the world and is used for not only human food and animal feed but also bioethanol production, for the added value enhancement.

### 2.2 Possible contribution of dry grinding to SDGs

Dry grinding processes have also been employed traditionally in mining industries (e.g., beneficiation). Recently, for example, Chelgani et al. (2019) investigated the grinding effects on the energy consumption in the mineral flotation separation. They found that the dry grinding mechanically activated the particle surfaces and increased the floatability, which can reduce the energy consumption during flotation separation. In various food industries, dry grinding processes have been widely used, and some review articles relating to SDGs have been published: e.g., superfine grinding (Gao et al., 2020), fruit and vegetable powders (Karam et al., 2016), moisture content effect (Jung et al., 2018). It is expected that technological progress on dry grinding in food industrial fields can contribute directly to meeting Goal 2: Zero Hunger.

For the achievement of SDGs, the improvement of energy consumption in the dry grinding processes is significantly important. Many researches relating to the analysis of energy consumption discuss the energy efficiency using the specific grinding energy and/or electric power consumption (Altun et al., 2015; Altun et al., 2019; Blanc et al., 2020; Katircioglu-Bayel et al., 2020; Ngamnikom and Songsermpong, 2011; Ogonowski et al., 2018; Tamura et al., 2017; 2020). In particular, Prziwara, Kwade and co-workers (Prziwara et al., 2018a; 2018b; 2018c; 2019; 2020a) have actively studied in detail the effects of grinding aids on the grinding efficiency in dry fine grinding processes. They carefully analyzed the obtained results focusing on the energy consumption and the surface energy of particles, and give us useful guidelines

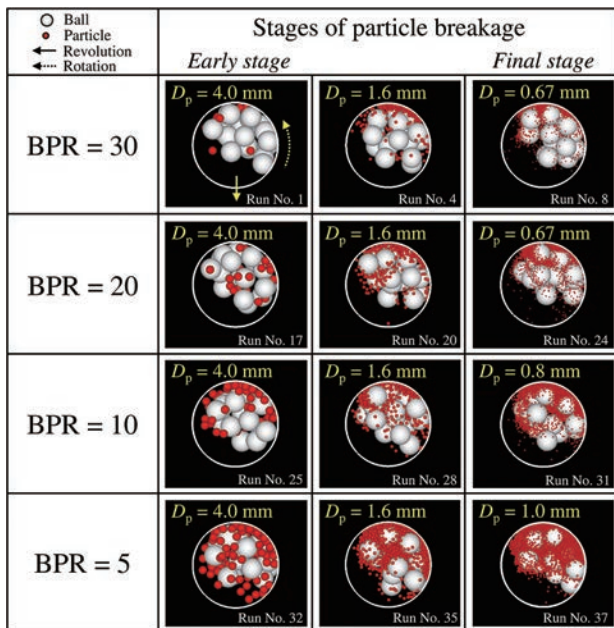


**Fig. 3** Snapshots of behaviors of particles and balls mimicking various stages of particle breakage at different values of ball-to-particle mass ratio (BPR) (ball diameter = 10 mm). Reprinted with permission from Ref. (Hirosawa and Iwasaki, 2021). Copyright: (2021) Elsevier.

for the selection of grinding aids. For example, they used the relative fineness increase, defined as the ratio of the specific surface area of product obtained with a grinding aid to that obtained without any grinding aid, as an index of the progress of grinding (Prziwara and Kwade, 2020b). The fineness increase was correlated with the energy consumption, which expressed quantitatively the difference of the grinding aid effects between amine-based and glycol-based additives. Therefore, their research results can contribute to reduction of the grinding energy consumption.

The work index (Chipakwe et al., 2020) and the impact energy of media calculated using the simulation of the behavior (Burmeister et al., 2018) have sometimes been utilized as the numerical index. Hirosawa and Iwasaki (2021) numerically analyzed the dissipated energy of particle in a planetary mill using the discrete element method (DEM) simulation of the behavior of the particles and balls to study the dependence of effective grinding energy on the conditions and the progress of grinding (i.e., particle size reduction) (Fig. 3). They found that using an appropriate size and number of balls in accordance with the stages of grinding is effective for precisely controlling the dissipated energy of particles even when the particle size decreased as the progress of grinding (Fig. 4). Therefore, the numerical simulation can give us the information relating to optimization of dry grinding processes.

In addition to above, some unique studies which can potentially contribute to meeting SDGs have been reported: e.g., analysis of grinding processes (Bu et al., 2019; 2020; Krauze et al., 2021; Nava et al., 2020; Prziwara et al.,

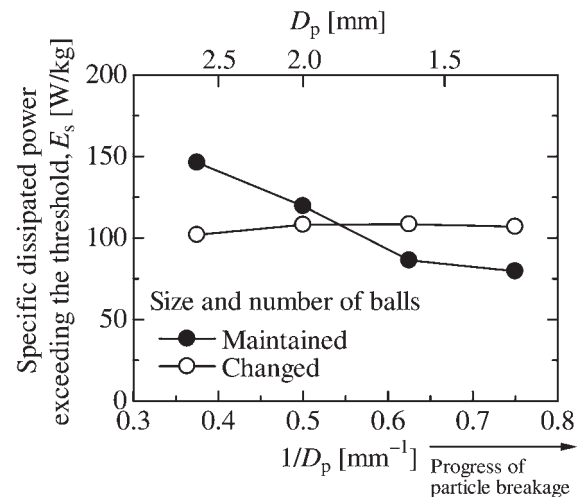


**Fig. 4** Effect of changing ball diameter and number of balls on variation in specific dissipated energy with particle breakage stage. Reprinted with permission from Ref. (Hirosawa and Iwasaki, 2021). Copyright: (2021) Elsevier.

2020a; Toraman, 2013), characterization and utilization of ground products (Arsoy et al., 2017; Choi et al., 2016; Gomez et al., 2019; Guzzo et al., 2019; 2020; Letelier et al., 2019; Liu et al., 2015; Makuza et al., 2021; Okazaki et al., 2022; Peltoniemi et al., 2020; Yang et al., 2021). However, the grinding mechanism considerably changes depending on the type of grinding machine, which makes it difficult to evaluate the energy efficiency using a unified standard. The standardization of the evaluation method is required for further contributions.

### 3. Dry mechanochemical process

#### 3.1 Outline

Generally, in dry grinding of particulate materials, the raw feed receives the mechanical energy induced by shear, compression, impact and friction, and then is ground into finer particles. At this moment, new particle surfaces form, of which the structure differs from that of the inside. By applying further the mechanical energy to the particles, the chemical bonding state of atoms microscopically changes (e.g., partial breaking), which can lead to increase in the disturbance of crystal lattice (lattice defect and lattice mismatch). Simultaneously, the plastic deformation energy can be accumulated in the particles. Such unstable state of the particles leads to a chemically activated state, which is so-called mechanical activation. This can result in various physicochemical changes, such as increase in the surface energy of particles, formation of radicals, adhesion and aggregation of particles, solid-phase reaction. In addition, this may cause chemical interaction between the particles and surrounding materials, i.e., mechanochemical reaction (Masuda et al., 2006). Mechanochemical effects are confirmed in many materials such as inorganic and organic materials and metals and can be practically applied to not only material synthesis but also material separation,

resource processing and recycling. For example, the mechanochemical synthesis of porous materials was reviewed by Szcześniak et al. (2020). The mechanical activation has been utilized for the reduction of reaction temperature of biochar (Tayibi et al., 2021) and the stabilization of heavy metals in fly ash for extraction control, i.e., reduction of the metal toxicity (Yuan et al., 2021). Mechanochemical treatments of natural and artificial resources can enable the recovery of valuables under mild conditions and the simultaneous grinding can act effectively as a pretreatment of the subsequent material processing.

### 3.2 Relationship between dry mechanochemical treatment and SDGs

Mechanochemical treatments have conventionally been used as an effective and powerful tool mainly for synthesis of materials in anticipation of local high-temperature and high-pressure environments, induced activation of reactants, rapid reaction, etc. In particular, dry (solvent-free) mechanochemical processes have been tried to apply to various inorganic and/or organic systems due to its simplicity and room-temperature operation. Many remarkable results of dry mechanochemical synthesis have been produced so far. Furthermore, a lot of articles reviewing various dry mechanochemical processes have also been published. Recently, Dong et al. (2022) review recent findings and potential applications of mechanochemical processes in the fields of environmental governance and energy storage, such as treatments of toxic compounds and recovery of valuables from energy storage materials. André et al. (2022) introduce the mechanochemical applications growing in Portugal, such as crystalline compounds of pharmaceuticals and bio-inspired metal-organic frameworks, ionic liquids, and liquid crystals. Kumar et al. (2020) present useful scientific knowledge on value-added recycling of biomass wastes through the mechanochemical synthesis of biochar-based materials via various ball milling treatments, which can contribute to the realization of carbon neutral society.

Dry mechanochemical syntheses of functional materials with high performance considering SDGs have been reported in recent years. For example, Danielis et al. (2021) synthesized the methane oxidation catalyst for natural gas fueled vehicles by a dry mechanochemical process using a planetary ball mill. The mechanochemical treatment may result in the formation of the particular structure suitable to high catalytic activity due to promotion of the surface oxygen mobility. The mechanochemically prepared catalyst showed excellent catalytic performance for simultaneous  $\text{NO}_x$  reduction and  $\text{CH}_4$  oxidation (Fig. 5). Sharma et al. (2022) used a software tool for evaluating greenness of some mechanochemical processes with different milling mechanisms for synthesis of nitrofurantoin from a standpoint of the 12 Principles of Green Chemistry (Anastas and

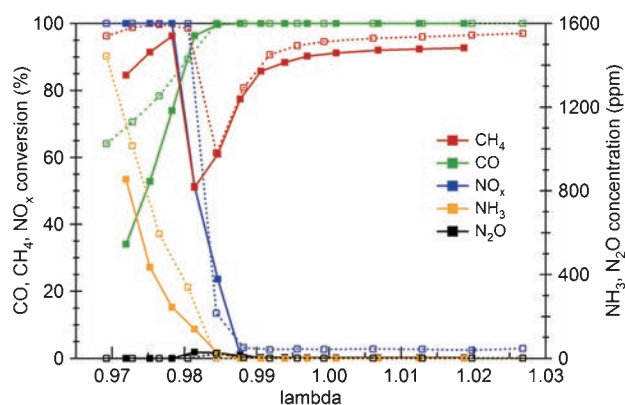


Fig. 5 Synthetic reactor results with full gas mixture at 823 K for the 2-modes aged Pd/CeO<sub>2</sub> catalyst sample (solid line, full symbols) and the 4-modes aged commercial Pd-based three-way catalyst (dotted line, open symbols). Reprinted with permission from Ref. (Danielis et al., 2021). Copyright: (2021) American Chemical Society.

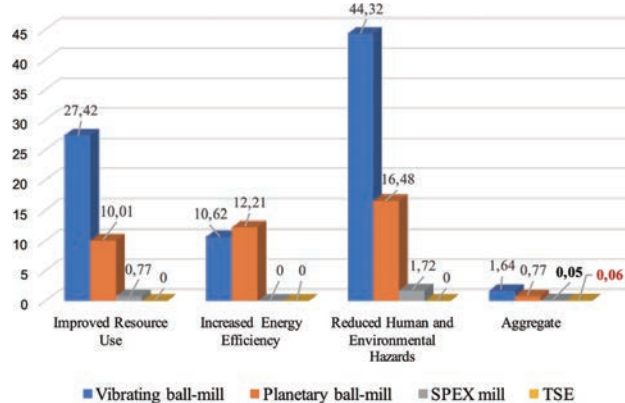
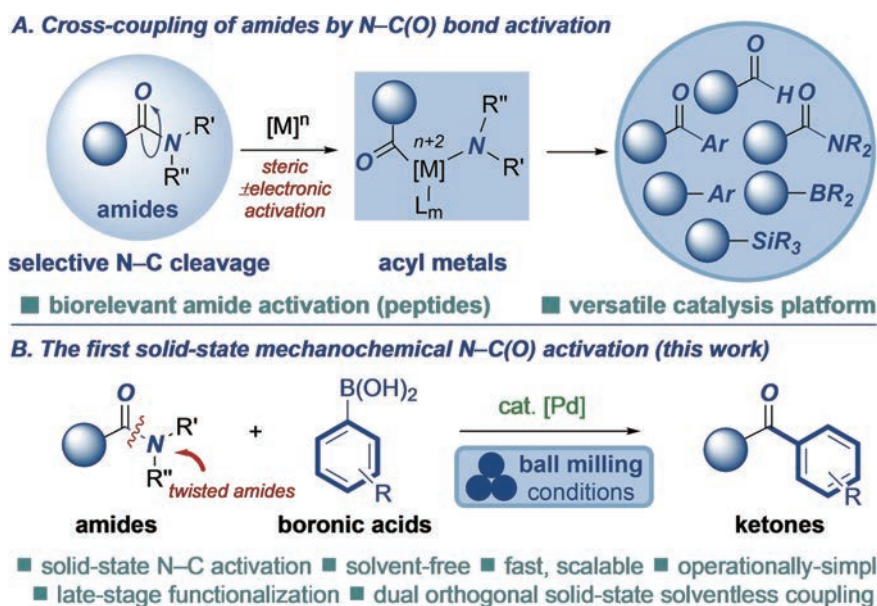


Fig. 6 Comparisons of greenness of batch vs continuous mechanochemical processes for the preparation of nitrofurantoin. Reprinted with permission from Ref. (Sharma et al., 2022). Copyright: (2022) American Chemical Society.

Warner, 1998). They show interesting results that a shaker mill and a twin-screw extrusion exhibit increased energy efficiency, improved resources use, and reduced human and environmental hazards compared to other commercial processes, which was determined based on the evaluation scores (Fig. 6). The difference in scores is mainly due to the difference in time of synthesis and in the product yield. This method may be useful for the development of greener mechanochemical processes.

### 3.3 Possible contribution of dry mechanochemical treatment to SDGs

Zhang et al. (2022) developed the mechanochemical solid-state cross-coupling of amides by nitrogen-carbon bond activation (Fig. 7), which is conducted under solventless conditions without external heating for short reaction time. The merit of the method is avoidance of potentially harmful solvents, which can lead to minimizing wastes and reducing environmental impacts. This mechanochemical cross-coupling can be applied to the synthesis of



**Fig. 7** General manifold of amide bond activation (A) and the solid-state mechanochemical N–C(O) activation (B). Reprinted with permission from Ref. (Zhang et al., 2022). Copyright: (2022) John Wiley and Sons.

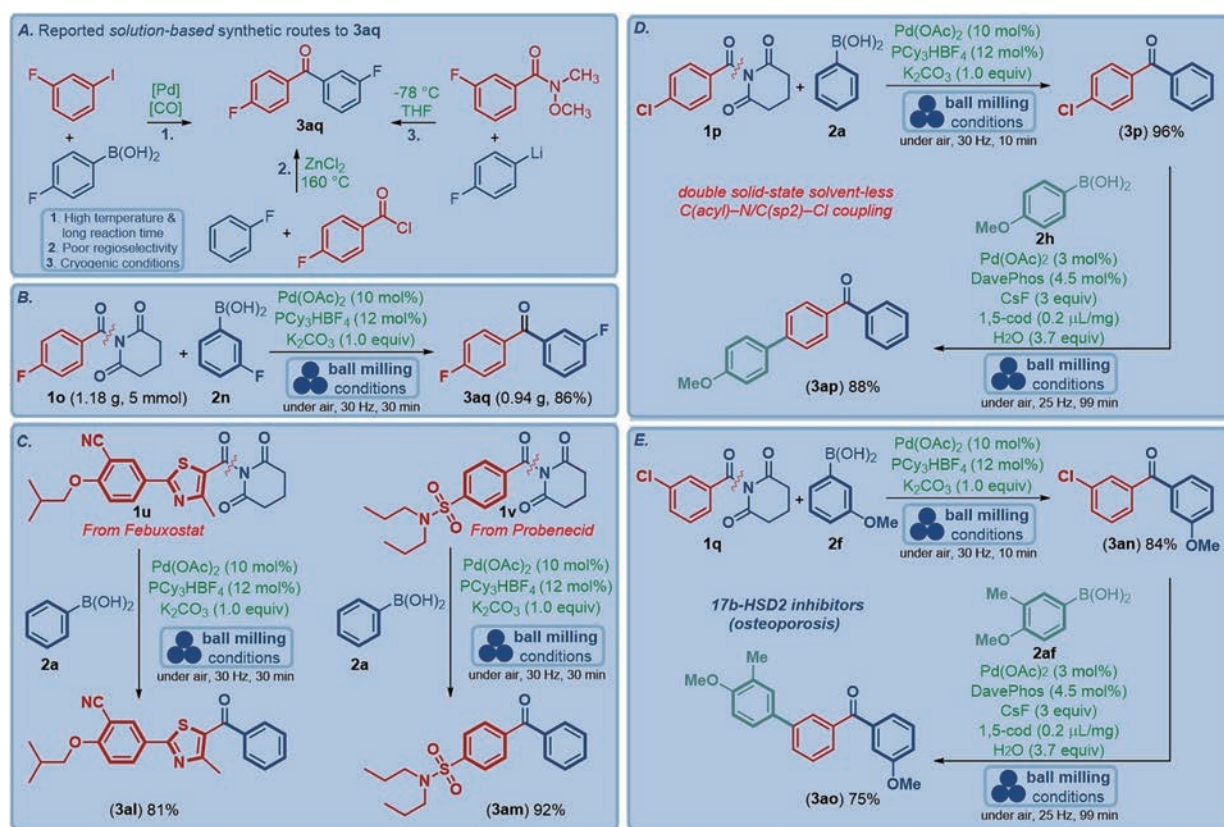


**Fig. 8** Application to the synthesis of pharmaceutical intermediates. Reprinted with permission from Ref. (Zhang et al., 2022). Copyright: (2022) John Wiley and Sons.

pharmaceutical intermediates (Fig. 8). The contribution of the method to various chemical processes may be quite large. Hirosawa et al. (2019) analyzed the rate of the mechanochemical reaction to form ZnFe<sub>2</sub>O<sub>4</sub> via high-energy ball milling of a mixture of ZnO and γ-Fe<sub>2</sub>O<sub>3</sub> based on the kinetic theories for thermal chemical reactions using

experimental and numerical approaches. The reaction rate constant was found to be correlated with the energy factor and frequency factor, similarly to the Arrhenius equation for thermal chemical reactions (Fig. 9). Their method of analyzing the rate of mechanochemical reactions can contribute to not only precise control of the reaction rate

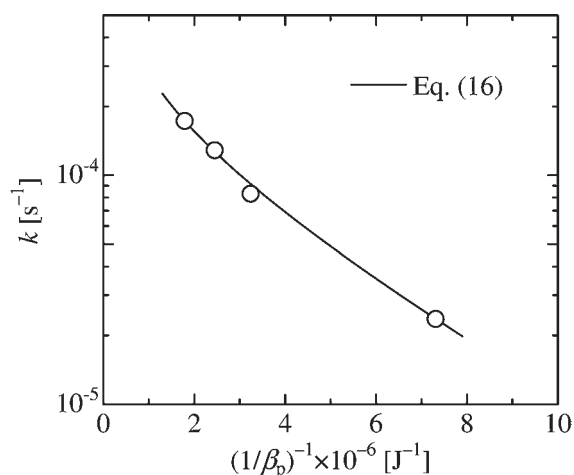


**Fig. 9** Relationship between the reaction rate constant and the reciprocal of a parameter representing the kinetic energy of particles. Reprinted with permission from Ref. (Hirosawa et al., 2019). Copyright: (2019) Elsevier.

but also the effective utilization of energy, the process optimization based on the mechanical energy, etc.

Many researchers have actively challenged to dry mechanochemical synthesis of various high-performance particles from inorganic (Goga et al., 2021; Hlova et al., 2014; Muh'd et al., 2015; Pal et al., 2018; Wu et al., 2021), organic (Oh et al., 2020; Otsuka and Goto, 2022; Zhang et al., 2018) and organic–inorganic (El Ajjouri et al., 2019; Martínez-Sarti et al., 2020; Tanaka et al., 2013) materials, which will probably lead to the achievement of SDGs in future. For example, the development of functional fertilizers by dry mechanochemical syntheses (Alrbaihat et al., 2021; Barčauskaite et al., 2020; Borges et al., 2021; Tan et al., 2021; Zheng et al., 2021) can contribute widely to SDGs such as the goals 2, 8, 9, 12 and 15.

### 3.4 Mechanochemically assisted process for particle synthesis

Mechanochemical treatments have often been used to assist the progress of chemical reactions. Štrukil and Sajko (2017) developed a novel mechanochemical approach for solid-state visible light photocatalysis. The method is very simple; the photochemical reaction proceeds during milling at room temperature using a visible (blue)-light-irradiated vibration mill with a glass jar. They demonstrated that both the light irradiation and the mechanochemical treatment are required to effectively promote the solid-state photocatalytic reaction. The method contains some potential applications in the growing field of photoredox catalysis and supramolecular chemistry. Onizuka and Iwasaki (2022) developed a novel solvent-free process for synthesizing hematite nanoparticles under environmentally friendly conditions. This method contains the mechanochemical treatment of ferric nitrate nonahydrate as the iron source and urea as the precipitant, which releases the

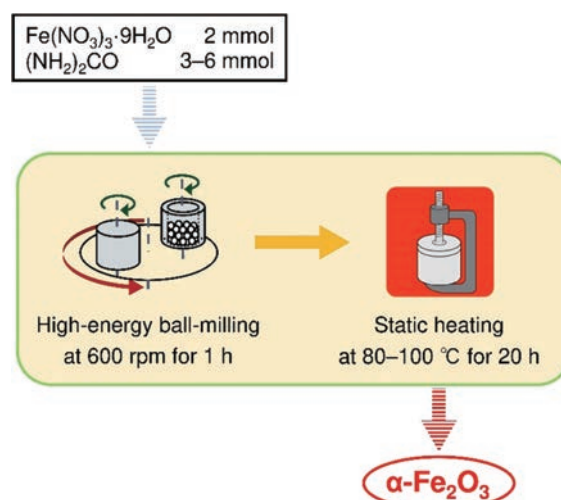


**Fig. 10** Mechanochemically assisted synthesis of hematite nanoparticles developed by Onizuka and Iwasaki (2022). Reprinted with permission from Ref. (Onizuka and Iwasaki, 2022). Copyright: (2022) Elsevier.

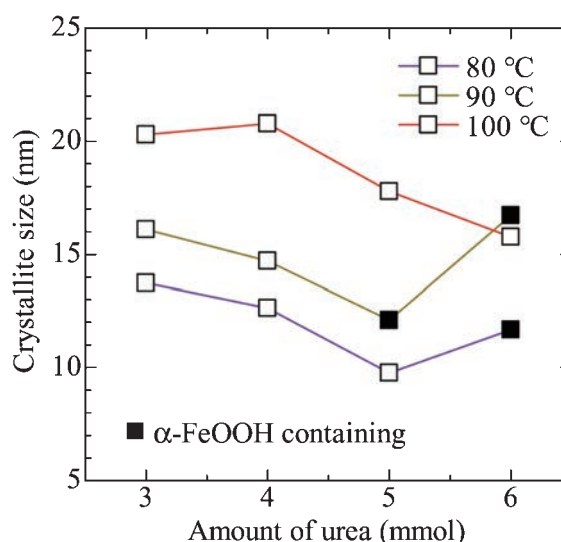


**Fig. 11** Crystallite sizes of hematite nanoparticles obtained with different amounts of urea at different heating temperatures. Reprinted with permission from Ref. (Onizuka and Iwasaki, 2022). Copyright: (2022) Elsevier.

crystal water from the iron source to be used for the urea hydrolysis (Fig. 10). In addition, the mechanochemical effects promote the hematite formation during heating even at low temperatures. The particle size was changed by the amount of urea and the heating temperature (Fig. 11). The low-temperature solvent-free method using urea hydrolysis may also be applicable to the environmentally friendly synthesis of other metal oxide nanoparticles. As an effective technique, dry mechanochemical pretreatments for activating the precursor of chemical reaction by thermal treatments, such as heating (Çolak et al., 2017; Iwasaki et al., 2016; Suetsugu, 2014), calcination (Ashiri, 2016; Bulina et al., 2017; Hashimoto et al., 2020; Kosova and Semykina, 2019; Lejda et al., 2020; Liu et al., 2020; Qiu



et al., 2021) and hydrothermal treatment (Kanie et al., 2018; Nada et al., 2019; Osuga et al., 2022; Zhang et al., 2020), have often been employed in the synthesis of various functional nanoparticles for weakening the thermal treatment conditions.

#### 4. Conclusion

Focusing on grinding and mechanochemical processes, this review presents the possibility of dry mechanical processes to the contribution of the achievement of the SDGs. In particular, from a viewpoint of the reduction of energy consumption and waste, dry mechanochemical processes may be suitable to an on-demand production of small quantity and large variety of high-performance fine particles in the consuming area. This may also lead to the contribution to the transition to a decarbonized society. For further enhancing the functionality and performance, the synthesis of nanosized particles cannot be avoided. However, nanoparticles have some concerns in health and environment. Thus, the nanoparticles should be used considering carefully the balance of valuables of nanoparticles and its contribution to the SDGs. Toward the realization of a sustainable society, various problems relating to fine particles, such as bioaccumulation of microplastics and nanoparticles discharged to environments, must be urgently solved. In addition, the automated system and labor saving is required for improvement of the work environment. Dry particle synthesis processes can play an important key role for the achievement of the SDGs. The author believes that the dry mechanical powder processes have the great potential to contribute directly or indirectly to all of the SDGs.

#### References

- Alrbaihat M.R., Al-Rawajfeh A.E., AlShamaileh E., A mechanochemical preparation, properties and kinetic study of kaolin-N, P fertilizers for agricultural applications, *Journal of the Mechanical Behavior of Materials*, 30 (2021) 265–271. DOI: 10.1515/jmbm-2021-0028
- Altun O., Benzer H., Toprak A., Enderle U., Utilization of grinding aids in dry horizontal stirred milling, *Powder Technology*, 286 (2015) 610–615. DOI: 10.1016/j.powtec.2015.09.001
- Altun D., Altun O., Zencirci S., Developing a methodology to model and predict the grinding performance of the dry stirred mill, *Minerals Engineering*, 139 (2019) 105867. DOI: 10.1016/j.mineng.2019.105867
- Anastas P.T., Warner J.C., *Green Chemistry: Theory and Practice*, Oxford University Press, New York, 1998, p. 30, ISBN: 0198502346.
- André V., Duarte M.T., Gomes C.S.B., Sarraguça M.C., Mechanochemistry in Portugal—A step towards sustainable chemical synthesis, *Molecules*, 27 (2022) 241. DOI: 10.3390/molecules27010241
- Arsoy Z., Ersoy B., Evcin A., Icduygu M.G., Influence of dry grinding on physicochemical and surface properties of talc, *Physicochemical Problems of Mineral Processing*, 53 (2017) 288–306. DOI: 10.5277/ppmp170124
- Ashiri R., On the solid-state formation of BaTiO<sub>3</sub> nanocrystals from mechanically activated BaCO<sub>3</sub> and TiO<sub>2</sub> powders: innovative mechanochemical processing, the mechanism involved, and phase and nanostructure evolutions, *RSC Advances*, 6 (2016) 17138–17150. DOI: 10.1039/C5RA22942A
- Assali M., Zaid A.-N., Features, applications, and sustainability of lipid nanoparticles in cosmeceuticals, *Saudi Pharmaceutical Journal*, 30 (2022) 53–65. DOI: 10.1016/j.jsps.2021.12.018
- Barčauskaite K., Braziene Z., Avižienyte D., Silva M., Drapanauskaite D., Honer K., Gvildiene K., Slinksiene R., Jancaitiene K., Mazeika R., Staugaitis G., Dambrauskas T., Baltakys K., Baltrusaitis J., Mechanochemically synthesized gypsum and gypsum drywall waste cocrystals with urea for enhanced environmental sustainability fertilizers, *Journal of Environmental Chemical Engineering*, 8 (2020) 103965. DOI: 10.1016/j.jece.2020.103965
- Bartolucci C., Antonacci A., Arduini F., Moscone D., Fraceto L., Campos E., Attaallah R., Amine A., Zanardi C., Cubillana-Aguilera L.M., Palacios Santander J.M., Scognamiglio V., Green nanomaterials fostering agrifood sustainability, *TrAC Trends in Analytical Chemistry*, 125 (2020) 115840. DOI: 10.1016/j.trac.2020.115840
- Bhardwaj A.K., Sundaram S., Yadav K.K., Srivastav A.L., An overview of silver nano-particles as promising materials for water disinfection, *Environmental Technology & Innovation*, 23 (2021) 101721. DOI: 10.1016/j.eti.2021.101721
- Blanc N., Mayer-Laigle C., Frank X., Radjai F., Delenne J.-Y., Evolution of grinding energy and particle size during dry ball-milling of silica sand, *Powder Technology*, 376 (2020) 661–667. DOI: 10.1016/j.powtec.2020.08.048
- Borges R., Soares Giroto A., Klaic R., Wypych F., Ribeiro C., Mechanochemical synthesis of eco-friendly fertilizer from eggshell (calcite) and KH<sub>2</sub>PO<sub>4</sub>, *Advanced Powder Technology*, 32 (2021) 4070–4077. DOI: 10.1016/j.apt.2021.09.013
- Bu X., Chen Y., Ma G., Sun Y., Ni C., Xie G., Differences in dry and wet grinding with a high solid concentration of coking coal using a laboratory conical ball mill: breakage rate, morphological characterization, and induction time, *Advanced Powder Technology*, 30 (2019) 2703–2711. DOI: 10.1016/j.apt.2019.08.016
- Bu X., Chen Y., Ma G., Sun Y., Ni C., Xie G., Wet and dry grinding of coal in a laboratory-scale ball mill: particle-size distributions, *Powder Technology*, 359 (2020) 305–313. DOI: 10.1016/j.powtec.2019.09.062
- Bulina N.V., Chaikina M.V., Prosanov I.Y., Dudina D.V., Solovyov L.A., Fast synthesis of La-substituted apatite by the dry mechanochemical method and analysis of its structure, *Journal of Solid State Chemistry*, 252 (2017) 93–99. DOI: 10.1016/j.jssc.2017.05.008
- Burmeister C., Titscher L., Breitung-Faes S., Kwade A., Dry grinding in planetary ball mills: evaluation of a stressing model, *Advanced Powder Technology*, 29 (2018) 191–201. DOI: 10.1016/j.apt.2017.11.001
- Chelgani S.C., Parian M., Parapari P.S., Ghorbani Y., Rosenkranz J., A comparative study on the effects of dry and wet grinding on mineral flotation separation – a review, *Journal of Materials Research and Technology*, 8 (2019) 5004–5011. DOI: 10.1016/j.jmrt.2019.07.053
- Chipakwe V., Semsari P., Karlkvist T., Rosenkranz J., Chelgani S.C., A comparative study on the effect of chemical additives on dry grinding of magnetite ore, *South African Journal of Chemical Engineering*, 34 (2020) 135–141. DOI: /10.1016/j.sajce.2020.07.011
- Choi H., Bor A., Sakuragi S., Lee J., Lim H.-T., The grinding behavior of ground copper powder for Cu/CNT nanocomposite fabrication by using the dry grinding process with a high-speed

- planetary ball mill, *Journal of the Korean Physical Society*, 68 (2016) 147–153. DOI: 10.3938/jkps.68.147
- Çolak H., Karaköse E., Derin Y., Properties of ZnO nanostructures produced by mechanochemical-solid state combustion method using different precursors, *Materials Chemistry and Physics*, 193 (2017) 427–437. DOI: 10.1016/j.matchemphys.2017.03.009
- Danielis M., Colussi S., Llorca J., Dolan R.H., Cavataio G., Trovarelli A., Pd/CeO<sub>2</sub> catalysts prepared by solvent-free mechanochemical route for methane abatement in natural gas fueled vehicles, *Industrial & Engineering Chemistry Research*, 60 (2021) 6435–6445. DOI: 10.1021/acs.iecr.0c05207
- Dong D., Zhang Y., Shan M., Yin T., Wang T., Wang J., Gao W., Application of mechanochemical technology for removal/solidification pollutant and preparation/recycling energy storage materials, *Journal of Cleaner Production*, 348 (2022) 131351. DOI: 10.1016/j.jclepro.2022.131351
- El Ajjouri Y., Chirvony V.S., Vassilyeva N., Sessolo M., Palazon F., Bolink H.J., Low-dimensional non-toxic A<sub>3</sub>Bi<sub>2</sub>X<sub>9</sub> compounds synthesized by a dry mechanochemical route with tunable visible photoluminescence at room temperature, *Journal of Materials Chemistry C*, 7 (2019) 6236–6240. DOI: 10.1039/C9TC01765H
- Gao W., Chen F., Wang X., Meng Q., Recent advances in processing food powders by using superfine grinding techniques: a review, *Comprehensive Reviews in Food Science and Food Safety*, 19 (2020) 2222–2255. DOI: 10.1111/1541-4337.12580
- García G.G., Coello-Velázquez A.L., Pérez B.F., Menéndez-Aguado J.M., Variability of the ball mill bond's standard test in a Ta ore due to the lack of standardization, *Metals*, 11 (2021) 1606. DOI: 10.3390/met11101606
- Goga M., Baláž M., Daneu N., Elečko J., Tkáčiková L., Marcinčinová M., Bačkor M., Biological activity of selected lichens and lichen-based Ag nanoparticles prepared by a green solid-state mechanochemical approach, *Materials Science & Engineering C*, 119 (2021) 111640. DOI: 10.1016/j.msec.2020.111640
- Gomez G.E., López C.A., Ayscue R.L., Knope K.E., Torres Deluigi M.D.R., Narda G.E., Strong photoluminescence and sensing performance of nanosized Ca<sub>0.8</sub>Ln<sub>0.1</sub>Na<sub>0.1</sub>WO<sub>4</sub> (Ln = Sm, Eu) compounds obtained by the dry “top-down” grinding method, *Dalton Transactions*, 48 (2019) 12080–12087. DOI: 10.1039/C9DT02109D
- Guzzo P.L., Marinho de Barros F.B., de Arruda Tino A.A., Effect of prolonged dry grinding on size distribution, crystal structure and thermal decomposition of ultrafine particles of dolostone, *Powder Technology*, 342 (2019) 141–148. DOI: 10.1016/j.powtec.2018.09.064
- Guzzo P.L., Marinho de Barros F.B., Soares B.R., Santos J.B., Evaluation of particle size reduction and agglomeration in dry grinding of natural quartz in a planetary ball mill, *Powder Technology*, 368 (2020) 149–159. DOI: 10.1016/j.powtec.2020.04.052
- Hashimoto T., Tagaya M., Kataoka T., Chatani S., Inui M., Higa Y., Motozuka S., Synthesis and photoluminescence properties of the Eu(III)-containing silica nanoparticles via a mechanochemical solid-state reaction between SiO<sub>2</sub> and EuCl<sub>3</sub>·6H<sub>2</sub>O, *Advanced Powder Technology*, 31 (2020) 3650–3656. DOI: 10.1016/j.apt.2020.07.013
- Hirosawa F., Iwasaki T., Iwata M., Kinetic analysis of mechanochemical reaction between zinc oxide and gamma ferric oxide based on the impact energy and collision frequency of particles, *Powder Technology*, 352 (2019) 360–368. DOI: 10.1016/j.powtec.2019.04.050
- Hirosawa F., Iwasaki T., Dependence of the dissipated energy of particles on the sizes and numbers of particles and balls in a planetary ball mill, *Chemical Engineering Research and Design*, 167 (2021) 84–95. DOI: 10.1016/j.cherd.2020.12.024
- Hlova I.Z., Gupta S., Goldston J.F., Kobayashi T., Pruski M., Pecharsky V.K., Dry mechanochemical synthesis of alane from LiH and AlCl<sub>3</sub>, *Faraday Discussions*, 170 (2014) 137–153. DOI: 10.1039/c3fd00161j
- Iwasaki T., Shimamura Y., Makino Y., Watano S., Mechanochemically assisted synthesis and visible light photocatalytic properties of lanthanum nickel oxide nanoparticles, *Optik*, 127 (2016) 9081–9087. DOI: 10.1016/j.ijleo.2016.06.125
- Jadoun S., Arif R., Jangid N.K., Meena R.K., Green synthesis of nanoparticles using plant extracts: a review, *Environmental Chemistry Letters*, 19 (2021) 355–374. DOI: 10.1007/s10311-020-01074-x
- Jung H., Lee Y.J., Yoon W.B., Effect of moisture content on the grinding process and powder properties in food: a review, *Processes*, 6 (2018) 69. DOI: 10.3390/pr6060069
- Kanie K., Sakaguchi M., Muto F., Horie M., Nakaya M., Yokoi T., Muramatsu A., Mechanochemically assisted hydrothermal synthesis of Sn-substituted MFI-type silicates, *Science and Technology of Advanced Materials*, 19 (2018) 545–553. DOI: 10.1080/14686996.2018.1497404
- Karam M.C., Petit J., Zimmer D., Djantou E.B., Scher J., Effects of drying and grinding in production of fruit and vegetable powders: a review, *Journal of Food Engineering*, 188 (2016) 32–49. DOI: 10.1016/j.jfoodeng.2016.05.001
- Katircioglu-Bayel D., Optimization of operating parameters on dry grinding of calcite in a stirred media mill using the Box-Behnken design, *Minerals*, 10 (2020) 251. DOI: 10.3390/min10030251
- Kerminen V.-M., Chen X., Vakkari V., Petäjä T., Kulmala M., Bianchi F., Atmospheric new particle formation and growth: review of field observations, *Environmental Research Letters*, 13 (2018) 103003. DOI: 10.1088/1748-9326/aad33c
- Khitab A., Ahmad S., Munir M.J., Kazmi S.M.S., Arshad T., Khushnood R.A., Synthesis and applications of nano titania particles: a review, *Reviews on Advanced Materials Science*, 53 (2018) 90–105. DOI: 10.1515/rams-2018-0007
- Kosova N.V., Semykina D.O., Mechanochemically assisted solid-state synthesis of sodium vanadium fluorophosphates, *Solid State Ionics*, 343 (2019) 115119. DOI: 10.1016/j.ssi.2019.115119
- Krauze O., Buchczik D., Budzan S., Measurement-based modelling of material moisture and particle classification for control of copper ore dry grinding process, *Sensors*, 21 (2021) 667. DOI: 10.3390/s21020667
- Kumar M., Xiong X., Wan Z., Sun Y., Tsang D.C.W., Gupta J., Gao B., Cao X., Tang J., Ok Y.S., Ball milling as a mechanochemical technology for fabrication of novel biochar nanomaterials, *Bioresource Technology*, 312 (2020) 123613. DOI: 10.1016/j.biortech.2020.123613
- Lejda K., Drygaś M., Janik J.F., Szczytko J., Twardowski A., Olejniczak Z., Magnetism of kesterite Cu<sub>2</sub>ZnSnS<sub>4</sub> semiconductor nanopowders prepared by mechanochemically assisted synthesis method, *Materials*, 13 (2020) 3487. DOI: 10.3390/ma13163487
- Letelier V., Henriquez-Jara B.I., Manosalva M., Parodi C., Ortega J.M., Use of waste glass as a replacement for raw materials in mortars with a lower environmental impact, *Energies*, 12 (2019) 1974. DOI: 10.3390/en12101974
- Liu S.-W., Guo S., Xia X.-Y., Chang X.-D., Effects of dry-

- wet- and freeze-grinding pretreatment methods on the physicochemical properties of maitake mushroom (*Grifola frondosa*) superfine powders, *Advance Journal of Food Science and Technology*, 7 (2015) 730–738. DOI: 10.19026/ajfst.7.1730
- Liu S., Li B., Wu Y., Luo K., Zhao Z., Zhang Y., Mechanochemically assisted synthesis of titanium carbonitride from metal and organic precursor, *Journal of the American Ceramic Society*, 103 (2020) 6112–6119. DOI: 10.1111/jace.17329
- Makuza B., Yu D., Huang Z., Tian Q., Guo X., Dry grinding – Carbonated ultrasound-assisted water leaching of carbonthermally reduced lithium-ion battery black mass towards enhanced selective extraction of lithium and recovery of high-value metals, *Resources, Conservation & Recycling*, 174 (2021) 105784. DOI: 10.1016/j.resconrec.2021.105784
- Martínez-Sarti L., Palazon F., Sessolo M., Bolink H.J., Dry mechanochemical synthesis of highly luminescent, blue and green hybrid perovskite solids, *Advanced Optical Materials*, 8 (2020) 1901494. DOI: 10.1002/adom.201901494
- Mastalska-Popławska J., Sikora M., Izak P., Góral Z., Role of starch in the ceramic powder synthesis: a review, *Journal of Sol-Gel Science and Technology*, 96 (2020) 511–520. DOI: 10.1007/s10971-020-05404-x
- Masuda H., Higashitani K., Yoshida H., Eds., *Powder Technology Handbook (Third Edition)*, CRC Press, 2006, pp. 239–246, ISBN: 1574447823. DOI: 10.1201/9781439831885
- Muh'd I.B., Talib Z.A., Zainal Z., Chyi J.L.Ying, Mofdal M.E.E., Mechanochemical solid state synthesis and optical properties of Cd<sub>0.5</sub>Zn<sub>0.5</sub>Se nanocrystals, *Journal of Materials Science*, 50 (2015) 457–462. DOI: 10.1007/s10853-014-8605-5
- Nada M.H., Larsen S.C., Gillan E.G., Mechanochemically-assisted solvent-free and template-free synthesis of zeolites ZSM-5 and mordenite, *Nanoscale Advances*, 1 (2019) 3918–3928. DOI: 10.1039/c9na00399a
- Nava J.V., Llorens T., Menéndez-Aguado J.M., Kinetics of dry-batch grinding in a laboratory-scale ball mill of Sn–Ta–Nb minerals from the Penouta mine (Spain), *Metals*, 10 (2020) 1687. DOI: 10.3390/met10121687
- Nawaz A., Goudarzi S., Asghari M.A., Pichiah S., Selopal G.S., Rosei F., Wang Z.M., Zarrin H., Review of hybrid 1D/2D photocatalysts for light-harvesting applications, *ACS Applied Nano Materials*, 4 (2021) 11323–11352. DOI: 10.1021/acsnm.1c01014
- Ngamnikom P., Songsermpong S., The effects of freeze, dry, and wet grinding processes on rice flour properties and their energy consumption, *Journal of Food Engineering*, 104 (2011) 632–638. DOI: 10.1016/j.jfoodeng.2011.02.001
- Nnadozie E.C., Ajibade P.A., Multifunctional magnetic oxide nanoparticle (MNP) core-shell: review of synthesis, structural studies and application for wastewater treatment, *Molecules*, 25 (2020) 4110. DOI: 10.3390/molecules25184110
- Ogonowski S., Wołosiewicz-Głąb M., Ogonowski Z., Foszcz D., Pawełczyk M., Comparison of wet and dry grinding in electromagnetic mill, *Minerals*, 8 (2018) 138. DOI: 10.3390/min8040138
- Oh C., Choi E.H., Choi E.J., Premkumar T., Song C., Facile solid-state mechanochemical synthesis of eco-friendly thermoplastic polyurethanes and copolymers using a biomass-derived furan diol, *ACS Sustainable Chemistry & Engineering*, 8 (2020) 4400–4406. DOI: 10.1021/acssuschemeng.9b06944
- Okazaki F., Hattori Y., Sasaki T., Otsuka M., Mechanochemical effect on controlled drug release of Konjac glucomannan matrix tablets during dry grinding, *Gels*, 8 (2022) 181. DOI: 10.3390/gels8030181
- Onizuka T., Iwasaki T., Low-temperature solvent-free synthesis of polycrystalline hematite nanoparticles via mechanochemical activation and their adsorption properties for Congo red, *Solid State Sciences*, 129 (2022) 106917. DOI: 10.1016/j.solidstatesciences.2022.106917
- Osuga R., Tanaka G., Yabushita M., Ninomiya K., Maki S., Nishibori M., Kanie K., Muramatsu A., Development of synthetic route for Fe-substituted MWW-type zeolite using mechanochemical method, *Journal of the Japan Petroleum Institute*, 65 (2022) 67–77. DOI: 10.1627/jpi.65.67
- Otsuka Y., Goto S., Dry mechanochemical synthesis of ethenzamide and saccharin 1:1 cocrystal and their evaluation using powder X-ray diffraction and FT-MIR and NIR spectroscopy, *Journal of Drug Delivery Science and Technology*, 67 (2022) 102918. DOI: 10.1016/j.jddst.2021.102918
- Pal P., Saha S., Banik A., Sarkar A., Biswas K., All-solid-state mechanochemical synthesis and post-synthetic transformation of inorganic perovskite-type halides, *Chemistry—A European Journal*, 24 (2018) 1811–1815. DOI: 10.1002/chem.201705682
- Parmar S., Kaur H., Singh J., Matharu A.S., Ramakrishna S., Bechelany M., Recent advances in green synthesis of Ag NPs for attenuating antimicrobial resistance, *Nanomaterials*, 12 (2022) 1115. DOI: 10.3390/nano12071115
- Peltoniemi M., Kallio R., Tanhua A., Luukkanen S., Perämäki P., Mineralogical and surface chemical characterization of flotation feed and products after wet and dry grinding, *Minerals Engineering*, 156 (2020) 106500. DOI: 10.1016/j.mineng.2020.106500
- Prziwara P., Breitung-Faes S., Kwade A., Impact of grinding aids on dry grinding performance, bulk properties and surface energy, *Advanced Powder Technology*, 29 (2018a) 416–425. DOI: 10.1016/j.apt.2017.11.029
- Prziwara P., Breitung-Faes S., Kwade A., Impact of the powder flow behavior on continuous fine grinding in dry operated stirred media mills, *Minerals Engineering*, 128 (2018b) 215–223. DOI: 10.1016/j.mineng.2018.08.032
- Prziwara P., Hamilton L.D., Breitung-Faes S., Kwade A., Impact of grinding aids and process parameters on dry stirred media milling, *Powder Technology*, 335 (2018c) 114–123. DOI: 10.1016/j.powtec.2018.05.021
- Prziwara P., Breitung-Faes S., Kwade A., Comparative study of the grinding aid effects for dry fine grinding of different materials, *Minerals Engineering*, 144 (2019) 106030. DOI: 10.1016/j.mineng.2019.106030
- Prziwara P., Hamilton L.D., Breitung-Faes S., Kwade A., Evaluation of the capturing of dry fine particles between grinding media by drop-weight tests, *Powder Technology*, 363 (2020a) 326–336. DOI: 10.1016/j.powtec.2020.01.012
- Prziwara P., Kwade A., Grinding aids for dry fine grinding processes – Part I: mechanism of action and lab-scale grinding, *Powder Technology*, 375 (2020b) 146–160. DOI: 10.1016/j.powtec.2020.07.038
- Qiu C., Chen Q., Chang C., Jiang W., Fan G., Mechanochemically assisted fabrication of ultrafine Pd nanoparticles on natural waste-derived nitrogen-doped porous carbon for the efficient formic acid decomposition, *International Journal of Hydrogen Energy*, 46 (2021) 656–665. DOI: 10.1016/j.ijhydene.2020.10.014
- Raheem D., Soltermann A.T., Tamiozzo L.V., Cogo A., Favén L., Punam N.J., Sarmiento C.R., Rainosalo E., Picco F., Morla F., Nilson A., Stammler-Gossmann A., Partnership for international development: Finland–Argentina conference on circular economy and bioeconomy with emphasis on food sovereignty and sustainability, *International Journal of*

- Environmental Research and Public Health, 19 (2022) 1773. DOI: 10.3390/ijerph19031773
- Rehman A.N., Bavoh C.B., Pendyala R., Lal B., Research advances, maturation, and challenges of hydrate-based CO<sub>2</sub> sequestration in porous media, ACS Sustainable Chemistry & Engineering, 9 (2021) 15075–15108. DOI: 10.1021/acssuschemeng.1c05423
- Shaikh W.A., Chakraborty S., Owens G., Islam R.U., A review of the phytochemical mediated synthesis of AgNP (silver nanoparticle): the wonder particle of the past decade, Applied Nanoscience 11 (2021) 2625–2660. DOI: 10.1007/s13204-021-02135-5
- Sharma P., Vetter C., Ponnusamy E., Colacino E., Assessing the greenness of mechanochemical processes with the DOZN 2.0 tool, ACS Sustainable Chemistry & Engineering, 10 (2022) 5110–5116. DOI: 10.1021/acssuschemeng.1c07981
- Soni A., Das, P.K., Hashmi A.W., Yusuf M., Kamyab H., Chelliapan S., Challenges and opportunities of utilizing municipal solid waste as alternative building materials for sustainable development goals: a review, Sustainable Chemistry and Pharmacy, 27 (2022) 100706. DOI: 10.1016/j.scp.2022.100706
- Štrukil V., Sajko I., Mechanochemically-assisted solid-state photocatalysis (MASSPC), Chemical Communications, 53 (2017) 9101–9104. DOI: 10.1039/c7cc03510a
- Suetsugu Y., Synthesis of lead vanadate iodoapatite utilizing dry mechanochemical process, Journal of Nuclear Materials, 454 (2014) 223–229. DOI: 10.1016/j.jnucmat.2014.07.073
- Swoboda P., Döring T.F., Hamer M., Remineralizing soils? The agricultural usage of silicate rock powders: a review, Science of the Total Environment, 807 (2022) 150976. DOI: 10.1016/j.scitotenv.2021.150976
- Szczeńniak B., Borysiuk S., Choma J., Jaroniec M., Mechanochemical synthesis of highly porous materials, Materials Horizons, 7 (2020) 1457–1473. DOI: 10.1039/d0mh00081g
- Tamura T., Ishikawa T., Kimata M., Potentiality of fine grinding using the horizontal dry bead mill, and relationship between required power and particle size, Journal of the Society of Powder Technology, Japan, 54 (2017) 648–653. DOI: 10.4164/sptj.54.648
- Tamura T., Ishikawa T., Kimata M., Effect of bead diameter on quartz sand grinding using horizontal dry bead mill, Journal of the Society of Powder Technology, Japan, 57 (2020) 627–632. DOI: 10.4164/sptj.57.627
- Tan Y., Zou Z., Qu J., Ren J., Wu C., Xu Z., Mechanochemical conversion of chrysotile asbestos tailing into struvite for full elements utilization as citric-acid soluble fertilizer, Journal of Cleaner Production, 283 (2021) 124637. DOI: 10.1016/j.jclepro.2020.124637
- Tanaka S., Kida K., Nagaoka T., Ota T., Miyake Y., Mechanochemical dry conversion of zinc oxide to zeolitic imidazolate framework, Chemical Communications, 49 (2013) 7884–7886. DOI: 10.1039/c3cc43028f
- Tayibi S., Monlau F., Fayoud N.-E., Abdeljaoued E., Hannache H., Zeroual Y., Oukarroum A., Barakat A., Production and dry mechanochemical activation of biochars derived from Moroccan red macroalgae residue and olive pomace biomass for treating wastewater: thermodynamic, isotherm, and kinetic studies, ACS Omega, 6 (2021) 159–171. DOI: 10.1021/acsomega.0c04020
- Toraman O.Y., Dry fine grinding of calcite powder by stirred mill, Particulate Science and Technology, 31 (2013) 205–209. DOI: 10.1080/02726351.2012.694135
- Wichaita W., Polpanich D., Tangboriboonrat P., Review on synthesis of colloidal hollow particles and their applications, Industrial & Engineering Chemistry Research, 58 (2019) 20880–20901. DOI: 10.1021/acs.iecr.9b02330
- Wu L., Kim S., Moriyoshi C., Kuroiwa Y., Suzuki M., Shinoda K., Aoyagi R., Akedo J., Synthesis of Pb(Zr, Ti)O<sub>3</sub> fine ceramic powder at room temperature by dry mechanochemical solid-state reaction evaluated using synchrotron radiation X-ray diffraction, Japanese Journal of Applied Physics, 60 (2021) SFFA02. DOI: 10.35848/1347-4065/ac0c6e
- Yang Y., Chen L., Mao Y., Different effects of wet and dry grinding on the activation of iron ore tailings, Journal of Renewable Materials, 9 (2021) 2261–2276. DOI: 10.32604/jrm.2021.015793
- Yuan Q., Zhang Y., Wang T., Wang J., Romero C.E., Mechanochemical stabilization of heavy metals in fly ash from coal-fired power plants via dry milling and wet milling, Waste Management, 135 (2021) 428–436. DOI: 10.1016/j.wasman.2021.09.029
- Zhang J., Zhang P., Shao L., Wang R., Ma Y., Szostak M., Mechanochemical solvent-free Suzuki–Miyaura cross-coupling of amides via highly chemoselective N–C cleavage, Angewandte Chemie International Edition, 61 (2022) e202114146. DOI: 10.1002/anie.202114146
- Zhang M., Lin Z., Huang Q., Zhu Y., Hu H., Chen X., Green synthesis of submicron-sized Ti-rich MWW zeolite powders via a novel mechanochemical dry gel conversion in mixed steam environment, Advanced Powder Technology, 31 (2020) 2025–2034. DOI: 10.1016/j.apt.2020.02.037
- Zhang Z.-Y., Ji D., Mao W., Cui Y., Wang Q., Han L., Zhong H., Wei Z., Zhao Y., Nørgaard K., Li T., Dry chemistry of ferrate(VI): a solvent-free mechanochemical way for versatile green oxidation, Angewandte Chemie International Edition, 57 (2018) 10949–10953. DOI: 10.1002/anie.201805998
- Zheng B., Kabiri S., Andelkovic I.B., Degryse F., Da Silva R., Baird R., Self P., McLaughlin M.J., Mechanochemical synthesis of zinc borate for use as a dual-release B fertilizer, ACS Sustainable Chemistry and Engineering, 9 (2021) 15995–16004. DOI: 10.1021/acssuschemeng.1c07111

## Author's Short Biography



### Tomohiro Iwasaki

Tomohiro Iwasaki is a Professor of Chemical Engineering at Osaka Metropolitan University in Japan. He received his master's degree in Chemical Engineering from Osaka Prefecture University. He also received his Ph.D. degree in Chemical Engineering from Osaka Prefecture University. His research interests include mechanochemical processes, organic–inorganic hybrid materials (organoclays, layered organosilicates) synthesized via intercalation, ferrite nanoparticles for magnetic hyperthermia treatments, and discrete element simulation of ball mills.

# Recent Advances in the Fabrication and Functionalization of Nanostructured Carbon Spheres for Energy Storage Applications<sup>†</sup>

Kiet Le Anh Cao<sup>1</sup>, Ferry Iskandar<sup>2,3</sup>, Eishi Tanabe<sup>4</sup> and Takashi Ogi<sup>1\*</sup>

<sup>1</sup> Chemical Engineering Program, Department of Advanced Science and Engineering, Graduate School of Advanced Science and Engineering, Hiroshima University, Japan

<sup>2</sup> Department of Physics, Institute of Technology Bandung, Indonesia

<sup>3</sup> Collaboration Research Center for Advanced Energy Materials, National Research and Innovation Agency - Institut Teknologi Bandung, Indonesia

<sup>4</sup> Western Region Industrial Research Center, Hiroshima Prefectural Technology Research Institute, Japan

## Abstract

The development of energy storage devices providing high energy and power densities and long-term stability will play an important role in the future utilization of sustainable energy sources. Numerous efforts have been devoted to achieving these requirements, especially the design of advanced electrode materials. For this reason, there is growing interest in the innovation of new carbon-based materials with enhanced electrochemical performance. Nanostructured carbon spheres (CSs) have attracted significant attention due to their prominent properties, such as high surface area, excellent electrical conductivity, tunable porosity, and surface functionality. This review offers a comprehensive overview into the recent advances of nanostructured CSs within the last five years, focusing on synthetic strategies for producing carbon particles with precisely controlled morphologies and interior structures, as well as the potential applications of these particles as high-performance electrode materials in rechargeable batteries and supercapacitors. The challenges and perspectives on future research directions are highlighted, focusing on the controlled synthesis and functionalization of nanostructured CSs with tunable structures and properties that are well-suited to practical applications. This review is intended to serve as a helpful resource to researchers involved in the fabrication of new CS materials and the development of methods to control their structure and morphology.

**Keywords:** carbon spheres, nanostructured particles, energy storage, batteries, supercapacitors

## 1. Introduction

The greenhouse effect is widely recognized as one of the main factors responsible for global climate change, which has begun to affect our daily life and has become a significant concern affecting the existence of all living species (Zhang et al., 2022; Tanno and Makino, 2018). Therefore, the development of renewable and green energy technologies for a sustainable future, which could mitigate the most severe impacts of climate change, is a highly desirable goal. Until now, numerous extensive research efforts are focused on the design of low-cost and environment-friendly energy storage devices with high electrochemical performance characteristics, including rechargeable batteries and supercapacitors (Long et al., 2017; Zhang M. et al., 2018). The

electrode materials in these electrochemical energy storage devices play a crucial role, which determine their overall performance. Consequently, the exploration of multifunctional electrode materials is still a hot and vital topic.

In order to meet these goals described above, the key aspects are the innovative design of nanostructured particulate materials and the discovery of fabrication processes that allow for the synthesis of materials having precisely tailored morphologies, structures and chemical characteristics. It will also be necessary to search for greener and more cost-effective synthetic processes to allow the widespread utilization of such devices. Interestingly, natural materials often tend to adopt spherical shapes because this morphology minimizes surface energy and is highly stable. From an engineering viewpoint, spherical particles also offer many advantages because they have no sharp edges and are thus less likely to be damaged during processing. In addition, the size and regular shape of spheres allow for the effective ordering of subjects in densely packed states, especially when necks and pores are present. Finally, spheres provide excellent fluidity (Tian et al., 2019; Cao et al., 2021b). As

<sup>†</sup> Received 20 June 2022; Accepted 7 July 2022  
J-STAGE Advance published online 23 September 2022

\* Corresponding author: Takashi Ogi;  
Add: 1-4-1 Kagamiyama, Higashi-Hiroshima, Hiroshima 739-8527, Japan  
E-mail: [ogit@hiroshima-u.ac.jp](mailto:ogit@hiroshima-u.ac.jp)  
TEL: +81-82-424-3765

a consequence of these advantages, carbon-based spheres have captivated vast attention due to the combined advantages of carbon materials with spherical colloids. These materials can exhibit several unique features, including regular geometry, high uniformity, good fluidity, superior packing density, and tunable particle size distribution (Liu et al., 2015; Tian et al., 2019). Despite the enormous achievements made in many fields, carbon spheres (CSs) continue to emerge and fabricate from smart synthetic strategies. These intriguing advantages and exciting prospects have stimulated worldwide research activities of CSs, particularly in energy-related applications. Therefore, the development and innovation of advanced CSs having well-defined structural and surface characteristics are expected to play a critical role in the energy field, which provide an opportunity to improve the performance in energy storage devices with both high power and energy densities.

Although several review articles concerning carbon-based materials (*e.g.*, mesoporous carbon, carbon nanotubes, graphene) have been published over the last decade (Zhang M. et al., 2018; Benzigar et al., 2018; Tian et al., 2019; Kerdnawee et al., 2017; Zhao et al., 2019), the scope of the review covers the critical advances of the nanostructured CSs, focusing on the recent progress in the fabrication with precisely controlled structures and functionalities through smart synthetic strategies. Such strategies are necessary to achieve better performance in energy storage devices. On this basis, the aim of the present review was to offer an overview into the fabri-

cation techniques of CSs, with a particular emphasis on new and promising developments. As a critical point, a comprehensive overview is provided that discusses the most up-to-date strategies (those devised primarily within the last five years) for the rational synthesis of CSs with diverse structures. In addition, the utilization of such materials as key components in a wide range of energy storage applications is explored. Fig. 1 provides a diagram summarizing various aspects of the nanostructured CSs considered herein. These aspects comprise fabrication processes and carbon sources, various methods for the tuning of morphology and architecture, functionalization, and applications in energy storage devices. To highlight the above-mentioned important point, the present review is organized as follows. Firstly, introducing the promising approaches for the design and synthesis of CSs using three routes (*e.g.*, template-free, soft templating, and hard templating) by combining the excellent work from worldwide researchers. Secondly, overviewing the performance of CSs with various structures and their composites in energy storage devices (*e.g.*, rechargeable batteries and supercapacitors). Furthermore, there is still a lack of a clear discussion regarding the specific relationship between carbon structures and electrochemical performance characteristics. As a matter of fact, the correlation between the synthesis strategy, structure, and characteristics of CSs would allow these materials to be used more extensively in energy storage devices; therefore, their preparation-structure-function relevance is expected to be understood. Finally, offering

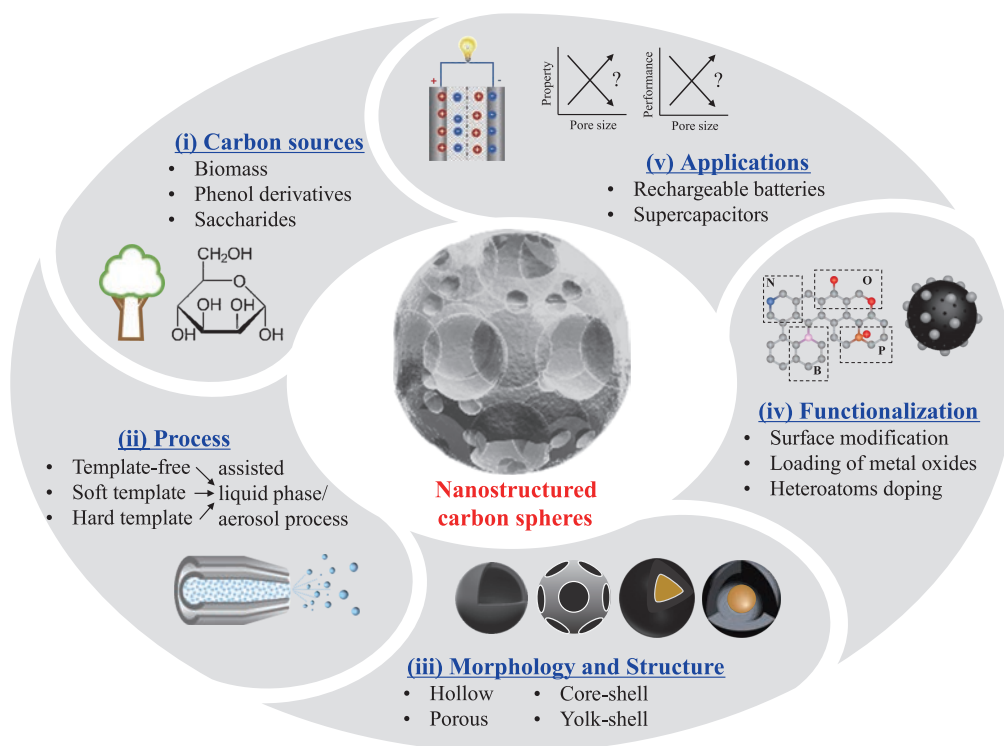


**Fig. 1** A comprehensive overview of the preparation and functionalization of nanostructured CSs for energy storage applications.

some concluding remarks on the current challenges and perspectives related to nanostructured CS materials, as well as highlighting the promising future progress in the field of energy-related devices.

## 2. Synthesis of carbon spheres

Various structures of CS materials can be obtained using numerous synthesis processes. Fig. 2 shows typical schemes for preparing nanostructured CSs with different strategies. These synthesis processes can generally be classified into three categories: template-free, soft template and hard template approaches, which will be highlighted in this section.

### 2.1 Template-free synthesis of carbon spheres

The large-scale production of CSs will require processes that are simple, energy efficient, environmentally friendly, and cost-effective. On this basis, the development of template-free approaches capable of producing CSs having a wide range of pore sizes would be preferable, as shown in Fig. 2(a). Three simple and commonly used template-free synthetic strategies, including hydrothermal carbonization (HTC) method, extension of the Stöber method, and aerosol-assisted method will be investigated. Common precursor materials for the fabrication of CSs in conjunction with template-free strategies and the respective physical properties of the obtained CSs are summarized in Table 1. Recently, numerous review articles have been carefully explained the synthesis of nanostructured CSs using HTC and extension of the Stöber methods (Liu et al., 2015; Tian et al., 2019). Therefore, in this section, we mainly focused on the fabrication of nanostructured CSs using aerosol-assisted techniques.

Aerosol-assisted techniques, such as spray drying and spray pyrolysis, are cost-effective, simple, continuous and scalable methods for the preparation of CSs (Ogi et al., 2014; Debecker et al., 2018; Leng et al., 2019; Gradon et al., 2020). Because of these advantages, such methods are frequently used to produce dry powders in the food, pharmaceutical, and chemical industries. Generally, depending on the operating conditions, solid or hollow spherical particles can be produced in the spray process (Cao et al., 2021b; 2021a; Nguyen et al., 2021; 2022). Feng et al. prepared pomegranate-like carbon microspheres (PCSs) by fabricating monodisperse, submicron CSs via a scalable template-free spray drying-assisted approach (Feng et al., 2019). In this process, monodisperse 3-aminophenol/formaldehyde (3-AF) resin spheres were initially synthesized based on the polymerization of 3-aminophenol and formaldehyde in deionized water without the use of a catalyst. The monodisperse resin colloids were subsequently spray dried to generate pomegranate-like resin microspheres during the spray drying process. Finally, after carbonization and potassium hydroxide (KOH) activation, the pomegranate-like

resin microspheres were converted into PCSs. These PCSs comprised well-defined microspheres with a high specific surface area (SSA) of 1477 m<sup>2</sup>/g and a relatively broad size distribution ranging from 1 μm to 5 μm.

Until now, considering the sustainable development of CS materials, the use of biomass as a precursor has received increasing attention due to its renewability, reproducibility, readily accessible, and environmental friendliness. Although biomass has been utilized as a raw material for the fabrication of carbon materials, there are few reports on the successful production of CSs from biomass-based materials using template-free spray drying method. Cao et al. has successfully fabricated spherical carbon particles using a template-free spray drying approach followed by the carbonization process, utilizing KOH as the activator and Kraft lignin as the carbon precursor (Fig. 3(a)) (Cao et al., 2021a; 2021b). Adjusting the KOH concentration in the reaction solution was found to allow tuning of the CS structure from dense to hollow, as shown in the TEM images (Fig. 3(b–d)). A possible mechanism for the formation of carbon particles is also studied in their research, with the aim of providing a more in-depth understanding of the process. In addition, hollow carbon spheres (HCSs) having a high SSA of 2424.8 m<sup>2</sup>/g along with a micro-mesoporous structure were obtained at KOH-to-lignin mass ratios below 1.5. Very recently, the same group has proposed a fundamental modification of the fabrication process of porous CSs by employing sodium hydroxide (NaOH) as the substitute activation agent in place of the more conventionally used KOH (Kitamoto et al., 2022). NaOH offers some advantages over KOH in terms of less corrosiveness, low cost, and simple handling procedure, all of which are appealing particularly from an industrial point of view. The results indicate that the structure of carbon particles can be tuned from a compact to hollow structure, and the surface textural characteristics can be easily adjusted by changing the amount of NaOH. The significant achievements and ongoing efforts in this field suggest that these processes will allow the development of advanced carbon materials and the high value-added utilization of Kraft lignin as a promising material for potential applications.

In the spray pyrolysis process, droplets of the liquid precursor are formed via ultrasonication (He and Wang, 2019; Ogi et al., 2020; Septiani et al., 2021; 2022; Le et al., 2022) and promptly carbonized at high temperatures under the protection of inert gases (Balgis et al., 2015; 2017). The size and morphology of the resulting CSs can be adjusted by changing the reaction conditions, reactant concentration ratios, and carbonization temperature. In recent years, there have been several publications regarding the synthesis of CSs using a template-free spray pyrolysis process. Guo et al. developed a novel strategy for producing hierarchical porous CSs by utilizing coal as the raw material in conjunction with ultrasonic spray pyrolysis (Guo et al., 2017). In

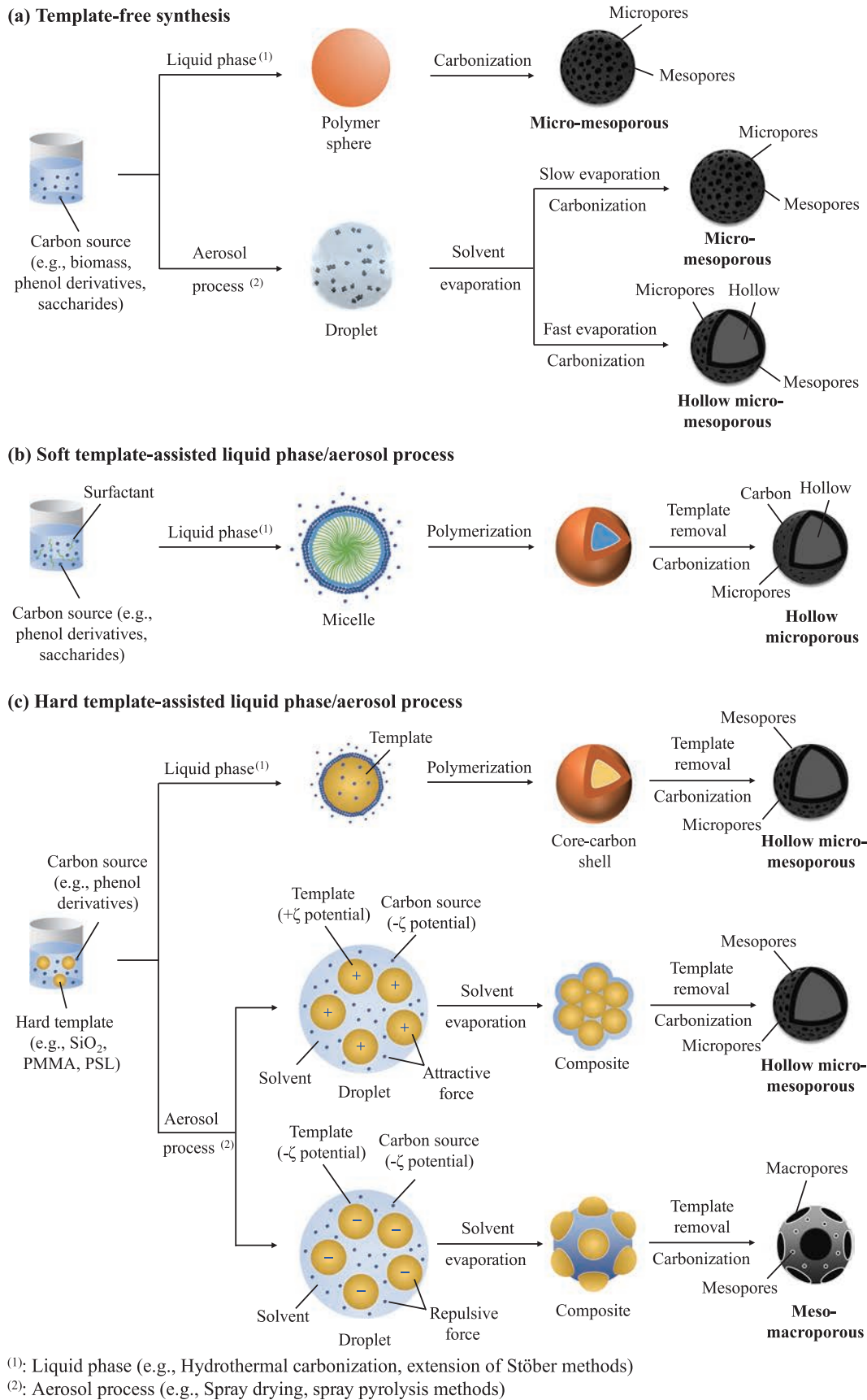


**Fig. 2** Synthetic strategies for the preparation of CSS using (a) template-free, (b) soft template, and (c) hard template approaches.



**Table 1** Summary of the conditions used for the template-free synthesis of functionalized CSs, the textural parameters of these materials and their potential applications.

No.	Material	Process	Precursor	Structure	$d_{\text{pore}}$ (nm)	SSA ( $\text{m}^2/\text{g}$ )	$V_{\text{total}}$ ( $\text{cm}^3/\text{g}$ )	Applications	Reference
1	N-ACSS <sup>a</sup>	HTC <sup>b</sup> + Activation	Glucose	Abundant microporous structure	1.6	1579	0.66	LSBs <sup>e</sup>	(Xiang et al., 2018)
2	N-CSs	Surfactant-assisted HTC	Glucose	Microporous structure	< 1.5	844	0.35	LIBs <sup>d</sup> and SIBs <sup>e</sup>	(Zhang H. et al., 2019)
3	ACSS	HTC + Activation	Xylose	Micro-mesoporous structure	—	2675	1.62	Supercapacitors	(Sun et al., 2020)
4	PCSS <sup>f</sup>	HTC	Starch	Hierarchical porous structure with coexistence of micro- and mesopores	2–3	393–973	0.18–0.27	Supercapacitors	(Lu et al., 2018)
5	PCSS	HTC + Activation	Starch	Porous structure with high content of micropores and sufficient mesopores	3.9	1973	0.89	Supercapacitors and SIBs	(Zhang J. et al., 2020)
6	PCSS	HTC + Activation	GAML <sup>g</sup>	Porous structure with dominant micropores and low content of mesopores	1.8–2.1	1746–2478	0.87–1.24	Supercapacitors	(Hao et al., 2018)
7	N-CSs	Extended the Stöber method	3-Aminophenol and formaldehyde	Microporous structure	< 2	61–356	—	PIBs <sup>h</sup>	(Wang S. et al., 2020)
8	N-HCSs <sup>i</sup> N-YS-CSs <sup>j</sup> N-SCSS <sup>k</sup>	Extended the Stöber method	Resorcinol and formaldehyde	Micro-/mesoporous structure. Different inner structures (solid, yolk-shell, hollow) can be obtained depending on the changed polymerization degree of internal RF resin	—	946 1263 501	0.51 0.68 0.29	Supercapacitors	(Zhang L. et al., 2019)
9	Pomegranate-like CSs	Spray drying + Activation	3-Aminophenol and formaldehyde	Pomegranate-like structure and rich packing voids with abundant micropores	—	1477	0.83	Supercapacitors	(Feng et al., 2019)
10	CSs	Spray drying + Carbonization	Kraft lignin	Dense structure with abundant micropores and small amounts of mesopores	0.7	936–1233	0.31–0.44	—	(Cao et al., 2021b)
11	HCSs	Spray drying + Carbonization	Kraft lignin	Porous hollow structure composed of micro- and mesopores	0.7, 2.4	1536–2425	0.75–1.57	Supercapacitors	(Cao et al., 2021a)
12	PCSS	Spray drying + Carbonization	Kraft lignin	By changing the NaOH concentration, the structure can be adjusted from a compact to hollow structure	0.7, 2.4, 20–100	761–1513	0.34–1.01	Supercapacitors	(Kitamoto et al., 2022)
13	HPCSs <sup>l</sup>	Spray drying + Carbonization	Sodium lignosulfonate	Hierarchical porous hollow structure comprised micro-, meso- and macropores	1–7, 10–100	963–1342	0.72–1.05	Supercapacitors	(Pang et al., 2018b)
14	MCSs <sup>m</sup>	Spray drying + Carbonization	Chitosan	Mesoporous structure with unique bimodal pore size distribution	~ 4, 7	645–1292	0.33–1.29	LSBs	(Zhou H. et al., 2018)
15	PCSS	Spray pyrolysis	Coal	Hierarchical porous structure composed of micro- and mesopores	1.7–2.5	547–948	0.23–0.52	Supercapacitors	(Guo et al., 2017)
16	N,S-PCSS <sup>n</sup>	Spray pyrolysis	Coal	Porous structure composed of micro- and mesopores	—	589–635	0.38–0.43	Supercapacitors	(Lv et al., 2020)
17	PCSS	Spray pyrolysis + Activation	Glucose	Honeycomb-like hierarchical porous structure including micro-, meso-, and macropores	< 1, 1–5, 100	1443–1837	1.23–1.40	Supercapacitors	(Tang et al., 2018)
18	N-HCSs	Spray pyrolysis + Carbonization	Glucose and glucosamine	Hollow structure with large number of mesopores within the shell	—	327	0.13	Supercapacitors	(Qu et al., 2018)

<sup>a</sup> N-ACSS: Nitrogen-doped activated CSs; <sup>b</sup> HTC: Hydrothermal carbonization; <sup>c</sup> LSBs: Lithium-sulfur batteries; <sup>d</sup> LIBs: Lithium-ion batteries; <sup>e</sup> SIBs: Sodium-ion batteries; <sup>f</sup> PCSS: Porous CSs; <sup>g</sup> GAML: 2-keto-L-gulonic acid mother liquor; <sup>h</sup> PIBs: Potassium-ion batteries; <sup>i</sup> N-HCSs: Nitrogen-doped hollow CSs; <sup>j</sup> N-YS-CSs: Nitrogen-doped yolk-shell CSs; <sup>k</sup> N-SCSS: Nitrogen-doped solid CSs; <sup>l</sup> HPCSs: Hollow porous CSs; <sup>m</sup> MCSs: Mesoporous CSs; <sup>n</sup> N,S-PCSSs: Nitrogen, sulfur co-doped porous CSs.

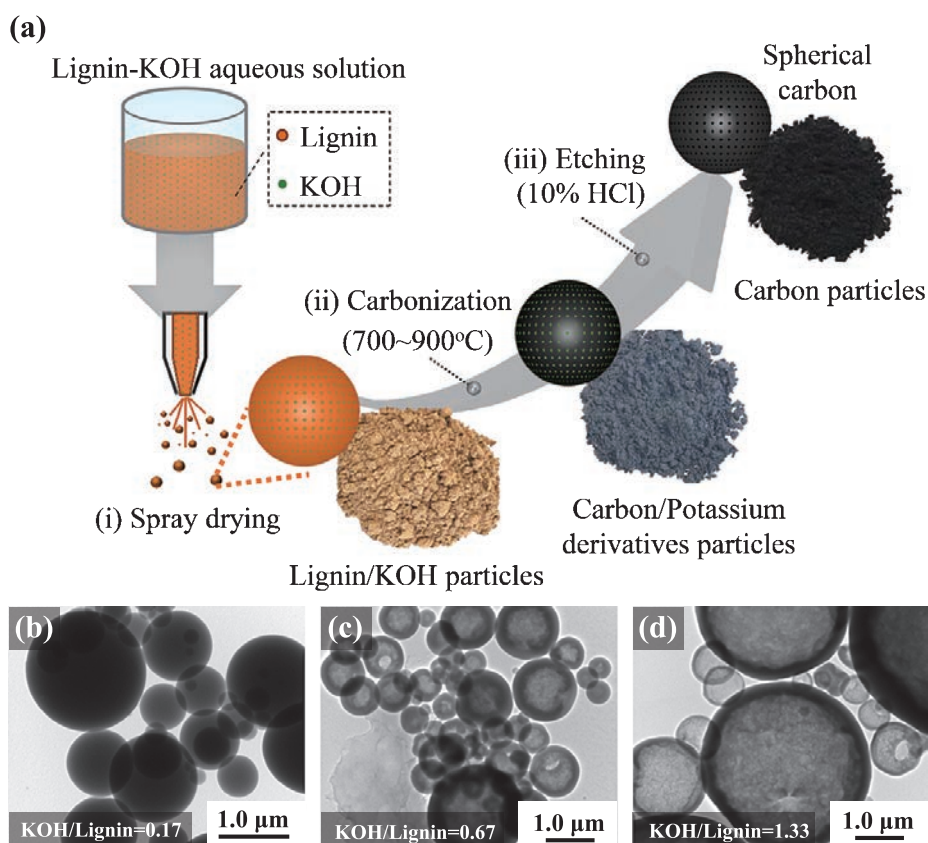


**Fig. 3** (a) An illustration of the synthesis of CSs from Kraft lignin via a spray drying process; Transmission electron microscopy (TEM) images of carbon particles generated using KOH/lignin mass ratios of (b) 0.17, (c) 0.67, and (d) 1.33.

this process, the raw coal is chemically oxidized by a highly concentrated mixture of sulfuric acid and nitric acid, such that numerous functional groups are introduced, including  $-C=O$ ,  $-OH$ ,  $-NH_2$ ,  $-SO_3H$ , and  $-NO_2$ . Subsequently, the as-prepared coal oxide can be readily dissolved in an alkaline solution to obtain a transparent precursor solution. The pyrolysis temperature was found to have a significant effect on the pore architecture and SSA of the CSs generated using this process. As the temperature was increased from 700 to 1000 °C, micro-/mesoporous structures were observed in these CSs with the SSA and total pore volume of the samples rapidly increasing from 547.2 to 948.5 m<sup>2</sup>/g and from 0.23 to 0.52 cm<sup>3</sup>/g, respectively. To further improve the electrochemical properties of carbon materials, the same group was developed multiple heteroatoms N/S doping porous CSs through ultrasonic spray pyrolysis method employing L-Cysteine as nitrogen and sulfur precursor along with coal as the carbon precursor (Lv et al., 2020). The results reveal that the homogeneous doping of N and S elements not only improves the hydrophilicity of the CSs but also provides more active sites, resulting in an increase in specific capacitance.

## 2.2 Soft template-assisted liquid phase/aerosol process

Soft templates are typically organic molecules, macro-

molecules or supramolecules that are easily decomposed at relatively low carbonization temperature (below 400 °C). The synthesis of porous CSs using the soft template typical involves several key steps (shown in Fig. 2(b)): (i) the dissolution of the template molecules and carbon precursor in a suitable solvent, (ii) the soft templates turn into micelles during solvent evaporation and simultaneous interaction of these micelles with the carbon precursor via hydrogen bonding as well as hydrophobic, hydrophilic or electrostatic interactions, and (iii) the heat treatment of the precursor/template composite in an inert atmosphere with complete decomposition of the soft template. Various carbon precursors and soft templates that are frequently used in the preparation of CSs, as well as the physical properties of the resulting materials, are summarized in Table 2.

Over the past decade, there has been significant process in the direct synthesis of mesoporous CSs from amphiphilic molecules such as surfactant or block copolymer self-assembles with carbon precursor, which is stabilized by thermal treatment. Different carbon precursors, such as phenolic resin or their derivatives, carbohydrates, nitrogen and carbon-rich compounds (e.g., dopamine), and natural polymers (e.g., cellulose, chitin and lignin) are commonly used for the fabrication of mesoporous CSs. Tang et al. prepared porous CSs with sub-micrometer particle size (about 300 nm) using the linear block copolymer PS-*b*-PEO as

**Table 2** Summary of the conditions used for the soft template synthesis of functionalized CSs, the textural parameters of these materials and their potential applications.

No.	Material	Process	Template	Precursor	Structure	$d_{\text{pore}}$ (nm)	SSA ( $\text{m}^2/\text{g}$ )	$V_{\text{total}}$ ( $\text{cm}^3/\text{g}$ )	Applications	Reference
1	N-MCSs <sup>a</sup>	Soft template + Activation	PS- <i>b</i> -PEO <sup>b</sup>	Dopamine	Interconnected hierarchical porous structure (micro- and mesopores). Mesopores are well-distributed on the sphere surface	4.2–16.0	397–2320	0.29–1.41	Supercapacitors	(Tang et al., 2017)
2	N-MCSs	Soft template	PS- <i>b</i> -PAA <sup>c</sup>	Dopamine	Core-shell structure with abundant mesopores in the core	14.8	449	0.60	SIBs	(Mao et al., 2020)
3	N-MCSs	Soft template + Pyrolysis	Pluronic F127	2-Aminophenol and formaldehyde	Mesoporous structure with uniform mesopore size (5 nm)	5	439	0.33	Supercapacitors	(Wang et al., 2018)
4	PCSs <sup>d</sup>	Soft template	Pluronic F127	Larch sawdust (biomass)	Hierarchical porous structure consisting of interconnected and worm-like pores	—	659–760	0.44–0.67	Supercapacitors	(Song et al., 2019)
5	N,O-CSs <sup>e</sup>	Soft template + HTC	Pluronic F127	3-Aminophenol and formaldehyde	Hierarchical micro-/mesoporous structure with interconnected and worm-like pores	0.6, 2–5	2012–3203	0.99–1.93	Supercapacitors	(Liu S. et al., 2016)
6	N-MCSs	Soft template	Pluronic F127	Melamine and formaldehyde	Porous structure composed of large mesopores	1.2, 6.7–8.1	791–883	1.3–1.5	SIBs	(Guo et al., 2021)
7	N-PCSs	Soft template + HTC	Pluronic F108	Phenol and formaldehyde	Porous structure with many micropores and few mesopores	—	1481	0.90	Supercapacitors	(Liang et al., 2019)
8	YS-CSs <sup>f</sup>	Soft template	CTAB <sup>g</sup>	Resorcinol and formaldehyde	Hierarchical porous yolk-shell structure	1.5, 2–10	543–703	0.59–1.47	PIBs	(Zhang H. et al., 2018)
9	N,O-YS-CSs <sup>h</sup>	Soft template + HTC	CTAB	Resorcinol and formaldehyde	Yolk-shell structure comprised dense core and porous shell layer (micro- and mesopores)	—	440–996	—	PIBs	(Chong et al., 2021)
10	N-HMCSs N-YS-MCSs	Soft template (Extended the Stöber method)	CTAC <sup>i</sup>	Resorcinol and formaldehyde	By changing amount of EDA, mesoporous yolk-shell and hollow structures are obtained	2.4 2.6	2001 1169	1.86 0.88	Supercapacitors	(Liu C. et al., 2016)
11	HCSs	Soft template (Extended the Stöber method)	CTAB	Phenol and formaldehyde	Increasing EtOH/H <sub>2</sub> O ratio, the structures were adjusted from irregular to hollow to core-shell. Abundant mesopores under appropriate EtOH/H <sub>2</sub> O ratio	2.9	544–1065	0.57–1.54	Supercapacitors	(Du et al., 2020)
12	APCSs	Soft template	DDAB <sup>j</sup>	3-Aminophenol and formaldehyde	Hollow structure with interconnected pores	—	259–1746	0.50–1.94	Supercapacitors	(Li et al., 2021)
13	N-PCSs	Soft template + HTC	[C <sub>12</sub> mim]Br <sup>k</sup>	3-Aminophenol and amphiphilic aliphatic aldehydes	Hierarchical porous structure including micro- and mesopores.	3.7–6.3, 25	812–1040	0.64–1.54	Supercapacitors	(Jia et al., 2022)
14	N-MCHSs	Soft template + HTC	Gemini <sup>l</sup>	3-Aminophenol and formaldehyde	Interconnected porous hollow structure (meso- and macropores)	< 2, 5–20, 20–110	1215–1517	1.12–3.22	Supercapacitors	(Li et al., 2020)

<sup>a</sup> N-MCSs: Nitrogen-doped mesoporous CSs; <sup>b</sup> PS-*b*-PEO: Polystyrene-*b*-poly(ethylene oxide); <sup>c</sup> PS-*b*-PAA: Polystyrene-*b*-poly(acrylic acid); <sup>d</sup> PCSs: Porous CSs; <sup>e</sup> N,O-CSs: Nitrogen, oxygen co-doped CSs; <sup>f</sup> YS-CSs: Yolk-shell CSs; <sup>g</sup> CTAB: Cetyltrimethylammonium bromide; <sup>h</sup> N,O-YS-CSs: Nitrogen, oxygen co-doped yolk-shell CSs; <sup>i</sup> CTAC: Cetyltrimethylammonium chloride; <sup>j</sup> DDAB: Didecyltrimethylammonium bromide; <sup>k</sup> [C<sub>12</sub>mim]Br: 1-dodecyl-3-methylimidazole bromide; <sup>l</sup> Gemini: Pentane-1,5-bis(dimethylcetyl ammonium bromide).

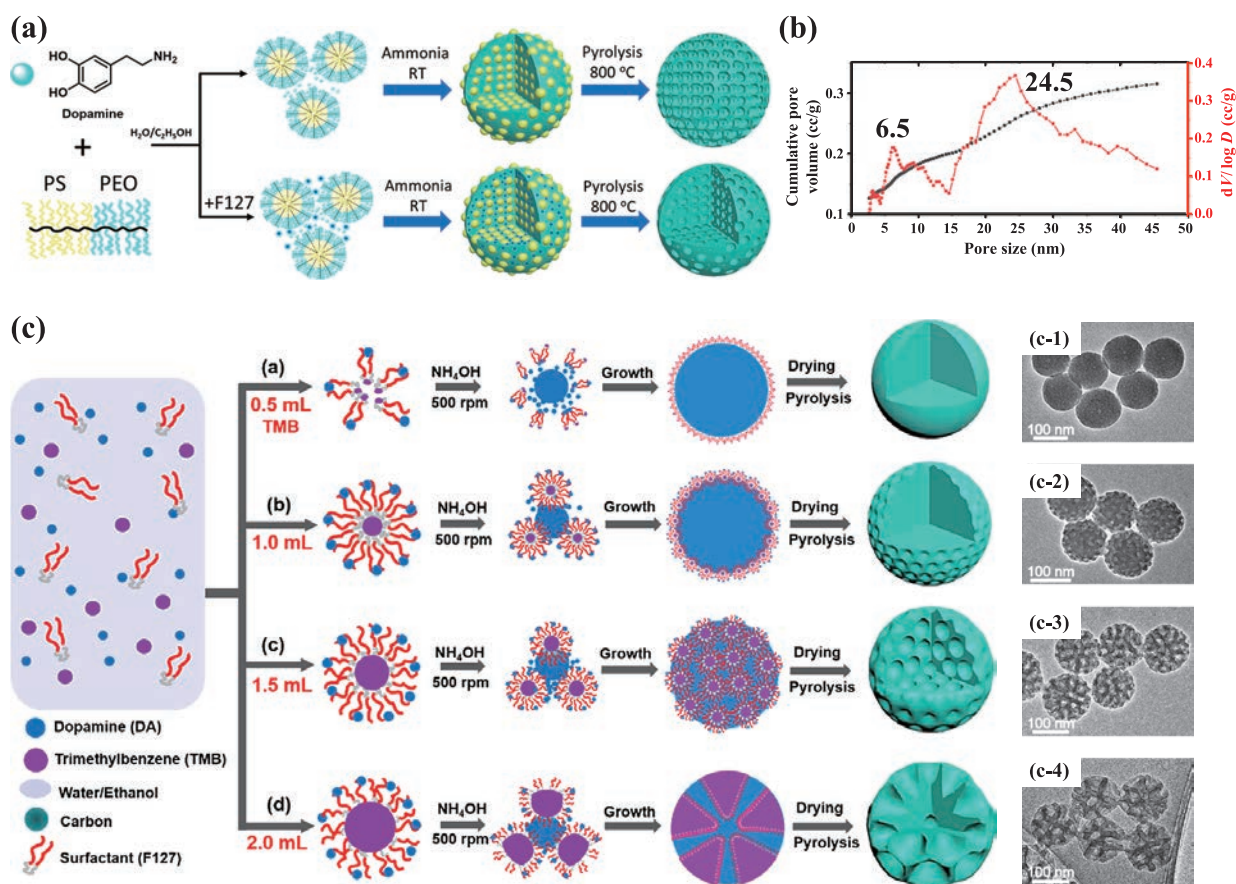


**Fig. 4** (a) An illustration showing the fabrication of monomodal and bimodal porous CSs through the self-assembly of dopamine, PS-*b*-PEO BCCPs, and Pluronic F127; (b) pore size distribution of mesoporous CSs. Reprinted with permission from Ref. (Fei et al., 2020). Copyright 2020, American Chemical Society. (c) An illustration showing the formation of N-doped mesoporous carbon nanospheres corresponded to TEM images with different morphologies and mesostructures using a versatile nano-emulsion assembly method. Reprinted with permission from Ref. (Peng et al., 2019). Copyright 2019, American Chemical Society.

the soft template and dopamine as the carbon source in conjunction with KOH activation (Tang et al., 2017). The size of mesopores could be precisely tuned from 4 to 16 nm by using PS-*b*-PEO copolymers having different molecular weights as pore forming agents in this process. Despite such prior work, the fabrication of mesoporous CSs with large pore size from soft templates as a means of providing efficient pathways for electrolyte diffusion remains a great challenge. On this basis, Fei et al. explored the fabrication of nitrogen-doped mesoporous CSs having ultra-large mesopore sizes (up to 24.5 nm) by utilizing PS-*b*-PEO brush block copolymers (BCCPs) along with a small molecule surfactant (Pluronic F127) as the template and dopamine as the carbon and nitrogen source followed by carbonization and thermal decomposition of the polymer templates, as illustrated in Fig. 4(a) (Fei et al., 2020). Mesoporous CSs with bimodal mesopore size distributions (having apexes at 6.5 and 24.5 nm) were confirmed by the peak in the  $dV/\log D$  curve (red line curve) and the cumulative pore volume is calculated by summing individual pore volumes (black line curve), as shown in Fig. 4(b). Specifically, BCCPs corresponded to the large mesopores and the

Pluronic F127 template was responsible for the small mesopores. This work demonstrated a unique and adaptable approach for synthesizing CSs with a precisely tailored morphology and bimodal pore sizes for potential applications in energy storage. Peng et al. reported the fabrication of highly uniform mesoporous CSs with adjustable pore sizes and structures (e.g., smooth, golf ball, multi-chambered, and dendritic nanospheres) (Fig. 4(c)) (Peng et al., 2019). In this work, Pluronic F127 was utilized as a soft template, dopamine was employed as a carbon and nitrogen source, and organic molecules (e.g., 1,3,5-trimethylbenzene) played a critical role in the evolution of pore size and also affected the interfacial interactions between the Pluronic F127 and dopamine. The CSs produced by this process had an ultra-large pore size of 37 nm, small average particle size of 128 nm, high SSA of 635 m<sup>2</sup>/g, and high nitrogen content of 6.8 wt%.

In some studies, ordered mesoporous CSs have been fabricated by a simple one-step process. Song et al. synthesized hierarchical porous CSs using Pluronic F127 as a soft template and biomass (e.g., larch sawdust) as the carbon precursor via a spray pyrolysis method (Song et al., 2019).

The morphology, particle size, and porosity of these CSs could be simply adjusted by varying the amount of F127 in the reaction system. The obtained porous CSs were found to have a high SSA up to 760.3 m<sup>2</sup>/g and mesopore sizes that could be adjusted within the range of 10–40 nm. In addition to block polymers, surfactants such as Triton X-100 have also been employed as the soft template to synthesize HCSs (Zhou et al., 2017). The HCSs obtained from this process had a SSA of approximately 893.3 m<sup>2</sup>/g and a total pore volume of 0.76 cm<sup>3</sup>/g.

Yolk-shell CSs with a unique core@void@shell structure have attracted tremendous interests as a consequence of their hierarchical pore architectures that are present in a controlled arrangement within each single particle (Zhang H. et al., 2018). Liu et al. prepared nitrogen-doped yolk-shell mesoporous CSs via a soft template approach, employing ethylenediamine (EDA) as both a nitrogen source and a base catalyst in a Stöber-silica/carbon assembly system (Liu C. et al., 2016). The resulting nitrogen-doped yolk-shell mesoporous CSs possessed a uniform mesopore size of 2.6 nm and a high SSA of 2001 m<sup>2</sup>/g. Shu et al. designed nitrogen-doped yolk-shell CSs with tunable mesoporous surfaces and particle sizes based on a soft template approach (Shu et al., 2018). The fabrication process used RF resin as the carbon precursor, melamine as the nitrogen precursor, cetyltrimethylammonium bromide (CTAB) as the pore-forming template, TEOS as the skeleton structure and ammonia as the catalyst. Because the rate of hydrolysis of TEOS was slower than the rate of polymerization of melanin resorcinol formaldehyde (MRF) in the initial stage of this process, a CTAB/MRF formed as the core and SiO<sub>2</sub>/CTAB/MRF formed as the shell. The subsequent carbonization of these particles at a high temperature produced a hollow core-shell structure and nitrogen-doped yolk-shell CSs were obtained after the SiO<sub>2</sub> template was removed using an NaOH solution.

### 2.3 Hard template-assisted liquid phase/aerosol process

The hard template approach, also known as the nanocasting approach, is commonly used materials with relatively rigid structures to guide the growth of materials based on providing limited space (Fuji et al., 2013; Li et al., 2016; Cao et al., 2020) such as SiO<sub>2</sub> (Wang H. et al., 2020), polystyrene latex (PSL) (Arif et al., 2016), poly(methyl methacrylate) (PMMA) (Ye et al., 2016) and calcium carbonate (CaCO<sub>3</sub>) (Ni et al., 2019). Several key processing steps are involved in the preparation of CSs using a hard template strategy, as shown in Fig. 2(c). These include (i) the fabrication of sphere-shaped hard template materials, (ii) the impregnation of these hard templates with a carbon precursor, (iii) the carbonization of the resulting carbon precursor/template composite in an inert atmosphere at a high temperature, and (iv) the removal of the hard template

via thermal decomposition or chemical etching methods, depending on the nature of the hard template. One of the key factors influencing the architecture and pore distribution is the dispersion of the hard template in the precursor solution. The resulting materials will possess rich pores with good connectivity if the template is well-dispersed in the precursor. Therefore, developing a method for enhancing the dispersion of hard template in the precursor solution is highly desirable (Ogi et al., 2017). Various CSs having different textural features have been prepared using different hard templates and the details of the materials and structural parameters are provided in Table 3.

SiO<sub>2</sub> spheres have been extensively applied as hard template to prepare CSs because they are inexpensive, have easily controllable sizes ranging from nanometer to micrometer and exhibit remarkable thermal stability together with a high degree of uniformity. Solid SiO<sub>2</sub> spheres are usually fabricated via the Stöber method, based on the hydrolysis of a SiO<sub>2</sub> precursor in a mixture of water and alcohol with ammonia as the catalyst (Stöber and Fink, 1968). HCSs can be obtained by coating of different carbon precursors on the surface of these SiO<sub>2</sub> particles followed by carbonization and etching process. Wang et al. synthesized N-doped HCSs using a simple interfacial sol-gel coating process, utilizing colloidal SiO<sub>2</sub> as the template, resorcinol/formaldehyde as the carbon precursor and EDA as both the nitrogen precursor and base catalyst (Wang et al., 2017). These HCSs possessed a uniform size of approximately 120 nm in diameter along with porous shells as thin as 10 nm. Density functional theory has demonstrated that N-doping could change the binding sites and enhance the adsorption of PF<sub>6</sub><sup>-</sup> ions in the carbon matrix. Zhang et al. developed a simple one-pot approach for synthesizing mesoporous HCSs with large controllable pore size based on a surfactant-free system (Zhang et al., 2016). Using a Stöber process, the reaction between resorcinol, formaldehyde and a TEOS/tetrapropyl orthosilicate (TPOS) mixture generated SiO<sub>2</sub>@SiO<sub>2</sub>/RF spheres without the addition of a cationic surfactant. In comparison with traditional TEOS-based system, the incorporation of TPOS, which undergoes hydrolysis and condensation rate more slowly than TEOS, provided better control over the formation of SiO<sub>2</sub> core and primary particles. The pore sizes in the mesoporous HCSs could be precisely tuned over the range from micropores to a size of 13.9 nm by adjusting the TEOS/TPOS or ethanol/water ratio.

PSL spheres with uniform sizes and good dispersion have been widely used as hard template, partly because these materials are readily removed by thermal annealing at 400 °C (Arif et al., 2016) or dissolution using organic solvents (Chen et al., 2016a). Balgis et al. synthesized nanostructured carbon particles via ultrasonic spray pyrolysis based on the self-assembly behavior of phenolic resin and PSL particles (Balgis et al., 2014; 2015). By adjusting

**Table 3** Summary of the conditions used for the hard template synthesis of functionalized CSs, the textural parameters of these materials and their potential applications.

No.	Material	Process	Template	Precursor	Structure	$d_{\text{pore}}$ (nm)	SSA ( $\text{m}^2/\text{g}$ )	$V_{\text{total}}$ ( $\text{cm}^3/\text{g}$ )	Applications	Reference
1	UHCSs <sup>a</sup>	Hard template	SiO <sub>2</sub> sphere	PTCDA <sup>b</sup>	Hollow structure with non-porous shells, ultrathin shell thickness	—	10	0.12	LSBs	(Song J. et al., 2018)
2	N,P-HPCSs <sup>c</sup>	Hard template	SiO <sub>2</sub> sphere	Dopamine	Hollow structure with abundant micropores	0.5–2	185–677	0.31–1.64	SIBs	(Wang H. et al., 2020)
3	N-HPCSs	Hard template + Activation	SiO <sub>2</sub> sphere	Dopamine	Hollow structure with abundant ultramicropores and reasonable supermicro- and mesopores	0.5, 0.8, 1.3, 2.7	860–1789	0.63–1.18	Supercapacitors	(Song Z. et al., 2018)
4	N-HMCSs <sup>d</sup>	Hard template	SiO <sub>2</sub> sphere	Dopamine	Hollow structure with abundant mesopores	9.1	457	1.04	LSBs	(Zhang et al., 2015)
5	N,P-PCSs <sup>e</sup>	Hard template	SiO <sub>2</sub> sphere	Melamine and formaldehyde	Hollow sphere with interconnected micro-, meso-, macroporous structure	2.6, 3.7	563–720	0.44–0.56	Supercapacitors	(Zhang et al., 2017)
6	N-HCSs	Hard template	SiO <sub>2</sub> sphere	<i>m</i> -Phenylenediamine and formaldehyde	Hollow structure (shell thickness ~25 nm). Micropores exist in the shell, while meso-/macropores correspond to the hollow cavity	< 2, 20–70	2044	1.60	Supercapacitors	(Xu et al., 2021)
7	N,P,S-PCSs <sup>f</sup>	Hard template	SiO <sub>2</sub> sphere	Aniline	Hierarchical porous structure with numerous pores within spheres	0.5–1, 2–4, 32	358–1258	0.68–1.96	Supercapacitors	(Yan et al., 2018)
8	HPCSs	Hard template	SiO <sub>2</sub> sphere	Furfuryl alcohol	Mesoporous structure with macro-hollow core	2–4	2489	1.45	Supercapacitors	(Zhou M. et al., 2018)
9	N-HMCSs	Hard template	SiO <sub>2</sub> sphere	PS/PAN <sup>g</sup>	Hollow structure Mesopores in the shells	4.1	807	0.87	Supercapacitors	(Chen et al., 2016b)
10	N-HCSs	Hard template	PS sphere	3-Aminophenol and formaldehyde	Hollow structure with micro-mesopores in the shells	—	365–772	—	Supercapacitors	(Anif et al., 2016)
11	Hierarchical PCSs	Hard template	PS sphere	Phenolic resin	Hollow structure: macropores covered by a thin carbon shell Porous structure: macropores exposed on the surface	2.8, 128	70–96	—	—	(Balgis et al., 2015)
12	N,O-HCSs	Hard template + Activation	PS sphere	Pyrrrole	Hierarchical hollow porous structure with abundant micro- and mesopores	0.5–15	558–1036	0.66–1.01	Supercapacitors	(Chen et al., 2017)
13	S,N-HCSs <sup>h</sup>	Hard template	PMMA sphere	Resorcinol and formaldehyde	Hollow spheres with microporous structure	—	486	—	SIBs	(Ye et al., 2016)
14	S,N-MHCSs	Hard template	CaCO <sub>3</sub> sphere	Dopamine	Interconnected hollow sphere structure with mesopores	5, 25	397	—	SIBs	(Ni et al., 2019)
15	N-HCSs	Hard template	Cu <sub>2</sub> O sphere	3-Aminophenol and formaldehyde	Micro-/mesoporous hollow structure with thin carbon shells (15–84 nm)	1.2–1.5	19–112	0.07–0.34	Supercapacitors	(Zhang D. et al., 2020)

<sup>a</sup> UHCSs: Ultrathin hollow CSs; <sup>b</sup> PTCDA: perylene-3,4,9,10-tetracarboxylic dianhydride; <sup>c</sup> N,P-HPCSs: Nitrogen, phosphorus co-doped hollow porous CSs; <sup>d</sup> N-HMCSs: Nitrogen-doped hollow mesoporous CSs; <sup>e</sup> N,P-PCSs: Nitrogen, phosphorus co-doped porous CSs; <sup>f</sup> N,P,S-PCSs: Nitrogen, phosphorus, sulfur co-doped porous CSs; <sup>g</sup> PS/PAN: Polystyrene/polyacrylonitrile; <sup>h</sup> S,N-HCSs: Sulfur, nitrogen co-doped hollow CSs.

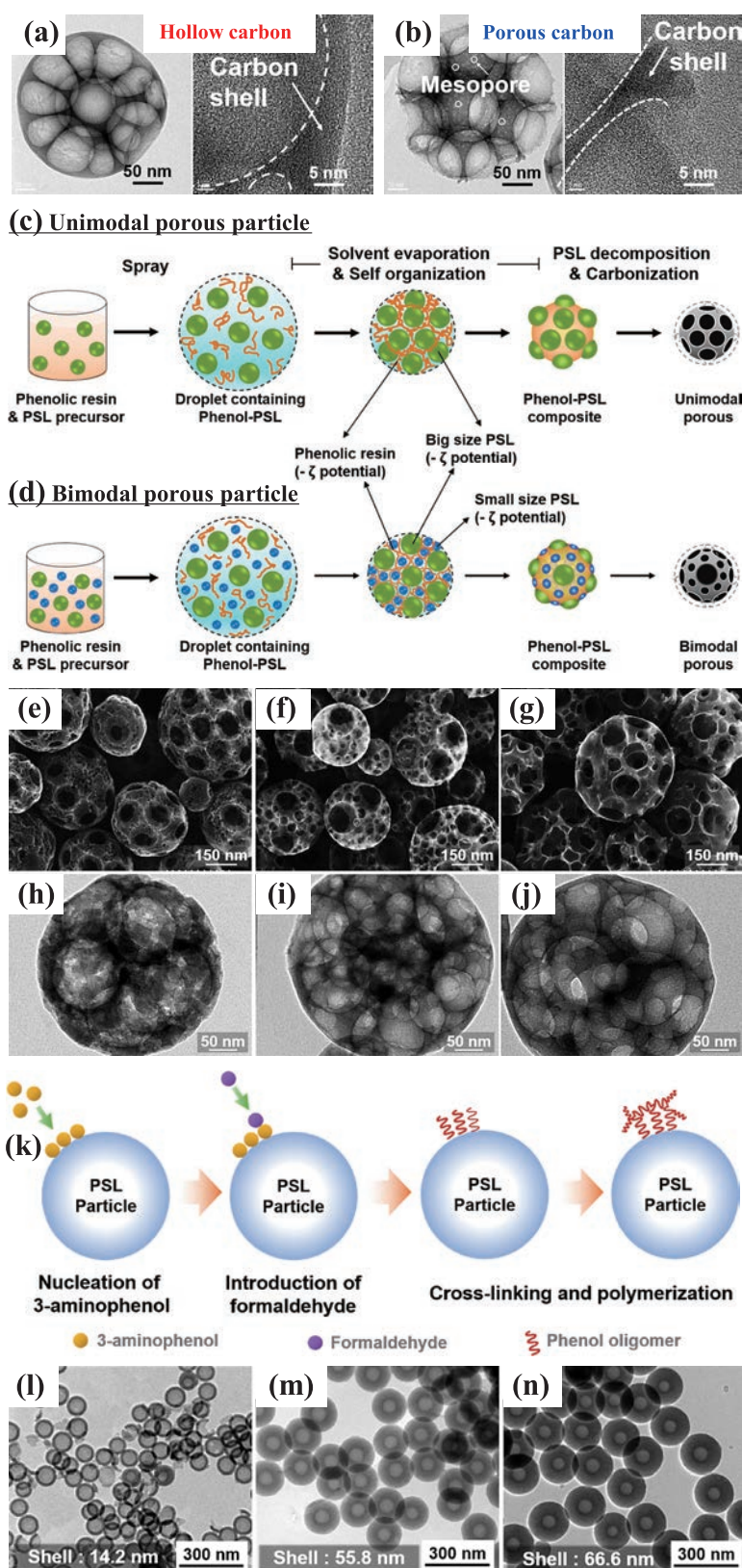


**Fig. 5** TEM images of carbon particle formation prepared via spray pyrolysis with (a) hollow CSs (using positively charged PSL), *the video is available publicly at <https://doi.org/10.50931/data.kona.21014023>* and (b) porous CSs (using negatively charged PSL), *the video is available publicly at <https://doi.org/10.50931/data.kona.21014023>*. Reprinted with permission from Ref. (Balgis et al., 2014). Copyright 2014, American Chemical Society. Illustrations showing the formation of (c) unimodal and (d) bimodal macroporous CSs, SEM and TEM images of bimodal porous CSs made using PSL particle sizes of (e, h) 230 and 40 nm; (f, i) 230 and 90 nm; and (g, j) 230 and 120 nm. Reprinted with permission from Ref. (Balgis et al., 2017). Copyright 2017, American Chemical Society. (k) An illustration of the shell growth on the surface of PSL particles, TEM images of HCSs prepared at 3-aminophenol/PSL mass ratio of (l) 1, (m) 10, and (n) 15 with 63 nm PSL particles in each case. Reprinted with permission from (Arif et al., 2016b). Copyright 2016, Elsevier.

the repulsive or attractive forces between the phenolic resin and PSL particles, the morphology of the prepared carbon particles can be precisely controlled. Strong electrostatic attraction between the highly positively charged PSL and phenolic resin resulted in hollow carbon particles (**Fig. 5(a)**), whereas the electrostatic repulsion occurred in the presence of negatively charged PSL formed porous carbon particles (**Fig. 5(b)**). The mechanism has been proposed in **Fig. 2(c)** and the detailed explanations are demonstrated in **Videos S1** and **S2** (available publicly at <https://doi.org/10.50931/data.kona.21014023>). Furthermore, the fabrication of hierarchical bimodal macroporous carbon nanospheres with interconnected pores (with applications as a catalyst support) using a spray pyrolysis technique with phenolic resin as the carbon source and PSL spheres as the template was also introduced, as shown in **Fig. 5(c–d)** (Balgis et al., 2017). The morphology of the resulting carbon particles was greatly influenced by changing the size of PSL particles, as shown in the SEM and TEM images (**Fig. 5(e–j)**). A bimodal macroporous structure can enhance the surface area available to accommodate Pt loading without sacrificing active site accessibility. As a means of improving the electron-transfer characteristics of carbon, Arif et al. fabricated HCSs having high-nitrogen content based on microwave-assisted polymerization together with carbonization process, using PSL as the template and 3-aminophenol as the carbon source (Arif et al., 2016). The plausible mechanism of shell formation and the chemical bond between PSL particles and 3-aminophenol during the nucleation process are demonstrated in **Fig. 5(k)**. By altering the 3-aminophenol/PSL mass ratio, the carbon shell thickness could be precisely adjusted from 14.2 to 66.6 nm, while the particle size could be easily controlled from 58.2 to 320 nm by changing the PSL particle size (**Fig. 5(l–n)**).

Another approach for producing porous CSs is by dissolution of the PSL using organic solvents. Chen et al. proposed a strategy for synthesizing mesoporous HCSs based on the “dissolution-capture” approach (Chen et al., 2016a). Polystyrene (PS) spheres serving as the template were prepared by emulsion polymerization and then coated with mesoporous SiO<sub>2</sub>. The PS cores were subsequently dissolved in tetrahydrofuran to form hollow cavities and was captured by the mesopores of the SiO<sub>2</sub> shells. The as-captured PS was then crosslinked based on Friedel-Crafts alkylation and was utilized as the carbon source. After carbonization and etching to remove SiO<sub>2</sub>, mesoporous HCSs with a uniform mesopore size (4.1 nm) were obtained.

### 3. Applications of carbon spheres

#### 3.1 Rechargeable batteries

With the rapid development of electric vehicles and portable electronics, there have been increasing demands for the development of lithium-ion batteries (LIBs) hav-

ing improved energy density, longer cycle life and faster charging rate. Graphite has traditionally been used as an anode material but provides a limited theoretical capacity (372 mAh/g) and a rate capability that cannot satisfy the requirements for enhanced performance, especially in the case of novel sodium-ion batteries (SIBs) or potassium-ion batteries (PIBs). Therefore, the development of new carbon-based materials for battery electrodes is critical. CSs are of particular interest among the variety of promising carbon materials because their small particle sizes and highly exposed surfaces ensure reduced charge transfer resistance during metalation/de-metalation. In addition, an isotropic spherical structure ensures a homogeneous distribution of current flow and allows a highly packed particle arrangement, resulting in higher volumetric energy densities. When employing CSs as an anode material for metal-ion batteries, large SSA, high pore volume, and good conductivity are crucial to obtaining the required metal-ion storage capacity and stability. Specifically, a high SSA provides for good contact with the electrolyte to sustain an elevated metal-ion flux through the interface, a large pore volume allows for metal ion and volume changes during metalation, while good conductivity ensures efficient electron transport.

The capacities and rate performances of anodes based on CSs have been significantly improved using two principal strategies. One such strategy involves doping single or dual heteroatoms (*e.g.*, O, N, B, S, P) into carbon materials to modulate the electronic and chemical structures. Such modifications can lead to enlarged interlayer distance, enhanced electronic conductivity, improved metal ion/electrolyte absorption and more active sites such that metal ion storage and cycling performance are enhanced (Long et al., 2017). In addition, the incorporation of such atoms modifies the pore structure. A hierarchical structure is desirable because micropores promote the reversible intercalation/de-intercalation of metal ions to afford high storage capacity, whereas meso-/macropores improve metal ion transfer kinetics and electrolyte mobility (Zhang J. et al., 2020). A representative example of these strategies was provided by Zhang et al., who synthesized nitrogen-doped CSs (N-CSs) through a HTC method followed by treatment with NH<sub>3</sub>, in addition to the use of glucose as the carbon precursor and CTAB as a surfactant (**Fig. 6(a)**) (Zhang H. et al., 2019). The resulting material showed excellent lithium/sodium ion storage capacity which delivered reversible capacities of 578 and 281 mAh/g for LIBs and SIBs, respectively, at 20 mA/g. As shown in **Fig. 6(b)**, when incorporated in LIBs, the N-CSs exhibited a capacity of 168.1 mAh/g at a high current density of 5 A/g, with a retention of 89.7 % even after 4,000 cycles. In contrast, the capacity of CSs (without nitrogen doping) was only 63.8 mAh/g, which was significantly lower than that of N-CSs. Similarly, in the case of trials with SIBs incorporating the N-CSs



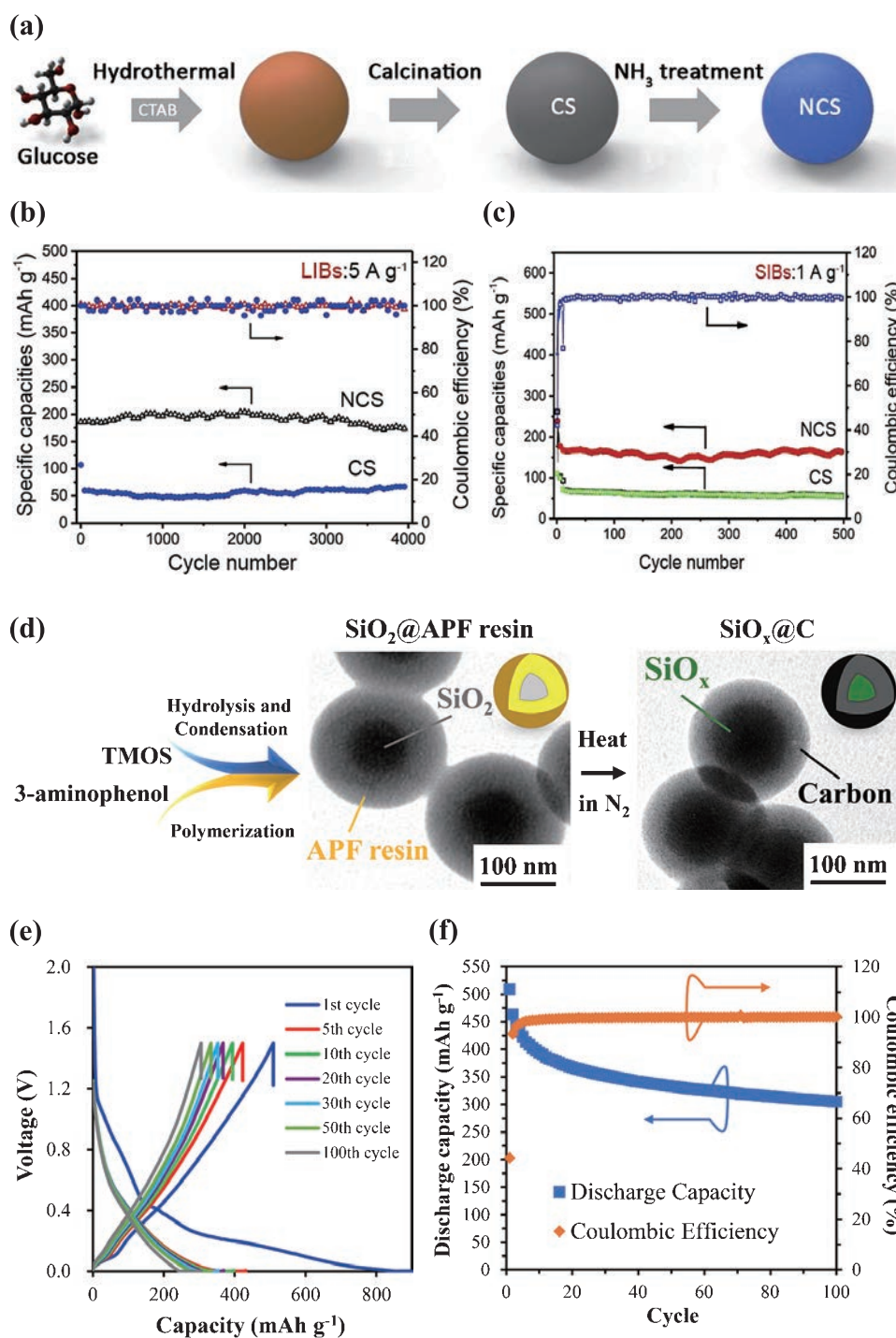


**Fig. 6** (a) An illustration showing the formation process of nitrogen-doped CSs (N-CSs), (b) cycling stability of N-CSs and CSs for LIBs at 5 A/g, and (c) cycling stability of N-CSs and CSs for SIBs at 1 A/g. Reprinted with permission from Ref. (H. Zhang et al., 2019). Copyright 2019, Elsevier. (d) An illustration showing the fabrication of  $\text{SiO}_x$ @C core-shell particles, (e) galvanostatic charge-discharge profile, and (f) cyclic performance of  $\text{SiO}_x$ @C particles as a LIB anode at different cycles. Reprinted with permission from Ref. (Cao et al., 2019). Copyright 2019, American Chemical Society.

(Fig. 6(c)), a high capacity of 163 mAh/g was retained after 500 cycles, whereas the CSs showed a lower specific capacity of 52 mAh/g at 1 A/g. These results indicate that nitrogen doping can improve the conductivity of CSs and provide additional active sites, both of which are crucial for enhancing electrochemical performance.

Interestingly, certain non-carbon materials provide large

theoretical capacities when used as battery anodes, including Si, Sn, Bi, P as well as various transition metal oxides (e.g., phosphides, sulfides, selenides) (Long et al., 2017). Even so, anodes made of these materials tend to undergo agglomeration and volume expansion/shrinkage during metalation/de-metalation and so exhibit poor cycling performance. CSs represent a means of addressing these

problems and high-capacity carbon-based anode materials (e.g.,  $\text{SiO}_x/\text{C}$ ,  $\text{Fe}_3\text{O}_4/\text{C}$ ) have been intensively investigated in attempts to achieve high energy densities. Cao et al. reported the synthesis of carbon-coated  $\text{SiO}_x$  ( $\text{SiO}_x@\text{C}$ ) core-shell particles through a sol-gel process (Cao et al., 2019). This work was based on the simultaneous hydrolysis-condensation of tetramethyl orthosilicate (TMOS) together with the polymerization of 3-aminophenol and formaldehyde in the presence of ammonia as a base catalyst and CTAB as a cationic surfactant, followed by the carbonization process (Fig. 6(d)). The resulting  $\text{SiO}_x@\text{C}$  particles were investigated as an anode material for LIBs and exhibited a reversible capacity of 509 mAh/g at 100 mA/g with approximately 80 % capacity retention after 100 cycles (Fig. 6(e–f)). This significantly improved electrochemical performance can be attributed to the structure of the material. The core-shell structure of these particles ensured optimal contact with the carbon matrix, while the round shape of carbon shell was highly resistant toward stress. These factors improved the conductivity of  $\text{SiO}_x$  and exerting the function of carbon.

On the cathode side, porous CSs have been successfully used as hosts for conductive sulfur in lithium-sulfur batteries (LSBs). The highly porous structure of these materials can accommodate a high proportion of sulfur while alleviating its isolating nature, thus facilitating the transport of electrons. Most studies show that sulfur is stored preferentially in the pores of carbon shells rather than in the interior of CSs, which is not conducive to inhibiting the shuttle effect and attaining high energy density. The process of sulfur material passing through the porous shell is difficult due to the capillary condensation effect and the absence of strong adsorption potential inside the carbon shell. As a result, the rational design of well-defined interior structure of CSs is an efficient method to suppress the “shuttle effect” of lithium polysulfides (LiPSs). Xu et al. proposed the fabrication of mesoporous nitrogen-doped yolk-shell CSs (N-YS-CSs) as novel sulfur encapsulators for LSBs through a Stöber method (Xu et al., 2018). The applied resorcinol-formaldehyde was acted as a carbon precursor and CTAB as a template to form the interior yolk and exterior shell under different hydrolysis polymerization rate. The N-YS-CSs@S cathode exhibited a high reversible capacity of 909 mAh/g at 0.2 C even after 500 cycles, which was higher than core-shell type architectures (323 mAh/g). The yolk-shell structure can effectively fulfill the synergistic effect of physisorption and chemisorption for LiPSs, and comprehensively absorb the LiPSs within the pores. In addition, the inner void between the yolk and shell provides sufficient cavity to accommodate the volume expansion during cycling, which contributes to the stability of the cycling performance. This strategy provides new ideas for the development of cathode structures for practical applications in LSBs. The structures, synthesis processes and

electrochemical performance characteristics of CSs and active material/CS composites used as electrode materials in rechargeable batteries are summarized in Table 4.

### 3.2 Supercapacitors

Typically, porous CSs have been employed as electrode materials in commercial electrical double-layer capacitor (EDLC) devices (Zhang M. et al., 2018). The spherical structure of these materials can decrease the distance that electrolyte ions are required to migrate so that an electric double-layer easily forms between the electrode and electrolyte. The capacitance of EDLCs is directly related to the contact area of the electrode with the electrolyte. In principle, increasing the pore volume, SSA and electrical conductivity of porous CS electrode will enhance charge accumulation in the electrical double layer formation and so improve capacitance (Pang et al., 2018b; Tang et al., 2018). It is generally considered that the presence of micropores in carbon materials significantly increases the SSA, which in turn plays an important role in enhancing specific capacitance. However, some investigations have discovered that ultrahigh SSAs may result in decreased volumetric capacitance as a consequence of relatively low packing densities (Kitamoto et al., 2022; Pang et al., 2018a). For this reason, it is critical to adjust pore sizes to maximize the ion-accessible SSA while decreasing dead volume. Both theoretical and experimental studies have confirmed that the highest capacitance is obtained in the case that the pore size (primarily micropores) is well matched to the ion size of the liquid electrolyte, because this scenario maximizes charge accommodation. However, the slow ion diffusion and desolvation in sub-nanometer micropores mean that high capacitance can only be realized at low or moderate charge-discharge rates, which limits the power density and rate capability. This issue can be resolved by incorporating macro-/mesopores into microporous carbon structures. In such cases, the mesopores can act as reservoirs to shorten ion transport pathways and so boost ion diffusion, allowing for high capacitance retention during rapid charging/discharging (Wang et al., 2018; Zhang et al., 2017). Thus, optimizing the proportions of micro-, meso-, and macropores in a porous CS electrode is critical to attaining high specific capacitance and rate performance.

The incorporation of heteroatoms (e.g., N, O, S, B, P) into porous CSs also plays a vital role to improve the electrochemical performance. Several studies have been conducted on the use of porous CSs doped with a variety of heteroatoms such as nitrogen (Xiong et al., 2017; Zhang L. et al., 2019), sulfur (Liu et al., 2017), or nitrogen co-doped with sulfur (Lv et al., 2020), oxygen (Chen et al., 2017; Liu S. et al., 2016), and phosphorus (Zhang et al., 2017) as electrodes in supercapacitors. Such modifications provide additional active sites for reversible redox reactions and so raise the overall capacitance of the sample. Yan et

**Table 4** Structures, synthesis processes, and electrochemical performance characteristics of CSs and active material/CS composites intended for use as electrode materials in rechargeable batteries.

No.	Material	Process	Template	Precursor	Battery	Reversible capability	Electrolyte	Reference
1	N-ACSS	HTC + Activation	—	Glucose	LSBs	1003.7 mAh/g at 0.1 C	1 M LiTFSI and 0.1 M LiNO <sub>3</sub> in DOL/DME	(Xiang et al., 2018)
2	N-CSS	Surfactant-assisted HTC	—	Glucose	LIBs	578 mAh/g at 20 mA/g	1 M LiPF <sub>6</sub> in DMC/EC/EMC	(Zhang H. et al., 2019)
3	PCSS	HTC + Activation	—	Starch	SIBs	281 mAh/g at 20 mA/g	1 M NaPF <sub>6</sub> in DMC/EC	(Zhang J. et al., 2020)
4	CSs	Extended the Stöber method	—	Resorcinol and formaldehyde	PIBs	210.3 mAh/g at 50 mA/g	1 M NaClO <sub>4</sub> in DEC/EC	(Wang S. et al., 2020)
	N-CSS			3-Aminophenol and formaldehyde		241 mAh/g at 25 mA/g	0.8 M KPF <sub>6</sub> in DEC/EC	
5	MCSs	Spray drying + Carbonization	—	Chitosan	LSBs	1163 mAh/g at 0.2 C	1 M LiTFSI in DOL/DME	(Zhou H. et al., 2018)
6	N-MCSS	Soft template	PS- <i>b</i> -PAA	Dopamine	SIBs	251 mAh/g at 100 mA/g	1 M NaClO <sub>4</sub> in PC + 5 % FEC	(Mao et al., 2020)
7	N-MCSS	Soft template	Pluronic F127	Melamine and formaldehyde	SIBs	373 mAh/g at 60 mA/g	1 M NaPF <sub>6</sub> in DEC/EC	(Guo et al., 2021)
8	YS-CSs	Soft template (Stöber method)	CTAB	Resorcinol and formaldehyde	PIBs	314 mAh/g at 50 mA/g	0.8 M KPF <sub>6</sub> in DEC/EC	(Zhang H. et al., 2018)
9	N,O-YS-CSs	Soft template + HTC	CTAB	Resorcinol and formaldehyde	PIBs	473.7 mAh/g at 20 mA/g	KPF <sub>6</sub> in DEC/EC/PC	(Chong et al., 2021)
10	UHCSS	Hard template	SiO <sub>2</sub> sphere	PTCDA	LSBs	1305 mAh/g at 0.2 C	1 M LiTFSI and 0.1 M LiNO <sub>3</sub> in DOL/DME	(Song J. et al., 2018)
11	N,P-HPCSS	Hard template	SiO <sub>2</sub> sphere	Dopamine	SIBs	302 mAh/g at 100 mA/g	1 M NaClO <sub>4</sub> in DEC/EC + 5 % FEC	(Wang H. et al., 2020)
12	N-HMCSS	Hard template	SiO <sub>2</sub> sphere	Dopamine	LSBs	1656 mAh/g at 0.2 C	1 M LiTFSI and 0.1 M LiNO <sub>3</sub> in DOL/DME	(Zhang et al., 2015)
13	S,N-HCSS	Hard template	PMMA sphere	Resorcinol and formaldehyde	SIBs	185 mAh/g at 500 mA/g	1 M NaClO <sub>4</sub> in DEC/EC + 2 % FEC	(Ye et al., 2016)
14	S,N-MHCSS	Hard template	CaCO <sub>3</sub> sphere	Dopamine	SIBs	240 mAh/g at 500 mA/g	1 M NaClO <sub>4</sub> in DEC/EC + 2 % FEC	(Ni et al., 2019)
15	SiO <sub>x</sub> @C core-shell	Soft template	CTAB	3-Aminophenol and formaldehyde	LIBs	509.2 mAh/g at 100 mA/g	1 M LiPF <sub>6</sub> in DMC/EC/EMC	(Cao et al., 2019)
16	Fe <sub>3</sub> O <sub>4</sub> @N-PCSS	Soft template	PS- <i>b</i> -PAA	Dopamine	LIBs	1240 mAh/g at 100 mA/g	1 M LiPF <sub>6</sub> in DEC/EC	(Mao et al., 2019)
17	Se@N-MCSS	Soft template	Pluronic F127	Dopamine	SIBs	378 mAh/g at 100 mA/g	1 M NaClO <sub>4</sub> in DEC/EC + 5 % FEC	(Sun et al., 2021)
18	Sn <sub>4</sub> P <sub>3</sub> -C core-shell	HTC + Phosphorization	—	Glucose and potassium stannate	LIBs	700 mAh/g at 500 mA/g	1 M LiPF <sub>6</sub> in DEC/EC + 2 % VC	(Choi et al., 2018)
19	Bi@C nanospheres	HTC	—	Glucose and bismuth nitrate	SIBs	680 mAh/g at 500 mA/g	1 M NaClO <sub>4</sub> in DMC/EC + 5 % FEC	(Zhu et al., 2020)
20	SnS QDs@N-CSS	HTC	—	Dopamine and tin(II) chloride	SIBs	400.3 mAh/g at 200 mA/g	1 M NaPF <sub>6</sub> in DME	(Veerabramani et al., 2020)
					SIBs	280 mAh/g at 100 mA/g	1 M NaClO <sub>4</sub> in EC/PC + 10 % FEC	

**Table 5** Structures, synthesis processes, and electrochemical performance characteristics of porous CSs as electrode materials in supercapacitors.

No.	Material	Process	Template	Precursor	Specific capacitance	Electrolyte	Reference
1	ACSS	HTC + Activation	—	Xylose	238.1 F/g at 1 A/g	1 M Na <sub>2</sub> SO <sub>4</sub>	(Sun et al., 2020)
2	PCSS	HTC + Activation	—	Starch	369.8 F/g at 1 A/g 331.4 F/g at 0.5 A/g	1 M H <sub>2</sub> SO <sub>4</sub> 6 M KOH	(Zhang J. et al., 2020)
3	PCSS	HTC + Activation	—	GAML	303.7 F/g at 0.04 A/g	6 M KOH	(Hao et al., 2018)
4	N-HCSS	Extended the Stöber method	—	Resorcinol and formaldehyde	196 F/g at 1 A/g 242 F/g at 1 A/g 160 F/g at 1 A/g	6 M KOH	(Zhang L. et al., 2019)
5	N-SCSS	—	—	—	—	—	—
5	Pomegranate-like CSs	Spray drying + Activation	—	3-Aminophenol and formaldehyde	338 F/g at 1 A/g	6 M KOH	(Feng et al., 2019)
6	HCSS	Spray drying + Carbonization	—	Kraft lignin	31.8 F/g at 0.2 A/g	6 M KOH	(Cao et al., 2021a)
7	PCSS	Spray drying + Carbonization	—	Kraft lignin	66.5 F/g at 10 mV/s	6 M KOH	(Kitamoto et al., 2022)
8	HPCSS	Spray drying + Carbonization	—	Sodium lignosulfonate	284 F/g at 0.1 A/g	7 M KOH	(Pang et al., 2018b)
9	N,S-PCSS	Spray pyrolysis	—	Coal	308 F/g at 1 A/g	6 M KOH	(Lv et al., 2020)
10	PCSS	Spray pyrolysis + Activation	—	Glucose	240 F/g at 0.5 A/g 80 F/g at 0.5 A/g	6 M KOH 1 M TEABF <sub>4</sub> /AN	(Tang et al., 2018)
11	N-HCSS	Spray pyrolysis + Carbonization	—	Glucose and glucosamine	266 F/g at 0.2 A/g	1 M H <sub>2</sub> SO <sub>4</sub>	(Qu et al., 2018)
12	N-MCSS	Soft template + Activation	PS- <i>b</i> -PEO	Dopamine	170 F/g at 1 A/g	EMIMBF <sub>4</sub>	(Tang et al., 2017)
13	N-PCSS	Soft template + Activation	Pluronic F127	Dopamine	111 F/g at 1 A/g	1 M TEABF <sub>4</sub> /AN	—
13	N-PCSS	Soft template + Activation	Pluronic F127	Dopamine	433 F/g at 0.5 A/g	6 M KOH	(Xiong et al., 2017)
14	PCSS	Soft template + Spray pyrolysis	Pluronic F127	Larch sawdust (biomass)	338.8 F/g at 0.2 A/g	6 M KOH	(Song et al., 2019)
15	N,O-CSs	Soft template + HTC	Pluronic F127	3-Aminophenol and formaldehyde	309 F/g at 0.1 A/g	6 M KOH	(Liu S. et al., 2016)
16	N-PCSS	Soft template + HTC	Pluronic F108	Phenol and formaldehyde	365 F/g at 0.5 A/g	6 M KOH	(Liang et al., 2019)
17	N-HMCSs	Soft template (Extended the Stöber method)	CTAC	Resorcinol and formaldehyde	300 F/g at 1 A/g 178 F/g at 1 A/g	1 M H <sub>2</sub> SO <sub>4</sub>	(Liu C. et al., 2016)
18	HCSs	Soft template	CTAB	Phenol and formaldehyde	265 F/g at 0.5 A/g	6 M KOH	(Du et al., 2020)
19	APCSs	Soft template	DDAB	3-Aminophenol and formaldehyde	256 F/g at 0.2 A/g	6 M KOH	(Li et al., 2021)
20	N-PCSS	Soft template + HTC	[C <sub>12</sub> mim]Br	3-Aminophenol and amphiphilic aliphatic aldehydes	181 F/g at 1 A/g	6 M KOH	(Jia et al., 2022)
21	N-MCHSS	Soft template + HTC	Gemini	3-Aminophenol and formaldehyde	240 F/g at 0.2 A/g	6 M KOH	(Li et al., 2020)
22	N-HPCSS	Hard template + Activation	SiO <sub>2</sub> sphere	Dopamine	353 F/g at 0.5 A/g	6 M KOH	(Song Z. et al., 2018)
23	N,P-PCSS	Hard template	SiO <sub>2</sub> sphere	Melamine and formaldehyde	208 F/g at 0.5 A/g	6 M KOH	(Zhang et al., 2017)
24	N-HCSS	Hard template	SiO <sub>2</sub> sphere	<i>m</i> -Phenylenediamine and formaldehyde	234 F/g at 0.5 A/g 221 F/g at 0.5 A/g	EMIBF <sub>4</sub> TEABF <sub>4</sub> /AN	(Xu et al., 2021)
25	N,P,S-PCSSs	Hard template	SiO <sub>2</sub> sphere	Aniline	274 F/g at 0.5 A/g	6 M KOH	(Yan et al., 2018)
26	N,O-HCSSs	Hard template + Activation	PS sphere	Pyrolyte	535 F/g at 0.2 A/g 473 F/g at 0.2 A/g	6 M KOH 1 M H <sub>2</sub> SO <sub>4</sub>	(Chen et al., 2017)
27	N-PCSS	Hard template	CaCO <sub>3</sub> sphere	Dopamine	270 F/g at 0.5 A/g	6 M KOH	(Guo et al., 2018)
28	N-HCSS	Hard template	Cu <sub>2</sub> O sphere	3-Aminophenol and formaldehyde	263.6 F/g at 0.5 A/g	6 M KOH	(Zhang D. et al., 2020)

al. fabricated N,P,S-codoped hierarchically porous CSs (N,P,S-PCSs) by utilizing silica colloid as a hard template, polyaniline as both a carbon and nitrogen precursor, phytic acid as a phosphorus precursor, and ammonium persulfate as a sulfur precursor (Yan et al., 2018). The well-dispersed pores provide a facile ion transportation path within the electrode. The resulting N,P,S-PCSs exhibited both high gravimetric and volumetric specific capacitance values of 274 F/g and 219 F/cm<sup>3</sup> at 0.5 A/g, which revealed a superior electrochemical performance. After 10,000 cycles, the N,P,S-PCSs samples showed the long-term cycling stability with 95 % initial capacitance retention at 10 A/g. This is mainly attributed to the uniform doping of N, P, and S as well as the hierarchically porous structure of the N,P,S-PCSs. **Table 5** summarizes the supercapacitor performance and the main characteristics of porous CSs prepared by various synthetic processes.

#### 4. Conclusions and outlook

Experimentation with spherical particles having attractive structures and multiple functions has proceeded for many years and these materials are expected to play a significant role in future energy sources. This review provides an overview of the latest advances and recent progress in the synthesis of CSs, with a particular focus on the applications of these materials in electrochemical energy storage. There have been significant advances in the fabrication of CSs with well-designed, controllable morphologies, desirable textural properties and adjustable functionalities. The primary techniques for fabricating CSs comprise template-free, soft template and hard template approaches, all of which are discussed in detail herein to provide a clear understanding of the capability of each synthesis route in terms of controlling structural features. It is vital to obtain specific chemical compositions and morphologies when fabricating CSs with targeted functionalities related to potential applications in rechargeable batteries and supercapacitors. This review demonstrates that CSs have been extensively employed because the porosity and other structural parameters of these materials are readily tuned. As such, CSs are of particular interest with regard to addressing critical issues related to rate capability and cycling stability, as well as facilitating their application in emerging energy storage devices. Despite the obvious advantages and significant achievements summarized above, CSs still face numerous challenges that need to be addressed before practical applications in energy storage devices are feasible. A number of suggested future research directions related to the advancement of this field of study are detailed below.

(1) The electrochemical performance of CSs requires further improvement to allow practical usage. As an example, the spherical carbon-based materials having core-shell structures with porous shells are especially appealing as

anode materials because they are able to host a number of active species that provide the electrical conductivity required for stable cycling and efficient use. It is important to prepare CS materials with pore structures that are tunable within the micropore and mesopore size ranges and to construct hierarchical structures by connecting micropores to mesopores and macropores. These features would improve the transport of ions and provide abundant active sites to increase the ion accessible SSA, leading to enhance the performance of energy storage devices. It will also be important to consider the packing density of CSs because this is a critical parameter that is rarely investigated. It is worth noting that the packing density of CSs is generally low (< 0.5 g/cm<sup>3</sup>). CSs typically possess hollow and porous structures, which result in improving the mass-ratio of the powder and energy density but decrease the volumetric energy density of the device. Consequently, some important applications of CSs are limited.

(2) The large-scale industrial applications of CSs are still restricted by the cost and the scale of production, which is vastly different from the estimated and makes them delayed in their adoption. For instance, to enhance the SSA and porosity, highly corrosive chemical activation treatment (e.g., KOH, H<sub>3</sub>PO<sub>4</sub>) followed by the removal of impurities is required. These processes typically consume extra energy and produce significant waste streams. Therefore, green chemical engineering processes are essential to the sustainable fabrication of porous CSs for energy storage devices. Future research may focus on the fabrication of CSs using less toxic and greener chemical activating agents at a reasonable cost.

Furthermore, it is important to note that the selection of carbon precursor has a pronounced effect on the performance of CSs. Biomass-based porous CSs are a promising material for emerging applications. However, biomass usually contains pollutants and other impurities. Important questions remain unanswered concerning the impacts of using these materials to construct CSs. How will these impurities migrate and transform during the preparation and application of CSs? What is the effect of these contaminants on the properties and performance of CSs? Answers to these questions must be determined to advance the use of biomass as a precursor for CS materials.

(3) The development of reliable synthetic pathways is still an emerging requirement and may be required to allow the scalable production of CSs with control over their structural properties. The innovation and simplicity of the new green synthesis protocol will be a prerequisite to produce CSs in conjunction with reduced costs, minimal environmental impact, and improved quality to facilitate their usage in large-scale energy storage devices. The use of green activation strategies typically provides enhanced yields. However, these approaches have been underdeveloped and more detailed studies are needed for their

optimization and advancement.

(4) Heteroatom doping is generally used to modify the surface chemistry of carbon materials but overdoping can vitiate the porous structure and an excess of some atoms can impair the electrical conductivity of the carbon. The future development of porous CSs will require an in-depth understanding of the structure-function relationship to allow the formation of desired structure and surface chemistry that meet the demands associated with various applications.

(5) The rapid evolution of CSs has been associated with advances in energy storage technologies. However, there remains an incomplete understanding of the relationships between structure and the electrochemical properties of CSs. More advanced characterizations in conjunction with numerical simulations may provide better insight into the connection between structures and electrochemical properties or reaction mechanisms.

In the future, there is likely to be increasing interest in CS materials for specific scientific and industrial applications and these materials will be used more frequently to support the development of energy storage devices. A better understanding of structure-performance relationships is also anticipated. Moreover, greener and simpler synthesis methods with reduced environmental impacts will be developed to enable the full use of renewable resources. There is no doubt that many opportunities are hidden, and the researchers should investigate more on utilizing the tremendous potential of functionalized CSs in the applications discussed herein. The progress achieved to date is expected to inspire future research and the authors hope that this review paper will accelerate further work toward a future sustainable society.

## Acknowledgements

This work was supported by a JSPS KAKENHI Grant Number 19H02500, International Network on Polyoxometalate Science at Hiroshima University, the JSPS Core-to-Core Program, the Hosokawa Powder Technology Foundation, and the Information Center of Particle Technology, Japan. We thank Michael D. Judge, MSc, from Edanz Group for editing a draft of this manuscript.

## Data Availability Statement

The video data of hollow carbon particle formation prepared via ultrasonic spray pyrolysis using phenolic resin (–) and PSL (+) is available publicly in J-STAGE Data (<https://doi.org/10.50931/data.kona.21014023>).

The video data of porous carbon particle formation prepared via ultrasonic spray pyrolysis using phenolic resin (–) and PSL (–) is available publicly in J-STAGE Data (<https://doi.org/10.50931/data.kona.21014023>).

## References

- Arif A.F., Kobayashi Y., Balgis R., Ogi T., Iwasaki H., Okuyama K., Rapid microwave-assisted synthesis of nitrogen-functionalized hollow carbon spheres with high monodispersity, *Carbon*, 107 (2016) 11–19. DOI: 10.1016/j.carbon.2016.05.048
- Balgis R., Ogi T., Arif A.F., Anilkumar G.M., Mori T., Okuyama K., Morphology control of hierarchical porous carbon particles from phenolic resin and polystyrene latex template via aerosol process, *Carbon*, 84 (2015) 281–289. DOI: 10.1016/j.carbon.2014.12.010
- Balgis R., Ogi T., Wang W.-N., Anilkumar G.M., Sago S., Okuyama K., Aerosol synthesis of self-organized nanostructured hollow and porous carbon particles using a dual polymer system, *Langmuir*, 30 (2014) 11257–11262. DOI: 10.1021/la502545d
- Balgis R., Widiyastuti W., Ogi T., Okuyama K., Enhanced electrocatalytic activity of Pt/3D hierarchical bimodal macroporous carbon nanospheres, *ACS Applied Materials and Interfaces*, 9 (2017) 23792–23799. DOI: 10.1021/acsami.7b05873
- Benzigar M.R., Talapaneni S.N., Joseph S., Ramadass K., Singh G., Scaranto J., Ravon U., Al-Bahily K., Vinu A., Recent advances in functionalized micro and mesoporous carbon materials: synthesis and applications, *Chemical Society Reviews*, 47 (2018) 2680–2721. DOI: 10.1039/C7CS00787F
- Cao K.L.A., Arif A.F., Kamikubo K., Izawa T., Iwasaki H., Ogi T., Controllable synthesis of carbon-coated SiO<sub>x</sub> particles through a simultaneous reaction between the hydrolysis-condensation of tetramethyl orthosilicate and the polymerization of 3-aminophenol, *Langmuir*, 35 (2019) 13681–13692. DOI: 10.1021/acs.langmuir.9b02599
- Cao K.L.A., Kitamoto Y., Iskandar F., Ogi T., Sustainable porous hollow carbon spheres with high specific surface area derived from Kraft lignin, *Advanced Powder Technology*, 32 (2021a) 2064–2073. DOI: 10.1016/j.apt.2021.04.012
- Cao K.L.A., Rahmatika A.M., Kitamoto Y., Nguyen M.T.T., Ogi T., Controllable synthesis of spherical carbon particles transition from dense to hollow structure derived from Kraft lignin, *Journal of Colloid and Interface Science*, 589 (2021b) 252–263. DOI: 10.1016/j.jcis.2020.12.077
- Cao K.L.A., Taniguchi S., Nguyen T.T., Arif A.F., Iskandar F., Ogi T., Precisely tailored synthesis of hexagonal hollow silica plate particles and their polymer nanocomposite films with low refractive index, *Journal of Colloid and Interface Science*, 571 (2020) 378–386. DOI: 10.1016/j.jcis.2020.03.064
- Chen A., Li Y., Yu Y., Li Y., Xia K., Wang Y., Li S., Zhang L., Synthesis of hollow mesoporous carbon spheres via “dissolution-capture” method for effective phenol adsorption, *Carbon*, 103 (2016) 157–162. DOI: 10.1016/j.carbon.2016.02.091
- Chen A., Xia K., Yu Y., Sun H., Liu L., Ren S., Li Y., “Dissolution-capture” strategy to form monodispersed nitrogen-doped hollow mesoporous carbon spheres, *Journal of The Electrochemical Society*, 163 (2016b) A3063–A3068. DOI: 10.1149/2.1021614jes
- Chen Z., Cao R., Ge Y., Tu Y., Xia Y., Yang X., N- and O-doped hollow carbonaceous spheres with hierarchical porous structure for potential application in high-performance capacitance, *Journal of Power Sources*, 363 (2017) 356–364. DOI: 10.1016/j.jpowsour.2017.07.037
- Choi J., Kim W.-S., Kim K.-H., Hong S.-H., Sn<sub>4</sub>P<sub>3</sub>-C nanospheres as high capacitive and ultra-stable anodes for sodium ion and lithium ion batteries, *Journal of Materials Chemistry A*, 6 (2018) 17437–17443. DOI: 10.1039/C8TA05586F
- Chong S., Yuan L., Li T., Shu C., Qiao S., Dong S., Liu Z.,

- Yang J., Liu H.K., Dou S.X., Huang W., Nitrogen and oxygen co-doped porous hard carbon nanospheres with core-shell architecture as anode materials for superior potassium-ion storage, *Small*, (2021) 2104296. DOI: 10.1002/sml.202104296
- Debecker D.P., Le Bras S., Boissière C., Chaumonot A., Sanchez C., Aerosol processing: a wind of innovation in the field of advanced heterogeneous catalysts, *Chemical Society Reviews*, 47 (2018) 4112–4155. DOI: 10.1039/C7CS00697G
- Du J., Zong S., Zhang Y., Hou S., Chen A., Co-assembly strategy for uniform and tunable hollow carbon spheres with supercapacitor application, *Journal of Colloid and Interface Science*, 565 (2020) 245–253. DOI: 10.1016/j.jcis.2020.01.021
- Fei H.F., Long Y., Yu H.J., Yavitt B.M., Fan W., Ribbe A., Watkins J.J., Bimodal mesoporous carbon spheres with small and ultra-large pores fabricated using amphiphilic brush block copolymer micelle templates, *ACS Applied Materials and Interfaces*, 12 (2020) 57322–57329. DOI: 10.1021/acsami.0c16566
- Feng S., Liu Z., Yu Q., Zhuang Z., Chen Q., Fu S., Zhou L., Mai L., Monodisperse carbon sphere-constructed pomegranate-like structures for high-volumetric-capacitance supercapacitors, *ACS Applied Materials and Interfaces*, 11 (2019) 4011–4016. DOI: 10.1021/acsami.8b19901
- Fuji M., Han Y.S., Takai C., Synthesis and applications of hollow particles, *KONA Powder and Particle Journal*, 30 (2013) 47–68. DOI: 10.14356/kona.2013009
- Gradon L., Balgis R., Hirano T., Rahmatika A.M., Ogi T., Okuyama K., Advanced aerosol technologies towards structure and morphologically controlled next-generation catalytic materials, *Journal of Aerosol Science*, 149 (2020) 105608. DOI: 10.1016/j.jaerosci.2020.105608
- Guo D., Fu Y., Bu F., Liang H., Duan L., Zhao Z., Wang C., El-Toni A.M., Li W., Zhao D., Monodisperse ultrahigh nitrogen-containing mesoporous carbon nanospheres from melamine-formaldehyde resin, *Small Methods*, 5 (2021) 2001137. DOI: 10.1002/smt.202001137
- Guo H., Ding B., Wang J., Zhang Y., Hao X., Wu L., An Y., Dou H., Zhang X., Template-induced self-activation route for nitrogen-doped hierarchically porous carbon spheres for electric double layer capacitors, *Carbon*, 136 (2018) 204–210. DOI: 10.1016/j.carbon.2018.04.079
- Guo M., Guo J., Tong F., Jia D., Jia W., Wu J., Wang L., Sun Z., Hierarchical porous carbon spheres constructed from coal as electrode materials for high performance supercapacitors, *RSC Advances*, 7 (2017) 45363–45368. DOI: 10.1039/c7ra08026c
- Hao Z.Q., Cao J.P., Zhao X.Y., Wu Y., Zhu J.S., Dang Y.L., Zhuang Q.Q., Wei X.Y., Preparation of porous carbon spheres from 2-keto-L-gulonic acid mother liquor by oxidation and activation for electric double-layer capacitor application, *Journal of Colloid and Interface Science*, 513 (2018) 20–27. DOI: 10.1016/j.jcis.2017.11.006
- He X., Wang W.-N., Rational design of efficient semiconductor-based photocatalysts via microdroplets: A review, *KONA Powder and Particle Journal*, 36 (2019) 201–214. DOI: 10.14356/kona.2019014
- Jia S., Guo Q., Shen M., Gao Q., Wang K., Controlled synthesis of carbon spheres via the modulation of the hydrophobic length of fatty aldehyde for supercapacitors, *Colloids and Surfaces A: Physicochemical and Engineering Aspects*, 636 (2022) 128064. DOI: 10.1016/j.colsurfa.2021.128064
- Kerdnawee K., Termvidhakorn C., Yaisanga P., Pakchamsai J., Chookiat C., Eiad-ua A., Wongwiriyan W., Chaiwat W., Ratchahat S., Faungnawakij K., Suttiponparnit K., Charinpanitkul T., Present advancement in production of carbon nanotubes and their derivatives from industrial waste with promising applications, *KONA Powder and Particle Journal*, 34 (2017) 24–43. DOI: 10.14356/kona.2017001
- Kitamoto Y., Cao K.L.A., Le P.H., Abdillah O.B., Iskandar F., Ogi T., A sustainable approach for preparing porous carbon spheres derived from Kraft lignin and sodium hydroxide as highly packed thin film electrode materials, *Langmuir*, 38 (2022) 3540–3552. DOI: 10.1021/acs.langmuir.1c03489
- Le P.H., Kitamoto Y., Cao K.L.A., Hirano T., Tanabe E., Ogi T., Synthesis of macroporous three-way catalysts via template-assisted spray process for enhancing mass transfer in gas adsorption, *Advanced Powder Technology*, 33 (2022) 103581. DOI: 10.1016/j.apt.2022.103581
- Leng J., Wang Z., Wang J., Wu H.-H., Yan G., Li X., Guo H., Liu Y., Zhang Q., Guo Z., Advances in nanostructures fabricated via spray pyrolysis and their applications in energy storage and conversion, *Chemical Society Reviews*, 48 (2019) 3015–3072. DOI: 10.1039/C8CS00904J
- Li B., Guo Q., Shen M., Li W., Gao Q., Controllable synthesis induced through cationic surfactant with two long hydrophobic chains from individual carbon spheres to 3D carbon frameworks for high performance supercapacitors, *Microporous and Mesoporous Materials*, 326 (2021) 111379. DOI: 10.1016/j.micromeso.2021.111379
- Li S., Pasc A., Fierro V., Celzard A., Hollow carbon spheres, synthesis and applications – a review, *Journal of Materials Chemistry A*, 4 (2016) 12686–12713. DOI: 10.1039/C6TA03802F
- Li W., Li B., Shen M., Gao Q., Hou J., Use of Gemini surfactant as emulsion interface microreactor for the synthesis of nitrogen-doped hollow carbon spheres for high-performance supercapacitors, *Chemical Engineering Journal*, 384 (2020) 123309. DOI: 10.1016/j.cej.2019.123309
- Liang Z., Zhang L., Liu H., Zeng J., Zhou J., Li H., Xia H., Soft-template assisted hydrothermal synthesis of size-tunable, N-doped porous carbon spheres for supercapacitor electrodes, *Results in Physics*, 12 (2019) 1984–1990. DOI: 10.1016/j.rinp.2019.01.074
- Liu C., Wang J., Li J., Hu X., Lin P., Shen J., Sun X., Han W., Wang L., Controllable synthesis of N-doped hollow-structured mesoporous carbon spheres by an amine-induced Stöber-silica/carbon assembly process, *Journal of Materials Chemistry A*, 4 (2016) 11916–11923. DOI: 10.1039/c6ta03748h
- Liu J., Wickramaratne N.P., Qiao S.Z., Jaroniec M., Molecular-based design and emerging applications of nanoporous carbon spheres, *Nature Materials*, 14 (2015) 763–774. DOI: 10.1038/nmat4317
- Liu S., Cai Y., Zhao X., Liang Y., Zheng M., Hu H., Dong H., Jiang S., Liu Y., Xiao Y., Sulfur-doped nanoporous carbon spheres with ultrahigh specific surface area and high electrochemical activity for supercapacitor, *Journal of Power Sources*, 360 (2017) 373–382. DOI: 10.1016/j.jpowsour.2017.06.029
- Liu S., Chen X., Li X., Huo P., Wang Y., Bai L., Zhang W., Niu M., Li Z., Nitrogen- and oxygen-containing micro-mesoporous carbon microspheres derived from m-aminophenol formaldehyde resin for supercapacitors with high rate performance, *RSC Advances*, 6 (2016) 89744–89756. DOI: 10.1039/C6RA16608C
- Long W., Fang B., Ignaszak A., Wu Z., Wang Y.J., Wilkinson D., Biomass-derived nanostructured carbons and their composites as anode materials for lithium ion batteries, *Chemical Society Reviews*, 46 (2017) 7176–7190. DOI: 10.1039/c6cs00639f

- Lu X., Jiang C., Hu Y., Zhong H., Zhao Y., Xu X., Liu H., Preparation of hierarchically porous carbon spheres by hydrothermal carbonization process for high-performance electrochemical capacitors, *Journal of Applied Electrochemistry*, 48 (2018) 233–241. DOI: 10.1007/s10800-018-1146-x
- Lv Y., Chen J., Jia W., Wu X., Guo J., Ding L., Jia D., Tong F., N/S co-doped coal-based porous carbon spheres as electrode materials for high performance supercapacitors, *RSC Advances*, 10 (2020) 11033–11038. DOI: 10.1039/d0ra00458h
- Mao J., Niu D., Jiang N., Jiang G., Chen M., Li Y., Shi J., Rational design of high nitrogen-doped and core-shell/mesoporous carbon nanospheres with high rate capability and cycling longevity for pseudocapacitive sodium storage, *Journal of Materials Chemistry A*, 8 (2020) 9768–9775. DOI: 10.1039/D0TA03229H
- Mao J., Niu D., Zheng N., Jiang G., Zhao W., Shi J., Li Y., Fe<sub>3</sub>O<sub>4</sub>-Embedded and N-doped hierarchically porous carbon nanospheres as high-performance lithium ion battery anodes, *ACS Sustainable Chemistry & Engineering*, 7 (2019) 3424–3433. DOI: 10.1021/acssuschemeng.8b05651
- Nguyen T.T., Miyauchi M., Rahmatika A.M., Cao K.L.A., Tanabe E., Ogi T., Enhanced protein adsorption capacity of macroporous pectin particles with high specific surface area and an interconnected pore network, *ACS Applied Materials & Interfaces*, 14 (2022) 14435–14446. DOI: 10.1021/acsmi.1c22307
- Nguyen T.T., Rahmatika A.M., Miyauchi M., Cao K.L.A., Ogi T., Synthesis of high specific surface area macroporous pectin particles by template-assisted spray drying, *Langmuir*, 37 (2021) 4256–4266. DOI: 10.1021/acs.langmuir.1c00232
- Ni D., Sun W., Wang Z., Bai Y., Lei H., Lai X., Sun K., Heteroatom-doped mesoporous hollow carbon spheres for fast sodium storage with an ultralong cycle life, *Advanced Energy Materials*, 9 (2019) 1900036. DOI: 10.1002/aenm.201900036
- Ogi T., Fukazawa H., Rahmatika A.M., Hirano T., Cao K.L.A., Iskandar F., Improving the crystallinity and purity of monodisperse Ag fine particles by heating colloidal sprays in-flight, *Industrial and Engineering Chemistry Research*, 59 (2020) 5745–5751. DOI: 10.1021/acs.iecr.9b05482
- Ogi T., Nandiyanto A.B.D., Okuyama K., Nanostructuring strategies in functional fine-particle synthesis towards resource and energy saving applications, *Advanced Powder Technology*, 25 (2014) 3–17. DOI: 10.1016/j.apt.2013.11.005
- Ogi T., Zulfijah R., Iwaki T., Okuyama K., Recent progress in nanoparticle dispersion using bead mill, *KONA Powder and Particle Journal*, 34 (2017) 3–23. DOI: 10.14356/kona.2017004
- Pang J., Zhang W., Zhang Hao, Zhang J., Zhang Huimin, Cao G., Han M., Yang Y., Sustainable nitrogen-containing hierarchical porous carbon spheres derived from sodium lignosulfonate for high-performance supercapacitors, *Carbon*, 132 (2018a) 280–293. DOI: 10.1016/j.carbon.2018.02.077
- Pang J., Zhang W.F., Zhang J.L., Zhang H.M., Cao G.P., Han M.F., Yang Y.S., Oxygen and nitrogen co-enriched sustainable porous carbon hollow microspheres from sodium lignosulfonate for supercapacitors with high volumetric energy densities, *ChemElectroChem*, 5 (2018b) 1306–1320. DOI: 10.1002/celec.201701384
- Peng L., Hung C.T., Wang S., Zhang X., Zhu X., Zhao Z., Wang C., Tang Y., Li W., Zhao D., Versatile nanoemulsion assembly approach to synthesize functional mesoporous carbon nanospheres with tunable pore sizes and architectures, *Journal of the American Chemical Society*, 141 (2019) 7073–7080. DOI: 10.1021/jacs.9b02091
- Qu H., Zhang X., Zhan J., Sun W., Si Z., Chen H., Biomass-based nitrogen-doped hollow carbon nanospheres derived directly from glucose and glucosamine: Structural evolution and supercapacitor properties, *ACS Sustainable Chemistry & Engineering*, 6 (2018) 7380–7389. DOI: 10.1021/acssuschemeng.7b04842
- Septiani E.L., Kikkawa J., Cao K.L.A., Hirano T., Okuda N., Matsumoto H., Enokido Y., Ogi T., Direct synthesis of submicron FeNi particles via spray pyrolysis using various reduction agents, *Advanced Powder Technology*, 32 (2021) 4263–4272. DOI: 10.1016/j.apt.2021.09.031
- Septiani E.L., Kikkawa J., Cao K.L.A., Hirano T., Okuda N., Matsumoto H., Enokido Y., Ogi T., DC bias characteristic enhancement of the powder core by using densified submicron sized FeNi particles through spray pyrolysis, *Journal of Materials Chemistry C*, 10 (2022) 8288–8295. DOI: 10.1039/D1TC05917C
- Shu C., Song B., Wei X., Liu Y., Tan Q., Chong S., Chen Y., Yang X.-d., Yang W.-H., Liu Y., Mesoporous 3D nitrogen-doped yolk-shelled carbon spheres for direct methanol fuel cells with polymer fiber membranes, *Carbon*, 129 (2018) 613–620. DOI: 10.1016/j.carbon.2017.12.049
- Song J., Zhang C., Guo X., Zhang J., Luo L., Liu H., Wang F., Wang G., Entrapping polysulfides by using ultrathin hollow carbon sphere-functionalized separators in high-rate lithium-sulfur batteries, *Journal of Materials Chemistry A*, 6 (2018) 16610–16616. DOI: 10.1039/c8ta04800b
- Song Y., Li W., Xu Z., Ma C., Liu Y., Xu M., Wu X., Liu S., Hierarchical porous carbon spheres derived from larch sawdust via spray pyrolysis and soft-templating method for supercapacitors, *SN Applied Sciences*, 1 (2019) 122. DOI: 10.1007/s42452-018-0132-6
- Song Z., Zhu D., Xue D., Yan J., Chai X., Xiong W., Wang Z., Lv Y., Cao T., Liu M., Gan L., Nitrogen-enriched hollow porous carbon nanospheres with tailored morphology and microstructure for all-solid-state symmetric supercapacitors, *ACS Applied Energy Materials*, 1 (2018) 4293–4303. DOI: 10.1021/acsaem.8b00928
- Stöber W., Fink A., Controlled growth of monodisperse silica spheres in the micron size range, *Journal of Colloid and Interface Science*, 26 (1968) 62–69. DOI: 10.1589/jpts.29.112
- Sun W., Guo K., Fan J., Min Y., Xu Q., Confined selenium in N-doped mesoporous carbon nanospheres for sodium-ion batteries, *ACS Applied Materials & Interfaces*, 13 (2021) 16558–16566. DOI: 10.1021/acsmi.1c02842
- Sun W., Zhang Y., Yang F., Tuning electrochemical performance of carbon-sphere-based supercapacitors by compressive stress, *Electrochimica Acta*, 357 (2020) 136874. DOI: 10.1016/j.electacta.2020.136874
- Tang J., Wang J., Shrestha L.K., Hossain M.S.A., Alothman Z.A., Yamauchi Y., Ariga K., Activated porous carbon spheres with customized mesopores through assembly of diblock copolymers for electrochemical capacitor, *ACS Applied Materials and Interfaces*, 9 (2017) 18986–18993. DOI: 10.1021/acsmi.7b04967
- Tang Z., Jiang S., Shen S., Yang J., The preparation of porous carbon spheres with hierarchical pore structure and the application for high-performance supercapacitors, *Journal of Materials Science*, 53 (2018) 13987–14000. DOI: 10.1007/s10853-018-2584-x
- Tanno K., Makino H., Development tendency and prospect of high performance coal utilization power generation system for low carbon society, *KONA Powder and Particle Journal*, 35 (2018) 139–149. DOI: 10.14356/kona.2018021
- Tian H., Liang J., Liu J., Nanoengineering carbon spheres



- as nanoreactors for sustainable energy applications, *Advanced Materials*, 31 (2019) 1903886. DOI: 10.1002/adma.201903886
- Veerasubramani G.K., Park M.-S., Choi J.-Y., Kim D.-W., Ultrasmall SnS quantum dots anchored onto nitrogen-enriched carbon nanospheres as an advanced anode material for sodium-ion batteries, *ACS Applied Materials & Interfaces*, 12 (2020) 7114–7124. DOI: 10.1021/acsami.9b18997
- Wang C., Wang F., Liu Z., Zhao Y., Liu Y., Yue Q., Zhu H., Deng Y., Wu Y., Zhao D., N-doped carbon hollow microspheres for metal-free quasi-solid-state full sodium-ion capacitors, *Nano Energy*, 41 (2017) 674–680. DOI: 10.1016/j.nanoen.2017.10.025
- Wang H., Lan J.L., Yuan H., Luo S., Huang Y., Yu Y., Cai Q., Yang X., Chemical grafting-derived N, P co-doped hollow microporous carbon spheres for high-performance sodium-ion battery anodes, *Applied Surface Science*, 518 (2020) 146221. DOI: 10.1016/j.apsusc.2020.146221
- Wang J.G., Liu H., Sun H., Hua W., Wang H., Liu X., Wei B., One-pot synthesis of nitrogen-doped ordered mesoporous carbon spheres for high-rate and long-cycle life supercapacitors, *Carbon*, 127 (2018) 85–92. DOI: 10.1016/j.carbon.2017.10.084
- Wang S., Li Y., Ma F., Wu X., Zhou P., Miao Z., Gao P., Zhuo S., Zhou J., Phenolic resin-based carbon microspheres for potassium ion storage, *Applied Surface Science*, 506 (2020) 144805. DOI: 10.1016/j.apsusc.2019.144805
- Xiang K., Cai S., Wang X., Chen M., Jiang S., Nitrogen-doped activated microporous carbon spheres as a sulfur matrix for advanced lithium-sulfur batteries, *Journal of Alloys and Compounds*, 740 (2018) 687–694. DOI: 10.1016/j.jallcom.2018.01.026
- Xiong S., Fan J., Wang Y., Zhu J., Yu J., Hu Z., A facile template approach to nitrogen-doped hierarchical porous carbon nanospheres from polydopamine for high-performance supercapacitors, *Journal of Materials Chemistry A*, 5 (2017) 18242–18252. DOI: 10.1039/c7ta05880b
- Xu J., Fan H., Su D., Wang G., Nitrogen doped yolk-shell carbon spheres as cathode host for lithium-sulfur battery, *Journal of Alloys and Compounds*, 747 (2018) 283–292. DOI: 10.1016/j.jallcom.2018.02.225
- Xu M., Liu Y., Yu Q., Feng S., Zhou L., Mai L., Phenylendiamine-formaldehyde chemistry derived N-doped hollow carbon spheres for high-energy-density supercapacitors, *Chinese Chemical Letters*, 32 (2021) 184–189. DOI: 10.1016/j.ccl.2020.11.004
- Yan L., Li D., Yan T., Chen G., Shi L., An Z., Zhang D., N,P,S-Codoped hierarchically porous carbon spheres with well-balanced gravimetric/volumetric capacitance for supercapacitors, *ACS Sustainable Chemistry & Engineering*, 6 (2018) 5265–5272. DOI: 10.1021/acssuschemeng.7b04922
- Ye J., Zang J., Tian Z., Zheng M., Dong Q., Sulfur and nitrogen co-doped hollow carbon spheres for sodium-ion batteries with superior cyclic and rate performance, *Journal of Materials Chemistry A*, 4 (2016) 13223–13227. DOI: 10.1039/c6ta04592h
- Zhang D., Shen S., Xiao X., Mao D., Yan B., Nitrogen-doped hollow carbon spheres with tunable shell thickness for high-performance supercapacitors, *RSC Advances*, 10 (2020) 26546–26552. DOI: 10.1039/D0RA02935A
- Zhang H., He H., Luan J., Huang X., Tang Y., Wang H., Adjusting the yolk-shell structure of carbon spheres to boost the capacitive K<sup>+</sup> storage ability, *Journal of Materials Chemistry A*, 6 (2018) 23318–23325. DOI: 10.1039/c8ta07438k
- Zhang H., Hu M., Lv Q., Yang L., Lv R., Monodisperse nitrogen-doped carbon spheres with superior rate capacities for lithium/sodium ion storage, *Electrochimica Acta*, 297 (2019) 365–371. DOI: 10.1016/j.electacta.2018.11.207
- Zhang H., Noonan O., Huang X., Yang Y., Xu C., Zhou L., Yu C., Surfactant-free assembly of mesoporous carbon hollow spheres with large tunable pore sizes, *ACS Nano*, 10 (2016) 4579–4586. DOI: 10.1021/acsnano.6b00723
- Zhang J., Chen Z., Wang G., Hou L., Yuan C., Eco-friendly and scalable synthesis of micro-/mesoporous carbon sub-microspheres as competitive electrodes for supercapacitors and sodium-ion batteries, *Applied Surface Science*, 533 (2020) 147511. DOI: 10.1016/j.apsusc.2020.147511
- Zhang L., Liu L., Liu M., Yu Y., Hu Z., Liu B., Lv H., Chen A., Controllable synthesis of N-doped hollow, yolk-shell and solid carbon spheres via template-free method, *Journal of Alloys and Compounds*, 778 (2019) 294–301. DOI: 10.1016/j.jallcom.2018.11.169
- Zhang M., He L., Shi T., Zha R., Nanocasting and direct synthesis strategies for mesoporous carbons as supercapacitor electrodes, *Chemistry of Materials*, 30 (2018) 7391–7412. DOI: 10.1021/acs.chemmater.8b03345
- Zhang N., Liu F., Xu S.-D., Wang F.-Y., Yu Q., Liu L., Nitrogen-phosphorus co-doped hollow carbon microspheres with hierarchical micro-meso-macroporous shells as efficient electrodes for supercapacitors, *Journal of Materials Chemistry A*, 5 (2017) 22631–22640. DOI: 10.1039/C7TA07488C
- Zhang Z., Zheng Y., Qian L., Luo D., Dou H., Wen G., Yu A., Chen Z., Emerging trends in sustainable CO<sub>2</sub>-management materials, *Advanced Materials*, (2022) 2201547. DOI: 10.1002/adma.202201547
- Zhang Z., Wang G., Lai Y., Li J., Zhang Z., Chen W., Nitrogen-doped porous hollow carbon sphere-decorated separators for advanced lithium-sulfur batteries, *Journal of Power Sources*, 300 (2015) 157–163. DOI: 10.1016/j.jpowsour.2015.09.067
- Zhao X., E J., Wu G., Deng Y., Han D., Zhang B., Zhang Z., A review of studies using graphenes in energy conversion, energy storage and heat transfer development, *Energy Conversion and Management*, 184 (2019) 581–599. DOI: 10.1016/j.enconman.2019.01.092
- Zhou H., Wang D., Fu A., Liu X., Wang Y., Li Y., Guo P., Li H., Zhao X.S., Mesoporous carbon spheres with tunable porosity prepared by a template-free method for advanced lithium-sulfur batteries, *Materials Science and Engineering B: Solid-State Materials for Advanced Technology*, 227 (2018) 9–15. DOI: 10.1016/j.mseb.2017.10.005
- Zhou L., Yang C., Wen J., Fu P., Zhang Y., Sun J., Wang H., Yuan Y., Soft-template assisted synthesis of Fe/N-doped hollow carbon nanospheres as advanced electrocatalysts for the oxygen reduction reaction in microbial fuel cells, *Journal of Materials Chemistry A*, 5 (2017) 19343–19350. DOI: 10.1039/c7ta05522f
- Zhou M., Lu Y., Chen H., Ju X., Xiang F., Excellent durable supercapacitor performance of hierarchical porous carbon spheres with macro hollow cores, *Journal of Energy Storage*, 19 (2018) 35–40. DOI: 10.1016/j.est.2018.07.007
- Zhu J., Wang J., Li G., Huang L., Cao M., Wu Y., Heterogeneous structured pomegranate-like Bi@C nanospheres for high-performance sodium storage, *Journal of Materials Chemistry A*, 8 (2020) 25746–25755. DOI: 10.1039/D0TA09164B

## Authors' Short Biographies



### Kiet Le Anh Cao

Kiet Le Anh Cao received his B.Sc. from University of Science, Vietnam National University, Ho Chi Minh City in 2014 and M.Sc. from Hanyang University, Korea in 2018. He obtained his Ph.D. degree in Chemical Engineering from Hiroshima University in 2021. He is currently working as a post-doctoral researcher in the Department of Advanced Science and Engineering, Hiroshima University, Japan. His research focuses on the rational design and development of novel nanostructured materials for energy storage and conversion.



### Ferry Iskandar

Ferry Iskandar studied transport phenomena at Hiroshima University, Japan, where he earned his doctorate. From 2007 until 2010, he worked as a faculty staff of Hiroshima University's Department of Chemical Engineering. He is currently an Associate Professor at the Department of Physics at the Institut Teknologi Bandung in Indonesia. Since 2016, Ferry Iskandar has also been a researcher at the Indonesian Research Center for Nanosciences and Nanotechnology. His broad research interests include material synthesis and physical characterisation, with an emphasis on nanostructured materials and their applications in the fields of photoenergy conversion and energy storage, including batteries and capacitors.



### Eishi Tanabe

Eishi Tanabe is a senior researcher of Hiroshima Prefectural Technology Research Institute. He received his bachelor's degree and master's degree of science in physics from Hiroshima University in 1993 and 1995, respectively. He started his career with electron microscopy in Hiroshima Prefecture Industrial Research Center in 1995. He received his Ph.D. degree in material science from Shimane University in 2005. His current research interests are TEM and FIB-SEM Tomography.



### Takashi Ogi

Takashi Ogi is a Full Professor in the Department of Advanced Science and Engineering, Hiroshima University. He received his Ph.D. degree in Chemical Engineering in 2008 from Hiroshima University. He was an Assistant Professor at Osaka Prefecture University from 2008–2010 and Associate Professor at Hiroshima University from 2015–2021. His current research interests include synthesis of nanostructured particles materials via liquid phase and aerosol process. Especially, he focuses on the development of rare earth free/less nanomaterials, and recovery of rare metal using biosorption.

# Computational Fluid Dynamic Modelling of Fully-Suspended Slurry Flows in Horizontal Pipes with Different Solids Concentrations<sup>†</sup>

Gianandrea Vittorio Messa<sup>1\*</sup>, Qi Yang<sup>1</sup>, Maria Graça Rasteiro<sup>2</sup>, Pedro Faia<sup>3</sup>,  
Vaclav Matoušek<sup>4</sup>, Rui C. Silva<sup>2</sup> and Fernando Garcia<sup>2</sup>

<sup>1</sup> Department of Civil and Environmental Engineering, Politecnico di Milano, Italy

<sup>2</sup> Chemical Process Engineering and Forest Products Research Centre, Department of Chemical Engineering, University of Coimbra, Portugal

<sup>3</sup> Center of Mechanical Engineering, Materials and Processes, Electrical and Computer Engineering Department, University of Coimbra, Portugal

<sup>4</sup> Department of Hydraulics and Hydrology, Faculty of Civil Engineering, Czech Technical University in Prague, Czech Republic

## Abstract

This research work is a significant step toward further understanding of the  $\beta$ - $\sigma$  two-fluid model for the simulation of fully-suspended slurry flows in pipeline systems, with the goal of enhancing its potential for scientific research and engineering applications. Particularly, the focus of the study is the characterization and handling of the two main empirical coefficients of the model, namely,  $\beta$  and  $\sigma$ , which require case-specific tuning based on a given set of experimental data. Reference is made to the relevant case of slurry transport in horizontal pipes with infinite length. The influence of  $\beta$  and  $\sigma$  on different features of the fluid dynamic solution has been extensively investigated, considering also the role played by the specific testing conditions. Based on these findings, a procedure for determining appropriate values of  $\beta$  and  $\sigma$  has been developed, which requires only two experimental measurements, namely the concentration profile from a test at moderate slurry concentration, and the hydraulic gradient from another test in which the same slurry flows at high concentration. The procedure has been satisfactorily tested against published experimental data on pipe transport of fine glass bead and sand slurry.

**Keywords:** Computational Fluid Dynamics, slurry pipelines, hydro-transport, two-fluid modelling, model calibration

## 1. Introduction

Pipeline transport of solid particles in the form of slurry is frequently encountered in several engineering fields, such as mining, chemical, oil and gas, pharmaceutical, food, among others. In addition, understanding the physical mechanisms and the complex phenomena occurring in a slurry pipe is an extremely challenging task, as well is the development of mathematical models for their description. Therefore, it is not surprising to see that slurry pipe flows have been driving the efforts of researchers for several decades.

From a technical point of view, there are a few relevant parameters which characterize slurry pipe flows. Probably the key role is played by the hydraulic gradient,  $i_m$  (pressure drop in meters of water per pipe unit length), which quantifies the energy dissipation produced by the flow, and, thus, dictates the selection of the pump capacity. The

hydraulic gradient for a certain solid volumetric concentration,  $C_{vi}$ , is often expressed as a function of the average slurry velocity,  $V_m$ , estimated by the ratio between the volumetric flow rate of the mixture,  $Q_m$ , and the pipe cross section area,  $A$ . When plotted, the trend of  $i_m$  versus  $V_m$ , for a certain  $C_{vi}$ , is called pipe characteristic curve. Actually, two types of concentrations can be defined for slurry pipe flows: one is the already mentioned  $C_{vi}$ , or in-situ concentration, which is the ratio between the volume of solids and the volume of slurry in a certain part of the system; the other is the delivered concentration,  $C_{vd}$ , which is the ratio between the volumetric flow rate of the solids,  $Q_s$ , and that of the mixture,  $Q_m$ . Finally, another important parameter is the deposition limit velocity,  $V_{dl}$ , which is the threshold value of average slurry velocity at which solids deposition starts to be observed.

The values of the just mentioned technical features and parameters, as well their relations, are strongly related with the internal structure of the flow. This has been usually quantified through several flow regimes, whose names and definitions are different in the literature. In this study, reference will be made to the well-established classification reported in the textbook of Wilson et al. (2006).

<sup>†</sup> Received 31 January 2022; Accepted 17 March 2022  
J-STAGE Advance published online 4 June 2022

\* Corresponding author: Gianandrea Vittorio Messa;  
Add: 20133 Milano, Italy  
E-mail: gianandreavittorio.messa@polimi.it  
TEL: +39-02-2399-6287

Homogeneous flow (**Fig. 1a**) is typically composed by very fine solids, smaller than say 40 microns, flowing at high velocity. In this regime, the distribution of particles is virtually uniform along the flow. The (Reynolds-averaged) velocity is axisymmetric across the pipe cross section and there is no local slip between particles and carrying fluid velocities. Slurries with particles in the range between 200 microns and up to 1.5 % of the pipe diameter show a heterogeneous behavior (**Fig. 1c**). In this regime, the particles tend to get separated from the carrying liquid. This

produces greater non-uniformity of the distributions of the solids concentration and velocity, especially at low velocities. In the case of coarse sands and fine gravel (size bigger than say 800 microns), heterogeneous flow becomes more distinctly stratified with a detectable sliding bed. Finally, fully stratified flow occurs when large and rapidly settling particles travel in the lower part of the pipe by either saltation or as a moving bed (**Fig. 1e**). Threshold conditions occur between the three main flow patterns described above. These are the pseudo-homogeneous regime (**Fig. 1b**), in-between the homogeneous and the heterogeneous ones, and the partially stratified regime (**Fig. 1d**), in-between the heterogeneous and the fully stratified ones. The pseudo-homogeneous regime is the focus of the present work. This pattern takes place when particles in the range in between 40 to 200 micron (typically fine sand) flow at relatively high velocities, and it is characterized by a moderate, yet clearly detectable, vertical concentration gradient and a slightly asymmetrical velocity profile.

Several sorts of models have been developed for the prediction of slurry parameters. Traditionally, they fit in two main categories. The first includes models based on integral (cross-section averaged) quantities which produce empirical or semi-empirical correlations for relevant parameters such as  $i_m$  or  $V_{dp}$ , as was done by Durand (1953) and Thomas (1979). The second category is that of mechanism-based layered models: Wilson (1976) developed one, starting from a simplified description of the inner structure of the flow.

Indeed, empirical and mechanistic models have been and still are a powerful tool for slurry pipeline design and management, as well as for researchers. At the same time, an intrinsic limitation is that, despite taking the basic transport mechanisms into account, these models are not able to characterize them at the local level. This does not allow deep insight into the flow, nor exploring geometries and flow conditions different from those considered for the calibration of the model coefficients and parameters. Numerical simulations based on Computational Fluid Dynamics (CFD) might allow overcoming such limits, since CFD modelling is inherently local and distributed. As discussed in Messa et al. (2021b), the CFD approach requires switching from a macroscopic description of the flow, i.e. the flow regimes in **Fig. 1**, on which traditional slurry models are based, to a particle-scale description based on the key physical mechanisms driving the flow at the local level. These are interaction between the particles and the turbulent fluid, quick particle–particle collisions, and long-lasting inter-granular contacts. As it is indicated by the color of the particles in **Fig. 1**, homogeneous and pseudo-homogeneous flow are driven by particle–fluid interactions, whereas fully stratified flow is contact-dominated. Conversely, all the three basic mechanisms play a role in heterogeneous and partially stratified flow.

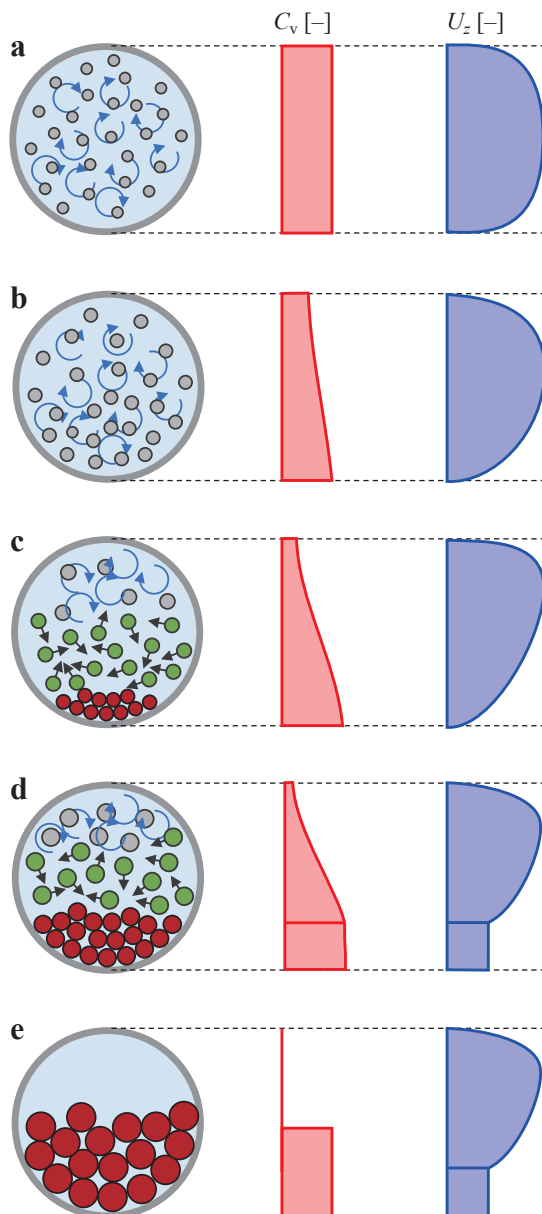


**Fig. 1** Main flow regimes of slurry pipe flow: (a) homogeneous flow; (b) pseudo-homogeneous flow; (c) heterogeneous flow; (d) partially stratified flow; (e) fully stratified flow. The sketches denoted by  $C_v$  and  $U_z$  indicate the typical solid volume fraction and Reynolds-averaged fluid velocity profiles along the vertical diameter. In the sketches on the left, the color of the particles indicates the key mechanism driving the flow: grey = particle–fluid interactions; green = quick particle–particle collisions; red = enduring particle–particle contacts.

There is no doubt that CFD has great potential as a tool for investigating slurry pipe flows. The local nature of a CFD model, in fact, opens up the possibility of (virtually) investigating geometries with no constraints in size and complexity, providing much more information when compared to laboratory testing. At the same time, this approach is also not free from criticisms. Depending on the modelling approach and type of flow, CFD simulations might require large computational costs, which could become practically unaffordable. For instance, describing particle–particle interactions in the Lagrangian framework is not currently feasible for the typical concentrations of slurry pipelines, making Eulerian-based methods (i.e. two-fluid model and mixture model) the preferred or even the only viable route for engineering computations. Apart from that, it must be noted that all CFD models for slurry flows are approximated in nature, and they include several closure parameters, and coefficients which, practically speaking, cannot be decided based on other criteria than the fitting of experimental data for certain conditions. This means that, in the end, CFD modelling cannot dismiss laboratory (or field) testing, but the two approaches should act in a synergistic way. And that is where the main challenges of CFD modelling arise, especially but not exclusively, in the context of its application to slurry pipelines.

As pointed out in Messa et al. (2021b), CFD modelling might have different scopes and impact. On the one hand, interpretative models are calibrated for specific flow conditions and then used to infer local and difficult-to-measure features of the flow under the same testing conditions only. This is the case, for instance, of a model whose calibration procedure uses a set of hydraulic gradient and concentration profile measurements, employed to gather information on the particle velocity distribution for the same experimental conditions. On the other hand, predictive models allow predicting one or more features of the flow outside the calibration conditions. Interpretative models are suitable for achieving a comprehensive and detailed picture of the flow overcoming the limitations of experiments; thus, they are very useful in research, in advanced design, and in the management of existing systems. Conversely, predictive models can be a fundamental tool for the design of new systems.

Although scientific research on the CFD usage in modelling of slurry pipe flows dates back to the 1980s, with an impressive increase in the number of published papers during the last 5–10 years, there is still a long way to go in the exploitation of its potential of application in this field. Among the most significant studies in the field, those authored by Roco and Shook (1983), Ling et al. (2003), Ekambara et al. (2009), Kaushal et al. (2012), Capecelatro and Desjardins (2013), Messa et al. (2014), Uzi and Levy (2018), Messa and Matoušek (2020) shall be mentioned. The interested reader is referred to Messa et al. (2021b) for

a comprehensive review of the state-of-the-art in the field. The aforementioned review paper concluded that most of the existing models might be regarded as interpretative, even if some works do not meet the proper verification and validation requirements, being the initial code verification stage via convergence testing one of them. For sure, very few models proved or even looked predictive in the sense previously introduced. This is not surprising, because the demonstration of the predictive capacity of a model requires going well beyond its evaluation with the existing experimental database, but also the extrapolation to new sets of conditions. Two different procedures have been followed in previous studies. The former consists of calibrating the model by referring only to a subset of the experimental database, while employing the remaining sets of data for validation. An attempt in this sense was reported, for instance, in Messa and Matoušek (2020). The second and different strategy was adopted in Ekambara et al. (2009) and Messa et al. (2014), and consists of the verification that the same combination of calibration coefficients allows for a reasonably good agreement with the largest possible experimental data available in the measurements database, which basically means that calibration and validation are no longer two distinct phases.

For about ten years, research work has been carried out at Politecnico di Milano on the development of CFD models for the simulation of slurry pipe flows. The main outcome of this research, achieved with important contributions from Concentration, Heat, and Momentum Limited (CHAM Ltd, London) and from Institute of Hydrodynamics of the Czech Academy of Sciences, is the already mentioned  $\beta$ - $\sigma$  two-fluid model. Whereas the first efforts were devoted to the definition of the model formulation (Messa and Malavasi, 2015), recently the focus has been directed mostly to the assessment of the predictive capacity of the model.

The research work illustrated in the present paper fits into this trend and represents an important step towards the usability increase of the two-fluid model in an industrial context. The role played by the two main tuning coefficients of the model,  $\beta$  and  $\sigma$ , has been established through an extensive sensitivity analysis. The goal was to understand which features of the CFD solution are mostly affected by  $\beta$  and  $\sigma$ , taking into account also the physical conditions of the simulated problem (pipe diameter, bulk velocity, in-situ concentration, etc.), in order to develop an appropriate procedure for calibration of the two parameters.

The remaining of the paper is divided into three sections, followed by the conclusions. In **Section 2**, the main features of the  $\beta$ - $\sigma$  two-fluid model and of the CFD setup are briefly illustrated. In **Section 3**, the results of the sensitivity analysis are presented, and the procedure for calibrating  $\beta$  and  $\sigma$  is proposed. Finally, in **Section 4**, three examples of application of the calibration strategy are presented

and discussed, referring to glass bead and fine sand slurry experimental data reported in the literature.

## 2. Mathematical model

### 2.1 Overview of the $\beta$ - $\sigma$ two-fluid model

The  $\beta$ - $\sigma$  two-fluid model is an extension of the IPSA (Inter-Phase Slip Algorithm) of Spalding (CHAM, 1994a) for turbulent slurry flow. Being a two-fluid model, it is based on the Eulerian-Eulerian approach, in which both phases are interpreted as interpenetrating continua and solved in the Eulerian, cell-based framework. The reader is referred to Messa and Matoušek (2020) for the complete set of conservation equations and closures. Only the essential features are summarized here.

The fundamental conservation equations of the  $\beta$ - $\sigma$  two-fluid model are for the mass and momentum of the two phases. Under steady-state conditions, the ones considered in this study, their formulation is as follows:

$$\nabla \cdot \Phi_l \rho_l \mathbf{U} = \nabla \cdot \left( \frac{\mu_l^t}{\sigma} \nabla \Phi_l \right) \quad (1)$$

$$\nabla \cdot \Phi_s \rho_s \mathbf{V} = \nabla \cdot \left( \frac{\mu_s^t}{\sigma} \nabla \Phi_s \right) \quad (2)$$

$$\begin{aligned} \nabla \cdot \Phi_l \rho_l \mathbf{U} \mathbf{U} = & -\Phi_l \nabla P + \nabla \cdot \Phi_l (\mu_l + \mu_l^t) \nabla \mathbf{U} \\ & + \Phi_l \rho_l \mathbf{g} + \mathbf{M}_l + \nabla \cdot \left( \frac{\mu_l^t}{\sigma} \mathbf{U} \nabla \Phi_l \right) \end{aligned} \quad (3)$$

$$\begin{aligned} \nabla \cdot \Phi_s \rho_s \mathbf{V} \mathbf{V} = & -\Phi_s \nabla P + \nabla \cdot \Phi_s (\mu_s + \mu_s^t) \nabla \mathbf{V} \\ & + \Phi_s \rho_s \mathbf{g} + \mathbf{M}_s + \nabla \cdot \left( \frac{\mu_s^t}{\sigma} \mathbf{V} \nabla \Phi_s \right) \end{aligned} \quad (4)$$

where:  $\Phi_l$ ,  $\mathbf{U}$ ,  $\mu_l$ , and  $\mu_l^t$  are the locally averaged volume fraction, the locally averaged velocity vector, the viscosity, and the eddy viscosity of the liquid phase, respectively;  $\Phi_s$ ,  $\mathbf{V}$ ,  $\mu_s$ , and  $\mu_s^t$  are the corresponding variables for the solid phase;  $P$  is the locally averaged pressure, shared by the phases;  $\mathbf{g}$  is the gravitational acceleration vector; and  $\mathbf{M}_l$  and  $\mathbf{M}_s$  are the generalized drag term, which will be discussed later. Clearly,  $\Phi_l$  and  $\Phi_s$  sum up to a unit value.

A key feature of the  $\beta$ - $\sigma$  two-fluid model, inherited from the original IPSA, is the presence of phase diffusion terms, which are the last terms on the right-hand side in Eqns. (1–4). The origin of these terms has been discussed in Messa et al. (2021b) on the grounds of the previous derivations of Burns et al. (2004): they basically arise from the modelling of the correlations between the fluctuating velocities and the fluctuating volume fractions, and they account for the effect of particle turbulent dispersion. The coefficient,  $\sigma$ , used to calculate the diffusion coefficient of the phase diffusion terms, is called turbulent Schmidt number for volume fractions, and it is one of the two main calibration parameters of the  $\beta$ - $\sigma$  two-fluid model.

The second calibration coefficient,  $\beta$ , appears in the

evaluation of the friction parameter  $\tilde{\mu}_m$ , which is expressed as a function of the volume fraction of the solid phase, through the following empirical correlation,

$$\tilde{\mu}_m = \mu_l \exp \left\{ \frac{2.5}{\beta} \left[ \frac{1}{(1 - \Phi_s)^\beta} - 1 \right] \right\} \quad (5)$$

built and based on the formal analogy with the correlation of Cheng and Law (2003) for the viscosity of the mixture of colloidal suspensions. Although  $\tilde{\mu}_m$  (and, thus, also  $\beta$ ) does not appear explicitly in Eqns. (1–4), it comes into play twice in the  $\beta$ - $\sigma$  two-fluid model. Firstly, it is used to evaluate the viscosity of the solid phase,  $\mu_s$ , assuming that  $\mu_l$ ,  $\mu_s$ , and  $\tilde{\mu}_m$  are related with each other through the following equation

$$\tilde{\mu}_m = \mu_l \Phi_l + \mu_s \Phi_s \quad (6)$$

The solid phase viscosity  $\mu_s$ , in turn, appears both in the momentum equation for that phase (Eqn. (4)) and in the wall boundary condition for the solid phase, which will be briefly illustrated later in Section 2.3. In addition to the evaluation of  $\mu_s$ ,  $\tilde{\mu}_m$  is used to calculate the generalized drag terms,  $\mathbf{M}_l$  and  $\mathbf{M}_s$ . These two terms account for the exchange of momentum between the two phases within each local control volume, and, considering the action-reaction principle, they are equal in intensity and opposite in sign. In the  $\beta$ - $\sigma$  two-fluid model, it is assumed that the inter-phase momentum exchange is uniquely due to the drag force, and so  $\mathbf{M}_l$  and  $\mathbf{M}_s$  are given by

$$\mathbf{M}_s = -\mathbf{M}_l = \frac{3}{4d_p} \Phi_s \rho_l C_d |\mathbf{U} - \mathbf{V}| (\mathbf{U} - \mathbf{V}) \quad (7)$$

where  $d_p$  is the volume-equivalent particle diameter, and  $C_d$  is the drag coefficient. As in many two-fluid models,  $C_d$  is obtained through the Schiller and Naumann (1935) correlation for a single spherical particle. However, a distinguishing feature in the  $\beta$ - $\sigma$  model resides in the fact that the input of the Schiller and Naumann's correlation is not the usual particle Reynolds number, but a modified Reynolds number based on  $\rho_l$ ,  $d_p$ ,  $|\mathbf{U} - \mathbf{V}|$ , and on the friction parameter  $\tilde{\mu}_m$ . The rationale behind this definition is the need to account for the increased flow resistance encountered by a single particle at high local solid concentration. Additionally, it is a simple way to account for the effect of particle shape through the empirical parameter  $\beta$ .

The eddy viscosities,  $\mu_l^t$  and  $\mu_s^t$ , are obtained from two-phase turbulence models. Particularly,  $\mu_l^t$  is calculated through the two-phase extension of the  $k$ - $\varepsilon$  standard turbulence model for high Reynolds number flows, which is embedded in the PHOENICS code (CHAM, 1994b). Thus,  $\mu_l^t$  is obtained through the solution of two partial differential equations for the turbulent kinetic energy per unit mass of the carrier fluid,  $k_l$ , and its dissipation rate per unit mass,  $\varepsilon_l$ . Conversely,  $\mu_s^t$  is directly obtained from  $\mu_l^t$  through the following algebraic constraint

$$\frac{\mu_l^t}{\rho_l} = \frac{\mu_s^t}{\rho_s} \quad (8)$$

### 2.2 Applicability conditions

The applicability conditions of the  $\beta$ - $\sigma$  two-fluid model have been individuated in Messa and Matoušek (2020). The first comes from the wall boundary condition of the solid phase, and it imposes that:

$$d_p^{+B} = \frac{d_p}{\frac{\mu_l}{\rho_l V_m} \left[ 0.039 \left( \frac{\rho_l V_m D}{\mu_l} \right)^{-0.25} \right]^{-0.5}} < 30 \quad (9)$$

where  $d_p^{+B}$  is the ratio between  $d_p$  and the viscous length scale estimated using the Blasius correlation for the coefficient of frictional resistance of turbulent single-phase flows in smooth straight pipes (Schlichting, 1979), and  $D$  is the pipe diameter. The two other constraints quantify the condition in which the flow must be dominated by particle turbulent interactions, without any role being played by particle-particle interactions. In Messa and Matoušek (2020), such condition has not been related to any of the flow regimes in Fig. 1, but it was referred to as “fully suspended flow”. However, it could be reasonably claimed that the flow regime in which the  $\beta$ - $\sigma$  two-fluid model is applicable, is the pseudo-homogeneous one (Fig. 1b). Mathematically speaking, the two constraints are:

$$V_m = 1.5V_{dl}^T \quad (10)$$

$$\Phi_s < 0.45 \quad (11)$$

where  $V_{dl}^T$  is the estimate of the deposition limit velocity obtained from the correlation of Thomas (2015).

### 2.3 CFD setup

The computational domain and the boundary conditions imposed are the same as in Messa and Matoušek (2020), namely, a cylindrical volume  $120D$  long, bounded by an inlet, an outlet, and a solid wall (Fig. 2).

At the inlet, uniform distributions have been imposed

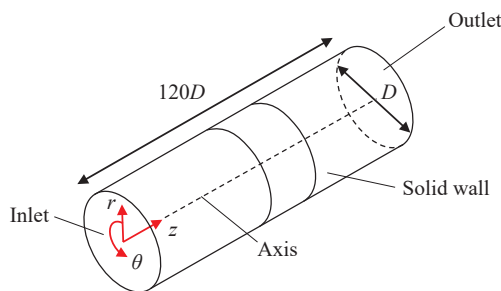


Fig. 2 Computational domain and boundary conditions.

for the axial velocities of the two phases,  $U_z^{in} = V_z^{in} = V_m$ , for their volume fractions,  $\Phi_s^{in} = 1 - \Phi_l^{in} = C_{vi}$ , for the turbulent kinetic energy of the liquid,  $k_l^{in}$ , and for its dissipation rate,  $\epsilon_l^{in}$ . The values of the last two parameters have been set based on a turbulence intensity of 0.05 and on a length scale of  $0.07D$ , as explained in Messa and Matoušek (2020). At the outlet, the pressure is set to zero, as well as the normal gradient of all solved variables. At the walls, the shear stress of the liquid,  $\tau_l^w$ , as well as the values of the turbulent parameters in the near-wall cells,  $k_l^w$  and  $\epsilon_l^w$ , are obtained from the equilibrium wall function option, available in PHOENICS (CHAM, 1994c). Conversely, the wall shear stress of the solid phase on the surface of the near-wall cells,  $\tau_s^w$ , was obtained through the following expression, implemented in PHOENICS through a user-defined function:

$$\tau_s^w = \Phi_s^w \rho_s s_s |\mathcal{V}^{\parallel}|^2 \quad (12)$$

where the  $\mathcal{V}^{\parallel}$  is the resultant velocity of the solid phase parallel to the wall at the first grid node,  $\Phi_s^w$  is the solid volume fraction in the near-wall cells, and  $s_s$  is the friction factor of the solid phase, given by the following implicit equation

$$s_s = \frac{\kappa^2}{\ln^2(E \cdot Re_s^w \sqrt{s_s})} \quad (13)$$

where  $\kappa = 0.41$  is the von Karman constant,  $E$  is a roughness parameter, set at 8.6 as recommended for smooth walls, and  $Re_s^w$  is a wall Reynolds number defined in terms of  $\rho_s$ ,  $|\mathcal{V}^{\parallel}|$ ,  $\mu_s$ , and of the normal distance of the first grid point to the wall,  $\delta$  (Fig. 3a). Since  $\mu_s$  is obtained from  $\mu_l^t$  (Eqn. (6)) which, in turn, is a function of  $\beta$  (Eqn. (5)), it is not surprising to see that this coefficient plays a role in the predictions of the frictional losses. Evidence of this claim will be given later.

In this study, the used code; PHOENICS version 2018 (CHAM, 2002) and all settings of the solution algorithm (FV formulation, differencing schemes, relaxation factors, convergence criteria, etc.) were the same as detailed in Messa and Matoušek (2020). Similarly, the grid was a structured one in cylindrical-polar coordinates, consisting of 30, 30, and 200 subdivisions along the azimuthal, radial, and axial directions, respectively (Fig. 3b). The azimuthal

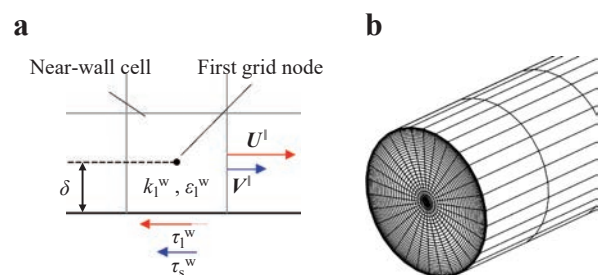


Fig. 3 Sketch of (a) a near wall cell and (b) of the computational mesh.

and axial subdivisions were uniform, whereas the radial ones were progressively reduced when moving away from the pipe axis. Thus, the smallest radial subdivisions were those adjacent to the pipe wall. On the grounds of the findings in Messa et al. (2021a), their size was set equal to 60 times the viscous length scale obtained by the Blasius correlation for turbulent single-phase flows in straight pipes. This implies that, although the total number of cells was the same for all simulations, their distribution over the pipe section was changed according to the inlet velocity,  $V_m$ . Note that, with the cylindrical-polar mesh, additional boundary conditions are needed along the pipe axis, which were of zero-flux type.

### 3. Analysis of the effects of $\beta$ and $\sigma$ on the key features of the CFD solution and development of a calibration strategy

Three necessary steps for proving that a model has a predictive capacity are (i) the identification of the calibration coefficients, (ii) the assessment of their role on the different features of the solution, and (iii) the development of a precise calibration strategy. The  $\beta$ - $\sigma$  two-fluid model has two main calibration coefficients,  $\beta$  and  $\sigma$ . Note that the number of empirical parameters becomes much higher if one includes the numerical constants in the turbulence model. However, dealing with a large number of tuning coefficients would make the calibration difficult and the model less robust; therefore, the turbulence model constants were simply set with the default values for single-phase flow (Launder and Spalding, 1974), and the  $\beta$ - $\sigma$  two-fluid model has been regarded as a two-parameter model.

Once the calibration parameters have been identified, their role in the different features of the CFD solution must be established. This requires not only to specify the range of variability of  $\beta$  and  $\sigma$  and to select the features of the solution of most interest, but also to define the physical conditions for the sensitivity analysis. In fact,  $\beta$  and  $\sigma$  might play different roles depending on the specific characteristics of the slurry flow subject of investigation, i.e. for different levels of concentration, pipe diameter, bulk mean velocity etc. Starting from this last task, it could be observed that the physical conditions characterizing a slurry pipe flow are defined by the pipe diameter,  $D$ , the pipe roughness, the slurry velocity  $V_m$ , the in-situ concentration  $C_{vi}$ , the particle properties, and the properties of the carrier fluid. In principle, the sensitivity analysis upon  $\beta$  and  $\sigma$  should be carried out within a suitable range of all the physical features above mentioned, and, for each physical condition, different values of  $\beta$  and  $\sigma$  should be considered. However, this would result in an unnecessarily large number of simulations and, therefore, some simplifications were made. Firstly, the pipe walls were considered hydraulically smooth, thereby neglecting the pipe roughness. The choice was made because, in its original formulation, the

$\beta$ - $\sigma$  two-fluid model is unable to account for pipe roughness. Indeed, a rough wall function option is available in PHOENICS for the liquid phase, but no study has been made for the solid phase. Additionally, the pipe roughness in the experiments used for calibrating and validating the  $\beta$ - $\sigma$  two-fluid model was generally very low (Kaushal and Tomita, 2007; Matoušek, 2002; Schaan et al., 2000). Secondly, also the particle properties, particle size and particle density were kept fixed in the sensitivity analysis, on the grounds of the following considerations. On one hand, typical materials used in slurry pipe flow experiments include glass beads and natural sand, whose densities are rather close to each other. On the other hand, preliminary simulations run at the beginning of this research work indicated that the role played by  $\beta$  and  $\sigma$  is substantially unaffected by the value of particle diameter within the typical range where this model applies, say 100  $\mu\text{m}$  to 200  $\mu\text{m}$ . Based on the above, the sensitivity analysis was performed considering particles with density of 2650  $\text{kg/m}^3$  and size of 150  $\mu\text{m}$ . Particle shape is very different for glass bead and sand, and also among sand grains. However, particle shape is not set a priori in the  $\beta$ - $\sigma$  model, but only indirectly through the empirical parameters  $\beta$  and  $\sigma$ .

Finally, also the properties of the carrier liquid have not been varied (density, viscosity, rheological model) but the characteristic features of water have been taken, namely  $\rho_1 = 998.23 \text{ kg/m}^3$ ,  $\mu_1 = 0.001 \text{ Pa}\cdot\text{s}$ , and Newtonian rheology. It is expected that reasonably small variations in terms of  $\rho_1$  and  $\mu_1$  will not alter the conclusions of the sensitivity analysis. The study of the effect of the rheological model will be addressed in future research, as it will require developing a non-Newtonian formulation of the  $\beta$ - $\sigma$  two-fluid model, currently unavailable.

Based on the considerations above, in the selection of the physical conditions of the sensitivity analysis, reference was made only to the pipe diameter,  $D$ , to the slurry velocity,  $V_m$ , and to the in-situ concentration,  $C_{vi}$ . For each of the three parameters, two “extreme” values have been considered to span the broadest possible range of applicability of the  $\beta$ - $\sigma$  two-fluid model, defined by the three applicability constraints in Section 2.2. In particular, the pipe diameter was either 50 mm (“small” pipe) or 500 mm (“large” pipe); the bulk velocity was either 2 m/s (“low” velocity) and 4.5 m/s (“high” velocity); the in-situ concentration was either 0.05 (“low” concentration) or 0.40 (“high” concentration). Only the “high” velocity was considered in the large pipe runs, as the 2 m/s value does not fulfil the constraint  $V_m = 1.5V_{dl}^T$  (Eqn. (10)). Thus, the total number of combinations was equal to six, as summarized in Table 1. For each of the six aforementioned scenarios, different combinations of  $\beta$  and  $\sigma$  were considered. Particularly,  $\sigma$  was either 0.50, 0.75, or 1.00, whereas  $\beta$  was either 0.50, 1.50, 2.50, or 3.50. The effects of varying  $\sigma$  were studied for  $\beta = 2.50$ , whereas that of varying  $\beta$  was investigated for  $\sigma = 0.75$ .



The target variables of the sensitivity analyses were those of most interest in slurry pipeline systems, namely, the hydraulic gradient,  $i_m$ , the chord-average volume fraction profile, the vertical profile of the locally-averaged fluid velocity, and the distributions of the wall shear stresses of the two phases over the pipe circumferences. Note that the vertical profile of the locally-averaged velocity of the solid phase has not been investigated, as the axial slip between the two phases was very small for all simulated cases, as typical of the pseudo-homogeneous regime.

Due to space limitations, only the most significant results will be provided in the form of tables and figures, but all of them are available upon request to the corresponding author. **Table 2** summarizes the values of hydraulic gradient,  $i_m$ , as obtained for all the combinations of  $\beta$  and  $\sigma$  and all testing conditions in **Table 1**. The results highlight that the effect of  $\sigma$  on  $i_m$  is negligible or even lacking, whereas  $\beta$  affects  $i_m$  but only at high concentration (cases C3, C4, C6). More generally, the effect of  $\beta$  at low concentration was found to be negligible not only in terms of hydraulic gradient, but also in terms of all other features of the flow under investigation, namely, concentration profile, velocity profile and wall shear stresses distributions. This is not surprising, if one considers that  $\beta$  plays a role in the model

through its appearance in the formula for the friction parameter  $\tilde{\mu}_m$  (Eqn. (5)) and, according to the mathematical formulation employed, the effect of  $\beta$  on  $\tilde{\mu}_m$  is very limited at low  $\Phi_s$ .

For all levels of concentration, the predicted concentration profiles are affected by the value of  $\sigma$ , as shown in **Fig. 4b, d** for the two exemplary cases C1 and C6. Increasing  $\sigma$  will increase the vertical concentration gradient, which is a clear consequence of the phase diffusion terms in the mass conservation equations (Eqns. (1) and (2)). As already mentioned, no effect of  $\beta$  can be detected at low concentration, as shown in **Fig. 4a** for case C1. Conversely,  $\beta$  was found to significantly affect the concentration profile at high concentration, as seen in **Fig. 4c** for case C6.

The predicted velocity profiles appear substantially insensitive to the values of  $\beta$  and  $\sigma$  for all the testing conditions. The greatest effect is observed when varying  $\beta$  at high concentration, but the change in the velocity values is still rather moderate (**Fig. 5**).

The wall shear stresses of the two phases are, in general, affected by both  $\beta$  and  $\sigma$ . At high concentration, an obvious increase in  $\tau_s^w$  is evident for increasing  $\beta$  (**Fig. 6a**), which is the direct consequence of the higher friction factor  $s_s$  produced by a higher wall Reynolds number  $Re_s^w$  (Eqn. (13)). At both low and high concentration, varying  $\sigma$  will modify the individual distributions of  $\tau_1^w$  and  $\tau_s^w$  (**Figs. 6b, c**). However, comparing the curves in **Figs. 6b, c** with the corresponding volume fraction profiles (shown in **Fig. 4b** for case C6 at  $\beta = 2.5$  only) suggests that the variations in  $\tau_1^w$  and  $\tau_s^w$  mainly arise from the effect of  $\sigma$  on the volume fraction in the near-wall cells rather than from a direct influence of  $\sigma$  on the friction factors of the two phases. It is interesting to note that, although  $\sigma$  has an effect on the individual wall shear stresses distribution, this parameter was found to have practically no influence on the hydraulic gradient (**Table 2**), which is related with the average value of their sum:

**Table 1** Simulation scenarios in the sensitivity analysis. The other physical parameters were  $\rho_1 = 998.23 \text{ kg/m}^3$ ,  $\mu_1 = 0.001 \text{ Pa}\cdot\text{s}$ ,  $\rho_s = 2650 \text{ kg/m}^3$ ,  $d_p = 150 \text{ }\mu\text{m}$ .

Case ID	$D$ [mm]	$V_m$ [m/s]	$C_{vi}$ [-]
C1	50	2	0.05
C2	50	4.5	0.05
C3	50	2	0.40
C4	50	4.5	0.40
C5	500	4.5	0.05
C6	500	4.5	0.40

**Table 2** Effect of  $\beta$  and  $\sigma$  on the predicted hydraulic gradient for the six testing conditions in **Table 1**.

Model parameters							
$\beta$	2.5			0.50	1.50	2.50	3.50
$\sigma$	0.50	0.75	1.00	0.75			
$i_m$ [-]							
C1	0.079	0.080	0.082	0.080	0.080	0.080	0.081
C2	0.331	0.333	0.335	0.332	0.332	0.333	0.333
C3	0.198	0.199	0.199	0.144	0.162	0.199	0.293
C4	0.825	0.825	0.825	0.607	0.680	0.825	1.203
C5	0.023	0.023	0.023	0.023	0.023	0.023	0.023
C6	0.051	0.051	0.051	0.040	0.044	0.051	0.071

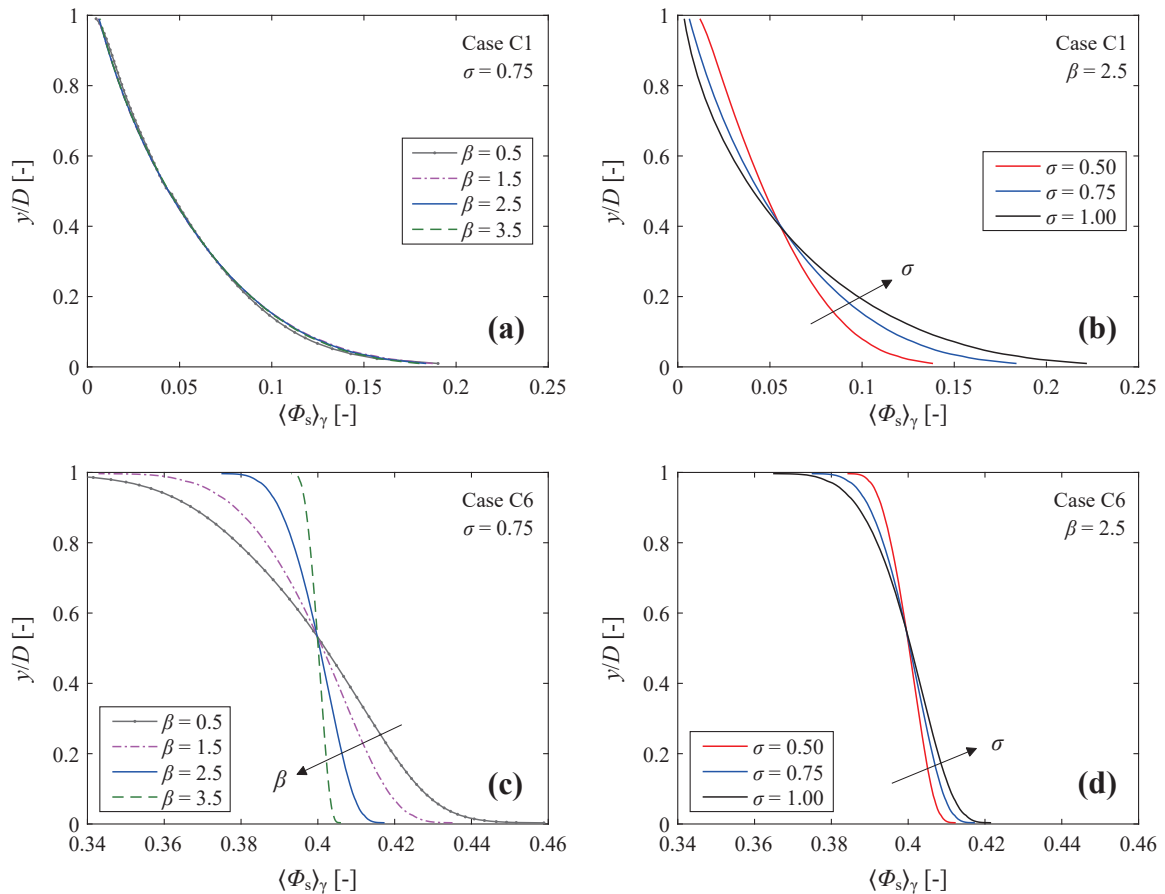


Fig. 4 Effect of  $\beta$  and  $\sigma$  on the predicted chord-averaged concentration profile for cases C1 and C6.

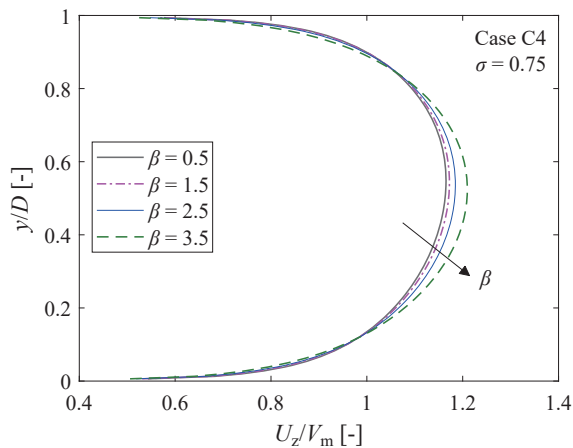


Fig. 5 Effect of  $\beta$  on the predicted fluid velocity profile for case C4.

$$\rho_l |g| i_m \left( \pi \frac{D^2}{4} \right) = \frac{D}{2} \int_0^{2\pi} (\tau_l^w + \tau_s^w) d\theta \quad (14)$$

Based on the results of the sensitivity analysis, a strategy was proposed for the calibration of the two parameters  $\beta$  and  $\sigma$ . The strategy is arranged into two steps in sequence. Firstly, in a first-attempt,  $\beta$  is chosen and an appropriate  $\sigma$  is determined by referring to the concentration profile data at low concentration. Secondly, using this value of  $\sigma$ , a more appropriate  $\beta$  is found by referring to the hydraulic

gradient data at high concentration. Therefore, in order to calibrate  $\beta$  and  $\sigma$ , one needs at least one experimentally determined concentration profile at low concentration (say 10 %) and one measured value of hydraulic gradient at high concentration (say 30–40 %). In the two calibration tests, the same type of particles shall be used, but no specific constraints are given in terms of mixture velocity and pipe diameter, provided that the three applicability conditions of the  $\beta$ - $\sigma$  model are fulfilled. As it will be demonstrated in Section 4, the two calibration tests might have different  $V_m$ . In principle, the pair of values of  $\beta$  and  $\sigma$  obtained from this calibration procedure should allow for reasonably accurate prediction over the entire range of  $C_{vi}$  spanned by the two calibration tests, and that they are also appropriate over the entire range of  $V_m$  determined by the two conditions defined by Eqns. (9) and (10) (which does not depend on the  $C_{vi}$ ).

The rationale behind the proposed strategy is the solution of the  $\beta$ - $\sigma$  two-fluid model is practically insensitive to the value of  $\beta$  for low concentration cases, as shown in Table 2 (cases C1, C2, C5) and Figs. 4a and 6a, whilst, for high concentration cases, the hydraulic gradient is not affected by  $\sigma$  but only by  $\beta$  (Table 2, cases C3, C4, C6). However, for the same high concentration cases,  $\beta$  does not influence only the hydraulic gradient, but also the concentration

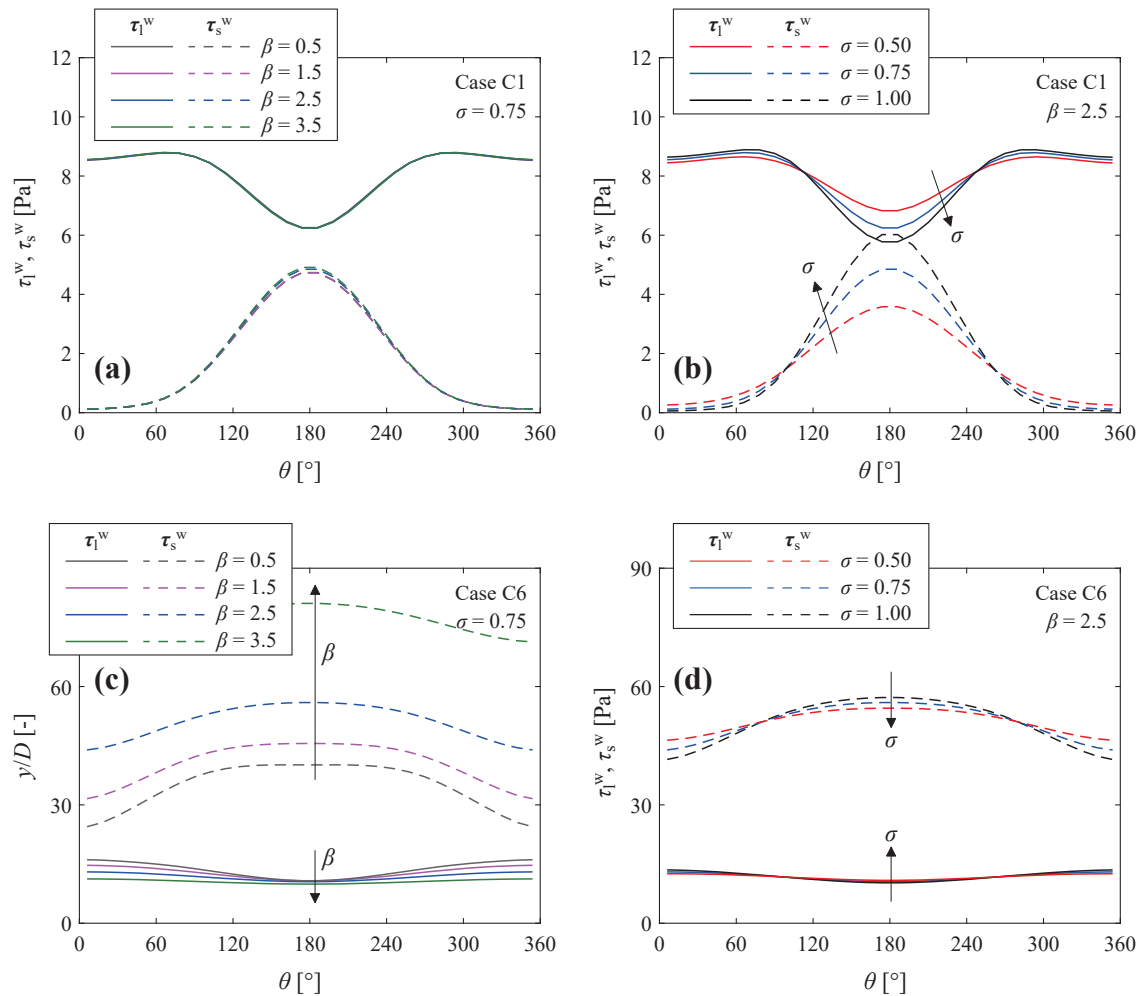


**Fig. 6** Effect of  $\beta$  and  $\sigma$  on the predicted distributions of the wall shear stresses of the two phases for cases C1 and C6. According to the coordinate system in **Fig. 1**,  $\theta = 0$  and  $\theta = 180^\circ$  indicate the crown and the invert of the pipe, respectively.

profile (**Fig. 4c**). Therefore, the effects of  $\sigma$  and  $\beta$  cannot be fully decoupled, as requested by the proposed calibration methodology; as a result, deviations might be expected for high concentration cases in terms of concentration profile. Strengths and weaknesses of the calibration strategy, and of the  $\beta$ - $\sigma$  formulation from a more general perspective, will be discussed in the next section. Three verification tests will be presented, employing experimental data reported in the literature.

## 4. Verification of the calibration strategy against experimental data

### 4.1 Experiments by Kaushal and Tomita (2007) on fine glass-bead slurry

The calibration strategy was firstly applied to the flow conditions extracted from the experimental tests on fine glass-bead slurry flow performed by Kaushal and Tomita (2007). The experiments were performed in a pipe with a diameter of 54.9 mm using glass beads with density of 2470 kg/m<sup>3</sup> and mean particle diameter of 150  $\mu$ m. The narrow particle size distribution enabled the assumption of

mono-disperse particles, inherent to the two-fluid modeling approach. The ranges of average velocity and in-situ concentration considered in the present study were 2 to 5 m/s and 10 to 40 %, respectively, disregarding the data at  $V_m = 1$  m/s and those at  $C_{vi} = 50$  % because they were out of the range of applicability of the  $\beta$ - $\sigma$  two-fluid model. For each condition, Kaushal and Tomita (2007) provided the hydraulic gradient and the concentration profile. In order to measure the latter quantity, they used a sampling probe and a  $\gamma$ -ray radiometric device, detecting full consistency of the two measurement techniques for fine glass beads. The concentration profiles obtained with the  $\gamma$ -ray device, which were the chord-average ones, were considered for comparison with the CFD simulations.

The first-attempt value of  $\beta$  was 0.5, and the case  $V_m = 4$  m/s and  $C_{vi} = 10$  % was chosen for the calibration of  $\sigma$ . As it is shown in **Fig. 7a**, the predicted concentration profile with  $\sigma = 0.5$  was in very good agreement with the experimentally determined for this case, and additional tests confirmed the same finding for the other flow velocities with  $C_{vi} = 10$  %. However, it must be observed that the

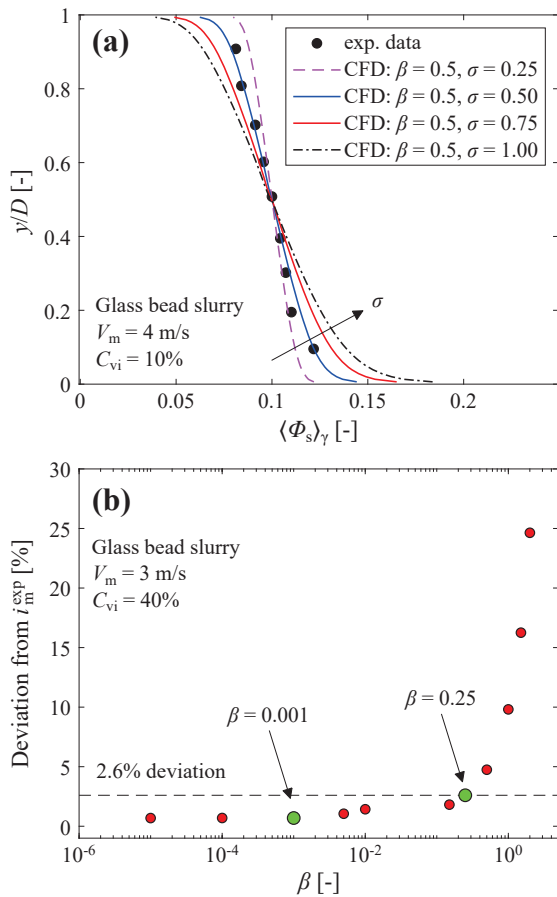


**Fig. 7** Calibration for glass bead slurry (data from Kaushal and Tomita 2007): (a) calibration of  $\sigma$  based on the measured concentration profile for  $V_m = 4 \text{ m/s}$  and  $C_{vi} = 10\%$  ( $\beta = 0.25$ ); (b) calibration of  $\beta$  based on the measured hydraulic gradient for  $V_m = 3 \text{ m/s}$  and  $C_{vi} = 40\%$  ( $\sigma = 0.50$ ).

uncertainty of the concentration data was not considered, as this information is difficult to estimate and it was not reported by the experimenters. Indeed, the consistency of the concentration profiles obtained by the sampling probe and the  $\gamma$ -ray device indicates the reliability of the data, but it is well known that local concentration values might be quite inaccurate close to the pipe bottom. This leads to the conclusion that it is not possible nor meaningful to seek for an “optimum” value for  $\sigma$  in a strict sense but, rather, the goal is to find “reasonably accurate” value of  $\sigma$ .

Once  $\sigma$  was defined as 0.5, an appropriate value of  $\beta$  was determined by referring to the measured hydraulic gradient for  $V_m = 3 \text{ m/s}$  and  $C_{vi} = 40\%$ . **Fig. 7b** shows the percentage deviation between predicted and measured  $i_m$  for different values of  $\beta$ . The CFD model overestimates  $i_m$  for every  $\beta$ . Particularly, for  $\beta$  ranging from  $10^{-5}$  to 0.25, the calculated hydraulic gradient is minorly affected by the value of  $\beta$ , both in absolute terms ( $i_m$  varies from 0.2437 m/m to 0.2483 m/m), as well as in terms of relative deviation from the experimental value (which is between 0.70 % and 2.60 %). The impossibility to find an “optimum” value of  $\beta$  which fully matches the experimentally-determined hydraulic gradient suggests that there exists some intrinsic

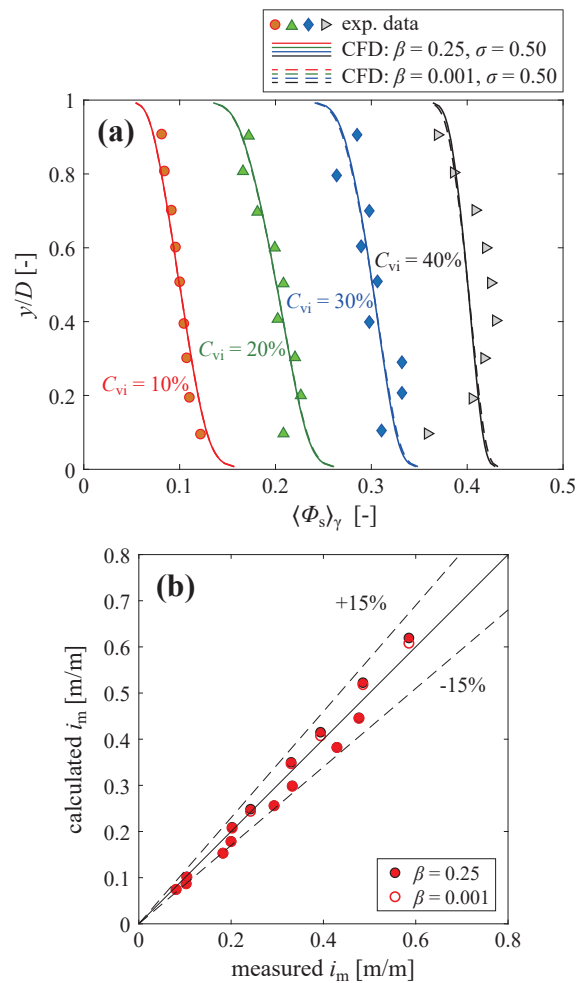


**Fig. 8** Validation of the model with  $\beta = 0.25$  and  $\sigma = 0.5$  (continuous lines, filled points) and  $\beta = 0.001$  and  $\sigma = 0.5$  (dotted lines, unfilled points) for glass bead slurry (data from Kaushal and Tomita 2007): (a) concentration profiles for  $V_m = 3 \text{ m/s}$  (b) hydraulic gradient.

limitation in the  $\beta$ - $\sigma$  formulation, which prevents its ability to capture accurately the physical processes driving slurry flows at high concentration. Nonetheless, in this first test case, the accuracy of the  $\beta$ - $\sigma$  two-fluid model in terms of hydraulic gradient is high (<2.60 %) for every  $\beta$  between  $10^{-5}$  and 0.25. Considering that the simulation convergence was more and more difficult to achieve as  $\beta$  decreased, probably because of issues in the numerical evaluation of  $\tilde{\mu}_m$  through Eqn. (5), initially it was decided to take  $\beta = 0.25$ . Such value did not produce any convergence issue, and resulted in a 2.6 % overestimation of the hydraulic gradient in the calibration case, which was judged a satisfactory enough level of agreement.

The conjecture underlying the proposed calibration strategy is that the pair of values  $\sigma = 0.5$  and  $\beta = 0.25$  allow for reasonably accurate prediction of concentration profile and hydraulic gradient for  $C_{vi}$  between 10 % to 40 % (that is, within the calibration conditions) and for  $V_m$  between 1.41 m/s and 5.95 m/s (as obtained from Eqns. (10) and (9), respectively). This could be partially verified through

validation with respect to all other testing conditions reported at the beginning of the present section (14 cases in total), for which however, the velocity range is a little bit narrower (2 m/s to 5 m/s).

With  $\beta = 0.25$  and  $\sigma = 0.5$ , reasonable agreement was obtained in terms of the concentration profile, as exemplified through the continuous lines in Fig. 8a for  $V_m = 3$  m/s and increasing  $C_{vi}$ . The  $\beta$ - $\sigma$  two-fluid model is able to accurately predict the concentration profiles up to  $C_{vi} = 30$  %. Conversely, for  $C_{vi} = 40$  %, the experimental data suggested a reverse slope close to the pipe invert, and this effect is not captured by the CFD model, resulting in rather poorly predicted concentration profile. This give strength to the claim that there exists some inherent inability of the  $\beta$ - $\sigma$  two-fluid model to capture the physics of highly concentrated slurry flows at high velocity, which cannot be remedied simply by adjusting  $\beta$ . Particularly, the absence of the lift force in generalized drag term could explain why the  $\beta$ - $\sigma$  two-fluid model is not able to reproduce the reversal in the slope of the concentration profile observed experimentally, as already guessed by Kaushal et al. (2013). Additionally, it is not excluded that particle–particle collisions could take place for slurry flows at  $C_{vi} = 40$  %, even at high flow velocity. The  $\beta$ - $\sigma$  formulation is not able to account for these effects, which is instead a peculiar feature of two-fluid models based on the Kinetic Theory of Granular flow, such as those used by Ekambara et al. (2009) and Kaushal et al. (2013).

Beyond these considerations, the parity plot in Fig. 8b indicates the capacity of the  $\beta$ - $\sigma$  two-fluid model with  $\beta = 0.25$  and  $\sigma = 0.5$  in predicting the hydraulic gradient with satisfactory accuracy (the filled points correspond to this combination of  $\beta$  and  $\sigma$ ). The maximum absolute deviation between calculated and measured  $i_m$  is 17.5 %, and the mean absolute deviation is 8.70 %.

A weak point in the analysis here above relies in the choice of the value of  $\beta = 0.25$ , which appears quite arbitrary. As already noticed, the points in Fig. 7b indicate that every value of  $\beta$  within  $10^{-5}$  and 0.25 produces broadly the same hydraulic gradient prediction, which is also close to the measured value (deviation  $< 2.60$  %), but the numerical convergence becomes more and more difficult as  $\beta$  decreases. In order to investigate the actual impact of  $\beta$  on the predictive capacity of the  $\beta$ - $\sigma$  two-fluid models, the simulations were repeated with  $\beta = 0.001$  and  $\sigma = 0.5$  and the new results are shown in Fig. 8 using dotted lines and unfilled points. No differences are detected in terms of concentration profile. At first glance, this finding might appear in contrast with the results of the sensitivity analysis shown in Fig. 4c, indicating an influence of  $\beta$  on the concentration profile for case C6 in which  $C_{vi} = 40$  %. However, the inconsistency might be explained considering that the two values of  $\beta$  compared in Fig. 8a (0.001 and 0.25) are lower than the range of  $\beta$  in the sensitivity analysis (0.5 to

3.5) and, additionally, that the horizontal axis is relatively narrow in Fig. 4c. Similar considerations can be made to explain why, in the parity plot in Fig. 8b, the effect of  $\beta$  on the predicted hydraulic gradient is very moderate, and visible only for a couple of points, whereas Table 2 indicates a higher degree of influence for cases with  $C_{vi} = 40$  % (C3, C4, C6). The comparison in Fig. 8 indicates that even the impossibility to identify an “optimum”  $\beta$  does not affect the overall degree of accuracy of the  $\beta$ - $\sigma$  model, thus its engineering effectiveness. It also gives strength to our claim that the poor agreement between measured and calculated concentration profiles at  $C_{vi} = 40$  % is not a consequence of an inappropriate value of  $\beta$ , but, rather, is due to some intrinsic modelling limitation.

#### 4.2 Experiments by Matoušek (2002) on fine sand slurry

A second verification of the calibration procedure was performed by referring to fine sand slurry flow experiments reported in Matoušek (2002), in which the pipe diameter is of 150 mm and the solids have a density of 2650 kg/m<sup>3</sup>

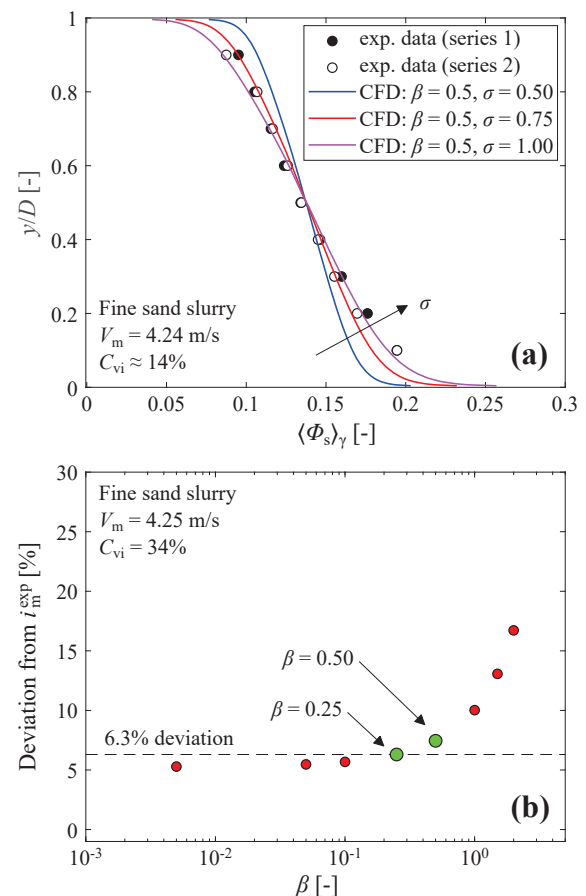


**Fig. 9** Calibration for fine sand slurry (data from Matoušek 2002): (a) calibration of  $\sigma$  based on the measured concentration profile for  $V_m = 4.24$  m/s and  $C_{vi} = 14$  % ( $\beta = 0.50$ ); (b) calibration of  $\beta$  based on the measured hydraulic gradient for  $V_m = 4.25$  m/s and  $C_{vi} = 34$  % ( $\sigma = 0.75$ ). Both repetitions are shown in plot (a), whether the mean hydraulic gradient between the two repetitions is considered in plot (b).

and a mean particle diameter of 130  $\mu\text{m}$ . Only six testing situations fulfill the applicability conditions of the  $\beta$ - $\sigma$  two-fluid model, corresponding to two values of  $V_m$  ( $\approx 4.2$  m/s and  $\approx 6$  m/s), and three levels of  $C_{vi}$  ( $\approx 14\%$ ,  $\approx 28\%$ ,  $\approx 33$ – $34\%$ ). For the six cases, the experimenter provided hydraulic gradient and chord-average concentration profiles by repeating the tests twice.

The concentration profile for  $V_m = 4.24$  m/s and  $C_{vi} \approx 14\%$  was used to decide an appropriate  $\sigma$ , using a first-attempt  $\beta$  equal to 0.5. The findings in Fig. 9a indicate that a good match with the experimental data is obtained for  $\sigma = 0.75$  and  $\sigma = 1$ , and the former value is used in the remaining simulations. Afterwards, a suitable value for  $\beta$  was determined from the measured hydraulic gradient for  $V_m = 4.25$  m/s and  $C_{vi} \approx 34\%$ . The points in Fig. 9b show some similarity with the corresponding ones for fine glass-bead slurry, shown in Fig. 7b. In both cases, in fact, the calculated  $i_m$  increases with increasing  $\beta$ , and shows a plateau for low values of this coefficient. However, a difference exists in terms of the deviation between the predicted and the calculated  $i_m$  within the plateau region, which is around 0.7%–2.6% in the previous glass-bead case (Fig. 7b, in which  $C_{vi} = 40\%$ ), and around 6% for the present fine sand case (Fig. 9b, in which  $C_{vi} = 34\%$ ). This indicates that, in the fine sand case, the inherent limitations in the  $\beta$ - $\sigma$  formulation for highly concentrated slurries have an obvious impact on the accuracy of the hydraulic gradient predictions despite the lower value of  $C_{vi}$  (34% instead of 40%). As a first-attempt, it was decided to use the same value of  $\beta$  of the glass-bead case, that is,  $\beta = 0.25$ , which corresponds to an overestimation of the hydraulic gradient of about 6.3%.

With  $\beta = 0.25$  and  $\sigma = 0.75$ , the predicted concentration profile was in a good agreement with the experimental data in Matoušek (2002) for all the five conditions (note that the sixth profile had been already used for calibrating  $\sigma$ ). Exemplary results are reported for  $V_m \approx 6$  m/s in Fig. 10a, using continuous lines to denote the CFD predictions with  $\beta = 0.25$  and  $\sigma = 0.75$ . In this second test case, the concentration profile is well predicted even for the highest value of  $C_{vi}$  (34%), in contrast to the findings of the first validation example (grey-black series in Fig. 8a, where the  $C_{vi}$  was 40%). This suggests that the limitations of the  $\beta$ - $\sigma$  formulation affect different features of the CFD solution, depending on the testing conditions. In the first validation example, the hydraulic gradient was well predicted but the concentration profile was not. In the second test case, the situation seemed to be the opposite. The deviation in terms of hydraulic gradient prediction is within 15% for five points out over six, and equal to 9.4% on average (filled points in Fig. 10b). This indicates that the predictive capacity of the calibrated model can be satisfactory for the applications, although obviously a six-point population is not sufficient to provide accurate statistics.

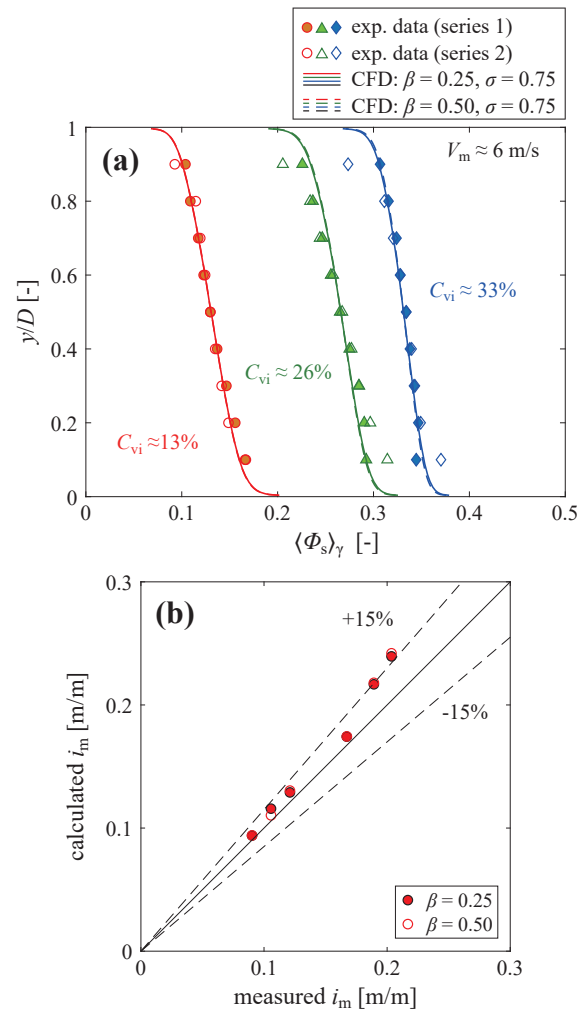


**Fig. 10** Validation of the model with  $\sigma = 0.75$  and  $\beta = 0.25$  (continuous lines, filled points) and  $\beta = 0.50$  (dotted lines, unfilled points) for fine sand slurry (data from Matoušek 2002): (a) concentration profiles (both repetitions are shown); (b) hydraulic gradient (experimental data are the average over the two repetitions).

As for the glass bead case, also in the fine sand one the first-attempt value of  $\beta$  is quite arbitrary, owing to the presence of a plateau in Fig. 9b. Thus, it was decided to investigate how the choice of a different value of  $\beta$  affects the predictive capacity of the model. The new value of  $\beta$  was 0.50, which, in Fig. 9b, is outside the plateau region and produces an overestimation of the hydraulic gradient of about 7.5%. In Fig. 10, the CFD results obtained with  $\beta = 0.50$  and  $\sigma = 0.75$  are shown using dotted lines or unfilled points. Similarly to what has been obtained in Section 4.1, changing  $\beta$  did not produce appreciable variations in terms of the concentration profiles and, except for a couple of points, even for the hydraulic gradient. Once again, the lack of influence of  $\beta$  even for the highest concentration observed in Fig. 9 is not inconsistent with the findings of the sensitivity analysis shown in Table 2 and Fig. 4. In fact, this can be explained through a number of reasons, such as: (1) the two values of  $\beta$  in Fig. 9 (0.25 and 0.50)

are quite close to each other and below the range used in the sensitivity analysis (0.5 to 3.5); (2) the horizontal axis in Fig. 10a is much more restricted than that in Fig. 4c; (3) the maximum  $C_{vi}$  in Fig. 10, equal to 34 %, is lower than the maximum  $C_{vi}$  in the sensitivity analysis, equal to 40 %.

### 4.3 Experiments by Schaan et al. (2000) on Lane Mountain sand slurry

In the final verification test, use was made of data reported in Schaan et al. (2000). Among the experiments described in the paper, calculations are directed to those performed in a 158.5 mm pipe using Lane Mountain sand. This type of sand is composed of small grains (median particle size is 90  $\mu\text{m}$ ) with high angularity, which produce significant frictional losses when flowing at high concentration. The density of the particles is the typical value for sand, that is 2655  $\text{kg}/\text{m}^3$ . Hydraulic-gradient data and a few chord-averaged concentration profiles were provided for  $V_m$  between 1 m/s and 5 m/s and three levels of  $C_{vi}$  between about 14 % and about 39 %.

The case  $V_m = 3 \text{ m/s}$  and  $C_{vi} \approx 14 \%$  was considered for determining an appropriate value of  $\sigma$  by imposing the agreement between the calculated and the measured

concentration profile. Based on the obtained results, shown in Fig. 11a, it was chosen to set  $\sigma$  equal to 0.75. Then,  $V_m = 3 \text{ m/s}$  and  $C_{vi} \approx 39 \%$  were used to decide on the  $\beta$  value. The relative deviation from the experimentally determined hydraulic gradient versus  $\beta$ , shown in Fig. 11b, suggests a similar trend to those of the two other test cases, if one considers that the horizontal axis in Fig. 11b is not in log-scale and that the range of  $\beta$  was narrower. The tendency of the points towards some limiting deviation for lower  $\beta$  is evident, which confirms the modelling limitations of the  $\beta$ - $\sigma$  formulation for high concentration. Nonetheless, here it was possible to identify a value of  $\beta$  (that is, 3.75) which fully matches the measured hydraulic gradient. Thus, the coefficients values  $\sigma = 0.75$  and  $\beta = 3.75$  were judged appropriate for Lane Mountain sand flow in a 150 mm pipe, with  $C_{vi}$  between 14 and 39 % (as obtained from the two calibration cases), and  $V_m$  between 1.79 m/s and 10 m/s (as obtained from Eqns. (10) and (9), respectively).

Validation was performed with respect to all other data reported in Schaan et al. (2000) fulfilling the conditions

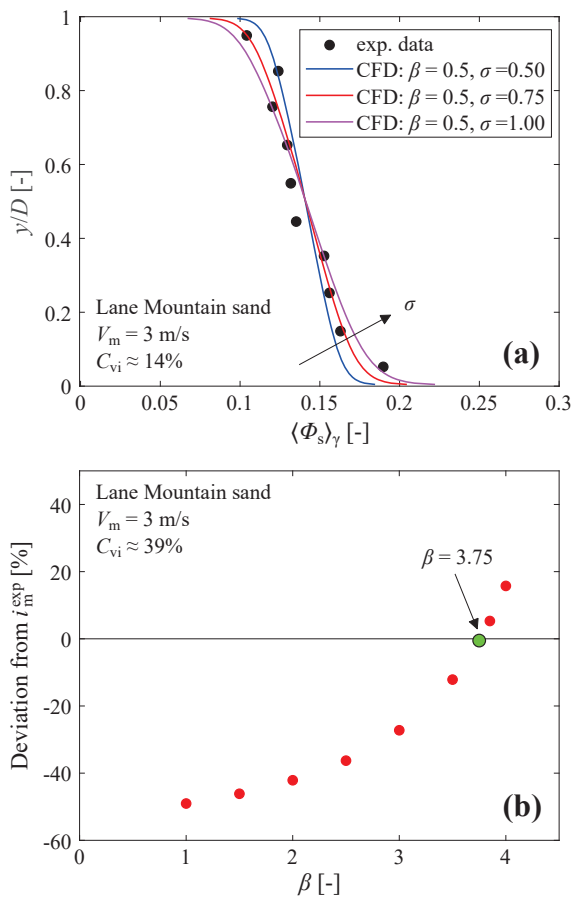


**Fig. 11** Calibration for Lane Mountain sand slurry (data from Schaan et al. 2000): (a) calibration of  $\sigma$  based on the measured concentration profile for  $V_m = 4.24 \text{ m/s}$  and  $C_{vi} = 14 \%$ ; (b) calibration of  $\beta$  based on the measured hydraulic gradient for  $V_m = 3 \text{ m/s}$  and  $C_{vi} = 40 \%$ .

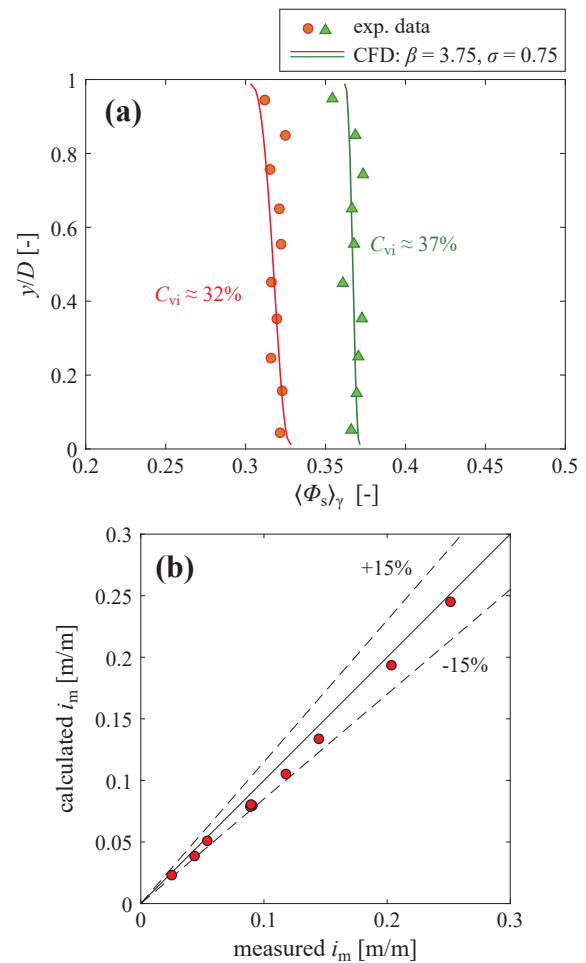


**Fig. 12** Validation of the model with  $\sigma = 0.75$  and  $\beta = 3.75$  for Lane Mountain sand (data from Schaan et al. 2000): (a) exemplary comparison of concentration profiles for  $V_m = 3 \text{ m/s}$ ; (b) parity plot of predicted vs measured hydraulic gradient.

above. The accuracy was satisfactory in terms of both concentration profiles and hydraulic gradient, as shown in **Fig. 12**.

As a final note, the value of  $\beta$  in the third validation example is significantly higher than that of the other two. This might be a consequence of the high angularity of the Lane Mountain sand particles used in the experiments of Schaan et al. (2000). This suggests that, as already guessed in one of the first papers concerning the  $\beta$ - $\sigma$  two-fluid models (Messa and Malavasi, 2015), the parameter  $\beta$  might be related with the effect of particle shape. Nonetheless, a full understanding of the features of the slurry flows dictating the values of  $\beta$  and  $\sigma$  has not been achieved yet, and it will drive the future research efforts of the authors.

## 5. Conclusions and open questions

The present research work marked a step forward in the use of the  $\beta$ - $\sigma$  two-fluid model as an engineering-effective tool with predictive capability. Particularly, the focus was on the analysis of the role played by the two main tuning coefficients of the model, namely,  $\beta$  and  $\sigma$ . The main findings are as follows:

- The value of  $\sigma$  mainly affects the slope of the predicted concentration profile, without any influence on the hydraulic gradient and on the velocity field. The value of  $\beta$  is important for slurries with high in-situ concentration and it affects both the hydraulic gradient and the solid concentration profile, but not the velocity field. The role played by  $\beta$  and  $\sigma$  on the different features of the CFD solution does not depend on flow velocity and pipe diameter.
- A procedure has been proposed for deciding the values of  $\beta$  and  $\sigma$  through experimental calibration. It consists firstly in evaluating  $\sigma$  based on a single concentration profile at low in-situ concentration (say around 10 %), followed by the calculation of an appropriate  $\beta$  based on a single hydraulic gradient point at high slurry concentration (say around 30–40 %). This strategy relies on the negligible effect of  $\beta$  on the solution of the  $\beta$ - $\sigma$  two-fluid model at low slurry concentration.
- The calibration procedure was verified based on experimental data reported in the literature, referring to both glass bead and sand slurry. The validation study indicated some degree of robustness of the calibrated parameters with respect to changes in velocity, particle size, and in-situ concentration. It has also been shown that, although in some cases it might not be possible to find a value of  $\beta$  which fully matches the measured hydraulic gradient for the high concentration calibration case, selecting different values of  $\beta$  within a reasonable range does not affect the overall performance of the  $\beta$ - $\sigma$  two-fluid model. The level of accuracy appears generally satisfactory for the application requirements but it might result in poor predictions for highly concentrated slurries

(in-situ concentration higher than about 35 %).

At the same time, some unresolved issues demand for further research. Two examples are given below.

Firstly, the calibration yielded for  $\sigma = 0.50$  and  $\sigma = 0.75$  intended for the validation tests on glass beads and the two types of sand, respectively. Bearing in mind that no optimum value of  $\sigma$  could be obtained in a strict sense, due to the uncertainty of the local volume fraction measurements, in order to provide a better characterization of  $\sigma$  it would be important to understand the origin of this difference. Is it due to the different material (glass beads versus sand) and/or to the different pipe size (54.9 mm versus 150 mm)? Or do other factors come into play? Similar open questions can be made for  $\beta$ , which appears related with the shape of the particles, but still lacks of a comprehensive characterization.

Additionally, the data in **Figs. 7b, 9b** and **11b**, indicate that, for highly concentrated slurries, the hydraulic gradient is insensitive to  $\beta$  below a certain threshold. This is a limitation of the  $\beta$ - $\sigma$  formulation, which appears incapable of reproducing all the physical mechanisms driving the transport of massive amounts of particles, thus demanding for further improvement. At the moment, the impact of this limitation varies according to the specific testing conditions. In the first two validation examples (glass bead slurry and fine sand slurry), it led to the already mentioned impossibility of finding an optimum  $\beta$  which matches the experimentally determined hydraulic gradient. Indeed, such limiting deviation is more significant for the fine sand case ( $\approx 6$  %, **Fig. 9b**) rather than for the glass bead one ( $< 2.6$  %, **Fig. 7b**), where, however, inaccuracies are observed in terms of the concentration profile (**Fig. 8a**, grey-black series). In the last validation example, which refers to slurry with highly angular particles, a best value of  $\beta$  was identified (**Fig. 11b**) and, based on the available data, the predictions are accurate in terms of both concentration profile and hydraulic gradient (**Fig. 12**).

## Acknowledgements

The research at University of Coimbra was sponsored by national funds through FCT—Fundação para a Ciência e a Tecnologia, under projects UIDB/00102/2020 and UIDB/00285/2020.

## Data Availability Statement

The data analysis file and the data supporting the findings of this study are available in J-STAGE Data (<https://doi.org/10.50931/data.kona.19861708>).

## References

Burns A.D., Frank T., Hamill I., Shi J.-M., The Favre averaged drag model for turbulent dispersion in Eulerian multi-phase flows, in: Proceedings of the 5<sup>th</sup> International Conference on Multiphase Flow (ICMF-2004), Yokohama, Japan, May



- 30–June 4, 2004.
- Capecelatro J., Desjardins O., Eulerian–Lagrangian modeling of turbulent liquid–solid slurries in horizontal pipes, *International Journal of Multiphase Flow*, 55 (2013) 64–79. DOI: 10.1016/j.ijmultiphaseflow.2013.04.006
- CHAM (Concentration, Heat and Momentum Limited), The PHOENICS encyclopaedia, Two-phase flows, 1994a, <www.cham.co.uk/phoenics/d\_polis/d\_lecs/ipsa/ipsa.htm> accessed 24.03.2022.
- CHAM (Concentration, Heat and Momentum Limited), The PHOENICS encyclopaedia, Turbulence models for two-phase flows, 1994b, <www.cham.co.uk/phoenics/d\_polis/d\_enc/turmod/enc\_tu7.htm> accessed 24.03.2022.
- CHAM (Concentration, Heat and Momentum Limited), The PHOENICS encyclopaedia, Equilibrium log-law wall functions, 1994c, <www.cham.co.uk/phoenics/d\_polis/d\_enc/turmod/enc\_tu8.htm> accessed 24.03.2022.
- CHAM (Concentration, Heat and Momentum Limited), PHOENICS Overview: CHAM Technical Report TR001, 2002, <www.cham.co.uk/phoenics/d\_polis/d\_docs/tr001/tr001.htm> accessed 24.03.2022.
- Cheng N.-S., Law A.W.-K., Exponential formula for computing effective viscosity, *Powder Technology*, 129 (2003) 156–160. DOI: 10.1016/S0032-5910(02)00274-7
- Durand R., Basic relationships of the transportation of solids in pipes – experimental research, in: *Proceedings of the 5<sup>th</sup> IAHR Congress*, Minneapolis, Minnesota, USA, 1–5 September 1953.
- Ekambara K., Sanders R.S., Nandakumar K., Masliyah J.H., Hydrodynamic simulation of horizontal slurry pipeline flow using ANSYS-CFX, *Industrial & Engineering Chemistry Research*, 48 (2009) 8159–8171. DOI: 10.1021/ie801505z
- Kaushal D.R., Thinglas T., Tomita Y., Kuchii S., Tsukamoto H., CFD modeling for pipeline flow of fine particles at high concentration, *International Journal of Multiphase Flow*, 43 (2012) 85–100. DOI: 10.1016/j.ijmultiphaseflow.2012.03.005
- Kaushal D.R., Tomita Y., Experimental investigation for near-wall lift of coarser particles in slurry pipeline using  $\gamma$ -ray densitometer, *Powder Technology*, 172 (2007) 177–187. DOI: 10.1016/j.powtec.2006.11.020
- Lauder B.E., Spalding D.B., The numerical computation of turbulent flows, *Computer Methods in Applied Mechanics and Engineering*, 3 (1974) 269–289. DOI: 10.1016/0045-7825(74)90029-2
- Ling J., Skudarnov P.V., Lin C.X., Ebadian M.A., Numerical investigations of liquid–solid slurry flows in a fully developed turbulent flow region, *International Journal of Heat and Fluid Flow*, 24 (2003) 389–398. DOI: 10.1016/S0142-727X(03)00018-3
- Matoušek V., Krupička J., Konfršt J., Pěnik V., Internal structure of settling-slurry flows: solids distribution and friction in horizontal pipe, in: *Proceedings of the 16<sup>th</sup> International Conference on Transport and Sedimentation of Solid Particles*, Rostock, Germany, 18–20 September 2013.
- Matousek V., Pressure drops and flow patterns in sand-mixture pipes, *Experimental Thermal and Fluid Science*, 26 (2002) 693–702. DOI: 10.1016/S0894-1777(02)00176-0
- Messa G.V., Malin M., Malavasi S., Numerical prediction of fully-suspended slurry flow in horizontal pipes, *Powder Technology*, 256 (2014) 61–70. DOI: 10.1016/j.powtec.2014.02.005
- Messa G.V., Malin M., Matoušek V., Parametric study of the  $\beta$ - $\sigma$  two-fluid model for simulating fully suspended slurry flow: effect of flow conditions, *Meccanica*, 56 (2021a) 1047–1077. DOI: 10.1007/s11012-021-01314-6
- Messa G.V., Malavasi S., Improvements in the numerical prediction of fully-suspended slurry flow in horizontal pipes, *Powder Technology*, 270 (2015) 358–367. DOI: 10.1016/j.powtec.2014.10.027
- Messa G.V., Matoušek V., Analysis and discussion of two fluid modelling of pipe flow of fully suspended slurry, *Powder Technology*, 360 (2020) 747–768. DOI: 10.1016/j.powtec.2019.09.017
- Messa G.V., Yang Q., Adedeji O.E., Chára Z., Duarte C.A.R., Matoušek V., Rasteiro M.G., Sanders R.S., Silva R.C., de Souza F.J., Computational fluid dynamics modelling of liquid–solid slurry flows in pipelines: state-of-the-art and future perspectives, *Processes*, 9 (2021b) 1566. DOI: 10.3390/pr9091566
- Roco M.C., Shook C.A., Modeling of slurry flow: the effect of particle size, *The Canadian Journal of Chemical Engineering*, 61 (1983) 494–503. DOI: 10.1002/cjce.5450610402
- Schaan J., Sumner R.J., Gillies R.G., Shook C.A., The effect of particle shape on pipeline friction for Newtonian slurries of fine particles, *The Canadian Journal of Chemical Engineering*, 78 (2000) 717–725. DOI: 10.1002/cjce.5450780414
- Schiller L., Naumann A., A drag coefficient correlation, *Zeitschrift des Vereins Deutscher Ingenieure*, 77 (1935) 318–320.
- Schlichting H., *Boundary-Layer Theory*, 7th ed., McGraw-Hill, New York, 1979, ISBN: 9780070553347.
- Thomas A.D., Predicting the deposit velocity for horizontal turbulent pipe flow of slurries, *International Journal of Multiphase Flow*, 5 (1979) 113–129. DOI: 10.1016/0301-9322(79)90040-5
- Thomas A., A modification of the Wilson & Judge deposit velocity equation, extending its applicability to finer particles and larger pipe sizes, in: *Proceedings of the 17<sup>th</sup> Conference on Transport and Sedimentation of Solid Particles*, Delft, The Netherlands, 22–25 September 2015.
- Uzi A., Levy A., Flow characteristics of coarse particles in horizontal hydraulic conveying, *Powder Technology*, 326 (2018) 302–321. DOI: 10.1016/j.powtec.2017.11.067
- Wilson K.C., A unified physically based analysis of solid-liquid pipeline flow, in: *Proceedings of the 4<sup>th</sup> International Conference on Hydrotransport*, Banff, Canada, 18–21 May 1976.
- Wilson K.C., Addie G.R., Sellgren A., Clift R., *Slurry Transport Using Centrifugal Pumps*, 3rd ed., Springer, New York, 2006, ISBN: 9780387232621.

## Authors' Short Biographies



### Gianandrea Vittorio Messa

Gianandrea Vittorio Messa studied Civil Engineering (Hydraulics) at Politecnico di Milano, where he received the M.Sc. cum laude and the PhD with honors in 2009 and 2013, respectively. Since 2021, he is Associate Professor at Politecnico di Milano, where he teaches courses of Fluid Mechanics and Hydraulics. His main research interest is the numerical modelling of particle-laden flows and related phenomena, such as slurry pipe transport and slurry erosion of pipeline components.



### Qi Yang

Qi Yang is currently a Ph.D. candidate in Civil and Environmental engineering at Politecnico di Milano. His doctoral work is focused on the CFD modelling of slurry flow in pipelines, including development and application of Eulerian-Eulerian two-fluids models.



### Maria da Graça Rasteiro

Maria da Graça Rasteiro graduated in Chemical Engineering at the University of Coimbra, did post graduate studies in Loughborough University, UK, and obtained a PhD in Chemical Engineering/Multiphase Processes, in 1988, at the University of Coimbra, under the co-supervision of Professor Brian Scarlett. She is presently an Associate Professor with Aggregation in the Chemical Engineering Department of the University of Coimbra in Portugal. She is a member of the working groups on Particle Characterization and Particle Mechanics of the European Federation of Chemical Engineering, and is presently a member of the Portuguese Engineers Association and a founding member of the Portuguese Society for Engineering Education (SPEE). Her research interests have always been in the field of Particle Technology and she started the first Portuguese laboratory on particle characterization. Presently, she has got research interests in the field of particle aggregation, development of natural polymers for particle flocculation including microplastics, rheology of particle suspensions, solid/liquid flow modelling including fiber flow modelling, and on experimental techniques for flow visualization including tomographic techniques.



### Pedro M. Faia

Pedro M. Faia received his degree in Electrical Engineering (1990), his M.S. in Automation (1994) and his Ph.D in Electronic Materials (2003) from the University of Coimbra. He is an Auxiliary Professor at the Department of Electrical Engineering and Computers of the University of Coimbra where he teaches. His research interest's concern: chemical and electrochemical sensors; impedance spectroscopy technique and applications; electric and ionic materials characterization; Electrical Impedance Tomography for multiphase flow visualization; Instrumentation.



### Václav Matoušek

Václav Matoušek is Full Professor of Water Engineering and Water Management at Faculty of Civil Engineering of Czech Technical University in Prague. He received the Master Degree in Civil Engineering at this university in 1986 and the PhD in Mechanical (Dredging) Engineering from the Delft University of Technology, the Netherlands, in 1997. His research focuses primarily on two-phase flows with a special attention to pipeline transport of slurries, slurry pumping, rheology of mixtures, flow of rheologically active slurries, sediment transport in open channels and river morphology.

## Authors' Short Biographies



### Rui César Silva

Rui César Silva has a background in chemical engineering from the University of Porto and in 2016 attained his PhD approval from the University of Coimbra, under the theme Solid-liquid suspension flow in pipes: modelling and experimental investigation where the first Portuguese electrical tomography system was successfully constructed. He worked at Hovione Farmaciência, a pharmaceutical CDMO, from 2016 until 2021, acting as technical scientific leader on several projects with topics ranging from particle engineering, hollow-fiber separations, chemical process modelling and data science. During his tenure at this company, he was one of the fastest members to achieve seniority and lead projects to commercialization, through process performance qualification, in record time. He authored several works presented at scientific conferences and served as a tutor on both Master and PhD thesis on hollow-fiber crystallization and particle size reduction technologies. Presently, he works in R&D Process Development and Scale-up at Amyris Portugal.



### Fernando A. P. Garcia

Fernando A. P. Garcia was graduated as a chemical engineer in the Instituto Superior Técnico of the Technical University of Lisbon. He obtained a Master degree in Biological Engineering in Chemical Engineering and then a PhD degree in Chemical Engineering in the University of Birmingham, UK. He started his academic career in the University of Coimbra, first as an assistant demonstrator in the areas of fluid dynamics and transport phenomena. After his doctorate he became an Assistant Professor and later an Associate Professor. Apart from the transport phenomena, his main interests are in the area of biocatalysis and downstream operations of fermentation processes and in treatment of industrial effluents. He is a member of several scientific institutions. He served as secretary of the ESAB, the European Section of Applied Biocatalysis of the European Federation of Biotechnology and later as a member of the Executive Board.

# Evaluation of a Coating Process for SiO<sub>2</sub>/TiO<sub>2</sub> Composite Particles by Machine Learning Techniques<sup>†</sup>

Taichi Kimura<sup>1\*</sup>, Riko Iwamoto<sup>2</sup>, Mikio Yoshida<sup>2</sup>, Tatsuya Takahashi<sup>3</sup>,  
Shuji Sasabe<sup>3</sup> and Yoshiyuki Shirakawa<sup>2\*</sup>

<sup>1</sup> Applied Chemistry, Graduated School of Science and Engineering, Doshisha University, Japan

<sup>2</sup> Department of Chemical Engineering and Materials Science, Faculty of Science and Engineering, Doshisha University, Japan

<sup>3</sup> Hosokawa Micron Corporation, Japan

## Abstract

In this study, in order to optimize a fabrication process for SiO<sub>2</sub>/TiO<sub>2</sub> composite particles and control their coating ratio ( $C_{Ti}$ ), regression models for the coating process were constructed using various machine learning techniques. The composite particles with a core (SiO<sub>2</sub>)/shell (TiO<sub>2</sub>) structure were synthesized by mechanical stress under various fabrication conditions with respect to the supply volume of raw materials ( $V$ ), addition ratio of TiO<sub>2</sub> ( $r_{Ti}$ ), operation time ( $t$ ), rotor rotation speed ( $S$ ), and temperature ( $T$ ). Regression models were constructed by the least squares method (LSM), principal component regression (PCR), support vector regression (SVR), and the deep neural network (DNN) method. The accuracy of the constructed regression models was evaluated using the determination coefficients ( $R^2$ ) and the predictive performance was evaluated by comparing the prediction coefficients ( $Q^2$ ). From the perspective of the  $R^2$  and  $Q^2$  values, the DNN regression model was found to be the most suitable model for the present coating process. Moreover, the effects of the fabrication parameters on  $C_{Ti}$  were analyzed using the constructed DNN model. The results suggested that the  $t$  value was the dominant factor determining  $C_{Ti}$  of the composite particles, with the plot of  $C_{Ti}$  versus  $t$  displaying a clear maximum.

**Keywords:** coated composite particles, machine learning techniques, neural network, coating ratio, SiO<sub>2</sub>/TiO<sub>2</sub>

## 1. Introduction

Composite particles synthesized by compounding techniques have been extensively utilized in various fields (Al-Salihi H.A. et al., 2019; Karger-Kocsis J. et al., 2014; Pierpaoli M. et al., 2019). Since powder properties play a key role in the suitability for a particular application (Kimura T. et al., 2020), selecting the optimal combination of particles is crucial for the performance of the composite particles (Deki Y. et al., 2018). For example, composite particles consisting of oxides, such as SiO<sub>2</sub> and TiO<sub>2</sub>, are utilized in cosmetics and ceramics because of their superior physical properties including optical and electrical properties (Adebisi A.A. et al., 2016; Himoto I. et al., 2016). Consequently, it is necessary to control the powder properties during the fabrication of composite particles.

In the synthesis of composite particles, compounding by mixing and dispersion, which involves convection, shear, and diffusion processes, is extensively applied. These

compounding techniques require a combination of impact, compression, and friction to overcome the aggregation forces. (Kim K. et al., 2016). In many cases of conventional processes using mixers and mechanical compounding machinery, premixing and compounding in other equipment is necessary because the mechanism of mixing of a single device is biased toward convection, shear, or diffusion (Thongnopkoon T. et al., 2018). Several fabrication methods for composite particles have been reported, although achieving control over the powder properties of the particles during the fabrication processes remains challenging owing to the complex relationships between the powder properties and fabrication conditions (Matsuoka Y. et al., 2021). Hence, it is essential to develop methods of predicting these complex relationships to control the powder properties of the composite particles.

Data with complex correlations are often analyzed by statistical and machine learning methods (Kaneko H. and Funatsu K., 2015; Wada S. et al., 2021; Zhao Z. et al., 2018), such as the least-squares method (LSM), principal component regression (PCR), and support vector regression (SVR) (De Backer A. et al., 2021; Tran H. et al., 2018; Zhang Z. et al., 2021). In addition, a deep neural network (DNN) analysis has proved useful in a variety of fields, including agriculture (Cai Y. et al., 2019; Qui Z. et al.,

<sup>†</sup> Received 11 March 2022; Accepted 12 May 2022  
J-STAGE Advance published online 25 June 2022

\* Corresponding Author: Taichi Kimura and Yoshiyuki Shirakawa;

<sup>1,2</sup> Add: 1-3 Tatara-Miyakodani, Kyotanabe, Kyoto 610-0321, Japan  
E-mail: cyjfl702@mail4.doshisha.ac.jp;  
yshiraka@mail.doshisha.ac.jp  
TEL: +81-774-65-6569 FAX: +81-774-6842

2018), environmental studies (Ghatak M.D. and Ghatak A., 2018; Tanzifi M. et al., 2018), and medicine (Basheer I.A. and Hajmeer M., 2000; Horie Y. et al., 2019; Stokes J.M. et al., 2020). DNN analysis is one of the typical machine learning methods and aims to replicate the neural circuits of the human brain by a mathematical model using multiple artificial neurons. A DNN learns by adjusting parameters in the model and can predict complex correlations (Basheer I.A. and Hajmeer M., 2000; Zhang G. et al., 1998).

In previous studies (De Backer A. et al., 2021; Tran H. et al., 2018; Zhang Z. et al., 2021), regression models were constructed to examine the relationships between several explanatory variables and the objective variables using various methods, including LSM, PCR, and SVR, and their predictive performance was improved by considering multiple explanatory variables. For example, Matsuoka et al. (Matsuoka Y. et al., 2021) investigated the relationships between the operating conditions and the physical properties of oral solid dosage tablets during a continuous manufacturing process using a DNN model, which successfully predicted the physical properties of the tablets from the operating conditions with high accuracy. In another study, regression models were constructed to estimate the volume loss of AA7075/Al<sub>2</sub>O<sub>3</sub> composites during wear test at various operating conditions using the LSM, SVR, and DNN methods, and the performance of the machine learning was compared with statistical analysis for this challenging situation involving complex correlations between the explanatory and objective variables (Aydin F., 2021).

In this study, the optimization of prediction techniques for the complex correlation between powder properties and fabrication conditions by constructing regression models using several methods was investigated. Furthermore, parameters affecting the powder properties of SiO<sub>2</sub>/TiO<sub>2</sub> composite particles were analyzed with a focus on the coating ratio ( $C_{Ti}$ ) of the composite particles. The SiO<sub>2</sub>/TiO<sub>2</sub> composite particles were synthesized using a powder processing system (NOB-MINI, HOSOKAWA Micron Co., Japan). Because of the balanced effects of compression, shear, and impact on individual particles, the fabrication apparatus used in this study enables particle design and particle processing, such as compounding, surface modification, and spheronization. To analyze the correlations between the fabrication conditions and  $C_{Ti}$  of the SiO<sub>2</sub>/TiO<sub>2</sub> composite particles, the supply volume ( $V$ ), addition ratio of TiO<sub>2</sub> ( $r_{Ti}$ ), operation time ( $t$ ), rotor rotation speed ( $S$ ), and temperature ( $T$ ) were varied. On the basis of the experimentally determined  $C_{Ti}$  values of the composite particles prepared under various fabrication conditions, regression models for  $C_{Ti}$  of the composite particles were obtained from the machine learning methods. Furthermore, the optimized models were used to predict  $C_{Ti}$  values of the composite particles under various fabrication conditions.

## 2. Experimental and construction methods for regression models

### 2.1 Materials and experimental procedure

The composite particles were prepared from SiO<sub>2</sub> (MT-150W, Tayca Co., Japan), as the core particle and TiO<sub>2</sub> (Silic T-1 (S-1), Yamamori Tsuchimoto Inc., Japan) as the shell particle. The SiO<sub>2</sub> and TiO<sub>2</sub> particles were supplied to the experimental apparatus (NOB-MINI, HOSOKAWA Micron Co., Japan). The supply volume of the raw materials ( $V$ ) and the addition ratio of TiO<sub>2</sub> ( $r_{Ti}$ ) were varied in the ranges of 25–125 mL and 5.0–15.0 wt%, respectively. The operation time ( $t$ ) was set to 1–15 min. The rotation speed ( $S$ ) and temperature ( $T$ ) were set to 2,200–5,700 min<sup>-1</sup> and 295–319 K, respectively. Under all experimental conditions, the electric current was maintained at constant value of 3.5 A. In total, the SiO<sub>2</sub>/TiO<sub>2</sub> composite particles were synthesized under 29 sets of experimental conditions, as summarized in **Table 1**. The surface morphology of the SiO<sub>2</sub>/TiO<sub>2</sub> composite particles was examined by scanning electron microscopy (SEM; SU3500 II; Hitachi High-Tech Science Co., Japan), and the Si and Ti distributions were measured using an energy-dispersive X-ray spectrometer (EDS; Ultim Max, Oxford Instruments Co., Japan) connected to the SEM. The mapping time was set at approximately 120 s. The coating ratio ( $C_{Ti}$ ) of the composite particles was calculated according to Eqn. (1) from the integrated areas of Si ( $S_{Si}$ ) and Ti ( $S_{Ti}$ ) in the elemental mapping images by using imaging software (WinROOF; Mitani Corp., Japan):

$$C_{Ti} = \frac{S_{Ti}}{S_{Si} + S_{Ti}} \quad (1)$$

### 2.2 Construction of regression model

The regression models were constructed as described in **Sections 2.2.1–2.2.4**. The fabrication parameters ( $V$ ,  $r_{Ti}$ ,  $t$ ,  $S$ , and  $T$ ) were employed as the explanatory variables to serve as the input values.  $C_{Ti}$  was chosen as the objective variable to serve as the output value. The 29 samples were split into training to construct the regression models (21 samples) and test data to evaluate the predictive performance of the constructed models (8 samples). The input and output values ( $z$ ) were auto-scaled by following

**Table 1** Summary of fabrication conditions for the SiO<sub>2</sub>/TiO<sub>2</sub> composite particles.

Experimental condition	
Supply volume ( $V$ ) [mL]	25–125
Addition ratio of Ti ( $r_{Ti}$ ) [wt%]	5.0–15.0
Operation time ( $t$ ) [min]	1–15
Rotation speed ( $S$ ) [min <sup>-1</sup> ]	2,200–5,700
Temperature ( $T$ ) [K]	295–319

Eqn (2):

$$z' = \frac{z - \mu}{\sigma} \tag{2}$$

where  $z'$  denotes the auto-scaled value, and  $\mu$  and  $\sigma$  represent the mean and standard deviation of each explanatory variable, respectively.

The determination coefficient ( $R^2$ ) was used to evaluate the accuracy of the regression models constructed from the training data. The predictive performance of the constructed models was assessed by calculating the predictive coefficient ( $Q^2$ ) using the test data. The root mean square error (RMSE) for each model was also calculated. The formulas used to calculate the  $R^2$ ,  $Q^2$ , and RMSE are given in Eqns. (3)–(5):

$$R^2 = 1 - \frac{\sum_{i=1}^n (y_i^{\text{calc.}} - y_i)^2}{\sum_{i=1}^n (y_{\text{mean}} - y_i)^2} \tag{3}$$

$$Q^2 = 1 - \frac{\sum_{i=1}^n (y_i^{\text{pred.}} - y_i)^2}{\sum_{i=1}^n (y_{\text{mean}} - y_i)^2} \tag{4}$$

$$\text{RMSE} = \sqrt{\frac{1}{n} \sum_{i=1}^n (y_i^{\text{calc.,pred.}} - y_i)^2} \tag{5}$$

where  $y_i$ ,  $y_i^{\text{calc.}}$ , and  $y_i^{\text{pred.}}$  represent the experimental value, the calculated value using the training data, and the predicted value using the test data, respectively, the subscript  $i$  denotes the  $i$ -th sample, and  $y_{\text{mean}}$  is the average of the experimental values.

The  $R^2$  value indicates the accuracy of model construction because it expresses the degree of agreement between the experimental values and the calculated values when training data are substituted into the models constructed from training data. Meanwhile, the  $Q^2$  value reflects the degree of agreement between the experimental values and the predicted values when test data are substituted into the models constructed from training data. The maximum value for both  $R^2$  and  $Q^2$  is 1.0, and values closer to 1.0 indicate a higher quality model. The RMSE has a positive value and is used to evaluate errors in the numerical prediction, where a smaller value indicates superior predictive performance (Barrasso D. et al., 2015).

### 2.2.1 Least-squares method (LSM)

LSM modeling is a construction method that involves determining the coefficients ( $\beta_{\text{LSM}}$ ) that minimize the sum-of-squares error ( $S_{\text{LSM}}$ ) between calculated values ( $y^{\text{calc.}}$ ) and experimental values ( $y$ ). When the numbers of samples and explanatory variables are  $m$  and  $n$ , respectively, the vector of error ( $\epsilon_{\text{LSM}}$ ),  $\beta_{\text{LSM}}$ ,  $y$ , and matrix of explanatory variables ( $X$ ) can be expressed as shown in Eqns. (6)–(9):

$$\epsilon_{\text{LSM}} = \begin{pmatrix} \epsilon_{\text{LSM}, 1} \\ \epsilon_{\text{LSM}, 2} \\ \vdots \\ \epsilon_{\text{LSM}, m} \end{pmatrix} \tag{6}$$

$$\beta_{\text{LSM}} = \begin{pmatrix} \beta_{\text{LSM}}^{(1)} \\ \beta_{\text{LSM}}^{(2)} \\ \vdots \\ \beta_{\text{LSM}}^{(n)} \end{pmatrix} \tag{7}$$

$$y = \begin{pmatrix} y_1 \\ y_2 \\ \vdots \\ y_m \end{pmatrix} \tag{8}$$

$$X = \begin{pmatrix} x_1^{(1)} & x_1^{(2)} & \dots & x_1^{(n)} \\ x_2^{(1)} & x_2^{(2)} & \dots & x_2^{(n)} \\ \vdots & \vdots & \ddots & \vdots \\ x_m^{(1)} & x_m^{(2)} & \dots & x_m^{(n)} \end{pmatrix} \tag{9}$$

Furthermore, the  $y^{\text{calc.}}$  and  $y$  vectors are given by Eqns. (10) and (11), respectively:

$$y^{\text{calc.}} = X\beta_{\text{LSM}} \tag{10}$$

$$y = X\beta_{\text{LSM}} + \epsilon_{\text{LSM}} \tag{11}$$

Because smaller errors between the  $y^{\text{calc.}}$  and  $y$  vectors were desired, the  $\beta_{\text{LSM}}$  vector minimizing the  $S_{\text{LSM}}$  matrix, which is determined by the square sum of the  $\epsilon_{\text{LSM}}$  vector, was sought by partial differentiation of Eqn. (11), to afford the relationship shown in Eqn. (12):

$$X^T X \beta_{\text{LSM}} = X^T y \tag{12}$$

Furthermore, when the inverse matrix of the  $X^T X$  matrix was multiplied from the left of both sides of Eqn. (12), the  $\beta_{\text{LSM}}$  vector was optimized as shown in Eqn. (13), thus constructing the LSM model:

$$\beta_{\text{LSM}} = (X^T X)^{-1} X^T y \tag{13}$$

For simple relationships, such as linear and quadratic functions consisting of a small number of parameters serving as explanatory variables, the LSM is a suitable method. Because the order of the explanatory variables was set to 1, the LSM model constructed in this study is a liner regression.

### 2.2.2 Principal component regression (PCR)

PCR modeling is a construction method in which explanatory variables are transformed into principal components that are uncorrelated with each other. The algorithm for PCR model construction consists of the following two steps (Hotelling H., 1957).

In the first step, principal component analysis (PCA) is conducted. When the score vector ( $t_{\text{PCR}}$ ) is defined as

a linear combination of the  $X$  matrix, the  $t_{\text{PCR}}$  vector is obtained as described by Eqn. (14):

$$t_{\text{PCR}} = Xp_{\text{PCR}} \quad (14)$$

where  $p_{\text{PCR}}$  is the weight of the linear combination, which is referred to as loading.

Because PCA is performed by maximization of the score, the sum-of-squares score ( $S_{\text{PCA}}$ ) is maximized by using the Lagrange multiplier ( $G_{\text{PCR}}$ ) expressed in Eqn. (15):

$$G_{\text{PCR}} = S_{\text{PCA}} - \lambda \left( \sum_{j=1}^n ((p_j)^2 - 1) \right) \\ = \sum_{i=1}^m (t_i)^2 - \lambda \left( \sum_{j=1}^n ((p_j)^2 - 1) \right) \quad (15)$$

where  $j$  represents the number of explanatory variables.  $n$  is the number of solutions of the equation represented by the  $\lambda$  value. The  $t_{\text{PCR}}$  vector with the  $n$ -th largest variance of  $\lambda$  is defined as the  $n$ -th principal component, and the principal component matrix ( $T$ ) is given by Eqn. (16):

$$T = \begin{pmatrix} t_{\text{PCR},1}^{(1)} & t_{\text{PCR},2}^{(1)} & \cdots & t_{\text{PCR},n}^{(1)} \\ t_{\text{PCR},1}^{(2)} & t_{\text{PCR},2}^{(2)} & \cdots & t_{\text{PCR},n}^{(2)} \\ \vdots & \vdots & \ddots & \vdots \\ t_{\text{PCR},1}^{(m)} & t_{\text{PCR},2}^{(m)} & \cdots & t_{\text{PCR},n}^{(m)} \end{pmatrix} \quad (16)$$

The PCR model was constructed by adopting the  $T$  matrix as the explanatory variables in a similar manner as described for LSM in Section 2.2.1, and the relationship between the output variables and the feature components was optimized by varying the number of principal components ( $N_{\text{PC}}$ ) within the range of 1–5.

For processes with a correlation between the explanatory variables, the PCR method is considered the optimal selection because the impact of explanatory variables with dependent relationships on the accuracy of the regression model is reduced.

### 2.2.3 Support vector regression (SVR)

An SVR model is constructed using a support vector machine (SVM) for regression analysis. In SVR modeling, a kernel trick along with SVM is applied to construct nonlinear models. The original form of the SVR minimizes the matrix ( $S_{\text{SVR}}$ ) shown in Eqn. (17), which is related to the vectors of error and coefficient in SVR:

$$S_{\text{SVR}} = \frac{1}{2} \|\mathbf{w}\|^2 + C \sum_{i=1}^N |y_i - f(\mathbf{x}_i)|_\varepsilon \quad (17)$$

where  $f$  and  $\mathbf{w}$  denote the SVR model and a weight vector, respectively,  $\varepsilon$  is a threshold,  $C$  is a penalty term that controls the trade-off between the model complexity and training errors, and  $N$  is the number of training data. The second term of Eqn. (17) is the  $\varepsilon$ -insensitive loss function, as defined in Eqn. (18):

$$|y_i - f(\mathbf{x}_i)|_\varepsilon = \max(0, |y_i - f(\mathbf{x}_i)| - \varepsilon) \quad (18)$$

Minimization of Eqn. (17) affords a regression model with a satisfactory balance between generalization capability and ability to adapt to training data. When an  $\mathbf{x}$  vector is inputted, a  $y$  value is predicted by Eqn. (19):

$$y = f(\mathbf{x}) = \sum_{i=1}^N (\alpha_i - \alpha_i^*) K(\mathbf{x}_i, \mathbf{x}) + u_{\text{SVR}} \quad (19)$$

where  $K$  is a kernel function, and  $u_{\text{SVR}}$  is a constant. As the kernel function for this study, the radial basis function kernel given by Eqn. (20) was adopted:

$$K(\mathbf{x}_i, \mathbf{x}) = \exp(-\gamma (\|\mathbf{x}_i - \mathbf{x}\|)^2) \quad (20)$$

where  $\gamma$  represents a turning parameter for controlling the width of the kernel function, and  $\alpha_i$  and  $\alpha_i^*$  in Eqn. (19) are obtained from Eqns. (17) and (18) by minimizing the Lagrange multiplier ( $G_{\text{SVR}}$ ), as expressed in Eqn. (21):

$$G_{\text{SVR}} = \frac{1}{2} \sum_{i=1}^N \sum_{j=1}^N K_{ij} (\alpha_i - \alpha_i^*) (\alpha_j - \alpha_j^*) \\ - \sum_{i=1}^N y_i (\alpha_i - \alpha_i^*) + \varepsilon \sum_{i=1}^N (\alpha_i - \alpha_i^*) \quad (21)$$

and the  $\alpha_i$  and  $\alpha_i^*$  values are subject to

$$\begin{cases} 0 \leq \alpha_i \\ \alpha_j^* \leq C \end{cases} \quad i = 1, 2, \dots, N \quad (22)$$

$$\sum_{i=1}^N (\alpha_i - \alpha_i^*) = 0 \quad (23)$$

and  $K_{ij}$  in Eqn. (21) is

$$K_{ij} = K(\mathbf{x}_i, \mathbf{x}_j) \quad (24)$$

In SVR modeling, the hyperparameters ( $C$ ,  $\varepsilon$ , and  $\gamma$  values) have to be set beforehand. The hyperparameters were selected by a comprehensive grid search (Kaneko H. and Funatsu K. et al., 2013).

The SVR method is suitable when it is necessary to construct a regression model to predict processes involving nonlinearities and negligible error ranges.

### 2.2.4 Deep neural network (DNN)

A neural network (NN) model is constructed by optimizing the hyperparameters, such as the numbers of hidden layers ( $N_{\text{H.L.}}$ ) and neurons ( $N_{\text{Neur.}}$ ), the activation function, and the number of learning times ( $N_{\text{L.T.}}$ ). An NN with an  $N_{\text{H.L.}}$  greater than two is referred to as a DNN. In this study, the  $N_{\text{H.L.}}$  and  $N_{\text{Neur.}}$  values were each varied in the range of 1–10. As the activation functions, the sigmoid function, tanh function, and rectified linear unit (ReLU) function were compared. The sigmoid function has a long history as an activation function for NN models. The tanh function has been reported to learn faster than the sigmoid function

(Ismail H.Y. et al., 2019; Shirazian S. et al., 2017). In recent years, the ReLU function has seen increasing use because of several advantages such as reduced gradient vanishing and faster calculation (Roggo Y. et al., 2020). The sigmoid function, tanh function, and ReLU function are expressed in Eqns. (25), (26), and (27), respectively:

$$h(x) = \frac{1}{1 + e^{-x}} \quad (25)$$

$$h(x) = \frac{e^x - e^{-x}}{e^x + e^{-x}} \quad (26)$$

$$h(x) = \begin{cases} x & (x > 0) \\ 0 & (x \leq 0) \end{cases} \quad (27)$$

In all cases, the stochastic gradient descent method was adopted as the optimization method.  $N_{L.T.}$  was varied in the range of 30–3,500. The hyperparameters are summarized in **Table 2**.

For systems in which the explanatory variables and objective variables are intricately related, the DNN method is an appropriate selection.

**Table 2** Summary of the hyperparameter ranges used to optimize the DNN method.

Parameter	
Number of hidden layers ( $N_{H.L.}$ ) [-]	1–10
Number of neurons ( $N_{Neur.}$ ) [-]	1–10
Activation function	Sigmoid Hyperbolic tangent Rectified linear unit
Loss function	Mean square error
Optimization method	Stochastic gradient descent
Learning times ( $N_{L.T.}$ ) [-]	30–3,500

### 3. Results and discussion

#### 3.1 Fabrication of SiO<sub>2</sub>/TiO<sub>2</sub> composite particles

To investigate the effects of the fabrication conditions on  $C_{Ti}$  of the SiO<sub>2</sub>/TiO<sub>2</sub> composite particles, the particles were synthesized under 29 sets of conditions by varying the values of  $V$  (25–125 mL),  $r_{Ti}$  (5.0–15.0 wt%),  $t$  (1–15 min),  $S$  (2,200–5,700 min<sup>-1</sup>), and  $T$  (295–319 K).  $V$ ,  $r_{Ti}$ ,  $t$ ,  $S$ , and  $T$  were set to include the maximum and minimum values within the operable range of experimental manipulations. The SEM and EDS images of the SiO<sub>2</sub>/TiO<sub>2</sub> composite particles for  $t$  values of 1 and 10 min are shown in **Fig. 1** to demonstrate the surface morphology and the state of the TiO<sub>2</sub> coating on the SiO<sub>2</sub> particles. The  $V$  and  $r_{Ti}$  values were 25 mL and 5.0 wt%, respectively. The  $S$  and  $T$  values were varied with an increase in the  $t$  value. From the EDS observations, the  $C_{Ti}$  values of the composite particles were calculated using Eqn. (1). The data obtained from the fabrication experiments are listed in **Table 3**. In addition, the data subjected to auto-scaling using Eqn. (2) are listed in **Table 4**. During the construction of the regression models using the machine learning methods, data from 21 of the fabrication experiments were used as training data. The data from the remaining eight fabrication experiments were used as test data to evaluate the predictive performance of the constructed models.

#### 3.2 Model construction using machine learning methods

The regression models were constructed using four machine learning methods, namely, LSM, PCR, SVR, and DNN. Regression analysis was performed to predict  $C_{Ti}$  of the SiO<sub>2</sub>/TiO<sub>2</sub> composite particles depending on the values of  $V$  (25–125 mL),  $r_{Ti}$  (5.0–15.0 wt%),  $t$  (1–15 min),  $S$  (2,200–5,700 min<sup>-1</sup>), and  $T$  (295–319 K), which were input as explanatory variables.  $C_{Ti}$  of the composite particles was set as the objective variable to serve as the output value. The accuracy of the constructed regression models with

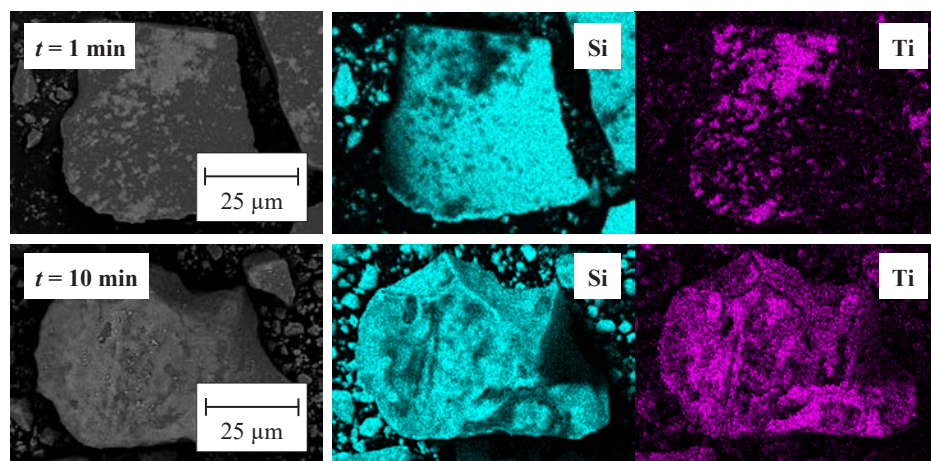


**Fig. 1** SEM and EDS images of the SiO<sub>2</sub>/TiO<sub>2</sub> composite particles obtained at  $t$  values of 1 min and 10 min.



**Table 3** Experimental data for the relationship between the fabrication conditions and  $C_{Ti}$  of the composite particles.

Run	$V$ [mL]	$r_{Ti}$ [wt%]	$t$ [min]	$S$ [min <sup>-1</sup> ]	$T$ [K]	$C_{Ti}$ [%]
1	25	5.0	1	5,500	295	34.6
2	25	5.0	3	5,600	316	57.1
3	25	5.0	5	5,500	308	35.2
4	25	5.0	10	5,600	317	40.5
5	25	5.0	15	5,700	317	41.0
6	50	5.0	10	3,500	305	44.5
7	50	5.0	15	3,500	306	35.5
8	100	5.0	10	2,500	302	37.1
9	100	5.0	15	2,500	303	45.7
10	50	10.0	10	3,700	307	39.5
11	50	10.0	15	3,700	308	42.5
12	100	10.0	10	2,600	303	46.7
13	100	10.0	15	2,600	304	45.1
14	75	5.0	10	2,800	304	52.7
15	75	5.0	15	2,800	304	36.2
16	125	5.0	10	2,200	301	61.5
17	125	5.0	15	2,200	301	40.0
18	100	5.0	3	2,500	310	34.7
19	100	5.0	5	2,500	313	37.6
20	100	5.0	10	2,500	315	39.6
21	100	10.0	3	2,600	312	43.6
22	100	10.0	5	2,600	315	53.1
23	100	10.0	10	2,600	316	53.0
24	100	15.0	3	2,800	315	49.3
25	100	15.0	5	2,800	317	57.2
26	100	15.0	10	2,700	319	63.9
27	50	15.0	3	3,800	319	59.8
28	50	15.0	5	3,800	315	52.1
29	50	15.0	10	3,800	316	63.8

respect to the training data was evaluated by calculating the  $R^2$  values according to Eqn. (3), and the predictive performances of the constructed models with respect to the test data were compared using the  $Q^2$  values calculated from Eqn. (4). The errors of the regression models were evaluated by calculating the RMSE values according to Eqn. (5).

### 3.2.1 Construction of the LSM model

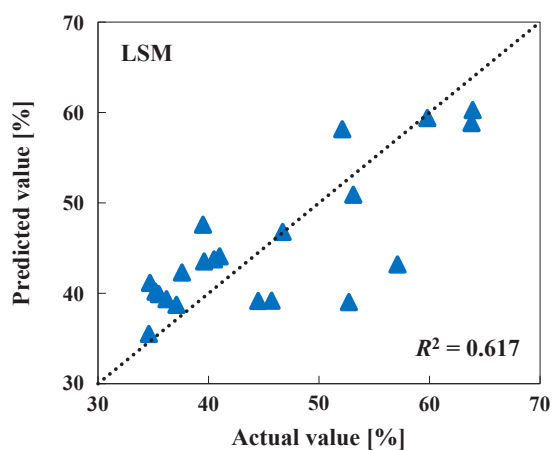
The LSM model represents the relationship between the explanatory variables and objective variable (Stojanovic B. et al., 2016). When the order of the explanatory variables is 1, as in this study, the relationship derived by the LSM is linear. Thus, the regression model constructed by the LSM according to Eqns. (6)–(13) is expressed in Eqn. (28):

$$C_{Ti}' = 0.0669V' + 0.616r_{Ti}' + 0.0215t' + 0.0532S' + 0.242T' \quad (28)$$

where  $V'$ ,  $r_{Ti}'$ ,  $t'$ ,  $S'$ , and  $T'$  denote the auto-scaled values of each fabrication parameter and  $C_{Ti}'$  is the auto-scaled value of  $C_{Ti}$  of the SiO<sub>2</sub>/TiO<sub>2</sub> composite particles. Hence the coefficients in Eqn. (28) reflect the influence of the corresponding parameter on  $C_{Ti}$  of the composite particles. All of the coefficients were positive, indicating that increasing the value of each fabrication parameter increased  $C_{Ti}$  of the composite particles. Furthermore, the contribution of each parameter to  $C_{Ti}$  of the composite particles was calculated by comparing the absolute values of the coefficients. The contributions of the parameters decreased in the following order:  $r_{Ti}$  (61.6 %) >  $T$  (24.2 %) >  $V$  (6.69 %) >  $S$

**Table 4** Auto-scaled data for the relationship between the fabrication conditions and  $C_{Ti}$  of the composite particles.

Run	$V$ [mL]	$r_{Ti}$ [wt%]	$t$ [min]	$S$ [min <sup>-1</sup> ]	$T$ [K]	$C_{Ti}$ [%]
1	-1.55	-0.82	-1.74	1.91	-2.24	-1.28
2	-1.55	-0.82	-1.30	2.00	0.96	1.18
3	-1.55	-0.82	-0.85	1.91	-0.34	-1.21
4	-1.55	-0.82	0.26	2.00	1.05	-0.63
5	-1.55	-0.82	1.37	2.08	1.07	-0.58
6	-0.78	-0.82	0.26	0.12	-0.74	-0.20
7	-0.78	-0.82	1.37	0.12	-0.52	-1.18
8	0.78	-0.82	0.26	-0.77	-1.20	-1.01
9	0.78	-0.82	1.37	-0.77	-1.10	-0.07
10	-0.78	0.43	0.26	0.30	-0.46	-0.75
11	-0.78	0.43	1.37	0.30	-0.20	-0.42
12	0.78	0.43	0.26	-0.68	-1.06	0.05
13	0.78	0.43	1.37	-0.68	-0.86	-0.13
14	0.00	-0.82	0.26	-0.50	-0.89	0.70
15	0.00	-0.82	1.37	-0.50	-0.86	-1.11
16	1.55	-0.82	0.26	-1.04	-1.32	1.66
17	1.55	-0.82	1.37	-1.04	-1.30	-0.69
18	0.78	-0.82	-1.30	-0.77	-0.02	-1.27
19	0.78	-0.82	-0.85	-0.77	0.43	-0.95
20	0.78	-0.82	0.26	-0.77	0.84	-0.74
21	0.78	0.43	-1.30	-0.68	0.41	-0.30
22	0.78	0.43	-0.85	-0.68	0.79	0.74
23	0.78	0.43	0.26	-0.68	0.98	0.73
24	0.78	1.68	-1.30	-0.50	0.76	0.33
25	0.78	1.68	-0.85	-0.50	1.16	1.19
26	0.78	1.68	0.26	-0.59	1.37	1.92
27	-0.78	1.68	-1.30	0.39	1.41	1.47
28	-0.78	1.68	-0.85	0.39	0.84	0.64
29	-0.78	1.68	0.26	0.39	1.02	1.91


**Fig. 2** Relationship between the actual and predicted  $C_{Ti}$  values for the LSM regression model.

(5.32 %) >  $t$  (2.15 %).

The relationship between the actual  $C_{Ti}$  values obtained from the experimental data and the calculated values obtained from the LSM regression model is presented in **Fig. 2**. The input values were 0.617 and 5.99 %, respectively. In general, the accuracy of a constructed regression model increases as the  $R^2$  value approaches 1.0 and the RMSE value decreases. The low  $R^2$  value was attributed to the features of LSM.

The correlation represented by the LSM is a linear variation of  $C_{Ti}$  of the composite particles with respect to five fabrication parameters (Arioli M. and Gratton S., 2012; Zhang Y. and Fearn T., 2015). Thus, when the correlation between the fabrication parameters and  $C_{Ti}$  of the composite particles is not linear, this nonlinear relationship cannot

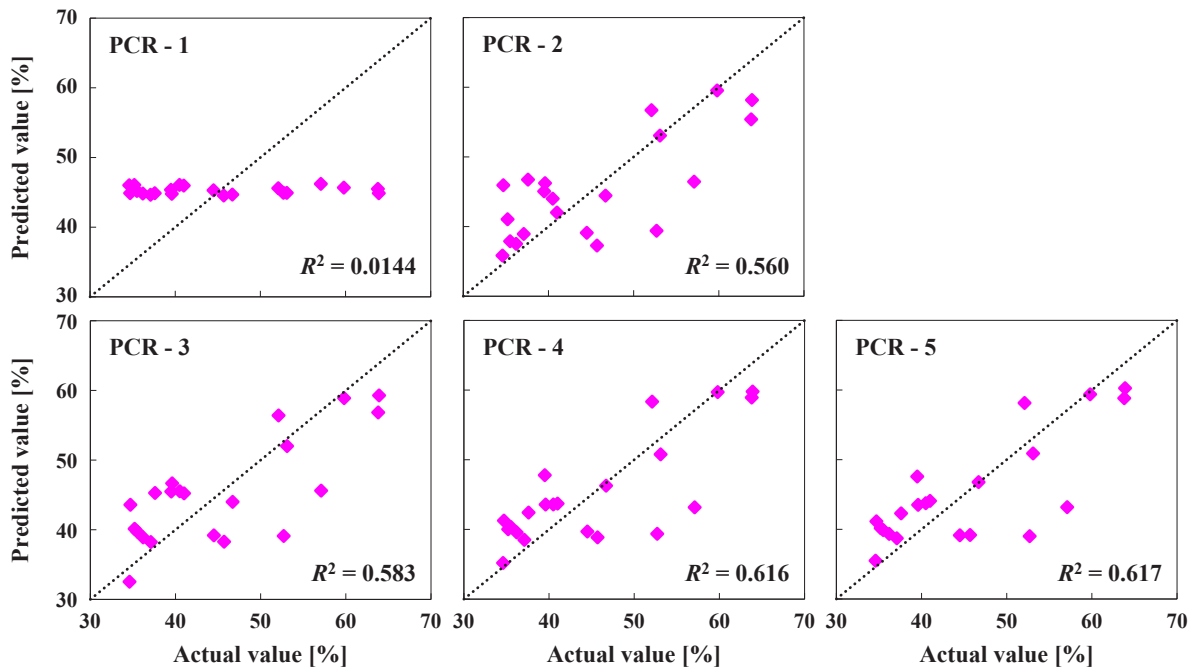


Fig. 3 Actual and predicted  $C_{Ti}$  values for the PCR regression model with various  $N_{PC}$  values.

be adequately expressed by a regression model based on the LSM (Arioli M. and Gratton S., 2012; Zhang Y. and Fearn T., 2015). Moreover, if the fabrication parameters are highly related to each other, the coefficients in Eqn. (28) could be anomalous owing to instability in the analytical calculations and the inaccuracy of the regression equation (Arioli M. and Gratton S., 2012; Zhang Y. and Fearn T., 2015).

### 3.2.2 Construction of the PCR model

In an effort to deal with the inaccuracy and instability of the regression model due to the correlation between the fabrication parameters as described in Section 3.2.1, the parameters were converted to principal components uncorrelated with each other by using PCA as expressed in Eqns. (14) and (15). Because the fabrication parameters highly related to each other were removed in advance, this allowed for prediction of  $C_{Ti}$  of the composite particles by a combination of fabrication parameters with low correlation (El Ghaziri A. and Qannari E.M., 2015).

The number of principal components ( $N_{PC}$ ) was varied within the range of 1–5, and the relationship between the actual  $C_{Ti}$  values obtained from the experimental data and the calculated values obtained from the PCR regression models for different  $N_{PC}$  values are presented in Fig. 3. The  $R^2$  values for each regression model are also indicated. When the data points are closer to the dotted line of  $y = x$  in the plots, the  $R^2$  values for the PCR regression models approach 1.0. Because the  $R^2$  values increased with increasing  $N_{PC}$ , all five of principal components were applied to the construction of the PCR regression model.

Table 5 Hyperparameters used in the SVR regression model.

$C$	$2^{-5}, 2^{-4}, \dots, 2^9, 2^{10}$	16 candidates
$\varepsilon$	$2^{-15}, 2^{-14}, \dots, 2^{-1}, 2^0$	16 candidates
$\gamma$	$2^{-20}, 2^{-19}, \dots, 2^9, 2^{10}$	31 candidates

The PCR regression model constructed with  $N_{PC}$  of 5 is expressed in Eqn. (29):

$$C_{Ti} = 0.635t_{PCR,1} + 0.249t_{PCR,2} + 0.0690t_{PCR,3} + 0.0549t_{PCR,4} + 0.0221t_{PCR,5} \quad (29)$$

where  $t_{PCR,i}$  represents the  $i$ -th principal component obtained by PCA. The effects of the principal components on  $C_{Ti}$  of the composite particles are expressed by each coefficient. The obtained  $R^2$  and RMSE values were 0.617 and 5.99 %, respectively. The fact that all of the principal components were applied to the construction of the regression model implies that the correlation between each fabrication parameter prior to PCR processing was not strong (El Ghaziri A. and Qannari E.M., 2015).

When all of the principal components were used to construct the regression model, the values calculated from the PCR regression model were identical to those calculated from the LSM model, because the application of the last principal component means that any effect of the fabrication parameters was not removed. Hence, the contribution of any correlation between the fabrication parameters to the low accuracy of the LSM regression model discussed in Section 3.2.1 was small. Thus, in an attempt to improve the accuracy of the regression models, we next considered the possibility of a nonlinear correlation between the

fabrication parameters and  $C_{Ti}$  of the composite particles.

### 3.2.3 Construction of SVR model

To consider a nonlinear correlation between the fabrication parameters and  $C_{Ti}$  of the composite particles, a regression model was constructed using SVR according to Eqns. (17)–(24). Regression models using SVR are constructed by minimizing the structural risk. The hyperparameters ( $C$ ,  $\varepsilon$ , and  $\gamma$ ) of the SVR model were optimized by adapting the comprehensive combination from the candidates listed in **Table 5** by exploring hyperparameters with maximum  $R^2$  values in verification results. The  $C$ ,  $\varepsilon$ , and  $\gamma$  values in the optimized SVR model were  $2^{-5}$ ,  $2^0$ , and  $2^{-2}$ , respectively.

The relationship between the actual  $C_{Ti}$  values obtained from the experimental data and the calculated values obtained from the SVR regression model is shown in **Fig. 4**. The  $R^2$  and RMSE values were 0.591 and 5.80 %, respectively. The former value is slightly lower than that obtained for the LSM model (0.617), indicating a lower accuracy. In contrast, the RMSE value was slightly smaller for the SVR model, indicating a high accuracy.

This comparison based on the  $R^2$  and RMSE values suggests that the SVR and LSM models had similar accuracy. Thus, under the conditions of this study, consideration

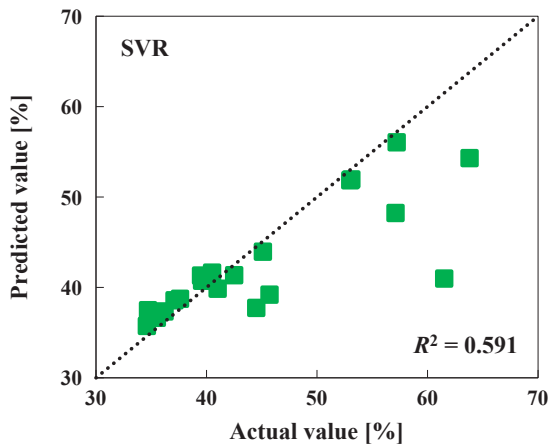


**Fig. 4** Relationship between the actual and predicted  $C_{Ti}$  values for the SVR regression model.

of the possibility of a nonlinear correlation between the fabrication parameters and  $C_{Ti}$  of the composite particles resulted in little change in the accuracy of the regression model. Therefore, we next considered the possibility of more complex correlations between the fabrication parameters and  $C_{Ti}$  of the composite particles.

### 3.2.4 Construction of DNN model

To consider more complex correlations between the fabrication parameters and  $C_{Ti}$  of the composite particles, a regression model was constructed using a DNN. For this model, the hyperparameters ( $N_{H.L.}$ ,  $N_{Neur.}$ , activation function and  $N_{L.T.}$ ) were optimized by exploring which hyperparameters afford the highest  $R^2$  values in the verification results.

The variation of the  $R^2$  values with  $N_{H.L.}$ ,  $N_{Neur.}$ , and  $N_{L.T.}$  is plotted in **Fig. 5**. In the case of  $N_{H.L.}$ , as shown in **Fig. 5a**), the  $R^2$  values were almost constant for  $N_{H.L.}$  values in the ranges of 1–5 layers and 6–10 layers but increased slightly when  $N_{H.L.}$  was increased from 5 layers to 6 layers. This increase in the  $R^2$  values with an increase in  $N_{H.L.}$  from 5 layers to 6 layers is caused by improved fit of the relation between the fabrication parameters and  $C_{Ti}$  of the composite particles. In the case of  $N_{Neur.}$ , as shown in **Fig. 5b**), the  $R^2$  values tended to increase with increasing  $N_{Neur.}$  in the range of 1–6 neurons, after which the  $R^2$  values remained almost constant irrespective of  $N_{Neur.}$ . This increase in the  $R^2$  values with increasing  $N_{Neur.}$  in the range of 1–6 neurons is caused by improved fit of the relation between the fabrication parameters and  $C_{Ti}$  of the composite particles. The minimal variation of the  $R^2$  values in the  $N_{Neur.}$  range of 6–10 neurons was attributable to the sufficiently good fit at the  $N_{Neur.}$  of 6 neurons. Finally,  $N_{L.T.}$  was varied in the range of 30–3,500 times. As shown in **Fig. 5c**), the  $R^2$  values rapidly increased as  $N_{L.T.}$  was increased from 30 to 700 times. Then, as  $N_{L.T.}$  was increased from 700 to 1,500 times, the  $R^2$  values increased more gradually. At  $N_{L.T.}$  values above 1,500, the  $R^2$  values remained almost constant irrespective of  $N_{L.T.}$ . Comparison of various activation functions revealed that the tanh afforded the highest  $R^2$  value, as

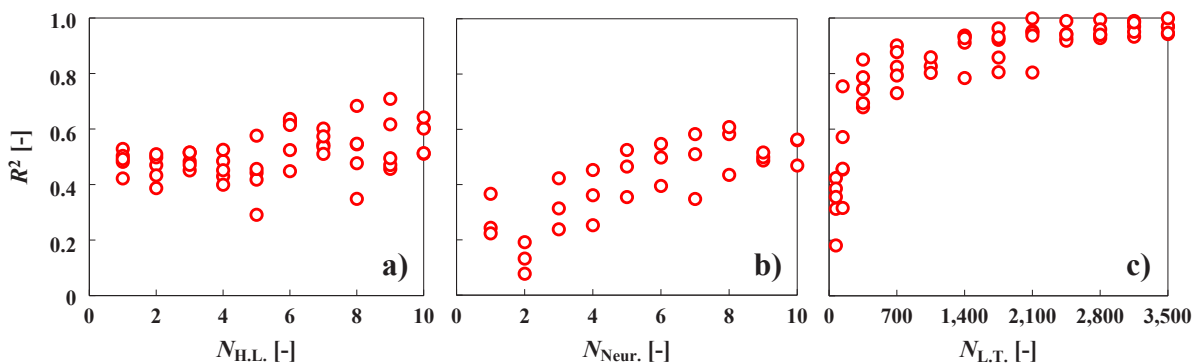


**Fig. 5**  $R^2$  values with variation in a)  $N_{H.L.}$ , b)  $N_{Neur.}$ , and c)  $N_{L.T.}$  for optimizing the DNN regression model.

summarized in **Table 6**. Hence, the optimized hyperparameters for the DNN regression model were an  $N_{H.L.}$  of six layers, an  $N_{Neur.}$  of six neurons, an  $N_{L.T.}$  of 1,500 times, and a tanh activation function.

The relationship between the actual  $C_{Ti}$  values obtained from the experimental data and the calculated values obtained from the DNN regression model is plotted in **Fig. 6**. The  $R^2$  and RMSE values were 0.941 and 2.19 %, respectively. Comparison of the results obtained for the DNN, LSM, and SVR regression models revealed that the DNN model displayed the highest accuracy, as indicated by its high  $R^2$  value and low RMSE value.

**Table 6** Relationship between the  $R^2$  values and activation functions for optimizing the DNN regression model.

Activation function	$R^2$ [-]
Sigmoid	0.0294
tanh	0.596
ReLU	0.152

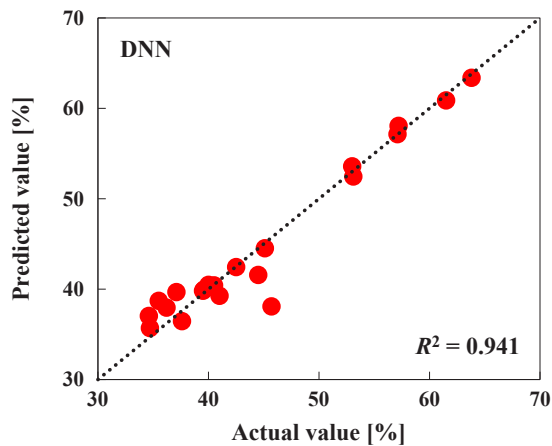


**Fig. 6** Relationship between the actual and predicted  $C_{Ti}$  values for the DNN regression model.

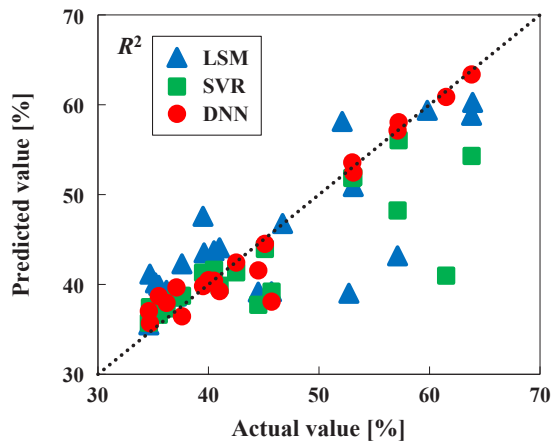


**Fig. 7** Comparison of the accuracy of the various regression models by  $R^2$  values based on the training data.

### 3.3 Comparison of constructed models

The LSM, PCR, SVR, and DNN regression models were used to predict  $C_{Ti}$  of the  $\text{SiO}_2/\text{TiO}_2$  composite particles under various fabrication conditions based on the test data. Moreover, the predictive performances of the constructed models were evaluated by comparison of their  $Q^2$ -values.

The relationship between the actual  $C_{Ti}$  values obtained from the experimental data and the calculated values obtained from the LSM, SVR, and DNN models for the training data are plotted in **Fig. 7**. Furthermore, to verify the predictive performances of the constructed models, the relationships between the actual  $C_{Ti}$  values obtained from the experimental data and the predicted values obtained from the three models for the test data are shown in **Fig. 8**. The results for the PCR regression model are excluded from these plots because they were identical to those obtained from the LSM model. The horizontal and vertical axes show the actual values obtained from the experimental data and the predicted values calculated from the training data or test data, respectively. The  $R^2$  and  $Q^2$  values become closer to 1.0 as the data points approach the dotted line of  $y = x$  in the plots. The  $R^2$  and  $Q^2$  values for each regression model are summarized in **Table 7**, along with the RMSE values for the training data ( $\text{RMSE}_{\text{train}}$ ) and test data ( $\text{RMSE}_{\text{test}}$ ).

Comparison of the  $R^2$  values for the three regression models revealed that the DNN model had the highest accuracy. Similarly, the DNN model displayed the highest  $Q^2$  value, indicating the best predictive performance. For

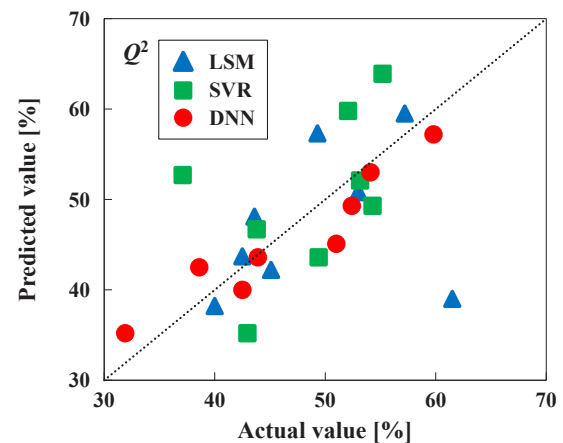


**Fig. 8** Comparison of the predictive performance of the various regression models by  $Q^2$  values based on the test data.

**Table 7** Summary of the  $R^2$ ,  $Q^2$ , and RMSE values for the various regression models.

	$R^2$ [-]	$\text{RMSE}_{\text{train}}$ [%]	$Q^2$ [-]	$\text{RMSE}_{\text{test}}$ [%]
LSM	0.617	5.99	-0.510	9.28
SVR	0.591	5.80	0.280	7.97
DNN	0.941	2.19	0.767	3.26

a regression model with high accuracy and predictive performance, higher  $R^2$  and  $Q^2$  values are required (Gurgenc T. et al., 2020). The high  $R^2$  and  $Q^2$  values of 0.941 and 0.767 obtained for the DNN regression model in this study demonstrate the successful construction of a regression model with high accuracy and predictive performance for estimating  $C_{Ti}$  of  $SiO_2/TiO_2$  composite particles. The RMSE values for the training data and test data were 2.19 % and 3.26 %, respectively. The average  $C_{Ti}$  of the  $SiO_2/TiO_2$  composite particles in the experimental data was 46.3 %. In comparison, the RMSE values for the training and test data were sufficiently small. Thus, the construction of a regression model for predicting  $C_{Ti}$  of  $SiO_2/TiO_2$  composite particles under various fabrication conditions was successfully realized by using the DNN method.

The DNN regression model displayed the highest accuracy in this study because the DNN method considers more complex correlations between explanatory variables and objective variables, including nonlinearities, by varying  $N_{H.L.}$  and  $N_{Neur.}$ . The LSM regression model attempts to predict the  $C_{Ti}$  values by calculating a formula based on simple relationships involving the explanatory variables. Meanwhile, the PCR regression model has similar features to the LSM model because the main difference between the two methods is the replacement of explanatory variables with principal components. The SVR regression model is constructed by using explanatory variables converted to support vectors by processing with kernel functions. Because the support vectors of SVR models are used in the same manner as the principal components of PCR models, SVR models possess similar characteristics to LSM and PCR models. Therefore, the constructed SVR regression model also predicted the  $C_{Ti}$  values from a calculation formula involving only simple relationships. In contrast, the application of the DNN method to construct a regression model leads to predictions based on complex correlations between the explanatory variables and objective variables because of the numerous hidden layers and neurons inherent to this approach.

### 3.4 Analyzing the effects of fabrication conditions on $C_{Ti}$ of $SiO_2/TiO_2$ composite particles by the DNN regression model

The DNN regression model was applied to analyze the relationship between the fabrication conditions and  $C_{Ti}$  of the  $SiO_2/TiO_2$  composite particles. The application range of the DNN regression model with respect to the five fabrication parameters was  $V = 25\text{--}125$  mL,  $r_{Ti} = 5.0\text{--}15.0$  wt%,  $t = 1\text{--}15$  min,  $S = 2,200\text{--}5,700$   $\text{min}^{-1}$ , and  $T = 295\text{--}320$  K. Each fabrication parameter serving as an input value was divided into 20 points over the corresponding range, and  $C_{Ti}$  of the  $SiO_2/TiO_2$  composite particles was predicted using the DNN regression model.

The calculated effects of the fabrication parameters on

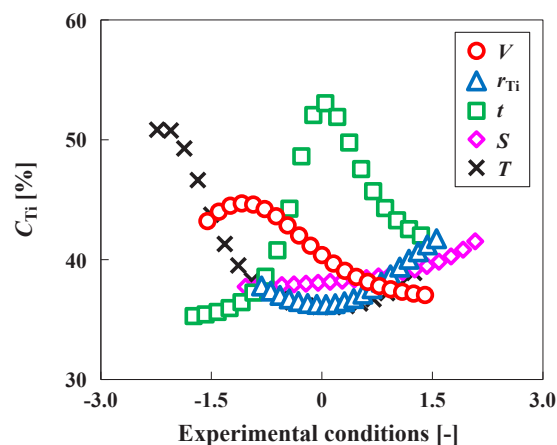


**Fig. 9** Calculated effects of the fabrication parameters on  $C_{Ti}$  of the composite particles.

$C_{Ti}$  of the  $SiO_2/TiO_2$  composite particles are plotted in **Fig. 9**. Comparison of the resulting curves revealed that the maximum gradients decreased in the following order:  $t > T > V > r_{Ti} > S$ . Because a higher gradient indicates a larger influence of the fabrication parameter on  $C_{Ti}$  of the composite particles, these results suggest that the effects of the fabrication parameters on  $C_{Ti}$  decrease in the same order. The  $V$ ,  $r_{Ti}$ ,  $t$ ,  $S$  and  $T$  values under the base condition when varying each parameter were 100 mL, 5.0 wt%, 5 min, 2,500  $\text{min}^{-1}$ , and 303 K, respectively.

The plot of  $C_{Ti}$  versus  $t$  revealed a clear maximum.  $C_{Ti}$  of the composite particles initially increased with increasing  $t$  owing to the gradual coating of  $TiO_2$  onto  $SiO_2$  over time. However, at higher  $t$  values,  $C_{Ti}$  of the composite particles decreased as a result of exfoliation of the surface coating.

Upon varying  $T$ ,  $C_{Ti}$  of the composite particles markedly decreased with increasing  $T$  in the low- $T$  range then remained almost constant with increasing  $T$  in the high  $T$  range. These findings suggest that lower  $T$  values are beneficial for enhancing  $C_{Ti}$  of  $SiO_2/TiO_2$  composite particles.

The variation of  $V$  initially had little effect on  $C_{Ti}$  of the composite particles, which remained almost constant with increasing  $V$  in the low- $V$  range. At higher values of  $V$ ,  $C_{Ti}$  of the composite particles decreased with increasing  $V$ , which was ascribed to a decrease in the contact frequency per single particle.

Examining of the relationship between  $r_{Ti}$  and  $C_{Ti}$  of the composite particles revealed that  $C_{Ti}$  slightly decreased with increasing  $r_{Ti}$  at lower  $r_{Ti}$  values. However, at higher  $r_{Ti}$  values,  $C_{Ti}$  increased with increasing  $r_{Ti}$ , which was attributed to the increased proportion of  $TiO_2$  particles with respect to  $SiO_2$ .

Finally, upon increasing  $S$ ,  $C_{Ti}$  of the composite particles slightly increased. This was ascribed to the progress of coating  $TiO_2$  onto  $SiO_2$ .

## 4. Conclusion

In this study, SiO<sub>2</sub>/TiO<sub>2</sub> composite particles with different  $C_{Ti}$  values were synthesized under various conditions ( $V$ ,  $r_{Ti}$ ,  $t$ ,  $S$ , and  $T$ ). To optimize the fabrication process of SiO<sub>2</sub>/TiO<sub>2</sub> composite particles, regression models were constructed to predict  $C_{Ti}$  of the composite particles using the LSM, PCR, SVR, and DNN approaches. Furthermore, the regression model with the highest accuracy and predictive performance was employed to analyze the effects of the fabrication parameters on  $C_{Ti}$  of the SiO<sub>2</sub>/TiO<sub>2</sub> coated composite particles. The obtained results can be summarized as follows:

- 1) SiO<sub>2</sub>/TiO<sub>2</sub> composite particles were fabricated by coating TiO<sub>2</sub> onto SiO<sub>2</sub> at various  $V$ ,  $r_{Ti}$ ,  $t$ ,  $S$ , and  $T$  values.
- 2) Comparison of the constructed regression models with respect to the training data revealed that the DNN regression model displayed the highest accuracy.
- 3) Comparison of the constructed regression models with respect to the test data indicated that the DNN regression model exhibited the best predictive performance.
- 4) Analysis of the effects of the fabrication parameters on  $C_{Ti}$  of the SiO<sub>2</sub>/TiO<sub>2</sub> composite particles using the DNN regression model revealed that  $t$  was the most influential factor governing  $C_{Ti}$  of the SiO<sub>2</sub>/TiO<sub>2</sub> composite particles.

## Acknowledgement

This study was financially supported by the HOSOKAWA Powder Technology Foundation (No. 20502), Osaka, Japan.

## References

- Adebisi A.A., Maleque M.A., Ali M.Y., Bello K.A., Effect of variable particle size reinforcement on mechanical and wear properties of 6061Al–SiCp composite, *Composite Interfaces*, 23 (2016) 533–547. DOI: 10.1080/09276440.2016.1167414
- Al-Salihi H.A., Mahmood A.A., Alalkawi H.J., Mechanical and wear behavior of AA7075 aluminum matrix composites reinforced by Al<sub>2</sub>O<sub>3</sub> nanoparticles, *Nanocomposites*, 5 (2019) 67–73. DOI: 10.1080/20550324.2019.1637576
- Arioli M., Gratton S., Linear regression models, least-squares problems, normal equations, and stopping criteria for the conjugate gradient method, *Computer Physics Communications*, 183 (2012) 2322–2336. DOI: 10.1016/j.cpc.2012.05.023
- Aydin F., The investigation of the effect of particle size on wear performance of AA7075/Al<sub>2</sub>O<sub>3</sub> composites using statistical analysis and different machine learning methods, *Advanced Powder Technology*, 32 (2021) 445–463. DOI: 10.1016/j.apt.2020.12.024
- De Backer A., Becquart C.S., Olsson P., Domain C., Modelling the primary damage in Fe and W: influence of the short-range interactions on the cascade properties: Part 2 – multivariate multiple linear regression analysis of displacement cascades, *Journal of Nuclear Materials*, 549 (2021) 152887. DOI: 10.1016/j.jnucmat.2021.152887
- Barrasso D., El Hagrasy A., Litster J.D., Ramachandran R., Multi-dimensional population balance model development and validation for a twin screw granulation process, *Powder Technology*, 270 (2015) 612–621. DOI: 10.1016/j.powtec.2014.06.035
- Basheer I.A., Hajmeer M., Artificial neural networks: fundamentals, computing, design, and application, *Journal of Microbiological Methods*, 43 (2000) 3–31. DOI: 10.1016/S0167-7012(00)00201-3
- Cai Y., Guan K., Lobell D., Potgieter A.B., Wang S., Peng J., Xu T., Asseng S., Zhang Y., You L., Peng B., Integrating satellite and climate data to predict wheat yield in Australia using machine learning approaches, *Agricultural and Forest Meteorology*, 274 (2019) 144–159. DOI: 10.1016/j.agrformet.2019.03.010
- Deki Y., Kadota K., Onda S., Tozuka Y., Shimosaka A., Yoshida M., Shirakawa Y., Crystallization behavior of glycine molecules with electrolytic dissociation on charged silica gel particles, *Chemical Engineering & Technology*, 41 (2018) 1073–1079. DOI: 10.1002/ceat.201700398
- Ghatak M.D., Ghatak A., Artificial neural network model to predict behavior of biogas production curve from mixed lignocellulosic co-substrates, *Fuel*, 232 (2018) 178–189. DOI: 10.1016/j.fuel.2018.05.051
- El Ghaziri A., Qannari E.M., A continuum standardization of the variables. Application to principal components analysis and PLS-regression, *Chemometrics and Intelligent Laboratory Systems*, 148 (2015) 95–105. DOI: 10.1016/j.chemolab.2015.09.008
- Gurgenc T., Altay O., Ulas M., Ozel C., Extreme learning machine and support vector regression wear loss predictions for magnesium alloys coated using various spray coating methods, *Journal of Applied Physics*, 127 (2020) 185103. DOI: 10.1063/5.0004562
- Himoto I., Yamashita S., Kita H., Design of heat emission controlled spherical container constructed with skeletal ceramic units based on heat transfer analysis, *Journal of Chemical Engineering of Japan*, 49 (2016) 850–863. DOI: 10.1252/jcej.15we122
- Horie Y., Yoshio T., Aoyama K., Yoshimizu S., Horiuchi Y., Ishiyama A., Hirasawa T., Tsuchida T., Ozawa T., Ishihara S., Kumagai Y., Fujishiro M., Maetani I., Fujisaki J., Tada T., Diagnostic outcomes of esophageal cancer by artificial intelligence using convolutional neural networks, *Gastrointestinal Endoscopy*, 89 (2019) 25–32. DOI: 10.1016/j.gie.2018.07.037
- Hotelling H., The relations of the newer multivariate statistical methods to factor analysis, *British Journal of Statistical Psychology*, 10 (1957) 69–79. DOI: 10.1111/j.2044-8317.1957.tb00179.x
- Ismail H.Y., Singh M., Darwish S., Kuhs M., Shirazian S., Croker D.M., Khraisheh M., Albadarin A.B., Walker G.M., Developing ANN-Kriging hybrid model based on process parameters for prediction of mean residence time distribution in twin-screw wet granulation, *Powder Technology*, 343 (2019) 568–577. DOI: 10.1016/j.powtec.2018.11.060
- Kaneko H., Funatsu K., Nonlinear regression method with variable region selection and application to soft sensors, *Chemometrics and Intelligent Laboratory Systems*, 121 (2013) 26–32. DOI: 10.1016/j.chemolab.2012.11.017
- Kaneko H., Funatsu K., Fast optimization of hyperparameters for support vector regression models with highly predictive ability, *Chemometrics and Intelligent Laboratory Systems*, 142 (2015) 64–69. DOI: 10.1016/j.chemolab.2015.01.001
- Kim K., Kim J., Core-shell structured BN/PPS composite film for high thermal conductivity with low filler concentration, *Composites Science and Technology*, 134 (2016) 209–216. DOI: 10.1016/j.compscitech.2016.08.024

- Kimura T., Wada Y., Kamei S., Shirakawa Y., Hiaki T., Matsumoto M., Synthesis of  $\text{CaMg}(\text{CO}_3)_2$  from concentrated brine by  $\text{CO}_2$  fine bubble injection and conversion to inorganic phosphor, *Journal of Chemical Engineering of Japan*, 53 (2020) 555–561. DOI: 10.1252/jcej.20we034
- Karger-Kocsis J., Bárány T., Single-polymer composites (SPCs): status and future trends, *Composites Science and Technology*, 92 (2014) 77–94. DOI: 10.1016/j.compscitech.2013.12.006
- Matsuoka Y., Ohsaki S., Nakamura H., Watano S., Analysis of continuous manufacturing process of oral solid dosage using neural network, *Journal of the Society of Powder Technology, Japan*, 58 (2021) 414–423. DOI: 10.4164/sptj.58.414
- Pierpaoli M., Zheng X., Bondarenko V., Fava G., Ruello M.L., Paving the way for a sustainable and efficient  $\text{SiO}_2/\text{TiO}_2$  photocatalytic composite, *Environments*, 6 (2019) 87–98. DOI: 10.3390/environments6080087
- Qui Z., Chen J., Zhao Y., Zhu S., He Y., Zhang C., Variety identification of single rice seed using hyperspectral imaging combined with convolutional neural network, *Applied Sciences*, 8 (2018) 212. DOI: 10.3390/app8020212
- Roggo Y., Jelsch M., Heger P., Ensslin S., Krumme M., Deep learning for continuous manufacturing of pharmaceutical solid dosage form, *European Journal of Pharmaceutics and Biopharmaceutics*, 153 (2020) 95–105. DOI: 10.1016/j.ejpb.2020.06.002
- Shirazian S., Kuhs M., Darwish S., Croker D., Walker G.M., Artificial neural network modelling of continuous wet granulation using a twin-screw extruder, *International Journal of Pharmaceutics*, 521 (2017) 102–109. DOI: 10.1016/j.ijpharm.2017.02.009
- Stojanović B., Babić M., Veličković S., Blagojević J., Tribological behavior of aluminum hybrid composites studied by application of factorial techniques, *Tribology Transactions*, 59 (2016) 522–529. DOI: 10.1080/10402004.2015.1091535
- Stokes J.M., Yang K., Swanson K., Jin W., Cubillos-Ruiz A., Donghia N.M., MacNair C.R., French S., Carfrae L.A., Bloom-Ackermann Z., Tran V.M., Chiappino-Pepe A., Badran A.H., Andrews I.W., Chory E.J., et al., A deep learning approach to antibiotic discovery, *Cell*, 180 (2020) 688–702.e613. DOI: 10.1016/j.cell.2020.01.021
- Tanzifi M., Yarak M.T., Kiadehi A.D., Hosseini S.H., Olazar M., Bharti A.K., Agarwal S., Gupta V.K., Kazemi A., Adsorption of Amido Black 10B from aqueous solution using polyani-line/ $\text{SiO}_2$  nanocomposite: Experimental investigation and artificial neural network modeling, *Journal of Colloid and Interface Science*, 510 (2018) 246–261. DOI: 10.1016/j.jcis.2017.09.055
- Thongnopkoon T., Chittasupho C., Curcumin composite particles prepared by spray drying and in vitro anti-cancer activity on lung cancer cell line, *Journal of Drug Delivery Science and Technology*, 45 (2018) 397–407. DOI: 10.1016/j.jddst.2018.04.006
- Tran H., Kim J., Kim D., Choi M., Choi M., Impact of air pollution on cause-specific mortality in Korea: results from Bayesian model averaging and principle component regression approaches, *Science of The Total Environment*, 636 (2018) 1020–1031. DOI: 10.1016/j.scitotenv.2018.04.273
- Wada S., Kagatani S., Nakagami H., Quantitative estimation of intra-subject variability in bioequivalence studies of generic solid oral dosage forms by multiple regression analysis, *Journal of Drug Delivery Science and Technology*, 64 (2021) 102656. DOI: 10.1016/j.jddst.2021.102656
- Zhang G., Eddy Patuwo B., Y. Hu M., Forecasting with artificial neural networks: the state of the art, *International Journal of Forecasting*, 14 (1998) 35–62. DOI: 10.1016/S0169-2070(97)00044-7
- Zhang Y., Fearn T., A linearization method for partial least squares regression prediction uncertainty, *Chemometrics and Intelligent Laboratory Systems*, 140 (2015) 133–140. DOI: 10.1016/j.chemolab.2014.11.011
- Zhang Z., Ding S., Sun Y., MBSVR: Multiple birth support vector regression, *Information Sciences*, 552 (2021) 65–79. DOI: 10.1016/j.ins.2020.11.033
- Zhao Z., Wang J., Sun B., Arowo M., Shao L., Mass transfer study of water deoxygenation in a rotor–stator reactor based on principal component regression method, *Chemical Engineering Research and Design*, 132 (2018) 677–685. DOI: 10.1016/j.cherd.2018.02.007

## Authors' Short Biographies



### Taichi Kimura

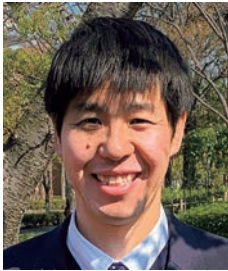
Taichi Kimura is a Ph.D. student at Doshisha University since 2020. He received his Bachelor and Master of Engineering degrees from Nihon University in 2017 and 2020, respectively. His research interests are analysis and design of particle fabrication processes using machine learning.

### Riko Iwamoto

Riko Iwamoto received her Bachelor of Engineering from Doshisha University in 2022. Her research interests were composite particle synthesis by mechano-chemical processes and materials designs using data science. She works for a company involved in data analysis since 2022.



## Authors' Short Biographies



**Mikio Yoshida**

Dr. Mikio Yoshida has been a Professor at Doshisha University since 2022. He received his Ph.D. degree from Doshisha University in 2005. After that, he worked as a post-doctoral researcher at Okayama University. He was employed as an Assistant Professor of Okayama University in 2007, and as an Associate Professor of Doshisha University in 2016. He was a scientific committee member of the 9th World Congress on Particle Technology (WCPT9) 2022 in Madrid, Spain. He has been an editorial board member of *Advanced Powder Technology* since 2017.



**Tatsuya Takahashi**

He received his Bachelor of Engineering degree, and Master of Engineering in Physics from Kwansei Gakuin University, Japan in 2013, and 2015, respectively. From 2015, he works Institute of Powder Engineering and ICT Digital Promotion Division, Hosokawa Micron Co., Ltd., Japan. His research topics cover area in semiconductor materials engineering technology, powder analysis technology.



**Shuji Sasabe**

Shuji Sasabe is a Division Manager of ICT Digital Promotion Division of Hosokawa Micron Corp. He received Master's degree in electrical engineering from Nippon Institute of Technology, Japan in 1991. He has been engaged in research on powder processing and powder characterization, and has been involved in the development of many powder characterization instruments. He is engaged in the promotion of Digital transformation.



**Yoshiyuki Shirakawa**

Dr. Yoshiyuki Shirakawa is a Professor at Doshisha University. He received his Ph.D. in 1993 from Niigata University. He started an academic carrier at Niigata University as a post-doctoral student for JSPS Research Fellowship Sciences in 1993 and worked at Osaka and Doshisha Universities. His research interests are composite particle synthesis by crystallization and mechano-chemical processes and materials designs using computer simulations.

# On the Similarity of Austin Model and Kotake–Kanda Model and Implications for Tumbling Ball Mill Scale-Up †

Ecevit Bilgili

*Otto H. York Department of Chemical and Materials Engineering, New Jersey Institute of Technology, USA*

## Abstract

The aim of this theoretical investigation is to seek any similarities between the Austin model and the Kotake–Kanda (KK) model for the specific breakage rate function in the population balance model (PBM) used for tumbling ball milling and assess feasibility of the KK model for scale-up. For both models, the limiting behavior for small particle size-to-ball size ratio and the extremum behavior for a given ball size are described by “power-law.” Motivated by this similarity, specific breakage rate data were generated using the Austin model parameters obtained from the lab-scale ball milling of coal and fitted by the KK model successfully. Then, using the Austin’s scale-up methodology, the specific breakage rate was scaled-up numerically for various mill diameter scale-up ratios and ball sizes of 30–49 mm and coal particle sizes of 0.0106–30 mm. PBM simulations suggest that the KK model predicts identical evolution of the particle size distribution to that by the Austin model prior to scale-up. Upon scale-up, the differences are relatively small. Hence, modification of the exponents in the Austin’s scale-up methodology is not warranted for scale-up with the KK model. Overall, this study has established the similarity of both models for simulation and scale-up.

**Keywords:** ball milling, breakage, population balances, Austin model, Kotake model, scale-up

## 1. Introduction

Tumbling ball mills have been commonly used in a multitude of industries, especially the minerals industry (Austin et al., 1984). Population balance modeling (PBM) enables engineers to simulate, design, control, and scale-up various particulate processes (Randolph and Larson, 1988; King, 2001), including the tumbling ball milling (Austin et al., 1984; Prasher, 1987). The size-discrete, time-continuous form of the PBM (Sedlatschek and Bass, 1953) for a well-mixed ball mill operating in batch mode is expressed as

$$\frac{dM_i}{dt} = -S_i M_i + \sum_{j=1}^{i-1} b_{ij} S_j M_j \quad \text{with } M_i(0) = M_{i,\text{ini}} \quad (1)$$

where  $i$  and  $j$  are the size-class indices running up to  $N_s$  (sink size class). Here,  $t$ ,  $M_i$ ,  $S_i$ , and  $b_{ij}$  represent time, mass fraction, specific breakage rate parameter, and breakage distribution parameter, respectively. Eqn. (1) also assumes first-order (linear) breakage kinetics and has been successfully used for simulating the milling of a wide variety of materials in different types of mills (Austin et al., 1984; King, 2001). Readers are referred to Bilgili and Scarlett (2005) and Capece et al. (2011) for an extensive review and a PBM framework for treatment of nonlinear breakage

kinetics.

It has been experimentally well-established that  $S_i$  varies significantly with design and operating conditions for a given material to be ground in ball mills (Austin et al., 1984). The celebrated Austin model describes how  $S_i$  varies as a function of particle size  $x_i$ :

$$S_i = a_T x_i^\alpha \frac{1}{1 + (x_i/\mu_T)^\Lambda} \quad (2)$$

Here,  $a_T$  and  $\mu_T$  are parameters that strongly depend on the milling conditions, the material, and the ball size, whereas  $\alpha$  and  $\Lambda$  are positive constants that largely depend on the properties of the material. Austin et al. (2007) assert that  $\Lambda$  can be satisfactorily taken as 3 for most materials. Some researchers assumed  $\Lambda = 3$  (e.g., Bwalya et al., 2014) or fitted  $\Lambda$  to find it within  $\pm 10\%$  of this value (Rogers et al., 1986; Petrakis et al., 2017); yet others found notably different values: 4.74 (Chimwani et al., 2013) and 2.4 (Shahcheraghi et al., 2019). Traditionally, these parameters have been estimated via either direct calculation of  $S_i$  by one-size-fraction method (Austin and Bhatia, 1971–72) or the optimization-based back-calculation method (Klimpel and Austin, 1977) using experimental data from small or pilot scale ball mills. As balls are an integral element of the ball mill design, the impact of ball size  $d_b$  on  $a_T$  and  $\mu_T$  has been extensively studied (Austin et al., 1976a; 1984; Katubilwa and Moys, 2009). The Austin model can be recast into the following form with explicit ball size dependence (e.g., Katubilwa and Moys, 2009, with slight

† Received 14 February 2022; Accepted 1 March 2022  
 J-STAGE Advance published online 23 April 2022  
 Add: Newark, NJ 07102, USA  
 E-mail: bilgece@njit.edu  
 TEL: +1-973-596-2998 FAX: +1-973-596-8436

differences in formalism):

$$S_i = a_0 x_i^\alpha \frac{(d_{B,0}/d_B)^\zeta}{1 + [x_i/(\mu_0 (d_B/d_{B,0})^\eta)]^A} \quad (3)$$

where  $a_0$  and  $\mu_0$  are the values of  $a_T$  and  $\mu_T$  for specific ball size  $d_{B,0}$  in the small/pilot scale batch milling experiments, while  $\eta$  and  $\zeta$  are constant ball-size exponents. For a mixture of balls, the specific breakage rate is calculated from the mass fraction of each ball size  $M_{B,p}$  and its corresponding  $S_{i,p}$  as follows:

$$\bar{S}_i = \sum_{p=1}^P M_{B,p} S_{i,p} \quad (4)$$

Scale-up of tumbling ball mills from small-scale batch mills to industrial scale mills has been successfully implemented within the context of PBM (Austin et al., 1984; Yildirim et al., 1999; Chimwani et al., 2014; De Oliveira and Tavares, 2018). In this approach, empirical equations are used for determining the dependence of the breakage parameters on ball/mill dimensions and operating variables at the lab-scale and large-scale industrial mills. It is important to emphasize that scale-up from a batch mill to continuous large-scale mills entails modification of the breakage parameters ( $S_i$  and  $b_{ij}$ ) as well as consideration of the residence time distribution and internal–external classification in the continuous mills (Herbst and Fuerstenau, 1980; Austin et al., 1984; Rogers and Austin, 1984; De Oliveira and Tavares 2018). Although each one of these aspects is important, this study focuses on the scale-up of the specific breakage rate  $S_i$ .

Upon scale-up,  $S_i$  is known to change significantly, whereas  $b_{ij}$  or its cumulative counterpart  $B_{ij}$  is generally assumed to remain invariant unless ball size/type changes significantly (Herbst and Fuerstenau, 1980; Austin et al., 1984). In accounting for scale-up related changes, the Austin’s methodology scales-up  $S_i$  in Eqn. (2) via correction factors  $K_1$ – $K_5$  that depend on the design parameters of the dry ball mill and operating conditions as follows:

$$S_i^* = a_T x_i^\alpha \frac{1}{1 + [x_i/(K_1 \mu_T)]^A} K_2 K_3 K_4 K_5 \quad (5)$$

$$K_1 = \left(\frac{D}{D_T}\right)^{N_2} \left(\frac{d_B}{d_{B,T}}\right)^{N_3}, K_2 = \left(\frac{d_{B,T}}{d_B}\right)^{N_0} \quad (6)$$

$$K_3 = \begin{cases} \left(\frac{D}{D_T}\right)^{N_1} & \text{if } D \leq 3.81 \text{ m} \\ \left(\frac{3.81}{D_T}\right)^{N_1} \left(\frac{D}{3.81}\right)^{N_1-N_4} & \text{if } D > 3.81 \text{ m} \end{cases} \quad (7)$$

$$K_4 = \frac{1 + 6.6J_T^{2.3}}{1 + 6.6J^{2.3}} \exp[-1.2(U - U_T)] \quad (8)$$

$$K_5 = \left(\frac{\phi_C - 0.1}{\phi_{C,T} - 0.1}\right) \left\{ \frac{1 + \exp[15.7(\phi_{C,T} - 0.94)]}{1 + \exp[15.7(\phi_C - 0.94)]} \right\} \quad (9)$$

where  $D$ ,  $J$ ,  $U$ , and  $\phi_C$  denote the mill diameter, the fractional mill filling by the balls, the void filling fraction, and the fraction of actual rotation speed compared to the critical speed  $N_C$ . The subscript T refers to the parameters used in the small-scale batch test, which are used to fit the model parameters in Eqns. (2) and (3). Typical scale-up exponents are  $N_0 = 1$ ,  $N_1 = 0.5$ ,  $N_2 = 0.2$ ,  $N_3 = 2$ , and  $N_4 = 0.2$  (Austin et al., 1984). However, other values of  $N_3$  were also used such as 1 (Yildirim, 1999) and 1.2 (Austin et al., 2007). One should note that  $N_0$  and  $N_3$  should be taken as  $\xi$  and  $\eta$  of Eqn. (3), respectively, from a study on the ball size impact on  $S_i$  at the test (T) scale, which is a preferred approach (Mulenga, 2017).

While the Austin model in Eqn. (2) or (3) has been the most widely used kinetic model for ball milling, Kotake et al. (2002, 2004) developed the following kinetic model for the breakage of narrowly sized feed with size  $x_f$ :

$$S_i = C_1 d_B^m x_f^\alpha \exp\left(-\frac{C_2 x_f}{d_B^n}\right) \quad (10)$$

which we briefly refer to as the KK (Kotake–Kanda) model for the sake of simplicity. The parameters  $C_1$  and  $C_2$  strongly depend on the milling conditions and material properties, whereas  $\alpha$  is a positive constant that largely depends on the properties of the material;  $m$  and  $n$  are material-dependent, ball size exponents. Kotake et al. (2002, 2004) and Deniz (2003) demonstrated the fitting capability of this model for ball milling of a multitude of minerals. The KK model, Eqn. (10), is appealing as it has 5 parameters as opposed to the Austin model with 6 parameters, when ball sizes are explicitly considered. The milling studies, where the back-calculation approach involved more than a few breakage parameters to be estimated, have shown that the accuracy decreases as the number of parameters to be estimated increases (Klimpel and Austin, 1977; Kwon and Cho, 2021). However, to the best knowledge of the author, the KK model has not been used for the PBM simulation of ball milling of a natural feed with a wide size particle size distribution (PSD), and no scale-up has been performed using it. More importantly, the KK model has never been compared to the Austin model.

The present theoretical investigation seeks answers to the following questions: (i) Are there any similarities between the Austin model and the KK model despite their different mathematical forms? (ii) Is the Austin’s scale-up methodology (scale-up correction factors) applicable to the KK model? (iii) Do these models predict similar time-wise evolution of PSD in ball mills before and after scale-up? To be able to answer these questions, we first generated synthetic specific breakage rate data using the Austin model, whose parameters were obtained from the lab-scale ball milling of coal. Next, this data was fitted by the KK model to determine its parameters. Then, using the Austin’s scale-up methodology, the specific breakage

rate was scaled-up numerically (virtual scale-up) using both models for various mill diameter scale-up ratios  $D/D_T$  from 4 to 10, ball sizes  $d_B$  of 30–49 mm, and coal particle sizes  $x_i$  of 0.0106–30 mm. PBM simulations assumed plug flow and invariance of  $b_{ij}$  in the large-scale mills and incorporated the scaled-up  $S_i$  values. The PBM simulations were performed for the small-scale mill and the large-scale mills. Upon scale-up, we find that the differences in both models' predictions are relatively small. Instead of just using  $N_1 = 0.5$  and  $N_2 = 0.2$  for the virtual scale-up with the KK model, which is based on the Austin's scale-up methodology, we also fitted these exponents to the  $S_i$  values generated by the Austin kinetic model, keeping the other scale-up exponents the same. Comparison of the PSD evolution prediction by the KK model (with/without modified  $N_1$  and  $N_2$ ) and the Austin model will allow us to find the answers to the above-mentioned questions.

## 2. Theoretical approach

### 2.1 Experimental data and model calibration

The KK model can be cast into the following form, which is valid for any arbitrary particle size  $x_i$

$$S_i = C_1 d_B^m x_i^\alpha \exp\left(-\frac{C_2 x_i}{d_B}\right) \quad (11)$$

Note that both Eqns. (3) and (11) are explicit in  $d_B$  and  $x_i$ , which enables us to discern any similarities or differences between the two models by analyzing the limiting behavior for small particle size-to-ball size ratio and the extremum behavior for a given ball size. To demonstrate that the KK model can predict the same  $S_i$  as that predicted by the Austin model, we need to have  $S_i$  parameters from an experimental data set on batch ball milling. Hence, we considered the experimental work on the batch ball milling of a South African coal (Katubilwa and Moys, 2009). They fitted and/or set the Austin model parameters as follows:  $\alpha_0 = 0.48 \text{ mm}^{-0.81} \cdot \text{min}^{-1}$ ,  $\mu_0 = 19.27 \text{ mm}$ ,  $d_{B,0} = 38.8 \text{ mm}$ ,  $\alpha = 0.81$ ,  $A = 3$ ,  $\xi = 1$ , and  $\eta = 1.96$ . Using this set of parameters, a synthetic data set for  $S_i$  was generated by the Austin model using Eqn. (3) for ball sizes of 30–49 mm with increments of 1 mm and coal particle sizes of 0.0106–30 mm with a geometric progression ratio of  $2^{1/13}$ . As the purpose of this study is to examine theoretical similarity of the KK model to the Austin model, we did not fit the KK model to the experimental data directly, but to the synthetic  $S_i$  data generated by the Austin model to minimize any bias. Both models have been shown to fit various ball milling data successfully in the milling literature; the question we seek to answer here is not how well they can fit specific experimental data. Therefore, the parameters of the KK model, Eqn. (11), were estimated by minimizing the sum-of-squared residuals between the KK model prediction and the synthetic data generated by the Austin model for the South African coal. In comparison to no transform

and logarithmic transform, a square-root transform of the response ( $S_i$ ) led to the best overall fitting and simulation results when the KK model with the estimated parameters were compared with the Austin model. Hence, only the KK model parameters obtained by fitting after the square-root transform of the response ( $S_i$ ) are presented. The optimization was performed via the Marquardt–Levenberg method in Minitab version 21.1.

### 2.2 Virtual scale-up

A virtual scale-up of the specific breakage rate  $S_i$  was performed from the small-scale batch mill to the large-scale continuous ball mills. Using the Austin's scale-up methodology, the specific breakage rate  $S_i$  obtained experimentally for the Austin model (Katubilwa and Moys, 2009) and the KK model with the estimated parameters (refer to Section 2.1) were scaled-up numerically for various mill diameter scale-up ratios  $D/D_T$  from 4 to 10, ball sizes  $d_B$  of 30–49 mm, and coal particle sizes  $x_i$  of 0.0106–30 mm. For simplicity,  $K_4$  and  $K_5$  are set to 1 in this study for the scale-up with both models regardless of any particular values of  $J$ ,  $U$ , and  $\phi_c$  values because  $K_4$  and  $K_5$  are independent of  $d_B/d_T \equiv d_B/d_{B0}$  and  $D/D_T$ , which were varied in this study. Hence, the scaled-up  $S_i$ , i.e.,  $S_i^*$ , was calculated by

$$S_i^* = a_0 x_i^\alpha \frac{(d_{B,0}/d_B)^\xi K_3}{1 + \left[ \frac{x_i}{\mu_0 (D/D_T)^{N_2} (d_B/d_{B,0})^\eta} \right]^A} \quad (12)$$

$$S_i^* = C_1 d_B^m x_i^\alpha \exp\left(-\frac{C_2 x_i}{(D/D_T)^{N_2} d_B^n}\right) K_3 \quad (13)$$

The above equations incorporate  $K_1$ ,  $K_2$ , and  $K_3$  directly, which depend on  $d_B/d_{B0}$  and  $D/D_T$ . First, Eqn. (12) was used to generate the  $S_i^*$  by the Austin model for all scale-up scenarios with various  $d_B/d_{B0}$  and  $D/D_T$ . These scaled-up data were taken as the “synthetic scale-up data” against which the scale-up with the KK model was compared. Then, two different virtual scale-up approaches for the KK model were used. In the first approach, the standard scale-up exponents of the Austin's scale-up methodology, i.e.,  $N_1 = 0.5$  and  $N_2 = 0.2$ , along with  $N_4 = 0.2$  were used in Eqn. (13) to predict the  $S_i^*$ . However, as there is no prior scale-up study with the KK model, one cannot assume that the Austin's scale-up exponents  $N_1$  and  $N_2$  are directly applicable for use in Eqn. (13). Hence, in the second approach, we fitted  $S_i^*$  values generated by Eqn. (12) for each  $D/D_T$  from 4 to 10 and ball sizes  $d_B$  of 30–49 mm using Eqn. (13) and minimizing the following standard error  $SE$ :

$$SE = \sqrt{\frac{\sum_{i=1}^N (\sqrt{S_{\text{Austin},i}^*} - \sqrt{S_{\text{KK},i}^*})^2}{N - N_p}} \quad (14)$$

which allowed us to estimate  $N_1$  and  $N_2$ . An additional fit

was performed to minimize  $SE$  for all  $D/D_T$  cases simultaneously. Here,  $N$  and  $N_p$  refer to the total number of data points and parameters estimated, respectively. Then, these simultaneously estimated values of  $N_1$  and  $N_2$  were used to predict  $S_i^*$  for each scale-up scenario separately.

### 2.3 PBM simulations

The scale-up from a small batch mill or a pilot-scale mill to a large-scale industrial continuous mill is a complex endeavor, entailing considerations of the residence time distribution (RTD), internal classification, and external classification in the continuous mill circuits (Herbst and Fuerstenau, 1980; Austin et al., 1984; Rogers and Austin, 1984; De Oliveira and Tavares, 2018) besides scale-up of the specific breakage rate. However, any consideration of these factors in the scale-up process would complicate the analysis to discern the differences between the Austin model and KK model in the scale-up of  $S_i$ . Hence, we followed the simplest approach for the modeling of an open-circuit continuous mill by assuming plug flow behavior and disregarding any internal classification in the mill. This simple approach purposefully isolates the problem of “breakage kinetics” in scale-up and allows us to focus on the discrimination of the KK model from the Austin model within the context of simulation and scale-up. The plug-flow is a viable assumption for some industrial scale ball mills (Austin, 1973). For example, a 10 tanks-in-series model represented the RTD data for a large-scale cement ball mill (Austin et al., 1975). The plug-flow assumption was also adopted by other researchers in the ball mill scale-up (Chimwani et al., 2014). Developing a sophisticated PBM for a continuous ball mill circuit with internal–external classification is not within the scope of this study.

Note that Eqn. (1) is applicable to mills operating in batch mode as well as plug-flow continuous mode. One can replace time  $t$  with contact time  $t^* = y/u$  for any axial position  $y$  in the mill with  $u$  denoting the average axial velocity of the particles:  $u = L/\tau = LF/M_h$ , where  $\tau$ ,  $L$ ,  $F$ , and  $M_h$  stand for the space-time (the average residence time), length of the mill, inlet mass flow rate, and mass hold-up at steady state, respectively. So, after replacing  $t$  with  $t^*$ , one can solve the set of ordinary differential equations (ODEs) in Eqn. (1) with the initial condition  $M_i(0) = M_{i,ini}$ , with  $M_{i,ini}$  representing the feed PSD, and predict the steady-state PSD at  $t^* = \tau$ . Henceforth, although we use the above formalism, for the sake of simplicity, we will still denote time as  $t$  in the results, but keeping in mind,  $t$  represents retention time in the batch mill and contact (residence) time in the plug-flow continuous mill at the steady state.

In the PBM simulations, we used the  $S_i$  values in Section 2.1 for the small-scale batch mill simulations and  $S_i^*$  values, as described in Section 2.2, for the continuous milling. The following cumulative breakage distribution parameters  $B_{ij}$  were taken from Katubilwa et al. (2011)

about the same South African coal for which  $S_i$  parameters were reported in Section 2.1:

$$B_{ij} = \phi(x_{i-1}/x_j)^\gamma + (1-\phi)(x_{i-1}/x_j)^\beta \quad (15)$$

Here,  $0 < \phi < 1$  is a breakage constant, and  $\gamma$  and  $\beta$  are breakage exponents. For the South African coal,  $\phi$ ,  $\gamma$ , and  $\beta$  were reported to be 0.51, 0.53, and 3.2, respectively. It is well-known that these parameters are largely material dependent, and are relatively insensitive to the milling conditions, except the ball size (Austin et al., 1984; Prasher, 1987; King, 2001). In a more elaborate model, one could incorporate the impact of ball size on  $B_{ij}$  by making  $\gamma$  dependent on the ball size (Austin et al., 2007). In the present simulations and scale-up, we assumed that  $B_{ij}$  remain invariant to ball size and scale-up, similar to what Chimwani et al. (2014) implemented. Using the  $B_{ij}$  values from Eqn. (15), we calculated  $b_{ij}$  via  $b_{ij} = B_{ij} - B_{i+1j}$ .

The initial PSD for the small batch mill simulation and the feed PSD for the continuous mill simulation were taken the same: a Gaussian PSD with a mean size of 20 mm and a standard deviation of 2 mm. The Gaussian PSD was generated using the function “normpdf” in MATLAB™ version 9.11. Considering the time scale of the batch milling experiments (Katubilwa and Moys, 2009), we simulated 0.5, 1, 2, 4, and 8 min of milling time (or residence time). Another rationale for the selection of 8 min is the following: power-station boilers usually demand 60–70 % of coal particles below 75  $\mu\text{m}$  (Prasher, 1987). Our exploratory simulations suggest 8 min residence time in the large-scale mills could meet this demand approximately. In all PBM simulations, the number of size classes  $N_s$  and the geometric progression ratio were set as 320 and  $2^{1/13}$ , respectively, which yields grid-independent simulation results. The set of ODEs in Eqn. (1) along with either Eqns. (3), (11), and (15) for the small batch mill or Eqns. (12), (13), and (15) for the large-scale continuous mill was solved using the function “ode15s” in MATLAB, which is a highly accurate, variable order–step-size ODE solver (Shampine et al., 2003). The relative error tolerance and the absolute error tolerance were set as  $10^{-4}$  and  $10^{-6}$ , respectively.

## 3. Results and discussion

### 3.1 Austin model vs. Kotake–Kanda model

Despite the differences in their mathematical forms, both the Austin model and the KK (Kotake–Kanda) model have similar limiting behavior and extremum behavior. Let us first consider the limiting case of  $x_i \ll d_B$ , for which Eqns. (3) and (11) reduce to

$$S_i = a_0 x_i^\alpha (d_{B,0}/d_B)^\xi \quad \text{and} \quad S_i = C_1 d_B^\alpha x_i^\alpha \quad (16)$$

respectively, because the dominator of Eqn. (3) and exponential term in Eqn. (11) approach 1. Clearly, both models provide power-law dependence of  $S_i$  on  $x_i$  and  $d_B$  in this

limit. Note that  $x_i \ll d_B$  has not been strictly defined and  $x_i/d_B < O(10^{-2})$  is reasonable for this limiting behavior. To prevent a possible confusion, we assert that this limiting behavior is not a practically irrelevant asymptotic limit. As demonstrated by Austin et al. (1976b) and De Oliveira and Tavares (2018), the whole milling kinetics could be governed by this limiting behavior if the feed or initial size is much smaller than the ball sizes used. The KK model can be made equivalent to the Austin model by imposing

$$C_1 = a_0 d_{B,0}^{\zeta} \text{ and } m = -\zeta \tag{17}$$

as well as the sameness of  $\alpha$  in both equations in terms of the limiting behavior.

Let us now consider the extremum behavior of  $S_i$  by setting  $dS/dx = 0$  after taking the equivalent particle size-continuous forms of Eqns. (3) and (11). This analysis yields the particle size  $x_m$  at which  $S_i$  is at a maximum and has the following  $S_m$ :

$$x_m = \mu_0 [\alpha / (\Lambda - \alpha)]^{1/\Lambda} (d_B / d_{B,0})^\eta \text{ with } \Lambda > \alpha \tag{18}$$

$$S_m = a_0 \mu_0^\alpha [\alpha / (\Lambda - \alpha)]^{\alpha/\Lambda} \left(1 - \frac{\alpha}{\Lambda}\right) \left(\frac{d_B}{d_{B,0}}\right)^{\alpha\eta - \zeta} \tag{19}$$

$$x_m = (\alpha / C_2) d_B^n \tag{20}$$

$$S_m = C_1 e^{-\alpha} (\alpha / C_2)^\alpha d_B^{\alpha n + m} \tag{21}$$

for the Austin model and the KK model, respectively. Similar to the limiting behavior, both models predict a power-law dependence of  $x_m$  and  $S_m$  on  $d_B$ . However, the exponents for the limiting behavior and the extremum behavior are different. One can make both models equivalent in terms of the extremum behavior alone, i.e., identical  $x_m$  and  $S_m$ , by setting the KK parameters as

$$C_1 = a_0 e^\alpha (1 - \alpha / \Lambda) d_{B,0}^\zeta \tag{22}$$

$$C_2 = (\alpha / \mu_0) (\Lambda / \alpha - 1)^{1/\Lambda} d_{B,0}^\eta \tag{23}$$

$n = \eta$ ,  $m = -\zeta$ , and same  $\alpha$  in both equations.

An interesting theoretical question arises as to what happens if the equivalence conditions, i.e., either Eqn. (17) for the limiting behavior or Eqns. (22)–(23) for the extremum behavior are imposed on the KK model. We note that the conditions imposed on  $C_1$  are incompatible because  $e^\alpha(1 - \alpha/\Lambda) = 1$  is overly restrictive and cannot be satisfied, except for  $\alpha = 0$ , which is untenable. If one imposes the equivalence in terms of the extremum behavior, then  $C_1$  provided by Eqn. (22) will be similar to  $C_1$  provided by Eqn. (17) in terms of the power-law dependence with the same exponent  $\zeta$ . However, Eqn. (22) will overpredict  $S_i$  by a factor of  $e^\alpha(1 - \alpha/\Lambda)$  in the limit  $x_i \ll d_B$ . This factor equals 1.641 (64.1 %) for the coal considered in Section 2.1, which is not acceptable.

The upshot of the above theoretical analysis is that the

KK model is similar, but not equivalent or identical, to the Austin model in terms of the limiting behavior and the extremum behavior. It is impossible to ensure equivalency of these models in terms of both limiting behavior in the size domain  $x_i \ll d_B$  and the extremum behavior in the neighborhood of  $x_i = x_m$ . Owing to the power-law dependence of  $S_i$  on  $x_i$  and  $d_B$  in the size domain  $x_i \ll d_B$  and that of  $x_m$  and  $S_m$  on  $d_B$ , we hypothesize that both models could predict similar  $S_i$  while satisfying the limiting behavior and the extremum in *some approximate statistical sense*. Note that they may differ significantly in the size domain  $x_i \ll d_B$  and near the extremum. This hypothesis can be tested by first fitting the KK model parameters to the  $S_i$  generated by the Austin model and then analyzing the resulting  $S_i$  profiles as well as these models' prediction of the temporal evolution of the PSD. To this end, the synthetic  $S_i$  data generated by the Austin model, whose parameters were obtained by fitting to the ball milling data on a South African coal (refer to Section 2.1), were fitted by the KK model. The parameters of the KK model are presented in Table 1. The sum-of-squared errors was  $4.08 \text{ min}^{-1}$ , and the standard error  $SE$  of the fit was  $3.69 \times 10^{-2} \text{ min}^{-0.5}$ . The parameters had low standard errors: all below 8 %. Clearly, the KK parameters in Table 1 will not satisfy the requirements of Eqn. (17) and Eqns. (22)–(23), which, respectively, ensure equivalency in terms of the limiting behavior and the extremum behavior. These strict conditions are not required for the models to be similar both qualitatively and quantitatively when experimental errors in determining  $S_i$  are considered (see later discussion).

Fig. 1 presents the specific breakage rate  $S_i$  data generated by the Austin model for the South African coal and its fitting by the KK model, which led to the estimated parameters in Table 1. While there are minor deviations, the KK model estimated the  $S_i$  profiles and the extremum behavior reasonably well. The KK model exhibited a slightly depressed, shifted peak as compared with the Austin model. Both models predict a cliff or falling off  $S_i$  for  $x_i > x_m$ , which can be explained by the inability of the balls to nip or capture the particles effectively. In view of Eqn. (16), the values of  $\zeta = 1$  and  $m = -1.444$  suggest that the smaller ball sizes are effective for  $x_i \ll d_B$  because for the smaller particles, the number frequency of the collisions with the

**Table 1** The KK model parameters obtained from fitting to the synthetic data generated by the Austin model.

Parameter	Value	Unit	SE (%)
$C_1$	107.5	$\text{mm}^{0.494} \cdot \text{min}^{-1}$	5.81
$m$	-1.444	–	1.10
$\alpha$	0.9496	–	0.242
$C_2$	370.6	$\text{mm}^{1.364}$	7.30
$n$	2.364	–	0.876

beads govern the specific breakage rate, which is suggested to be scaled by the inverse of  $d_B$ , as signified by  $\zeta = 1$  (Austin et al., 1984). Overall, both models' phenomenological representation of the breakage kinetics appears to be qualitatively and quantitatively similar.

The location of the extremum points in Fig. 1 are given by  $x_m - S_m$ , which depend on the ball size  $d_B$  and are obtained via Eqs. (18)–(21) for the Austin model and the KK model, respectively, as follows:

$$x_m = 1.063 \times 10^{-2} d_B^{1.96} \text{ and } S_m = 0.3423 d_B^{0.588} \quad (24)$$

$$x_m = 2.562 \times 10^{-3} d_B^{2.36} \text{ and } S_m = 0.1439 d_B^{0.801} \quad (25)$$

Fig. 2 depicts the variation of  $x_m$  and  $S_m$  with  $d_B$  based on Eqs. (24) and (25). According to the Austin model, each

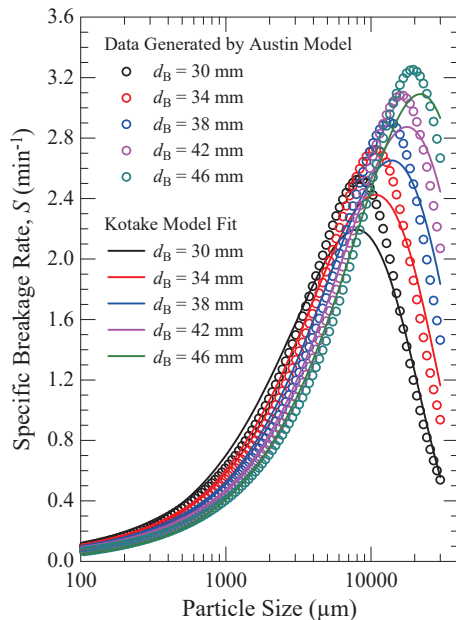


Fig. 1 Size dependence of  $S_i$  for various ball sizes: fitting by the KK (Kotake) model to the synthetic data generated by the Austin model.

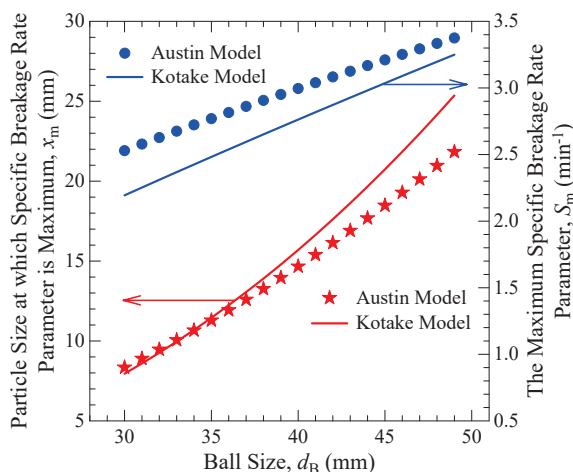


Fig. 2 Dependence of  $S_m$  and  $x_m$  on the ball size: Austin model with Eqn. (24) and the KK model with Eqn. (25).

ball size most effectively breaks a certain particle size. Large balls are the best for breaking coarse particles; small balls are the best for breaking small particles. For example, 46 mm balls are most effective for breaking  $\sim 20$  mm particles; yet, they are the worst for breaking  $< \sim 8$  mm particles; 30 mm balls are most effective for the latter. Practically, for a feed with wide PSD, the common practice is to use a mixture of different ball sizes (Austin et al., 1984; Prasher, 1987; Katubilwa and Moys, 2009).

As can be seen from Fig. 2, the KK model provides a similar ball size dependence of  $S_m$  and  $x_m$  to that by the Austin model although there is some deviation. The mean relative deviation for  $S_m$  and  $x_m$  were 8.18 % and 7.31 %, respectively, while the maximum relative deviation for  $S_m$  and  $x_m$  were 13.2 % and 16.1 %, respectively. One interesting trend is that as  $d_B$  increased, the  $S_m$  deviation of the KK model from the Austin model decreased, while the  $x_m$  deviation increased, which counter each other. This observation along with  $< 10$  % mean relative deviation overall imply that the deviations may have small impact on the PBM simulation and scale-up results. This is indeed the case, as will be demonstrated next through PBM simulations before and after scale-up.

To develop a deeper understanding of the ball size effects, one must resort to Discrete Element Modeling (DEM) of tumbling ball mills. DEM provides significant fundamental insights and microdynamic information such as collision energies among the balls–particles–mill wall/liners and their frequencies (Tavares, 2017; Rodriguez et al., 2018). In an excellent critical analysis, Rodriguez et al. (2018) pointed out some fundamental learnings from the DEM: (i) Collision energies involving events with only particles (particle–particle and particle–liner) are not sufficiently high to cause breakage of particles and (ii) a fraction of the collisions inside the ball mill do not involve particles; hence, they do not directly contribute to particle breakage. In agreement with the above, the multi-scale PBM–DEM modeling of the experimental tumbling ball mill (Kotake et al., 2002) by Capece et al. (2014) predicted the  $S_i$  profile similar to those in Fig. 1. Moreover, their simulations suggest that for a given narrow feed size, an effective ball size that maximizes the specific breakage rate exists. This effective ball size appears to maximize collision frequency with the particles (ball–particle collisions) with sufficiently high impact energy above a minimum threshold impact energy that is particle size-dependent. Such minimum impact energies required to break individual particles under impact loading should be determined experimentally (Tavares and King, 1998; Vogel and Peukert, 2003; Tavares, 2007).

While the analysis of the data in Figs. 1 and 2 suggests that the KK model is similar to the Austin model and they both provide similar  $S_i$ ,  $x_m$ , and  $S_m$ , one would argue about the deviations. At this juncture, it is imperative to mention the errors involved in the determination of  $S_m$  and

$x_m$ . For example, Kotake et al. (2002; 2004) described an averaging procedure to determine  $S_m$  and  $x_m$  because of the experimental scatter around the maxima. The experimental deviations were certainly greater than the  $\sim 10\%$   $S_m$  and  $x_m$  deviations of the KK model from the Austin model observed here. Moreover, the 85 % of the fitted  $S_i$  values by the KK model were within a band of  $\pm 20\%$ , with 15 % of the values outside this band (Kotake et al., 2004); similarly notable deviations can be seen in Deniz (2003). Most importantly, a long-due study (Shahcheraghi et al., 2019) clearly demonstrated that at 95 % confidence level, the experimentally determined  $S_i$  parameters of the Austin model had 21.7–34.1 % uncertainty, whereas the  $B_{ij}$  parameters had 7.8–17.8 % uncertainty. Hence, the deviations shown in Figs. 1 and 2 between the Austin model and the KK model would most likely be within the range of experimental uncertainty when the two models are fitted to the same experimental data with repeats. This has never been done in the experimental ball milling literature. In this study, we will confirm the similarity of the two models via PBM simulations next.

A batch ball milling process was simulated by PBM, as described in Section 2.3 to assess if the deviations between the two models'  $S_i$  values could cause significant difference in the simulated time-wise evolution of the PSD. To the best knowledge of the author, this is the first study in which a batch milling process has been simulated by the KK model. Fig. 3 clearly illustrates that despite the  $S_i$  deviations illustrated in Fig. 1, the two models simulated the temporal evolution of the PSD almost identically. The

maximum deviations in the PSDs estimated by the KK model and the Austin model are within a few percentages. In view of the above discussion and the simulation results, it is clear that the PBM with either the KK model or the Austin model yields a similar temporal evolution of the PSD in a batch mill prior to scale-up. The KK model has one less parameter than the Austin model (5 vs. 6); its use may be advantageous for parameter estimation.

### 3.2 Virtual scale-up with the KK model

Historically, the Austin kinetic model has been used along with Austin's methodology for ball mill scale-up (Austin et al., 1984). As the KK model has never been used for ball mill scale-up, it is doubtful if it can be integrated with the Austin's scale-up methodology. In Section 2.2, we developed the scaled-up specific breakage rate parameter  $S_i^*$  using this methodology. To the best knowledge of the author, this is the first attempt to use the KK model for scale-up, albeit virtual. This virtual scale-up will allow us to assess if the KK model could provide (or fit to)  $S_i^*$  similarly to the Austin model upon scale-up. Table 2 presents the virtual scale-up scenarios and the standard error  $SE$ , as per Eqn. (14). Four diameter scale-up ratios  $D/D_T$  with ball sizes of 30–49 mm and coal particle sizes of 0.0106–30 mm were considered. The Austin model, via Eqn. (12), was used to produce the synthetic scale-up  $S_i^*$  data to which the  $S_i^*$  generated by the KK model, via Eqn. (13), will be compared (SU1–4 in Table 2). In SU1–SU4, standard values of the scale-up correction exponents, i.e.,  $N_1 = 0.5$  and  $N_2 = 0.2$  were used. In SU5–SU8,  $N_1$  and  $N_2$  were estimated by fitting Eqn. (13) to the synthetic scale-up

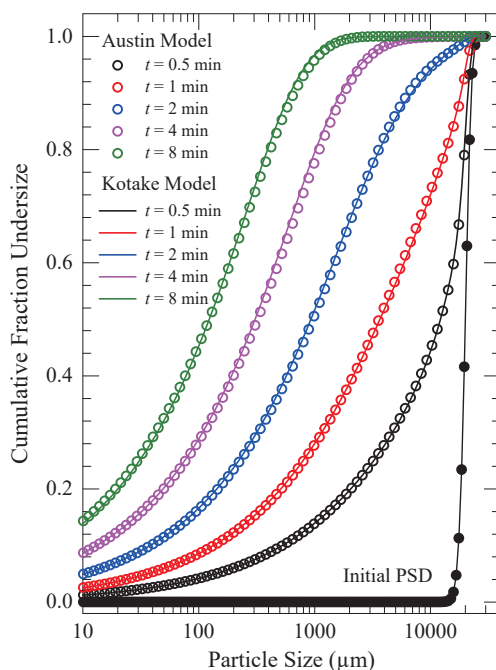


**Fig. 3** PBM simulation of the time-wise evolution of the cumulative PSD in a batch mill with an initial Gaussian PSD (mean size: 20  $\mu\text{m}$ ,  $SD$ : 2  $\mu\text{m}$ ) and  $d_b = 38$   $\mu\text{m}$ .

**Table 2** Standard error  $SE$  calculated or estimated by Eqn. (14) with the KK model estimation and the synthetic scale-up data generated by the Austin model. The analytical data is available publicly at <https://doi.org/10.50931/data.kona.19596367>

Scale-up no.	$D/D_T$ (-)	$N_1$ (-)	$N_2$ (-)	$SE$ ( $\text{min}^{-0.5}$ )
SU1	4	0.5	0.2	$5.79 \times 10^{-2}$
SU2	6	0.5	0.2	$6.90 \times 10^{-2}$
SU3	8	0.5	0.2	$7.78 \times 10^{-2}$
SU4	10	0.5	0.2	$8.47 \times 10^{-2}$
SU5	4	0.455	0.239	$5.07 \times 10^{-2}$
SU6	6	0.455	0.241	$5.56 \times 10^{-2}$
SU7	8	0.455	0.242	$5.88 \times 10^{-2}$
SU8	10	0.455	0.242	$6.07 \times 10^{-2}$
SU9 <sup>a</sup>	4	0.455	0.241	$5.07 \times 10^{-2}$
SU10 <sup>a</sup>	6	0.455	0.241	$5.56 \times 10^{-2}$
SU11 <sup>a</sup>	8	0.455	0.241	$5.88 \times 10^{-2}$
SU12 <sup>a</sup>	10	0.455	0.241	$6.07 \times 10^{-2}$

<sup>a</sup> The  $SE$  of simultaneous fitting with SU9–12 was  $5.66 \times 10^{-2} \text{ min}^{-0.5}$ .



data for each  $D/D_T$  separately. In SU9–SU12, they were fitted to the synthetic scale-up data for all  $D/D_T$  data together.

Fitting of the scaled-up specific breakage rate parameter  $S_i^*$  by the KK model to the synthetic scale-up  $S_i^*$  data (Austin model) either one-at-a-time for each scale-up scenario (SU5–8) or simultaneously for all scenarios (SU9–12) led to almost identical exponents of the scale-up correction factor:  $N_1 = \sim 0.46$  and  $N_2 = \sim 0.24$ , which deviated only by 8 % and 20 % from the standard values of the Austin's scale-up methodology, i.e.,  $N_1 = 0.5$  and  $N_2 = 0.2$  (SU1–4). Hence, one set of modified  $N_1$  and  $N_2$  can be used for the scale-up of  $S_i$  of the KK model. When the  $SE$  of SU9–12 was compared with that of SU1–SU4, the modified  $N_1$  and  $N_2$  reduced  $SE$  by 12 %, 19 %, 24 %, and 28 %, respectively, for  $D/D_T$  values of 4, 6, 8, and 10.

At the small-scale, the fitting of the KK model to the synthetic  $S_i$  data for its parameter estimation has a  $SE$  of  $3.69 \times 10^{-2} \text{ min}^{-0.5}$ . Upon scale-up, the  $SE$  values in **Table 2** for SU1–4 are 57 %–130 % higher than that associated with the parameter estimation. The situation is somewhat better when the newly estimated, modified  $N_1 = 0.455$  and  $N_2 = 0.241$  are used. The  $SE$  values for SU9–12 (upon scale-up) are 37 %–65 % higher than that associated with the parameter estimation. Clearly, the  $S_i$  differences between the KK model and the Austin model become more pronounced upon scale-up whether the standard Austin scale-up correction exponents or the modified exponents are used. While the  $SE$  increased upon scale-up, as intuitively expected, in absolute terms, the  $SE$  values are still low which will become apparent once the deviations are presented in visual form next.

**Figs. 4** and **5** present the synthetic  $S_i^*$  data by the Austin model and  $S_i^*$  provided by the KK model (SU1 and SU3) and fitted by the KK model (SU9 and SU11). The data from the other scale-up scenarios were not presented in graphical form for the sake of brevity. It suffices to state that **Figs. 4** and **5** are representative of the general scale-up trends for all scenarios.

A cursory look at **Figs. 4** and **5** vs. **Fig. 1** reveals the remarkable impact of the scale-up on the specific breakage rate. Upon scale-up and an increase in  $D/D_T$ , the specific breakage rate increases, which accords well with the experimental ball milling literature (Austin, 1973; Austin et al., 1984).  $N_1$  captures the increase in mill power as mill diameter increases (Austin, 1973).  $S_m$  and  $x_m$  also increase, which suggests the maximum point moves to the right and its peak is heightened. With an increase in  $D/D_T$ , the cliff after  $x_i > x_m$  becomes less pronounced and the abnormal breakage region shrinks. In fact, for  $d_b = 46$  mm, the maximum point almost disappears. Obviously, for a higher  $D/D_T$  value, the balls are dropped from a greater height, and they hit the particles at a much higher impact force. According to a semi-theoretical analysis (Hayashi and Tanaka, 1972), the impact force for free-falling balls scales with  $D^{0.5}$ . A

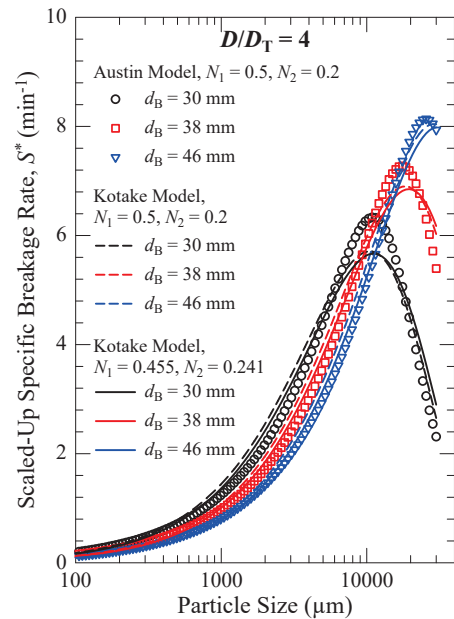


**Fig. 4** Comparison of  $S_i^*$  generated by the Austin model and the KK model with two sets of  $N_1$ – $N_2$  ( $D/D_T = 4$ ).

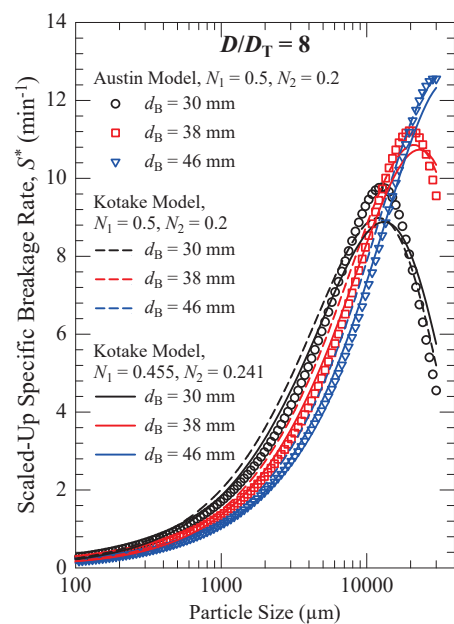


**Fig. 5** Comparison of  $S_i^*$  generated by the Austin model and the KK model with two sets of  $N_1$ – $N_2$  ( $D/D_T = 8$ ).

recent advanced DEM simulation study (De Carvalho et al., 2021) provides a more fundamental explanation. Their DEM simulations point out a significant expansion of the collision frequency–collision energy envelope as the ball milling is carried out at larger scales: from batch to pilot and then to industrial mills. They determined the specific collision frequency to be 2404 collisions/kg·s, 2746 collisions/kg·s, and 3795 collisions/kg·s at the batch, pilot, and industrial scales, respectively. Overall, higher impact forces, collision energies, and specific collision frequency explain the higher specific breakage rates upon scale-up

fundamentally.

The differences in  $S_i^*$  between the Austin model and the KK model, with/without the modified  $N_1$  and  $N_2$  exponents, illustrated in Figs. 4 and 5 seem to be unremarkable and most likely statistically insignificant when actual ball milling data are considered. The readers are referred to the discussion and the references in Section 3.1. However, proving this point with comparative experimental study is beyond the scope of this study. We pose a different, yet quite relevant question: can the  $S_i^*$  differences depicted in Figs. 4 and 5 translate into significant differences in terms of the PSD evolution with residence time in a continuous mill?

Fig. 6 illustrates that the PSD shifts from the Gaussian feed PSD to the left monotonically along the axial direction of a continuous mill with  $D/D_T = 4$ , which is scaled from the small batch mill whose PSD evolution is shown in Fig. 3. The time refers to retention time in the batch mill (Fig. 3) and the residence time in the continuous mill (Fig. 6), which corresponds to different axial locations in the mill. A cursory look at Fig. 6 vs. Fig. 3 reveals that the product becomes much finer upon scale-up, which is in agreement with the higher specific breakage rate parameter upon scale-up ( $S_i^*$  in Fig. 4 vs.  $S_i$  in Fig. 1). A larger diameter mill with  $D/D_T = 8$  (Fig. 7) exhibits similar behavior; the PSDs are finer as compared with those in Fig. 6, which again can be attributed to the respective  $S_i^*$  values in Figs. 4 and 5.

Let us now answer the question posed earlier: the Austin model and the KK model, with either the standard scale-up

exponents  $N_1 = 0.5$  and  $N_2 = 0.2$  or the modified scale-up exponents estimated in this study, i.e.,  $N_1 = 0.455$  and  $N_2 = 0.241$ , predict very similar PSDs in a plug flow continuous mill. Although the differences increased slightly upon scale-up to a larger mill with  $D/D_T = 8$  (Fig. 7), both the Austin model and the KK model estimated similar PSDs, with a max. deviation of 4 % at 10  $\mu\text{m}$  in the cumulative mass fraction.

An interesting finding from the continuous mill simulations presented in Figs. 6 and 7 is that the modification of the Austin's scale-up exponents  $N_1$  and  $N_2$  was not warranted for the integration of the KK model with the Austin's scale-up methodology. The KK model with the modified scale-up exponents showed less deviation from the Austin model than that with the standard exponents at the earlier residence time values. However, this trend was reserved at the later residence time points and at the exit of the mill ( $t = \tau = 8$  min). Despite the lower  $SE$  values of the  $S_i^*$  associated with the modified scale-up exponents in Table 2, these differences in the  $SE$  values did not seem to make a significant difference in terms of the PSD change along the mill axis and the product PSD, as proven by the simulation results in Figs. 6 and 7. Longer residence times were not considered for two reasons. First, the product PSD ( $t = 8$  min) in the large-scale continuous mills reached the desired target approximately for coal applications: 60–70 % below 75  $\mu\text{m}$ . Second, the Austin model parameters were estimated using the one-size-fraction data from a ball milling study on South African coal (Katubilwa and Moys, 2009; Katubilwa et al., 2011). In these studies, the

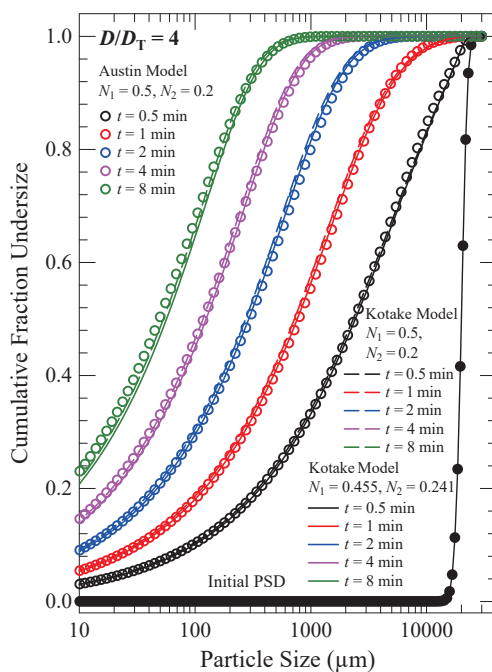


Fig. 6 The variation of the PSD at different residence times of the particles (different axial locations) in a continuous ball mill with plug-flow,  $D/D_T = 4$ , and  $d_B = 38$  mm.

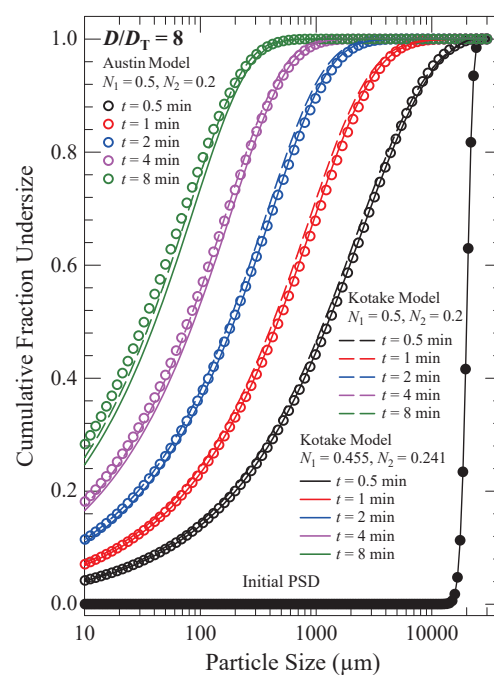


Fig. 7 The variation of the PSD at different residence times of the particles (different axial locations) in a continuous ball mill with plug-flow,  $D/D_T = 8$ , and  $d_B = 38$  mm.

smallest feed size fraction studied contained 300–425  $\mu\text{m}$  coal particles. Hence, both the Austin and the KK models extrapolate  $S_i$  of the finer particle range ( $< 300 \mu\text{m}$ ) based on the coarser particles' breakage kinetics. While this is a common practice, we suspect that the  $\alpha$  parameter in both models could be sensitive to the particle size domain in the model calibration. Hence, the slightly higher deviation of the KK model from the Austin model for particles smaller than 100  $\mu\text{m}$  (refer to Fig. 7) could be indirectly linked to the model calibration and the slight differences in the  $\alpha$  value ( $\alpha = 0.81$  for the Austin model and  $\alpha = 0.95$  for the KK model).

#### 4. Concluding remarks and outlook

This theoretical study presents a comparative analysis of the Austin kinetic model and the Kotake–Kanda (KK) kinetic model in terms of their prediction of the specific breakage rate parameter as a function of particle size and ball size. Both models have been shown to be similar in terms of their limiting behavior and the extremum behavior because both behaviors are governed by power-law relationships. Mathematical requirements have been formulated to ensure equivalency of both models under these conditions; however, ensuring equivalency for both behaviors through these derived conditions is shown to be severely restrictive or incompatible. Hence, to investigate their similarities further, synthetic specific breakage rate  $S_i$  data were generated by the Austin model and fitted by the KK model reasonably well. The PBM simulations of a batch (reference) mill have demonstrated almost identical PSD evolution, confirming the similarity of the two models. Then, a virtual scale-up from the batch reference mill to a continuous plug-flow mill with different  $D/D_T$  has been performed. Using the Austin's scale-up methodology along with the Austin model, the scaled-up specific breakage rate parameter  $S_i^*$  has been determined. The KK model has also been scaled-up using the Austin's scale-up methodology with and without modified scale-up correction exponents. Also, the large-scale continuous mill operation has been simulated via PBM with the  $S_i^*$ . This study has overall demonstrated that (i) the KK model is similar, but not equivalent, to the Austin model, (ii) the KK model and the Austin model provide similar PSD evolution after scale-up, (iii) the modification of the Austin's scale-up exponents  $N_1$  and  $N_2$  is not warranted, and (iv) the Austin's scale-up methodology is applicable to the KK model as well as the Austin model.

This theoretical study has generated additional questions and ideas for further research. A well-designed experimental ball milling study, using both one-size fraction method and the optimization-based back-calculation method on several natural feed PSDs, should be conducted. The models should be discriminated based on their goodness-of-fit, parameter uncertainties and confidence intervals,

and statistical significance. Such studies could reveal if the KK model has some advantages in terms of parameter uncertainties over the Austin model as the former has one less parameter than the Austin model. Such a future study is especially important to the calibration of the KK model (parameter estimation) as the currently used method with one-size-fraction milling experiments is conducive to accumulation of experimental errors. Finally, it is hoped that the Kotake–Kanda model will be used within the Austin's scale-up methodology for ball mill scale-up in the future.

#### Acknowledgements

The author would like to thank his PhD student Mr. Nontawat Muanpaopong for preparing the figures and proof-reading the manuscript. This theoretical research did not receive any specific grant from funding agencies in the public, commercial, or not-for-profit sectors.

#### Data Availability Statement

The data analysis file and the data supporting the findings of this study are available in J-STAGE Data (<https://doi.org/10.50931/data.kona.19596367>).

#### Nomenclature

$a_T$	model parameter in the Austin model ( $\text{mm}^{-\alpha}\cdot\text{min}^{-1}$ )
$a_0$	value of $a_T$ for specific ball size $d_{B,0}$ ( $\text{mm}^{-\alpha}\cdot\text{min}^{-1}$ )
$b_{ij}$	breakage distribution parameter (–)
$B_{ij}$	cumulative breakage distribution parameter (–)
$C_1$	model parameter in the KK model ( $\text{mm}^{-(m+\alpha)}\cdot\text{min}^{-1}$ )
$C_2$	model parameter in the KK model ( $\text{mm}^{n-1}$ )
$d_B$	ball size (mm)
$d_{B,0}$	reference ball size (mm)
$D$	mill diameter (m)
DEM	Discrete Element Modeling
$F$	inlet mass flow rate ( $\text{kg}\cdot\text{min}^{-1}$ )
$J$	ball filling fraction (–)
KK	Kotake–Kanda
$K_1$ – $K_5$	Austin's scale-up correction factors (–)
$L$	mill length (m)
$m, n$	ball-size exponents in the KK model (–)
$M_{B,p}$	mass fraction of ball size with index $p$ (–)
$M_h$	mass hold-up (kg)
$M_i$	mass fraction in size class $i$ (–)
$N$	total number of data points (#)
$N_C$	critical speed (rpm)
$N_p$	total number of parameters estimated (#)
$N_s$	total number of size classes, sink size class (#)
$N_0$ – $N_4$	Austin's scale-up correction exponents (–)
ODE	Ordinary Differential Equation
$P$	total number of ball sizes in a ball mixture (#)

PBM	Population Balance Modeling
PSD	Particle Size Distribution
RTD	Residence Time Distribution
$SD$	standard deviation (mm)
$SE$	standard error ( $\text{min}^{-0.5}$ )
$S_i$	specific breakage rate parameter ( $\text{min}^{-1}$ )
$S_m$	maximum specific breakage rate parameter ( $\text{min}^{-1}$ )
$S_i^*$	scaled-up specific breakage rate parameter ( $\text{min}^{-1}$ )
$\bar{S}_i$	specific breakage rate parameter for a ball mixture ( $\text{min}^{-1}$ )
SU	scale-up
$t$	time (min)
$t^*$	contact or residence time (min)
$u$	average axial velocity ( $\text{m}\cdot\text{s}^{-1}$ )
$U$	void filling fraction (–)
$x$	particle size (mm)
$x_f$	feed particle size (mm)
$x_m$	particle size at which specific rate parameter is maximum (mm)
$y$	axial position in a continuous mill (m)

#### Greek letters

$\alpha$	particle size exponent in both the Austin model and the KK model (–)
$\beta, \gamma$	breakage distribution exponents (–)
$\xi, \eta$	constant ball-size exponents in the Austin model (–)
$A$	abnormal breakage exponent in the Austin model (–)
$\mu_T$	a size parameter in the Austin model (mm)
$\mu_0$	value of $\mu_T$ for specific ball size $d_{B,0}$ (mm)
$\tau$	space-time or average residence time (min)
$\phi$	breakage distribution constant (–)
$\phi_C$	fraction of operating rotation speed compared to critical speed (–)

#### Subscripts

$i, j$	size-class indices
ini	initial
m	maximum
$p$	ball size index
T	test condition as reference for the scale-up

#### References

- Austin L.G., Understanding ball mill sizing, *Industrial Engineering Chemistry Process Design and Development*, 12 (1973) 121–129. DOI: 10.1021/i260046a001
- Austin L.G., Bhatia V.K., Experimental methods for grinding studies in laboratory ball mills, *Powder Technology*, 5 (1971–72) 261–266. DOI: 10.1016/0032-5910(72)80029-9
- Austin L.G., Luckie P.T., Wightman D., Steady-state simulation of a cement-milling circuit, *International Journal of Mineral Processing*, 2 (1975) 127–150. DOI: 10.1016/0301-7516(75)90017-4
- Austin L.G., Shoji K., Luckie P.T., The effect of ball size on mill performance, *Powder Technology*, 1 (1976a) 71–79. DOI: 10.1016/0032-5910(76)80009-5
- Austin L., Shoji K., Bhatia V., Jindal V., Savage K., Klimpel R., Some results on the description of size reduction as a rate process in various mills, *Industrial & Engineering Chemistry Process Design and Development*, 15 (1976b) 187–196. DOI: 10.1021/i260057a032
- Austin L.G., Klimpel R.R., Luckie P.T., *Process Engineering of Size Reduction: Ball Milling*, Society of Mining Engineers of the AIME, Littleton, CO, USA, 1984, ISBN: 9780895204219.
- Austin L.G., Julianelli K., De Souza A.S., Schneider C.L., Simulation of wet ball milling of iron ore at Carajas, Brazil, *International Journal of Mineral Processing*, 84 (2007) 157–171. DOI: 10.1016/j.minpro.2006.09.010
- Bilgili E., Scarlett B., Population balance modeling of non-linear effects in milling processes, *Powder Technology*, 153 (2005) 59–71. DOI: 10.1016/j.powtec.2005.02.005
- Bwalya M.M., Moys M.H., Finnie G.J., Mulenga F.K., Exploring ball size distribution in coal grinding mills, *Powder Technology*, 257 (2014) 68–73. DOI: 10.1016/j.powtec.2014.02.044
- Capece M., Bilgili E., Dave R., Identification of the breakage rate and distribution parameters in a non-linear population balance model for batch milling, *Powder Technology*, 208 (2011) 195–204. DOI: 10.1016/j.powtec.2010.12.019
- Capece M., Bilgili E., Davé R., Insight into first-order breakage kinetics using a particle-scale breakage rate constant, *Chemical Engineering Science*, 117 (2014) 318–330. DOI: 10.1016/j.ces.2014.06.019
- Chimwani N., Glasser D., Hildebrandt D., Metzger M.J., Mulenga F.K., Determination of the milling parameters of a platinum group minerals ore to optimize product size distribution for flotation purposes, *Minerals Engineering*, 43–44 (2013) 67–78. DOI: 10.1016/j.mineng.2012.09.013
- Chimwani N., Mulenga F.K., Hildebrandt D., Glasser D., Bwalya M.M., Scale-up of batch grinding data for simulation of industrial milling of platinum group minerals ore, *Minerals Engineering*, 63 (2014) 100–109. DOI: 10.1016/j.mineng.2014.01.023
- De Oliveira A.L.R., Tavares L.M., Modeling and simulation of continuous open circuit dry grinding in a pilot-scale ball mill using Austin's and Nomura's models, *Powder Technology*, 340 (2018) 77–87. DOI: 10.1016/j.powtec.2018.09.016
- De Carvalho R.M., Campos T.M., Faria P.M., Tavares L.M., Mechanistic modeling and simulation of grinding iron ore pellet feed in pilot and industrial-scale ball mills, *Powder Technology*, 392 (2021) 489–502. DOI: 10.1016/j.powtec.2021.07.030
- Deniz V., A study on the specific rate of breakage of cement materials in a laboratory ball mill, *Cement and Concrete Research*, 33 (2003) 439–445. DOI: 10.1016/S0008-8846(02)00976-6
- Hayashi M., Tanaka T., Analysis of the selection function of comminution kinetics, *Journal of Chemical Engineering of Japan*, 5 (1972) 308–310. DOI: 10.1252/jcej.5.308
- Herbst J.A., Fuerstenau D.W., Scale-up procedure for continuous grinding mill design using population balance models, *International Journal of Mineral Processing*, 7 (1980) 1–31. DOI: 10.1016/0301-7516(80)90034-4
- Katubilwa F.M., Moys M.H., Effect of ball size distribution on milling rate, *Minerals Engineering*, 15 (2009) 1283–1288. DOI: 10.1016/j.mineng.2009.07.008
- Katubilwa F.M., Moys M.H., Glasser D., Hildebrandt D., An attainable region analysis of the effect of ball size on milling, *Powder Technology*, 210 (2011) 36–46. DOI: 10.1016/j.

- powtec.2011.02.009
- King R.P., *Modeling and Simulation of Mineral Processing Systems*, Butterworth-Heinemann, Oxford, 2001, ISBN: 0750648848.
- Klimpel R.R., Austin L.G., The back-calculation of specific rates of breakage and non-normalized breakage distribution parameters from batch grinding data, *International Journal of Mineral Processing*, 4 (1977) 7–32. DOI: 10.1016/0301-7516(77)90028-X
- Kotake N., Suzuki K., Asahi S., Kanda Y., Experimental study on the grinding rate constant of solid materials in a ball mill, *Powder Technology*, 122 (2002) 101–108. DOI: 10.1016/S0032-5910(01)00405-3
- Kotake N., Daibo K., Yamamoto T., Kanda Y., Experimental investigation on a grinding rate constant of solid materials by a ball mill—effect of ball diameter and feed size, *Powder Technology*, 143–144 (2004) 196–203. DOI: 10.1016/j.powtec.2004.04.014
- Kwon J., Cho H., Investigation of error distribution in the back-calculation of breakage function model parameters via nonlinear programming, *Minerals*, 11 (2021) 425. DOI: 10.3390/min11040425
- Mulenga F.K., Sensitivity analysis of Austin’s scale-up model for tumbling ball mills — Part 2. Effects of full-scale milling parameters, *Powder Technology*, 317 (2017) 6–12. DOI: 10.1016/j.powtec.2017.04.043
- Petrakis E., Stamboliadis E., Komnitsas K., Identification of optimal mill operating parameters during grinding of quartz with the use of population balance modeling, *KONA Powder and Particle Journal*, 34 (2017) 213–223. DOI: 10.14356/kona.2017007
- Prasher C.L., *Crushing and Grinding Process Handbook*, Wiley, Chichester, 1987, ISBN: 9780471105350.
- Randolph A.D., Larson M.A., *Theory of Particulate Processes (Second Edition)*, Academic Press, San Diego, 1988, ISBN: 9780125796521.
- Rodriguez V.A., De Carvalho R.M., Tavares L.M., Insights into advanced ball mill modelling through discrete element simulations, *Minerals Engineering*, 127 (2018) 48–60. DOI: 10.1016/j.mineng.2018.07.018
- Rogers R.S.C., Austin L.G., Residence time distribution in ball mills, *Particulate Science and Technology*, 2 (1984) 191–209. DOI: 10.1080/02726358408906404
- Rogers R.S.C., Austin L.G., Brame K.A., Mill sizing for phosphate grinding in mills of 0.2 to 5 meters in diameter. *Mining, Metallurgy & Exploration*, 3 (1986) 240–246. DOI: 10.1007/BF03402488
- Sedlatschek K., Bass L. Contribution to the theory of milling processes, *Powder Metallurgy Bulletin*, 6 (1953) 148–153.
- Shahcheraghi S.H., Mulenga F.K., Tavakoli Mohammadi M.R., Mousavi S.M., How precise are ore breakage parameters measured from direct batch milling tests?, *Minerals Engineering*, 137 (2019) 157–159. DOI: 10.1016/j.mineng.2019.04.010
- Shampine L.F., Gladwell I., Thompson S., *Solving ODEs with MATLAB*, Cambridge University Press, New York, 2003, ISBN: 9780521530941.
- Tavares L.M., Chapter 1 Breakage of Single Particles: Quasi-Static, in: Salman A.D., Ghadiri M., Hounslow M.J. (Eds.), *Handbook of Powder Technology*, Elsevier Science B.V., 2007, pp. 3–68, ISBN: 0167-3785. DOI: 10.1016/S0167-3785(07)12004-2
- Tavares L.M., A review of advanced ball mill modelling, *KONA Powder and Particle Journal*, 34 (2017) 106–124. DOI: 10.14356/kona.2017015
- Tavares L.M., King R.P., Single-particle fracture under impact loading, *International Journal of Mineral Processing*, 54 (1998) 1–28. DOI: 10.1016/S0301-7516(98)00005-2
- Vogel L., Peukert W., Breakage behaviour of different materials—construction of a mastercurve for the breakage probability, *Powder Technology*, 129 (2003) 101–110. DOI: 10.1016/S0032-5910(02)00217-6
- Yildirim K., Cho H., Austin L.G., The modeling of dry grinding of quartz in tumbling media mills, *Powder Technology*, 105 (1999) 210–221. DOI: 10.1016/S0032-5910(99)00140-0

## Author’s Short Biography



### Ecevit Bilgili

Dr. Ecevit Bilgili is a Professor, AIChE Fellow, master teacher, and associate chair of the Chemical and Materials Engineering department at NJIT. He holds a PhD in chemical engineering from Illinois Institute of Technology, Chicago, USA. His Particle Engineering and Pharmaceutical Nanotechnology Lab has been conducting research in designing formulations and processes for high-value-added products like pharmaceuticals with enhanced functionalities. His research entails development, optimization, intensification, and scale-up of various particulate processes such as milling, granulation, and drying. Dr. Bilgili also models various milling processes via combined DEM–PBM. He currently serves as the Associate Executive Editor of *Advanced Powder Technology* journal.

# A Hybrid PBM-DEM Model of High-Pressure Grinding Rolls Applied to Iron Ore Pellet Feed Pressing<sup>†</sup>

Victor A. Rodriguez<sup>1</sup>, Túlio M. Campos<sup>1</sup>, Gabriel K.P. Barrios<sup>1</sup>,  
Gilvandro Bueno<sup>2</sup> and Luís Marcelo Tavares<sup>1\*</sup>

<sup>1</sup> Department of Metallurgical and Materials Engineering, Universidade Federal do Rio de Janeiro, Brazil

<sup>2</sup> Vale S.A., Complexo de Tubarão, Brazil

## Abstract

Mathematical models of high-pressure grinding rolls (HPGR) have attracted great attention, owing to their role in optimization of operating machines as well as in the design and selection of new ones. Although population balance models (PBM) and the discrete element method (DEM) have been used in this task, both suffer from important limitations. Whereas PBMs have challenges associated to the prediction of operating gap and to the validity of several of its assumptions in different formulations in the literature, application of DEM has its own challenges, in particular when fed with distributions containing large amounts of fines. This work proposes a hybrid approach in which the coupling of DEM to particle replacement models and multibody dynamics is used to predict operating gap, throughput and power, as well as providing information along the rolls length that is used in PBM to predict the product fineness. The hybrid approach is then compared to both DEM and a PBM (Modified Torres and Casali), demonstrating similar results to the later when applied to simulating a pilot-scale machine operating under different conditions, but improved prediction when applied in scale-up to an industrial-scale HPGR.

**Keywords:** high-pressure grinding rolls, discrete element method, population balance method, modelling, simulation

## 1. Introduction

Since the introduction of the high-pressure grinding rolls (HPGR) technology, various authors have proposed different approaches to its mathematical modelling, which may be classified as predominantly empirical, phenomenological or mechanistic.

Schönert (1988) was the first to propose relationships among key performance variables, involving geometrical variables of the HPGR such as rolls diameter and length; operating variables as rolls velocity, working gap, nip angle, working pressure and material variables such as flake density. Based on experimental evidence, Austin et al. (1993; 1995) and Morrell et al. (1997), proposed relationships to predict the porosity of the product flakes, as well as the working gap as a function of the specific grinding force, including a correction factor for the effects of rolls surface, feed top size, scale of the machine, moisture content and rolls speed.

In regard to prediction of product fineness, Klymowsky

and Liu (1997) and Morrell (2004; 2010; 2022) developed work indices that characterize empirically the relationship between the energy that is applied by an HPGR to a particle bed and the resultant product fineness. Application of the HPGR work index to predict the specific energy consumed by the machine demands the use of correction factors that reflect the effect of top feed particle size, fines, moisture content, mode of operation (open- or closed-circuit), material strength, and roll surface. More recently, Chelgani et al. (2021) and Tohry et al. (2021) proposed yet another empirical approach that is based on the so-called Explainable Artificial Intelligence (EAI). Although it requires large databases originated from monitoring variables in industrial-scale plants, it demonstrated to be able to predict accurately the 80 % passing size in the product and the power draw using linear and nonlinear multivariable assessment, being useful in optimizing a machine in operation. These approaches may be regarded as predominantly empirical since they do not rely on a consistent description of the underlying physics of machine operation.

Phenomenological models have been widely used to predict the HPGR product particle size distribution. Different authors have developed approaches based on the self-similarity concept (Fuerstenau et al., 1991; Lim et al., 1996), different formulations of the population balance model (PBM) (Austin et al., 1993; Dundar et al., 2013;

<sup>†</sup> Received 18 April 2022; Accepted 23 May 2022  
J-STAGE Advance published online 2 July 2022

\* Corresponding author: Luís Marcelo Tavares;  
Add: COPPE/UFRJ, Cx. Postal 68505, CEP 21941-972, Rio de Janeiro, Brazil  
E-mail: [tavares@metalmat.ufrj.br](mailto:tavares@metalmat.ufrj.br)  
TEL: +55 21 2290-1544 (ext. 246)

Thivierge et al., 2022), including those considering different breakage zones (pre-crushing, edge and compression zones) and mechanisms (Daniel and Morrell, 2004; Morrell et al., 1997), which are often characterized using the piston-and-die, besides laboratory- and pilot-scale HPGR tests (Rashidi et al., 2017).

Torres and Casali (2009) proposed a PBM formulation of the HPGR that refined the description of the edge and central products, relying on an empirical parabolic variation of axial pressure profile along the rolls. In their model, the specific breakage rates are a function of the specific energy input. As such, good predictions of product fineness rely on the ability of the model to properly predict HPGR throughput and power. Based on a large number of experiments, Campos et al. (2019a) identified some limitations of the Torres and Casali approach when applied to a pilot-scale HPGR processing iron ore pellet feed. The authors proposed modifications of the expressions originally used to describe HPGR throughput, associated to the material ejection from the edge of the rolls, as well as to the power consumption equation. Additional modifications were also proposed and validated in industrial-scale HPGRs, including a breakage saturation model and an equation to account for variations of the axial pressure profile (Campos et al., 2021a).

One important application of mathematical models is in sizing and scale-up of HPGRs (Daniel and Morrell, 2004; Morrell et al., 1997; Schönert, 1988), where limitations are recognized when they deal with prediction of HPGR throughput (Banini et al., 2011), working gap and product fineness (Daniel and Morrell, 2004). Many of the mentioned scale-up studies are based on HPGR testing in pilot- and industrial-scale machines. However, experimental tests require a large mass of material even at the laboratory scale (Rashidi et al., 2017). The piston-and-die test is adopted by many researchers to study interparticle breakage and obtain information of the compressibility and breakage response of the particle bed. Models based on the PBM and piston-and-die tests include the description of the energy absorption in different size classes of a compressed particle bed (Liu and Schönert, 1996) and the creation of new surface area and particle bed porosity (Dundar et al., 2013; Esnault et al., 2015) to describe the HPGR product particle size distribution. In addition, the piston-and-die test has also been used to predict and scale-up HPGR performance variables (Davaanyam et al., 2015; Hawkins, 2008; Nadolski et al., 2011; Pamparana and Klein, 2021).

The application of mechanistic models to simulate comminution machines has been increasing in recent years. Mechanistic models are meant to describe in detail the effect of operating and design variables since they can decouple material from machine contributions in the process. This is accomplished by both characterizing and modelling in detail each of the breakage mechanisms, almost invari-

ably using the Discrete Element Method (Weerasekara et al., 2013). However, simulation of large-scale industrial comminution machines using DEM deals with challenges that include the large number of elements (up to several million particles), boundaries containing large numbers of elements, wide particle size ranges and need to couple with other tools describing the additional relevant physics of the system, which include particle breakage, dynamic geometry interactions, solid-fluid interactions, etc. (Cleary, 2004).

In particular, laboratory- and pilot-scale DEM simulations of HPGRs allowed to describe the effect of feed size distribution, roll dimensions and speed, applied specific force, besides features such as lateral confinement, roll wear profile and feed segregation. These have then been used to predict performance variables that include throughput, working gap, power consumption and compressive force profile along the rolls, besides skewing (Barrios and Tavares, 2016; Cleary and Sinnott, 2021; Nagata et al., 2020; Quist and Evertsson, 2012; Rodriguez et al., 2021; 2022a; 2022b).

However, prediction of size distribution of the product remains a great challenge in DEM simulations of HPGRs. In this regard, two publications are worth mentioning. Herbst and co-workers (2011) combined Metso's proprietary Fast Breakage simulation approach in DEM, experimental data from piston-and-die tests and the energy-based population balance model as alternatives to ore characterization and equipment selection by HPGR pilot-plant testing. The validated physics-based model was then successfully used to predict the performance of industrial-scale HPGRs using the proposed energy-based scale-up method. Although promising, their approach did not account for the axial force and throughput distribution along the rolls.

Cleary and Sinnott (2021) simulated an industrial-scale HPGR using DEM including a particle replacement model (PRM) to predict the variation of flow, pressure and particle breakage response along the rolls. Yet, the authors recognized that it is not possible to include all fine particles in the DEM simulations owing to the large computational effort, so that a minimum cut-off size was applied to represent the HPGR product, representing the fines as additional mass in the finest resolved size class. While good predictions were reached, such approach is not suitable to predict HPGR operation with very fine feeds.

The present work proposes a hybrid modelling approach, through which HPGR throughput and power are described as a function of roll axial position for a given set of design and operating conditions through coupled DEM-MBD-PRM simulations (Rodriguez et al., 2022a; 2022b), whereas size reduction is also predicted as a function of roll axial position using PBM considering the breakage distribution and selection functions. The approach has been applied to a base case, consisting of a pilot-scale HPGR in size reduction of iron ore pellet feed with 80 % passing size

as fine as 103  $\mu\text{m}$ , from which model parameters have been fitted. The approach was validated by comparing model predictions to data from the HPGR operating under different specific forces and roll velocities. The greatest potential of the model has then been demonstrated by predicting the performance of an industrial-scale HPGR based on breakage parameters calibrated at pilot-scale.

## 2. Modelling background

### 2.1 Proposed hybrid model

The model consists of linking outputs from DEM simulations to the population balance model (PBM). This later is represented by the energy-specific selection function proposed by Herbst and Fuerstenau (1980), a non-normalizable breakage distribution function used by Campos et al. (2019a) and selected expressions proposed by Torres and Casali (2009). Following this approach, DEM simulations allow to capture the effect of design and operating variables on the HPGR performance, while the PBM model allows dealing with the entire range of particle sizes fed to the machine.

As presented in detail in recent publications by the authors (Rodriguez et al., 2022a; 2022b), outputs provided by the DEM simulations correspond to total power ( $P_{\text{DEM}}$ ), total throughput ( $Q_{\text{DEM}}$ ), compressive axial force profile in the region between the gap and the nip angle ( $F_k$ ), and axial mass flowrate profile in the region between the gap and the nip angle ( $V_k$ ).

Following the PBM approach proposed by Torres and Casali (2009), the roll length is discretized in  $N_B$  sections. In each of the  $k$  sections, the mass of material contained in every size class  $i$  is given by:

$$v_{z,k} \frac{d}{dz} w_{i,k}(z) = \sum_{j=1}^{i-1} S_{j,k} b_{ij} w_{j,k}(z) - S_{i,k} w_{i,k}(z) \quad (1)$$

where  $w_{i,k}$  is the fraction of material in size class  $i$  and section  $k$ ,  $z$  is the distance between the beginning of the compression zone and the extrusion zone,  $v_{z,k}$  is the material flow velocity in the  $z$  direction for each section  $k$ ,  $S_{i,k}$  is the breakage rate for each size class  $i$  and section  $k$ , and  $b_{ij}$  is the breakage function in distributed form.

Two functions must be known in order to solve the resulting system of differential equations:  $b_{ij}$  and  $S_{i,k}$ . Campos et al. (2019a) and Faria et al. (2019) observed that, for some Brazilian iron ores, the non-normalizable breakage function proposed by King (2001) was required to describe their response, being given by:

$$B_{ij} = \phi \left( \frac{x_i}{x_j} \right)^\gamma + (1 - \phi) \left( \frac{x_i}{x_j} \right)^\beta \quad \text{for } x_i \geq \omega \quad (2)$$

$$B_{ij} = \phi \left( \frac{x_i}{\omega} \right)^\eta \left( \frac{x_i}{x_j} \right)^\gamma + (1 - \phi) \left( \frac{x_i}{x_j} \right)^\beta \quad \text{for } x_i < \omega$$

where  $\gamma$ ,  $\beta$ ,  $\phi$ ,  $\omega$  and  $\eta$  are fitting parameters and  $b_{ij} =$

$B_{i-1,j} - B_{ij}$ . The specific selection function can be calculated using the polynomial equation given by Herbst and Fuerstenau (1980):

$$\ln \left( \frac{s_i^E}{s_1^E} \right) = \zeta_1 \ln \left( \frac{\bar{x}_i}{\bar{x}_1} \right) + \zeta_2 \left[ \ln \left( \frac{\bar{x}_i}{\bar{x}_1} \right) \right]^2 \quad (3)$$

where  $s_1^E$  (t/kWh),  $\zeta_1$  and  $\zeta_2$  are the parameters to be fitted from a base case,  $\bar{x}_i$  is the representative size given by  $\bar{x}_i = \sqrt{x_{i-1}x_i}$  and  $\bar{x}_1$  is a reference size. In the present work  $\bar{x}_1$  was set to 1 mm. Following the Torres and Casali modelling approach, Eqn. 4 calculates the breakage rates ( $S_{i,k}$ ), giving

$$S_{i,k} = s_i^E \frac{P_k}{M_k} \quad (4)$$

where  $P_k$  and  $M_k$  are the power profile and the mass of solids profile along the roll length gathered from the DEM simulations. Power profile is hereby calculated by normalizing the compressive force profile ( $F_k$ ) and multiplying it by the total HPGR power, with both variables gathered from the DEM simulation (Eqn. 5). The throughput profile in Eqn. 6 is then calculated on the basis of the total throughput and mass flowrate of solids profile from DEM:

$$P_k = P_{\text{DEM}} \frac{F_k}{\sum_{j=1}^{N_B} F_j} \quad (5)$$

$$Q_k = Q_{\text{DEM}} \frac{V_k}{\sum_{j=1}^{N_B} V_j} \quad (6)$$

where  $P_{\text{DEM}}$  is power consumption (kW),  $Q_{\text{DEM}}$  is total throughput (t/h), and  $F_k$  is the compressive force profile (kN) predicted by DEM. Given their direct relationship to power, compression forces ( $F_k$ ), provided by DEM simulation, are used in Eqn. 5. In the hybrid model approach, the mass flowrate profile of solids ( $V_k$ ) is then defined on the basis of the mean particle residence time ( $\lambda_k$ ) and the total mass ( $M_k$ ) in each block ( $k$ ) along the rolls:

$$V_k = \frac{M_k}{\lambda_k} \quad (7)$$

The solution of Eqn. 1 allows calculating the fraction retained in each size class of every block ( $k$ ) following the Torres and Casali model approach, which is based on the Reid's analytical solution (Reid, 1965):

$$p_{i,k} = \sum_{j=1}^i A_{ij,k} \exp \left( -s_j^E \frac{P_k}{Q_k} \right) \quad (8)$$

where  $A_{ij,k}$  is a matrix given by:

$$A_{ij,k} = \begin{cases} 0 & i < j \\ \sum_{l=j}^{i-1} \frac{b_{il} S_{l,k}}{S_{i,k} - S_{j,k}} A_{lj,k} & i > j \\ f_i^{\text{IP}} - \sum_{l=1}^{i-1} A_{il,k} & i = j \end{cases} \quad (9)$$



where is the fraction retained in each size class  $i$  in the feed.

Finally, the overall product size distribution is calculated from the weighted average product size distributions of each section  $k$  and is given as:

$$p_i^{\text{HPGR}} = \frac{1}{Q_{\text{DEM}}} \sum_{k=1}^{N_B} p_{i,k} Q_k \quad (10)$$

## 2.2 Modified Torres and Casali model

In the present study, the Modified Torres and Casali (MTC) model (Campos et al., 2019a) represents the purely phenomenological model that is compared to the proposed hybrid approach. A summary of its main expressions and the comparison with the corresponding ones in the hybrid model is presented in **Table 1**. Throughput and power models in the Modified Torres and Casali model required fitting four parameters ( $\varphi$ ,  $v$  and  $\tau$  for the throughput model and  $\kappa$  for the power model). That was done on the basis of a selected base case. The throughput profile is assumed as uniform. On the other hand, whereas the Torres and Casali (2009) model assumes a parabolic pressure profile along the rolls, the MTC model allows for different profiles, given evidence from both experiments and DEM simulations (Cleary and Sinnott, 2021; Rodriguez et al., 2021).

## 3. Materials and methods

### 3.1 Experimental

In the present study, the material selected is an iron ore concentrate processed in the production line of the Com-

plexo the Tubarão (Vitoria, Brazil) and used in the production of iron ore pellets. The iron ore concentrate, originally from the Itabira region, in the Iron Quadrangle from Minas Gerais (Brazil), is essentially composed of hematite with minor amounts of quartz as contaminant (Campos et al., 2019b).

Experiments consisted in both pilot-scale tests and an industrial survey. Pilot-scale tests were carried out in an RPR 03.6 – 100/32 roller press manufactured by KHD Humboldt Wedag AG with 1 m-diameter rolls (**Fig. 1**). A sample of 100 tons was collected from the production line in the HPGR feed located in the pre-grinding stage (Campos et al., 2019b). The feed moisture content was 7.5 %, which is very similar to the value practiced in industrial-scale operations, although close to the maximum value allowable for pressing iron ore concentrates (Van der Meer, 1997). A total of eight experiments were carried out varying the specific force (2.5 and 3.5 N/mm<sup>2</sup>) and the peripheral roll velocity (0.20, 0.35, 0.50 and 0.70 m/s). Throughput, power consumption, specific energy, operating gap, roll velocity and operating pressure were obtained from the supervisory system. During each test, a sampling apparatus was introduced underneath the rolls to collect samples from five parallel sections of the discharge. The apparatus was introduced manually and allowed characterizing the axial variation of the product fineness along the rolls (Campos et al., 2019b). Additional pilot-scale tests were carried out with a blend composed of iron ore concentrates from the Iron Quadrangle, normally used to feed the pelletizing

**Table 1** Summary of expressions and approaches used for estimating the key performance variables in both the Modified Torres and Casali model (Campos et al., 2019a; Campos et al., 2021a) and the proposed hybrid model.

Model	Modified Torres and Casali	Hybrid approach
Throughput	$Q = LU_g \rho_g x_g \left( \frac{100}{100 - \delta} \right)$ $\ln \left( \frac{\delta}{\varphi} \right) = -v \frac{\chi_g}{D} \left( \frac{U}{U_{\max}} \right)^\tau \quad U_g = \frac{x_c U \rho_a^*}{x_g \rho_g}$	Mass flow sensor underneath the working gap in DEM simulations
Throughput profile	Uniform, with step bypass flow	Eqn. 7 Extracted from $N_B$ sections positioned in the compression zone (i.e. between the working gap and nip angle) along the rolls in the DEM simulations. Each section moves as a plug
Power consumption	$P = 2F \sin \left( \frac{\kappa \alpha_{\text{ip}}}{2} \right) U$	$P = 4\pi \tau_{\text{DEM}} U$
Power distribution along the rolls	$P_k = \frac{4}{\pi} \sum_{n=1}^{100} \frac{1 - \cos n\pi}{2n} e^{-\mu(n^2\pi^2)} \sin n\pi \bar{y}_k$	Force profile extracted from $N_B$ bins located in the compression zone (i.e. between the working gap and nip angle) along the rolls in the DEM simulations
Breakage model	$p_i^{\text{HPGR}} = \frac{1}{N_B} \sum_{k=1}^{N_B} p_{i,k}$	$p_i^{\text{HPGR}} = \frac{1}{Q_{\text{DEM}}} \sum_{k=1}^{N_B} p_{i,k} Q_k$

$D$ : roll diameter,  $L$ : roll length,  $U$ : roll velocity,  $U_g$ : material velocity;  $\rho_a$ : bulk density  $\rho_g$ : flake density,  $x_c$ : critical size,  $x_g$ : operating gap,  $\delta$ : the percentage of material ejected by the edge of the rolls;  $F$ : compressive force,  $\alpha_{\text{ip}}$ : nip angle,  $\tau_{\text{DEM}}$ : torque on the rolls extracted from DEM simulation,  $\omega$ : angular velocity of the roll,  $\kappa$ : nip angle parameter,  $\varphi$ ,  $v$  and  $\tau$ : throughput model parameters,  $\mu$ : power profile parameter,  $\bar{y}_k$ : normalized average position,  $N_B$ : number of sections along the roll length. \*Only used in simulations of industrial-scale machines



**Fig. 1** Pilot-scale HPGR (left) and industrial-scale HPGR (right) used in the experimental campaigns.

**Table 2** Summary of the main design and operating conditions of HPGRs in the experimental campaigns.

Variables	Pilot-scale study	Scale-up study	
		Pilot	Industrial
Roll diameter (m)	1.0	1.0	1.4
Roll length (m)	0.32	0.32	1.6
Specific force (N/mm <sup>2</sup> )	2.5–3.5	2.5	2.5
Operating pressure (bar)	37.0–52.0	40.0	60.9
Rolls velocity (m/s)	0.20–0.70	0.32	1.30
Operating gap (mm)	6.8–8.2	13.8	6.0
Maximum roll velocity (m/s)	0.90	0.90	1.95
Feed 80 % passing size (μm)	103	143	143
Feed % passing 45 μm	28	26	26
Feed BSA (cm <sup>2</sup> /g)	450 ± 10	490 ± 10	470 ± 10

plant in question (Campos et al., 2021a). A previous study demonstrated relatively minor differences in pressing response between the samples (Campos et al., 2021b), making comparisons valid between them. Operating conditions and main feed characteristics are presented in **Table 2**.

In addition, industrial-scale data were obtained from a survey on an HPGR manufactured by KHD/WEIR (**Fig. 1**). The machine has 1.4 m-diameter rolls, with 15.9 mm diameter studs, and cheek plates. During the survey the HPGR operated at a specific compressive force of 2.5 N/mm<sup>2</sup> and roll velocity of 1.3 m/s. Performance variables of the HPGR were captured using the supervisory system. Samples from the feed and product were collected from belt cuts for size analysis.

Particle size distributions from samples of the feed and product were measured by laser scattering in a Malvern Mastersizer<sup>TM</sup> 2000 (Malvern Instruments Inc), whereas Blaine specific surface area (BSA) was measured in a PC-Blaine-Star (Zünderwerke Ernst Brün GmbH).

### 3.2 Coupled DEM-MBD-PRM simulations

Simulations using DEM were carried out coupled to multibody dynamics (MBD), describing the translation of the movable roll, and particle replacement method (PRM), following the approach proposed and adopted as part of earlier studies by the authors (Rodriguez et al., 2021; 2022a). In the present work, DEM simulations were carried out using the commercial software Altair EDEM version 2020.3. The Hertz–Mindlin contact model was used, in which the normal force component is described on the basis of Hertz contact theory, whereas the tangential force model is based on Mindlin–Deresiewicz work (Mindlin 1949; Mindlin and Deresiewicz 1953). Furthermore, these particles are allowed to break owing to the use of a sphere-based particle replacement (PRM) strategy, recently proposed by Tavares et al. (2021) and coded in an application programming interface (API). Finally, a two-way coupled model based on MBD and DEM was implemented to calculate the dynamics of the floating roll as initially proposed elsewhere (Edwards et al., 2013; Barrios and Tavares, 2016). Since this DEM-MBD coupling was embedded in the EDEM software, the use of co-simulation tools became unnecessary.

#### 3.2.1 Material properties

Due to the large number of particles demanded in HPGR simulations, the authors selected a coarser particle size distribution, with a top size 8 mm, to represent the iron ore pellet feed. This approach was already successfully used in this application in previous studies (Rodriguez et al., 2021; 2022a). From this and bench-scale tests, which included measurement of the static and dynamic angles of repose (Rodriguez et al., 2022a), material and contact parameters were calibrated (**Table 3**). Addition material properties were estimated on the basis of a piston-and-die test, resulting in the selection of values of Poisson's ratio of 0.25, particle density of 3,011 kg/m<sup>3</sup> and shear modulus of 2 GPa (Rodriguez et al., 2022a). Finally, values of breakage model parameters were taken from previous publications (Rodriguez et al., 2021; 2022a). The same set

**Table 3** Hertz–Mindlin contact parameters used in the DEM simulations.

Coefficient	Ore-steel	Ore-ore
Restitution	0.15	0.20
Static friction	0.49	0.55
Rolling friction	0.47	0.51

of material, contact and breakage parameters were used to simulate both pilot- and industrial-scale HPGRs.

### 3.2.2 Equipment setup

At first, computer Aided Designs (CAD) of the HPGR units simulated were generated. The translational dynamics in the floating roll was described by a force controlled in the longitudinal direction “x”, while only the kinematics of the rotating movement in both rolls with a fixed angular velocity was described. Being a one-dimensional model, it does not allow for skewing of the rolls, studied by Rodriguez et al. (2022b). The rolls movement started only when DEM particles filled the hopper from a particle factory located above the rolls. From this point on in the simulation, new particles were added continuously until steady-state conditions were reached, and then analysis were performed.

The hopper level is an important aspect in DEM simulation of HPGRs, since particles located in this region only apply pressure to the particle bed sitting between the rolls (Cleary and Sinnott, 2021; Nagata et al., 2020). In the present study, the recommendation from Cleary and Sinnott (2021) was followed, where the minimum mass in the hopper ( $m_{\text{hopper}}$ ) is given by:

$$m_{\text{hopper}} \geq L_h W^2 \rho_{af} \quad (11)$$

where  $L_h$  is the length along the diameter of the rolls and  $W$  the width of the feed hopper, and  $\rho_{af}$  is the bulk density of the feed. During simulations, this minimum mass of particles filling the hopper was maintained approximately unchanged.

Even though the present approach already used virtual particles that are larger than those in the real operations (upscaled particles), maintaining the hopper level to meet Eqn. 11 imposes a major computational challenge when dealing with simulations of industrial-scale machines. As such, in order to reduce the number of elements required in the simulation, the final portion of the hopper silo was filled with particles of even coarser size (60 mm diameter) and density ( $10,000 \text{ kg/m}^3$ )—called column-pressure particles—so as to match the same pressure that would have been generated by piling up additional feed particles. Fig. 2 illustrates this scheme, where these column-pressure particles are placed without interfering with the rolls. It is worth mentioning that, although these particles move downwards

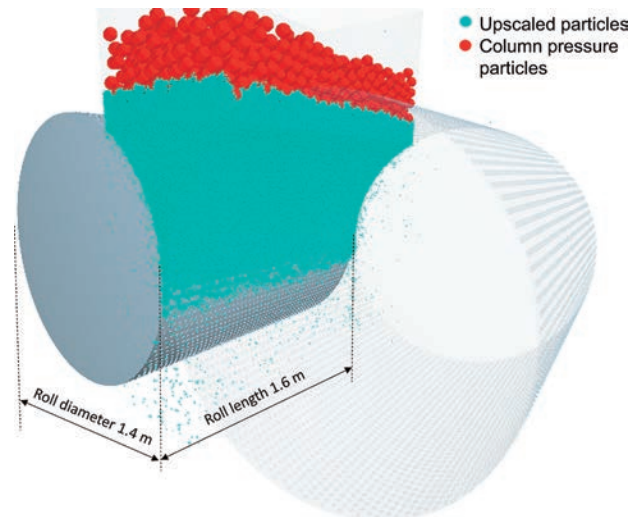


**Fig. 2** Representation of industrial HPGR simulation using the coupled DEM-MBD-PRM with both feed (upscaled) particles and column-pressure particles.

as rolls rotate, the short simulation times required to reach steady state conditions prevented them from ever contacting the rolls.

### 3.2.3 Measurement of key variables in DEM simulations

As part of the hybrid simulation approach, the DEM simulations directly provide throughput and power of the HPGR, as informed in Table 1. Indeed, total throughput between the rolls was estimated with a cylindrical geometry sensor positioned underneath the working gap. The total power was calculated based on the torque required to rotate the rolls multiplied by the rotation frequency. The mass flowrate in each block ( $V_k$ ) and axial compressive force ( $F_k$ ) profiles were estimated from a grid bin located in the compression zone, presented in detail elsewhere (Rodriguez et al., 2022a).

With the aim of providing an additional comparison with both phenomenological and hybrid approaches, the size distribution from the DEM simulations using PRM was also computed. The approach used to obtain the particle size distribution using the Tavares PRM can be found elsewhere (Tavares et al., 2021).

### 3.3 PBM parameter estimation

The proposed Hybrid model was implemented in Matlab™ (version R2021a, Mathworks Inc.), which is the platform also used in predictions using the Modified Torres and Casali model. Initially, the parameter optimization was performed on a base case test, which consisted in the pilot-scale experiment with a peripheral roll velocity of 0.35 m/s and specific compressive force of 2.5 N/mm<sup>2</sup> (reference test #1 in Table 4). Breakage function parameters (Eqn. 2) were estimated as part of previous studies

by Campos et al. (2019a), being also used in the present work. The three remaining parameters in Eqn. 3 were then calibrated from reference test #1.

Parameter optimization for DEM simulations, used in power and mass flowrate predictions in the Hybrid model was conducted as part of an earlier work (Rodriguez et al., 2022a), whereas in the case of the Modified Torres and Casali model, reference tests #1 and #2 (Table 4) were used. Two parameters from the throughput model (Table 1) were kept constant and equal to values from a previous study ( $\varphi = 100$  and  $\tau = 0.1$ ), since they were found to be valid for a range of machines (Campos et al., 2019a). The single fitting parameters for the nip angle model ( $\kappa$ ) and the remaining parameter for the throughput model ( $\nu$ ) were then calibrated on the basis of the reference tests in Table 4. This was used to ensure that the model was properly calibrated to capture variations when the HPGR was operating under different conditions. In order to ensure a parabolic pressure profile as assumed by Campos et al. (2019a), parameter  $\mu$  from Table 1 was set to 0.05. From the fitted parameters, prediction of the remaining pilot-scale experiments as well as the industrial-scale survey was performed.

The optimal parameters were fitted using the function *fminsearch* from Matlab™ (version R2021a, Mathworks Inc.), which allows finding the minimum of unconstrained multivariable function using the derivative-free method. The objective function consisted of the sum of squares of the differences in the logarithms of the experimental and fitted cumulative particle size distribution values of reference test #1.

Comparison between predictions by the different models and the experimental results were carried out from computations of the relative absolute deviation given by  $\varepsilon_{\text{ABS}} = 100|var_{\text{Exp}} - var_{\text{Calc}}|/var_{\text{Exp}}$ , where  $var_{\text{Exp}}$  is the ex-

perimental variable and  $var_{\text{Calc}}$  is the calculated variable. Besides power, throughput and product size distribution, Blaine specific surface area (BSA) was also analyzed. Predictions of BSA from simulated product size distributions were computed using the approach described elsewhere (Campos et al., 2019b).

## 4. Results and discussion

### 4.1 Parameter fitting

Different base cases were used for predictions of throughput and power in each approach. The DEM-MBD-PRM approach, used in the proposed Hybrid model, was able to make predictions of power and throughput of the pilot HPGR campaign. In that procedure, Rodriguez et al. (2022a) based their results on reference test #2 (Table 4). No particular calibration was carried out using industrial data. On the other hand, selected parameters of the power and throughput equations (Table 1) for the Modified Torres and Casali model (Campos et al., 2019a; Campos et al., 2021a) were calibrated from reference tests #1 and #2 in Table 4, resulting in the values of  $\nu = 155$  and  $\kappa = 3.2$ . The different values for these parameters from those previously fitted on the basis of data from pressing dry pellet feed fines may be attributed to the effect of moisture content.

In predicting size reduction, the optimal parameters fitted for the Hybrid model and the Modified Torres and Casali model are shown in Table 5. Both the non-normalizable breakage and the selection functions are illustrated in Fig. 3, which show that nearly identical specific selection functions were obtained from the parameter optimization procedure. The results compared to the experimental data are presented in Fig. 4, demonstrating that good agreement was reached between model and experiments, with values of the objective function of 0.038 for the Hybrid model and 0.040 for the MTC model. Results allow to conclude that the non-normalizable breakage function parameters proposed in a previous study (Campos et al., 2019a) remain valid in the present work. A closer examination of predicted product BSA shows that good agreement between

**Table 4** Operating conditions of the reference tests.

Variable	Reference test	
	#1	#2*
Specific force (N/mm <sup>2</sup> )	2.5	3.5
Operating pressure (bar)	38.6	48.5
Operating gap (mm)	8.2	7.4
Roll peripheral velocity (m/s)	0.35	0.50
Throughput (t/h)	19.9	26.8
Power consumption (kW)	47.2	66.1
Specific energy (kWh/t)	2.37	2.47
Passing 45 $\mu\text{m}$ in product (%)	52.3	52.0
Product BSA (cm <sup>2</sup> /g)	800	820

\*Additionally used to calibrate the power and throughput model in the Modified Torres and Casali model.

**Table 5** Fitted selection and breakage function parameters.

Equation	Parameter	MTC	Hybrid model
Breakage function (Eqn. 2)	$\gamma$	0.896	0.896
	$\beta$	5.461	5.461
	$\phi$	0.857	0.857
	$\eta$	0.46	0.46
	$\omega$ (mm)	0.013	0.013
Selection function (Eqn. 3)	$\xi_1$	-0.491	-0.492
	$\xi_2$	-0.191	-0.190
	$s_1^E$ (t/kWh)	0.260	0.247

fitted and predicted values for size reduction was obtained, since absolute deviations from measurements were 0.7 % and 0.5 % for the Modified Torres and Casali and Hybrid models, respectively. It is worth mentioning that values of

the specific selection function in **Table 5** differ from those reported in earlier studies (Campos et al., 2019a) primarily due to setting  $\bar{x}_1 = 1$  mm in Eqn. 3.

#### 4.2 Pilot-scale HPGR simulations

Based on the calibrations from **Section 4.1**, both modelling approaches were applied to predict the remaining pilot-scale tests (**Table 2**) pressing iron ore concentrates. Initially, **Fig. 5** compares measured and predicted throughputs, highlighting the good agreement between both model approaches and experiments. As discussed by Rodriguez et al. (2022a), good predictions were achieved using DEM-MBD-PRM simulations with average absolute deviation of 7.2 %, with larger overestimations for tests at higher throughputs (peripheral roll velocity of 0.70 m/s). Predictions of the Modified Torres and Casali model, on the other hand, show a smaller deviation of 4.6 %, underestimating values for roll peripheral velocity of 0.70 m/s.

A comparison between measured and predicted power consumptions in the pilot-scale HPGR using the Hybrid model and the MTC model is presented in **Fig. 6 (top)**. Very good agreement is evident between the Hybrid model and experiments, with mean absolute deviations of 7.9 %. Likewise, the MTC model, with  $\kappa = 3.2$  fitted based on the two pilot-scale tests (**Section 4.1**), also exhibited good agreement with experiments, with mean deviation of 9.5 %. Likewise, similar deviations of the specific energy predictions were observed in **Fig. 6 (bottom)**, being equal to 7.2 % for the Hybrid model and 8.2 % for the MTC model. Those estimates are very important for both approaches since the predicted product size distributions are directly influenced by them.

**Fig. 7** shows experimental results and predictions of product size distribution from two selected tests run at the roll peripheral velocity of 0.50 m/s. Reasonable agreement is evident, demonstrating the acceptable ability of both

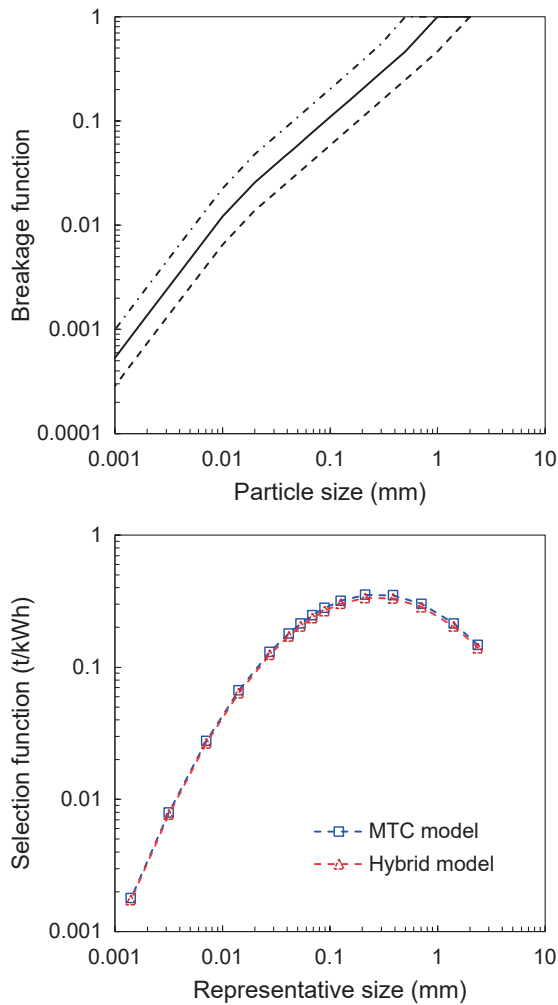


**Fig. 3** Non-normalizable breakage function of selected feed particle sizes (**top**) and comparison between specific selection function fitted for the Hybrid model and for the Modified Torres and Casali (MTC) model (**bottom**).

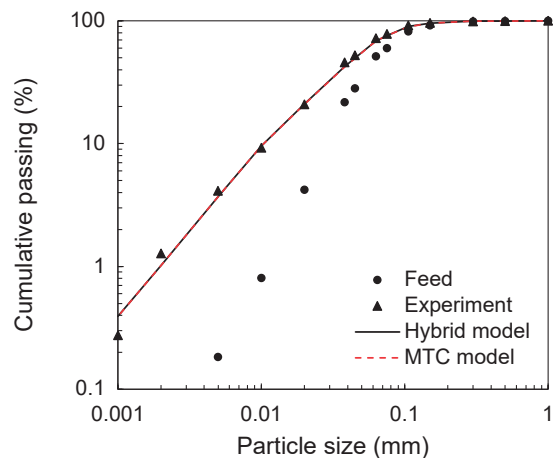


**Fig. 4** Comparison of fitted and experimental product size distributions of base case (reference test #1).

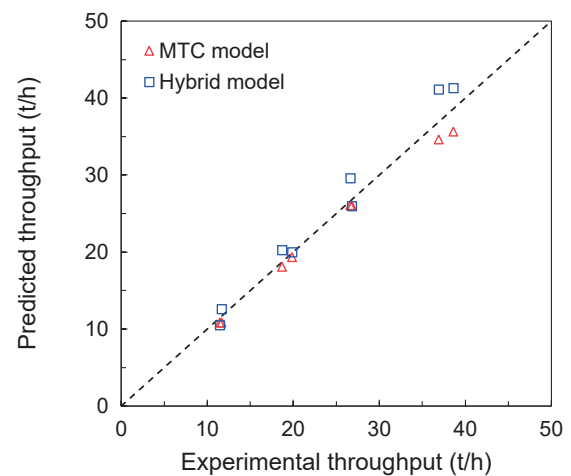


**Fig. 5** Comparison between measured and predicted throughput in the pilot-scale HPGR using the Hybrid and the Modified Torres and Casali models.

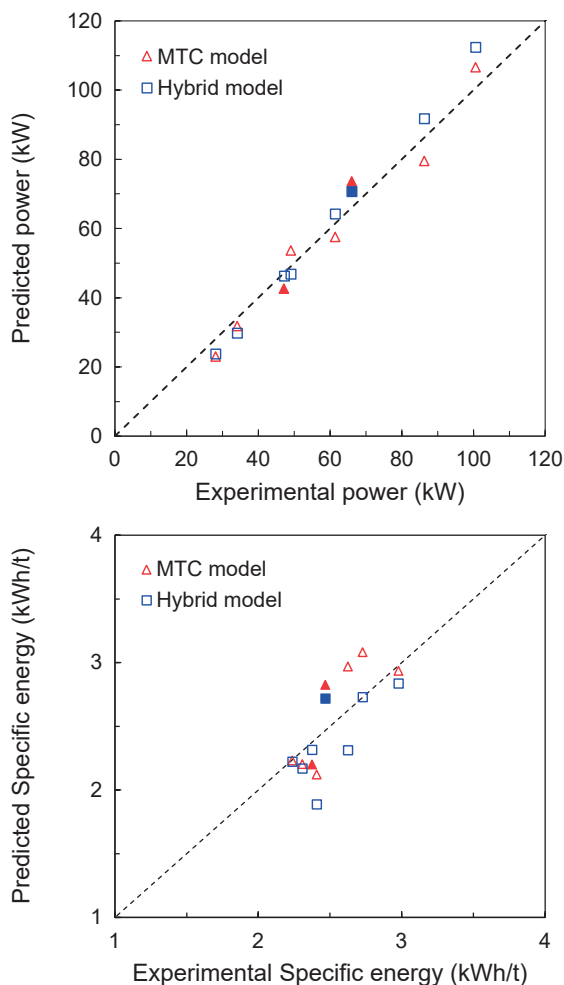


**Fig. 6** Comparison between measured and predicted power (**top**) and specific energy consumption (**bottom**) in the pilot-scale HPGR for the Modified Torres and Casali and Hybrid models. Filled markers correspond to the base cases used in model calibration.

modelling approaches in predicting product size distribution when operating conditions are varied. In application of HPGRs to iron ore concentrate pressing, it is routine to check the percent passing the 45  $\mu\text{m}$  sieve to assess the coarser part of the product size distribution, whereas the Blaine specific surface area (BSA) is strongly influenced by its finer portion. As such, **Fig. 8** presents a comparison between experimental and predicted values for both indices for all tests performed in the pilot-scale HPGR. In general, Hybrid model predictions are in only reasonable agreement with experiments, with values of average absolute deviations of 5.5 % and 6.2 % for passing in 45  $\mu\text{m}$  and the BSA, respectively. Marginally higher deviations were observed for the MTC model, where average absolute deviations of 5.9 % were obtained for the percentage passing the 45  $\mu\text{m}$  sieve and 6.7 % for the BSA.

A more detailed inspection is also possible from **Fig. 9** with a relationship between specific energy consumption and the product BSA. Unlike expected, experimental BSA values did not show clear trend with specific energy. In

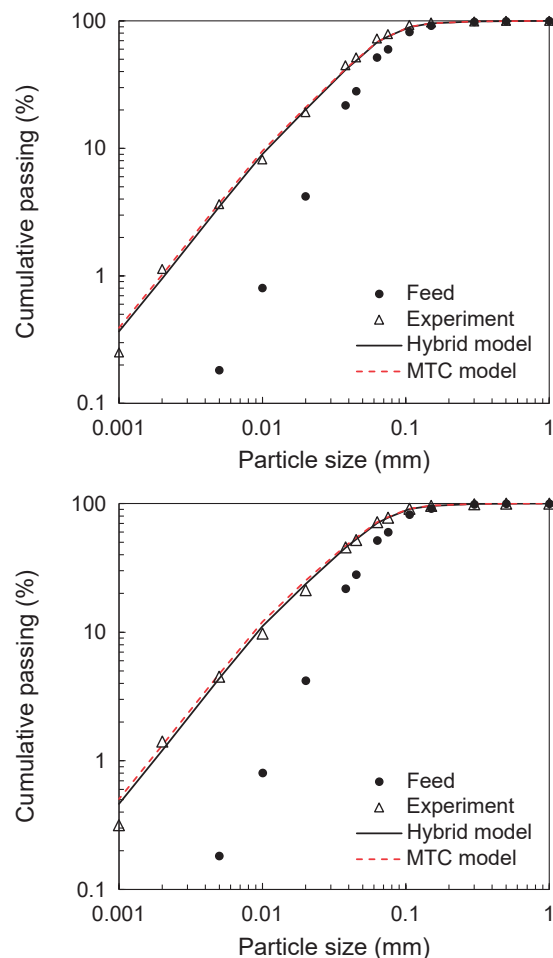


**Fig. 7** Comparison between predicted and experimental product size distributions in the pilot-scale HPGR with roll peripheral velocity of 0.5 m/s and specific compressive forces of 2.5  $\text{N}/\text{mm}^2$  (**top**) and 3.5  $\text{N}/\text{mm}^2$  (**bottom**).

general, although recent works showed no improvement in size reduction given the increment in roll peripheral velocity (Campos et al., 2019b; Van der Meer and Leite, 2019), it is worth mentioning that HPGR operations with high moisture content as in the present work would provide some acceleration on the compression zone and increase the proportion of material ejected from the edge of the rolls. These features can, at least in part, be responsible for the dispersion of the data in **Figs. 8** and **9**.

On the other hand, **Fig. 9** shows that results from the two models exhibited a clear and direct improvement in the BSA with the increase in specific energy. These results can be explained by the modelling approach adopted in both models, which relies on breakage rates (Eqn. 4) that are calculated from the product of the specific selection function and the ratio between the power consumption and the holdup. As such, although DEM provides a more detailed description, the use of the PBM limits the capability of the model in providing improved descriptions of the effect of operating variables when compared to the phenomenological (MTC) model.

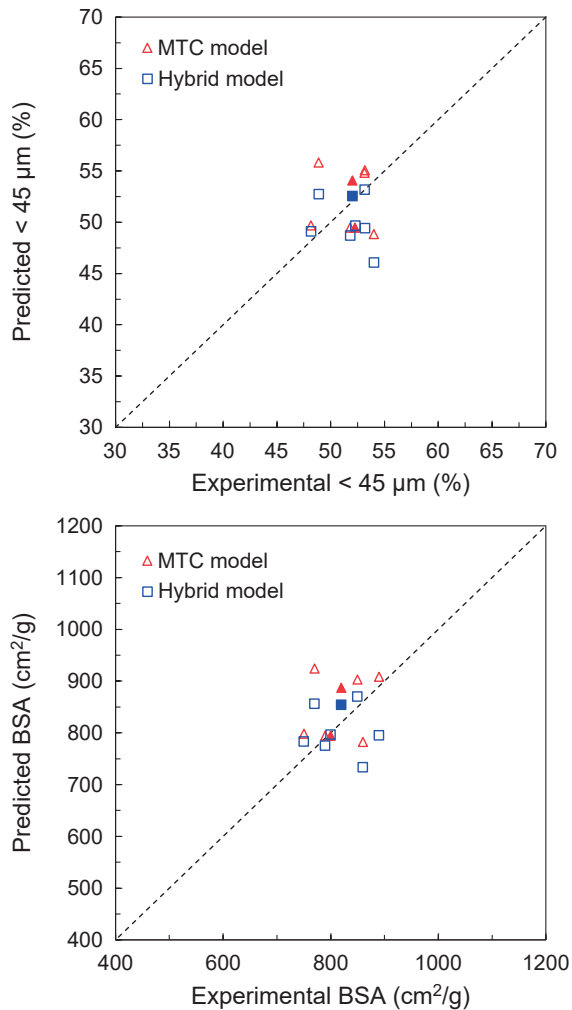


**Fig. 8** Comparison of experimental and predicted passing the 45  $\mu\text{m}$  sieve (**top**) and the BSA (**bottom**) using both the Hybrid and the Modified Torres and Casali models. Filled markers correspond to the base cases used in model calibration.

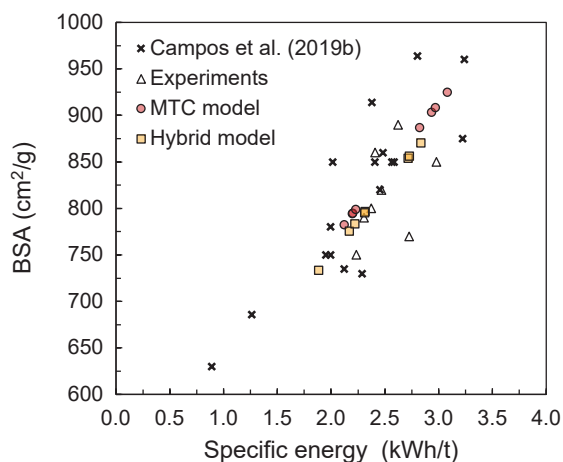


**Fig. 9** Relationship between product BSA and specific energy consumption for the tests carried out in the pilot-scale HPGR. For comparison, data are also included for the experimental campaign carried out by Campos et al. (2019b).

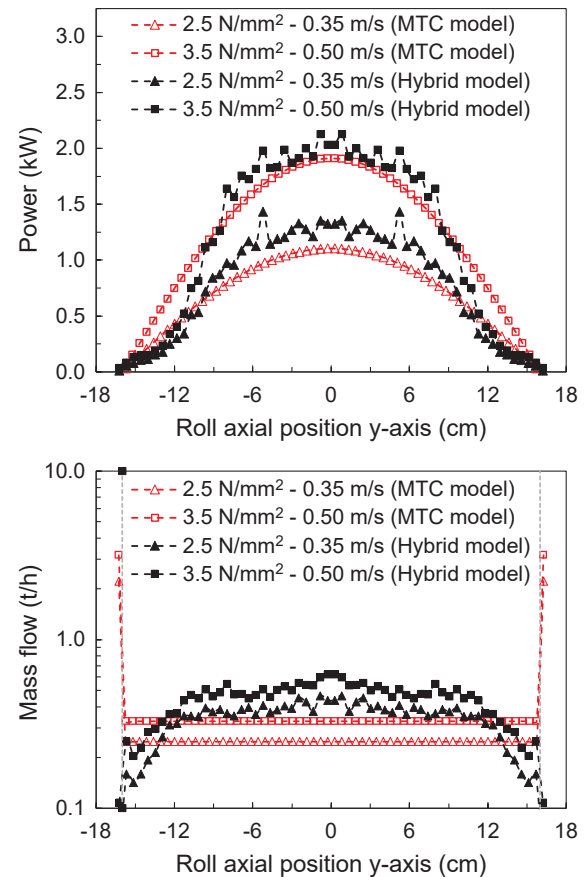


**Fig. 10** Comparison between the Hybrid model and MTC model of the power (**top**) and mass flowrate (**bottom**) profiles for the pilot-scale HPGR. Vertical dotted lines identify the projection of the rolls length.

### 4.3 Axial variation in pilot-scale HPGR

Similarities and important differences appear on how the two model approaches deal with the axial variation of power and mass flow in the HPGR, as illustrated in **Fig. 10**. Regarding the power profile, as mentioned in **Table 1**, a parabolic pattern is associated to the MTC model with the highest value at the centre of the rolls, vanishing to zero towards the edges. DEM simulations show a similar pattern, but with a more marked drop towards the edge of the rolls.

Greater differences are found in the throughput profiles, whereas the MTC model gives uniform values between the rolls and a marked step increase at the by-pass region, due to the material ejected beyond the length of the rolls (**Fig. 10 bottom**). On the other hand, the mass flowrates in the Hybrid model do not show the by-pass effect, since its values are computed within the particle bed. In addition, this approach results in higher values towards the centre of the rolls and lower values towards its edge.

As explained in **Section 3.1**, samples were collected underneath the rolls to capture the axial variation of the particle size distribution along the rolls. This is an important aspect in HPGR operation since products with coarser particle sizes are known to appear close to the edge of the rolls (Campos et al., 2019b; Lubjuhn and Schönert, 1993;

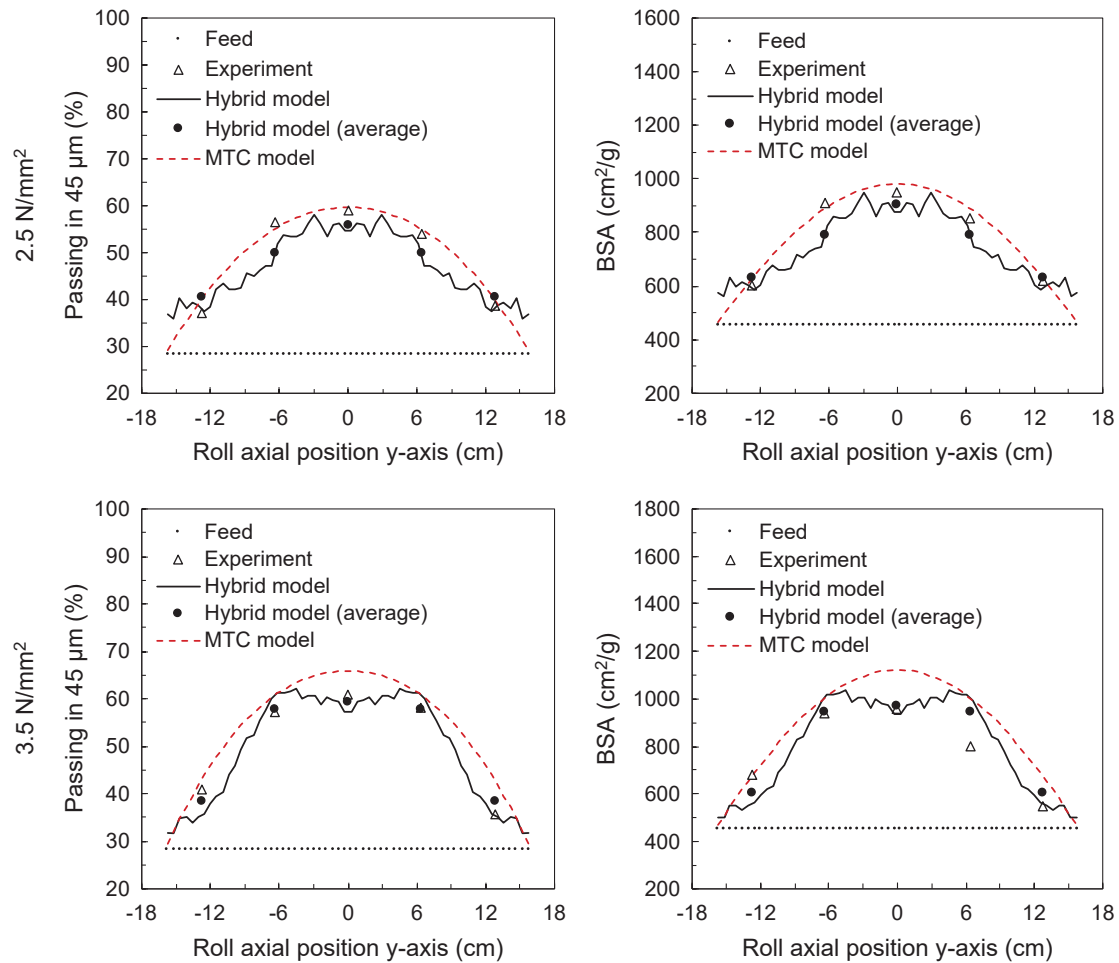


**Fig. 11** Comparison between experimental and predicted values for the percentage passing of the 45  $\mu\text{m}$  sieve and BSA using the Hybrid and the Modified Torres and Casali models for pilot-scale tests at a peripheral roll speed of 0.50 m/s.

Morrell et al., 1997; Torres and Casali, 2009), in spite of efforts that have been made to prevent it (Van der Ende et al., 2019; Herman et al., 2013). In order to check the ability of the models to describe the variation of product size distribution along the length of the rolls, predictions of selected tests are compared to experiments in Fig. 11 for the pilot-scale HPGR operating at the roll peripheral velocity of 0.50 m/s. Good agreement is evident for both test conditions simulated, in particular for the Hybrid model. Also, as already discussed by Campos et al. (2019a), the parabolic shape profile demonstrates a reasonable description for the pilot-scale HPGR studied in pressing iron ore concentrates.

#### 4.4 HPGR Scale-up

At first, a snapshot of the DEM-MBD-PRM simulation of the industrial scale HPGR is presented in Fig. 12. Around 2.5 million particles were processed in the simulation, in which the reduction in particle size becomes clear as the bed of particles move towards and through the gap. A summary of the simulation results is presented in Table 6, which shows that the Hybrid model provided reasonable predictions of total power, with a deviation of 17.8 % from the experimental results, with an even closer

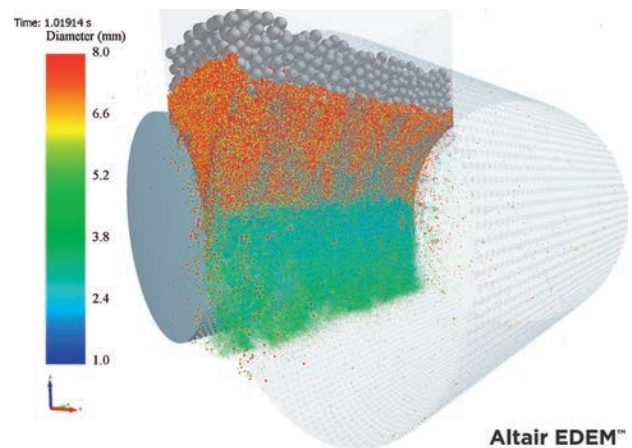


**Fig. 12** 3D rendered DEM simulation image of the industrial-scale HPGR with particles colored by size operating at specific force of 2.5 N/mm<sup>2</sup> and roll velocity of 1.30 m/s. Column-pressure particles colored in gray.

prediction of throughput, with a deviation of only 2.0 %. Greater deviations are, however, observed when comparing predictions using the modified Torres and Casali model to experiments, with 12.3 % deviation in the case of power



and 74.1 % in the case of throughput. This significant overestimation of throughput may be explained by the greater proportion of material ejected by the bypass zone in the model prediction. Similar mass transfer in the centre of the roll was predicted by both models, with around 9 % larger from that estimated from the DEM simulation as part of the hybrid model.

A comparison of the pressure profiles in pilot- and industrial-scale HPGRs predicted using DEM, shown in Fig. 13, demonstrates that the pressure profile in the industrial-scale machine is more constant in the central portion of the rolls. Indeed, the DEM simulation was able to capture this effect that was already reported experimentally by some authors (Campos et al., 2021b; Morley, 2010).

On the basis of the parameters calibrated from a base case test from the pilot-scale test campaign, presented in Section 4.1, predictions of product size distribution of the industrial HPGR survey were carried out using both the Hybrid and the Modified Torres and Casali models. Predictions are presented in Fig. 14, where the Hybrid model shows good agreement with experiments, with an average absolute deviation of 8.0 %. The poor prediction of throughput (Table 6), which directly affects the specific energy, led to the high value of absolute deviation (15.8 %) for the Modified Torres and Casali model. An additional

hypothetical case was then simulated. This condition consisted in matching the experimental specific energy in each model and make prediction of the industrial test. These results are presented as dashed lines in Fig. 14, with reductions in absolute deviations to 6.2 % and 6.9 % for the MTC and Hybrid models, respectively.

A final comparison is shown in Fig. 15, where predictions

**Table 6** Key variables of industrial-scale HPGR with both modeling approaches, with deviations (%) from experiments in parentheses

Measure	Survey	MTC	Hybrid
Power (MW)	1.17	1.31 (12.3)	1.37 (17.8)
Throughput (t/h)	520	905 (74.1)	509 (2.0)
Spec. energy (kWh/t)	2.24	1.45 (35.5)	2.70 (20.2)
Prod. % <45 $\mu\text{m}$	48.8	42.5 (13.1)	52.0 (6.6)
Prod. BSA ( $\text{cm}^2/\text{g}$ )	890	680 (23.5)	858 (3.6)

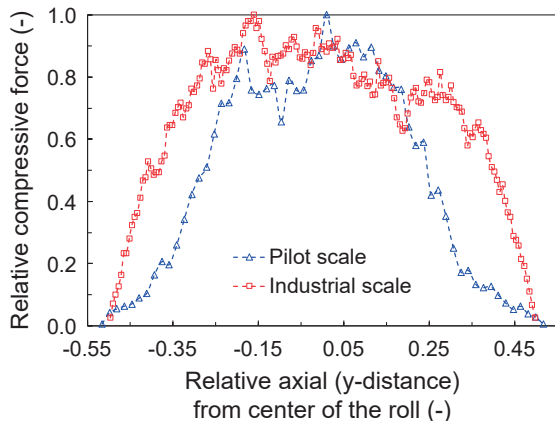


**Fig. 13** Relative compressive force profile along the roll in pilot- and industrial-scale HPGRs obtained from DEM-MBD-PRM simulations. Pilot-scale HPGR operating at 2.5 N/mm<sup>2</sup> and rotating at 0.32 m/s.

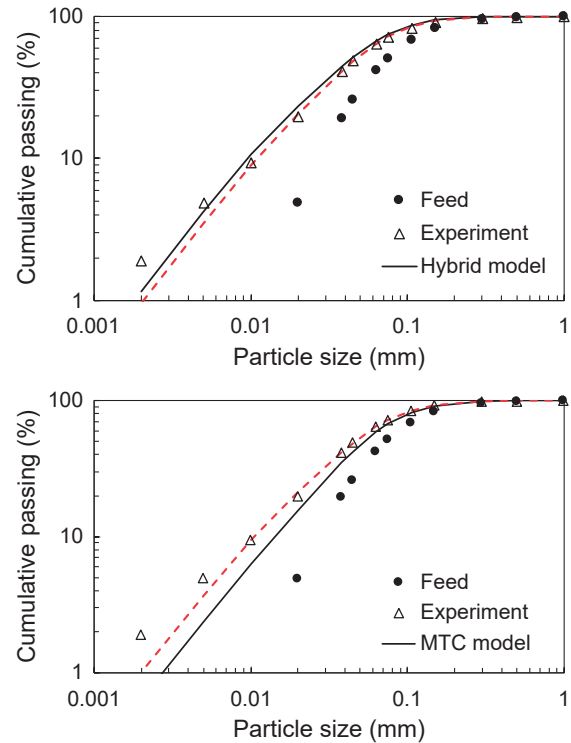


**Fig. 14** Comparison of predicted and experimental product size distribution using the Hybrid (top) and the Modified Torres and Casali models (bottom) of the industrial HPGR operating at 2.5 N/mm<sup>2</sup> and 1.30 m/s. Dashed lines correspond to hypothetical case matching the experimental specific energy in each model.

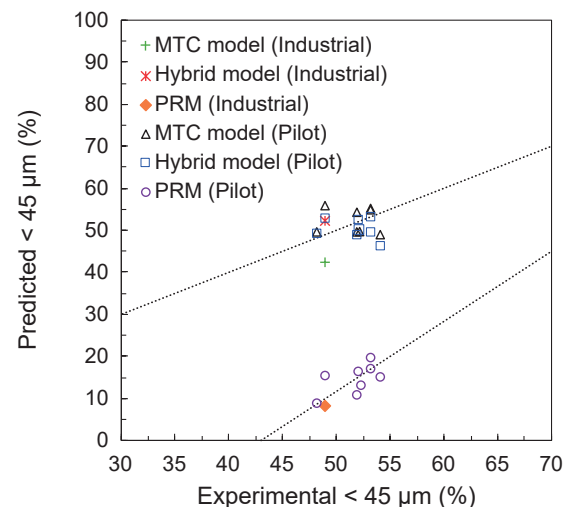


**Fig. 15** Comparison of experimental and predictions of 45  $\mu\text{m}$  of the product size distribution in both pilot and industrial scale, including the PRM.

of percentage passing the 45  $\mu\text{m}$  sieve for all tests are compared to those obtained using the particle replacement model (PRM) in DEM. As demonstrated in the earlier work (Rodriguez et al., 2022a), the PRM was unable to reach quantitative agreement with experiments. However, although biased, its predictions were more aligned with experiments than both Hybrid and the MTC models, thus demonstrating its great future potential.

## 5. Conclusions

In order to deal with the limitations of DEM-MBD-PRM approach in predicting quantitatively the fineness of iron ore pellet feed in the HPGR product, a Hybrid model was proposed. The model used throughput and power, besides mass flowrate and force profiles predicted along the rolls obtained from DEM simulations as input to a population balance model (Modified Torres and Casali model), fitted on the basis of a base case test.

The approach was able to predict the product particle size distributions of a pilot-scale HPGR operating at different roll velocities and pressures in size reduction of iron ore pellet feed, but with predictions that were comparable to those obtained using the Modified Torres and Casali model. Advantages of the Hybrid model in this case would only appear if changes are made to the machine in question, such as replacement of cheek plates by flanges or changes in stud patterns, for instance. In these cases, the Hybrid model would be able to capture their effect, whereas the phenomenological model would not.

The Hybrid model demonstrated to provide superior predictions of throughput, power and product fineness than the phenomenological approach when used to predict the performance of an industrial-scale HPGR when the models were fitted using data from pilot-scale tests. This demonstrates the great potential of the Hybrid model to be used in scale-up and design of HPGRs in the future.

## Acknowledgements

The authors would like to thank Vale S.A. for financial and technical support to the research, as well as permission to publish the work. We also thank the additional financial support by the Brazilian research agencies CNPq (grant number 151862/2022-2 and 313425/2021-3), FAPERJ (grant number E-26/202.574/2019) and CAPES (finance Code 001 and grant number - 88881.188860/2018-01).

## Data Availability Statement

The data analysis file and the data supporting the findings of this study are available in J-STAGE Data (<https://doi.org/10.50931/data.kona.20129942>).

## References

Austin L.G., Trubeljal M.P., von Seebach H.M., Capacity of high-pressure grinding rolls, *Mining, Metallurgy & Explora-*

- tion, 12 (1995) 65–73. DOI: 10.1007/BF03403080
- Austin L.G., Weller K.R., Lim I.L., Phenomenological modelling of the high pressure grinding rolls, in: XVIII International Mineral Processing Congress, Sydney, 1993, pp. 87–96.
- Banini G., Evaluation of scale up effect on high pressure grinding roll (HPGR) implementation at PT Freeport Indonesia, in: SAG Conference, Vancouver, Canada, 2011.
- Barrios G.K.P., Tavares L.M., A preliminary model of high pressure roll grinding using the discrete element method and multi-body dynamics coupling, *International Journal of Mineral Processing*, 156 (2016) 32–42. DOI: 10.1016/j.minpro.2016.06.009
- Campos T.M., Bueno G., Tavares L.M., Modeling comminution of iron ore concentrates in industrial-scale HPGR, *Powder Technology*, 383 (2021a) 244–255. DOI: 10.1016/j.powtec.2020.12.075
- Campos T.M., Bueno G., Böttcher A., Kwade A., Mayerhofer F., Tavares L.M., Relationships between particle breakage characteristics and comminution response of fine iron ore concentrates, *Minerals Engineering*, 164 (2021b) 106818. DOI: 10.1016/j.mineng.2021.106818
- Campos T.M., Bueno G., Barrios G.K.P., Tavares L.M., Pressing iron ore concentrate in a pilot-scale HPGR. Part 2: modeling and simulation, *Minerals Engineering*, 140 (2019a) 105876. DOI: 10.1016/j.mineng.2019.105876
- Campos T.M., Bueno G., Barrios G.K.P., Tavares L.M., Pressing iron ore concentrate in a pilot-scale HPGR. Part 1: experimental results, *Minerals Engineering*, 140 (2019b) 105875. DOI: 10.1016/j.mineng.2019.105875
- Chelgani C.S., Nasiri H., Tohry A., Modeling of particle sizes for industrial HPGR products by a unique explainable AI tool—A “Conscious Lab” development, *Advanced Powder Technology*, 32 (2021) 4141–4148. DOI: 10.1016/J.APT.2021.09.020
- Cleary P.W., Large scale industrial DEM modelling, *Engineering Computations*, 21 (2004) 169–204. DOI: 10.1108/02644400410519730
- Cleary P.W., Sinnott M.D., Axial pressure distribution, flow behaviour and breakage within a HPGR investigation using DEM, *Minerals Engineering*, 163 (2021) 106769. DOI: 10.1016/j.mineng.2020.106769
- Daniel M.J., Morrell S., HPGR model verification and scale-up, *Minerals Engineering*, 17 (2004) 1149–1161. DOI: 10.1016/j.mineng.2004.05.016
- Davaanyam Z., Klein B., Nadolski S., Using piston press tests for determining optimal energy input for an HPGR operation, in: SAG Conference, Vancouver, Canada, 2015, pp. 1–20.
- Dundar H., Benzer H., Aydogan N., Application of population balance model to HPGR crushing, *Minerals Engineering*, 50–51 (2013) 114–120. DOI: 10.1016/j.mineng.2013.07.005
- Edwards W., Pérez-Prim J., Barrios G.K.P., Tavares L.M., Edward D., Santhanam P., A coupling interface for co-simulation of EDEM with multi-body dynamics, in: 6th International Conference on DEM, Colorado, 2013.
- Esnault V.P., Zhou H., Heitzmann D., New population balance model for predicting particle size evolution in compression grinding, *Minerals Engineering*, 73 (2015) 7–15. DOI: 10.1016/j.mineng.2014.12.036
- Faria P.M.C., Rajamani R.K., Tavares L.M., Optimization of solids concentration in iron ore ball milling through modeling and simulation, *Minerals*, 9 (2019) 366. DOI: 10.3390/min9060366
- Fuerstenau D.W., Shukla A., Kapur P.C., Energy consumption and product size distributions in choke-fed, high-compression roll mills, *International Journal of Mineral Processing*, 32

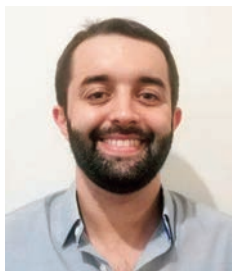
- (1991) 59–79. DOI: 10.1016/0301-7516(91)90019-F
- Hawkins R.A., A Piston and die test to predict laboratory-scale HPGR performance, MPhil Thesis, University of Queensland, 2008. DOI: 10.14264/158721
- Herbst J.A., Fuerstenau D.W., Scale-up procedure for continuous grinding mill design using population balance models, *International Journal of Mineral Processing*, 7 (1980) 1–31. DOI: 10.1016/0301-7516(80)90034-4
- Herbst J.A., Mular M.A., Pate W.T., Qiu X., Detailed modeling of an HPGR/HRC for prediction of plant scale unit performance, in: *International Autogenous Grinding, Semiautogenous Grinding and High Pressure Grinding Rolls Technology Conference*, Vancouver, Canada, 2011, pp. 1–20.
- Herman V., Knorr B., Whalen D., HRC<sup>TM</sup>: taking HPGR efficiency to the next level by reducing edge effect, in: *International Mineral Processing Conference*, Santiago de Chile, 2013, pp. 195–202.
- King R.P., *Modeling and Simulation of Mineral Processing Systems*, Butterworth Heinemann, Elsevier, 2001, ISBN: 978-0-08-051184-9. DOI: 10.1016/C2009-0-26303-3
- Klymowsky I.B., Liu J., *Towards the development of a work index for the roller press*, Society for Mining, Metallurgy and Exploration, Inc., Littleton, CO (United States), 1997.
- Lim I.L., Voigt W., Weller K.R., Product size distribution and energy expenditure in grinding minerals and ores in high pressure rolls, *International Journal of Mineral Processing*, 44–45 (1996) 539–559. DOI: 10.1016/0301-7516(95)00064-X
- Liu J., Schönert K., Modelling of interparticle breakage, *International Journal of Mineral Processing*, 44–45 (1996) 101–115. DOI: 10.1016/0301-7516(95)00022-4
- Lubjuhn U., Schönert K., Material flow in the acceleration zone and throughput of high pressure roller mills, in: *XVIII International Mineral Processing Congress (IMPC)*, Sydney, 1993, pp. 161–168.
- Mindlin R.D., Compliance of elastic bodies in contact, *Journal of Applied Mechanics*, 16 (1949) 259–268. DOI: 10.1115/1.4009973
- Mindlin R.D., Deresiewicz H., Elastic spheres in contact under varying oblique forces, *Journal of Applied Mechanics*, 20 (1953) 327–344. DOI: 10.1115/1.4010702
- Morley C., HPGR-FAQ, *Journal of the Southern African Institute of Mining and Metallurgy*, 110 (2010) 107–115. <http://www.scielo.org.za/pdf/jsaimm/v110n3/03.pdf>
- Morrell S., An alternative energy–size relationship to that proposed by Bond for the design and optimisation of grinding circuits, *International Journal of Mineral Processing*, 74 (2004) 133–141. DOI: 10.1016/j.minpro.2003.10.002
- Morrell S., Predicting the specific energy required for size reduction of relatively coarse feeds in conventional crushers and high pressure grinding rolls, *Minerals Engineering*, 23 (2010) 151–153. DOI: 10.1016/j.mineng.2009.10.003
- Morrell S., Lim W., Shi F., Tondo L., Modelling of the HPGR crusher, in: Kawatra S.K. (Eds.), *Comminution Practices*, Society for Mining Metallurgy, 1977, pp.117–126, ISBN: 978-0873351492.
- Morrell S., Helping to reduce mining industry carbon emissions: a step-by-step guide to sizing and selection of energy efficient high pressure grinding rolls circuits, *Minerals Engineering*, 179 (2022) 107431. DOI: 10.1016/j.mineng.2022.107431
- Nadolski S., Bamber A.S., Klein S., Drozdak J., Investigation into laboratory scale tests for the sizing of high pressure grinding rolls, in: *SAG Conference*, Vancouver, Canada, 2011, pp. 1–18.
- Nagata Y., Tsunazawa Y., Tsukada K., Yaguchi Y., Ebisu Y., Mitsuhashi K., Tokoro C., Effect of the roll stud diameter on the capacity of a high-pressure grinding roll using the discrete element method, *Minerals Engineering*, 154 (2020) 106412. DOI: 10.1016/j.mineng.2020.106412
- Pamparana G., Klein B., A methodology to predict the HPGR operational gap by using piston press tests, *Minerals Engineering*, 166 (2021) 106875. DOI: 10.1016/j.mineng.2021.106875
- Quist J., Evertsson M., Simulating pressure distribution in HPGR using the discrete element method, in: *8th International Comminution Symposium*, 2012, pp. 1–14.
- Rashidi S., Rajamani R.K., Fuerstenau D.W., A review of the modeling of high pressure grinding rolls, *KONA Powder and Particle Journal*, 34 (2017) 125–140. DOI: 10.14356/kona.2017017
- Reid K.J., A solution to the batch grinding equation, *Chemical Engineering Science*, 20 (1965) 953–963. DOI: 10.1016/0009-2509(65)80093-8
- Rodriguez V.A., Barrios G.K.P., Bueno G., Tavares L.M., Investigation of lateral confinement, roller aspect ratio and wear condition on HPGR performance using DEM-MBD-PRM simulations, *Minerals*, 11 (2021) 801. DOI: 10.3390/min11080801
- Rodriguez V.A., Barrios G.K.P., Bueno G., Tavares L.M., Coupled DEM-MBD-PRM simulations of high-pressure grinding rolls. Part 1: calibration and validation in pilot-scale, *Minerals Engineering*, 177 (2022a) 107389. DOI: 10.1016/j.mineng.2021.107389
- Rodriguez V.A., Barrios G.K.P., Tavares L.M., Coupled DEM-MBD-PRM simulations of high-pressure grinding rolls. Part 2: investigation of roll skewing, *Minerals Engineering*, 178 (2022b) 107428. DOI: 10.1016/j.mineng.2022.107428
- Schönert K., A first survey of grinding with high-compression roller mills, *International Journal of Mineral Processing*, 22 (1988) 401–412. DOI: 10.1016/0301-7516(88)90075-0
- Tavares L.M., Rodriguez V.A., Souza M., Padros C.B., Ooi J.Y., An effective sphere-based breakage model for simulation in DEM, *Powder Technology*, 392 (2021) 473–488. DOI: 10.1016/j.powtec.2021.07.031
- Thivierge A., Bouchard J., Desbiens A., Unifying high-pressure grinding rolls models, *Minerals Engineering*, 178 (2022) 107427. DOI: 10.1016/j.mineng.2022.107427
- Tohry A., Yazdani S., Hadavandi E., Mahmudzadeh E., Chelgani S.C., Advanced modeling of HPGR power consumption based on operational parameters by BNN: a “Conscious-Lab” development, *Powder Technology*, 381 (2021) 280–284. DOI: 10.1016/j.powtec.2020.12.018
- Torres M., Casali A., A novel approach for the modelling of high-pressure grinding rolls, *Minerals Engineering*, 22 (2009) 1137–1146. DOI: 10.1016/j.mineng.2009.04.011
- Van der Ende R., Knapp H., Van der Meer F., Reducing edge effect and material bypass using spring-loaded cheek plates in HPGR grinding, in: *SAG Conference 2019*, pp. 1–9.
- Van der Meer F.P., Roller press grinding of pellet feed. Experiences of KHD in the iron ore industry. In: *Proceedings from the AusIMM Conference on Iron Ore Resources and Reserves Estimation*, Perth WA Australia, 1997.
- Van der Meer F.P., Leite I.A., Aspects of HPGR in iron ore pellet feed preparation, in: *6th Brazilian Ore Agglomeration Symposium*, São Paulo, 2018, pp. 102–115. DOI: 10.5151/2594-357X-31516
- Weerasekara N.S., Powell M.S., Cleary P.W., Tavares L.M., Evertsson M., Morrison R.D., Quist J., Carvalho R.M., The contribution of DEM to the science of comminution, *Powder Technology*, 248 (2013) 3–24. DOI: 10.1016/j.powtec.2013.05.032

## Authors' Short Biographies



### Victor Alfonso Rodriguez

Victor Rodriguez received his Materials Engineering degree from Universidad del Valle in Colombia. He then spent four years working as an R&D engineer in a company focused on refining, manufacturing and recycling precious metals. After that, he joined Universidade Federal do Rio de Janeiro (UFRJ), where he was awarded master's and doctorate degrees for research dealing with mechanistic modeling and simulation of ball mills and HPGRs, respectively. Victor is currently a post-doctoral fellow at the Laboratório de Tecnologia Mineral (LTM/COPPE/UFRJ) and his research interests include discrete element methods, mechanistic modeling and material characterization.



### Túlio Moreira Campos

Túlio Campos is a Metallurgical Engineer graduated at UFRJ and is currently pursuing a master's degree in Metallurgical and Materials Engineering at the Alberto Luiz Coimbra Institute for Postgraduate Studies and Engineering Research (COPPE/UFRJ). Túlio is a research assistant at the Laboratório de Tecnologia Mineral (LTM/COPPE/UFRJ) and works with mathematical modelling of comminution, process simulations, particle breakage, grinding circuit optimization, multicomponent operations and digital twin technology. Túlio is interested in developing and applying advanced, practical and robust process models to improve and integrate total process simulation as a tool for innovation in the minerals industry.



### Gabriel Kamilo Pantoja Barrios

Gabriel Barrios is a Chemical Engineer graduated at Universidad del Valle in Colombia, with master's and doctorate degrees from UFRJ in Brazil. He is currently a post-doctoral fellow at the Laboratório de Tecnologia Mineral of the Alberto Luiz Coimbra Institute for Postgraduate Studies and Engineering Research (LTM/COPPE/UFRJ). His research interests include particle characterization, mathematical modelling and simulation of mineral processing equipment, simulation using the discrete element method and geometallurgy. He has experience in experimental work in metallurgical laboratory, mineral processing plant surveying, and computational simulation.



### Gilvandro Bueno

Gilvandro Bueno is a Master Engineer at Vale S.A. He is a Metallurgical Engineer, graduated from the Universidade Federal de Ouro Preto and has a master's degree in Metallurgical and Materials Engineering from UFRJ. Prior to his current engagement he worked at Taboca Mineração S.A., Votorantim Cimentos S.A. and Samarco S.A., with a total of 30 years of industrial experience in mineral, cement and pelletizing processes.



### Luís Marcelo Tavares

Luís Marcelo Tavares is a Professor at UFRJ in Brazil. He received his bachelor's degree in Mining Engineering (honors) and his master's degree from Universidade Federal do Rio Grande do Sul. He was awarded a Ph.D. degree in Extractive Metallurgy at the University of Utah. He has been a member of the faculty of UFRJ since 1998, where he is head and founder of the Laboratório de Tecnologia Mineral and has been Department chairman. His research interests include particle breakage, advanced models of comminution and of degradation during handling, DEM, physical concentration, classification, iron ore processing and development of pozzolanic materials. He is a founding member and currently president of the Global Comminution Collaborative (GCC) and has received several awards from the Brazilian Association of Metallurgy, Materials and Mining (ABM).

# The 54th Symposium on Powder Technology and Special Lecture for the 30th Anniversary of the Establishment of HPTF

The 54th Symposium on Powder Technology organized by Hosokawa Powder Technology Foundation took place at Imperial Hotel Osaka, in Japan on Monday, September 5, 2022. It was held by the planning of Council of Powder Technology, Japan and with the sponsorship of Hosokawa Micron Corporation. Nearly 180 people from the industries and universities attended this symposium. The theme of the symposium this year was “Frontiers of Powders and Powder Processing for SDGs”. There were seven lectures including three special ones given by the 2019 KONA Awardee Prof. Makio Naito, 2020 KONA Awardee Prof. Brij M. Moudgil and 2022 Queen Elizabeth Prize winner Dr. Masato Sagawa. This 54th symposium was scheduled to be held two years ago, but due to the COVID-19 pandemic, this time it was held after three year interval in a hybrid style (on-site and online) for the first time.

At the beginning of the symposium, Mr. Yoshio Hosokawa, the president of the Foundation, gave the opening address mentioning that this symposium was started in 1968, more than 50 years ago and has been continued almost annually since then. The Hosokawa Foundation established 30 years ago took over the role of organizer from Hosokawa Micron Corporation. Prior to the lectures, the KONA Award presentation ceremony was held and the plaques of KONA Award were handed from the president to the 2019 KONA Awardee Professor Makio Naito (Osaka Univ., Japan), the 2020 KONA Awardee Professor Brij M. Moudgil (Univ. of Florida, USA) and one of the 2021 KONA Awardees Professor Shuji Matsusaka (Kyoto Univ., Japan). The other awardee of the KONA Award 2021 Professor Wolfgang Peukert (Friedrich-Alexander-Univ. Erlangen-Nuremberg, Germany) was handed the plaque at ICCCI 2022 last November. The KONA Award has been presented to the researchers who have greatly contributed to the research and development as well as education in the field of Powder and Particle Science and Technology since 1990. It was given originally by Hosokawa Micron Corporation but now is presented to the researchers from all over the world by the Hosokawa Powder Technology Foundation annually.

The contents of the symposium are shown below. In the morning session, Prof. Naito and Prof. Moudgil gave the KONA Award lectures, in which they introduced their research results on various materials, in which the structural control and interfacial design of fine particles and powders have been used to improve their properties and enhance their performance for a wide range of industrial applications. Then, three leading researchers gave thought-provoking lectures on resources circulation, solid-state batteries, and direct methane reforming (DMR) reaction using iron-based catalysts to address the SDGs from the perspective of advanced powder processing and particle bonding technologies, followed by an introduction of latest equipment and technology development with the SDGs in mind from Hosokawa Micron Corporation.

The last lecture was Special Lecture for the 30th Anniversary of the Establishment of HPTF, which was given by Dr. Masato Sagawa, who discovered and globally commercialized the world’s most powerful permanent magnet, Nd-Fe-B Sintered Magnets, in which he explained the history of the discovery and development of neodymium magnets, their characteristics, and applications for such as electric vehicles, robots and wind generators in an easy-to-understand manner.



At the KONA Award presentation ceremony, President Hosokawa (Left) and 2019 KONA Awardee Professor Makio Naito (Osaka Univ., Japan).



At the KONA Award presentation ceremony, President Hosokawa (Left) and 2020 KONA Awardee Professor Brij M. Moudgil (Univ. of Florida, USA) .

**The 54th Symposium on Powder Technology and Special Lecture  
for the 30th Anniversary of the Establishment of HPTF**

**Theme: Frontiers of Powders and Powder Processing for SDGs**

**Date:** Monday, September 5, 2022 **Place:** Imperial Hotel Osaka

**Opening address** Mr. Yoshio Hosokawa (*President of Hosokawa Powder Technology Foundation, Chairman of Hosokawa Micron Corporation*)

- 2019-2021 KONA Award presentation ceremony

**Session 1** Chaired by Prof. Masayoshi Fuji (*Nagoya Institute of Technology, Japan*)

- Lecture 1 (Special lecture by the 2019 KONA Awardee)  
**“Microstructure Control of Particles and Powders for High Quality Advanced Materials”**  
 Prof. Makio Naito (*Osaka University, Japan*)

- Lecture 2 (Special lecture by the 2020 KONA Awardee)  
**“Surface Engineered Particle Systems for Industrial Applications”**  
 Prof. Brij M. Moudgil (*University of Florida, USA*)

**Session 2** Chaired by Associate General Manager, Dr. Yoshio Sakka (*NIMS, Japan*)

- Lecture 3  
**“Resources Circulation Through Advanced Powder Processing”**  
 Prof. Chiharu Tokoro (*Waseda University, The University of Tokyo, Japan*)

- Lecture 4  
**“Powder Joining Technologies for Realizing Solid-State Batteries”**  
 Dr. Kazunori Takada (*National Institute for Materials Science, Japan*)

**Session 3** Chaired by Prof. Shuji Matsusaka (*Kyoto University, Japan*)

- Lecture 5  
**“Efforts for SDGs by Direct Methane Reforming (DMR) Reaction with Iron-Based Catalysts”**  
 Dr. Toshiki Matsui (*Toda Kogyo Corporation, Japan*)

- Lecture 6  
**“Hosokawa Micron’s Equipment and Technology Development Considering SDGs”**  
 Dr. Kenji Murata (*Hosokawa Micron Corporation, Japan*)

**Session 4** Chaired by Honorary Research Advisor, Dr. Hisao Makino (*CRIEPI, Japan*)

**Special Lecture for the 30th Anniversary of the Establishment of HPTF**

- Lecture 7  
**“40 Years of Nd-Fe-B Sintered Magnet Development”**  
 Dr. Masato Sagawa (*Advisor, Daido Steel Co., Ltd., Japan*)

**Closing remarks** Emeritus Prof. Hiroyuki Kage (*Kyushu Institute of Technology, President of Council of Powder Technology, Japan*)



Symposium on Powder Technology.



Special Lecture for the 30th Anniversary of the Establishment of HPTF (Left: presenter, Dr. Sagawa; Right: questioner, Prof. Fuji).

# The KONA Award 2021

The KONA Award has been presented to the researchers who have greatly contributed to the research and development as well as education in the field of Powder and Particle Science and Technology since 1990. It was given originally by Hosokawa Micron Corporation but now is presented to the researchers from all over the world by the Hosokawa Powder Technology Foundation annually. The application for this award requires a specified recommendation form written in English to be submitted to the President of the Hosokawa Powder Technology Foundation. The award candidates are reviewed by the KONA Award Committee members and the results are reported to the Selection Committee of the Foundation for the nomination of the awardee. It needs to be finally approved at the Board of Directors’ meeting of the Foundation. The KONA Award is presented at a ceremony in or outside of Japan with a plaque and a prize of one million yen.

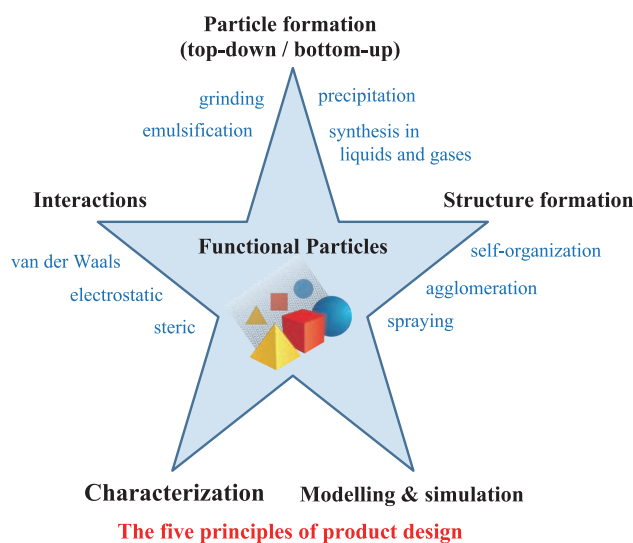
There were three candidates recommended from around the world for The KONA Award 2021, and it has been presented to two researchers this year, namely Professor Wolfgang Peukert of Friedrich-Alexander-University Erlangen-Nuremberg, Germany and Professor Shuji Matsusaka of Kyoto University, Japan. The KONA Award plaque was presented to Prof. Matsusaka at the 54<sup>th</sup> Symposium on Powder Technology on September 5, 2022 and to Prof. Peukert at the 7<sup>th</sup> International Conference on the Characterization and Control of Interfaces for High Quality Advanced Materials (ICCCI 2022) in November 2022.

Prof. Peukert has brought particle technology forward like no other European and probably no other professors at all in the last decade. With his forward-looking approaches to focus research activities on particle interactions, he has given particle technology as an engineering discipline a new direction. From the fundamental and in-depth research of individual processes in mechanical process engineering, which was predominant 20 years ago, his influence has clearly shifted the discipline towards process-structure-property relationships and, thus, towards the design of products made of the finest particles, which are often in the nanometer range. He has published his research results in more than 550 refereed publications with over 11800 citations (according to Scopus as of Oct. 10, 2022), whereby he has achieved an extremely high h-index of 57 for the research subject “process engineering”.

His pioneering concepts have led to the acquisition of the Cluster of Excellence “Engineering of Advanced Materials – Hierarchical Structure Formation for Functional Devices”, which he successfully coordinated for 12 years of funding. He was also awarded the Gottfried Wilhelm Leibniz Prize (1.55 million €) for his scientific achievements. Within the Process-Net association (as part of DECHEMA and VDI/GVC), he has been intensively promoting the subject for many years as chairman of the division “Particle Technology and Product Design”. These outstanding achievements are complemented by many other smaller successes and activities.



At the KONA Award presentation ceremony, President Hosokawa (Left) and 2021 KONA Awardee Prof. Wolfgang Peukert (Friedrich-Alexander-University Erlangen-Nuremberg, Germany).



Selected research achievements for the KONA Award 2021 (Prof. Wolfgang Peukert): Particle based product innovations by understanding and controlling particle interactions.



At the KONA presentation ceremony, President Hosokawa (Left) and 2021 KONA Awardee Prof. Shuji Matsusaka (Kyoto Univ., Japan).

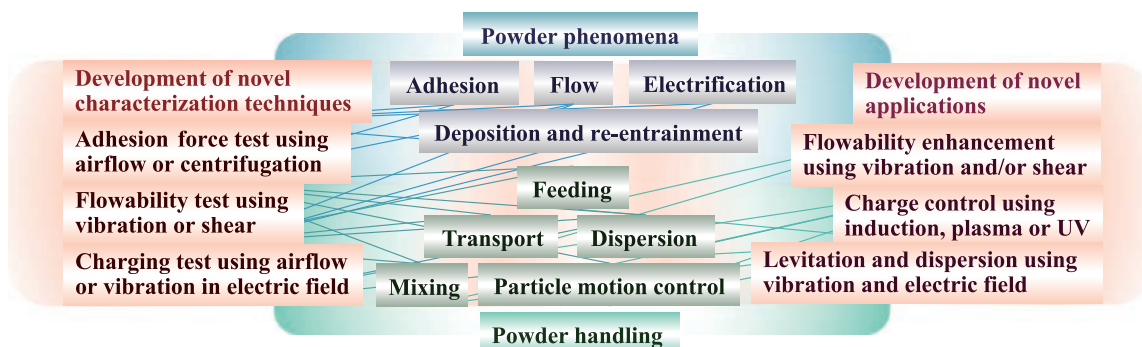
Prof. Shuji Matsusaka has been conducting research at Kyoto University focusing on powder technology, particularly with regards to the advanced characterization of fine particles in gases, for 32 years. This area of study covers a number of fundamentally related topics including electrostatic charging, deposition and re-entrainment, adhesion and agglomeration, and powder flowability and mechanics. He has used the characterization methods to develop novel powder handling systems for feeding, transport, and particle motion control systems. Furthermore, he established the theory and control method of particle charging based on contact potential difference in an external electric field.

He also developed novel methods using atmospheric pressure plasma jets and the photoelectric effect arising from ultraviolet radiation. In addition, he established a dynamic model for particle deposition layers formed in gas-solid pipe flow, considering simultaneous particle deposition and re-entrainment. Applying the airflow method, he developed a system measuring the adhesive strength distribution of fine particles to characterize different adhesion forces including van der Waals forces and electrostatic forces. To analyze and evaluate the flowability of highly cohesive powders, he invented the vibration shear method, which was effective for micro-feeding of nanoparticles and micron-sized particles. Furthermore, he developed the constant-volume shear method and the vibration-induced fluidization method for characterization and applications.

For the above achievements, he was awarded the APT Distinguished Paper Award in 2018, Best Paper Award of the Society of Powder Technology, Japan in 2018, SCEJ Award for Outstanding Research Achievement in 2018, Best Paper Award of the Imaging Society of Japan in 2010, Distinguished Achievement Award of the Information Center of Particle Technology, Japan in 2002, Best Paper Award of the Society of Powder Technology, Japan in 2002, Iinoya Award of the Japan Association of Aerosol Science and Technology in 1995, among other awards.

In recognition of his research achievements, he was appointed as Editor-in-Chief of Advanced Powder Technology. During his tenure, he elevated the journal to a top ranking in the field by increasing the impact factor from 1.6 (2013) to 4.2 (2019). To achieve this objective, he made effective use of the financial support provided by the Japanese government and established overseas editorial boards in Europe and North America. He has been a longstanding proponent of various international programs.

Prof. Matsusaka is an acknowledged world leader in powder technology and has made significant contributions to the formation of a global network of researchers in the field.



Selected research achievements for the KONA Award 2021 (Prof. Shuji Matsusaka): Advanced characterization of fine particles and the development of novel powder handling systems.



## General Information

### History of the Journal

The KONA journal (currently called “KONA Powder and Particle Journal”) was first published in 1983 by the Council of Powder Technology, Japan (CPT), which had been established in 1969 by Hosokawa Micron Corporation as a nonprofit organization to promote powder technology, in order to introduce excellent Japanese papers to the world. From the issue of No.8, the CPT changed its editorial policy to internationalize the KONA journal and to incorporate papers by authors throughout the world. In response to this change, three editorial blocks have been organized in the world: Asian-Oceanian, American and European. The issues from No.1 (1983) to No.12 (1994) of the KONA were published by the CPT and the issues from No.13 (1995) by the Hosokawa Powder Technology Foundation. The policy and system have not changed even after the Hosokawa Foundation has taken over the publication from the CPT. From the issue of No.27 (2009), publication of translated papers has been terminated and only original papers have been published.

### Aims and Scope

KONA publishes review and original research papers in a broad field of powder & particle science and technology, ranging from fundamental principles to practical applications. The papers on critical reviews of existing knowledge in special areas are very welcome.

The submitted papers are published only when they are judged by the Editor to contribute to the progress of powder science and technology, and approved by any of the three Editorial Committees.

The paper submitted to the Editorial Secretariat should not have been previously published.

### Category of Papers

- Invited articles  
Review papers and feature articles invited by the KONA Editorial Committees.
- Contributed papers  
Original review papers and some limited number of original research papers of high quality submitted to the KONA Editorial Committees, and refereed by the reviewers and editors.

### Submission of Papers

You can submit your paper online via **Editorial Manager® for KONA Online Paper Submission and Peer Review System**. For all further information, please go to the journal’s homepage on <https://www.kona.or.jp/jp/journal/info.html>

Publication in KONA is free of charge.

### Publication Schedule

KONA is published annually. The publication date is around January 10<sup>th</sup>.

### Subscription

KONA is distributed free of charge to senior researchers at universities and laboratories as well as to institutions and libraries in the field throughout the world. The publisher is always glad to consider the addition of names of those, who want to obtain this journal regularly, to the mailing list.

### Instructions to Authors

#### (1) Language

All submissions should be written in good English. Authors may choose either British or American English, provided that the chosen style is used consistently. Authors from non-English-speaking countries are encouraged to use a professional English editing service to proofread their manuscript.

#### (2) Data Repository Information

In order to promote open data discoverability and use of research outputs, this journal encourages authors to submit the data files supporting your manuscript work, which can be deposited in the journal’s J-STAGE Data site <<https://jstagedata.jst.go.jp/kona>> after acceptance of the paper through the peer-review process.

These data may describe observations, experiments, modeling or analyses and may take the form of databases, simulations, movies, large figures or as otherwise appropriate.

If you have any questions or would like more information, please contact the KONA Editorial Office (contact\_zainq@hmc.hosokawa.com).

### (3) Manuscript format

- Electric files should be submitted to the Editorial Secretariat by online. Authors’ short biography with less than 100 words per person and color photographs of all the authors should be attached to the final version.
  - The structure of manuscripts should follow the following order; title, authors, affiliations, abstract, graphical abstract, keywords, main text, (acknowledgement), (appendix), (nomenclature), references. The items with parentheses are not mandatory.
  - Full postal addresses must be given for all the authors. Indicate the corresponding author by the asterisk“\*” after the name. Telephone and fax numbers and e-mail address should be provided for the corresponding author.
  - Abstract should not exceed 200 words.
  - Graphical abstract should be a concise, visual summary of the article which will be displayed in the contents list both online and print.
  - The appropriate number of keywords is 5 or 6.
  - The maximum pages printed in KONA are supposed to be: 15 for an original paper and 25 for a review paper.
  - Symbols and units should be listed in alphabetical order with their definition and dimensions in SI units.
  - The color figures will appear in color both on the KONA Website (<http://www.kona.or.jp>) and also in the paper version.
  - Concerning references, the alphabetical system should be adopted. Please use reference management software such as Endnote to manage references as far as possible.
- List:** References should be arranged first alphabetically and then further sorted chronologically if necessary. More than one reference from the same author(s) in the same year must be identified by the letters “a”, “b”, “c”, etc., placed after the year of publication.

Examples:

- Reference to a book:

Strunk Jr. W., White E.B., *The Elements of Style*, fourth ed., Longman, New York, 2000, ISBN: 9780205309023.

- Reference to a chapter in an edited book:

Mettam G.R., Adams L.B., How to prepare an electronic version of your article, in: Jones B.S., Smith R.Z. (Eds.), *Introduction to the Electronic Age*, E-Publishing Inc., New York, 2009, pp.281–304.

- Reference to a journal publication:

Tsuji Y., Tanaka T., Ishida T., Lagrangian numerical simulation of plug flow of cohesionless particles in a horizontal pipe, *Powder Technology*, 71 (1992) 239–250. DOI: 10.1016/0032-5910(92)88030-L

**Text:** All citations in the text should refer to:

1. Single author: the author’s name (without initials, unless there is ambiguity) and the year of publication;
2. Two authors: both authors’ names and the year of publication;
3. Three or more authors: first author’s name followed by “et al.” and the year of publication.

Citations may be made directly (or parenthetically). Groups of references should be listed first alphabetically, then chronologically.

Examples:

“as demonstrated (Hidaka J. et al., 1995; Tsuji Y., 1992a, 1992b, 1993). Mori Y. and Fukumoto Y. (2002) have recently shown ...”

### (4) Copyright and permission

- The original paper to be submitted to KONA has not been published before in any language or in any journals or media; it is not submitted and not under consideration for publication in whole or in part elsewhere.
- Authors are responsible for obtaining permission from the copyright holders to reproduce any figures, tables and photos for which copyright exists.
- The KONA Journal applies the Creative Commons Attribution License to all works published by the Journal. Copyright stays with the agreed copyright owner, and the Hosokawa Powder Technology Foundation is granted the exclusive right to publish and distribute the work, and to provide the work in all forms and media.
- Users of the journal will be able to reuse the contents in any way they like, provided they are accurately attributed. No permission is required from either the authors or the publisher.



# HOSOKAWA ALPINE

Process technologies for tomorrow.

**YOUR PROCESS.  
YOUR FLEXIBILITY.  
YOUR PICOLINE.**

*Particle processing  
for smallest lab batches.*



*More than 100 research institutes and R&D departments  
in the world trust in the Picoline.*

- System for fine grinding, classifying or mixing powders or suspensions
- Containment systems available
- 10 function modules allow 12 different process setups by using various mill types and mixers
- Combine one platform with various function modules and accessories for dry or wet processing

Get detailed  
information here:



[www.hosokawa-alpine.com](http://www.hosokawa-alpine.com)

## » MIXING, DRYING & AGGLOMERATION TECHNOLOGIES



Hosokawa Micron B.V. is a global supplier of process equipment and complete systems for the mechanical and thermal processing of dry and wet powders. The company specializes in the design and manufacture of mixing, drying and agglomeration technologies.

In the Netherlands, Hosokawa Micron B.V. maintains extensive facilities for R&D, testing, manufacturing, toll processing and after sales services.



# HOSOKAWA MICRON B.V.

Gildenstraat 26  
7005 BL Doetinchem  
NETHERLANDS

[www.hosokawa-micron-bv.com](http://www.hosokawa-micron-bv.com)



# HOSOKAWA MICRON POWDER SYSTEMS

## Analytical Innovation in Particle Size Analysis Mikro Air Jet Sieve<sup>®</sup> MAJSx<sup>2</sup>

- CFR 21 Part 11 registration audit trail
- 12 language options
- Compatible with multiple balances & printers
- Comparative 'overlay' of analysis results
- Vacuum pressure displayed in multiple formats
- Slit wand boost rotation speed for difficult materials



**CONTACT US TODAY**

[www.hmicronpowder.com](http://www.hmicronpowder.com) • (908) 273-6360 • [help@hmps.hosokawa.com](mailto:help@hmps.hosokawa.com)



**HOSOKAWA MICRON LTD**

### Containment Solutions for Powders, Particles, Liquids and Vapours

Hosokawa Micron Ltd offers a portfolio of standard and bespoke containment equipment perfect for laboratories, pilot-scale processing and R&D, including gloveboxes, isolators, fume cupboards and downflow booths.

Each product is engineered and manufactured to meet the highest international safety standards and provide operator protection when handling and processing potentially hazardous, toxic and sensitizing materials while also maintaining material integrity as well as protecting the process and environment.

Our ranges of high-performance containment equipment can be designed and manufactured for standalone use or to complement Hosokawa Micron Group's extensive range of processing and analysis equipment for applications such as milling, classifying, mixing and blending, particle design and drying.

[hosokawa.co.uk](http://hosokawa.co.uk)

Hosokawa Micron Ltd, Whitehouse Industrial Estate,  
Rivington Road, Runcorn, Cheshire, WA7 3DS, UK

**+44 (0)1928 755100**

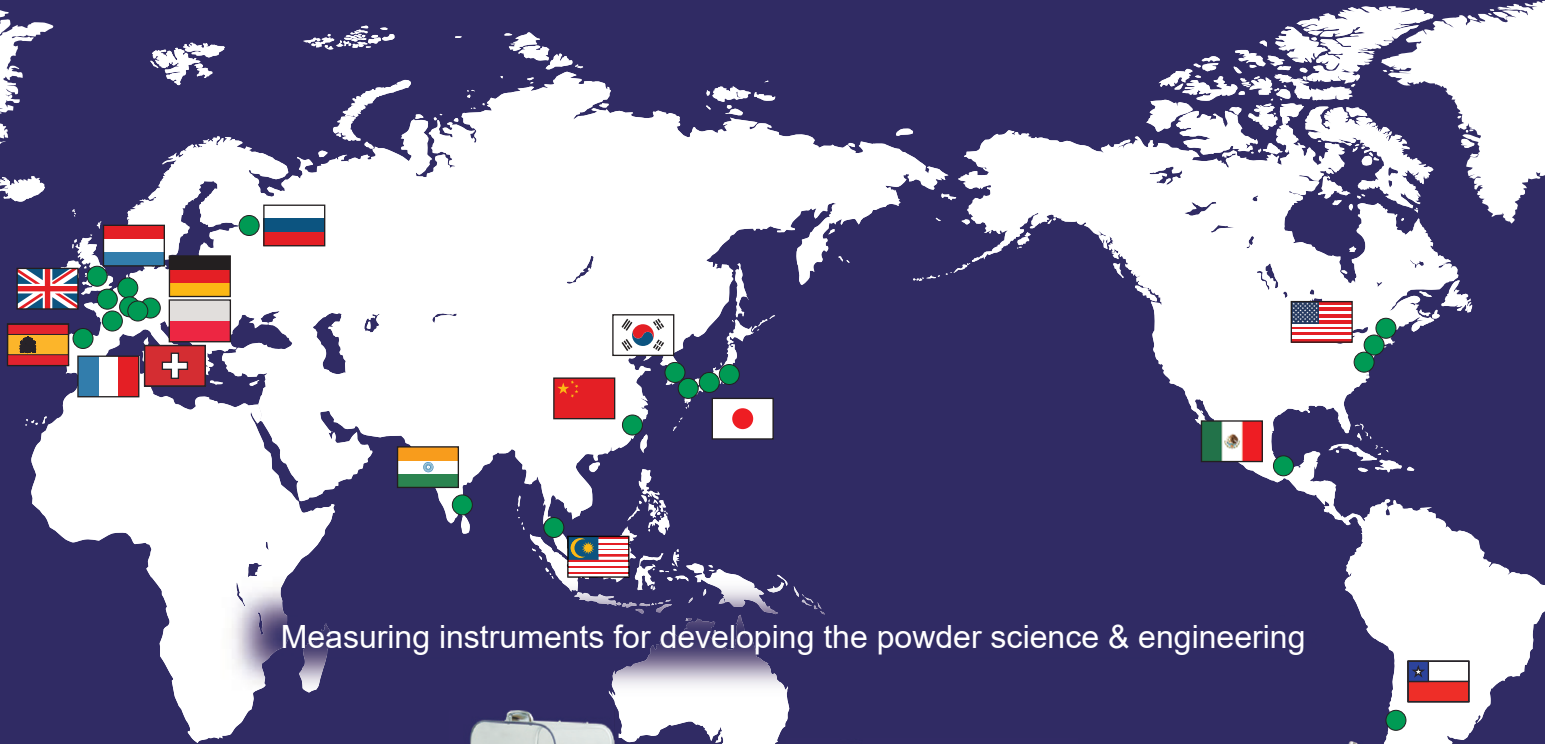


At the Forefront of Powder Processing Technologies



# HOSOKAWA MICRON GROUP

The Hosokawa Micron Group will always be the leading global company covering the mountain range of Powder Technologies. The Group has been a pioneer in the field of powder and particle processing and blown film processing. We provide R&D, engineering, manufacturing and services in various fields of the world's major industrial markets.



Measuring instruments for developing the powder science & engineering



Dynamic Particle Image Analyzer  
Parshe Analyzer



Penetration speed  
Peneto Analyzer, PNT-N



Carr's indices  
Powder characteristics tester, PT-X



Wet sieving  
Viblette, VBL-F



Process Technologies for Tomorrow

## HOSOKAWA MICRON CORPORATION

Headquarters Location :

**HOSOKAWA MICRON CORPORATION**

URL : [www.hosokawamicron.com](http://www.hosokawamicron.com)